DOE-ER-0313/58
Distribution
Categories
UC-423, -424

FUSION MATERIALS
SEMIANNUAL PROGRESS REPORT
FOR THE PERIOD ENDING

June 30, 2015

Prepared for
DOE Office of Fusion Energy Sciences
(AT 60 20 10 0)

DATE PUBLISHED: September 2015

Prepared by
OAK RIDGE NATIONAL LABORATORY
Oak Ridge, Tennessee 37831
Managed by
UT-Battelle, LLC
For the
U.S. DEPARTMENT OF ENERGY

FOREWORD

This is the fifty-eight in a series of semiannual technical progress reports on fusion materials science activity supported by the Fusion Energy Sciences Program of the U.S. Department of Energy. It covers the period ending June 30, 2015. This report focuses on research addressing the effects on materials properties and performance of exposure to the neutronic, thermal and chemical environments anticipated in the chambers of fusion experiments and energy systems. This research is a major element of the national effort to establish the materials knowledge base for an economically and environmentally attractive fusion energy source. Research activities on issues related to the interaction of materials with plasmas are reported separately.

The results reported are the products of a national effort involving a number of national laboratories and universities. A large fraction of this work, particularly in relation to fission reactor irradiations, is carried out collaboratively with partners in Japan, Russia, and the European Union. The purpose of this series of reports is to provide a working technical record for the use of program participants, and to provide a means of communicating the efforts of fusion materials scientists to the broader fusion community, both nationally and worldwide.

This report has been compiled under the guidance of F. W. (Bill) Wiffen and Susan Noe, Oak Ridge National Laboratory. Their efforts, and the efforts of the many persons who made technical contributions, are gratefully acknowledged.

Gene Nardella
Research Division
Office of Fusion Energy Sciences

TABLE OF CONTENTS

TABLE OF CONTENTS

TABLE OF CONTENTS

TABLE OF CONTENTS

TABLE OF CONTENTS

TABLE OF CONTENTS

TABLE OF CONTENTS

TABLE OF CONTENTS

TABLE OF CONTENTS

TABLE OF CONTENTS

TABLE OF CONTENTS

TABLE OF CONTENTS

TABLE OF CONTENTS

TABLE OF CONTENTS

1.1 DEVELOPMENT OF ADVANCED REDUCED ACTIVATION FERRITIC/MARTENSITIC STEELS —

L. Tan (Oak Ridge National Laboratory)

OBJECTIVE

Traditional reduced activation ferritic/martensitic (RAFM) steels suffer noticeable strength reduction at temperatures above 500°C, which limits their high temperature applications for DEMO and beyond DEMO fusion reactors. This project is to develop cast nanostructured alloys (CNAs) that are manufacturable and affordable advanced RAFM steels having optimized alloy composition and thermomechanical treatment (TMT) to produce a high density of stable nanoprecipitates to retain superior high temperature performance.

SUMMARY

New heats of CNAs have been fabricated, which showed superior yield and tensile strength at test temperatures up to 750°C. The superior strength is explained by their refined microstructure with significantly increased amount of MX-type nanoprecipitates. Charpy impact toughness of the CNAs was assessed in this work, which showed excellent upper shelf energies that are more than double that of Grade 91 steel and about 8–10 times that of oxide dispersion strengthened (ODS) steels. The ductile-brittle transition temperature (DBTT) of the CNAs is comparable or lower than Grade 91 steel. Characterization of the high-dose Fe^{2+} ion-irradiated samples containing VN nanoprecipitates exhibited evolution with irradiation depth, that is, with increasing irradiation dose. The growth of VN particles was found to be dependent on the irradiation direction.

PROGRESS AND STATUS

Introduction

Two heats of CNAs were fabricated using arc melting followed by drop casting into 1" × 1" × 6" bars. The bars were hot-rolled into 0.3"-thick plates. The plates were subjected to standard heat treatments using normalization at ~1100°C/0.5 h followed by tempering at 750°C/0.5 h and air-cooling. Samples of the heats have shown excellent yield and tensile strength at testing temperatures up to 750°C as compared to F82H and Eurofer97. The effect of increased number density of MX in CNA on helium management is being conducted by one of colleagues using ion irradiation. This report describes the Charpy impact toughness of the CNAs. Additionally, the characterization of high-dose Fe^{2+} ion-irradiated samples bearing TaC, TaN and VN nanoprecipitates, respectively, has been continued using TEM, with new findings briefly reported here.

Experimental Procedure

Charpy impact tests were conducted on a Tinius Olsen Charpy 300 ft-lb machine according to the ASTM Standard E23-12c, "Standard test methods for notched bar impact testing of metallic materials." Sub-size V-notch (1 mm deep) Charpy specimens with a dimension of 5 × 5 × 25 mm were extracted from the plates along the T-L orientation.

A FEI CM200 field-emission-gun transmission electron microscope (TEM) equipped with an EDAX energy dispersive X-ray spectroscopy (EDS) detector was primarily used to characterize the Fe^{2+}-irradiated samples. TEM specimens, perpendicular to the surfaces (i.e., parallel to the ion irradiation direction), were lifted out and thinned to electron-transparent using focused ion beam (FIB) on a Hitachi NB5000. Specimen thickness of the characterized regions was estimated using convergent beam electron diffraction (CBED) technique.

Results

The Charpy impact resistance of the specimens in the transition region was tested at temperatures from –100°C to above room temperature. Oxide-dispersion strengthened (ODS) ferritic steel 14YWT was also tested using the same type of specimens, which yielded Charpy impact toughness comparable to other 12-14Cr ODS ferritic steels. The measured absorbed Charpy energy of each specimen of CNAs was normalized to that of ODS ferritic steel 14YWT and plotted as a function of testing temperature as shown in Figure 1. Literature data of Grade 91 steel are included for comparison [1]. The Charpy data are fitted with a function of $y = \frac{a_1+a_0}{2} + \frac{a_1-a_0}{2} tanh\left(\frac{T-T_0}{k}\right)$, where T is testing temperature, a_1, a_0, T_0, and k are fitting parameters for upper shelf energy, lower bound energy, transition temperature and slope of the fitting curve changing from upper shelf to lower bound, respectively. The results indicate that CNAs have noticeably increased upper shelf energies about 8 to 12 times of ODS ferritic steels, which are also more than double of Grade 91 steel. The ductile-brittle transition temperature (DBTT) of the CNAs is comparable or lower than that of Grade 91 steel. As compared to conventional RAFM and FM steels, the CNAs were found to have refined microstructure with significantly increased amount of MX-type precipitates, which may have benefited the improved Charpy impact toughness.

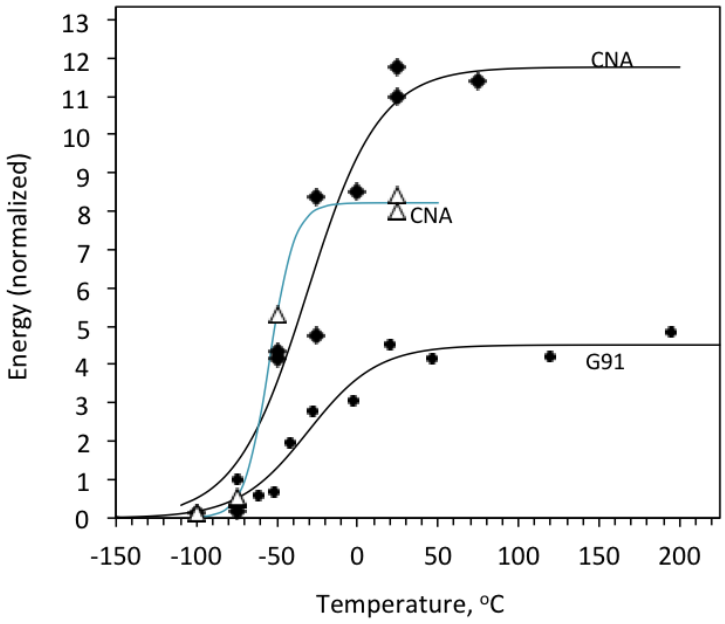

Figure 1. Normalized Charpy absorbed energy (referring to ODS ferritic steels) of CNAs and Grade 91 steels.

The stability of VN nanoprecipitates in a ferritic steel under Fe^{2+} ion irradiation at 500°C for up to ~50 dpa and ~246 dpa was characterized using TEM in both bright-field and dark-field modes. Analysis of the nanoprecipitates exhibited evolution with irradiation depth, namely irradiation dose. The low-dose irradiation results have been reported in Ref. [2,3]. The high-dose irradiation results will be reported in a Journal article. An interesting observation during comparison of the results is that the growth of the nanoprecipitates is dependent upon the irradiation direction. Figure 2 shows an example of the nanoprecipitate in two orientations referring to the irradiation direction. The particle length of the two VN nanoprecipitates in Figure 2 (left) aligns the irradiation direction. The irradiation (~20 dpa) slightly elongated the particle length but did not alter the lattice fringes of the particles. In contrast, the particle length of the VN nanoprecipitate in Figure 2(right) is perpendicular to the irradiation direction. The irradiation (~150 dpa) significantly altered the lattice fringes and increased the thickness of the particle.

Additional FIB-TEM specimens from the high-dose irradiated sample with VN-particle orientation aligning the irradiation direction are being characterized to confirm the phenomenon. Neutron-irradiated VN samples will be characterized to elucidate potential difference from ion irradiation results.

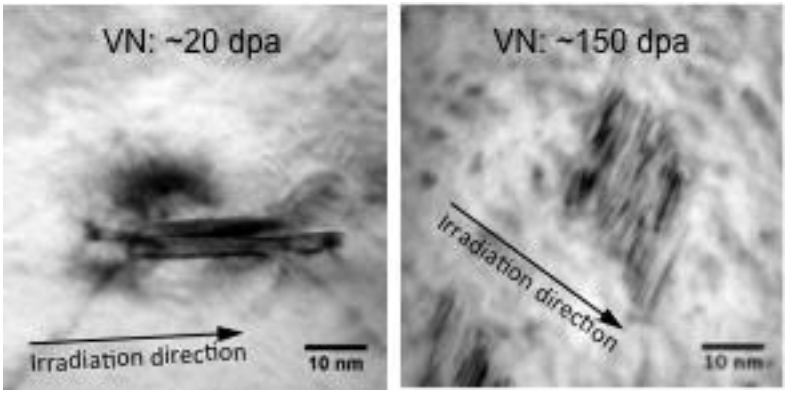

Figure 2. Effect of ion-irradiation direction on the growth of VN nanoprecipitates at 500°C.

References

[1] W.R. Corwin, A.M. Hougland, Effect of specimen size and material condition on the Charpy impact properties of 9Cr-1Mo-V-Nb steel, in: W.R. Corwin, G.E. Lucas (Eds.), The Use of Small-Scale Specimens for Testing Irradiated Material, ASTM STP 888, American Society for Testing and Materials, Philadelphia, 1986, pp. 325-338.

[2] L. Tan, Y. Kotah, L.L. Snead, Stability of the strengthening nanoprecipitates in reduced activation ferritic steels under Fe^{2+} ion irradiation, Journal of Nuclear Materials 445 (2014) 104-110.

[3] L. Tan, T.S. Byun, Y. Katoh, L.L. Snead, Stability of MX-type strengthening nanoprecipitates in ferritic steels under thermal aging, stress and ion irradiation, Acta Materialia 71 (2014) 11-19.

1.2 NEW BAINITIC STEEL FOR FUSION STRUCTURAL APPLICATIONS — Y. Yamamoto (Oak Ridge National Laboratory)

OBJECTIVE

This work aims to develop new bainitic steel, based on 3Cr-3WV(Ta) steels originally developed at ORNL, with mechanical properties of both base metal and weldments superior to those of existing commercial bainitic steels or ferritic-martensitic (F-M) steels. The target applications are high temperature structural components in fusion reactors such as vacuum vessel, structural ring which supports the blanket modules, and magnet shields, to be used at or above 400-500ºC range. Improvement of long-term creep properties by introducing additional fine, stable second-phase dispersions, as well as maintaining a good weldability, is targeted via optimization of alloy composition and thermo-mechanical heat treatment.

SUMMARY

Four heats of 3Cr-3WV base bainitic steels were delivered to ORNL. Minor alloying additions of Mn, Si, and N did not affect the as-normalized and tempered microstructure, viewed in an optical microscope, but increased the micro-Vickers hardness. The bainitic transformation kinetics during continuous cooling were measured using a Gleeble™ thermal mechanical simulator, which indicated that the transformation temperature was significantly lowered by the minor alloying additions. This indicates a wider window for the carbide-free acicular bainite ferrite formation in the modified steels compared to the base steels, which would play an important role in improving the creep properties. Creep-rupture property evaluation of these heats was initiated, and the tests of two base steels were completed.

PROGRESS AND STATUS

Introduction

With the alloy design strategy of improving creep performance, two new bainitic steels based on 3Cr-3WV and 3Cr-3WVTa [1,2] with minor alloying additions of Mn, Si, and N were proposed with guidance from computational thermodynamics. The calculation predicted that the minor alloying additions result in formation of stable MN (M: mainly V) in a wide temperature range below ~1100ºC and increase the stability of $M_{23}C_6$ (M: mainly Cr) relative to M_7C_3 (M: mainly Cr). Since both MN and $M_{23}C_6$ are the key strengthening phases of the bainitic steels at elevated temperatures, the proposed alloys would have a potential of improved creep properties compared to the base steels. The calculated continuous-cooling-transformation (CCT) diagram predicted wider austenite stable regions (retarding the transformation to ferrite or pearlite) with lower the bainitic transformation start temperature compared the base steels, indicating that the stable “carbide-free acicular bainite ferrite formation” would be expected which plays an important role to improve the creep properties of the bainitic steels. In this report, the experimental efforts to verify the calculated predictions have been presented.

Experimental Procedure

The 55 kg forged plates of two base bainitic steels and two modified steels have been prepared by Carpenter Technology Corporation. Table 1 summarizes the target and analyzed compositions of the steels in the present study. The heats with nominal 88 kg were vacuum induction melted and cast into a mold with a size of 10 cm x 10 cm x 20 cm (+ hot-top). The ingots were homogenized and forged at 1100ºC to make plates with a size of 25 mm thickness x 15 cm width x ~40 cm length, followed by normalized at 1100°C. A part of each plate was sectioned, and applied tempering at 700ºC for 1h, followed by air cooling.

Microstructure of the as-normalized and tempered materials was characterized by using light optical microscopes, and the same metallographic specimens were used for micro-Vickers hardness analysis with 1kg load. Dilatometry analysis was conducted by using Gleeble™ thermal mechanical simulator. The round bar shape specimens were heated in a backfilled Ar gas atmosphere up to 1100ºC, held for 5min, and then cooled to room temperature with cooling rates at 10 and 1ºC/s. The specimen diameter was

measured by using an extensometer with a ceramic tip during heating and cooling process. Tensile creep-rupture test was conducted at 600ºC and 250MPa in a laboratory air by using dog-bone shape sheet specimens with a size of 0.7 x 3.2 x 12.7 mm at gage portion.

Table 1. Target and analyzed compositions of the steels in the present study.

Heat	Status	Composition, wt%								Remarks
		C	Mn	Si	Cr	N	V	W	Ta	
2750	Target	0.10	0.40	0.16	3.00	-	0.20	3.00	-	3Cr-3WV
	Analyzed	0.10	0.40	0.15	2.95	0.00	0.20	3.01	<0.01	
2751	Target	0.10	0.40	0.16	3.00	-	0.20	3.00	0.10	3Cr-3WVTa
	Analyzed	0.10	0.40	0.14	2.95	0.00	0.20	3.03	0.10	
2752	Target	0.10	1.00	0.50	3.00	0.05*	0.20	3.00	-	3Cr-3WV + MSN
	Analyzed	0.10	0.98	0.49	2.98	0.017	0.20	3.02	<0.01	
2753	Target	0.10	1.00	0.50	3.00	0.05*	0.20	3.00	0.10	3Cr-3WVTa + MSN
	Analyzed	0.11	1.00	0.48	2.95	0.014	0.20	3.03	0.09	

* Assumed that the nitrogen yield would ~30% after melting

Results

Cross-sectional microstructure of both as-normalized and tempered samples exhibited 100% bainitic microstructure for all four steels, with no indication of the delta-ferrite or the retained austenite in the matrix from the optical micrographs. Figure 1 shows typical microstructures of as-normalized and tempered bainitic steels obtained from heat #2753 (the modified 3Cr-3WVTa steel). No significant difference in the OM microstructure was observed among the four different heats.

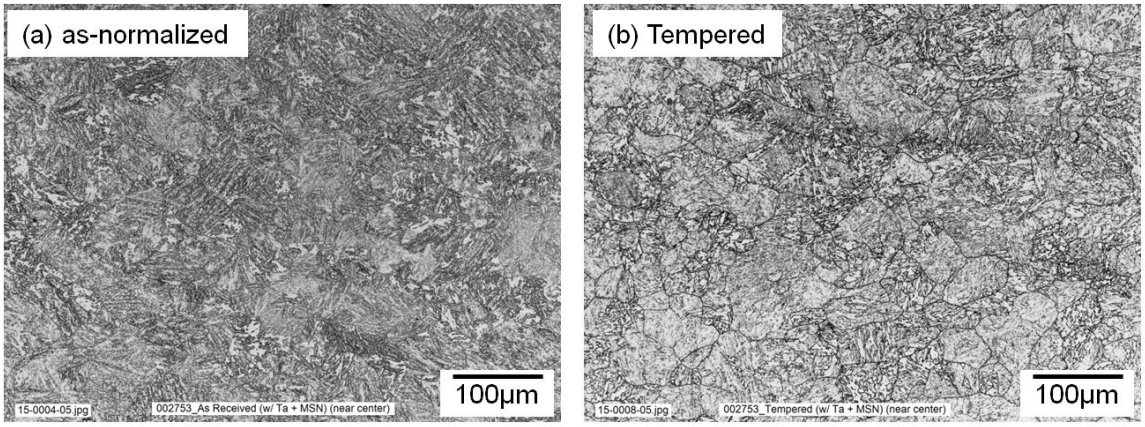

Figure 1. Optical micrographs of the heat #2753; (a) as-normalized, and (b) tempered.

Micro-Vickers hardness measurements of the four different heats at as-normalized and tempered conditions were completed, as summarized in Figure 2. The base steels (heats #2750 and #2751) at as-normalized condition showed ~340-350HV with almost no difference between with and without Ta addition, although #2751 exhibited significantly higher hardness than #2750 after tempering (280HV and 220HV, respectively). This result is consistent with the alloy design strategy that the Ta addition promotes the formation of strengthening carbides (TaC) [1,2] which appear not at as-normalized state but after tempering. The hardness increased to ~370HV by the additions of Mn, Si, and N (#2752 and #2753) at as-normalized conditions, but no significant improvement in the hardness at the tempered conditions compared to the Ta addition in #2751. This result indicates that the minor alloying additions potentially

have an impact on transformation kinetics lowering the bainite transformation temperature which promotes the formation of carbide-free acicular bainite ferrite to strengthen the materials, rather than the formation of strengthening carbides or carbonitrides.

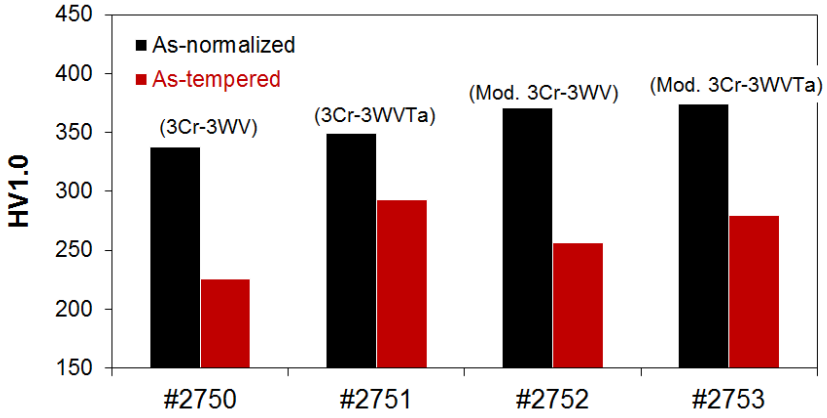

Figure 2. Micro Vickers hardness test results (load: 1kg) of the four different heats.

Dilatometer analysis of the heats confirmed that the minor alloying additions successfully lowered the bainite transformation temperatures. Figure 3 showed the bainitic transformation percentage during continuous cooling calculated from the obtained dilatometry curves, plotted as a function of temperature. The base steels (heats #2750 and #2751) showed relatively rapid transformation kinetics since the bainitic transformation was mostly completed within very narrow temperature range from 520 to 480ºC during cooling at 10ºC/s. The additions of Ta seemed not to impact the transformation kinetics. On the other hand, the modified steels (#2752 and #2753) started the bainitic transformation a little higher temperature than the base steels, but the transformation kinetics was significantly slow and the 90% bainitic transformation occurred around 65-70°C lower than that of the base metals. Similar result was obtained in the case of the cooling rate at 1ºC/s. These results indicate that the transformed bainite ferrite would contain larger amounts of supersaturated carbon and nitrogen than the base steels because the transformation temperature is low enough to expect limited transportation of such elements in the matrix. This would result in wider window of the carbide-free acicular bainite ferrite formation in the modified steels compared to the base steels. Detailed microstructure characterization is required to verify the mechanism, and is currently in progress.

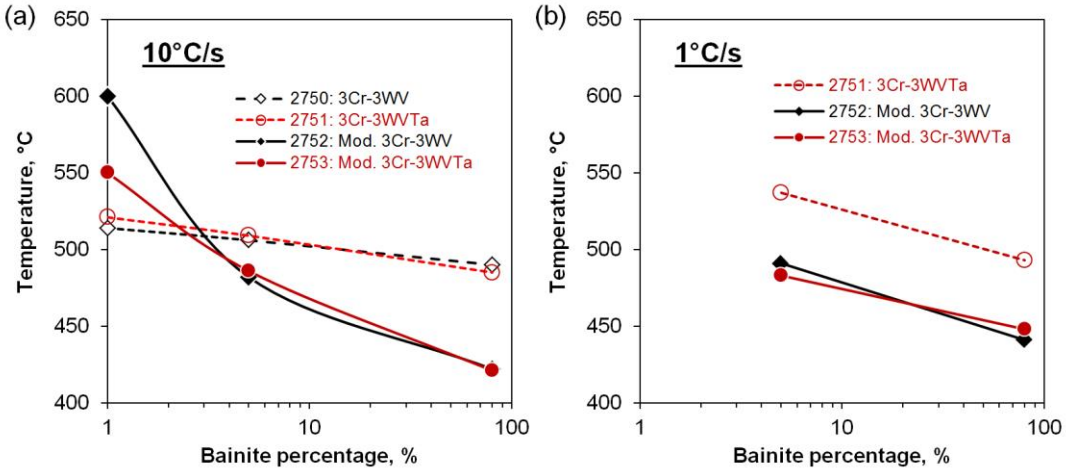

Figure 3. Bainitic transformation temperatures of four different bainitic steels plotted as a function of the transformation percentage; (a) cooled at 10ºC/s and (b) at 1ºC/s.

Creep-rupture test of the bainitic steels was initiated. The creep-rupture life of the base steels (heats #2750 and #2751) tested at 600ºC and 250MPa are shown in Figure 4. The rupture life of Grade 92 (9Cr-2W base) F-M steel reported in NIMS Creep Data Sheet is also shown for comparison. The results indicate the advantage of the base steels to the existing F-M steel at the test condition, which is consistent with the report by Klueh et al [1,2]. The tests of the modified steels (#2752 and #2753) are currently in progress.

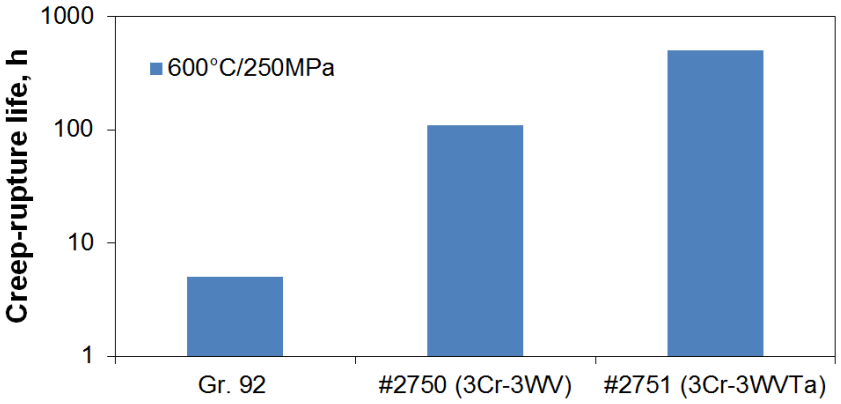

Figure 4. Creep-rupture life of the heats #2750 and #2751 tested at 600ºC and 250MPa compared with that of Grade 92 (reported in NIMS Creep Data Sheet, http://smds.nims.go.jp/creep/index_en.html).

References

[1] R.L. Klueh, Elevated-Temperature Ferritic and Martensitic Steels and Their Application to Future Nuclear Reactors, ORNL/TM-2004/176, November 2004.

[2] R.L. Klueh, N.D. Evans, P.J. Maziasz, V.K. Sikka, Creep-rupture behavior of 3Cr-3W-V bainitic steels, International Journal of Pressure Vessels and Piping, 84 (2007) 29-36.

1.3 MICROSTRUCTURAL CHARACTERIZATION OF A Fe+ IRRADIATED Fe-6%Cr ALLOY — Y. Wu, P. Wells, G. R. Odette, T. Yamamoto (University of California Santa Barbara), S. Roberts and C. Hardie (University of Oxford), D. Bhattacharyya *(*Australian Nuclear Science and Technology Organization)*,* M. Bachhav and E. A. Marquis (University of Michigan)

OBJECTIVES

The objective of this work is to carry out correlative atom probe tomography (APT) and transmission electron microscopy (TEM) studies on the effects of Fe-ion and neutron irradiation on microstructural evolution in a simple binary Fe-6Cr alloy.

SUMMARY

Both ion-beam and neutron irradiations of candidate structural alloys produce large populations of interstitial dislocation loops that lead to hardening and other effects on mechanical properties. Here we report on the number density, size distribution and character of the loops produced by high energy Fe-ions in a Fe-6Cr binary alloy; and we further compare these results to the corresponding microstructures produced by neutron irradiation. While the two types of irradiations produce qualitatively similar features, there are possibly some notable differences. In particular, it appears that only Si segregates to the loops in the Fe-ion irradiations, while both Si and Cr are associated with the loops in the case of neutron irradiations.

BACKGROUND

Simple Fe-Cr simple binary “model” alloy variants of the complex tempered martensitic and ODS structural alloys that are leading candidates for use in future fission and fusion reactors have been extensively studied [1-4]. At less than 9%Cr, the primary effect of both ion and neutron irradiations at ≈ 300°C is to produce a large population of segregated dislocation loops, often along with impurity atom segregation and solute clustering. For example, Bachhav et al. found two kinds of dislocation loops in APT studies of a Fe-6%Cr alloy neutron irradiated to ≈ 1.8 dpa at ≈ 290°C [1]: small loops with Si and Cr segregated along the dislocation lines and larger loops with Cr segregated along the dislocation lines and Si inside the loops. Here we report on both APT and TEM studies on the same alloy Fe-ion irradiated to ≈ 1.7 dpa at ≈ 290°C.

PROGRESS AND STATUS

Experimental Procedure

The Fe-6 wt.%Cr alloy was heat treated under an argon atmosphere at 950°C for 15 minutes followed by air cooling and then annealed at 750°C followed by air cooling. Irradiation was conducted at the Ion Beam Center in the Rossendorf Institute in Dresden, Germany (Hardies and Roberts). The implantation was designed with multiple ion charges, energies and beam currents to maintain an approximately constant level of dpa damage and dose rate with depth into the sample. The implantation temperature was measured and controlled at a nominal 290°C by thermocouples mechanically clamped to the base plate. The Fe-ion beam produced an average dose of 1.7 dpa in ≈ 2 μm deep layer.

The surface of the Fe+-irradiated samples were prepared by polishing for scanning electron microscopy (SEM) and electron back–scattered diffraction (EBSD) observations. Atom probe tomography (APT) specimens were fabricated by focused ion beam (FIB) micromachining with a FEI Helios tool using standard lift-out procedures. The technique for preparing TEM specimen can be found in Ref. [5].

The APT specimens were run at 55K in voltage mode with a pulse fraction of 20% and a pulse repetition rate of 200 kHz, with an ion detection rate of 0.003-0.005/pulse. Data were reconstructed and analyzed using the Cameca Visualization and Analysis Software (IVAS 3.6.6). The average evaporation field (33V/nm), and the detector efficiency (0.36) were used in the reconstruction of the analysis. The APT

atom maps contain a number of solute segregated dislocation loops. The loops were also characterized using weak-beam transmission electron microscopy (TEM) [6].

Results and Discussion

The measured APT compositions of the Fe+ irradiated Fe-6%Cr alloy for three different runs are in good agreement with the nominal Cr content (≈ 6 at.%). Various trace impurities were also observed, most notably ≈ 0.04 at.% Si.

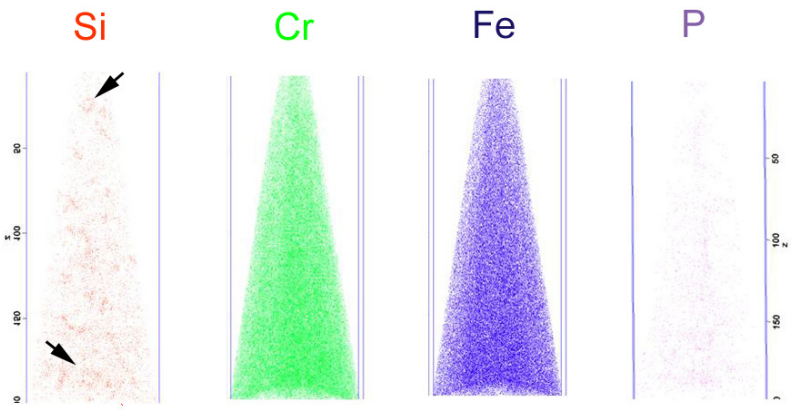

Figure 1. APT element maps, showing the distribution of Si, Cr, Fe and P, respectively.

Visual inspection of the atom maps in Figure 1 show that Si is segregated at the loops, but Cr is not. Note there are some indications of Cr clustering, but may be an artifact, since these atoms are concentrated along low index crystallographic zone lines and towards poles, and are not clearly associated with loops. Likewise, identification of apparent P clusters that emerge in low iso-concentration threshold images are not considered to be fully reliably identified features, although some segregation of this element to loops is observed, along with impurity C. These Fe-ion irradiation results differ from those for the same Fe-6%Cr alloy neutron irradiated to 1.8 dpa at 290°C, where both Si and Cr segregate to dislocation loops [1].

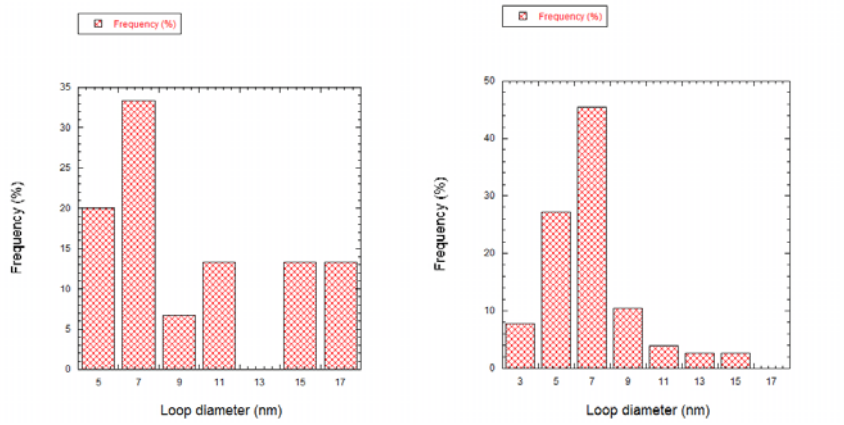

Figure 2. The size distribution of loops measured by APT a) and TEM b).

The dislocation loops found in the APT characterization are ≈ 7-10 nm in diameter with a number density of ≈ $1.4\times10^{22}/m^3$. A histogram of the loop sizes is shown in Figure 2a. There are also some smaller features in the iso-surface with Si threshold of ≈ 0.41% images, that we suspect to be small highly segregated loops. The concentrate profile shown in Figure 3 demonstrates that the dominant segregating species is Si along with smaller amounts of P and C. A comparison of the observed blue line (Cr/20) while the horizontal dashed blue line, which is the nominal Cr concentration, divided by 20 may indicate a slight enrichment. Examination of six composition profiles suggests that any average enrichment of Cr between the Si peaks is less than a factor of ≈ 1.2.

a)

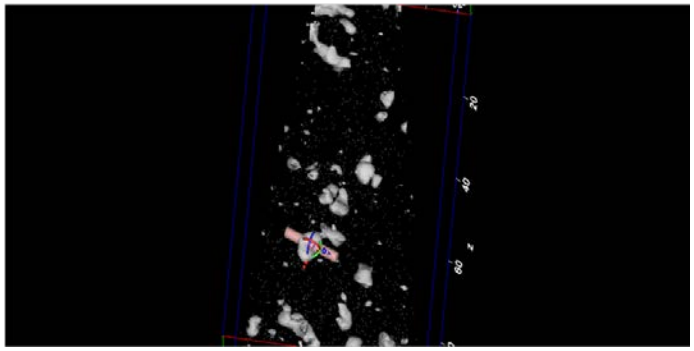

b)

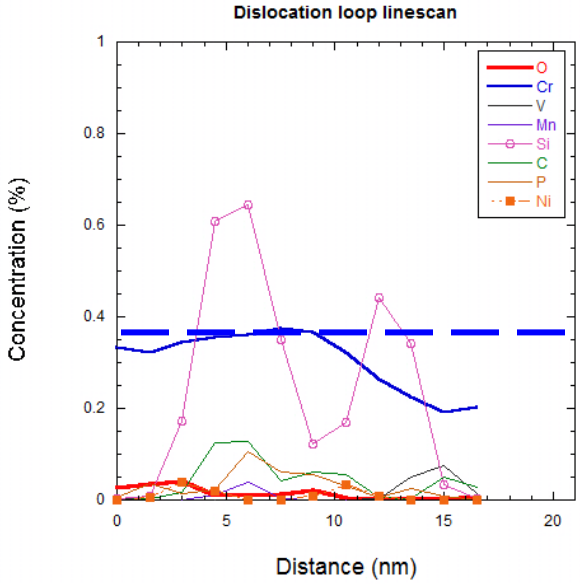

Figure 3. a) Isosurface of Si with the region of interest is getting through one of the dislocation loops; b) APT composition profiles across the highlighted dislocation loop (Cr concentration are divided by 20).

An example of a weak beam bright field TEM images, shown in Figure 4, reveals both <100>{200} and ½<111>{111}-type loops, but the latter are more frequent. The loops have an average diameter of ≈ 6.4 nm. A population of smaller features and black spot type damage are also observed, but details are difficult to resolve in TEM. The corresponding histogram of TEM loop sizes is shown in Figure 2b. While on average the loops are smaller, the TEM results are broadly consistent with the APT data.

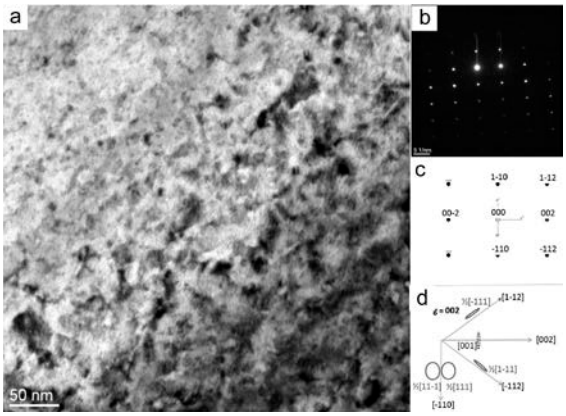

Figure 4. a) Weak-beam bright field image showing dislocation loops near the [110] zone axis using g002; b) The corresponding selected area diffraction (SED); c) The simulated diffraction pattern of bcc-Fe under [110] zone axis; d) A dislocation-loop map showing that the projected dislocation-loops are excited by g002.

Summary

The TEM and APT characterization data on dislocation loops in the ion irradiated Fe-6Cr alloy are summarized in Table 1 and compared to the corresponding neutron data.

Table 1. Comparison of the dislocation loops in ion irradiated and neutron irradiated samples

	Ion		Neutron		Neutron (limited)	
	TEM	APT	APT		TEM	
Loop types	Mostly ½<111>{111}		Mostly ½<111>{111}		Small segregated loops* + larger loops?	
Segregation		Si on loop dislocations lower C & P	Cr at loop periphery Si inside	Si&C on loop dislocations lower C & P	Small segregated loops?	Larger segregated loops
Diameter (nm)	6.4	8	8-10	18-20	2.5	5.4
# density(/m^3)	$1.3x10^{22}$	$1.4x10^{22}$	$2.9x10^{22}$		$4.3x10^{22}$	$1.3x10^{21}$

* Seen as solute clusters?

References

[1] M. Bachhav, L. Yao, G. R. Odette, E. A. Marquis, J. Nucl. Mat. 453 (2014) 334.
[2] M. Bachhav, G. R. Odette, E. A. Marquis, J. Nucl. Mat. 454 (2014) 381.
[3] M. Bachhav, G. R. Odette, E. A. Marquis, ScriptaMater. 74 (2014) 48.
[4] M. Matijasevic, and A. Almazouzi, J. Nucl. Mat. 377 (2008) 147.
[5] Y. Wu, T. Yamamoto, N. Cunningham, G. R. Odette, S. Kondo, and A. Kimura, Fusion Reactor Materials Program June 30, 2013 DOE/ER-0313/54 – Volume 54, PP 42-50.
[6] B. Yao, D. J. Edwards, R. J. Kurtz, J. Nucl. Mat. 434 (2013) 402-410.

1.4 ON THE EFFECTS OF HELIUM-DPA INTERACTIONS ON CAVITY EVOLUTION IN TEMPERED MARTENSITIC STEELS UNDER DUAL ION-BEAM IRRADIATION —— Takuya Yamamoto, Yuan Wu, G. Robert Odette (University of California Santa Barbara), Kiyohiro Yabuuchi, Sosuke Kondo, Akihiko Kimura (Kyoto University)

OBJECTIVE

The objective of this research is to characterize how cavities and other microstructural features evolve in irradiated 9Cr tempered martensitic steels (TMS) and nanostructured ferritic alloys (NFA) are affected by the starting microstructure and irradiation variables, including temperature, displacements per atom (dpa), dpa rate and the helium/dpa (He/dpa) ratio.

SUMMARY

Cavity evolution in normalized and tempered 8Cr martensitic steels (TMS) F82H under Fe^{3+} and He^{+} dual ion beam irradiation (DII) at 500°C was characterized for a number of new dpa and He conditions. The cavity evolution TMS alloy database at 500°C now includes 280 material-dpa-He-dpa rate DII conditions. In summary, key observations on swelling include: a) the f_v-dpa trend is controlled by the He/dpa; b) better accounting for local microstructure effects and run-to-run variations partly rationalized the observed large data f_v "scatter"; c) f_v is somewhat lower in the reference case and similar runs; d) f_v is lower in the Ta modified variant of F82H than in the IEA heat and f_v in the latter decreases with increasing cold work.

BACKGROUND

As reported previously [1-5], we have been carrying out systematic DII studies at 500°C in DuET facility in Kyoto University at various nominal He/dpa and dpa rates (defined at the depth of 600 nm) in TMS and NFA. Here we update the DII database and report an analyses cavity evolution (and swelling) trends in F82H Mod.3 (M3) and IEA TMS encompassing a very wide range of DII dpa, He and He/dpa. We also compared the behavior of F82H to that in the NFA.

PROGRESS AND STATUS

Experiment

While details of alloys and DII experiments can be found in [3], Table 1 summarizes nominal He and dpa conditions at two reference depth locations encompassed by the current database. The irradiations targeted two nominal doses, three He/dpa and two dpa rate conditions. Taking advantage of the varying spatial distributions of dpa, He and He/dpa with the example shown Figure 1a, we characterized the microstructures over a very wide range of He and dpa conditions. Figure 1b shows all the available conditions for F82H IEA in both as-tempered and two cold worked conditions and Ta-modified F82H Mod.3 for a wide range of dpa and He/dpa ratios. Here we report TEM quantitative characterization of cavity (bubbles and voids) structures in a series of 100nm slices from near the beginning to beyond the end of the range of the 6.4 MeV Fe^{3+} ions. The specific conditions shown in Figure 1b represent the average dpa, He and He/dpa in each of the 100 nm slices. The dpa are based on SRIM using the Kinchin-Pease with Fe displacement energy of 40 eV [6,7].

RESULTS

Void swelling as a function of He and He/dpa and root causes of observed scatter

Here cavity evolution trends as a function of dpa and He/dpa are quantified in terms of average diameter, $\langle d \rangle$, number density, N, and volume fraction, f. Earlier analyses showed that variations in the void $\langle d_v \rangle$ and N_v are less sensitive to local microstructure variations; and that the total $f \approx f_v$. We separate voids from bubbles by assuming a (≈ critical) threshold diameter of 4 nm for the latter. This threshold is not fixed or rigorous, but corresponds to a dip that is often observed between two bubble-void peaks in the cavity size distribution. We have also previously noted that there is significant scatter in the data trends,

including f, which is likely due to variations in the local microstructure and the uncertainty in the irradiation temperature [1].

Table 1. Irradiation conditions analyzed in this report.

Exp ID	Alloys	T (°C)	Nominal Condition (@550-650nm)				Peak He (@1000-1100nm)		
			dpa	He (appm)	He/dpa	dpa/s	dpa	He (appm)	He/dpa
DI10B1	FM3	500	26	1210	47	5.0×10^{-4}	45	2100	47
DI10B2			9.9	457	46	5.2×10^{-4}	17	795	46
DI10B3			10	480	47	5.1×10^{-4}	18	840	47
DI13A1	FM3	500	26	390	15	5.1×10^{-4}	44	670	15
DI13B1	FM3, FIA	500	30	848	29	1.5×10^{-3}	51	1467	29
DI13B2	FIB, FID	500	27	730	28	1.5×10^{-3}	46	1262	28
DI14A1	FM3, FIA	500	30	1340	45	1.3×10^{-3}	52	2320	45
DI14A2	FIB, FID	500	30	1400	46	1.5×10^{-3}	52	2430	46
DI14B	FM3, FIA, FID	500	45	1290	28	8×10^{-4}	79	2230	28
D15A	FM3, FIA, FIB, FID	500	51	1360	27	8.6×10^{-4}	88	2350	27

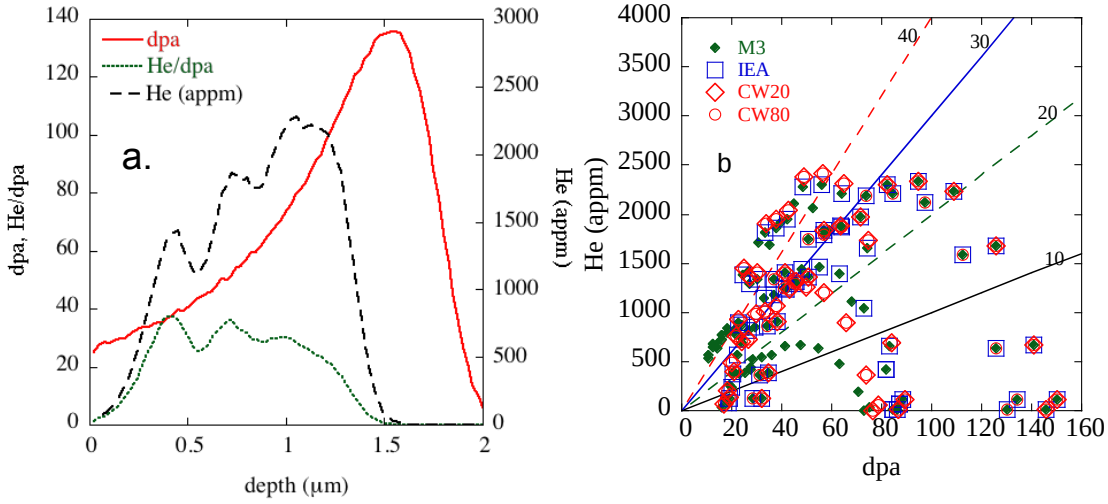

Figure 1. a) The dpa, He (appm) and He/dpa profile for DI14B irradiation as an example; and, b) the He/dpa, dpa conditions for all the DI runs for the TMS materials.

For example, areas containing large carbides have a larger number of finer bubbles at the interface, compared to in carbide free regions of the matrix. This local variation in the He bubbles affects the corresponding void N_v, d_v and f (f_v). Thus we have re-analyzed and added many other areas to previous results. We also found that the pyrometer temperature measurement system may have been miscalibrated during periods when the system upgrades were carried out, leading to possible run-to-run and within run deviations from the nominal 500°C. Hence, for the latest experiment, D15A, the temperature was calibrated every hour using thermocouples welded onto one of the samples, away from the beam area. Using D15A as a reference, all the other runs were analyzed to identify the run-to-run variations. We have also accumulated a significant amount of new data for the F82H IEA steel with 20%

and 80% cold work (CW). These results are tabulated in a large and growing DII database that currently contains 104 dpa-He-dpa rate DII conditions for F82H Mod.3, 64 for as-tempered (AT) F82H IEA, 48 for 20% CW and 64 for 80% CW F82H IEA.

Figure 2 shows the N_v, $<d_v>$ and f_v for voids in the as-tempered F82H M3 and IEA groups by the nominal He/dpa ratio based on SRIM estimates rounded to the nearest single digit value in general increments of 10. The filled symbols are for runs in late 2013 (2013B) and early 2014 (2014A). The unfilled symbols are for all the other runs, which are in better agreement with the trends observed in the reference run D15A.

As shown in Figure 2a and 2b, the data group that ran at ≈ nominal temperature (NT) including the reference runs forms a single f vs dpa trend for each He/dpa level. Swelling incubation dpa_o for He/dpa of 40, 30, 20, 10 and <5 are ≈ 40, ≈ 90, ≈ 110 and ≈ 130 (dpa), respectively. Those incubation doses are lower in the other group. While the actual temperatures for the runs were yet to be evaluated, these runs were at ≈ 50°C or more higher temperature (HT) than NT. The HT runs also form consistent trend within themselves showing dpa_o of ≈ 20, ≈ 40, ≈ 60, ≈ 70, and ≈ 80 (dpa) for He/dpa of 40, 30, 20, 10 and <5, respectively. Apparently the effect of He/dpa is more enhanced in NT group.

In the NT group, at the incubation doses especially when f < 1%, N_v increases sharply while $<d_v>$ stays ≈ 5 nm, suggesting that nucleation (transformation from bubbles to voids) is dominant process. For He/dpa = 30 in F82H IEA, the large f ≈ 2% at dpa ≈ dpa_o + 20 is accompanied by a significant growth of voids as $<d_v>$ > 10 nm. In the HT group the N_v and $<d_v>$ trends are different as both increase sharply at the dpa_o. These differences can be caused by the difference in the temperature range where void nucleation and/or growth are active. Further investigation of the trends will be covered in a future experiment that will include more systematic and controlled variation of the irradiation temperature.

Figure 3 shows the corresponding a) volume fraction, b) number density, and c) average diameter of "voids" vs. dpa plots for F82H IEA at two CW levels, 20 and 80%. Here we also show the data in the NT and HT groups. Within each group, the trends are consistent and similar to the as-tempered conditions. He/dpa effects on reducing dpa_o is observed in 80% CW.We currently do not have enough data to see the dpa_o in the 20%CW alloy. While the exact HT condition is not determined, in each group the data shows the effect of CW since these 20 vs 80%CW samples were side-by-side irradiated whenever possible. An interesting trend is that the effect of CW on f reverses between HT and NT. At HT larger f is observed in 20%CW, so that including AT, a higher dislocation density (ρ) reduces f, which may be due to a higher number density of smaller bubbles at higher ρ. In the NT condition, higher ρ shows slightly more swelling in all He/dpa levels. ISHI experiments also showed that higher ρ refines bubbles that would otherwise reach critical sizes for void transformation. However, higher ρ enhances the imbalance of vacancies to self-interstitial atoms flowing into cavities. This effect can accelerate void-swelling by reducing the critical size for transformation and increasing void growth rates. These contradicting effects at different temperatures may have resulted in the observed behaviors, but further experimental investigation along with comparison with models are also included in the future study.

Summary

This is work in progress and will be discussed in more detail in future reports and publications. The summary of key observations on swelling includes: a) the f_v-dpa trend is controlled by the H/dpa; b) better accounting for local microstructure effects and run-to-run variations partly rationalized the observed large data f_v "scatter"; c) f_v is somewhat lower in the reference case and similar runs; d) f_v is lower in M3 than IEA and f_v in IEA decreases with increasing cold work.

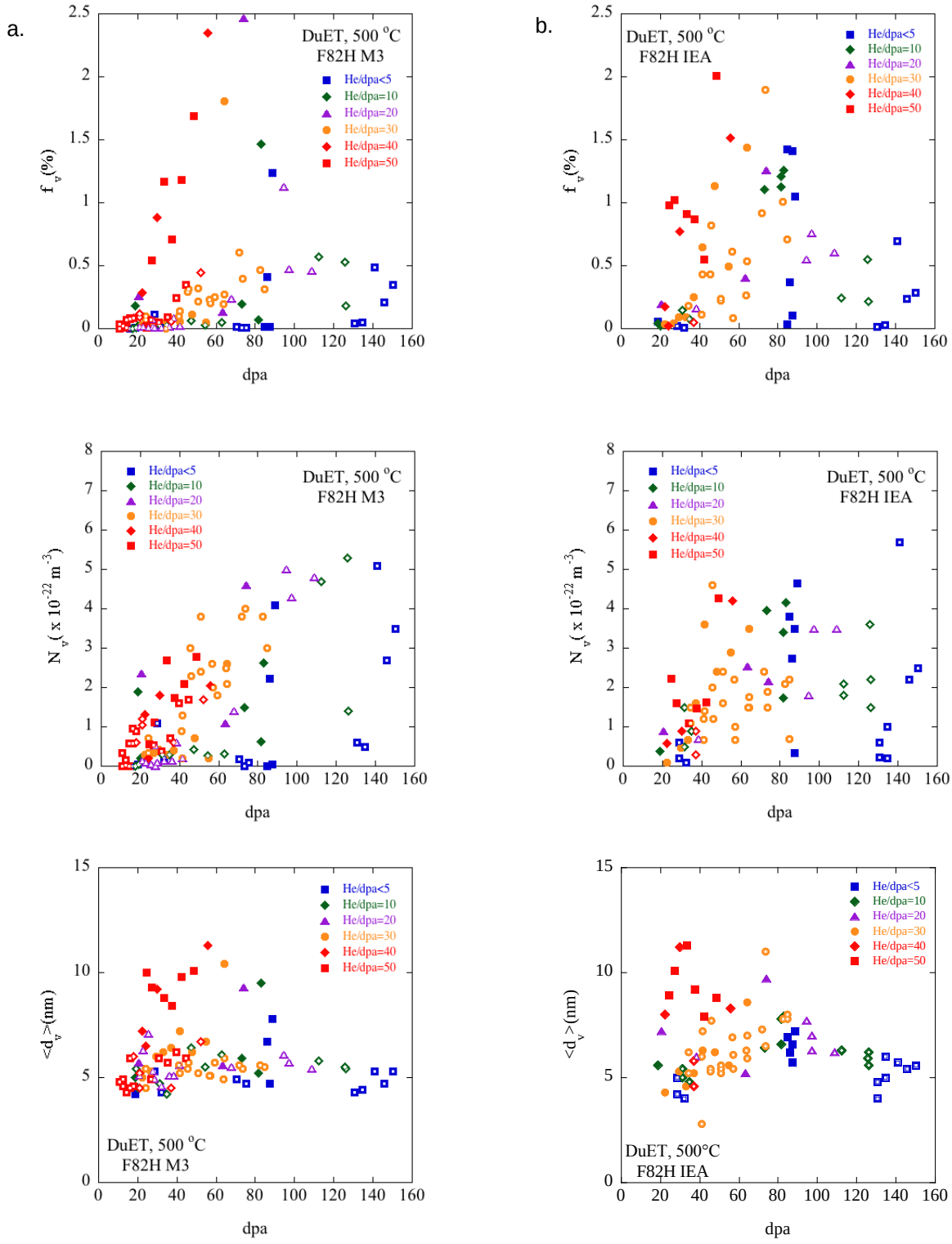

Figure 2. The fv, dv and Nv for the as-tempered condition of a) F82H M3; and, b) IEA.

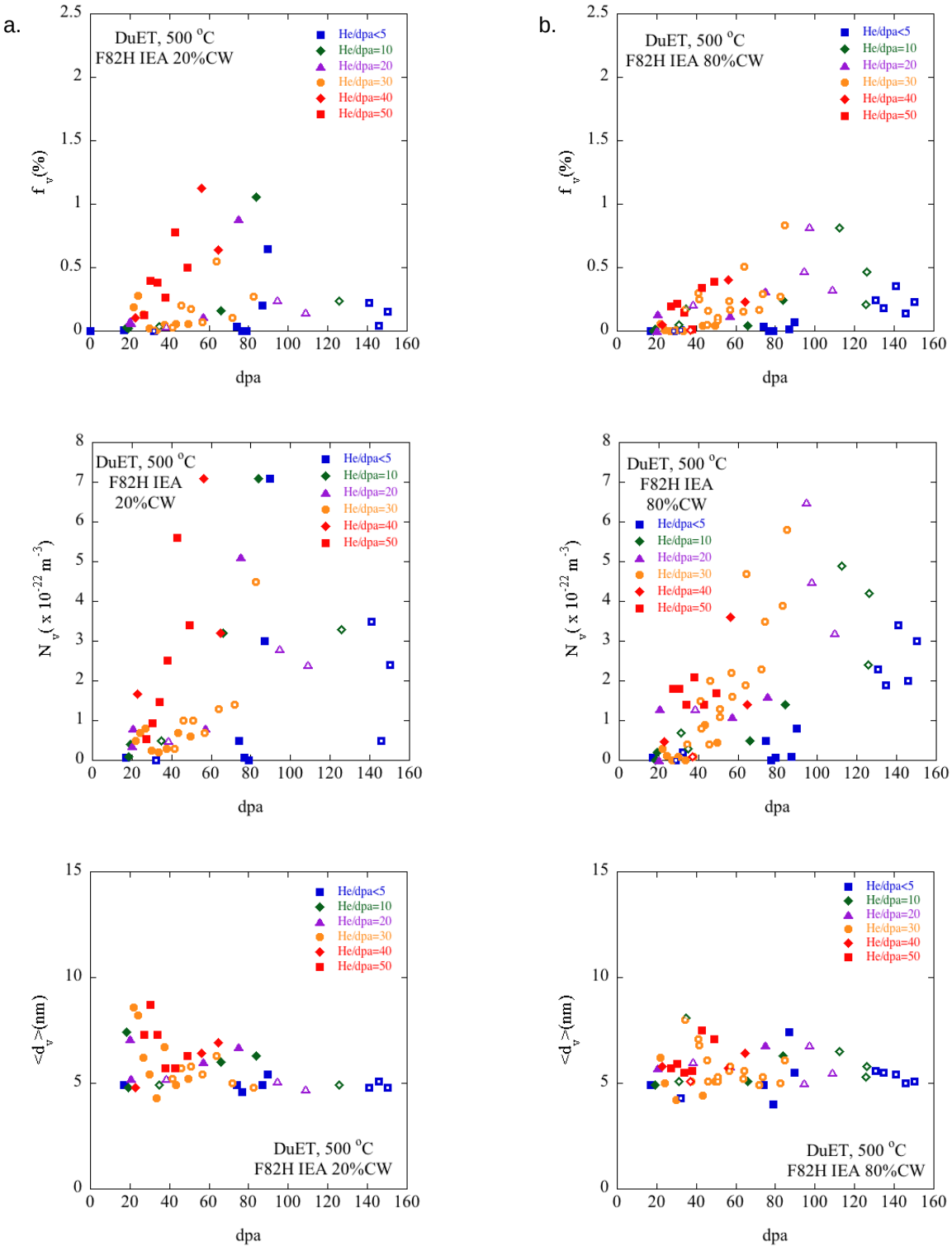

Figure 3. The f_v, d_v and N_v for the CW conditions of F82H IEA of a) 20%; and, b) 80%.

Acknowledgements

The dual ion-beam irradiations were conducted under the support of the "Joint Research Program on Zero-Emission Energy Research, Institute of Advanced Energy, Kyoto University (ZE28A-22, ZE26A-16, 25A-19, 24A-13 and 23B-3). The work performed at UCSB was supported by the U. S. Department of Energy, Office of Fusion Energy Sciences, under contract DE-FG03-94ER54275. We acknowledge the contributions of the NSF sponsored UCSB Microstructure and Microanalysis Facility. We are also grateful for generous support of research materials, F82H mod.3 from Dr. K. Shiba, (JAEA, Japan).

References (need updates)

[1] G.R. Odette, T. Yamamoto, Y. Wu, S. Kondo, A. Kimura, *Fusion Materials Semiannual Report 12/31/2014* DOE/ER-313/57 (2015) 8
[2] T. Yamamoto, Y. Wu, G.R. Odette, S. Kondo, A. Kimura, *Fusion Materials Semiannual Report 6/30/2014* DOE/ER-313/56 (2014) 194
[3] T. Yamamoto, Y.Wu, G.R. Odette, K. Yabuuchi, S. Kondo, A. Kimura, J. Nucl. Mater. 449 (2014) 190
[4] T. Yamamoto, Y.Wu, G.R. Odette, S. Kondo, A. Kimura, *Fusion Materials Semiannual Report 6/30/2013* DOE/ER-313/54 (2013) 6.
[5] T. Yamamoto, Y. Wu, G.R. Odette, K. Yabuchi, A. Kimura, *Fusion Materials Semiannual Report 12/31/2010* DOE/ER-313/49 (2011) 1.
[6] ASTM E521-96 (2009), ASTM
[7] R.E. Stoller, M.B. Toloczko, G.S. Was, A.G. Certain, S. Dwaraknath, F.A. Garner, Nuc Instr Mehtods Phys Res B 310 (2013) 75.

1.5 THREE DIMENSIONAL FRACTOGRAPHY OF HFIR-IRRADIATED F82Hs – H. Sakasegawa, H. Tanigawa (Japan Atomic Energy Agency), and Y. Katoh (Oak Ridge National Laboratory)

OBJECTIVE

The objective of this work is to perform 3D fractography on HFIR-irradiated F82Hs to study details of irradiation effects on the tensile rupture mechanism. This work is part of the U.S. Department of Energy – Japan Atomic Energy Agency fusion materials collaboration.

SUMMARY

The 3D fractography was performed using a scanning electron microscope. Three pictures of tensile specimen rupture surfaces were taken from different tilt angles and 3D images were produced from these pictures using a software program. From the representative result shown here, it was revealed that the irradiated specimen of F82H-MOD3 heat irradiated to 2.7 dpa at 573 K showed a shear rupture mode, with a small area fraction of dimpled surface.

PROGRESS AND STATUS

Introduction

3D fractography is very useful technique to study rupture mechanisms. For example, FRActure Surface Topography Analysis (FRASTA) technology was developed and published [1]. This technology focuses on the growth history of a crack, which is strongly correlated to the remaining useful life of a material, and reveals how a crack front interacts with microstructural features. This result can contribute to understanding the rupture mode in detail and help in the development of materials with more appropriate mechanical properties. In the case of F82H, it is well known that its ductility drastically degrades and uniform elongation becomes near zero after irradiation around 573 K to less than a few dpa. This irradiation embrittlement should be understood and allowed for in planning to actually use F82H as a blanket material with appropriate structural soundness.

Experimental

In this work, scanning electron microscopy (SEM) images were obtained on ruptured HFIR irradiated tensile specimens (SS-J3 type) using the JEOL JSM-6010LA in cell 4 in Building 3025E, Oak Ridge National Laboratory. Three or five pictures were taken from different tilt angles. These pictures were then processed with the software, Alicona MeX, to produce a 3D image of the rupture surface [2].

Results and Discussion

Figure 1 shows the result of tensile test at 573 K on F82H-MOD3 heat (Fe-0.1C-8Cr-2W-0.2V-1.0Ta) [3] irradiated at 573 K to 2.7 dpa (ID: HX4) [4]. The irradiated sample clearly showed irradiation embritllement and the uniform elongation was reduced to 0.1 %, compared to that of unirradiated F82H which is generally larger than 2 %. The tensile ruptured surface is shown in Figure 2 (a). Though the upper right position was contaminated, we clearly observed some dimples which indicated that this specimen had a local ductile fracture mode. Figure 2 (b) shows the image of the rotated and tilted specimen. This picture gives three dimensional information of the fracture surface, but it is difficult to observe the topographical detail.

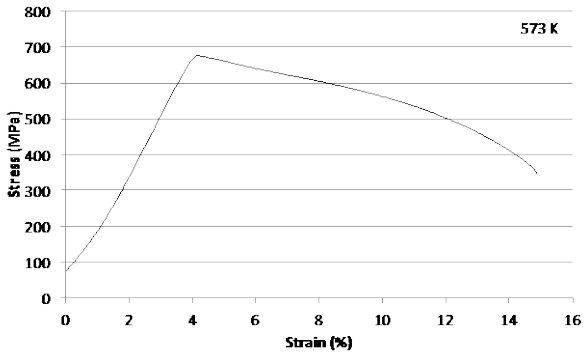

Figure 1. Tensile test result on specimenID: HX4, F82H MOD3 heat, irradiated to 2.7 dpa at 573 K and tested at the irradiation temperature.

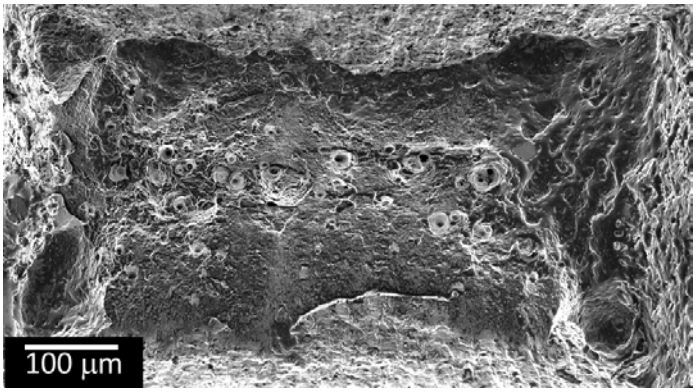

(a) Top view

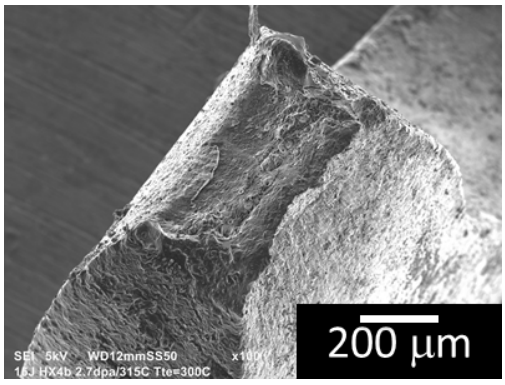

(b) Skew view

Figure 2. Two SEM images of the fracture surface of the specimen described in Figure 1.

Figure 3 (a) shows three pictures taken at tilt angles of -5, 0, and +5 degrees to produce a 3D image. These images were then processed using the software MeX and obtained the 3D profile image shown in Figure 3 (b). The corresponding quantitative data are shown in Figure 4. These data indicated that the fracture surface slanted and showed a shear rupture mode with an angle of about 54 degrees to the tensile axis. This information cannot be obtained from Figure 2, which was the result of ordinary fracture surface analysis. This information is expected to be very helpful to understand details of irradiation effects on rupture mechanism, and it may be possible to obtain true fracture initiation strain, which value is more consistent with the true tensile fracture nature than is reduction in area. In future work, we will evaluate more tensile ruptured specimens after irradiation and perform the 3D topography using this technique to clarify the irradiation embrittlement.

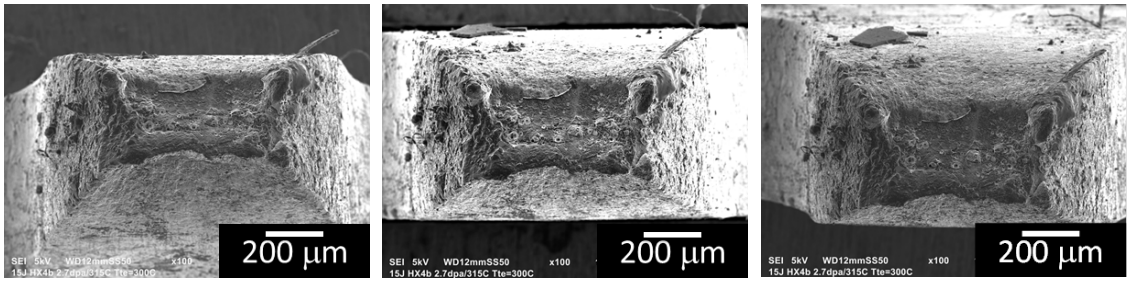

+5 degree **0 degree** **-5 degree**

(a) Tilted views to process for 3D image of tensile fracture surface of HX4

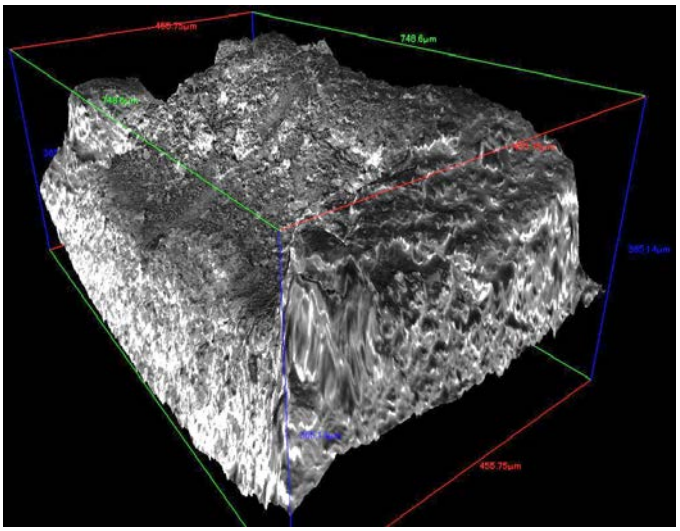

(b) Obtained 3D image of the tensile fracture surface of HX4

Figure 3. Detailed images processed to provide a 3D image of the fracture surface.

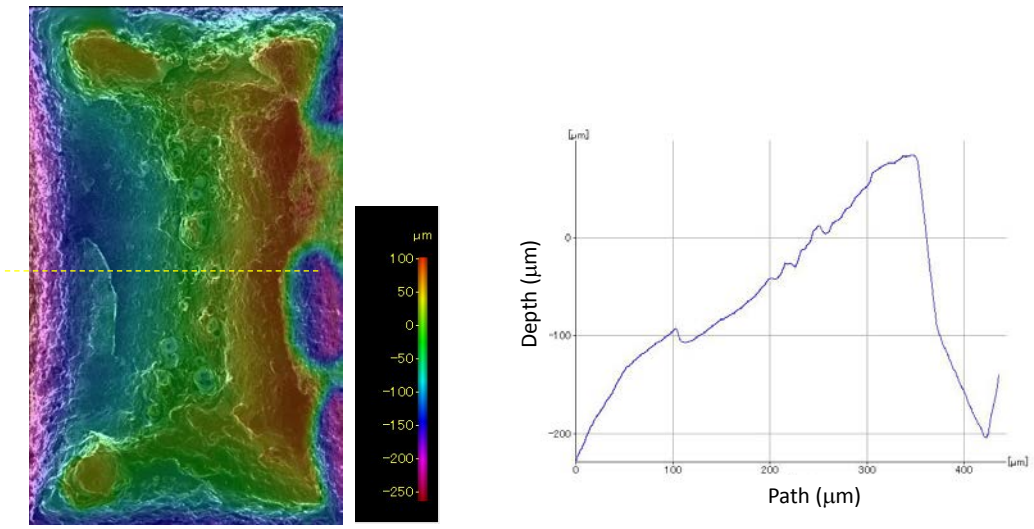

Figure 4. 3D profile of the tensile fracture surface (Left) and line profile (Right) of the relative heights along the broken yellow scan line indicated on the 3D profile.

Acknowledgements

This research was sponsored by the Japan Atomic Energy Research Institute and the Office of Fusion Energy Sciences, U.S. Department of Energy, under contracts NFE-10-02779 and DE-AC05-00OR22725, respectively, with UT-Battelle, LLC. The authors would like to acknowledge the assistance of Patrick S. Bishop in Building 3025 hot cell facility in the experimental work and the supports of FMNS Group staff.

References

[1] T. Kobayashi et al., Metall. Trans. A. 18A (1987) 1941-1949.
[2] http://www.alicona.com/home/products/mex.html
[3] K. Shiba et al., Fusion Sci. Tech. 62 (2012) 145-149.
[4] T. Hirose et al., Fusion Materials Semi-annual Progress Report, DOE/ER-0313/46, (June 30) 72-78.

2.1 DEVELOPMENT OF ODS FeCrAl FOR FUSION REACTOR APPLICATIONS – B. A. Pint, K. A. Unocic, S. Dryepondt and D. T. Hoelzer (Oak Ridge National Laboratory, USA)

OBJECTIVE

The dual coolant lead-lithium (DCLL) blanket concept requires improved Pb-Li compatibility with ferritic steels in order to demonstrate viable blanket operation in a DEMO-type fusion reactor. The goal of this work is to develop an oxide dispersion strengthened (ODS) alloy with improved compatibility with Pb-Li and excellent mechanical properties. The current focus is characterizing the performance of a group of ODS alloys based on Fe-12Cr-5Al.

SUMMARY

Characterization of the first four experimental ODS FeCrAl heats (based on Fe-12Cr-5Al) is nearing completion. Creep testing of the alloys containing Y_2O_3 + ZrO_2 and Y_2O_3 + HfO_2 at 800°C/100 MPa has shown exceptional lifetimes for these materials. Additional Pb-Li compatibility experiments were completed at 700°C including similar composition ODS FeCrAl alloys made for a nuclear energy project. All of the alloys showed low mass changes in these experiments. suggesting superior Pb-Li compatibility compared to wrought and ODS Fe-Cr compositions. A thin (~1 μm) reaction product of $LiAlO_2$ was observed in all cases and additional characterization is in progress. The final phase of this project will examine two new alloys made with the same Fe-12Cr-5Al powder and several new alloys where Zr was added as an alloy addition rather than an oxide dispersion.

PROGRESS AND STATUS

Introduction

The DCLL blanket concept (Pb-Li and He coolants) is the leading U.S. design for a test blanket module (TBM) for ITER and for a DEMO-type fusion reactor.[1] With reduced activation ferritic-martensitic (FM) steel as the structural material, the DCLL is limited to ~475°C metal temperature because Fe and Cr readily dissolve in Pb-Li above 500°C and Eurofer 97 plugged a Pb-Li loop at 550°C.[2-3] For a higher temperature blanket for DEMO, structural materials with enhanced creep and compatibility are needed. ODS FeCrAl alloys are one possibility to meet this objective and considerable research on ODS FeCr alloys has shown an excellent combination of creep strength and radiation resistance.[4-7] However, these ODS FeCr alloys do not have adequate compatibility with Pb-based coolants, such as Pb-Bi eutectic (LBE) [8-11]. With the addition of Al, isothermal compatibility tests have shown low mass losses at up to 800°C [12] and a recent thermal convection loop was operated for 1000h at 550°C with only small mass changes measured for the commercial Fe-21Cr-5Al-3Mo alloy (Kanthal APMT) specimens in the hot and cold legs [13] . Therefore, a materials development effort is underway, specific to this application. ODS FeCrAl was commercialized in the 1970's for its high temperature (>1000°C) creep and oxidation resistance [14] and other research groups are currently investigating new FeCrAl alloy compositions for fission and fusion applications with liquid metals [15-17].

Previous initial work [18-21] had identified Fe-12wt.%Cr-5Al as a target composition with low Cr to minimize α' formation during irradiation [22], while maintaining 5%Al for Pb-Li compatibility.[18,21] Using diffusion couples, combinations of oxides also were identified that could form stable ternary compounds. The microstructure and property assessment of this first generation of composition is nearly complete [23,24] and a second generation is being designed based on the information learned.

Experimental Procedure

Four experimental ODS FeCrAl ferritic alloys were produced by mechanical alloying (MA). Powder of specified composition Fe-12.1wt.%Cr-5.0Al and particle size range ~45-150 μm was prepared by Ar gas atomization by ATI Metal Powders. The FeCrAl powder was blended with 0.3%Y_2O_3 powder (17-31 nm crystallite size, produced by Nanophase, Inc.) and subsequent 1kg batches included additions of 0.4ZrO_2, 0.22HfO_2 and 0.2TiO_2 powders (<100 nm diameter from American Elements). Each batch was ball milled for 40 h in Ar gas atmosphere using the Zoz CM08 Simoloyer ball mill. After ball milling, the powders were placed in mild steel cans, degassed at 300ºC under vacuum and sealed. The cans were equilibrated at 950ºC for 1 h and then extruded through a rectangular shaped die. Table 1 shows the as-extruded compositions of each alloy. The alloys with additional ZrO_2, HfO_2 and TiO_2 oxide additions showed higher O contents and the Cr and Al contents were lower than the starting powder. Other typical impurities were Co, Cu, Ni and Mn at the 0.01-0.02% level and the C and N pickups from the milling process were acceptable. Table 1 also includes several additional alloys with higher Cr contents that were produced for a nuclear energy project. These alloys were made by a similar process but with only Y_2O_3 additions. For comparison, a commercial ODS (PM2000) and a powder metallurgy (APMT) FeCrAl alloy are shown.

Because of the relatively small amount of material fabricated, creep testing of the new alloys was performed at 800°C using 25mm long specimens parallel to the extrusion axis and with a 2 x 2 mm gauge section that was 7.6mm long. Static Pb-Li capsule tests were performed using Mo (inert to Pb-Li) inner capsules and type 304 stainless steel (SS) outer capsules to protect the inner capsule from oxidation. The ODS FeCrAl specimens were ~1.5 mm thick and 4-5 cm^2 in surface area with a 600 grit surface finish and were held with 1 mm diameter Mo wire. The capsules were loaded with 125 g of Pb-Li in an Ar-filled glove box. The most recent capsule tests were conducted with commercial Pb-Li from the same supplier used for the loop experiment [13]. The Mo and SS capsules were welded shut to prevent the uptake of impurities during the isothermal exposure. After exposure, residual Pb-Li on the specimen surface was removed by soaking in a 1:1:1 mixture of acetic acid, hydrogen peroxide and ethanol for up to 72 h. Mass change was measured with a Mettler-Toledo balance with an accuracy of ±0.04 mg or 0.01 mg/cm^2.

Post-test specimen surfaces were examined using x-ray diffraction (XRD) and secondary electron microscopy (SEM) equipped with energy dispersive x-ray (EDX) analysis. After surface characterization, the specimens were metallographically sectioned and polished and examined by light microscopy, SEM and transmission electron microscopy (TEM). Specimens for TEM analysis were prepared by Focused Ion Beam (FIB, Hitachi model NB500) using the in-situ lift-out method. A Philips model CM200 FEG-TEM/STEM (Scanning TEM) with XEDS was used for analysis. Bright-Field (BF) and High Angle Annular Dark Field (HAADF) STEM imaging methods were used in the microstructural investigations.

Table 1. Alloy chemical compositions (mass% or ppmw) by inductively coupled plasma analysis and combustion analysis.

Material	Fe%	Cr%	Al%	Y%	O	C	N	S	Other
Powder	82.8	12.1	5.0	<	64	31	11	<3	0.004Si
125Y	83.3	11.4	4.8	0.19	842	380	455	20	0.05W, 0.02Si, 0.01Ti
125YZr	82.8	11.5	4.9	0.18	1920	250	160	10	0.30Zr, 0.01Hf, 0.01Si
125YHf	82.3	11.7	4.8	0.17	2280	220	110	10	0.68Hf, 0.01Zr, 0.01Si
125YTi	82.4	12.0	4.9	0.16	2220	350	135	30	0.20Ti,0.01Si
134Y	82.5	12.8	4.4	0.17	1360	310	140	10	0.01Si
155YT	79.9	14.6	4.7	0.16	950	340	240	10	0.44Ti, 0.02Si
155YMT	79.0	14.6	4.8	0.16	830	370	130	<10	0.44TI,0.88Mo,0.02Si
PM2000	74.1	19.1	5.5	0.39	2480	14	86	8	0.48Ti, 0.02Si
APMT	69.8	21.2	4.8	0.21	519	360	530	<3	2.8Mo,0.1Zr,0.2Hf,0.5Si

< indicates below the detectability limit of <0.01%

Table 2. Measurements of the grain size and grain aspect ratio (GAR) of the ODS FeCrAl ferritic alloys.

Alloy	Grain Size (μm)		GAR
	Parallel to Extrusion Axis	Normal to Extrusion Axis	(Parallel/Normal)
125Y	0.83 ± 0.17	0.56 ± 0.09	1.48
125YZ	0.27 ± 0.06	0.17 ± 0.02	1.59
125YH	0.70 ± 0.16	0.39 ± 0.06	1.79
125YT	0.14 ± 0.02	0.12 ± 0.01	1.17

Results and Discussion

A large amount of microstructural information has been reported previously on the ODS Fe-12Cr-5Al alloys as well as aging and hardness data [20,23-25]. Table 2 summarizes the completed comparison of grain size for each of the four alloys.

Figure 1 compares the creep performance at 800°C of the ODS Fe-12Cr-5Al alloys to the commercial alloys PM2000 and APMT. Data from Plansee for fine grain (FG) PM2000 are also included. One PM2000 specimen failed during loading at 80 MPa, while an on-going 125YT test has reached 285 h with the same applied stress. For testing at 100 MPa, one 125YH specimen failed after 1242 h and one 125YZ specimen has passed 4000 h without failure. To reach a minimum lifetime of 1000h at 800ºC, alloys APMT and FG PM2000 are limited to ~25 MPa and ~45 MPa, respectively. For the new 12Cr-5Al alloys, the stress can be increased to at least 80MPa. A 100MPa test is planned for 125YT and further work is needed to confirm that 125YZ exhibits the best creep properties among the new alloys.

For the Pb-Li compatibility assessment, the most recent mass change data after 1000 h at 700°C in static Pb-Li is summarized in Figure 2 with the previous result for a 125YZ specimen. In the initial set of capsule experiments under the same conditions, a 125YH specimen lost 1.3 mg/cm^2, but showed no visual indication of attack. A second 125YH specimen was exposed in this set of experiment and showed a low

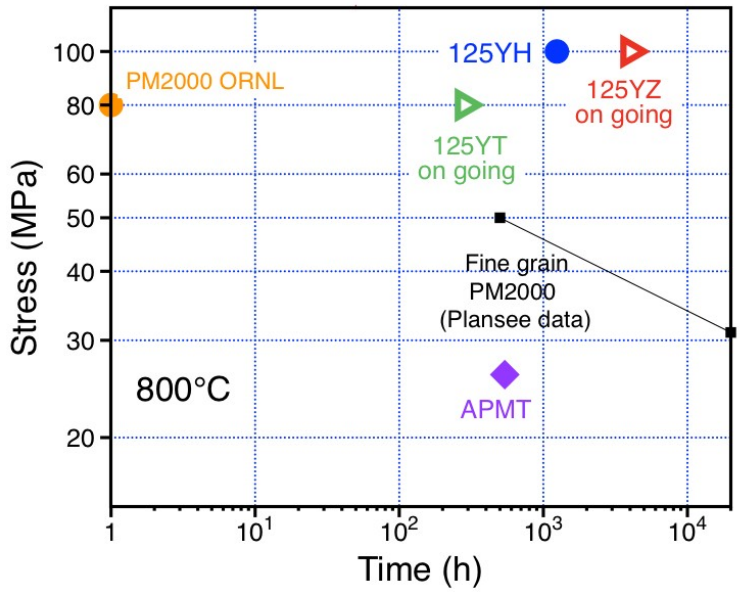

Figure 1. Lifetime at 800°C versus applied stress for the ODS Fe-12Cr-5Al, PM2000 and APMT alloys.

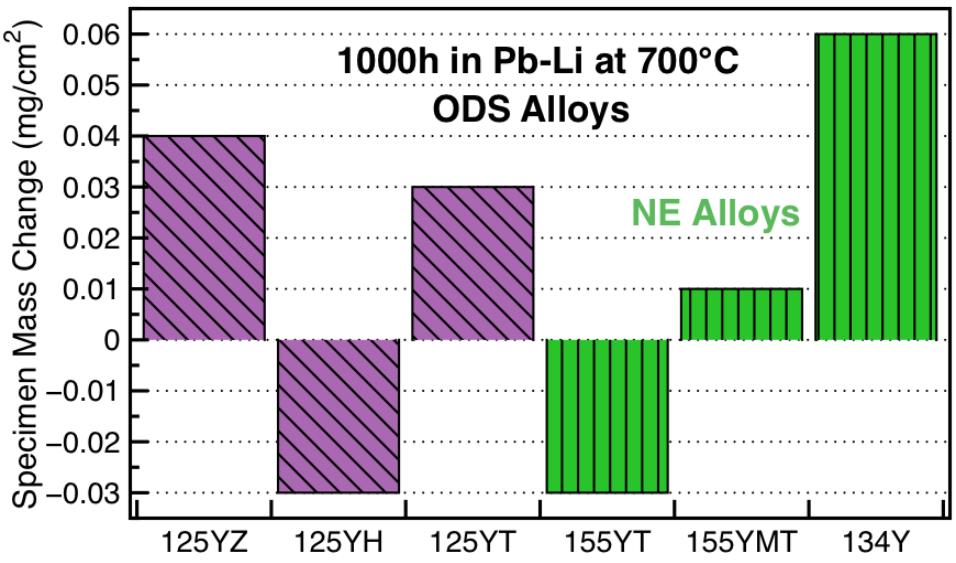

Figure 2. Specimen mass change for alloy specimens exposed for 1000h at 700°C in static Pb-Li.

mass change like the other specimens. In addition to the 12Cr-5Al specimens, ODS FeCrAl alloy specimens from another project were included that contained higher Cr contents, Table 1. These specimens also showed low mass changes after exposure and cleaning, consistent with prior work on commercial FeCrAl alloys PM2000 and APMT [12,26]. Also consistent with these prior studies, XRD identified the reaction products as $LiAlO_2$ in all cases. This oxide formed due to O impurities in the Pb-Li and presumably inhibited dissolution of the alloy into the liquid metal. However, the mass losses observed in the recent loop test at ~450-550°C suggest that this layer does not prevent dissolution.

Figure 3 shows cross-sections of the 12Cr-5Al ODS alloy specimens exposed in Pb-Li. In several cases, the ~1μm thick $LiAlO_2$ layer fractured or delaminated during specimen preparation. Previously, the Al content in the alloy was measured using electronprobe microanalysis but only minor Al depletion was observed in the 125YH and 125YZ specimens [23,25]. In order to further study the reaction product, TEM cross-sections were made. Figures 4 and 5 show initial results for the 125YZ specimen. The oxide appeared to have a columnar grain structure, Figure 4. At higher magnification, voids and oxide precipitates could be observed in the $LiAlO_2$ layer. Voids appear light in the bright field image and dark in the HAADF image. Oxides rich in Zr should appear bright in the HAADF image and dark in the bright field image, Figure 5. The incorporation of oxides into the reaction product suggests that the layer grew by the inward transport of O, rather than outward transport of Al. Unfortunately, $LiAlO_2$ was easily damaged by the electron beam (as was found earlier [26]) and only limited analysis has been possible of this specimen.

In the final year of this 3-year effort, several new alloys will be briefly investigated. Two new alloys have been extruded with the same Fe-12Cr-5Al powder with additions of La_2O_3-ZrO_2 and Y_2O_3-Fe_2O_3. The former was selected to examine the oxide precipitates formed in the alloy with La rather than Y and the latter was made to replace the 125Y alloy baseline alloy that had a lower O content than the other alloys (Table 1) and was contaminated with Fe-Cr powder resulting in questionable mechanical properties and Pb-Li compatibility [25]. In addition, new powder was ordered with Fe-12Cr-5.6Al and Fe-10Cr-6Al base compositions and alloys additions of Zr, Hf or Zr and Ti. The primary goal with these powders is to determine if different oxides form if, for example, the Zr is added as an alloy addition rather than as ZrO_2.

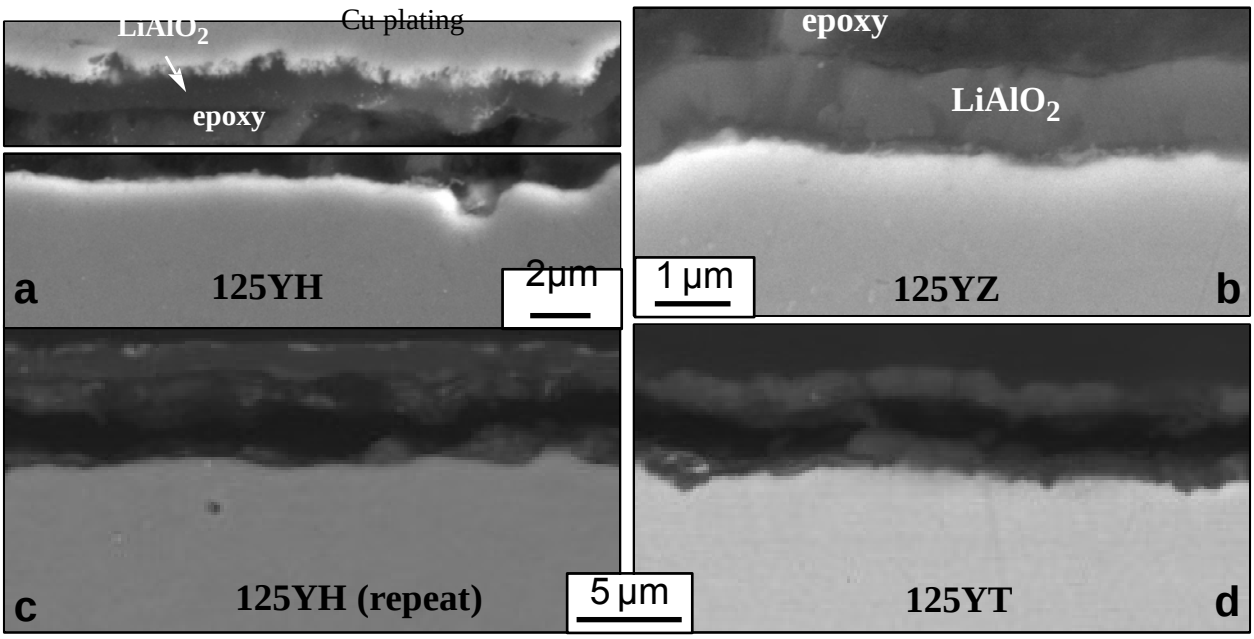

Figure 3. SEM backscattered electron images of polished cross-sections after 1000 h in Pb-Li at 700°C of (a) 125YH, (b) 125YZ, (c) 2nd 125YH specimen and (d) 125YT. In (a), (c) and (d) the oxide delaminated during specimen preparation.

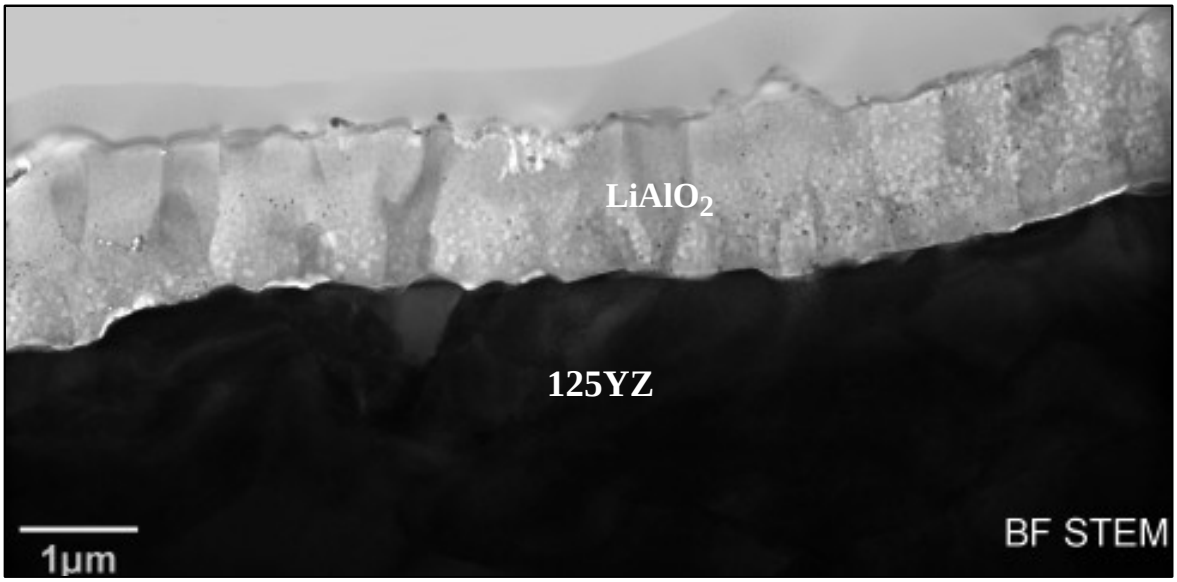

Figure 4. Bright field STEM image of the oxide formed on 125YZ after 1000h at 700°C in PbLi.

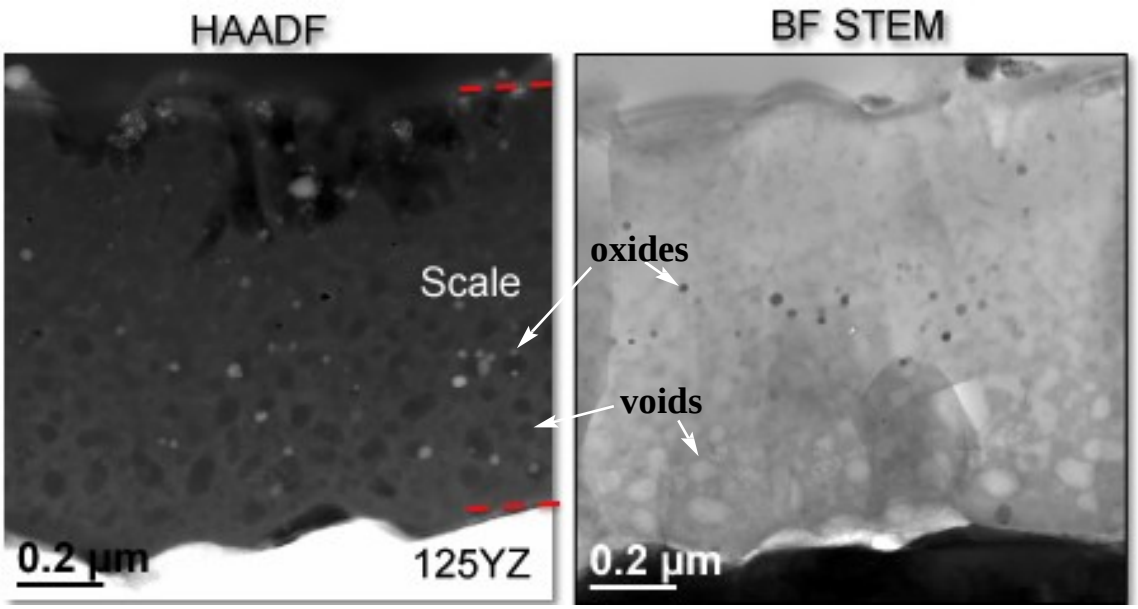

Figure 5. STEM cross-sectional images of the oxide formed on 125YZ after 1000h at 700°C in PbLi.

References

[1] M. Abdou, D. Sze, C. Wong, M. Sawan, A. Ying, N. B. Morley and S. Malang, Fus. Sci. Tech., 47 (2005) 475.
[2] O. K. Chopra, D. L. Smith, P. F. Tortorelli, J. H. DeVan and D. K. Sze, Fusion Technol., 8 (1985) 1956.
[3] J. Konys, W. Krauss, J. Novotny, H. Steiner, Z. Voss and O. Wedemeyer, J. Nucl. Mater. 386-88 (2009) 678.
[4] S. Ukai and M. Fujiwara, J. Nucl. Mater. 307 (2002) 749.
[5] G. R. Romanowski, L. L. Snead, R. L. Klueh, D. T. Hoelzer, J. Nucl. Mater., 283-287 (2000) 642.
[6] R. L. Klueh, J. P Shingledecker, R. W. Swindeman, D. T. Hoelzer, J. Nucl. Mater. 341 (2005) 103.
[7] D. A. McClintock, M. A. Sokolov, D. T. Hoelzer and R. K. Nanstad, J. Nucl. Mater., 392 (2009) 353.
[8] T. Furukawa, G. Müller, G. Schumacher, A. Weisenburger, A. Heinzel and K. Aoto, J. Nucl. Mater. 335 (2004), 189.
[9] P. Hosemann, H.T. Thau, A.L. Johnson, S.A. Maloy and N. Li, J. Nucl. Mater. 373 (2008) 246.
[10] C. Schroer, J. Konys, T. Furukawa and K. Aoto, J. Nucl. Mater. 398 (2010) 109.
[11] A. Weisenburger, K. Aoto, G. Müller, A. Heinzel, G. Schumacher and T. Furukawa, J. Nucl. Mater. 358 (2006) 69.
[12] B. A. Pint, L. R. Walker and K. A. Unocic, Mater. High Temp. 29 (2012) 129.
[13] S. J. Pawel, DOE-ER-0313/56 (2014) 178.
[14] J. D. Whittenberger, Met. Trans. 9A (1978) 101.
[15] J. Lim, H.O. Nam, I.S. Hwang and J.H. Kim, J. Nucl. Mater. 407 (2010) 205.
[16] A. Kimura, et al., J. Nucl. Mater. 417 (2011) 176.
[17] S. Takaya, et al., J. Nucl. Mater. 428 (2012) 125.
[18] B. A. Pint, D. T. Hoelzer, D. Shin, J. O. Kiggans, Jr., K. A. Unocic, DOE/ER-0313/53 (2012) 10.
[19] B. A. Pint, D. T. Hoelzer and K. A. Unocic, DOE/ER-0313/54 (2013) 27.
[20] D. T. Hoelzer, K. A. Unocic, S. Dryepondt and B. A. Pint, DOE/ER-0313/55 (2013) 5.
[21] K. A. Unocic and B. A. Pint, J. Nucl. Mater. 455 (2014) 330.

[22] C. Capdevila, M.K. Miller, K.F. Russell, J. Chao, J.L. González-Carrasco, Mater. Sci. Eng. A 490 (2008), 277.
[23] B. A. Pint, S. Dryepondt, K. A. Unocic and D. T. Hoelzer, JOM 66 (2014) 2458.
[24] K. A. Unocic, D. T. Hoelzer and B. A. Pint, Mater. High Temp. 32 (2015) 123.
[25] B. A. Pint, K. A. Unocic, S. Dryepondt and D. T. Hoelzer DOE-ER-0313/56 (2014) 31.
[26] B. A. Pint and K. L. More, J. Nucl. Mater. 376 (2008) 108.

2.2 CHARACTERIZATION OF THE MICROSTRUCTURE AND TEXTURE OF NFA-1 FOR TWO DEFORMATION PROCESSING ROUTES -- S. Pal, M.E. Alam, G. R. Odette (UCSB), J. Lewandowski (Case Western University) D. T. Hoelzer (ORNL) and S. A. Maloy (LANL)

OBJECTIVE

The objective of this research is to characterize the effect of different processing routes on the microstructural development and texture evolution of the FCRD-NFA-1alloy to facilitate the fabrication of component structures.

SUMMARY

Our previous investigation showed that NFA-1 produced through ball milling and hot extrusion followed by hot cross rolling suffers from severe micro-cracking on planes parallel to the plate surface and normal to the thickness direction. The microcracking inhibits fabrication of components, such as thin wall tubing, by conventional processing routes. This work reveals that a strong {001}<110> brittle texture component develops in NFA-1 during thermo-mechanical processing. Dislocation pile-ups at low angle boundaries result in formation of cleavage micro-cracks on {001} planes. In contrast, tubes formed by hydrostatic extrusion develop a strong {110}<211> "J_1-shear texture" component and low angle grain boundaries. Since preferred slip occurs on {110} planes in bcc Fe, deformation is readily accommodated by easy dislocations glide in the hydrostatic tube extrusion case. This is in contrast to {001} slip planes with pile ups that lead to stress concentrations and micro-crack nucleation in the extruded and cross rolled plate.

PROGRESS AND STATUS

Introduction

A nanostructured ferritic alloy (NFA), called FCRD NFA-1, was processed and is being qualified as part of collaboration between UCSB, LANL and ONRL [1-2]. Processing the plate involved a series of steps, including: 1) ball milling to produce powders with dissolved Y, Ti and O; 2) consolidation by hot extrusion at 850°C that also precipitated nano-oxides; and, 3) annealing and cross rolling at 1000°C. Following steps produce the base material, in the form of a plate, which is later used as a starting material for the thin wall tube formation through cold working process, such as pilgering. Presence of severe micro-cracks in the through thickness direction of plate, shatters the whole component during tubing by propagating along the radial direction of the tube. Very recently, hot hydrostatic extrusion method has been employed to produce tube from this NFA-1 alloy at Case Western University. It is well reported that application of hydrostatic pressure can change the ductility and fracture behavior of a brittle monolithic metal [3]. Component fabrication from brittle intermetallic material such as NiAl was successfully carried out using hydrostatic extrusion method near to its brittle to ductile transition temperature [4]. Present study is a prelude to understand the microstructural development and texture formation; when, same NFA-1 alloy processed through two different routes, hot extrusion followed by cross-rolling and hydrostatic extrusion.

Materials and Methods

The nominal composition of NFA-1 is 14Cr-3W-0.4Ti-0.21Y-balance Fe. Hot consolidation results in precipitation of an ultrahigh density (order $5x10^{23}/m^3$) of Y-Ti-O nano-oxides (NO), primarily $Y_2Ti_2O_7$, with average diameters of 2-3 nm. These NO provide exceptional strength accompanied by high ductility, thermal stability and irradiation tolerance, including trapping helium in nm-scale bubbles at their interfaces.

The processing sequence described above resulted in a 12.5 mm thick plate that is characterized by pancake shaped grains. The grain size is taken as the average of the long (l) and short (s) dimensions d = (l + s)/2 and the grain aspect ratio as r = l/s. The plates also contain a high density of micro-cracks on planes parallel to the plate surface and normal to the thickness direction. The cross rolled plate (or as extruded bar) can, in principle, serve as the starting point for subsequent fabrication of NFA components.

However, the micro-cracks severely limit the conventional cold workability of NFA-1, and more generally similarly processed NFA [1, 2]. For example, tube processing typically involves multiple room temperature pilgering and high temperature annealing step sequences [5-7]. Very recently, hot hydrostatic extrusion was used to produce a small length of thin wall tubing from the NFA-1 plate with remarkable success [8]. Hot extrusion was performed two times with an area reduction ratio of 4:1, which is equivalent to 44% applied strain. An aluminum mandrel was used to promote uniform wall thickness and stable deformation. The final product is completely free from micro-cracking. This motivated in-depth characterization of the microstructure and texture of NFA-1, for both of these processing routes. The microstructure of the plate and hydrostatically extruded tube were observed by SEM, TEM on FIBed liftouts and EBSD were used to characterize the corresponding textures. The characterization studies led to a micromechanical hypothesis regarding formation of the microcracks. The plate and tubing reference directions and specimen orientation are schematically illustrated in Figure 1.

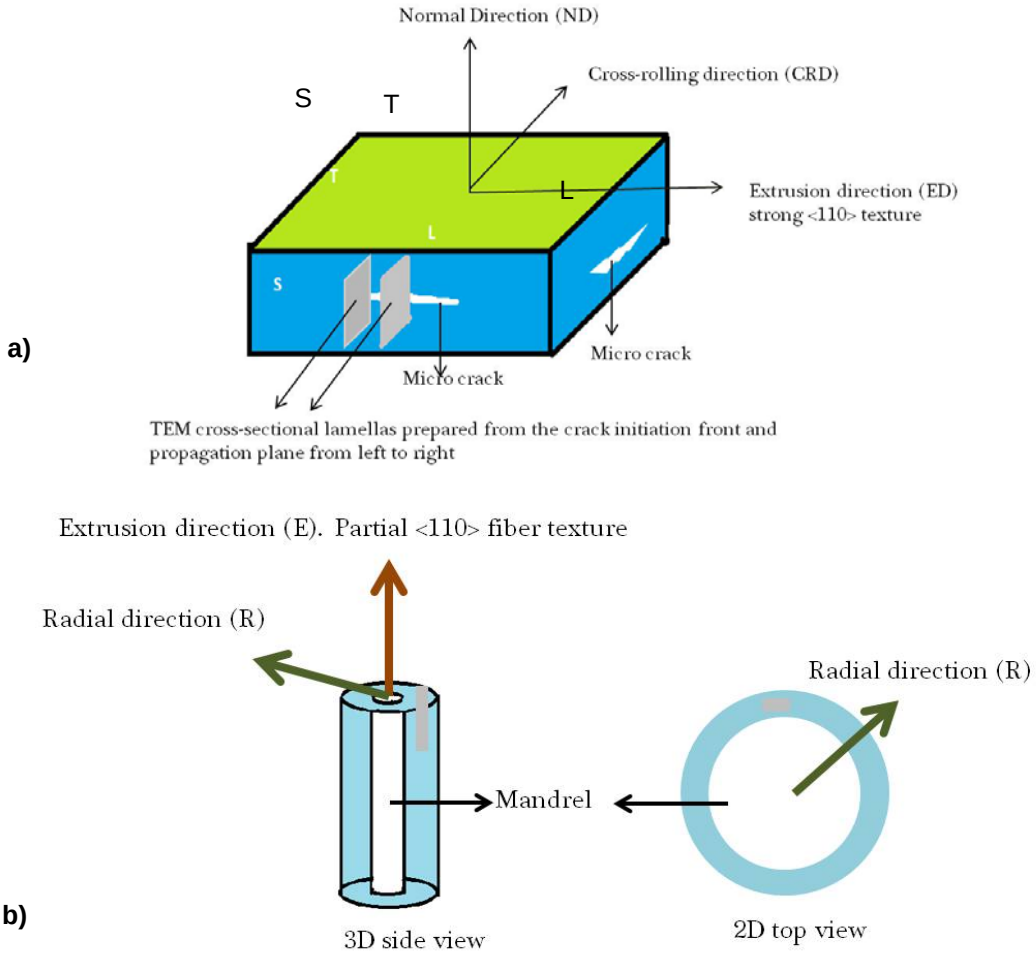

Figure 1. a) Schematic of a plate orientations referenced to the prime deformation directions. Micro-cracks, which are also shown in the image, run perpendicular to the short (S)-thickness direction. The tensile and cracked specimen orientation (L, T, and S) convention is also shown in Figure 1a. and, b) a schematic of the hydrostatically extruded tube showing the two key extrusion (E) and radial (R) directions. The region from where the TEM lamella is prepared is marked by grey box.

For cracks this convention is that the first letter defines the direction parallel to the front: L, T and S, and the second letter the direction of propagation. For tensile tests the letter defines the specimen axis. Planes and surfaces can also be defined in terms of L, T, S as parallel to the top (LT), side (LS) and front (ST);

Results

The two NFA-1 conditions characterized are: a) plates deformation processed by hot extrusion, annealing and cross rolling; and, b) tubes fabricated by hydrostatic extrusion. The hot extrusion, at Case Western University, was carried out starting with a gun drilled thick wall tube on a mandrel. The tube was taken from the cross-rolled plate with its axis in the extrusion direction. Therefore, it is very important to define the primary deformation orientations for both processing conditions by referencing physically relevant directions. Figure 1a shows a schematic of the plate, defining the longitudinal (L), transverse (T) and short (S) directions as labeled accordingly along with primary deformation extrusion (L) and cross-rolling (T) coordinate system. Figure 1b shows the two relevant radial and extrusion directions for hydrostatic processing.

Microstructural characterization by SEM

Figure 2a and b show SEM images for LS and LT views, respectively, of the NFA-1 plate. Grains are elongated in the extrusion direction in case of LS view. Black Ti/Y rich precipitates along with the micro-cracks are seen in the SEM image for the LS view in Figure 2a, No microcracks are found for the LT view shown in Figure 2b. In case of tube, Figure 3 shows the SEM image of the polished surface of the sectioned tube normal to the extrusion direction.

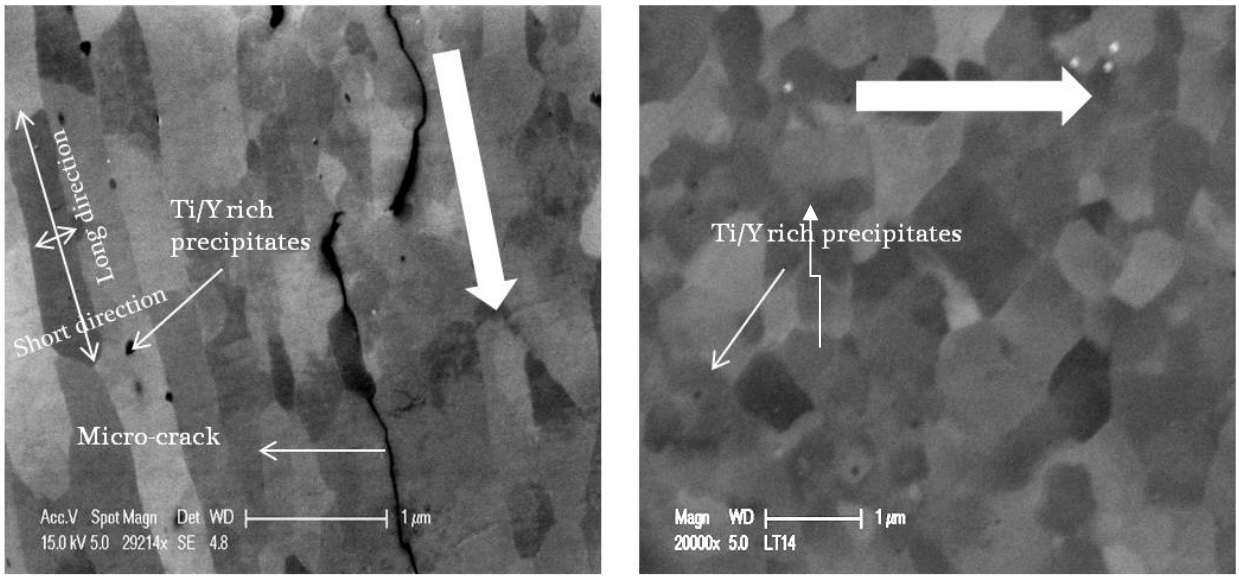

Figure 2. a) A SEM image for the LS view; b) a SEM image for the LT view. The large arrows mark the extrusion direction. Other components of the microstructure are labeled. The long and short dimensions of an individual grains are seen in the Figure 3a. The same method for grain size measurement is followed for the microstructural characterization of both tube and plate.

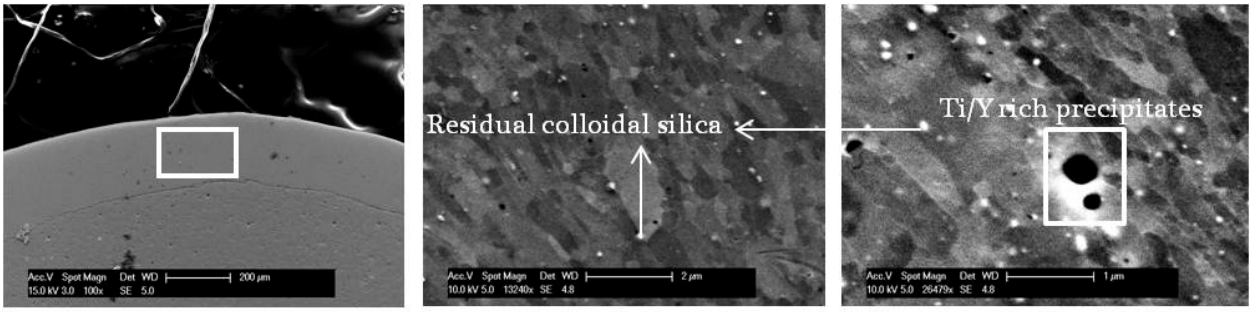

Figure 4. a) A low magnification SEM micrograph showing the tube wall cross section with the mandrel. The extrusion direction is normal to the image plane; b) a magnified view of the location marked by the white box in Figure 3a and, c) grains elongated in the radial direction (maximum sheer stress direction) of the hydrostatically extruded tube (see Figure 1b), where the dark particles are either Ti and Y rich precipitates, while the bright particles are residual colloidal silica.

The corresponding average grain sizes and standard deviations for the plane parallel to the top (LT) and side surface (LS) of the plate are summarized in Table 1. Here the grain size is taken as the average of the long and short dimension and the aspect ratio as the long divided by short dimension. The grains observed in the LS view parallel to the thickness direction have "flattened" shapes and are elongated along the observed extrusion direction. The grain size distributions and aspect ratio for the tube are also given in Table 1. The SEM micrographs of the tube section in Figure 3b and c reveal grains elongated in the radial direction. SEM images in Figure 2a and Figure 3c clearly show the plate's side (LS) view, the contrast-orientation differences between the elongated grains are much stronger in comparison to the tube. Most notably, hydrostatic extrusion does not result in the formation of the microcracks.

Table 1. Showing the grain size and aspect ratio for the plate and tube conditions.

Sample surface	Average grain size (μm)	Grain aspect ratio
LT plane for plate	454 ± 142	1.2 ± 0.2
LS plane for plate	1077 x 397	2.7 ± 1.1
Cross-sectional plane for tube	590 ± 210	2.1 ± 1.1

Microstructural characterization by TEM

Figure 4a shows a SEM image of the tube cross-section indicating the location of a FIB lift out at a ≈ 45° angle to the radial, maximum shear, direction. The FIBed foil face is parallel to the extrusion direction as shown in Figure 4b.

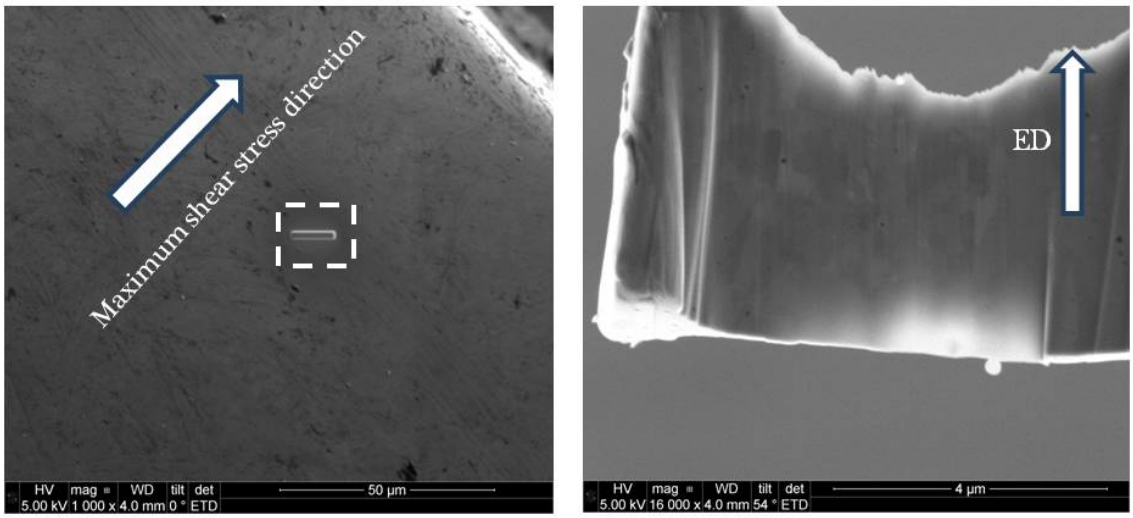

Figure 5. a) The location of TEM lift-out for the tube; and, b) the corresponding FIBed TEM foil.

The bright field (BF) TEM images in Figures 5a to d clearly demonstrate that hydrostatically extruded tube contains a significant population of dislocations in the vicinity of a low angle boundary, marked in Figures 5c and d. The boundary between the grains, marked by the dashed box, is ill defined, with minimum contrast between the two sides, indicating a low angle character.

In order to accurately determine the grain sizes in the tube, the circled grain in Figure 6a is tilted in a two-beam condition (see Figure 6b) and the corresponding dark field image is shown in Figure 6c. The SAD pattern from the circled region using the smallest 20 µm aperture in Figure 6b, shows overlap of the near <111> grains, with only a small angle of misorientation. The corresponding dark field (DF) image in Figure 6c shows that all the bright grains are roughly equiaxed. These observations lead to the conclusion that low angle grain boundaries exist in what appear in BF to be elongated grains. This also confirms our SEM observation of grains elongated along the radial direction of the tube with a minimal contrast between grains of either side of the boundary, as shown in Figure 3b and c. Both SEM and TEM observe a similar average small grain diameter of ~ 0.5 µm.

Figure 7 show BF and DF TEM images of the plate side LS view, where the foil area is perpendicular to the extrusion direction. Figure 7a shows that microcracks track the elongated grain with lengths of ~ 0.4 ± 0.1 and ~ 3± 1 µm along the short and elongated directions, respectively. The plate condition contains a high dislocation density. SAD patterns, at a 0° tilt, are shown in Figures 7b and c, for the two circled regions in Figure 7a. The SAD patterns show the two bcc <110>-zone axis are only slightly misoriented with respect to each other. The DF image in Figure 7d shows a trans-granular crack propagating through a (001) grain (the corresponding (002) spot is marked in Figure 7b with a white circle). The BF image shown in Figure 7f is for a <110>-zone axis. These results show that, in contrast to the tubing, in the NFA-1 plate condition, elongated grains are separated by high angle boundaries.

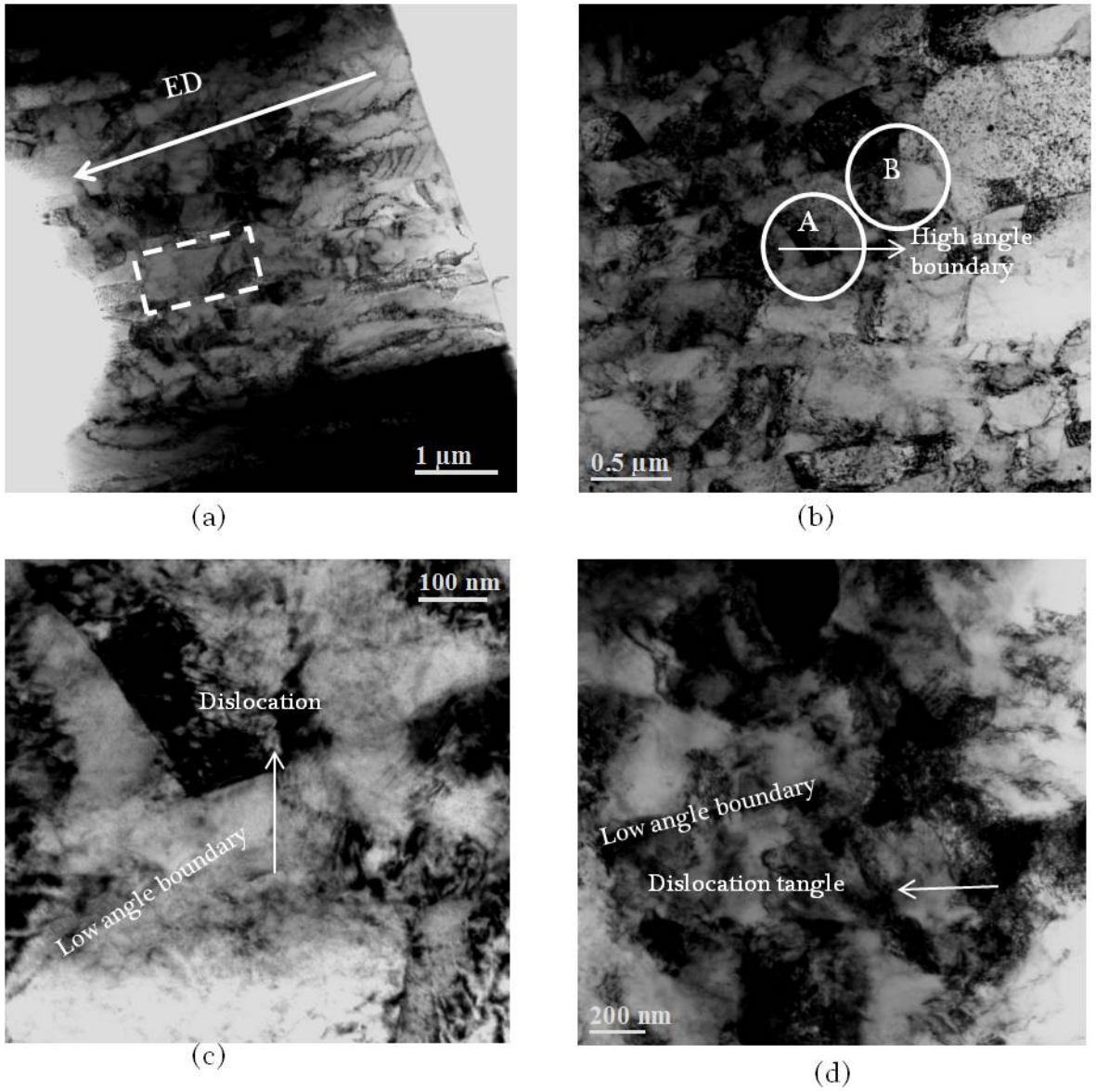

Figure 6. A bright field image of the tube microstructure at different magnifications:. a) the extrusion direction elongated grain structure; b) a high angle grain boundary; c) a magnified view of region marked as (A) in Figures 5b; d) a magnified view of region marked as (B) in Figure 5b showing low angle boundaries and dislocations tangles.

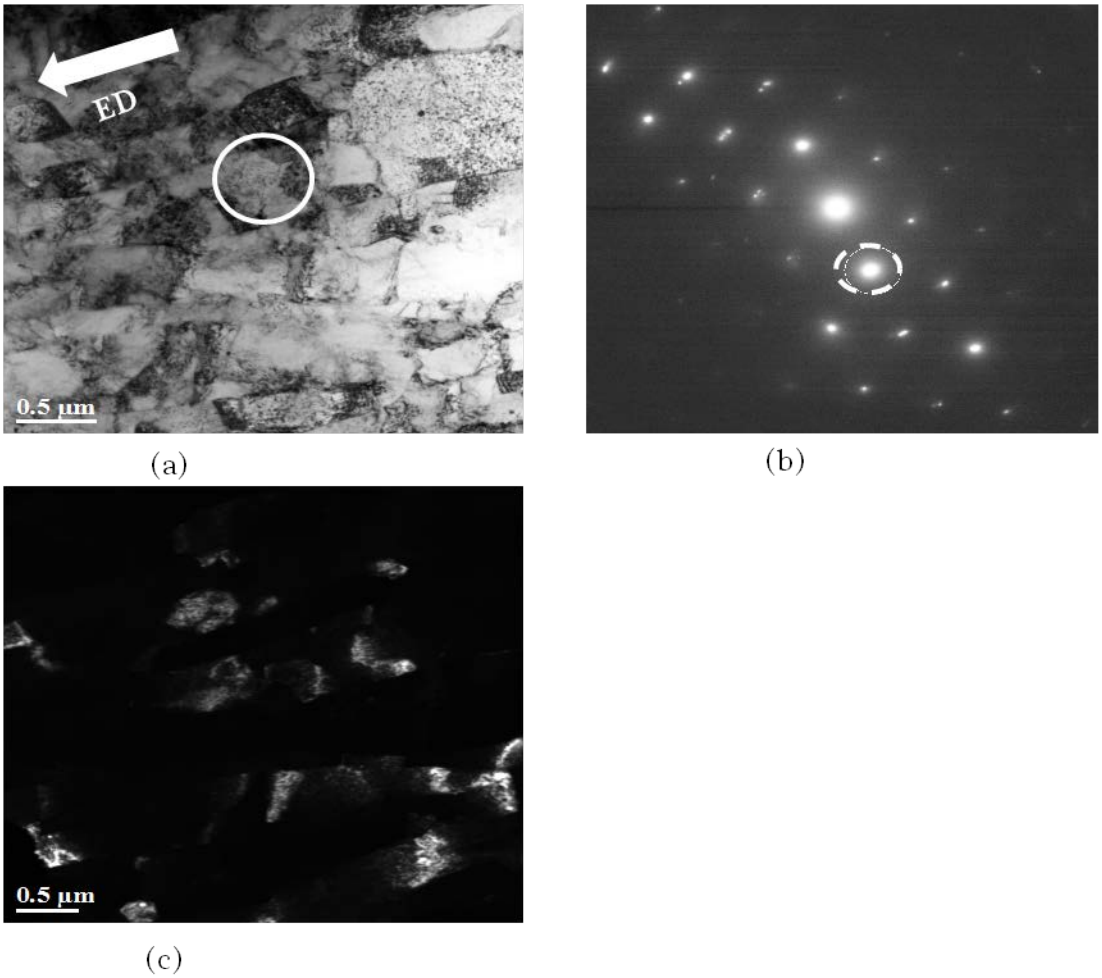

Figure 7. a) BF image of the tube microstructure; b) the SAD pattern for the circled region along the <111> zone axis under two beam conditions with the (110) bright spot circled; and, c) the dark field image of the (110) spot

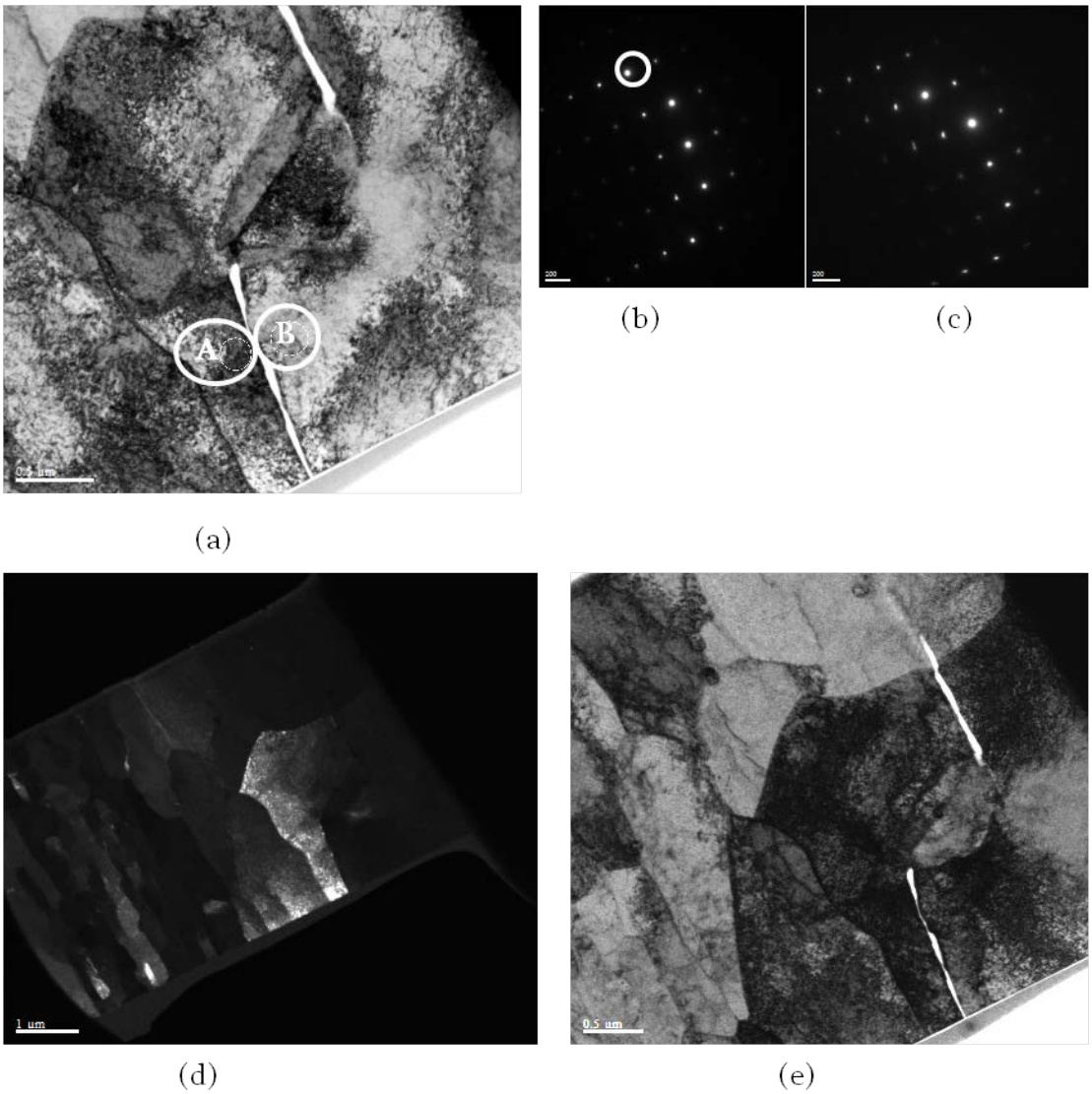

Figure 8. a) shows the BF image of the LS sample; b) and c) are the SAD patterns from the circled regions in a; d) a DF image from the circled SAD spot in Figure 6b; and, e) a BF image for a<110> zone axis.

Texture Characterization by EBSD

Texture measurements for both the NFA-1 processed conditions were carried out by EBSD. For the plate, EBSD was carried out on both the side-parallel (LS) and top-parallel (LT) views (as shown in the schematic Figure 1a). Pole figure (PF) maps for the LT and LS parallel surface planes are shown in Figure 8. The PF show that the plate contains strong α-fiber texture along the extrusion direction with a partial α-fiber along the cross-rolling direction. A prominent <100>-texture component is observed in the direction normal to LT parallel surface planes.

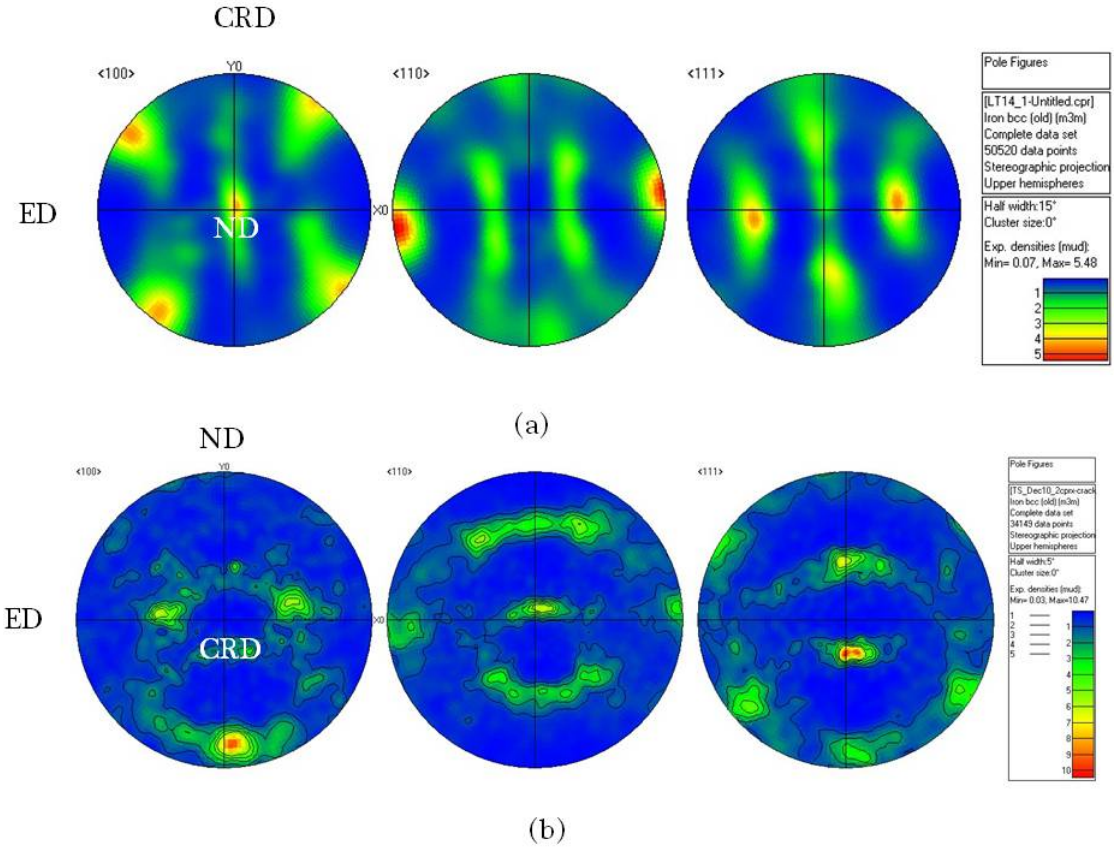

Figure 9. a) LT, and b) LS views: EBSD <100>, <110>, <111> poles of the plate sample, respectively. Equivalent deformation directions for the plate are also shown in the PF respectively by following the convention defined in Figure 1a and following text.

Texture measurements were carried out on a polished surface shown in the Figure 3a, normal to the extrusion direction. The texture of the tube is quite different compared to the plate as shown in Figure 9. The tube has a partial α-fiber texture in the extrusion direction.

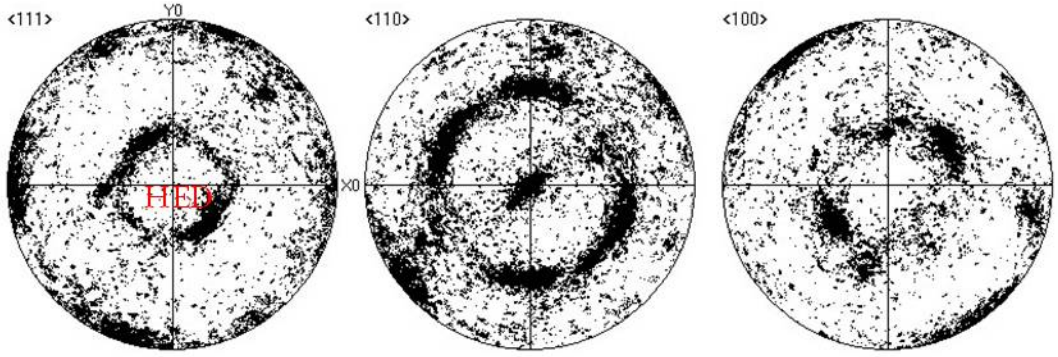

Figure 10. Pole <111>, <110>, <100> poles figures of the tube. Hydrostatic extrusion direction for the tube, schematically shown in Figure 1b, is also marked in the <111> pole figure of <111> pole.

PF analysis shows development of α-fiber along the extrusion direction for both the tube and the plate, while for the direction normal to the plate surface parallel planes and tube radius, the texture components are <100> and <111>, respectively. This observation is further corroborated in the inverse pole figures (IPF) in Figure 10, which show density of pole projections on a stereographic triangle with <001>, <110> and <111> vertices for the plate in the prime deformation directions.

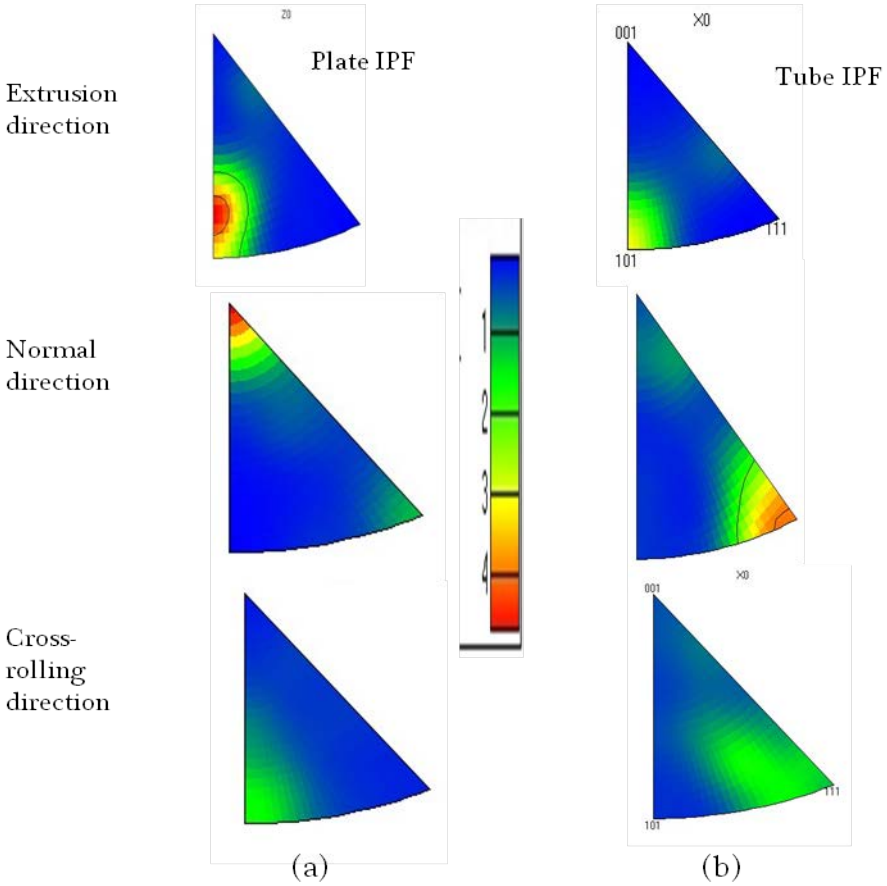

Figure 11. IPF maps of the tube and plate: a) the plate IPF for extrusion, surface normal and cross-rolling directions following the convention in Figure 1a; b) the tube radial direction, which is equivalent to the both cross-rolling and normal directions for the plate (see Figure 1b.) The extrusion direction is the same for both tube and plate.

The IPF analysis clearly demonstrates that while along the extrusion direction texture is similar for both the tube and plate, it differs in the normal direction: a strong <100> in along the normal direction for the plate, and <111> in the normal radial direction for the tube. The latter is also the direction of the maximum sheer stress in the case of the hydrostatic extrusion.

PF and IPF maps are basically a 2D stenographic projection of either crystallographic directions or the deformation directions for the plate or tube. A fully accurate description of the texture and its components is not possible using PF or IPF plots. A more accurate way of representing texture requires an orientation distribution function (ODF) analysis. All the possible orientations in a sample are projected in a 3D Euler space (defined by three Euler's angles of, ϕ, ϕ_1 and ϕ_2) as shown in Figure 11. Preferred orientations produce a high-density region around a certain combinations of these angles. Figure 12a shows a 3D ODF plot created from the PF data using the series expansion method [9]. For the ease of visualization, 2D sections of the 3D cube containing ϕ and ϕ_1 from 0 to 90° for constant value of ϕ_2 is shown in Figure 11.

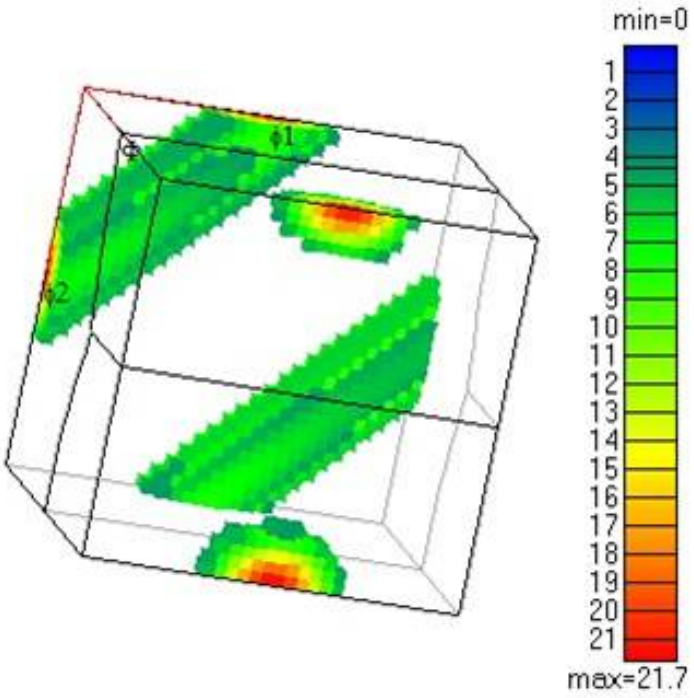

Figure 12. A 3D ODF plot for the plate.

The most important texture components for bcc steels occur at ϕ_2 = 0 and 45° sections [8], which are shown in Figures 12a, d and 12b,f for the plate and tube, respectively. Figures 12c and f show the ideal texture components for bcc steels (reproduced from Ref. [8]). These sections show the texture is completely different in the plate versus the tube. These ODF maps are compared with ideal ϕ_2 = 0 and 45° sections of bcc steel [8] shown in Figures 12c and f.

The texture components in the plate and tube are also shown on the ideal ODF plots as brown circle (plate) and blue box (tube), respectively. Notably the plate contains strong {001} <110> brittle cleavage texture components. Note, the PF and IPF analysis mainly showed a <110> α-fiber in the plate. However, the ODF analysis shows that α-fiber family contains three strong texture components: {001}<110>, {112}<110>, {111}<110>, with {001} <110> being by far the most dominant. Again, the {001}<110> α-fiber texture is also the most brittle cleavage system in bcc iron. This partly explains the origins of microcracking on (001) planes in the plate. The texture of the tube is quite different with dominant

components of {011}<211> and a lower fraction of {011}<111>. These two components belong to the ζ-fiber texture family as shown by the brown line in Figure 12c.

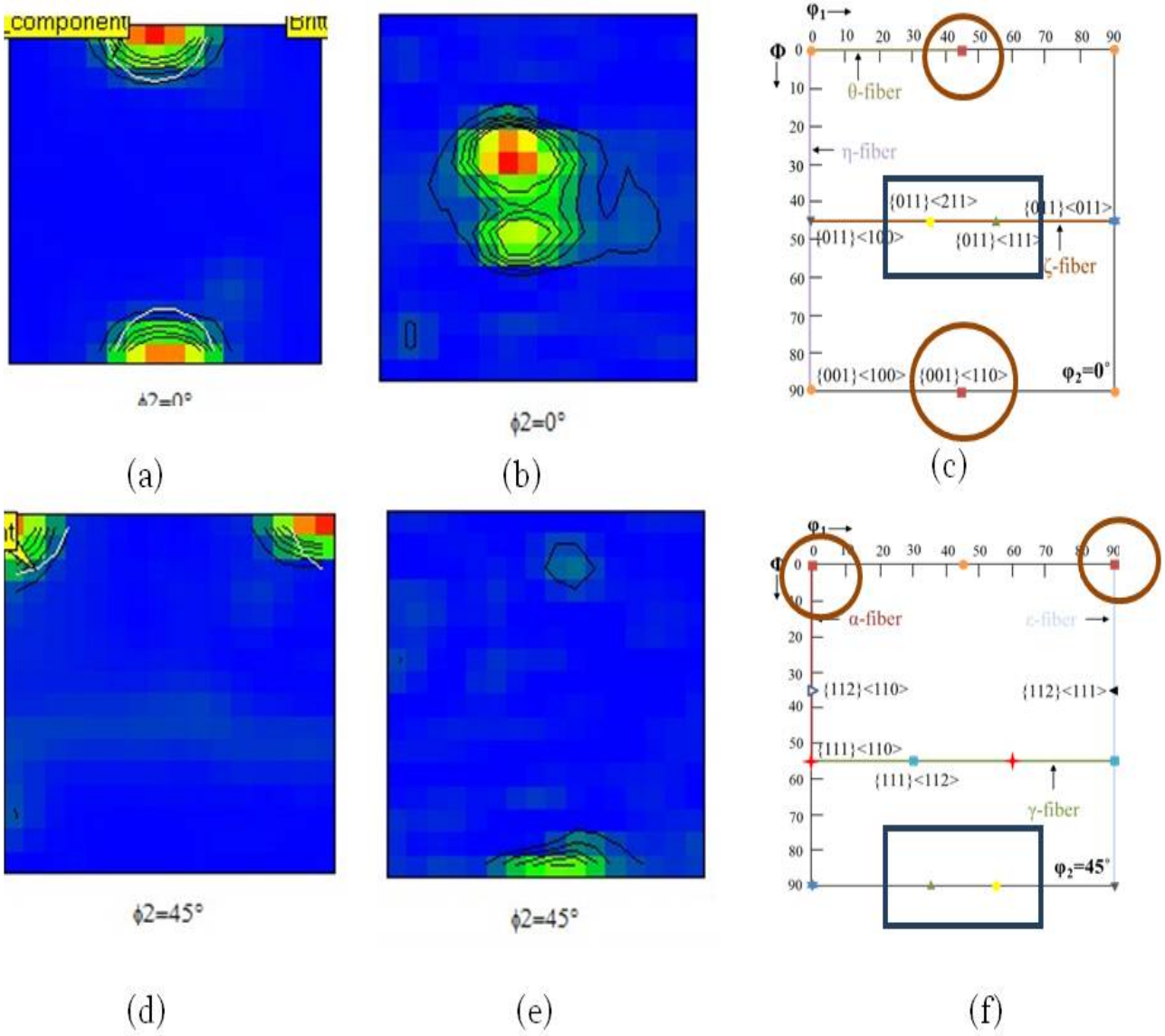

Figure 13. a), b) and c) (top) are ϕ_2 = 0 sections for the plate, tube and ideal ODF texture components for bcc steel, respectively [8]. Figures 12 d), e) and f) (bottom) are for the corresponding ϕ_2 = 45° section.

Conclusions

- Various characterization methods have been used to explore the microstructures and crystallographic textures that develop in NFA-1 under two deformation processing paths.
  In the case of the hot extruded and cross-rolled plate, the grains are elongated along the extrusion direction and a strong α-fiber texture develops along with a brittle cleavage {100}<011>-fracture system. This restricts glide on {100} planes lead to dislocation pile ups and stress concentrations with increasing strain, resulting in formation of corresponding population of micro-cracks.

- In case of hydrostatic extrusion of tubes, the grains are elongated along the maximum sheer stress direction and develop corresponding sheer texture components of {110} <112> and {110}<111>. Deformation occurs on {110}-bcc easy glide planes and is accompanied by formation of low angle sub grain boundaries. These microstructures and textures are not brittle, hence, cracking is not observed in the hydrostatically extruded tube.

Acknowledgments

This work is part of a multi-laboratory collaboration between LANL, UCSB and ORNL. The DOE Office of Fusion Energy Sciences partially supported the research reported here. NFA-1 was produced under the sponsorship of the DOE Office of Nuclear Energy through both a NEUP grant and the FCRD program.

References

[1] G.R. Odette, “Recent progress in developing and qualifying nanostructured ferritic alloys for advance fission and fusion applications”, JOM, Vol-66, Number-12, 2012, 2427-2441.
[2] M.E. Alam, N. J. Cunningham, D. Gragg, K. Fields, G. R. Odette, D. T. Hoelzer and S. A. Maloy**, “**Mechanical Properties Characterization of a Larger Best Practice Heat of 14YWT NFA1**”**, Fusion Reactor Materials Program, June 30, 2014, *DOE/ER-0313/56 – Volume 56.*
[3] J.J. Lewandowski and P. Lowhaphandu, **“**Effects of hydrostatic pressure on mechanical behaviour and deformation processing of materials”, International Materials Review, 43(4), (1998), 145-187.
[4] J.J Lewandowski, B. Berger, J.D. Rigney, and S. N. Patankar, "Effects of Dislocation Substructure on Strength and Toughness in Polycrystalline NiAl Processed via High Temperature Hydrostatic Extrusion", Philosophical Magazine A, 78 (3), (1998), 643-656.
[5] S. Ukai, “Perspective of ODS alloys application in nuclear environments”, Journal of Nuclear Materials, 307-311, (2002), 749-757.
[6] B. Leng, “Recrystallization texture of cold-rolled oxide dispersion strengthen ferritic steel”, ISIJ International, 51 (2011), 951.
[7] L. Toualbi, “Assessment of a new fabrication route for for Fe-9Cr-1W ODS cladding tubes”, Journal of Nuclear Materials, 442 (2013) 410-416.
[8] Un-published work – “Effect of tube processing methods on the texture and grain boundary characteristics of 14YWT Nanostructured Ferritic Alloys” - work carried out in LANL.
[9] H.J. Bunge, “Texture Analysis in Material Science: Mathematical methods”, Butterworths, London, p-323, 1982.

2.3 FABRICATION AND CHARACTERIZATION OF FE–{100}YTO BILAYERS —T. Stan, Y. Wu, and G. R. Odette (University of California Santa Barbara), H. D. Zhou (University of Tennessee)

OBJECTIVE

The objective of this work is to fabricate surrogate bulk Fe:$Y_2Ti_2O_7$ interfaces in the form of bilayers that are amenable to detailed characterization techniques and irradiation experiments.

SUMMARY

Nanostructured Ferritic Alloys (NFAs) have a Fe-Cr matrix and are dispersion strengthened by < 5 nm Y-Ti-O nano-oxide (NO) phases. The interfaces between the Y-Ti-O NO, such as $Y_2Ti_2O_7$ (YTO), and the surrounding matrix provide many favorable characteristics pertinent to fusion environments, such as trapping He in fine-scale bubbles. As a supplement to current characterization efforts of the NOs themselves, surrogate bulk Fe-YTO interfaces have been fabricated by electron beam Fe deposition on {100} YTO substrates. Grains with the {110}Fe||{100}YTO and <111>Fe||<110>YTO orientation relationship (OR) matched the two-fold symmetry of the {100}YTO substrate. This OR is not observed in embedded NOs. These results will support the development of computational models to predict NFA behavior.

PROGRESS AND STATUS

Introduction

Materials for nuclear fusion applications must reliably perform at high temperatures and manage high levels of helium (He). Nanostructured Ferritic Alloys (NFAs) are a promising class of Fe-Cr-based stainless steels that have remarkable mechanical properties, are thermally stable up to 1000 °C, and are irradiation tolerant [1-3]. NFAs contain a high density (~$10^{23}/m^2$) of 2-3 nm Y-Ti-O nano-oxide (NO) which help impede dislocation climb and glide, stabilize dislocation and grain structures, and trap He in fine-scale bubbles at matrix-NO interfaces that prevent void swelling and He embrittlement. Indeed, NFAs may turn He from a liability to an asset. For example, He bubbles act as recombination sites for vacancies and interstitials, thus promoting self-healing. The high density of matrix-NO interface pinning sites prevents He from collecting at grain boundaries, which would otherwise degrade creep and fracture properties.

There is ongoing research to determine the compositions, structures, and matrix-NO orientation relationships (ORs) for the NOs. A summary of these studies and other NFA properties was recently published by Odette [1]. The most common reported NO is $Y_2Ti_2O_7$ (YTO) fcc pyrochlore. Characterization and analysis of the NO:matrix interfaces is needed to develop first-principles atomic interface models necessary for predicting NFA performance in fusion reactor environments. YTO-matrix orientation relationships (ORs) are of interest because they affect interface defect structures, misfit strains, and energies.

There is a difference between bulk ORs and interfacial ORs. Bulk ORs refer to the overall relationship between two crystal lattices. The nomenclature involves listing any two non-linearly related parallel planes and directions between the lattices. Interfacial ORs describe the specific planes that are touching at an interface. The nomenclature involves listing the specific plane names and at least one set of parallel directions. Thus, a NO particle has only one bulk OR with the matrix, but may have many different interfacial ORs depending on the particle shape. In many cases, the 2-3 nm NOs have been shown to be cuboidal with flat matrix-YTO interfaces [4-6].

Cube-on-cube [4,5] and edge-on-cube [4,6] bulk ORs have been reported for embedded NOs. Their associated interfacial ORs have been summarized in Table 1, and are referred to as OReA – OReF where e refers to embedded. A schematic of each interfacial OR is shown with the surface orientation pointing out of page. The cube-on-cube bulk OR has interfaces where both matrix and NO faces (OReA), edges (OReB), or corners (OReC) are touching. The cuboidal NOs with cube-on-cube bulk OR have predominantly OReA and OReB interfacial ORs, and very small areas with OReC. The edge-on-cube bulk

OR has interfaces where a cube face is touching another face, or an edge. Note that some NO edges were blurry in Dawson et al. [4]; thus, the OReE interface may actually have been OReD. The ORs observed in this study are also listed in Table 1 as ORd1 – ORd3 where d refers to deposited.

Table 1. Reported bulk orientation relationships (ORs) and associated interfacial ORs.

Name	Bulk OR	Interfacial OR	Schematic	Reference
OReA	**Cube on Cube**	$\{100\}_{Fe} \parallel \{100\}_{YTO}$ $\langle 100\rangle_{Fe} \parallel \langle 100\rangle_{YTO}$ $\langle 110\rangle_{Fe} \parallel \langle 110\rangle_{YTO}$	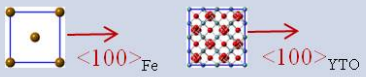	Dawson et al. Ribis et al.
OReB	**Cube on Cube**	$\{110\}_{Fe} \parallel \{110\}_{YTO}$ $\langle 100\rangle_{Fe} \parallel \langle 100\rangle_{YTO}$ $\langle 110\rangle_{Fe} \parallel \langle 110\rangle_{YTO}$	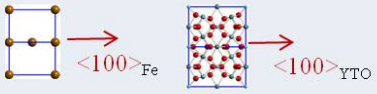	Dawson et al.
OReC	**Cube on Cube**	$\{111\}_{Fe} \parallel \{111\}_{YTO}$ $\langle 110\rangle_{Fe} \parallel \langle 110\rangle_{YTO}$	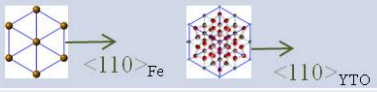	Dawson et al.*
OReD	*Cube on Edge*	$\{100\}_{Fe} \parallel \{100\}_{YTO}$ $\langle 110\rangle_{Fe} \parallel \langle 100\rangle_{YTO}$ $\langle 100\rangle_{Fe} \parallel \langle 110\rangle_{YTO}$	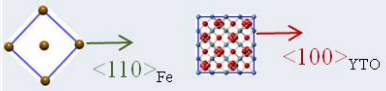	Dawson et al. Ciston et al.
OReE	*Cube on Edge*	$\{110\}_{Fe} \parallel \{100\}_{YTO}$ $\langle 100\rangle_{Fe} \parallel \langle 100\rangle_{YTO}$ $\langle 110\rangle_{Fe} \parallel \langle 100\rangle_{YTO}$	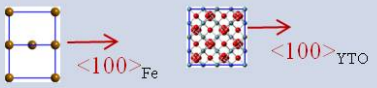	Dawson et al.**
OReF	*Cube on Edge*	$\{100\}_{Fe} \parallel \{110\}_{YTO}$ $\langle 100\rangle_{Fe} \parallel \langle 100\rangle_{YTO}$ $\langle 100\rangle_{Fe} \parallel \langle 110\rangle_{YTO}$	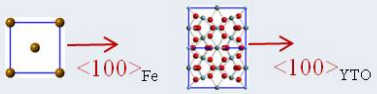	Ciston et al.
ORd1	**Edge on Corner**	$\{110\}_{Fe} \parallel \{111\}_{YTO}$ $\langle 100\rangle_{Fe} \parallel \langle 110\rangle_{YTO}$ $\langle 110\rangle_{Fe} \parallel \langle 112\rangle_{YTO}$	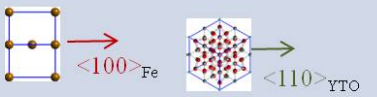	Fast Fe-{111}YTO
ORd2	*Cube on Corner*	$\{100\}_{Fe} \parallel \{111\}_{YTO}$ $\langle 100\rangle_{Fe} \parallel \langle 110\rangle_{YTO}$ $\langle 100\rangle_{Fe} \parallel \langle 112\rangle_{YTO}$		Slow Fe-{111}TYO 2-5 nm interfacial MO_x layer
ORd3	**Rotated Edge on Cube**	$\{110\}_{Fe} \parallel \{100\}_{YTO}$ $\langle 112\rangle_{Fe} \parallel \langle 110\rangle_{YTO}$ $\langle 111\rangle_{Fe} \parallel \langle 110\rangle_{YTO}$	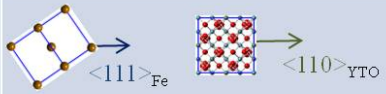	Fast Fe-{100}YTO

**The OReC interface is the least common. **The OReE interface may not actually be seen in NFAs.*

The nm-scale NOs are difficult to characterize using conventional microscopy techniques due to their small size. The research approach in this study is to deposit Fe on oriented YTO single crystal substrates to create surrogate mesoscopic-scale interfaces. These bilayers may or may not have similar interfacial characteristics to those found for embedded NO. Even if the bilayers do not have same characteristics as the embedded ones, this study will further the general understanding of metal-oxide interfaces. Surrogate interfaces are also amenable to irradiation studies such as interactions with point defects and He. Characterization of the Fe-YTO interfaces will help develop and improve first-principles atomic interface models, and help predict NFA performance.

Studies of Fe deposited on {111}YTO and {110}YTO were previously reported by Stan et al. [7] and in other Fusion Semiannual Reports [8,9]. This study is a continuation of the previous results by reporting depositions on {100}YTO single crystal substrates. The naturally selected interfaces are characterized and their implications to NOs in NFAs are discussed.

Experimental

The details of how samples were fabricated and the characterization instruments are covered in a previous publication [7]. In summary, YTO single crystals were {100} surface oriented and 2 mm thick wafers were cut using a wire saw. An Allied Multiprep instrument was used to polish the wafers using a sequence of diamond lapping films, followed by a final 15 minute polishing step using a 0.02 μm non-crystallizing colloidal silica suspension. Immediately after colloidal silica polishing and prior to Fe deposition, the substrates were placed under running water and gently scrubbed with Micro-Organic soap. This was followed by an acetone sonic bath for 10 minutes, and finally an isopropanol bath for 10 minutes.

An electron beam system was used to deposit Fe on the {100}YTO substrates at 800°C with a 10°C/min ramp up and down rate. While in the system and prior to Fe deposition, all of the substrates were left in vacuum at 800 ^{o}C for 1 hour. The deposition parameters are summarized in Table 2.

Table 2. Summary of deposition conditions.

Sample Name	Vacuum	Fe Thickness	Rate	Deposition time
Slow	8 x 10^{-6} torr	≈ 0.2 μm	0.3 nm/s	600 s
Fast	3 x 10^{-6} torr	≈ 2.0 μm	8.0 nm/s	250 s

Results

The following figures, each with parts a – g, show SEM and EBSD data that describe the depositions in this study. Part a is an SEM image or EBSD band contrast image showing grain size and shape. Part b shows EBSD inverse pole figure (IPF) maps depicting the out-of-plane crystallographic orientation of the Fe grains. Part c shows the same data as part b but represented as Euler pole figure (PF) maps indicating the full orientation of the Fe grains. In all figures, parts a – c show representative 10 μm by 10 μm areas such that the results can be easily compared for different depositions. Part d shows three PFs (<100>, <110> and <111> reflections) of the data shown in the maps of part a, colored according to the out-of-plane grain orientation (IPFZ). Part e shows three PFs of the Euler map in part c. Part f shows the substrate orientation as represented by PFs. Part g shows the 3D rendering of the Fe grains and substrate. The Fe-YTO ORs were obtained by overlapping spots in the Fe PFs with the accompanying YTO PFs.

<u>Slow Fe</u>

The first deposition was done using a slow rate of 0.3 nm/s to a total film thickness of 0.2 μm. The Fe grain size and topology are seen in Figures 1a-c. The grain size ranges from 0.5 – 2 μm, and the grains have an ~ 1:1 aspect ratio. Figure 1b is completely colored green indicating strong {110}Fe texturing. The Euler map in Figure 1c shows two dominant colors (blue and light orange) indicating two in-plane orientations of the Fe grains. The green areas in Figure 1c are believed to be mis-indexed portions of the blue grains.

The Fe PFs in Figures 1d–e have rings which usually imply a lack of in-plane orientation. However, the blue and light orange coloring indicates that there are two dominant orientations. The lack of distinct spots was previously believed to be caused by charging of the Fe film and misindexing of some grains. This effect was also present in later scans but removed for clarity. By overlapping select spots from the Fe PFs in Figure 1d with spots from the YTO PFs in Figure 1f, the following OR is obtained:

ORd3: {110}Fe || {100}YTO and <111>Fe || <110>YTO

This type of edge-on-cube orientation has not been observed for embedded NO in NFA. The 3D renderings in Figure 1g show that the Fe grains have a <111>Fe direction matched with one of the two <110>YTO in-plane directions. The blue and light orange grains have the exact same OR with the substrate, but are 90° rotated from one another and match the 2-fold symmetry of the underlying YTO.

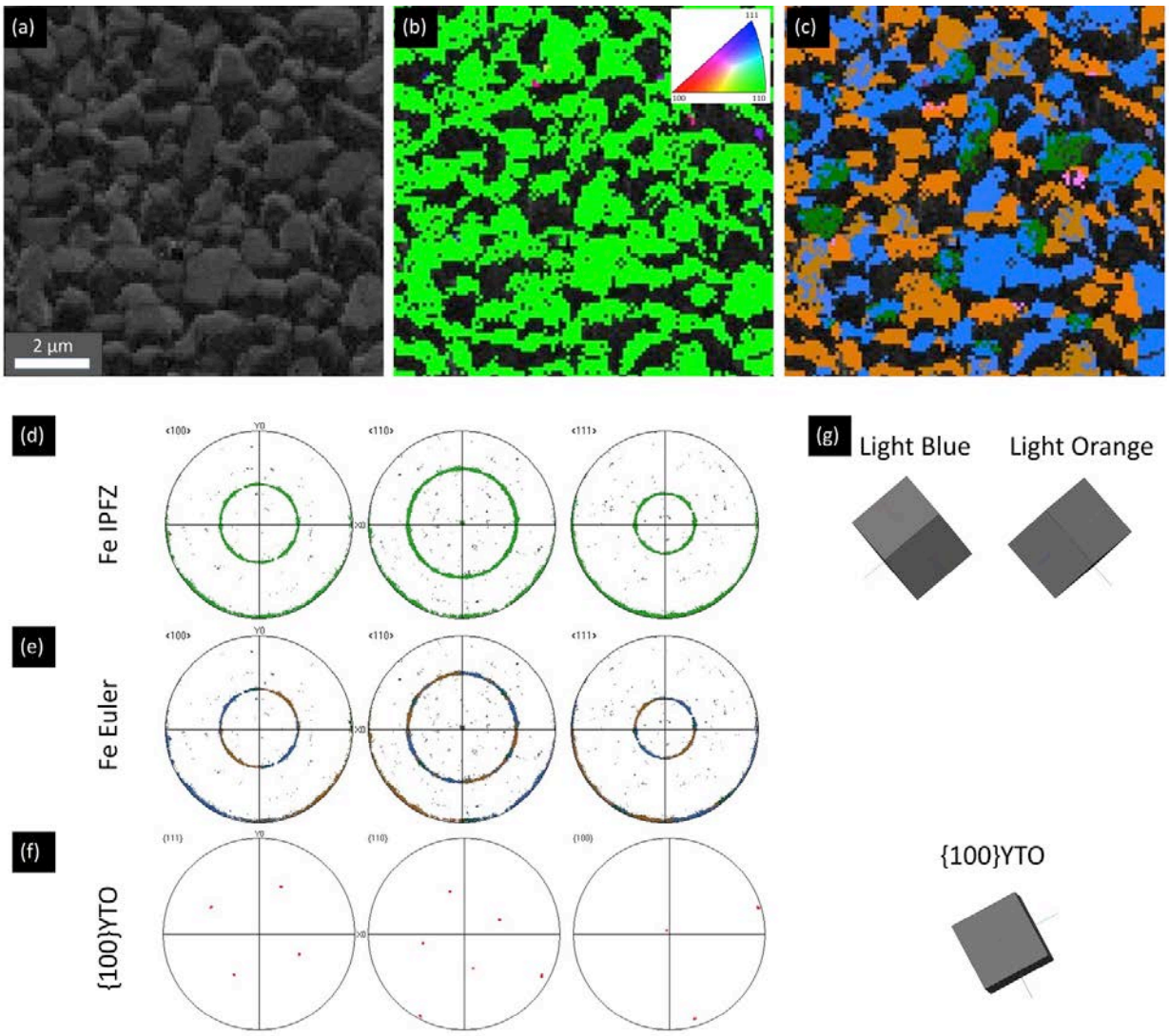

Figure 1. a) Band contrast, b) inverse PF map, and c) Euler map of the Fe film for the slow deposition. Fe PFs colored according to the d) out-of-plane orientation and e) Euler representation. f) YTO substrate PFs. g) 3D renderings of the Fe grains and YTO substrate.

Fast Fe

The previous deposition did not yield a large Fe film with a single dominant OR as desired. Thus the film was removed and the substrate was polished to have a new {100}YTO surface. The sample was cleaned and a thicker 2.0 µm film was deposited at a higher rate of 8 nm/s. A thicker film was chosen to ensure full coalescence of the Fe layer. A faster deposition was used to get a higher purity Fe film.

Figure 2a is an SEM image of the Fe film showing larger ~2 µm grains. Surface charging prevented large EBSD scans, thus smaller 6 µm by 6 µm data sets were collected. The EBSD data are shown in

Figures 2a–f and the results are consistent with the slow deposition. The rings in the PFs have been digitally removed and the dominant ORs are clearly visible as:

ORd3: {110}Fe || {100}YTO and <111>Fe || <110>YTO

The light blue and light orange grains are 90° rotated from each other and have only one OR with the substrate. This OR was not observed for embedded NOs.

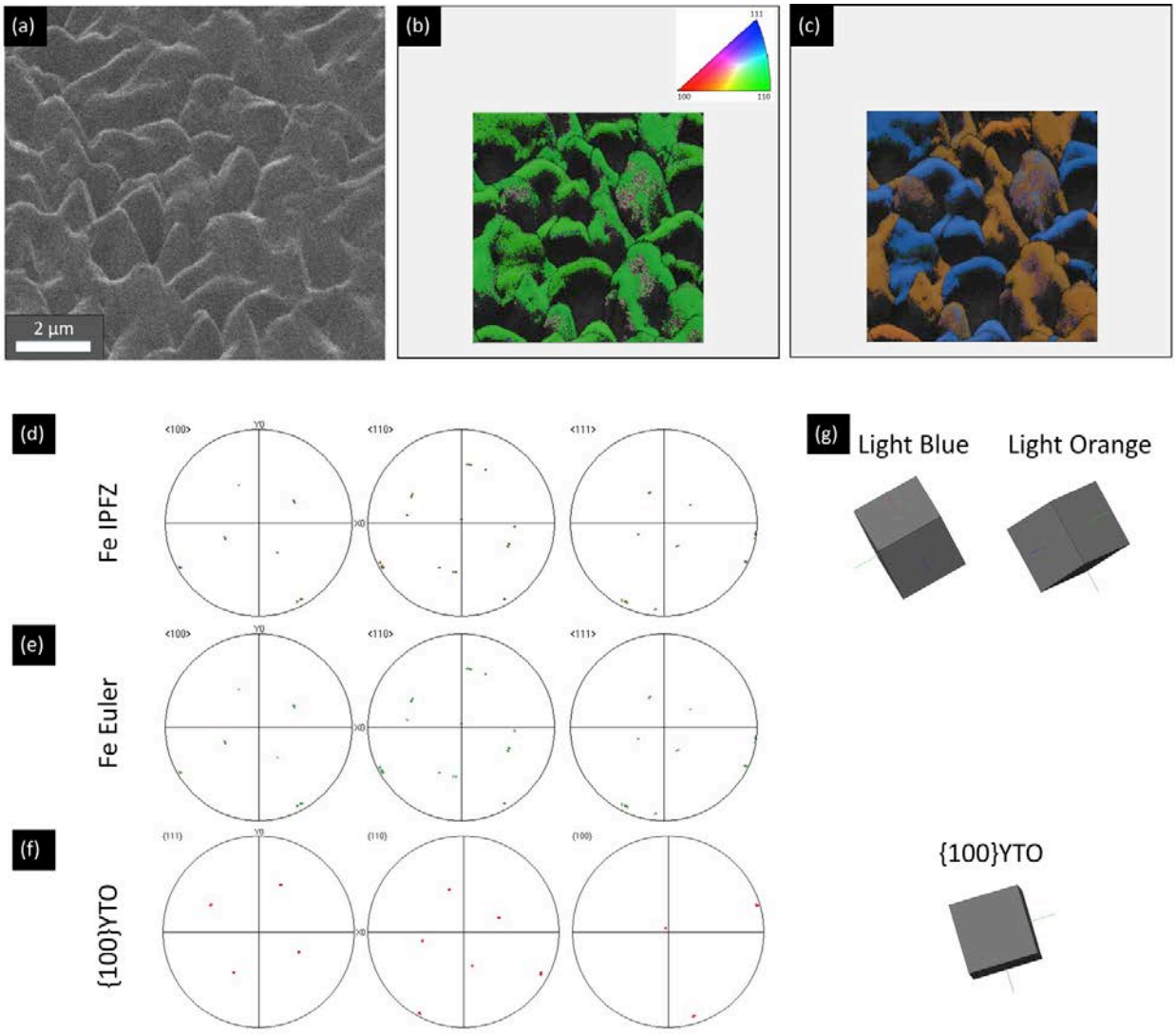

Figure 2. a) SEM image, b) inverse PF map, and c) Euler map of the Fe film for Area 1 of the fast deposition. Fe PFs colored according to the d) out-of-plane orientation and e) Euler representation. Note that the rings in the PFs were removed to isolate the dominant grain orientation. f) YTO substrate PFs. g) 3D renderings of the Fe grains and YTO substrate.

Discussion and Future Studies

The OR observed for the deposited film is {110}Fe||{100}YTO and <111>Fe||<110>YTO. Preliminary HRTEM and STEM data indicate that the grains have a relatively thick interlayer (~ 5 nm). This was

seen previously [7] where the presence and thickness of a metallic oxide interlayer directly affected the Fe grain orientation. Further, some areas of the two previously discussed films had areas with {110} textured Fe grains but no low-index in-plane matching. The cause of these areas will be investigated.

Three other depositions on {100}YTO were carried out, but the results were clearly affected by artifacts during the deposition. The Fe films had randomly oriented grains which are not useful for Fe-YTO studies. These films will be removed and the substrates will be re-polished. The e-beam system has been cleaned and repaired in preparation for future depositions.

Further, two depositions of Fe on amorphous silica substrates were carried out. The first used the Fe electron beam deposition system at a temperature of 800°C and ~10^{-6} torr as in previous studies. The Fe grains were mostly randomly oriented, with some grains exhibiting a {100}Fe texturing and random in-plane orientation. A similar experiment was done using an electron beam in a molecular beam epitaxy system at 100°C and ultrahigh vacuum of 10^{-10} torr. The two experiments yielded similar grain morphologies with mostly randomly oriented Fe grains and some {100} Fe texturing. These results are being analyzed in more detail.

The bilayers are being prepared for future He implantation and dual-beam irradiation studies. The results will help inform first-principle models of metallic oxide interfaces, as well as reaction-rate theory models for predicting NFA behavior.

References

[1] G. R. Odette, JOM. 66, 12, (2014) 2427
[2] G. R. Odette, M. J. Alinger, B. D. Wirth, Annu. Rev. Matter. Res. 38 (2008) 471
[3] Y. Dai, G. R. Odette, T. Yamamoto, Comp. Nuc. Mat. (2012) Elsevier
[4] K. Dawson, G. J. Tatlock, J. Nuc. Mat. 444 (2014) 252
[5] J. Ribis, Y. de Carlan, Acta Mat. 60 (2012) 238
[6] J. Ciston, Y. Wu, G. R. Odette, et al., Fus. Mat. Semiann. Prog. Rep. (2012) DOE-ER-0313/51
[7] T. Stan, Y. Wu, G. R. Odette, et al., Metal. and Mater. Trans. A, 44, 10 (2013) 4505
[8] T. Stan, Y. Wu, G. R. Odette, Fus. Semiann. 56 (2013) DOE-ER-0313/56
[9] T. Stan, Y. Wu, S. Kraemer, et al., Fus. Semiann. 57 (2014) DOE/ER-0313/57

2.4 IRRADIATION-DAMAGE BEHAVIOR IN ADVANCED STEELS — C. M. Parish, Y. Katoh, M. E. Bannister, K. A. Unocic, L. Tan, B.-K. Kim, D. T. Hoelzer (Oak Ridge National Laboratory), and S. J. Zinkle (University of Tennessee)

OBJECTIVE

Determine the helium mitigation response of candidate steels (NFA, CNA, ODS-FeCrAl) and compare relative to each other.

SUMMARY

Four iron-based alloys were investigated: a 9Cr NFA "9YWTV" containing Y-Ti-oxides, a 9Cr CNA containing TaC precipitates, and two Fe-12Cr-5Al ODS alloys containing mixed populations of Y-Al-oxides, Y-Zr-oxides and Y-Hf-oxides. In a D-T burning plasma environment, the 14 MeV neutrons produce copious helium transmutation and the materials ability to mitigate helium effects must be characterized for future fusion materials selection and development. Here, sequential He and Fe ion irradiation is combined with advanced post-irradiation characterization to compare the four materials' helium mitigation.

PROGRESS AND STATUS

Introduction

As a screening experiment to begin understanding helium mitigation effects, 650°C sequential irradiations were performed at the ORNL MIRF facility; simultaneous dual-beam irradiations are presently underway at the Kyoto University DuET facility. 9YWTV NFA (nanostructured ferritic alloy), 9Cr CNA (cast nanostructured alloy), and two Fe-12Cr-5Al ODS (oxide-dispersion strengthened) alloys (Y-Zr FeCrAl and Y-Hf FeCrAl) were irradiated. Advanced characterization was used with the intent of analyzing the changes to the microstructure driven by the irradiation, particularly to determine how helium bubbles are dispersed in the four different materials. Because no intense 14 MeV neutron sources are available, these accelerator-based tests are the most effective way to screen candidate alloys for helium mitigation potential.

Experimental Procedure

The alloys were mechanically polished to colloidal silica and irradiated at 650°C to provide ~800 appm He, followed by 2.75 MeV Fe ion irradiation to produce a midrange dose of ~50 dpa at 650°C; Figure 1.

Samples for electron microscopy were prepared by FIB (focused ion beam) milling from the irradiated areas. S/TEM (Scanning / transmission electron microscopy) was performed using FEI Tecnai T20 or FEI Talos F200X instruments at ORNL. In particular, STEM imaging using conventional and Fresnel-STEM [1] modes were used to image precipitates and helium bubbles simultaneously. X-ray spectrum images (SIs) were taken using the F200X instrument's high-efficiency, 4-detector system. Some of the SIs were analyzed using the Sandia National Laboratory AXSIA computer code [2] to perform multivariate statistical analysis [3].

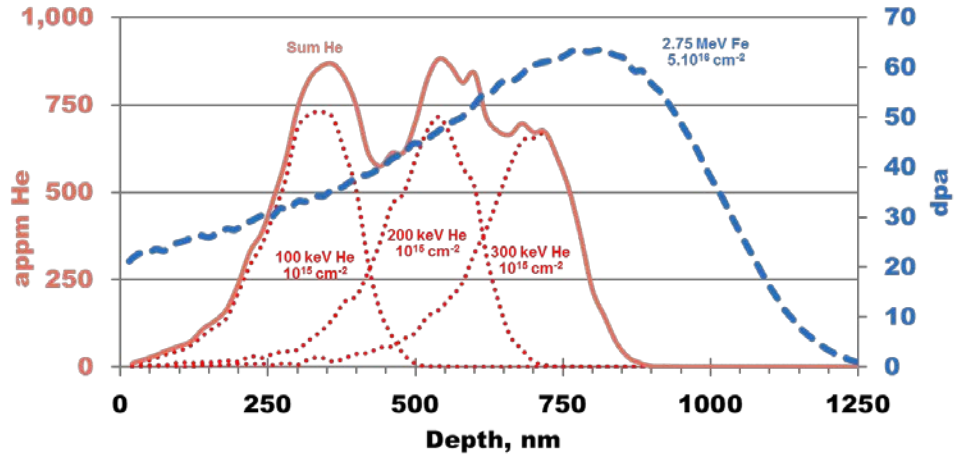

Figure 1. SRIM-software calculations of the expected He and dpa profiles for the irradiations. The appm/dpa ratio is ~10-20, reasonably representative for a fusion spectrum on a ferritic steel.

Results

Analysis of the samples is presently underway; however, preliminary scoping results, especially indicating the capabilities of the new F200X microscope at ORNL to explore helium mitigation, will be presented here.

The 9YWTV NFA material, under the present sequential 650°C irradiations, appears to have best sequestered the helium in terms of uniform matrix dispersal, compared to the other three materials (CNA, Y-Zr FeCrAl, Y-Hf FeCrAl). Experiments are ongoing and this preliminary observation may be revised. The 9YWTV shows the smallest helium bubbles, and a large fraction of the bubbles are captured in the grain interiors, away from the grain boundaries.

For instance, Fresnel-contrast BF STEM and HAADF STEM at ~700 nm depth (~800 ppm He, ~50 dpa) shows a high density of very fine bright/dark features in Fresnel imaging, presumed to be bubbles, along with bands of dark features in HAADF, presumably nanoclusters (Figure 2). An X-ray mapping experiment was performed in the F200X instrument, which provided a high statistical confidence for mapping the locations of the nanoclusters (Figure 3).

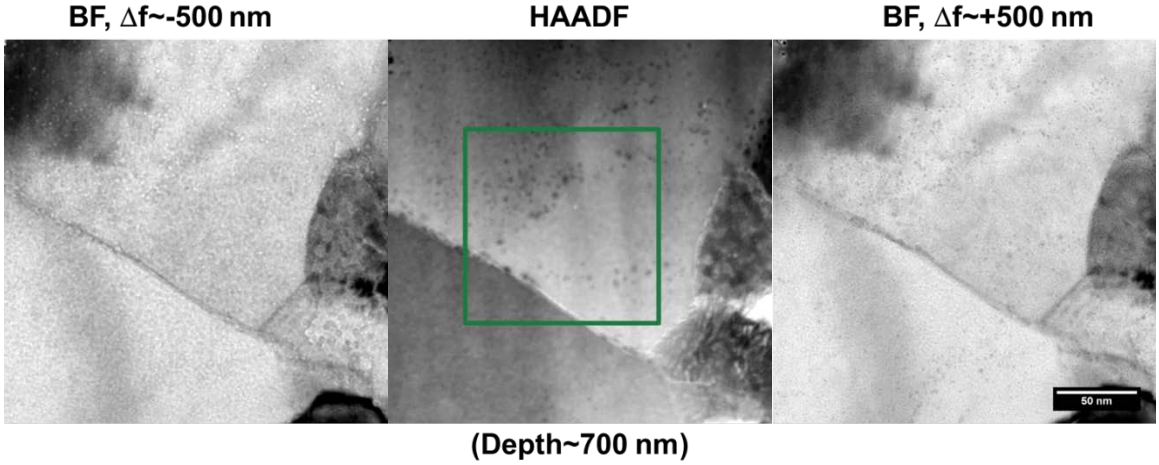

Figure 2. 9YWTV, sequential He + Fe irradiation, 650°C. Fresnel BF-STEM and HAADF-STEM images showing void-like contrast (presumably He bubbles) along with grain boundary and precipitates.

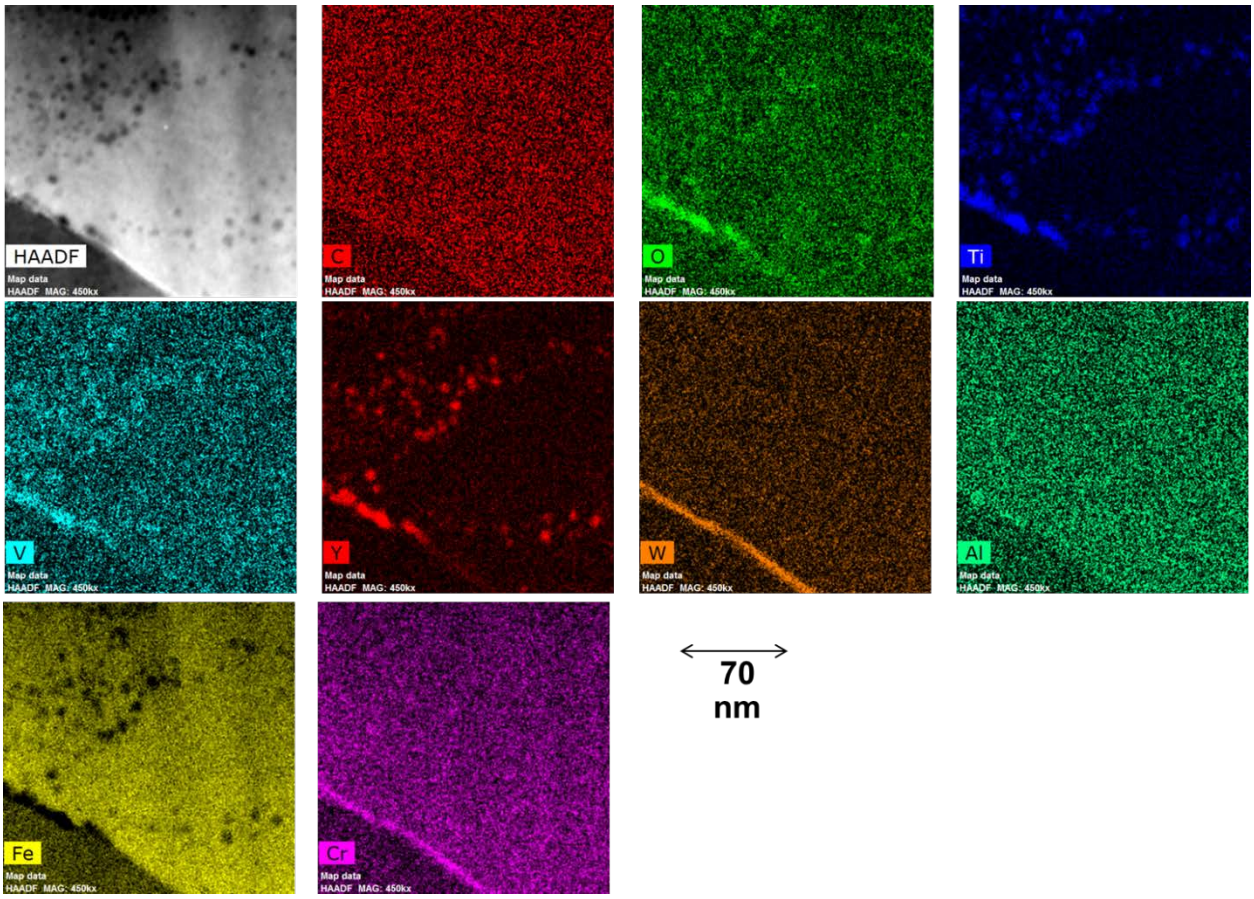

Figure 3. Same area as Figure 2, X-ray mapping. Note Cr-W on grain boundary and Y-Ti-O in nanoclusters.

The distribution of the nanoclusters can be more precisely defined by applying MVSA to the spectrum image dataset from which the X-ray maps (Figure 3 above) were extracted. MVSA analysis (Figure 4) decomposed the data into three underlying components, indicating matrix (Fe-Cr), grain boundary enrichment (Cr-W) and nanoclusters (Ti-Y-O). Most importantly, the visibility (contrast) of the nanoclusters is improved (Figure 3, right panel) compared to their visibility in the X-ray maps (Figure 2) due to the statistical ensemble averaging of the data.

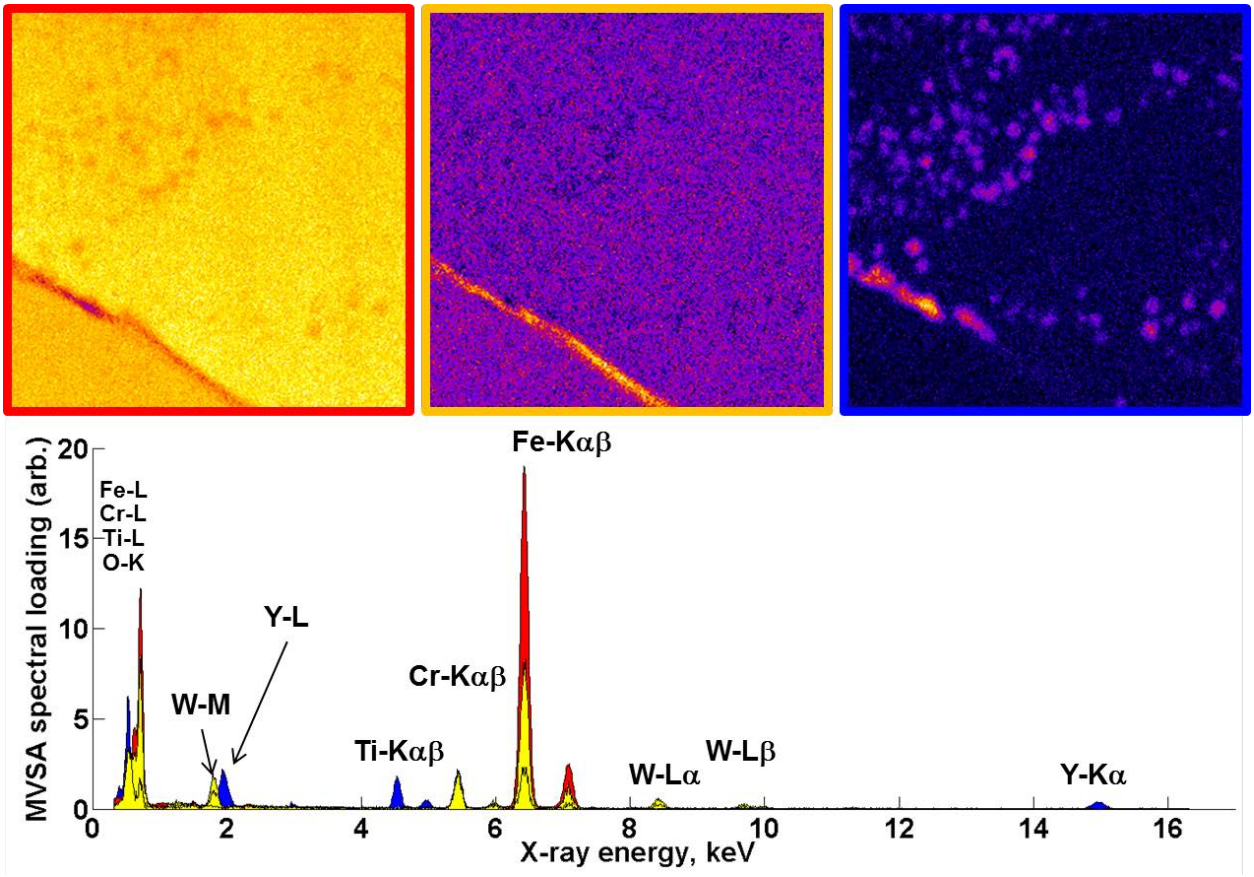

Figure 4. Multivariate statistical analysis of the X-ray mapping data in Figure 3. Note improved visibility of the nanoclusters (blue spectrum, blue-bordered image) compared to the X-ray maps (Figure 3).

Combining the MVSA component image with the Fresnel-contrast STEM image (Figure 5) indicates that the bubble-like contrast and the nanoclusters appear to be closely associated; there appear to be slightly more bubbles than nanoclusters, however. This implies that the nanoclusters are sequestering the helium effectively, although further confirming experiments are needed.

The CNA alloy appears to show more helium bubbles at dislocations, grain boundaries and lath boundaries, and larger bubbles, than the 9YWTV alloy (Figure 6). X-ray analysis indicates significant Ti content at or near the same locations as the Fresnel contrast of the bubbles. X-ray mapping (Figure 7) and MVSA (Figure 8) show the same result.

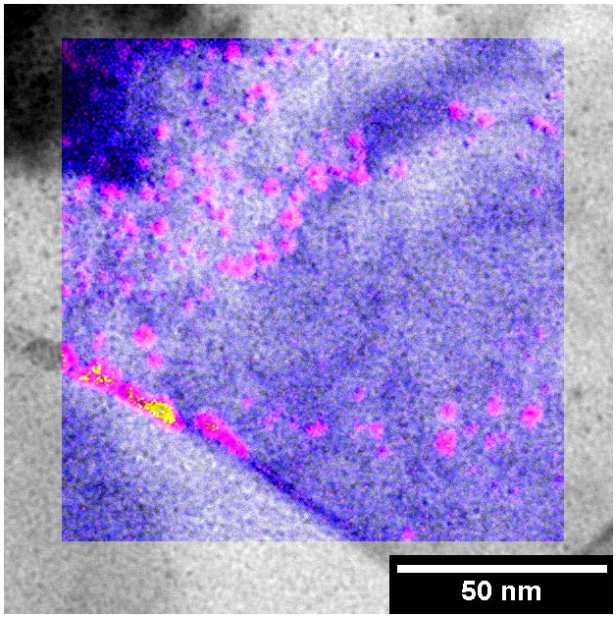

Figure 5. MVSA nanocluster map overlaid onto the Fresnel-STEM image. It appears that the presumed bubble contrast is mostly associated with the nanocluster features.

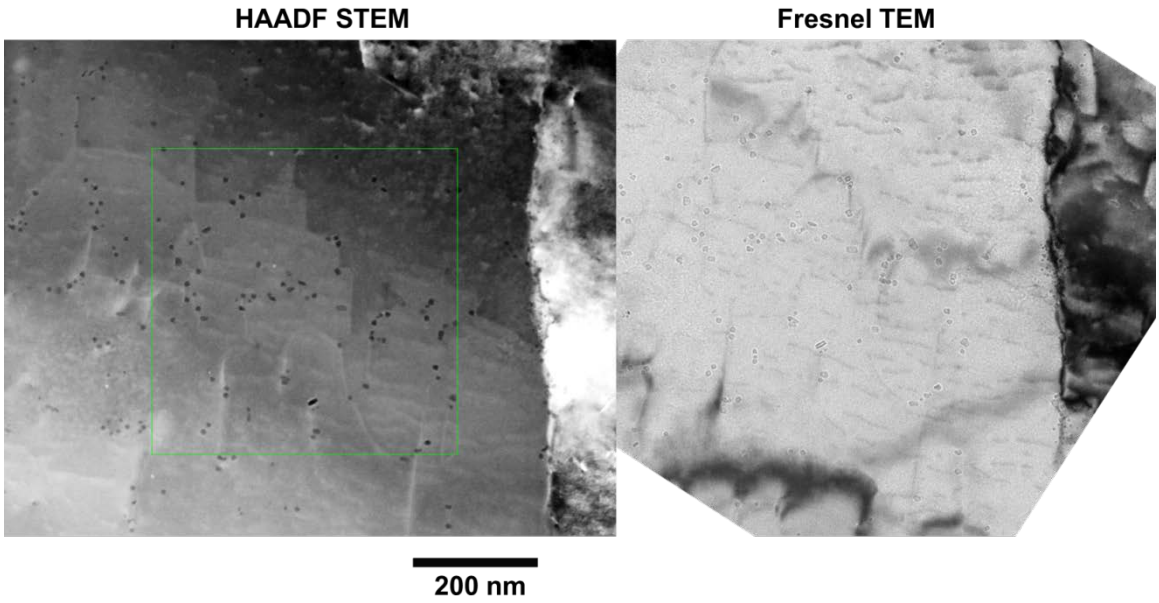

Figure 6. HAADF-STEM image showing low-atomic-number regions (bubbles or precipitates), and Fresnel TEM image, showing void contrast.

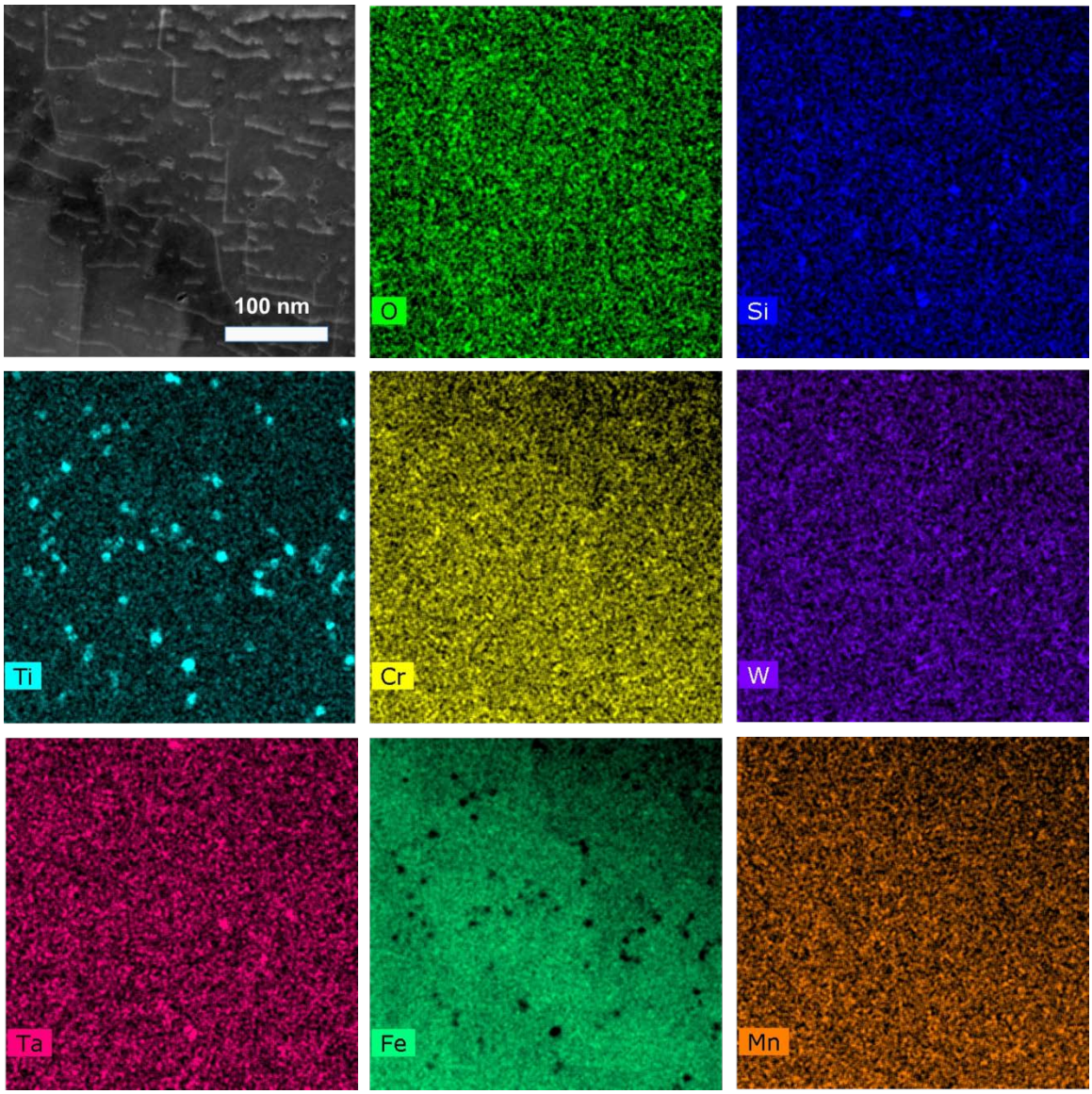

Figure 7. HAADF-STEM image and X-ray maps from the area of Figure 6. Note the Ti-rich regions that appear associated with cavity-like contrast.

Although further microscopy, and perhaps atom probe tomography, is needed, it is possible that the Ti-rich features in Figures 7 and 8 may be helium bubbles, showing Ti-enrichment to the region of the bubbles, or perhaps to their surfaces.

Further work on unirradiated regions of the CNA alloy (to compare to Figures 6-8), and characterization of the bubbles in the He+Fe irradiated FeCrAl samples, is presently underway. The dual-ion-beam irradiated samples will also be examined for comparison to these sequentially-irradiated samples.

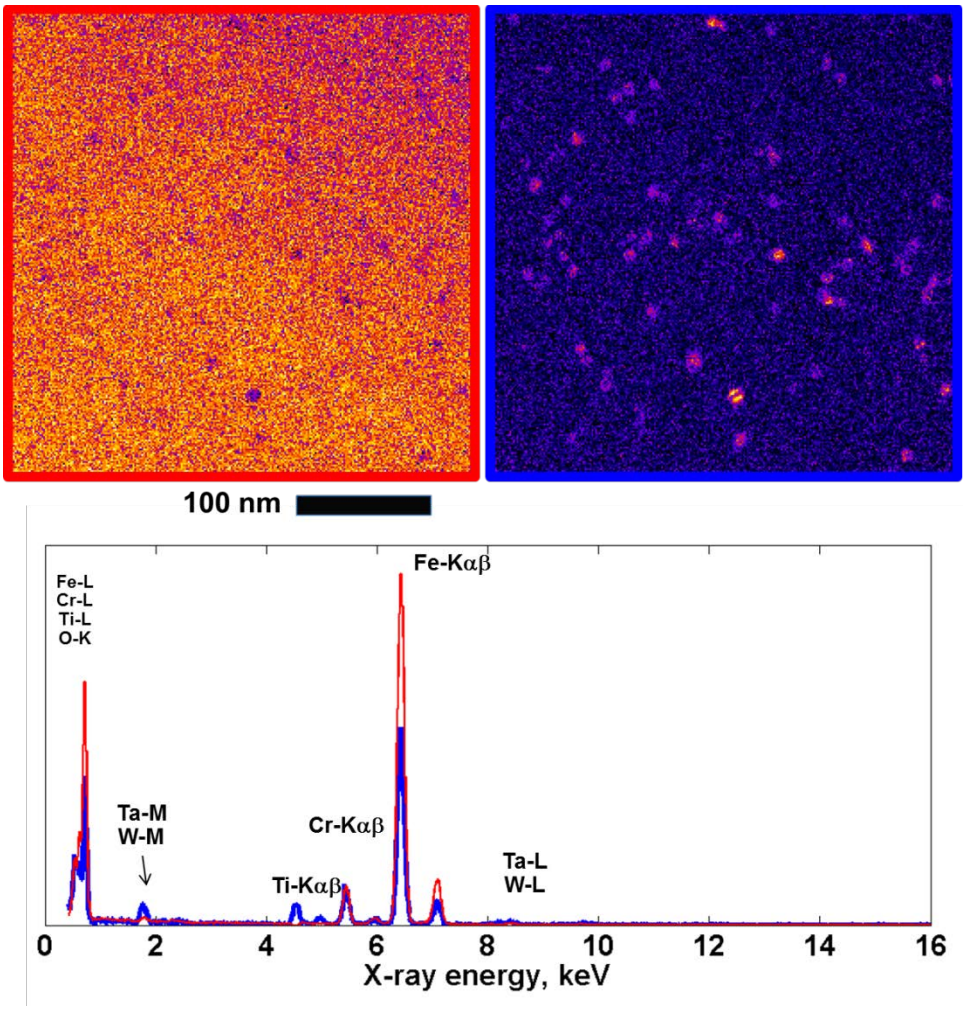

Figure 8. MVSA component maps and spectra of the X-ray data presented in Figure 7. Strong Ti contrast is associated with the features seen in the X-ray maps.

Acknowledgements

9YWTV material provided by Dr. T. S. Byun. Talos F200X STEM provided by the Department of Energy, Office of Nuclear Energy, Fuel Cycle R&D Program and the Nuclear Science User Facilities.

References

[1] C.M. Parish, M.K. Miller, Aberration-Corrected X-Ray Spectrum Imaging and Fresnel Contrast to Differentiate Nanoclusters and Cavities in Helium-Irradiated Alloy 14YWT, Microscopy and Microanalysis, 20 (2014) 613-626.

[2] P.G. Kotula, M.R. Keenan, J.R. Michael, Automated analysis of SEM X-ray spectral images: a powerful new microanalysis tool, Microscopy and Microanalysis, 9 (2003) 1-17.

[3] C.M. Parish, Multivariate Statistics Applications in Scanning Transmission Electron Microscopy X-Ray Spectrum Imaging, in: P.W. Hawkes (Ed.) Advances in Imaging and Electron Physics, Vol 168, 2011, pp. 249-295.

2.5 MICROSTRUCTURAL SUMMARY OF ODS FERRITIC ALLOYS (14YW, 14YWT, 12YWT, MA957FR, PM2000) AND RAFM STEELS (F82H MOD.3-CW, EUROFER97) FROM JP27 IN-SITU HE INJECTION (ISHI) EXPERIMENT AT 500°C —

H. J. Jung, D. J. Edwards, R. J. Kurtz (Pacific Northwest National Laboratory), G. R. Odette, Y. Wu, T. Yamamoto (University of California Santa Barbara)

OBJECTIVE

To summarize the microstructural response of oxide dispersion strengthened (ODS) ferritic alloys (14YW, 14YWT, 12YWT, MA957Fr, PM2000) and reduced activation ferritic/martensitic (RAFM) steels (F82H mod.3-CW, Eurofer97) irradiated in the JP27 irradiation experiment in HFIR at 500°C with *in situ* He injection (ISHI).

SUMMARY

A TEM characterization of various ferritic-based alloys has been conducted to document the changes in microstructure under neutron irradiation with and without the impact of high levels of He injection. Microstructural features such as dislocation loops, network dislocations, He bubbles and voids were characterized in five ODS alloys, 14YW, 14YWT, 12YWT, MA957Fr, PM2000, and two RAFM steels, F82H mod.3+CW and Eurofer97. The total neutron dose was ~21.2 dpa and the total He level was ~1230 appm injected into an ~6 μm uniform region below the surface of the sample. The results indicated that He injection significantly impacts the microstructure evolution path, producing changes in the dislocation structure and cavity distribution that are closely related to the size, density and chemistry of the oxide particles, or the lack thereof in the case of the RAFM alloys.

PROGRESS AND STATUS

Introduction

Oxide-dispersed strengthened (ODS) ferritic alloys, nanostructured ferritic alloys (NFA) and reduced activation ferritic/martensitic (RAFM) steels are generally swelling-resistant under neutron irradiation [1,2]. However, the swelling resistance of RAFM steels could degrade in the presence of high levels of helium (10 appm He per dpa) produced by transmutation in the fusion nuclear environment [3]. Over the lifetime of the first wall, up to ~2000 appm of helium will accumulate in these materials, leading to helium bubble formation, hardening of the matrix, and possibly loss of creep-rupture strength at high irradiation temperatures. A potential consequence of helium accumulation is that small bubbles (d<2 nm) can grow to a critical size and convert to unstably growing voids, thereby causing significant swelling [4]. In order to prevent the transition of He bubbles to voids, microstructures are being designed to provide a high density of nanoscale trapping sites such as nano-size oxide particles to broadly disperse He gas atoms [1] so that bubbles do not reach the critical size. We are currently examining the effectiveness of oxide dispersions, as well as elucidating the mechanisms of He movement, trapping, and interaction with various defects and interfaces in ODS ferritic alloys and RAFM steels under irradiation.

Due to practical difficulties in exploring material performance in a fusion-relevant irradiation environment, the *in situ* He injection (IHSI) technique has been developed to explore the effects of simultaneous neutron irradiation and He injection on microstructural evolution of candidate materials, as detailed in the recent literature [5-9]. Here we present analytical transmission electron microscopy (TEM) characterization of neutron-irradiated and He/neutron-irradiated effects on ODS ferritic alloys, nanostructured ferritic alloys and RAFM steels with a NiAl layer deposited on one surface. When irradiated with neutrons, the ^{59}Ni isotope undergoes a ^{59}Ni(n, α) reaction and injects some fraction of the energetic He into the ferritic alloy. Cross-sectional TEM samples were prepared to characterize microstructural features such as He bubbles/voids, dislocation loops/line dislocations, and oxide or carbide particles.

Experimental Procedure

Three NFAs, 14YWT, 12YWT, MA957Fr, two ODS ferritic alloys 14YW and PM2000, and two RAFM steels (F82H mod.3-CW, Eurofer97) were neutron irradiated in the JP27 experiment to a dose of 21.2 dpa at 500°C in the High Flux Isotope Reactor (HFIR) at Oak Ridge National Laboratory (ORNL). A list of the various alloys and their nominal compositions in the as-irradiated state as determined by energy dispersive spectroscopy (EDS) is provided in Table 1. Note that the alloys containing W have experienced some degree of transmutation in the highly thermalized neutron environment of HFIR such that some of W has converted into Os and Re. A 4 µm NiAl coating used for the ISHI was applied to one side of a 3-mm TEM disc, which allows FIB lamella to be extracted from either side of a TEM disc to explore the impact of neutron irradiation with or without concurrent helium injection. At 21.2 dpa, the NiAl coating produced a He concentration of about 1230 appm in the ferritic matrix extending to a depth of ~6 µm below the coating. Cross-sectional TEM samples, prepared by a FIB (FEI Quanta 3D), were finalized with low-energy surface cleaning (2 keV Ga^+ ion) at ±2° tilt angles. The TEM lamellae were extracted from each side of the TEM disc.

TEM characterization was performed using a JEOL 2010F and a newly installed Cs-corrected JEOL ARM 200CF microscope operated at 200 keV. Bright-field TEM/STEM images of dislocation loops and line dislocations were acquired under weak ***g***=200 two-beam conditions near 001 zone axis following the approach outlined by Yao et al [10]. This approach allows the <100>/{100} and 1/2<111>/{111} type dislocation loop populations to be measured separately at a given orientation based on loop inclination, shape of the loop, and the ***g.b=0*** invisibility criterion. Bright-field TEM (BFTEM) images of He bubbles and voids were acquired using an over/under-focus technique, and measured bubble sizes are about 87% of the actual bubble size at an under-defocus of 750 nm as determined from a previous modeling study [11-13].

Table 1. Composition of alloys

Alloy	Composition (wt.%) with Fe balance											
	Al	Si	Ti	Cr	Mn	Fe	Ni	Y	Mo	W	Re	Os
14YW	1.6	0.8	0.0	13.7	1.9	80	0.1	0.1	0.0	2.0	0.1	0.5
14YWT	0.8	0.2	0.4	13.8	2.2	79	0.1	0.1	0.1	2.0	0.2	0.5
12YWT	0.8	0.1	0.4	12.0	2.1	81	0.4	0.1	0.3	1.7	0.2	0.5
MA957Fr	0.4	0.3	---	8.9	2.4	87	0.1	---	---	0.8	---	0.2
PM2000	6.0	1.0	0.5	18.5	1.8	71	0.1	0.3	0.1	0.00	0.1	0.0
F82H.mod3 +CW	---	0.1	---	8.2	0.3	88	---	---	---	1.3	0.2	0.5
Eurofer	0.5	0.9	---	8.6	2.7	80	0.8	---	0.6	0.8	0.1	0.3

Results and Discussion

The microstructural information is provided for the He-injected/neutron irradiated side versus the neutron-irradiated side of the same sample. Figure 1 presents examples of the dislocation loops and line dislocations taken in BFTEM using a weak **g**=200 two-beam condition near a 001 zone axis. For brevity the two types of loops will be referred to as <100> or <111> loops to represent the <100>/{100} and 1/2<111>/{111} loops, respectively, documented in this work. Figure 2 provides examples of the cavity microstructure present in each irradiated material and condition; each image was taken in an underfocus/overfocused condition of 750 nm. Histograms of the loop and cavity sizes for each alloy and irradiation condition are provided in Figure 3 - Figure 5. The density and average size values are summarized in Table 2.

Table 2. Microstructure summary at 500 °C of JP27 ODS ferritic alloys and RAFM steels under irradiation of only neutron and dual He/neutron

Sample	Irradiation Condition @ 500 °C	Dislocation loops Density [10^{20}/m^3] (Size [nm])		Line Dislocation Density [10^{13}/m^2]	Cavities (He bubbles or voids)	
		<100>{100}	1/2<111>{111}		Density [10^{22}/m^3]	Size [nm]
14YWT	neutron	18 (11.2 ±7.1)	15 (8.9 ±6.6)	6.3	N/A	N/A
	He/neutron	36 (17.1 ±11.2)	18 (16.4 ±9.2)	5.6	19	1.4 ±0.3
12YWT	neutron	28 (6.1 ±2.8)	20 (6.9 ±3.7)	18	N/A	N/A
	He/neutron	34 (14.5 ±8.8)	28 (10.5 ±3.8)	17	19	1.2 ±0.2
MA957Fr	neutron	16 (10.1 ±4.8)	8 (13.3 ±5.0)	17	N/A	N/A
	He/neutron	30 (21.9 ±19.2)	11 (27.4 ±20.0)	27	He bubbles	
					0.4	1.9 ±0.4
					Voids in matrix	
					0.8	6.6 ±2.9
PM2000	neutron	8 (17 ±7.3)	4 (19.6 ±6.7)	22	He bubbles	
					N/A	N/A
					Voids within ODS	
					0.01	8.8 ±5.0
	He/neutron	38 (40 ±25.7)	14 (30.5 ±18)	3.7	He bubbles	
					2	1.4 ±0.2
					Voids within ODS	
					0.2	7.8 ±2.5
14YW	neutron	12 (21.7 ±15.6)	11 (17.3 ±8.9)	1.6	0.6	11.6 ±4.9
	He/neutron	27 (27.5 ±24.9)	12 (23.2 ±16.4)	2.4	11	3.1 ±1.9
F82H mod.3+CW	neutron	15 (10.3 ±5.8)	9 (10.1 ±4.9)	27	2.1	1.3 ±0.3
	He/neutron	48 (34 ±24.6)	28 (36.6 ±25.2)	30	11	2.7 ±1.6
Eurofer97	neutron	16 (9.3 ±2.7)	8 (10.2 ±4.3)	22	N/A	N/A
	He/neutron	28 (27.7 ±10.1)	11 (28.5 ±12.3)	32	He bubbles	
					0.2	1.8 (0.5)
					Voids in matrix	
					0.75	6.9 (3.6)

There are many notable differences in the response of the different materials to the presence of high helium levels. The dislocation analysis revealed that the line dislocation density and the loop densities were usually higher on the He-injected side of the sample for all of the materials. In the case of the dislocation loops, the general trend is higher dislocation loop density of both types, and a larger average diameter for both types of loops compared to the side of the sample that experienced only neutron irradiation. In addition, a consistent trend among all of the alloys is that the <100> loops are present at a higher density and larger average size compared to the <111> loops, and this trend applies equally to both sides of the sample, i.e., with and without helium injection. Perhaps the biggest surprise is the PM2000 alloy, which is a very large grained material with a relatively low density of coarse Y-Al-O particles. Large dislocation loops of both types formed during irradiation, growing to sizes of over 100 nm in the presence of helium injection. Evidently the loops were stabilized by nucleation and growth of fine helium bubbles that formed on the periphery of each <100> and <111> loop. This association between loops and helium bubbles was not observed in any of the other alloys, and is thought to have arisen in PM2000 because of the absence of a high density of grain or lath boundaries, which provide effective, competing sinks for both helium and point defects.

Under helium injection, the RAFM steels possess the lowest swelling resistance of all of the alloys due to the formation of comparatively large voids in the interiors of the martensitic laths, as well as small bubbles

on lath boundaries. These voids are often aligned in stringers that are assumed to have formed on dislocations that have migrated away under irradiation. A low density of bubbles was found in the matrix of the neutron irradiated side of the RAFM steels samples, presumably from helium produced via transmutation of the bulk alloy. At the other end of the spectrum are the two NFA 14YWT and 12YWT, which do not form any voids, only a high density of small bubbles in the helium-injected side of the TEM disc. It is assumed that helium bubbles form on the high density of nano-oxide particles (<2 nm in size) present in both alloys. MA957Fr is another NFA that exhibits mostly bubble formation, however, there were cases of void-like features that formed on particles in limited areas of the TEM foil. These may be coalescence of small bubbles on the periphery of the particles. The 14YW alloy, an analogue to 14YWT but without the titanium addition that refines the oxide particle distribution, exhibited the worst response of the NFA alloys, exhibiting both bubbles and voids that were attached to the oxide particles, as shown in Figure 6. The particles proved to be effective sinks, but their density is too low to provide the kind of sink strength that prevents helium bubbles from reaching critical size leading to unstable void growth. The oxide particles in 14YW are large enough to be easily visible in TEM, unlike those present in the 14YWT and 12YWT. It was also noted in Figure 6 that some of the bubbles and voids were aligned along the <100> planes in the 14YW alloy, perhaps because of a prior dislocation structure that no longer exists in the irradiated samples. PM2000 proved to be resistant to large-scale void formation also, but by a different mechanism. The oxide dispersion in the PM2000 consists of Y-Al-O particles with an average size of 30 nm, which amorphosized under irradiation. Their distribution is too coarse to provide the same sink strength as the nano-oxide dispersions in 14YWT and 12YWT, however, the dislocation loops that formed under irradiation proved to be effective sinks for helium, promoting a more uniform distribution of helium bubbles on the periphery of the growing loops. The only voids found in this alloy were voids that formed inside the amorphous oxide particles. Voids were found in every particle in the helium-injected side, but in only ~22% of the amorphous particles on the side of the disc without helium injection. Other microstructural changes were observed in this alloy, and have been reported in a previous semiannual report. The most notable changes are fine precipitation of a Fe-Al-Ti phase, α□ or possibly σ phase. It is unclear how the chemistry of this alloy affects helium transport and capture, nor its impact on the dislocation loop stability versus the lack of competing sinks because of the much larger grain size.

In summary, the NFA alloys 14YWT, 12YWT and MA957Fr are more resistant to void swelling due to trapping of helium by the high density of small nano-oxide clusters dispersed in the matrix. The PM2000 alloy also appears to be relatively resistant to void formation due to the ability of the loops to grow and continuously capture helium at the periphery of each <100> and <111> loop. The effect of the oxide particle distribution and its chemistry on helium trapping efficiency are illustrated by comparing the 14YWT versus the 14YW alloy, where the coarser distribution of particles in the 14YW allows helium bubbles to reach the critical size for unstable void growth. Since each visible particle in 14YW has a helium bubble or void associated with it, the particles appear to be effective trapping sites, but are not at a high enough density to prevent void formation. The RAFM steels are, not surprisingly, the poorest of the group of alloys investigated here with respect to void swelling in the presence of high helium.

Future work will continue to explore the microstructure of these irradiated alloys, expanding the matrix to higher doses and exploring samples irradiated at 400°C under similar helium injection levels. 3D-APT measurements are also being done on certain alloys to help understand the fate of the nano-oxide dispersion, as well as the presence of any precipitation in the matrix.

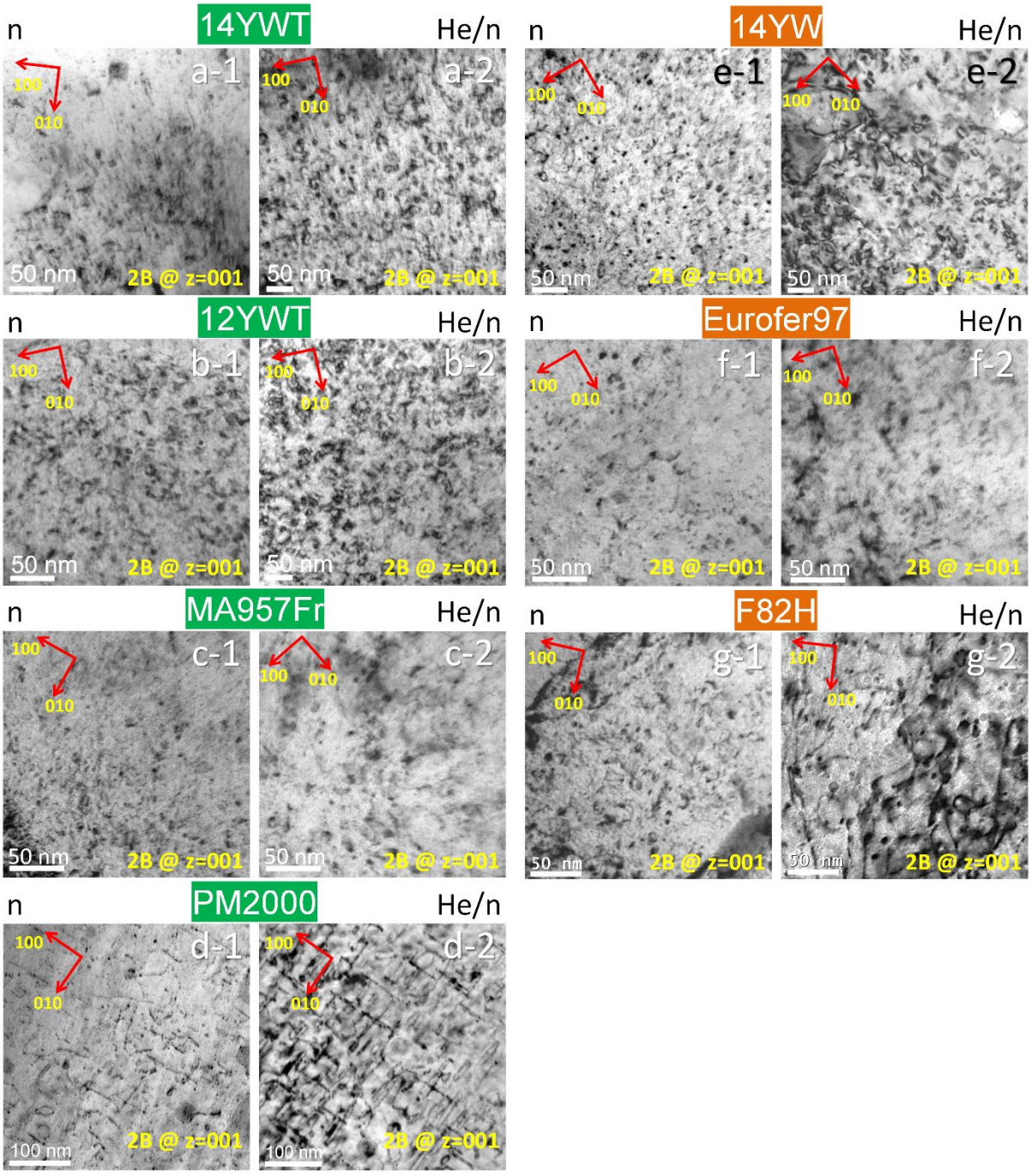

Figure 1. Examples are shown of the dislocation loop microstructure and the network dislocations that form in the irradiated samples. The images provide a comparison of both sides of the TEM disc, that is, with and without helium injection. PM2000 is the only alloy that shows a high density of large, arrayed loops.

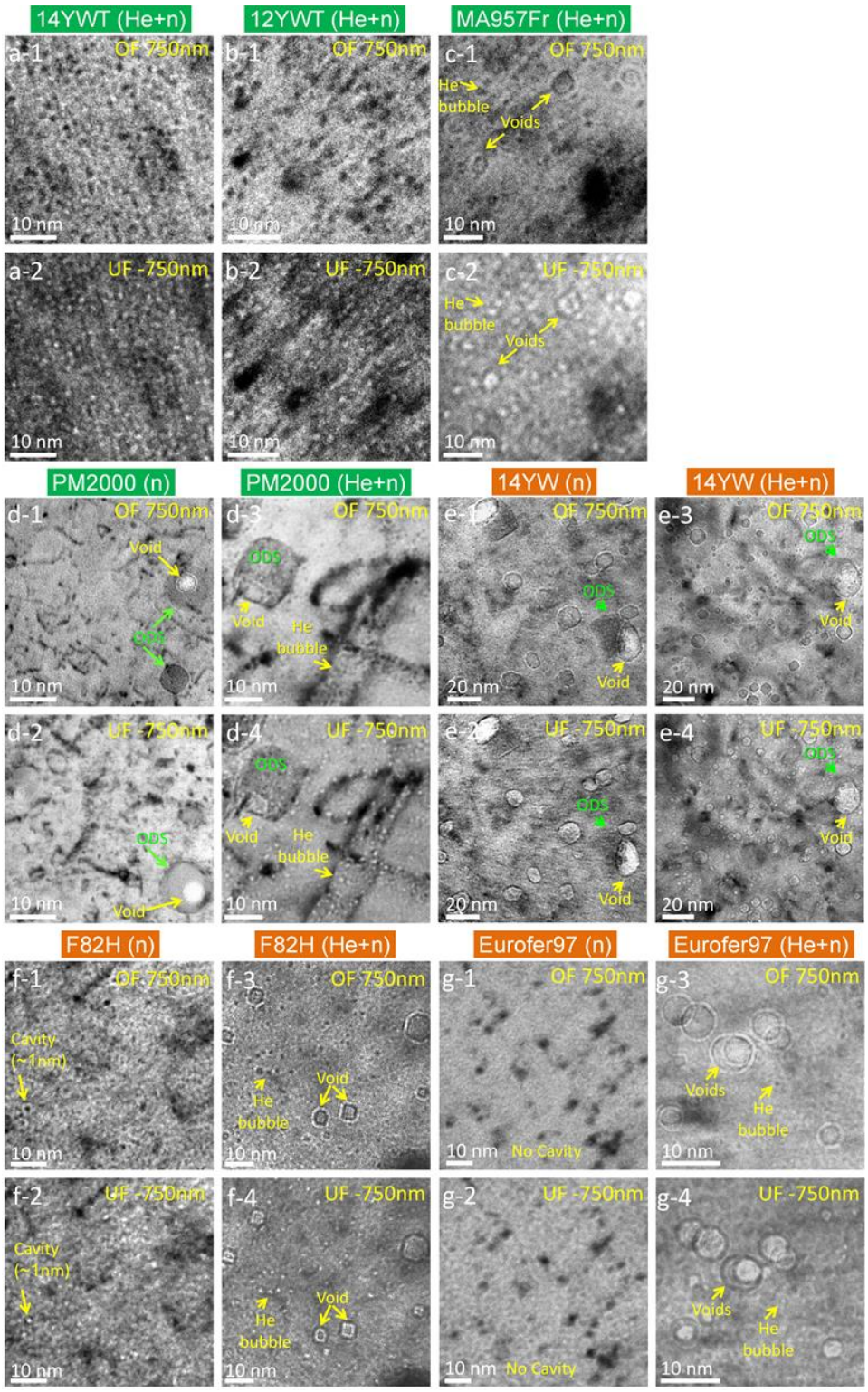

Figure 2. Helium bubbles and void microstructures are shown for each of the irradiated alloys and conditions in this study. Examples are provided for the helium-injected side along with a comparison of the non-injected side of the foil.

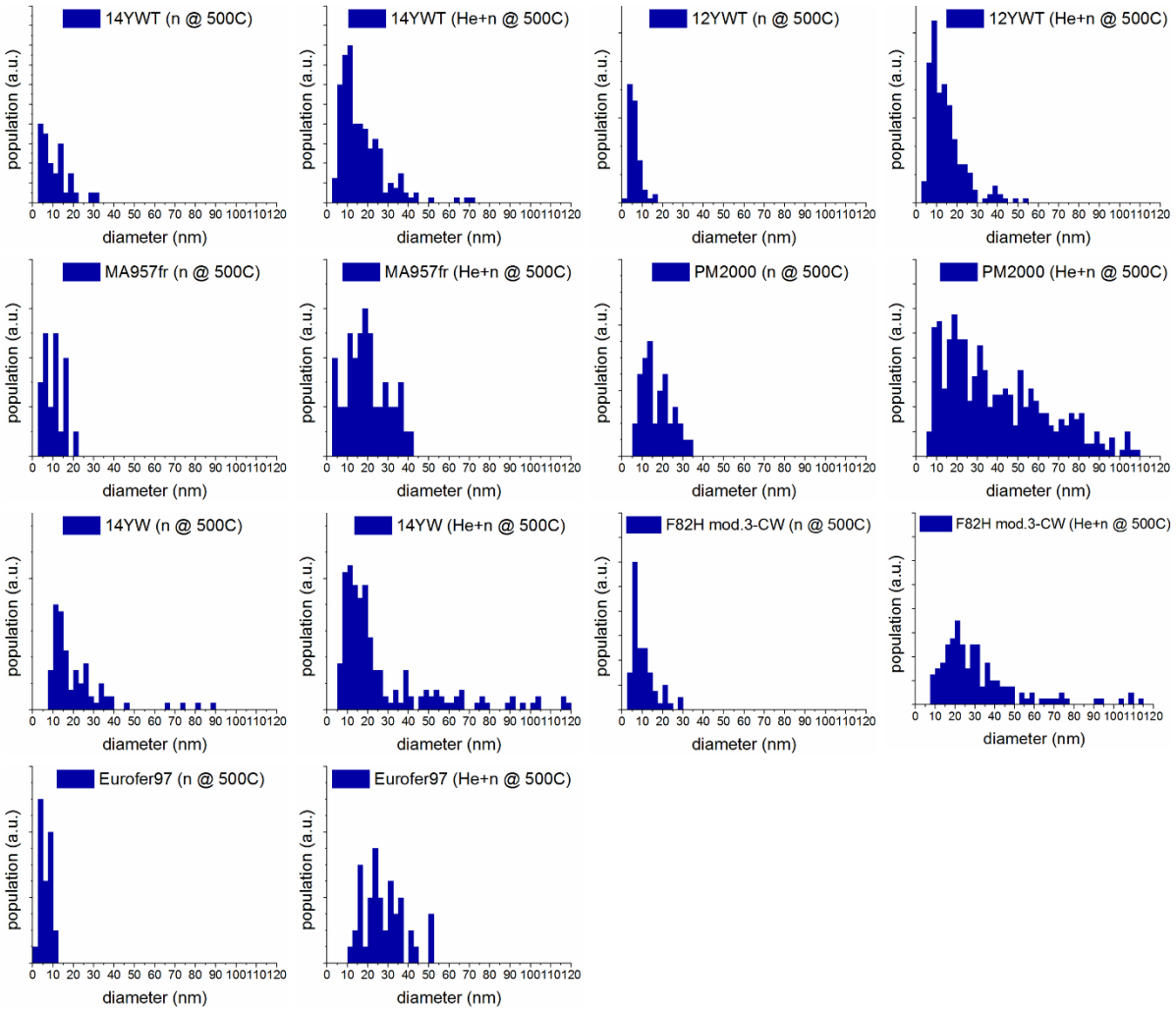

Figure 3. Histograms of <100>/{100} loop size in ODS ferritic alloys (14YWT, 12YWT, MA957Fr, PM2000, 14YW) and RAFM steels (F82H mod.3-CW, Eurofer97) under only neutron-irradiation (left) and He/neutron-irradiation (right) at 500°C.

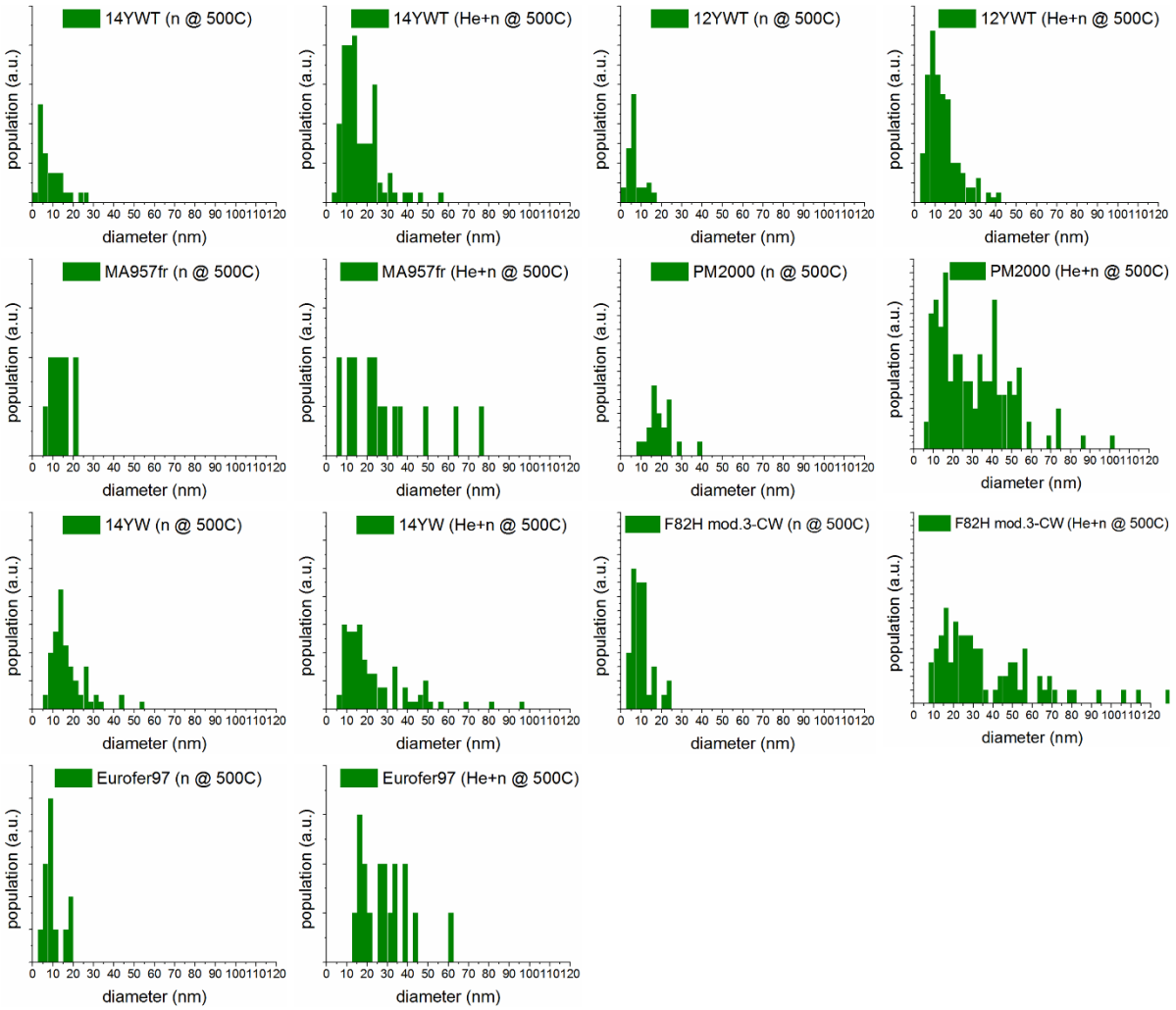

Figure 4. Histograms of 1/2<111>/{111} loop size in ferritic alloys (14YWT, 12YWT, MA957Fr, PM2000, 14YW) and RAFM steels (F82H mod.3-CW, Eurofer97) under only neutron-irradiation (left) and He/neutron-irradiation (right) at 500°C.

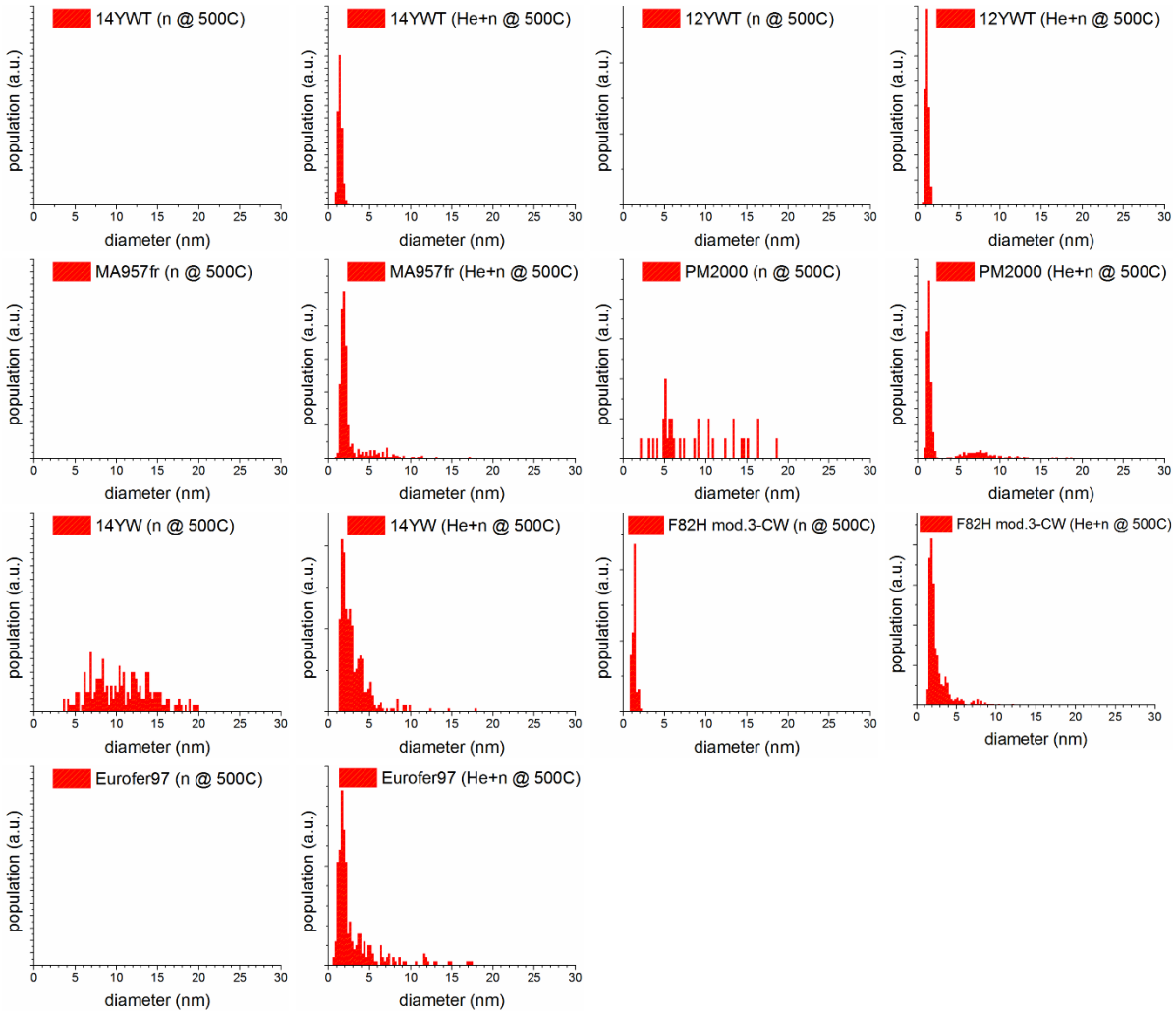

Figure 5. Histograms of bubble and voids in ferritic alloys 14YWT, 12YWT, MA957Fr, PM2000, 14YW and RAFM steels (F82H mod.3-CW, Eurofer97) under only neutron-irradiation (left) and He/neutron-irradiation (right) at 500 °C.

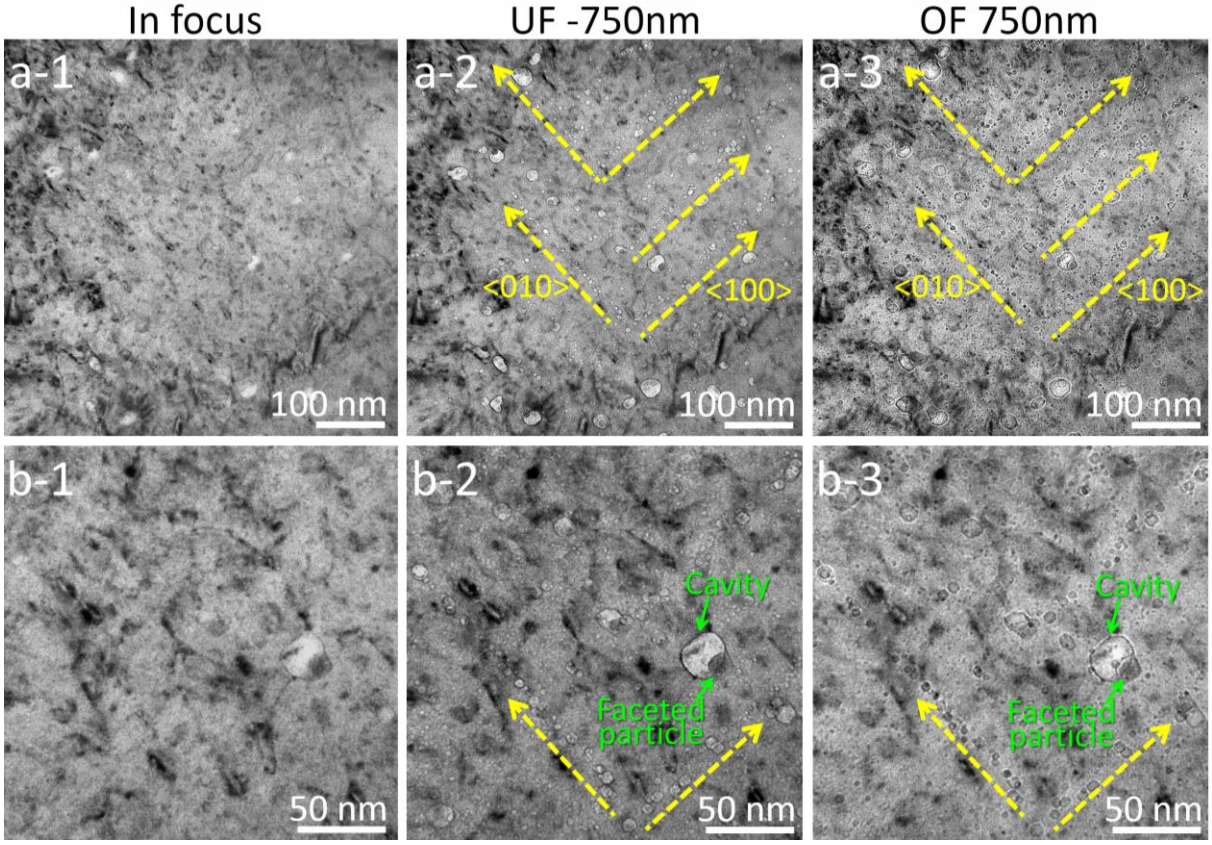

Figure 6. Two sets of through-focus BFTEM images taken near an [001] zone axis in the He-injected side of alloy 14YW show (a) He bubbles and cavities aligned to <100> directions (along yellow arrow), (b) large cavities (green) attached to rounded rectangular particle surface.

Acknowledgements

This research was supported by the U. S. Department of Energy, Office of Fusion Energy Sciences, under contract DE-AC06-76RLO1830 and DE-FG03-94ER54275. A portion of the research was performed using EMSL, a national scientific user facility sponsored by the DOE's Office of Biological and Environmental Research and located at PNNL.

References

[1] G.R. Odette, M.J. Alinger, B.D. Wirth, Annu. Rev. Mater. Res. 38 (2008) 471.
[2] R.J. Kurtz, A. Alamo, E. Lucon, Q. Huang, S. Jitsukawa, A. Kimura, R.L. Klueh, G.R. Odette, C. Petersen, M.A. Sokolov, P. Spätig, J.W. Rensman, J. Nucl. Mater. 386-388 (2009) 411.
[3] N. Baluc, K. Abe, J.L. Boutard, V.M. Chernov, E. Diegele, S. Jitsukawa, A. Kimura, R.L. Klueh, A. Kohyama, R.J. Kurtz, R. Lässer, H. Matsui, A. MÖslang, T. Muroga, G.R. Odette, M.Q. Tran, B. van der Schaaf, Y. Wu, J. Yu, and S.J. Zinkle, Nucl. Fusion 47 (2007) S696.
[4] R.E. Stoller, G.R. Odette, J. Nucl. Mater. 131 (1985) 118.
[5] T. Yamamoto, G.R. Odette, L.R. Greenwood, Fusion Materials Semiannual Progress Report for Period Ending June 30, 2005, DOE/ER-313/38 (2005) 95.

[6] T. Yamamoto, G.R. Odette, P. Miao, et al. J. Nucl. Mater. 367 (2007) 399.
[7] R.J. Kurtz, G.R. Odette, T. Yamamoto, D.S. Gelles, P. Miao, B.M. Oliver, J. Nucl. Mater. 367-370 (2007) 417.
[8] T. Yamamoto, G.R. Odette, P. Miao, J. Nucl. Mater. 386-388 (2009) 338.
[9] G.R. Odette, P. Miao, D.J. Edwards, T. Yamamoto, R.J. Kurtz, H. Tanigawa, J. Nuc. Mater. 417 (2011) 1001.
[10] B. Yao, D.J. Edwards, and R.J. Kurtz, J. Nucl. Mater. 434 (2012) 402.
[11] B. Yao, D.J. Edwards, R.J. Kurtz, G. R. Odette, T. Yamamoto, Fusion Materials Semiannual Progress Report for the Period Ending December 31, 2011, DOE-ER-0313/51 (2011) 85.
[12] B. Yao, D.J. Edwards, R.J. Kurtz, G.R. Odette, and T. Yamamoto, J. Electron Micros. 61(6) (2012) 393.
[13] H.J. Jung, D.J. Edwards, B. Yao, R.J. Kurtz, G.R. Odette, T. Yamamoto, Y. Wu, Fusion Materials Semiannual Progress Report for the Period Ending June 30, 2014, DOE-ER-0313/56 (2014) 19.

2.6 MICROSTRUCTURE, TEXTURING, MICROCRACKING AND DELAMINATION BEHAVIOR OF NFA-1 — S. Pal, M. E. Alam and G. R. Odette (UCSB), D. Hoelzer (ORNL), S. Maloy (LANL)

OBJECTIVE

The objective is to determine the origins of microcracking in 14YWT NFA-1 plate.

SUMMARY

NFA-1 was processed by gas atomization of powders, mechanical alloying by powder ball milling, consolidation by hot extrusion, annealing and hot cross-rolling. NFA-1 has highly anisotropic microstructures and mechanical properties. View planes parallel to the plate side show pancake-shaped grains of ~ 0.5 μm average thickness and aspect ratios of 2-3. Larger and a few much larger grains are also seen**.** Extrusion and cross rolling induce a strong <110> fiber texture, accompanied by brittle {001}<110> cleavage system planes parallel to the plate surface. Sessile dislocations with a Burgers vector of <001> on {001} planes along low-angle subgrain boundaries form during the the initial stages of deformation. Further deformation results in dislocation pile-ups at the subgrain boundaries, creating stress concentrations and opening displacements that nucleate microcracks on the brittle cleavage system. Microcrack propagation is driven by residual stresses that develop during the deformation.

PROGRESS AND STATUS

Introduction

Hot extruded and cross-rolled FCRD-NFA-1 is severely microcracked on planes surface of the as-processed plate [1-2]. The microcracks form during thermo-mechanical processing. This work is aimed at identifying the detailed micro-mechanisms leading to microcracking and subsequent delamination.

Experimental Methods

Microstructural characterization was carried out using SEM and TEM. EBSD was used for texture characterization. Selected region TEM lamellas were fabricated by the FIB lift out method and examined using a variety of imaging, diffraction, and micro-analytical methods.

Results

Deformation processed nano-structured ferritic (NFA-1) alloy exhibits strong anisotropy in both its mechanical properties and microstructure [1]. A significant difference in the measured values of fracture toughness and tensile strength along the thickness and longitudinal directions is observed [1-2]. The sample geometry and directions are schematically shown in Figure 1.

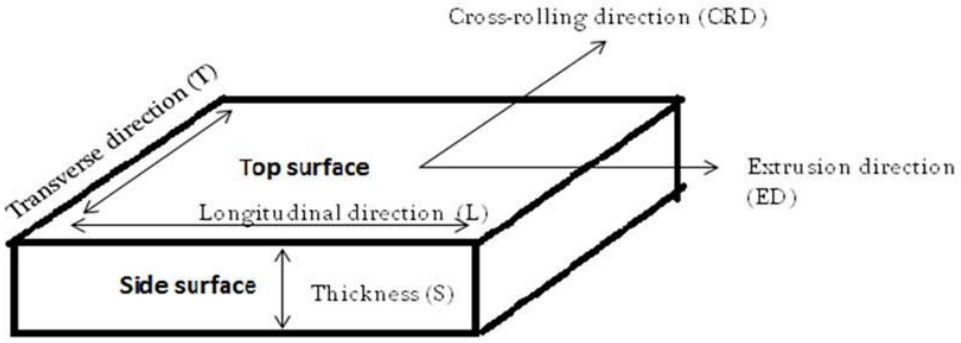

Figure 1. A schematic of the NFA-1 plate showing longitudinal (L), transverse (T) and short thickness (S) directions.

Planes parallel to the side surface is defined as LS, parallel to the top LT and parallel to the front face as TS. Extrusion and cross-rolling of the plate was carried out along the L and T direction as marked accordingly. Microstructural characterization using SEM reveals a significant difference in grain morphology and apparent sizes along the plane parallel to top surface, versus parallel to the thickness direction, as described in Figure 1. Equiaxed ~ 0.2-0.7 μm grains are observed on the plane parallel to top surface (LT view), whereas the plane parallel to thickness direction (LS view) contains elongated "pancake" shaped grains of thickness ~0.2-0.5 μm and an aspect ratio of ~ 6-7.

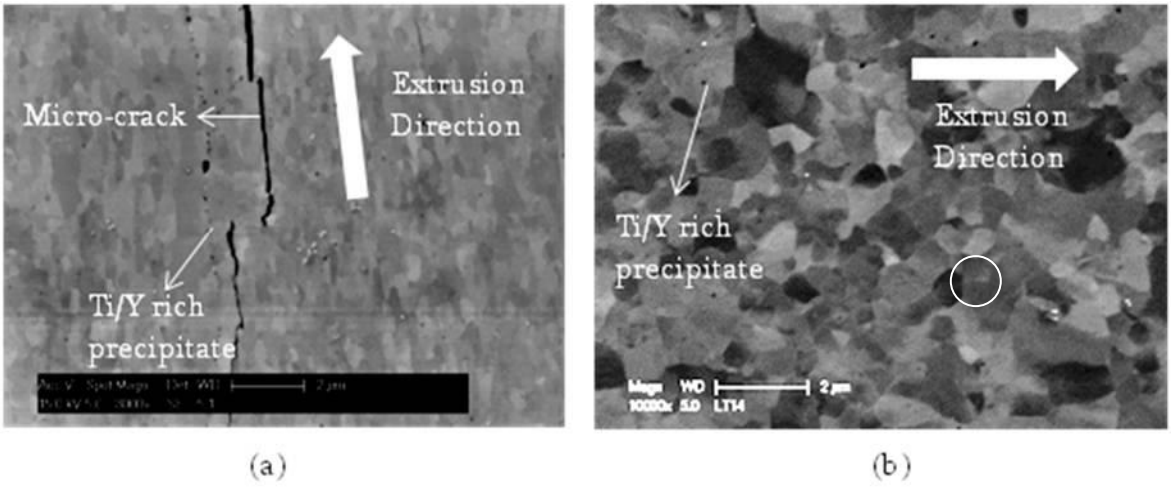

Figure 2. Polished SEM micrographs of the plate's a) LS view and b) LT view. The microstructural features (visible in the SEM micrographs) and extrusion direction for the sample are labeled accordingly.

SEM images of both the LS and LT views show the presence of Ti- and Y-rich precipitates, which are detrimental to mechanical properties. Compositional maps for both the LS view shown in Figure 3a-f and the LT view shown in Figure 4a-f were characterized using electron probe microanalysis (EPMA). The elemental composition map shown in Figure 3 and Figure 4 confirm the presence of Ti- and Y-rich precipitates in the hot extruded and cross-rolled plate. The number density of the Y-rich precipitates is lower compared to the Ti-rich features, as seen in Figure 3b and d and Figure 4b and d. The precipitates are aligned in stringers along the extrusion direction, as seen in Figure 3f and Figure 4f. EPMA maps also show that the cracked region contains oxidation peaks. Elemental maps for the LT and LS views are similar. A more detailed investigation of these Ti/Y-rich particles was carried out by TEM EDX in the high angle annular dark field (HAADF) mode as shown in Figure 5a. It was previously proposed that the microcracks might nucleate at the coarse precipitates, especially along prior powder particle boundaries. This now does not seem to be the case, since TEM clearly reveals that these features do not influence microcrack nucleation. The precipitates, which span a size range from about 15 to 150 nm and are found both in the matrix and on grain boundaries, degrade the ductility of NFA-1. The compositions of the precipitates and matrix are summarized in Table 1.

Table 1. EDX composition analysis of the Ti/Y rich precipitates and the matrix.

Feature	Composition (atom %)					
	Fe	Cr	W	Ti	Y	Cu*
Ti rich particle	2.91	1.13	-	78.94	-	16.97
Y rich particle	40.02	8.96	-	-	40.02	8.71
Matrix	78.38	14.74	0.94	-	0.28	5.22

* Cu in the EDX spectrum is due to use of a Cu grid.

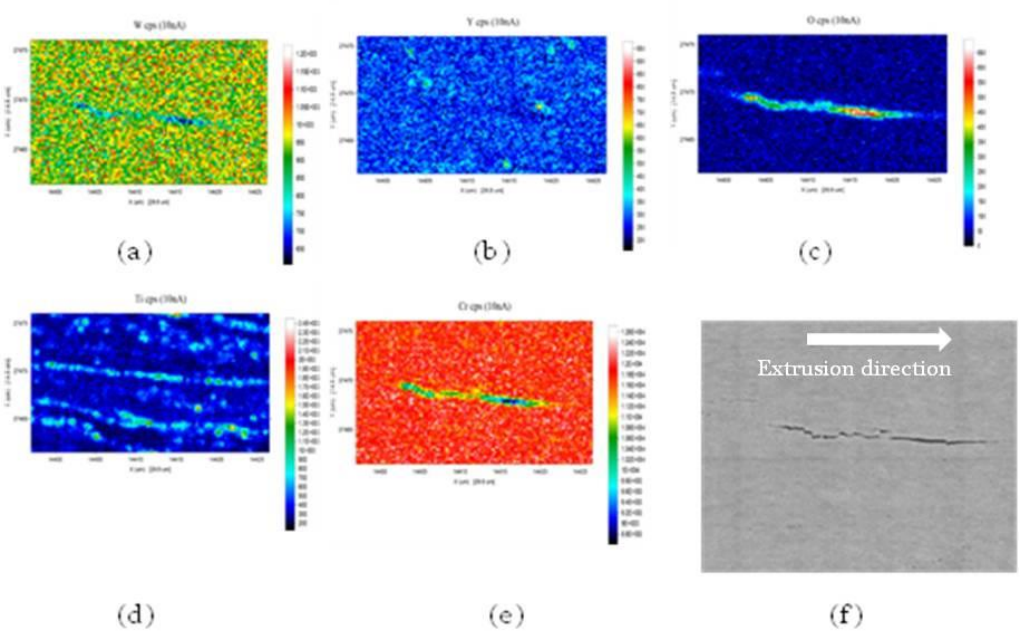

Figure 3. a-e) Elemental compositional maps for the LS view and f) the cracked region of interest.

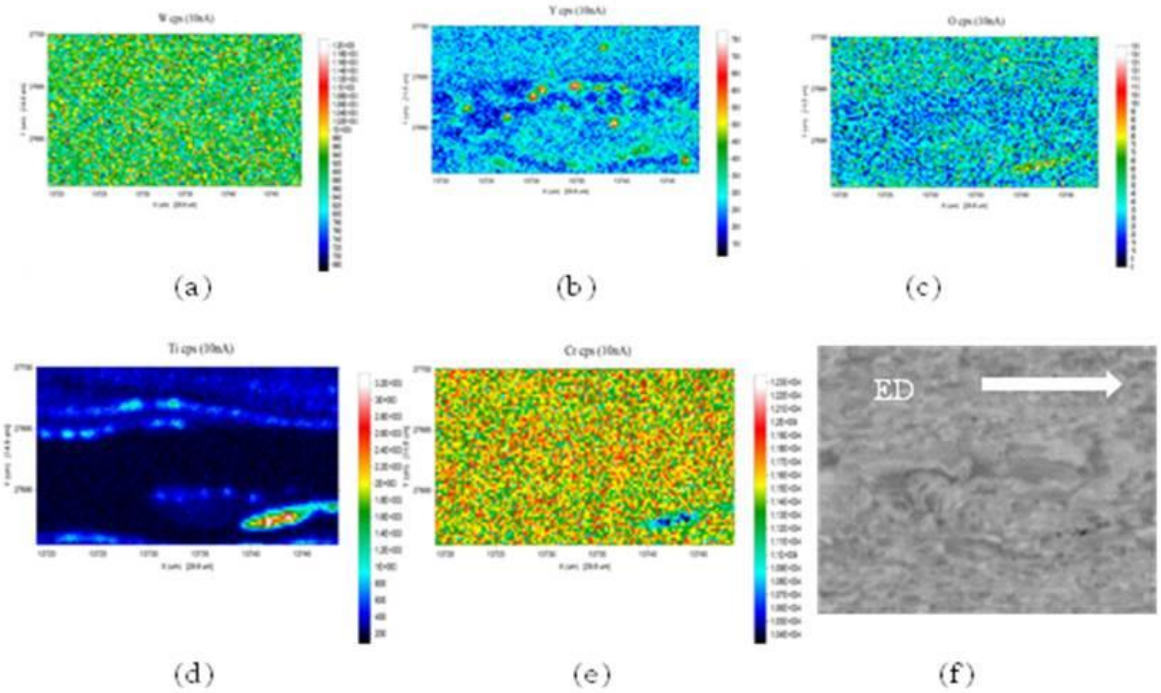

Figure 4. a-e) Elemental compositional maps of LT view and f) the cracked region of interest.

Microcracks are observed only in the plate side SL view, running throughout the plate thickness (S). Similar microcracking has been previously reported in the literature [3-4]. The microcrack size, number density, inter-crack spacing, and opening dimensions are summarized in Table 2. The microcracks play a very critical role in determining the fracture toughness of NFA-1, especially by nucleating delaminations

that relax the triaxial stress state towards a plane strain condition, thereby lowering internal stresses and suppressing cleavage; alternately, delaminations cause crack deflections for LS orientations. However, microcracks reduce the tensile ductility and strength in the thickness (S) direction [1].

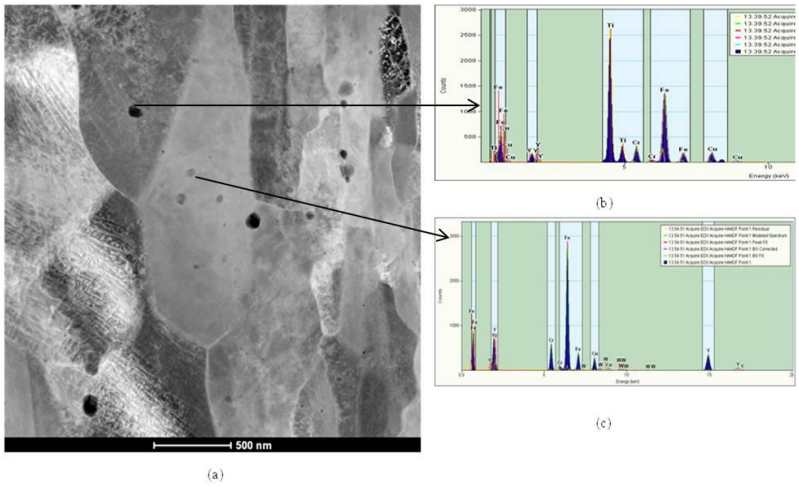

Figure 5. a) HAADF image showing Ti/Y-rich precipitates with darker contrast; b) EDX spectrum of the Ti rich precipitates; and c) EDX spectrum for the Y rich precipitates.

Table 2. Microcrack Statistics

Item	Number	Standard Deviation
Average crack separation (µm)	~ 16.3	± 4.7
Crack length (µm)	~ 10.2	± 8.9
Number density (/m^2)	~ 3.45×10^9	± 1.2×10^9
Crack mouth opening displacement (nm)	~ 252	± 142

Texture characterization

Figure 6 shows the directions and planes that are used to define texturing with respect to the primary deformation orientations. Texture measurements for different views of the plate planes were first carried out by pole figure (PF) analysis. Projections of two major deformation axes, along with the plate normal direction, are shown in stereogram in Figure 6b and c for both the LT and LS views, respectively.

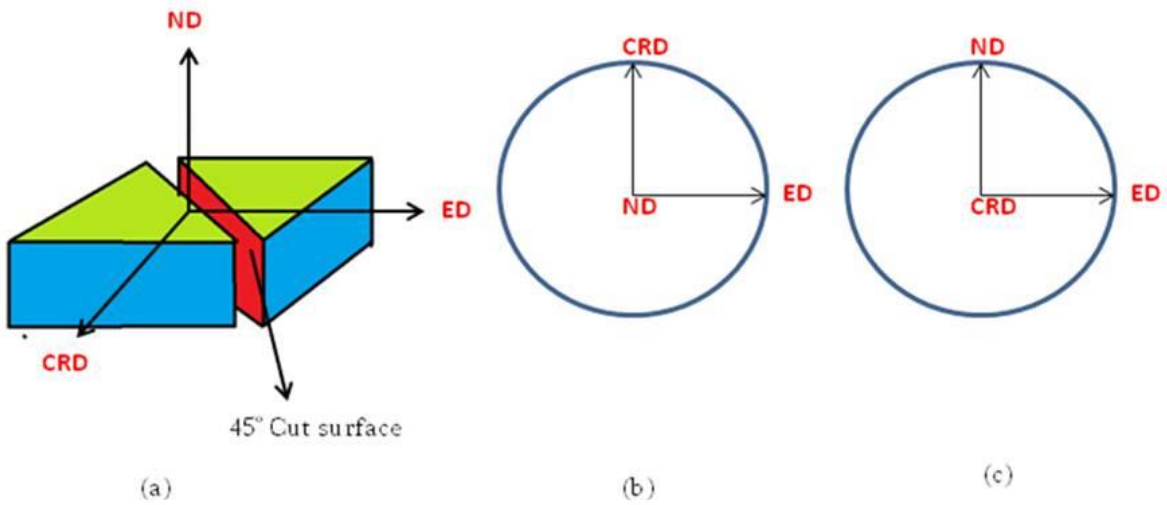

Figure 6. a) A schematic representation of the plate along with primary deformation axes of extrusion (ED), cross-rolling (CRD) and normal direction to the plate (ND). b) and c) Stereogram equivalent deformation axis directions for the LT and LS views, respectively.

EBSD PF maps in in Figure 7a show that the plate has an expected strong α-fiber texture (<110>) along the extrusion direction. Figure 7b shows that a partial α-fiber also develops along the cross-rolling direction. This suggests that both the primary deformation processes (hot extrusion and cross-rolling) induce a similar type of <110>-fiber texture. PF analysis also shows that the texture component developed along the surface normal direction is <001>. EBSD characterization of surface cuts at 45° with respect to the extrusion direction (as illustrated in Figure 6a) in Figure 8 also show that the texture for the LT plate surface normal is predominantly <100>. The PF analysis in Figure 8 also shows that the planes parallel to the 45° cut surface are {100}-type. These observations are further corroborated by the inverse pole figure (IPF) analysis in Figure 9.

More quantitative and accurate determination of the texture components was carried out based on an orientation distribution function (ODF) analysis. The Φ_2 = 0 and 45° ODF sections, shown in Figure 9a and b, demonstrate that a strong {001}<110> texture is dominant in the plate. This is also the low-toughness cleavage system in bcc Fe.

Taken together, the most important conclusion is that a strong {001}<110> texture system develops in the thickness direction of the extruded and cross-rolled plate.

Characterization of crack propagation and initiation by TEM

A brittle crack is characterized by its direction and plane of propagation. TEM was used to characterize the propagation plane-direction and the microcrack formation mechanism. TEM lamellas in Figure 11b and d, taken from locations shown in Figure 11a and c, were prepared using FIB lift-out method. The largest separation between the crack surfaces indicates the crack initiation site.

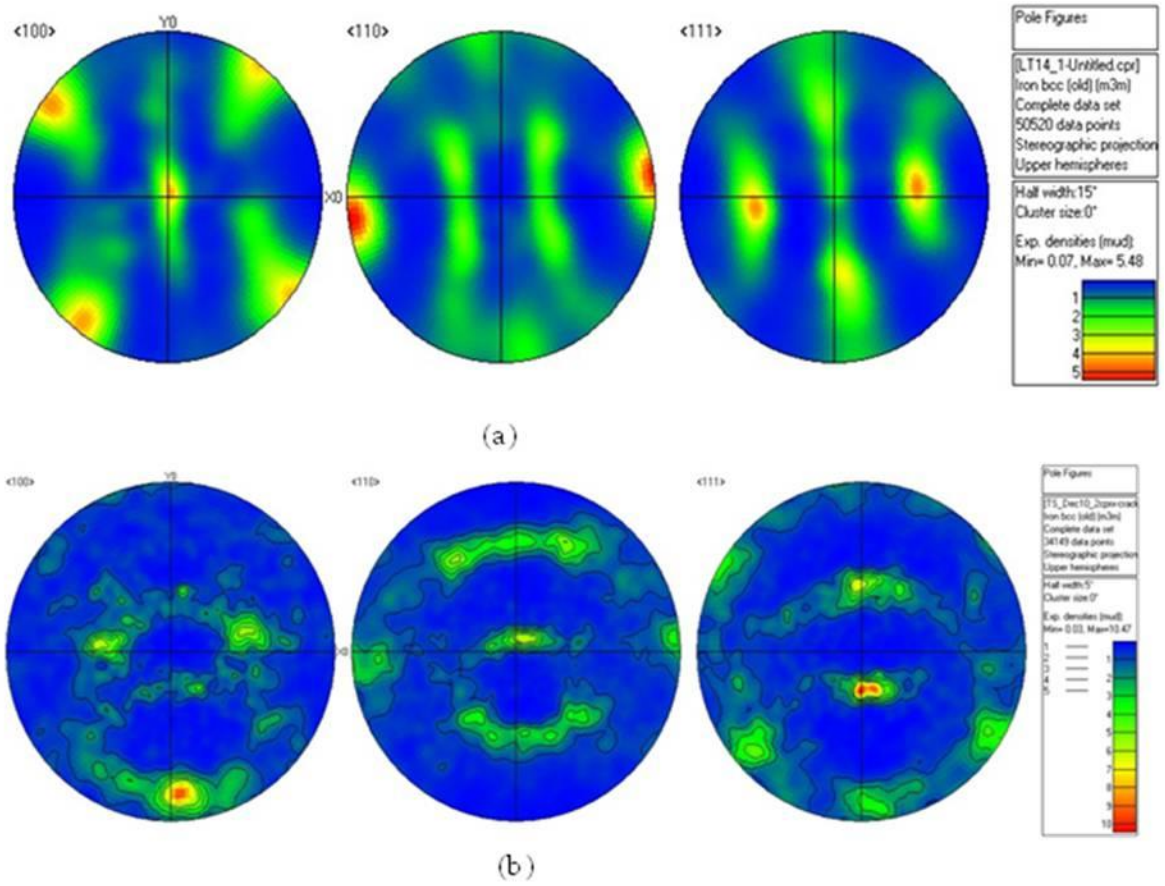

Figure 7. Pole figures of a) LT view and b) LS view of the as-extruded plate showing projection of <100>, <110>, and <111> poles.

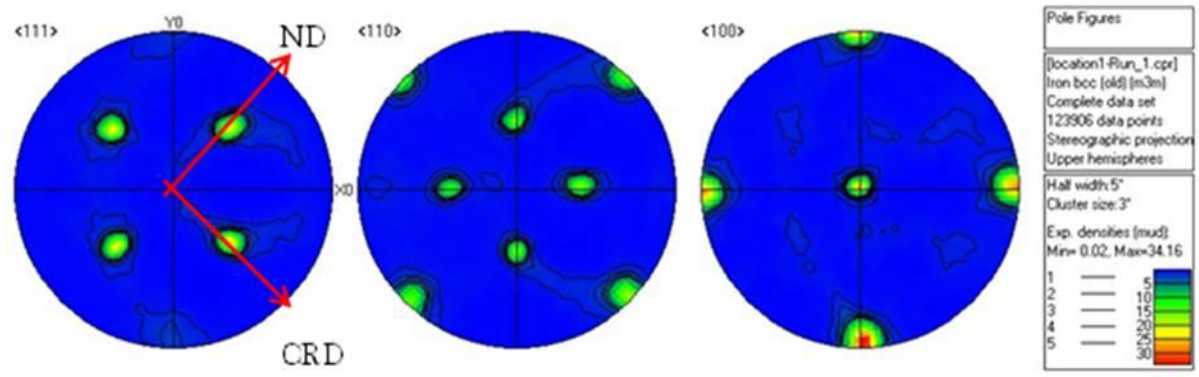

Figure 8. PF for the 45° cut surfaces showing <111>, <110>, and <100> projections. Red arrows indicate the deformation directions of the plate for the <111> projection.

.

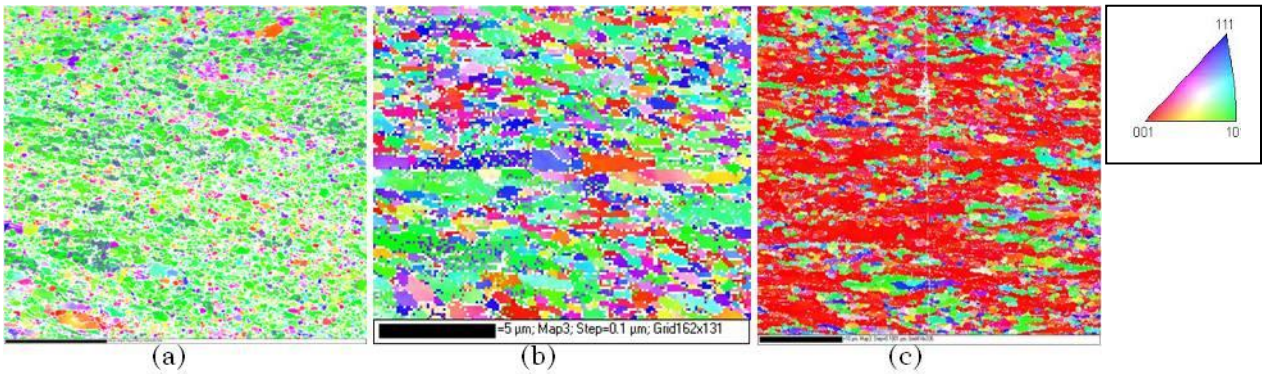

Figure 9. IPF maps of a) LT, b) TS, and c) 45° cut section showing density of the planes parallel to the surface of respective samples.

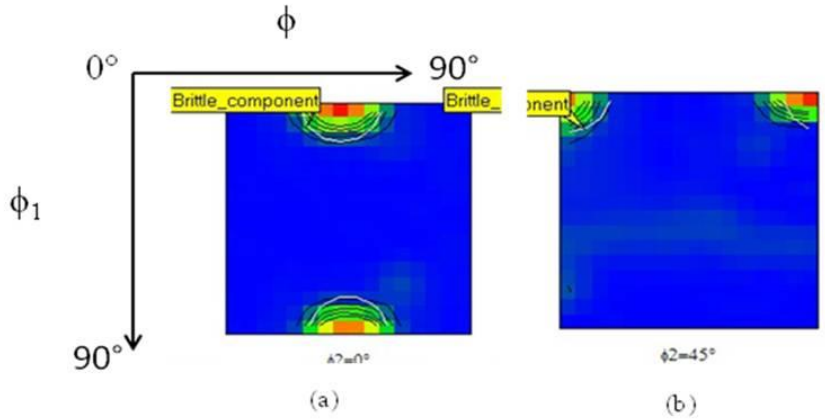

Figure 10. a) Φ_2 = 0 and b) Φ_2 =45° ODF sections of the plate.

Figure 11 shows the FIB locations where TEM lamella were extracted along both the propagated crack front and initiation site. Figure 12a is a bright field (BF) TEM image of the propagation front lamella shown in Figure 11b. The crack runs through a single grain with a contrast variation due to a high dislocation density and a low-angle boundary. Selected area diffraction (SAD) patterns for the marked locations in Figure 12a, along with dark field (DF) imaging, confirm that the crack is confined to a single (001) oriented grain. The SAD patterns from the near crack tip locations, marked as 1 and 2 in Figure 12a, show that the foil normals are near <110>, and are only slightly misoriented with respect to each other. The weak beam dark field (WBDF) image in Figure 12b uses the (002) reflection, marked by the dashed circle in Figure 12c, in the g-3g condition. Dislocations, seen as the bright contrast in Figure 12b, are concentrated around the crack and low-angle boundary.

A BF image of the propagating crack region is shown in Figure 13a. The WBDF in Figure 13b, and the HAADF image in Figure 13c, also show dislocation pile-ups in the vicinity of a crack. Further, Figure 13 suggests that a low-angle subgrain boundary is formed in a grain by the accumulation of dislocations. Contrast in HAADF images is sensitive to variations in mass-thickness and local strain fields. Since the FIB lamella thickness is nearly uniform, the contrast variation in the Figure 13c can be largely ascribed to corresponding variations in the local strain fields. Eight TEM lamellas were prepared from the crack initiation regions and illustrative BF and DF images are shown in Figure 14a and c. along with the corresponding SAD patterns in Figure 14b. Clearly, the microcrack nucleates on a {100}-type plane and propagates in a transgranular mode.

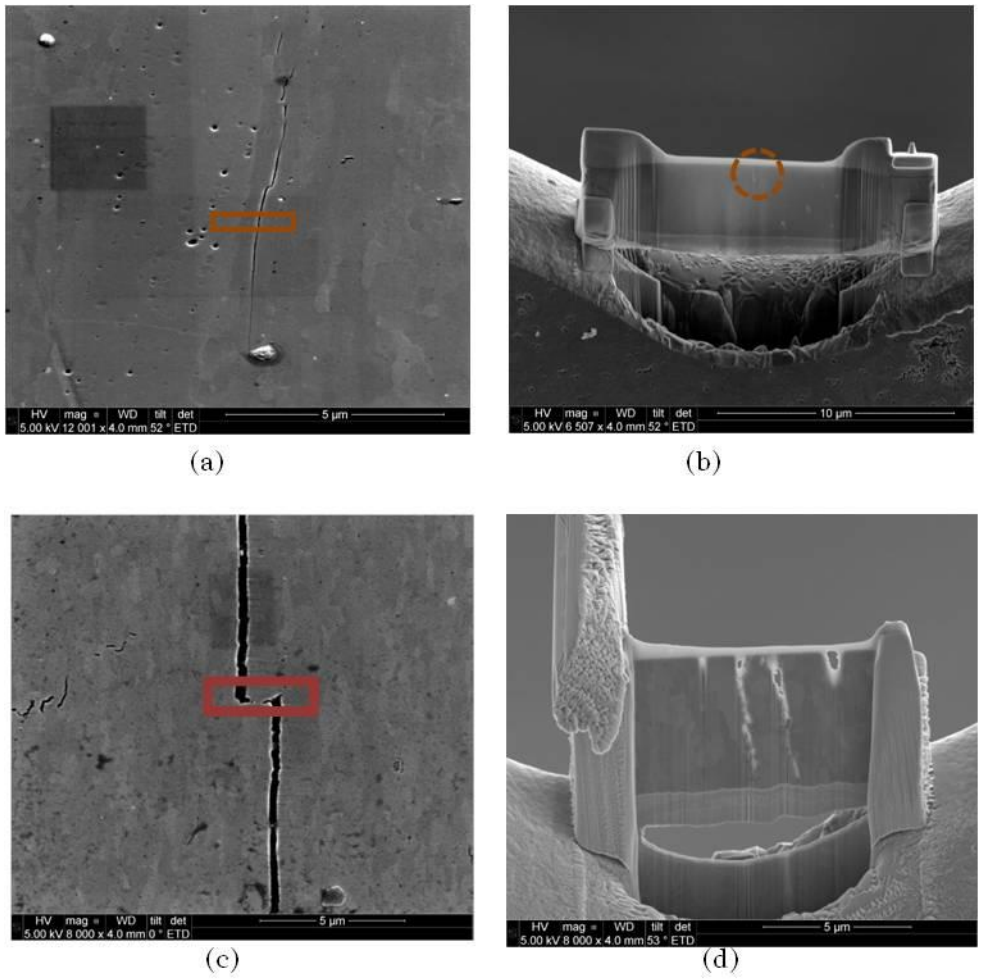

Figure 11. a) The marked location where the TEM lamella was extracted to characterize the crack propagation front; b) the corresponding FIBed lamella; c) the marked location crack initiation front where the TEM lamella was extracted; and d) the corresponding FIBed lamella.

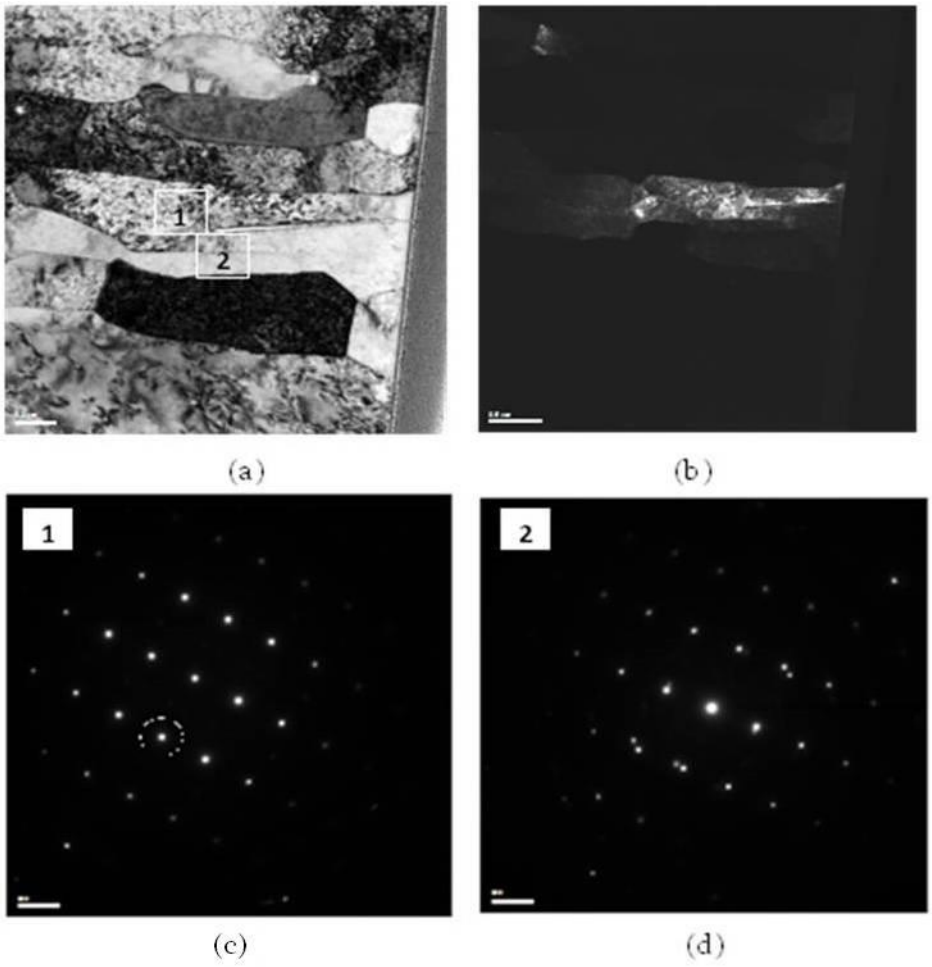

Figure 12. a) BF image, b) WBDF image using the (002) reflection marked in Figure 12c, and c-d) SAD patterns for the marked locations in Figure 12a.

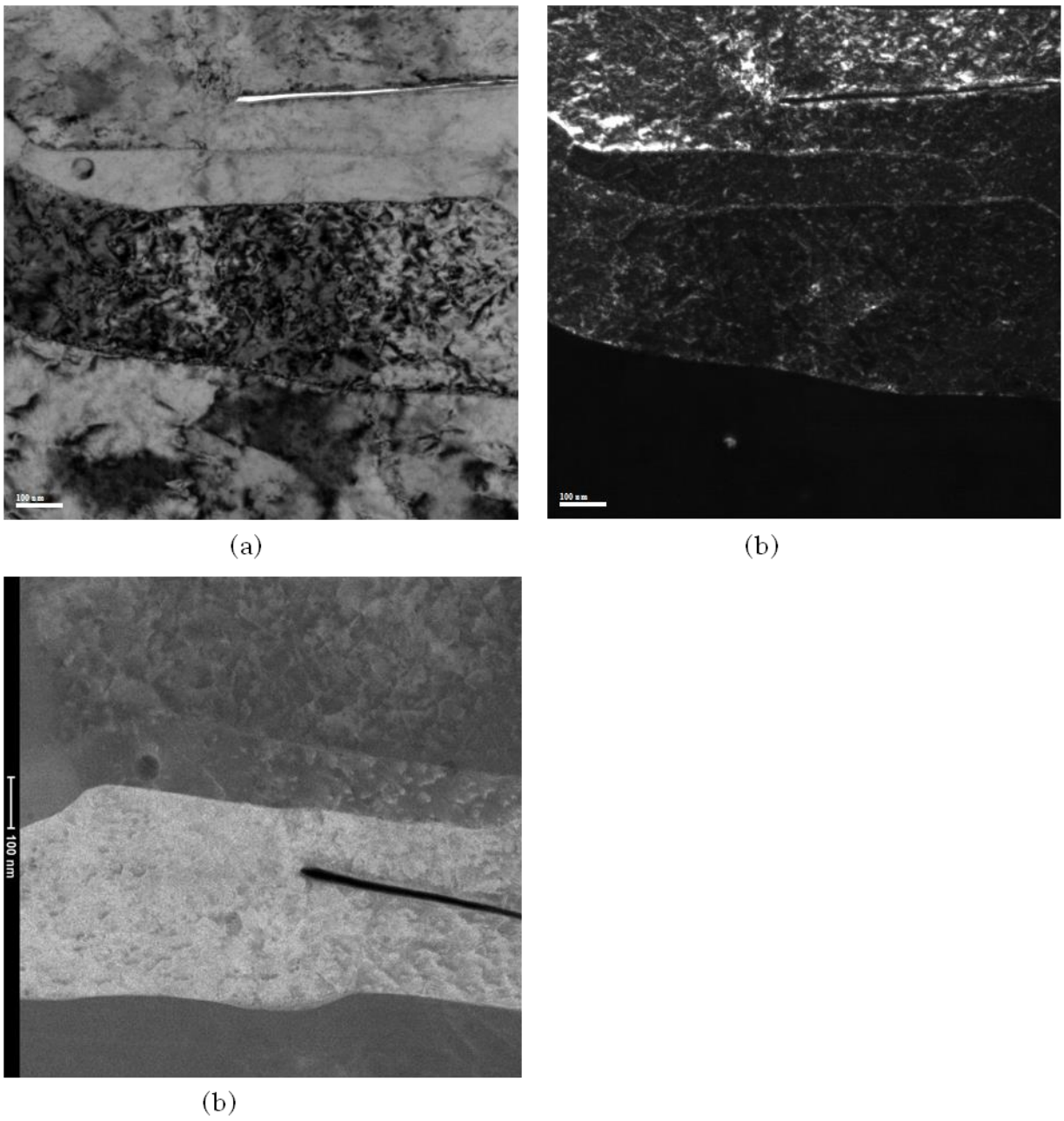

Figure 13. a) BF, b) WBDF, and c) HAADF images of the crack propagation plane.

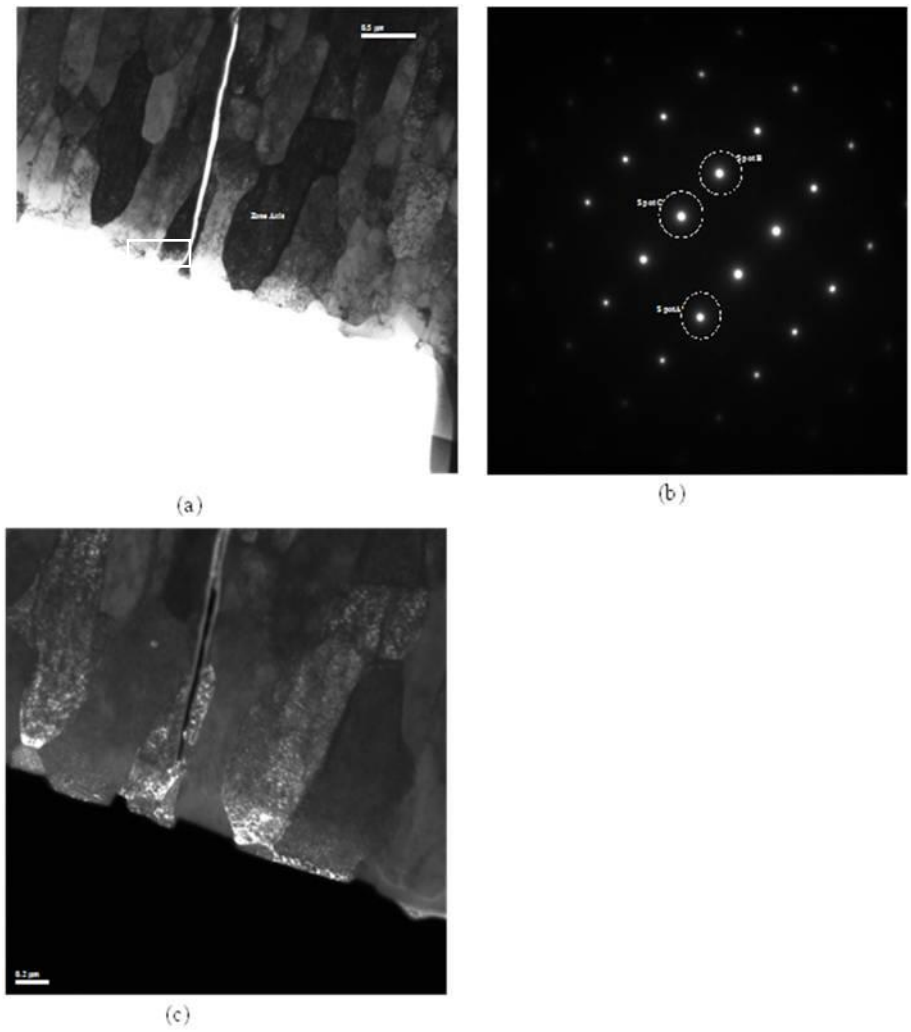

Figure 14. a) BF image of the crack initiation front. Marked grain is tilted to the zone axis conditions. b) SAD pattern of <110> zone axis captured from the grain marked using white box in Figure 14a. c) DF image captured from the (002) spot labeled in Figure 14b.

The higher-magnification view of the crack region in Figure 15 shows very diffuse boundary-like contrast parallel to the crack. Dislocation tangles are clearly seen inside the grain in Figure 15a and b. Figure 15b shows that cracks propagate along the subgrain boundary, which originated from dislocation a pile-up.

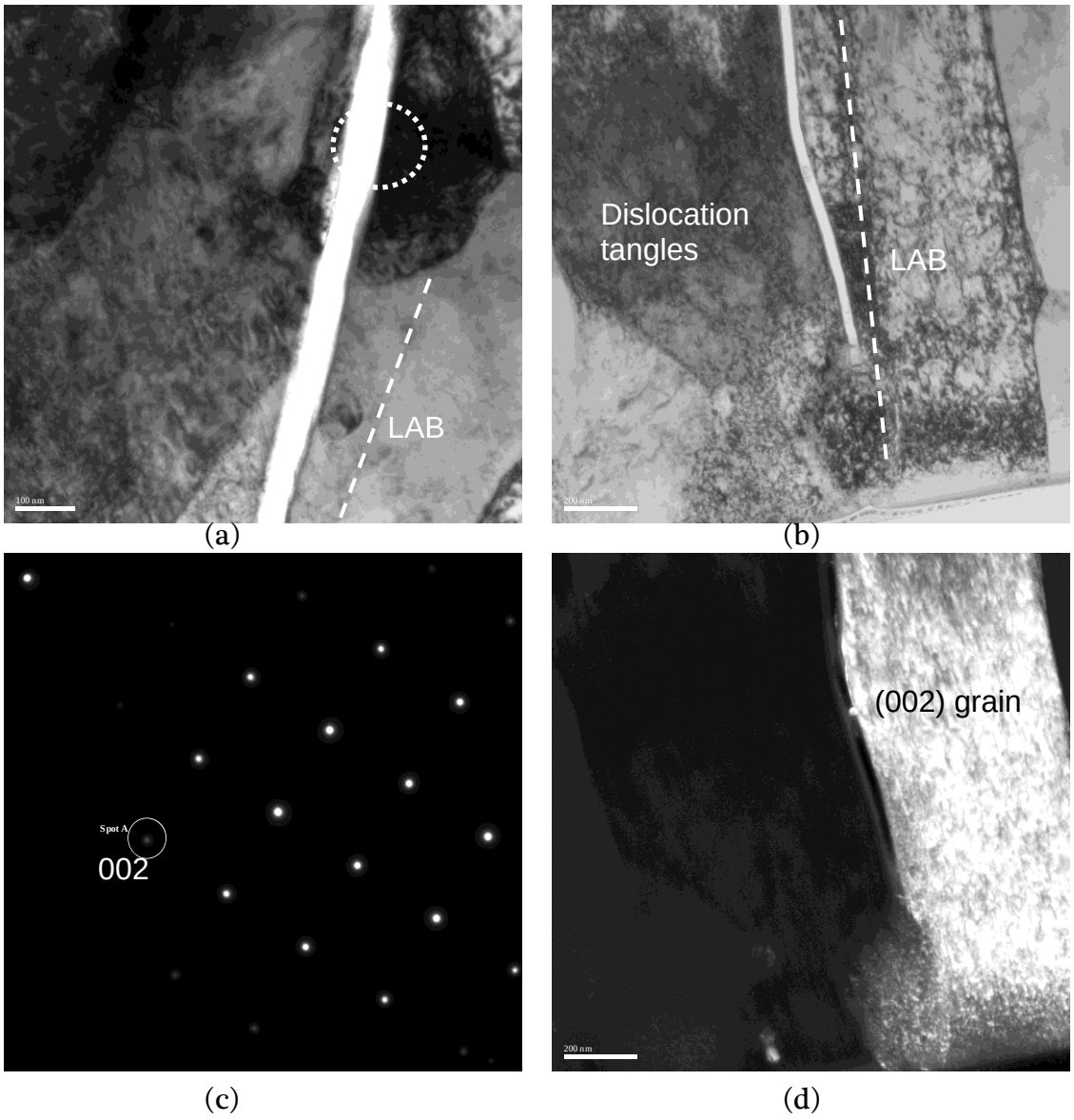

Figure 15. a) BF image of a cracked region showing low-angle boundary (LAB) in a grain; b) BF image of the same location under different tilting conditions; c) SAD pattern from the marked region in Figure 15a showing the grain orientation <110>; and d) DF image corresponding to the (002) reflection of the SAD pattern shown in Figure 15c.

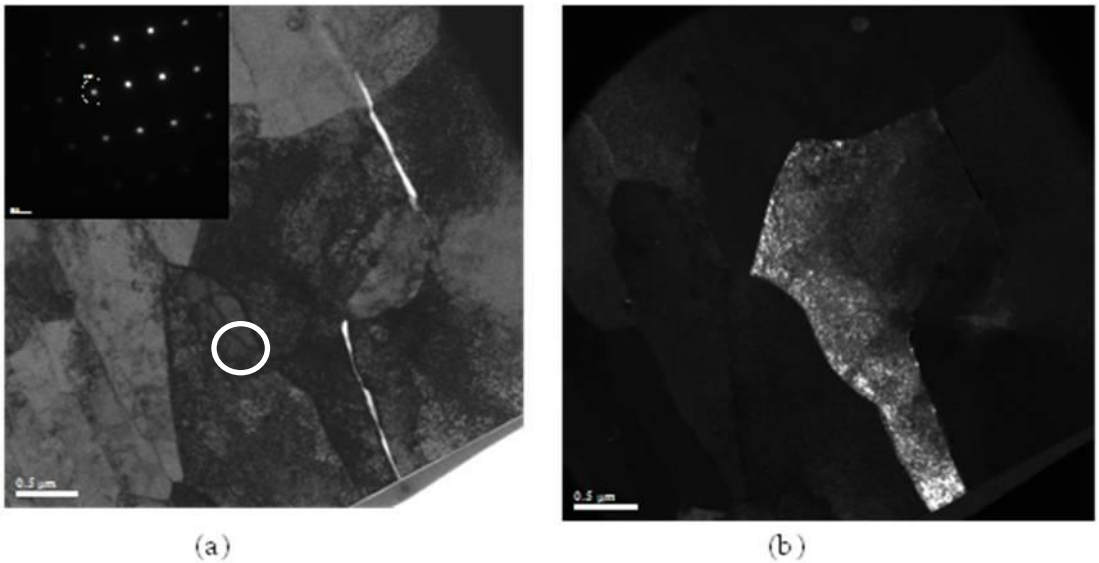

Figure 16. a) BF image of the cracked region, where the insert shows the SAD pattern for the (110) zone axis at the marked location; and b) DF image corresponding to the (002) reflection in the inset SAD pattern of Figure 16a.

Figure 16 and Figure 17 lend additional support to our hypothesis regarding the nucleation of microcracks associated with dislocation pile-up at low-angle subgrain boundaries. Figure 16 again shows that crack originates on a {001} plane in a grain that contains a high density of dislocations. The SAD patterns shown in Figure 17 for different locations near the crack, as marked by red circles in the BF image, show that all the SAD patterns belong to a nearly common zone axis with only minor deviations from <110>. These results clearly demonstrate that cracks are formed in association with low-angle grain boundaries by dislocation pile-ups. All the microstructural components are contained in the HAADF image in Figure 18, taken from the same locations seen in Figure 16a and Figure 17. The HAADF micrograph clearly shows the low-angle boundary parallel to the crack and that the dislocation pile-ups develop the boundary.

Thus we hypothesize that the sequence of events leading to microcracking is as follows: a) the initial deformation is accommodated by formation of low-angle dislocation subgrain boundaries; b) further deformation creates dislocation pile-ups at these low-angle subgrain boundaries; c) the local stress concentrations and accumulated opening displacements nucleate microcracks on {100}-type planes; d) once nucleated, the microcracks propagate transgranularly along the low-angle subgrain boundaries on {100}-type cleavage planes.

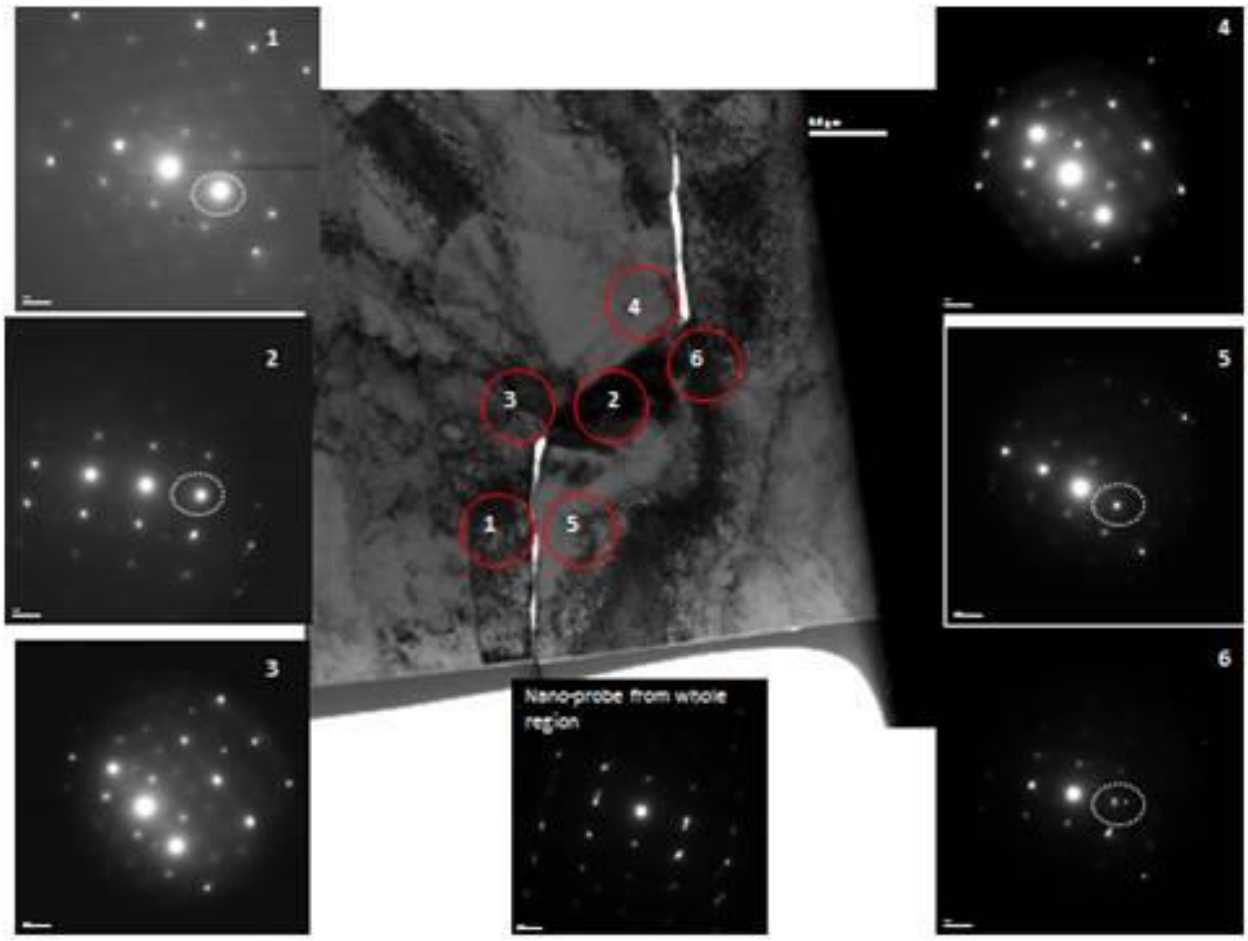

Figure 17. SAD patterns and their corresponding locations in the same cracked region as shown in Figure 16. The misorientations between all the patterns are very low.

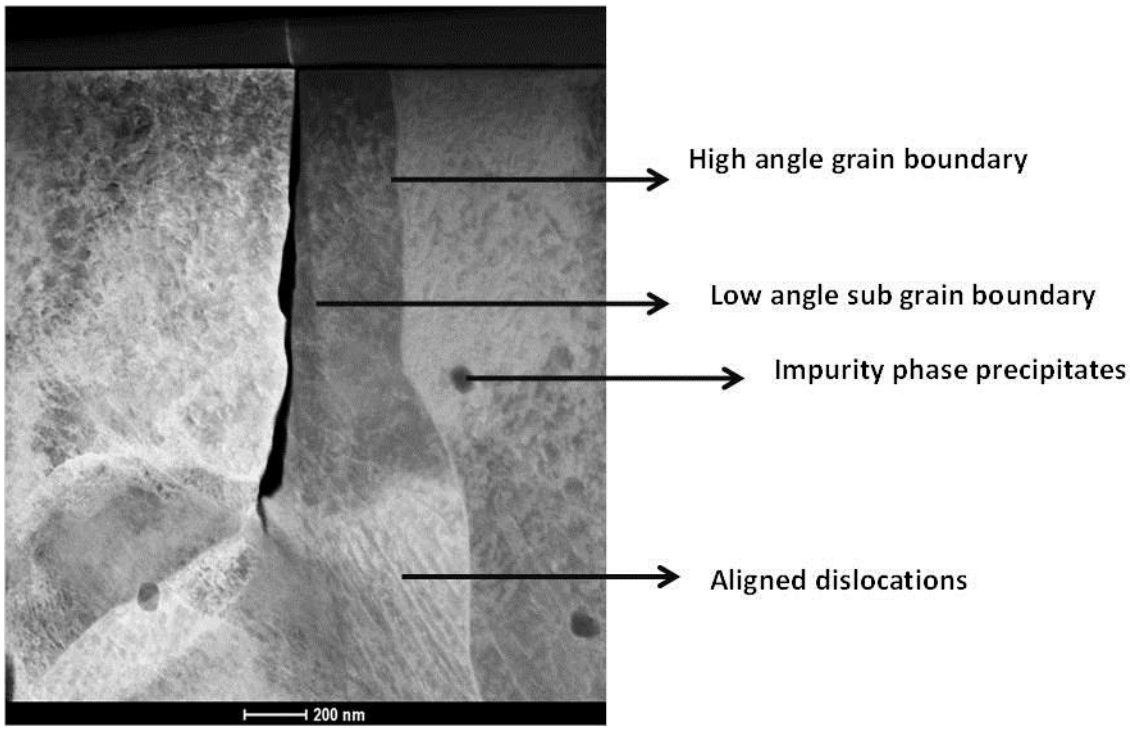

Figure 18. HAADF image of the crack front showing different microstructural components.

Summary and Discussion

Microcracking and delamination in pipeline steels are well-established phenomena. Various reasons for this behavior have been proposed, including: inter-phase boundary fracture, the presence of carbide and inclusion particles, texture, banding, and anisotropic plastic deformation [3-4]. Unfortunately a clear responsible micro-mechanism operating during thermo-mechanical processing and texture development is not in hand. Most of these reported results are for dual-phase steels containing combinations of ferrite/austenite/martensite constituent grains and their biphasic interfaces [3-4]. In the present investigation, microcracking and delamination occur in a fully ferritic steel (14YWT NFA-1). The extruded and cross-rolled NFA-1 plate exhibits a strong α-fiber texture (<110>∥ ED). ODF analysis coupled with IPF mapping shows that presence of a {001}<110>-texture component in planes normal to the short, plate thickness direction. This is the most brittle cleavage system in bcc Fe. TEM clearly shows that cracks nucleate and propagate on {100}-type planes and run along low-angle subgrain boundaries parallel to {100} in the <110> direction. Since {110} are the easy glide planes in bcc structures, grains containing these planes become elongated along the extrusion direction. In contrast, glide is difficult on {100}-type planes. Under sufficiently high stress, two a/2[111] + a/2[-1-11] dislocations react on a {001} plane to form a sessile [001] dislocation [5]. Subsequent dislocation pile-ups create stress concentrations and opening displacements that nucleate a microcrack. The fracture toughness for the {001} <110> cleavage system is extremely low, of order ~ 5-10 MPa$\sqrt{m}$. This microcrack growth is further driven by the residual stresses that develop during the thermo-mechanical processing.

The existence of residual stress is supported by streaking in the SAD patterns in Figure 19b collected from different locations near the cracks within a single grain marked in Figure 19a. These SAD patterns are taken along the <111> zone axis of bcc Fe. Streaking of the diffraction spots usually could be attributed to residual stress that generates strain even within a single grain. Initially the deformation is accommodated through low-angle subgrain boundary formation on {001} planes by creating sessile <001> dislocations that form subgrain boundaries. These subgrain boundaries are also aligned along the primary deformation direction. Further deformation causes dislocation pile-ups and produces crack

opening displacements. These cracks propagate on the brittle cleavage system {001}<110> aligned along the subgrain boundaries.

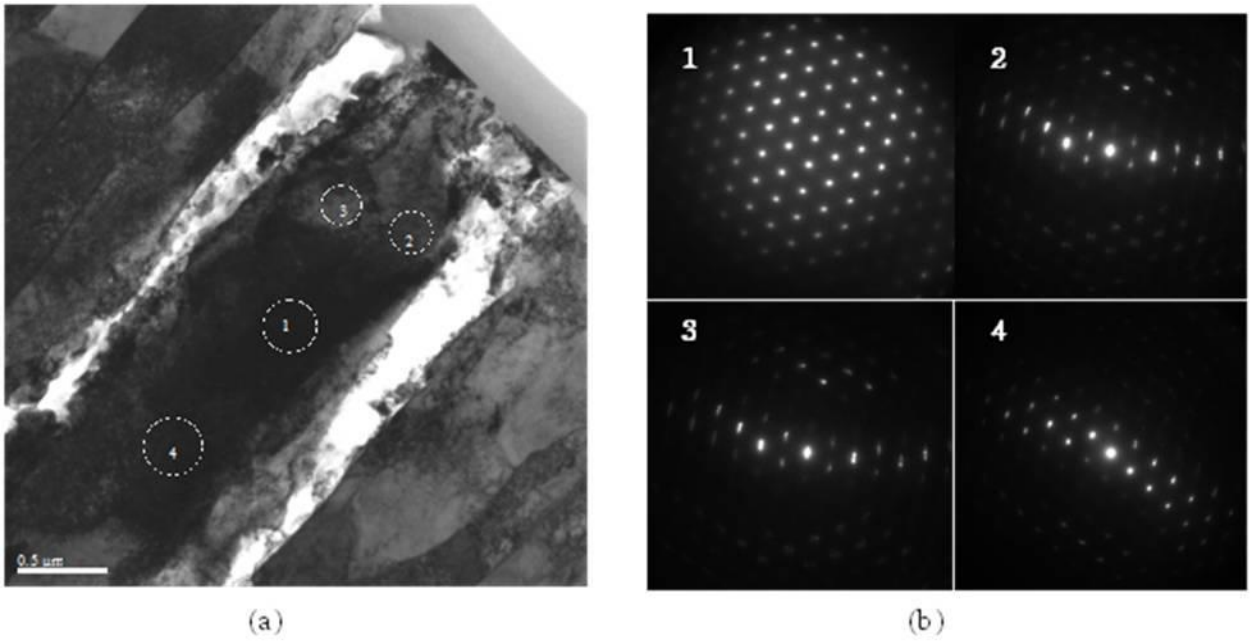

Figure 19. a) BF image of the cracked regions and (b) streaked SAD patterns from the locations marked in the BF image.

Conclusions

- Thermo-mechanical processing of the NFA-1 alloy produces a microstructure containing a tri-modal distribution of small (< 1 μm), medium (1 – 10 μm) and large grains. The pancake-shaped grains are compressed in the plate reduced-thickness direction and elongated in the cross-rolling and especially extrusion directions, with and average aspect ratio ranging from 2-3 when viewed along a side LS view surface.

- NFA-1 contains coarser Ti- or Y-rich precipitates/inclusions in the size range of ~ 15-150 nm. However, these features do not appear to affect microcracking.

- Microcracking of as-processed NFA-1 alloy is related to texture development during deformation processing. The plate develops α-fiber texture along the extrusion and cross-rolling directions, which results in alignment of the {001}<110> brittle cleavage plane-direction system normal to the plate thickness direction.

- Initial deformation is accommodated by a/2[110] dislocation glide. Dislocations react to form low-angle subgrain boundaries composed of sessile a[001]-type dislocations on {001} planes. Further deformation leads to additional dislocation pile-ups at the subgrain boundaries that create stress concentrations and opening displacements, which nucleate a cleavage microcrack. Transgranular cleavage microcrack propagation occurs on the {001} <110>-cleavage system and is further driven by residual stresses that develop during deformation processing.

References

[1] G.R. Odette, “Recent progress in developing and qualifying nanostructured ferritic alloys for advance fission and fusion applications” JOM, 66-12 (2014) 2427.

[2] M. E. Alam, N. J. Cunningham, D. Gragg et al., **"**Mechanical property characterization of a larger best practice heat of 14YWT NFA1**"**, DOE/ER-0313/56 (63-69)

[3] H.C.Chao, "Mechanism of anisotropic lammellar fractures", Met. Trans. A, 9A (1978) 509.

[4] D. L. Bourell and O. D. Sherby "Texture induced cleavage delamination of warm-rolled low carbon steel", Met. Trans. A, 14A (1983) 2563.

[5] A.H. Cottrell, "Theory of brittle fracture in steel and similar metals**",** Trans. A.M.I.E, 212 (1958), 192-203.

2.7 CRACK HEALING BY ANNEALING IN 14YWT NANOSTRUCTURED FERRITIC ALLOY, FCRD NFA-1 — M.E. Alam, S. Pal, G. R. Odette (UCSB), D. T. Hoelzer (ORNL) and S. A. Maloy (LANL)

OBJECTIVE

The objective of this study is to explore the effects of annealing on the microstructural and mechanical properties of a newly developed larger best practice heat of 14YWT nanostructured ferritic alloy, NFA-1.

SUMMARY

FCRD NFA-1 is a new 14YWT nanostructured ferritic alloy (NFA) processed to form a 12.5 mm thick plate. Plane sections parallel to the broad plate surface have a nearly equiaxed, ultrafine grain structure. In contrast, the plane sections parallel to the narrow plate thickness side contain pancake shaped grains with a tri-modal size distribution, including some that are very large, and a population of microcracks running normal to the thickness direction. At 23°C tensile specimens loaded in the short thickness direction have flat, faceted fracture surfaces and no ductility due to cleavage initiation of the microcracks. The corresponding tensile ductility increases with test temperature due to a brittle to ductile transition near about ~150°C. Annealing at 1300°C/1h appears to heal the microcracks, resulting in ductile fracture for short thickness direction axis loading. Annealing also appears to alter the grains and reduces the room temperature (23°C) yield stress by ≈ 13%. Tensile tests at 600°C showed relatively isotropic properties in both conditions, and a smaller reduction in strength following annealing.

PROGRESS AND STATUS

Materials and Methods

The nanostructured ferritic alloys (NFAs) are a promising candidate alloy class for the advanced nuclear fission and future fusion reactor applications, since they have high tensile, fatigue and creep strengths over a wide range of temperature, as well as unique irradiation tolerance and outstanding thermal stability up to 1000°C. These attributes derive from the presence of submicron size grains, high dislocation densities and especially an ultrahigh population of nanometer size Y-Ti-O rich multifunctional nano-oxides (NO) [1]. NFA-1 was developed in collaboration between UCSB, ORNL and LANL to explore including Y in the Fe-14Cr-3W-0.4Ti-0.2Y melt prior to gas atomization by ATI Powder Metals (Pittsburgh, PA). However, the Y was phase separated after atomization. Thus a low interstitial alloy powder (15 kg) variant was ball milled for 40 hours with FeO (52.5 g) to increase the O content and to mechanically alloy the Y into solution. The milling was carried out by Zoz GmbH (Wenden, Germany) using a CM100b attritor mill with a ball mass-to-charge ratio of 10:1 and ball size of 5 mm. The milled powders were then consolidated at ORNL by hot extrusion at 850°C. The extruded bar was annealed for 1 hour and then hot cross-rolled to a ≈ 50% thickness reduction, both at 1000°C, to produce an ≈ 12.5 mm thick plate [2]. The as-fabricated plate has been extensively characterized as reported elsewhere [3]. Tensile specimens extracted from the plate wrapped in a molybdenum getter foil were annealed in a low pressure Ar environment at 1300°C for 1 h.

The as fabricated and annealed NFA-1 conditions were characterized using a scanning electron microscope (SEM) equipped with energy dispersive spectroscopy (EDS) and electron backscatter diffraction (EBSD) detectors. The tensile specimens were ground (to 1500 grit) and polished (to 20 nm colloidal silica), then etched with Kroll's reagent (92% distilled water, 6% nitric acid and 2% hydrofluoric acid) prior to examination in a FEI x30, Netherland SEM. Longest (l) and shortest (s) individual grain dimensions were tabulated from the SEM micrographs using 'ImageJ64' software. The effective grain diameter was taken as d = (l+s)/2 and the aspect ratio as r = l/s. EBSD was used to characterize the texture in the plate induced by hot extrusion and cross rolling. Vickers microhardness measurements were performed on polished coupon surfaces at a 500g load using LECO M-400A semi-automated hardness tester, based on the average of 10 to 15 indents. Tensile tests were performed on flat dog-bone shaped sub-sized specimens with a gage section length, width and thickness of 5.0x1.2x0.5 mm^3. The

tensile tests were performed for longitudinal (L), transverse (T) and short (S) thickness directions as illustrated in Figure 1, at both room temperature and 600°C, on a 810 MTS servo-hydraulic universal testing machine equipped with a clam shell furnace. The tensile specimens were sanded with 1500 grit to remove surface contamination, minor defects and local residual stresses due to the EDM used to fabricate them. The specimens were heated to the target temperature in atmosphere, and held for 10 minutes before testing. Loading was carried out at a crosshead speed of 0.30 mm/min, or a strain rate of ≈10^{-3}/s. Except for the small size of the specimens, the tensile properties were determined in accordance with ASTM Standard E8M-13. The fracture surfaces of the broken tensile specimens were extensively characterized by SEM.

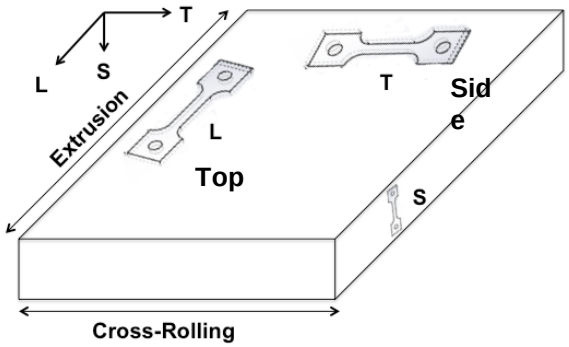

Figure 1. NFA-1 specimen orientations labeled with respect to the extrusion, cross-rolling and plate thickness directions.

Results and Discussion

- Microstructure

Figs. 2a and d show SEM micrographs of the plate normal (L-T or top) view with nearly equiaxed, unimodal and ultrafine grains, in both the as fabricated and 1300°C annealed conditions. The grains are ≈ 20% larger following annealing. Figs. 2b and c show that the as-fabricated L-S (side) plane contains a number of microcracks running on planes normal to the plate thickness direction. The corresponding grains are elongated and pancake-shaped with a tri-modal grain size distribution (many < 1 μm, some 1-10 μm and a few very large grains). As shown in Figs. 2e and f, microcracks are not observed in the L-S (side) view of the annealed specimens. Both the corresponding grain size and aspect ratio appear slightly smaller in the annealed versus as-fabricated condition. An EDS scan indicates the presence of Ti-rich precipitates in stringers along the extrusion direction. High temperature annealing appears to heal the cracks, presumably by surface diffusion, perhaps assisted by recrystallization and grain boundary migration [4].

Table 1. Grain morphology and microhardness of as-fabricated and 1300°C annealed NFA1

Location, Condition	Grain Size (nm)	Aspect Ratio	Microhardness (Hv)
Top, as-fabricated	454 ± 142	1.2 ± 0.2	376 ± 18
Side, as-fabricated	(1077 ± 509) x (397 ± 124)	2.7 ± 1.1	352 ± 39
Top, annealed	705 ± 346	1.2 ± 0.4	294 ± 13
Side, annealed	(822 ± 516) x (341 ± 115)	2.4 ± 1.4	304 ± 17

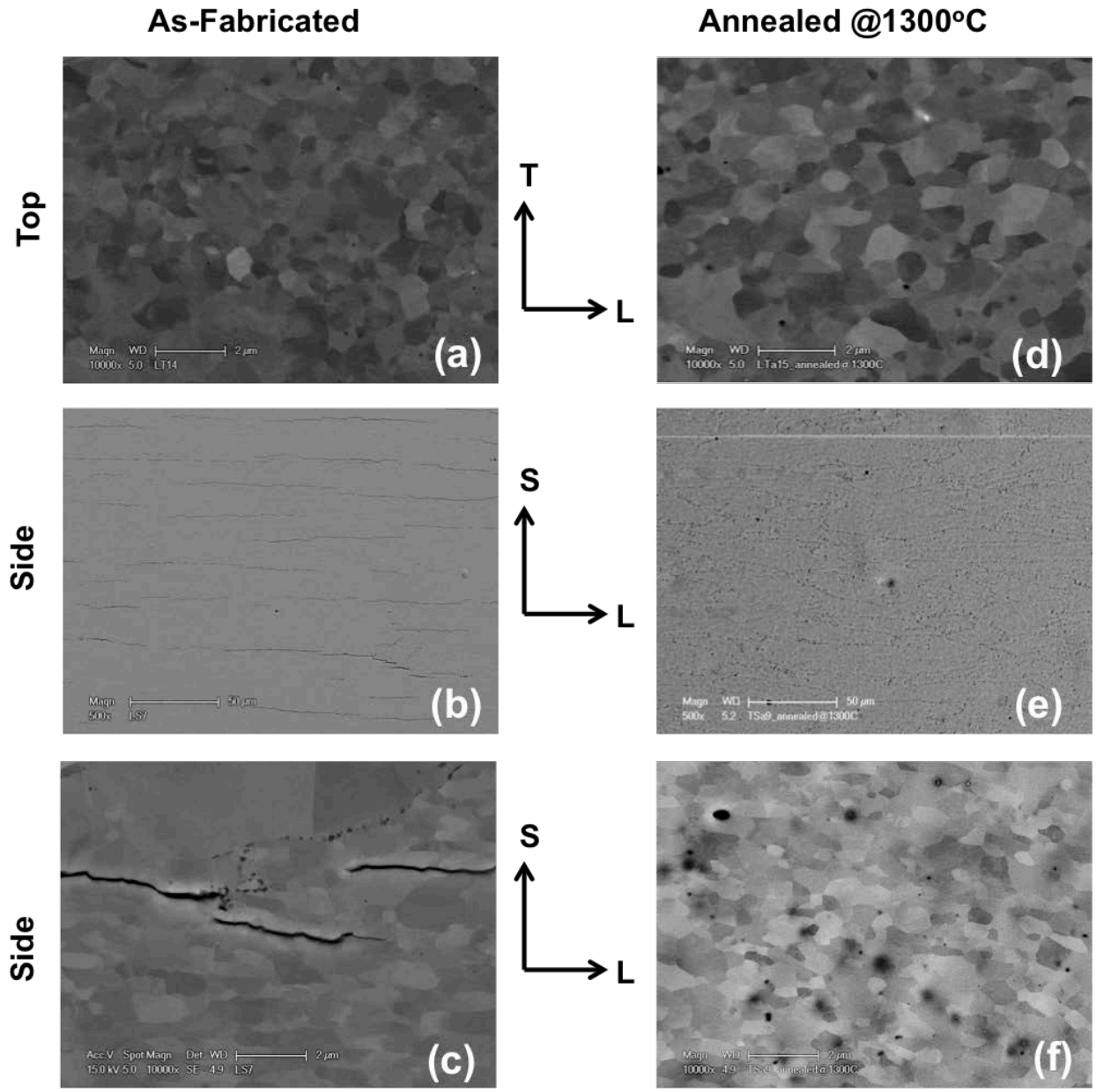

Figure 2. SEM images showing plate's: a) top; b and c, side view morphology, respectively, for as-fabricated (left) and 1300°C annealed samples (right).

Figure 3 shows inverse pole figure (IPF) maps for as-fabricated and annealed conditions with both top and side views measured using EBSD techniques. Subgrains and grains were characterized by means of misorientation angle distribution (MAD) measured using EBSD. A misorientation angles greater than 3° (red) and less than 15° is considered as subgrain boundary, while, above 15° (black) it is taken as a grain boundary.. Consistent with the SEM observations, Figure 3a shows small and nearly equiaxed grains in the plate's L-T (top) view, while Figure 3b shows larger and grains elongated in the extrusion direction in the side views in the as-fabricated condition. Some very large and highly elongated grains are also observed, including one in the vicinity of a microcrack. Low angle grain boundaries are found inside the larger grains (marked as red). The IPF maps highlight the strong preferential crystallographic orientation

of most of the grains with a <110> direction parallel along with the extrusion directions. As shown elsewhere [5], the texturing is accompanied by the development of (100) planes normal to the thickness direction, thus creating a corresponding (100)<110> texture component, which is the most brittle cleavage system for bcc Fe. In combination with stress concentrations, this leads to the formation of the population of microcracks. In contrast, the side view of the annealed condition is crack-free, relatively equiaxed and nontextured with a bimodal grain distribution as seen in Figure 3d.

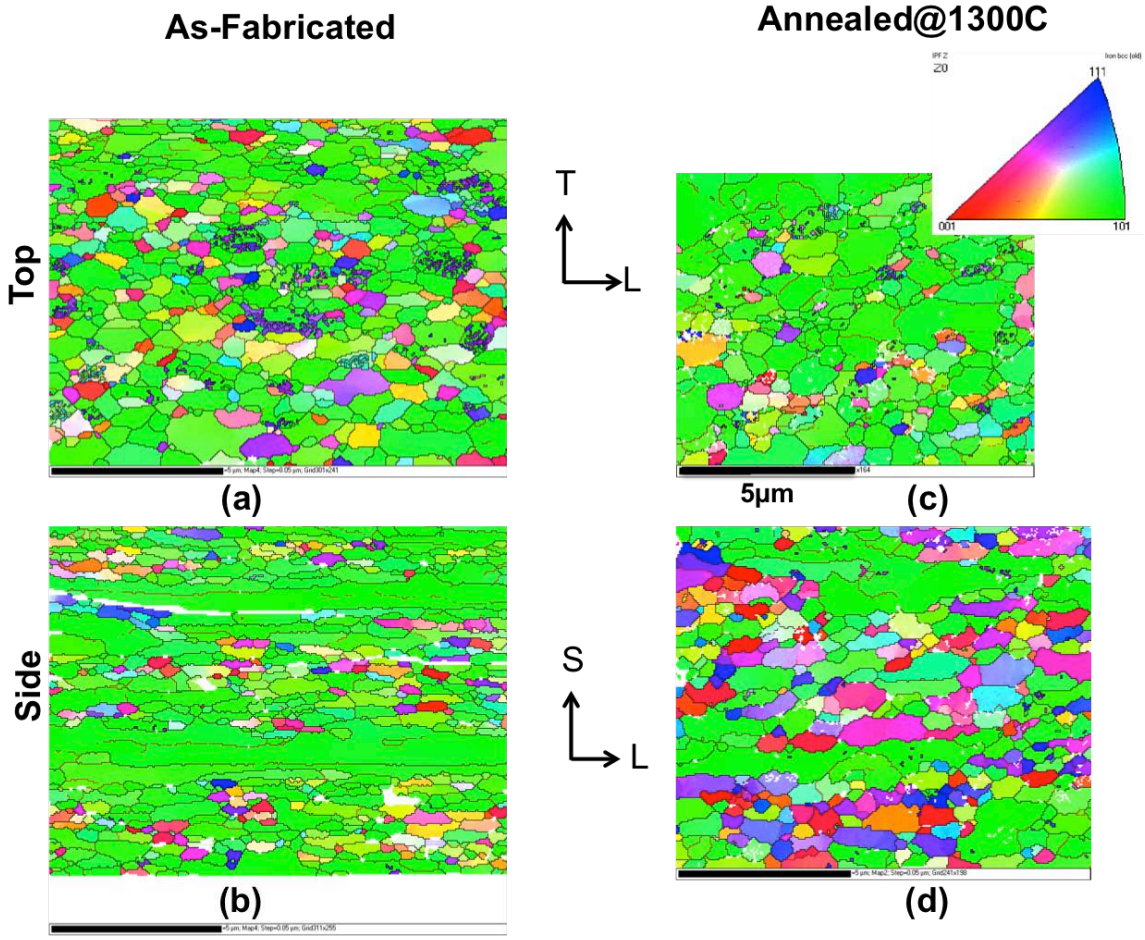

Figure 3. IPF maps obtained by EBSD for the as-fabricated condition (left) with a) top and b) side views; the corresponding IPF map for the annealed condition (right) with c) top and d) side views.

Microhardness

Vicker's microhardness (H_v) data for the NFA-1 are also summarized in Table 1. For the as-fabricated condition H_v averages 376 ± 18 (kg/mm^2) for the top surface and 352 ± 39 (kg/mm^2) for the side surface for specimens. These differences can probably be attributed to some coarsening of the NO and grains. The lower H_v and higher standard deviation for the side surface might be due to softening associated with delamination. The H_v is lower after annealing and similar for the two surfaces, with smaller standard deviations.

Tensile Properties

Figure 4 shows engineering stress-strain s(e) curves from room temperature tensile tests in the three L, T and S orientations (see Figure 1), for both the as-fabricated and annealed conditions. The as-fabricated L and T orientations have similar s(e), with 0.2% yield stress (YS) and ultimate tensile strength (UTS) values varying from 951-961 MPa and 1062-1082 MPa, respectively. The total elongations range from 12.8 to 15.3%. In contrast, the as-fabricated S orientation has the lowest strength with YS = UTS = 652 MPa, fracturing in the elastic region, without any plastic strain. The s(e) for the L and T oriented annealed condition are also similar to each other, with ≈ 14% lower strength than the as-fabricated condition. While the as-fabricated S oriented tensile specimen failed in the elastic region at room temperature, the corresponding annealed condition has a large total elongation of ≈ 18%, with slightly higher YS ≈ 700 MPa and a significantly higher UTS of ≈ 874 MPa compared to the as fabricated condition. The strength and ductility for annealed condition in the S orientation is comparable to the annealed L and T oriented specimens. These improvements in strength and ductility are associated with the absence of microcracks (Table 1 and Figure 2). The lower YS in this case is due to a lower stress marking the deviation from the elastic loading line. But this may be an experimental artifact since all three orientations have otherwise very similar s(e) curves.

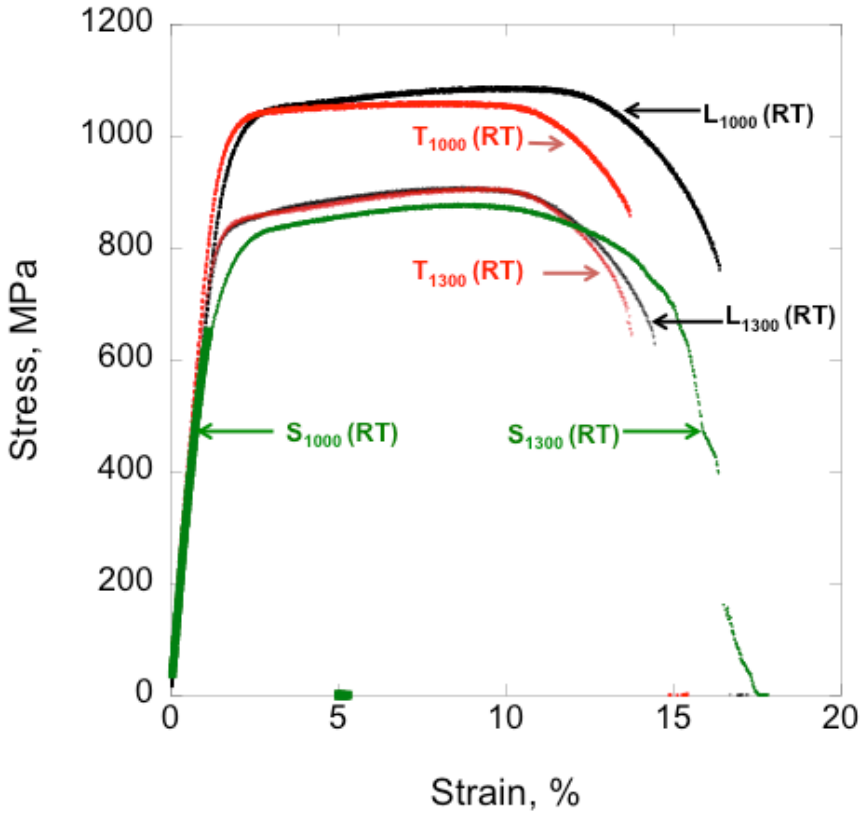

Figure 4. Room temperature engineering stress-strain curves of as-fabricated (1000°C) and annealed (1300°C) NFA-1 specimens tested in three different orientations.

Figures 5 and 6 show the fracture surfaces of the broken tensile specimens. Delaminations occurred in both the as-fabricated condition L and T specimens normal to the thickness direction in planes parallel to the plate surfaces. In contrast, the annealed condition is delamination-free. Again the fracture surface is

flat and brittle for the S orientation in the as-fabricated condition, in contrast to fully ductile fracture in the annealed condition. Corresponding higher magnification images in Figure 6 show ductile dimples in all the annealed specimen along with shallow crater-like features, which might be partly responsible for lower strength along with higher grain size compared to the as-fabricated specimens. The crater like features may partially healed microcracks.

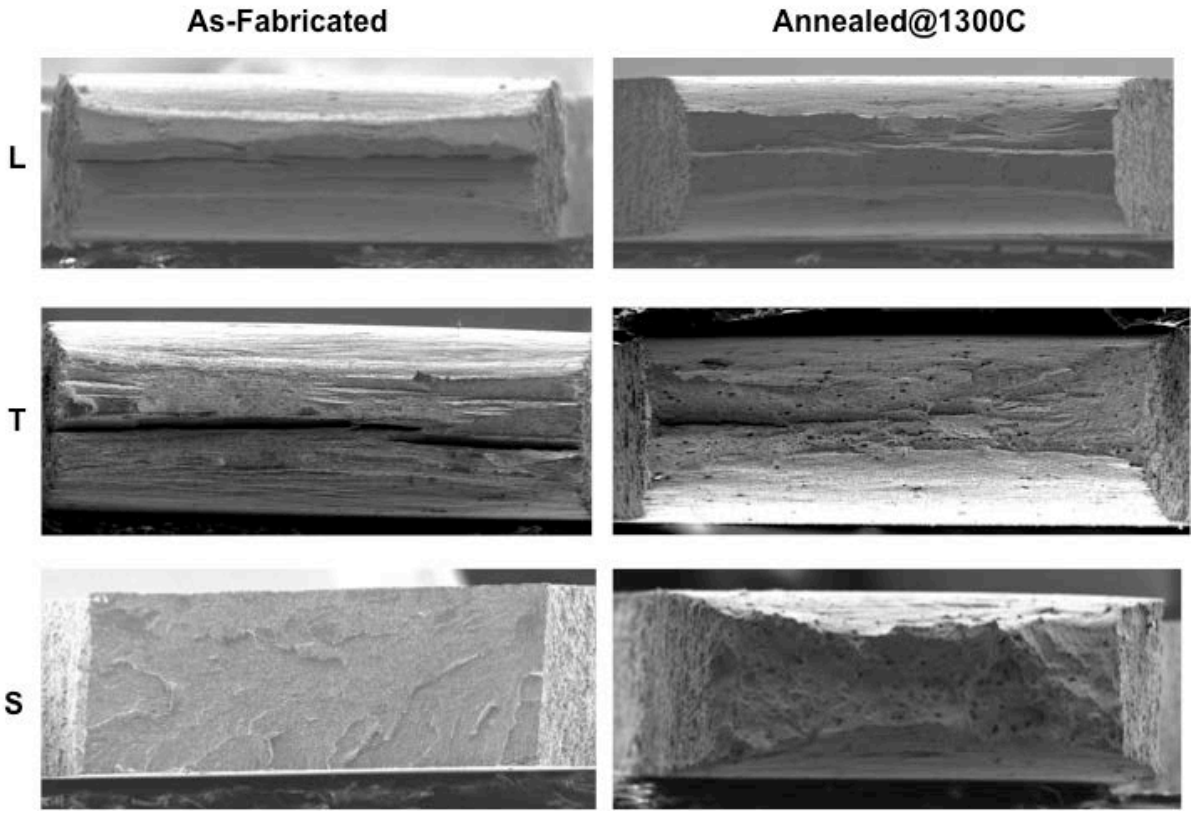

Figure 5. Low magnification SEM fractographs of room temperature as-fabricated and annealed tensile fracture surfaces for different orientations.

Figure 7a shows the s(e) for tensile test on annealed T and S oriented specimens at 600°C. Both the strength (YS and UTS) and ductility decrease at higher temperature. In both cases, the uniform elongations are quite low (~1.3%) compared to at room temperature (7-8%). However, the annealed specimens retained significant strength levels of YS = 432-489 MPa and UTS = 469-502 MPa, and ductility, with total elongation strains of 9-10%. This compares to corresponding as-fabricated strength and ductility values of YS ≈ 484-547 MPa, UTS ≈ 529-580 and total elongation strains of 13.5-14.4%. As seen in Figure 7b, no delaminations are observed in the annealed condition. Relatively flat fracture surfaces were observed for both T and S orientations with reductions in area of ≈31% and ≈12%, respectively. Higher magnification SEM images in Figure 7b, show dimples associated with coarser oxide particles in both cases, along with crater-like features. However, the dimples for the S orientation appear to be composed of larger and smaller features. The larger features are filled with small dimples on their sidewalls. Note the surfaces are oxidized during high temperature testing. In the annealed condition L, T and S orientations strength and ductility values are comparable both for the room temperature and 600°C tests. Thus NFA-1 exhibits nearly isotropic behavior when annealed at 1300°C.

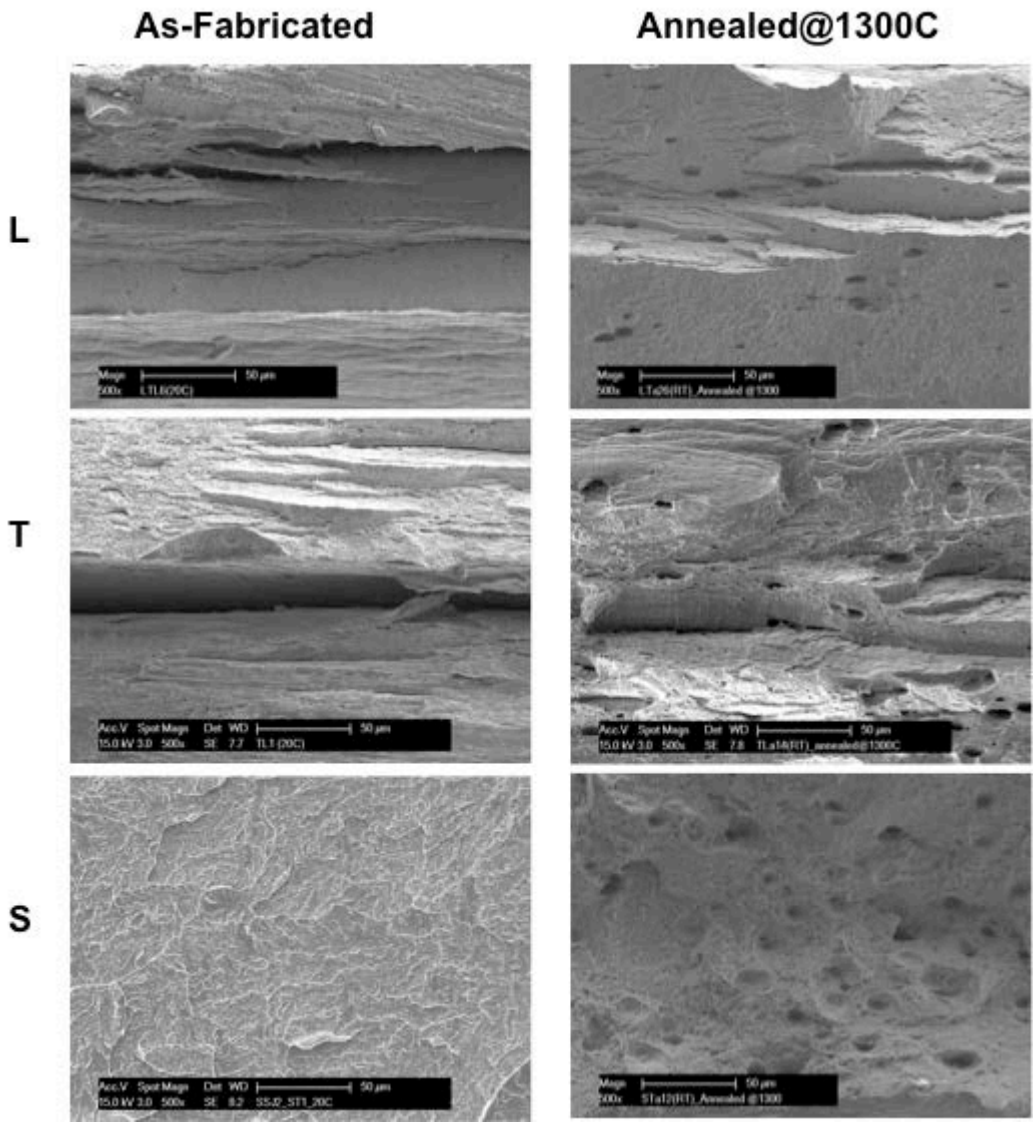

Figure 6. High magnification SEM fractographs of room temperature as-fabricated and annealed tensile fracture surfaces at different orientations.

Summary and Future Work

The effect of annealing 1300°C for 1 h on as-fabricated NFA-1 was characterized in terms of grain structures, microcracks, microhardness and tensile properties. High temperature annealing appears heal the microcracks that exist in the as-fabricated plate. Annealing also increases the average grain size by ≈ 20% reduces both the microhardness by ≈ 18% and room temperature tensile YS and UTS by ≈ 13% lower. The room temperature tensile properties are more isotropic after annealing.

The effect of different annealing temperatures and times will be explored and more detailed observations on microcrack healing will be carried out along with the corresponding effects on the grain, dislocation and NO nanostructures will be characterized. Mechanical property measurements will be extended to fracture toughness.

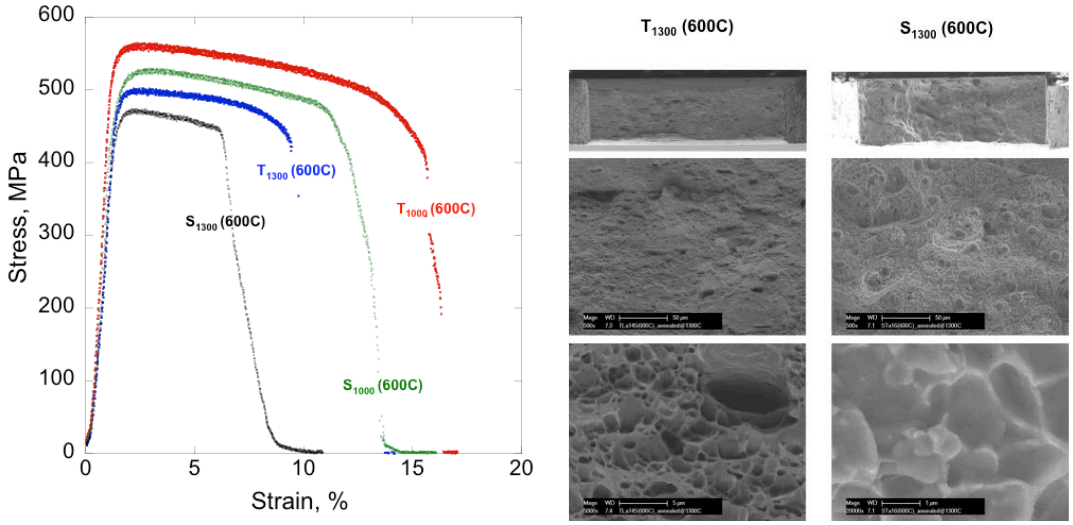

(a) (b)

Figure 7. a) Engineering stress-strain curves of annealed specimens tested at 600°C, and b) their SEM fractographs.

Acknowledgments

This work is part of a multi-laboratory collaboration between LANL, UCSB and ORNL. The DOE Office of Fusion Energy Sciences supported some of the mechanical testing reported here. NFA-1 was produced under the sponsorship of the DOE Office of Nuclear Energy through both a NEUP grant and the FCRD program.

References

[1] G.R. Odette, "Recent progress in developing and qualifying nanostructured ferritic alloys for advanced fission and fusion applications," JOM. 66 (2014) 2427.

[2] N.J. Cunningham, Y. Wu, G.R. Odette, D.T. Hoelzer, S.A. Maloy, " Characterization of a larger best practice heat of 14YWT in annealed powder, HIP consolidated and extruded forms", Fusion Materials Semiannual Progress Report for Period Ending June 30, 2013, DOE/ER-0313/54, U. S. Department of Energy, 15.

[3] M.E. Alam, K. Fields, G. R. Odette, D. T. Hoelzer and S. A. Maloy, "Tensile property characterization of 14YWT nanostructured ferritic alloy NFA1" Fusion Materials Semiannual Progress Report for Period Ending December 31, 2014, DOE/ER-0313/57, U. S. Department of Energy, 39.

[4] K.W. Gao, L.J. Qiao, and W. Y. Chu, "In situ TEM observation of crack healing in □α-Fe", Scripta Materialia, 44 (2001) 1055.

[5] A. G. Junceda, M. H. Mayoral and M. Serrano, " Influence of the microstructure on the tensile and impact properties of a 14Cr ODS steel bar", Materials Science and Engineering A, 556 (2012) 696.

2.8 FRICTION STIR WELDING OF ODS STEELS AND ADVANCED FERRITIC STRUCTURAL STEELS

— Z. Feng, W. Tang, X. Yu, G. Chen, D. Hoelzer, and L. Tan (Oak Ridge National Laboratory)

OBJECTIVE

This project addresses the critical technology gap of joining oxide dispersion strengthened (ODS) steels, nanostructured ferritic alloys (NFAs), reduced-activation ferritic/martensitic (RAFM) steels, and dissimilar metal joints of ODS/NFAs and RAFM steels through friction stir welding (FSW) technology. The research focuses on understanding the stability of the strengthening phases in the weld region, and the bonding mechanisms between dissimilar structural steels as a function of FSW process conditions.

Specific project objectives are (i) developing the process parameter space to consistently produce defect-free welds of the same and dissimilar metals, (ii) developing the knowledge base and practical applicable approaches to tailor and optimize the microstructure features in the weld to match the properties of the base metal through process innovation, and (iii) producing representative weld joints and welded components to support future testing and evaluation at high temperature and irradiation environments in collaboration with JAEA and other international teams.

SUMMARY

For this final reporting period of the project, the baseline FSW process conditions for joining ODS steels and RAFM steels have been successfully developed. A computational fluid dynamics (FCD) based model has been developed and applied to understand of temperature and material flow during FSW of these advanced structural materials. A unique high temperature digital image correlation (DIC) strain measurement technique enabled experimentally determining the local deformation behavior in different regions of FSW of RAFM steel in high temperature creep test. The DIC measurement revealed drastic increase in creep resistance (i.e. reduced creep rate) in the stir zone, and reduced creep resistance in the heat affected zone (HAZ), an area requiring further process optimization. Finally, the sizes of the oxides/nano-cluster features, the primary strengthening phase in ODS alloys, is highly dependent on the FSW process conditions. This shows the feasibility of using FSW to join advanced fusion structural materials with better than base metal properties.

PROGRESS AND STATUS

Microstructure characterization of the dissimilar materials ODS alloy and RAFM steel FSW joint

A defect-free dissimilar materials joint between 14YWT and 9Cr advanced steels was produced by friction stir welding (FSW) and was reported previously. Both alloys were developed and produced at Oak Ridge National Laboratory (ORNL). Optical microstructures in various metallurgical zones of the dissimilar materials joint were also reported. Though optical images of the weld confirmed the joint was free of defects, detailed grain structures and hardening precipitates, which are important strengthening factors, are need to be characterized to further evaluate the joint quality.

In this period of study, we concentrated on examining the microstructure of this dissimilar materials joint using scanning electron microscope (SEM). Three regions on the 14YWT side, including stir zone (SZ), heat affected zone (HAZ) and base metal (BM) were characterized in details. Backscattered electron images of the ODS alloy 14YWT BM, SZ and HAZ are shown in Figure 1. In the SZ of 14YWT, significant grain growth was observed. Grain size of SZ is about 5-10 microns compared to 0.3 microns in base metal (BM). In addition, the HAZ also exhibits grain growth (grain size is about 1-2 microns) due to the heat introduced by friction stir process.

Figure 2 shows backscatter electron images of SZ and BM. For BM, most of the precipitates were not resolved by SEM since these precipitates are on the order of 2-5nm (nano-clusters). Only sub-micron ferritic grains were observed in BM. In SZ, t*he “bright” precipitates inside grains indicate they are enriched with greater atomic number elements. As a result, these precipitates could be oxides enriched

with Y and Ti, which need to be confirmed by further atom probe tomography or transmission electron microscopy.

In our study reported in previous reporting periods, it was found that FSW can preserve the nano-size precipitates in 14YWT. Similar phenomenon was also observed in the current report. Precipitates were observed in SZ.

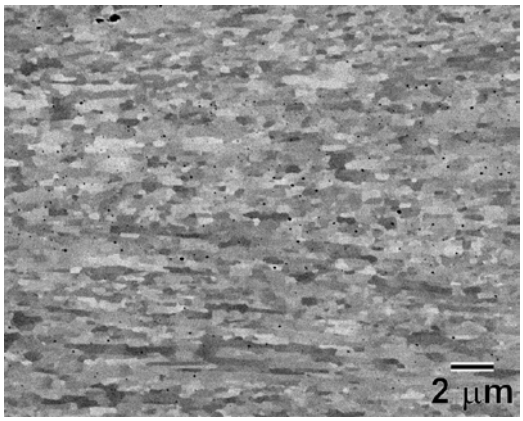

(a) Base metal

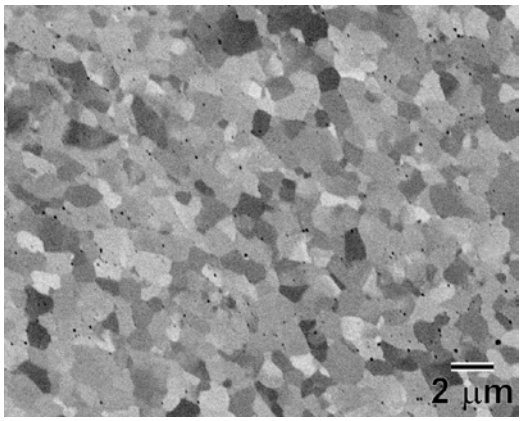

(b) Heat affected zone (HAZ)

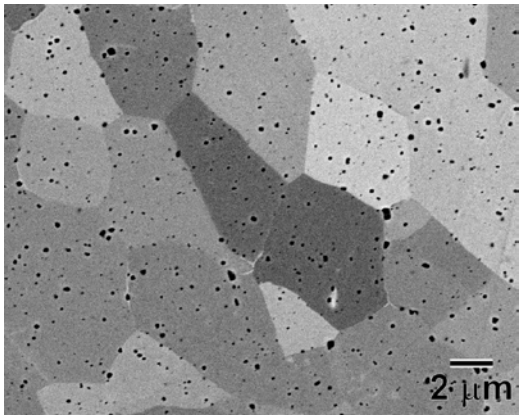

(c) Stir zone (SZ)

Figure 1. Electron backscatter images of 14YWT at various metallurgical zones

In the SZ, the interface between 9Cr and 14YWT also studied. Figure 3 shows backscattered electron image of 9Cr/14YWT interface. Ferrite grains 14YWT near the interface are elongated. The elongated grains are due to great deformation introduced by FSW. In addition, voids were observed in 9Cr steel adjacent to the interface, but not in 14YWT. The voids are in the size of 1-3 microns and mainly locate at the 9Cr prior austenite grain boundaries. The presence of the voids is on consistent along the interface. Some regions in 9Cr adjacent to the interface were free of voids (in the center of Figure 3a). Possible reasons for those voids appearance include the FSW tool wear effect and base metal precipitates etching effect. FSW of high temperature materials is very harsh to the FSW tool due to the elevated welding temperature (it can reach to 1000 °C easily) and high reaction forces. In another study of FSW stainless steel, voids were observed in certain regions of the joint stir zone after polycrystalline cubic boron nitride (PCBN) FSW tool was worn. The tool geometry change, features change and particles falling off from the tool may result voids in SZ. Meanwhile, the 9Cr base metal contains a couple of micrometer sizes particles, which are shown in Figure 4. It is possible that those particles were preferentially etched by the chemical etchant.

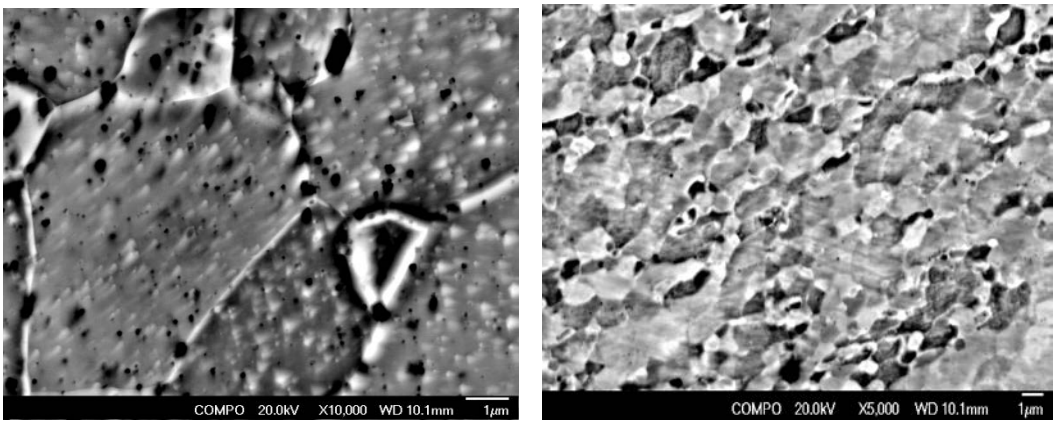

(a) 14YWT stir zone *(b) 14YWT base metal*

Figure 2. Grain and precipitates growth in the 14YWT SZ after FSW

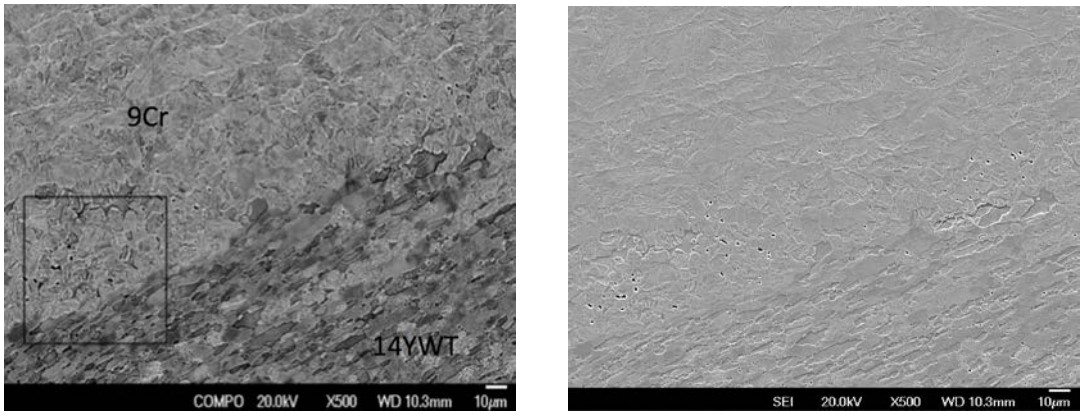

(a) backscattered electron imaged *(b) Secondary electron image*

Figure 3. *Image of 9Cr/14YWT interface showing voids at 9Cr prior austenite grain boundaries*

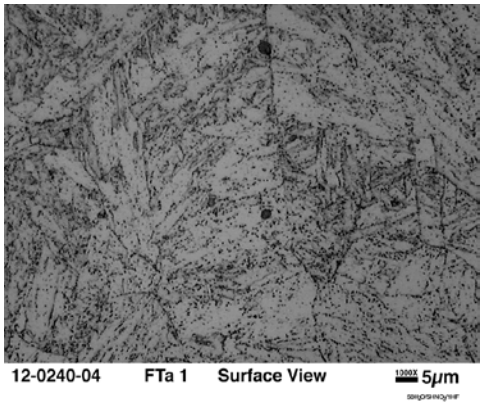

Figure 4. Micron size particles in 9Cr base metal

High temperature creep testing and characterization of RAFM friction stir welded joints

RAFM steel F82H was joined by FSW previously. Optical microscopy results as well as microhardness distributions of the welded joint were reported.

Cross-weld creep tests were performed on F82H FSW joints. Round bar specimens were machined out from the F82H FSW joint perpendicular to the welding direction for tensile creep-rupture test. The weld zone was located in the middle of each specimen. Specimens were machined to 6 mm diameter with a gage length of 40 mm, as shown in Figure 5. A unique feature of our creep test was the use of digital image correlation (DIC) technique to study the anticipated non-uniform deformation and creep behavior in the cross-weld specimen, due to the fact of the highly non-uniform microstructure gradient in the SZ and HAZ region. Before the creep test, special high-temperature random speckle pattern was applied on the specimen surface for DIC measurement of local deformation. Thermocouples were attached to the specimen to record the testing temperature.

Figure 5. Tensile creep-rupture specimens

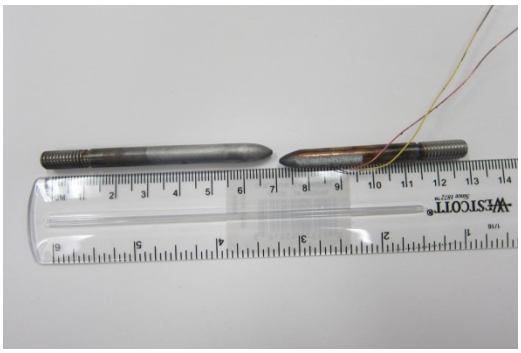

Figure 6. Broken tensile creep-rupture specimen

Tensile creep-rupture tests of welded joints were performed using a Gleeble^{TM} thermal mechanical simulator. Two test temperatures were chosen, 550°C and 650°C, which are typical temperatures for nuclear structural materials application. The sample was heated to 550°C or 650°C at 5°C/s, and a constant stress of 100 MPa was applied during the creep test.

For the sample tested at 650°C, it failed after 16 hours of testing. Post-test analysis showed that the failure location was in FSW HAZ, and the broken specimen is shown in Figure 6. Traverse creep strain across the sample from DIC analysis 5 minutes before fracture is shown in Figure 7. From Figure 7, clearly the strain peak value is located at the HAZ and the strain valley is located in the FSW stir zone. Therefore, high temperature creep plastic deformation was concentrated in the HAZ of the welded joint and the stir zone plastic deformation was even lower than that in the base metal.

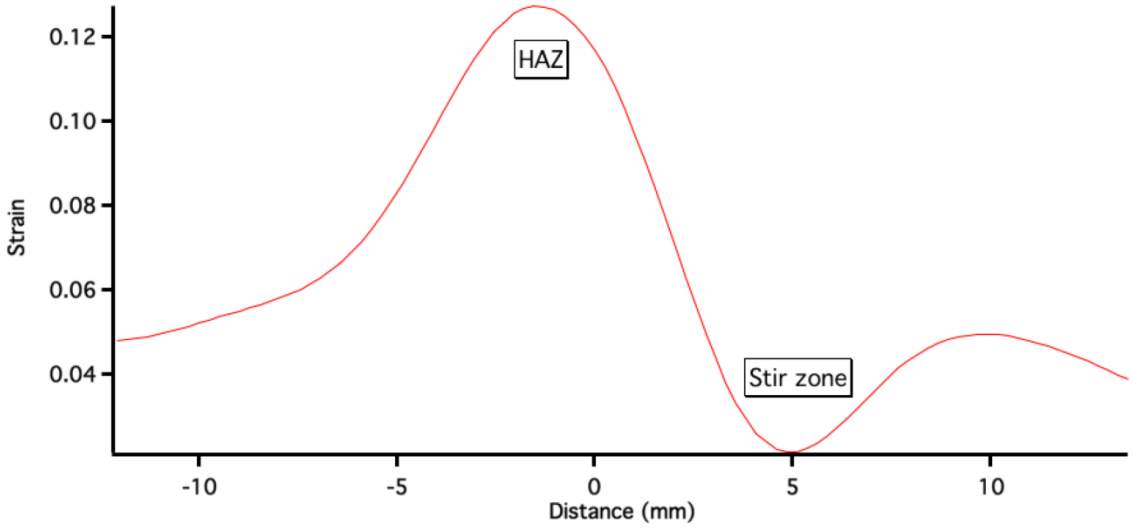

Figure 7. Traverse creep strain distribution of the sample tested at 650°C before fracture

The stress-rupture test at 550°C was interrupted at 89 hours, and the specimen didn't show obvious deformation or necking. After the stress-rupture test, the strain histories of SZ, HAZ and BM were plotted in Figure 8. In general, the system error of current DIC strain measurement is less than 3 X 10^{-4}. Before the loading in creep testing, HAZ and BM showed strain of 0.0083 and SZ showed strain of 0.0070. Those strains were thermal strains at 550°C. When stress was applied, the sample started to creep with time went by but there were almost no creep deformation in SZ at all. For BM, the secondary creep started at about 10.2 hours and the secondary creep rate was 2.9 X10^{-5} /h. For HAZ, the secondary creep started early at about 2.5 hours and the secondary creep rate was 4.8X10^{-5} /h. For SZ, creep strain should be less than 3 X 10^{-4} (system error of DIC). Assume the creep strain is 3 X 10^{-4}, which result in creep rate of 3.4 X10^{-6}/h. In general, the secondary creep rate in HAZ of a fusion welded ferritic steel joint is almost 5 times higher than that in BM. However, the secondary creep rate in HAZ is only about 1.7 times higher than that in BM for current friction stir welded RAFM joint.

Stress vs. creep rate was plotted in Figure 9. The base metal creep behavior follows Norton's power law. For HAZ, creep rate is only slightly above the power law curve. However, creep rate of SZ is significant lower than power law curve. The stir zone is expected to have much better creep resistance than base material.

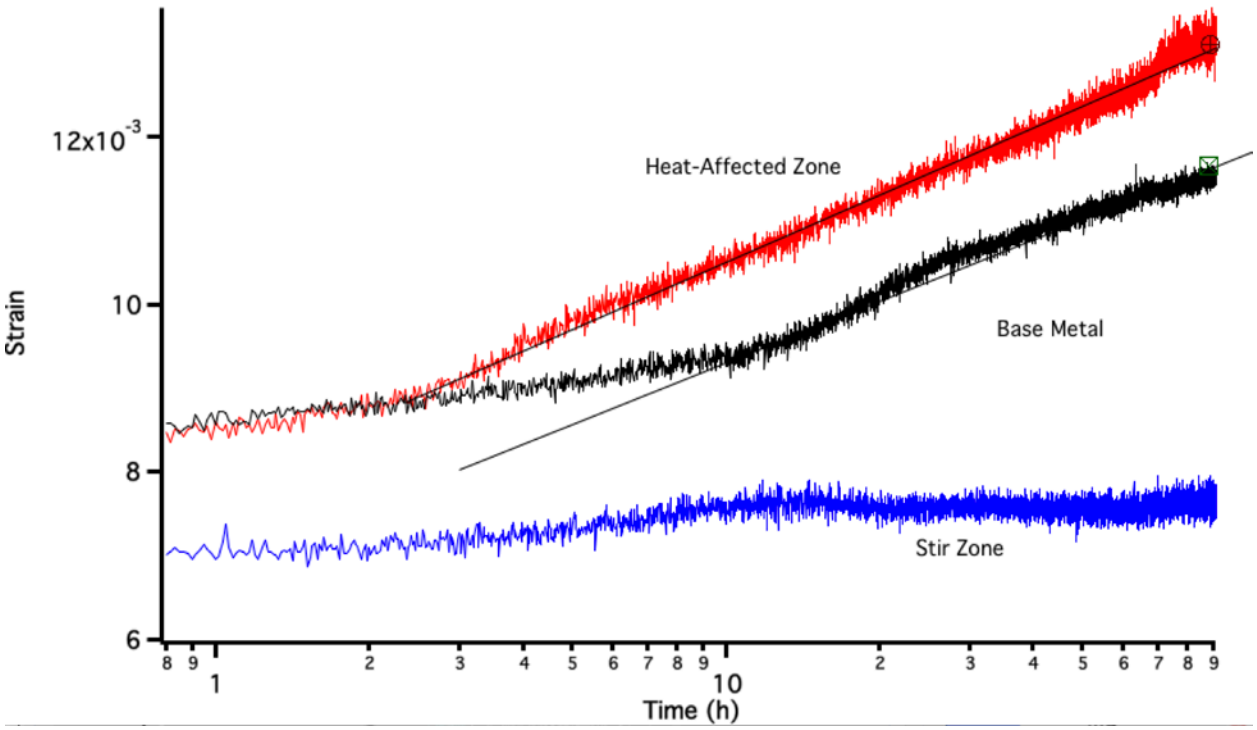

Figure 8. Strain vs. time for BM, SZ and HAZ of a RAFM FSW joint in creep-rupture test.

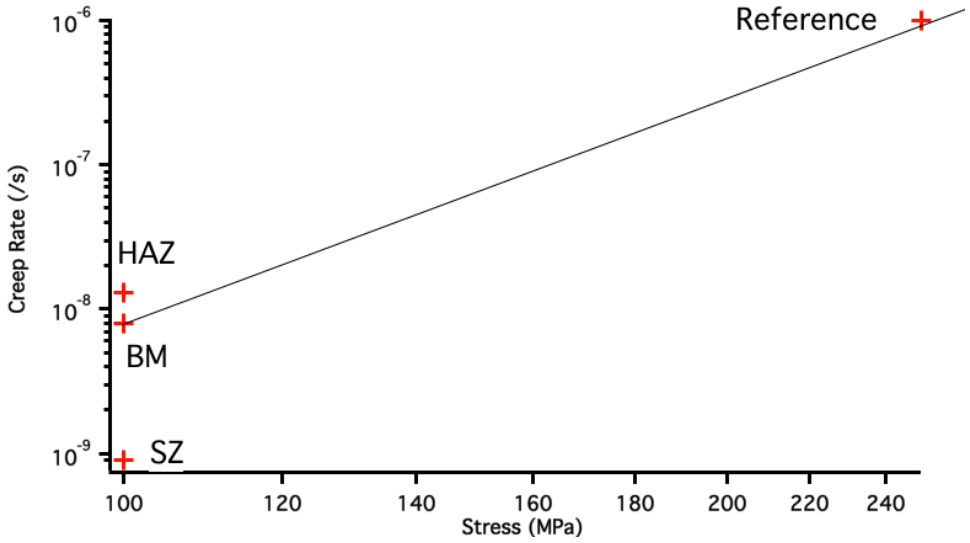

Figure 9. Stress vs. strain rate for different regions of the friction stir weld

Friction-induced material behavior in FSW thermal-mechanical coupled computer modeling

Fundamental studies of thermal-mechanical conditions, such as temperature, strain and strain rate, in FSW of ODS and RAFM steels were carried out by 3D thermally-mechanically coupled numerical models developed based on Computational Fluid Dynamics (CFD). Reasonable FSW temperature fields and material flow patterns were obtained by using the computer models developed in last year. This period of

study was focused on enhancing the developed numerical models, in order to predict the thermal-mechanical conditions in wide range of welding parameters, which facilities the understanding of material behaviors in different welding conditions. The temperature dependency of material flow strength is critical in predicting the variations of heat generation, temperature and material flow in different conditions owing to the thermal-mechanical nature of FSW process. The numerical modeling in this period of study was enhanced by taking into consideration of material flow stresses measured at various elevated temperatures from publications. The enhanced computer models were used to simulate the material behavior in different conditions. Various modeling conditions and parameters in the simulations are shown in Table 1. By applying those conditions and parameters, different FSW temperature distributions are obtained from modeling results and they are shown in Figure 10. From Figure 10, it is obvious that the welding temperature of 400 rpm FSW is higher than austenite phase transformation temperature while that of 100 rpm FSW processes is around the austenite phase transformation temperature value for the modeled material Eurofer 97 RAFM steel (A_{c1b} = 820 °C and A_{c1e} = 890 °C). In FSW, the peak temperature is mainly affected by welding power input and welding power input is mainly affected by FSW tool rotating rate. From the previous experimental results, martensitic was the major grain microstructure in 400 rpm condition FSW stir zone, and partially martensitic microstructure was observed in 100 rpm condition FSW stir zone. The modeling results of FSW temperature fields evolved the reason behind those experimental results.

Table 1. Parameters in the computation

Tool rotation rate/ rpm	Welding speed/ ipm	Magnitude of frictional stress between tool and workpiece/ MPa
100	2.0	15.0~25.0
200	2.0	15.0~25.0
400	2.0	15.0~25.0

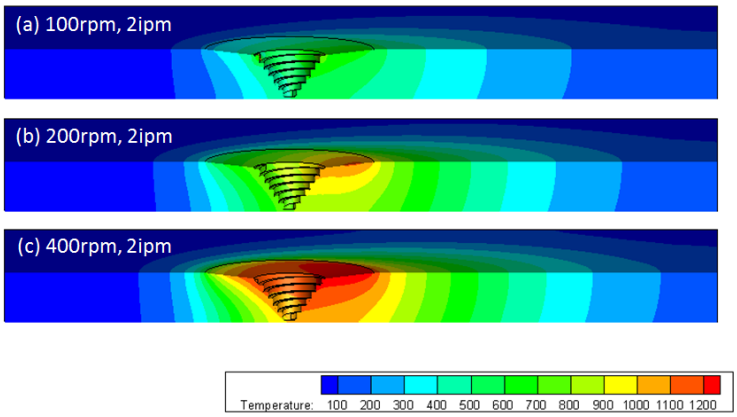

Figure 10. Temperature fields with different welding parameters from computer modeling.

Fundamentally, the FSW joint properties are highly depended on its thermal – mechanical history during the welding process, but lots of the thermal – mechanical information will not show after the FSW because of materials recovering and recrystallization. Based on the numerical simulating development, the thermal-mechanical history of material deposited in the weld is studied by particle tracing to obtain material deformation facts. The distributions of plastic strain and peak temperature at a FSW joint cross section are shown in Figure 11. It is clear that plastic strain and peak temperature distributed inside the stir zone unevenly, and that explains stir zone grain size and microstructure dissimilarities in metallographic study.

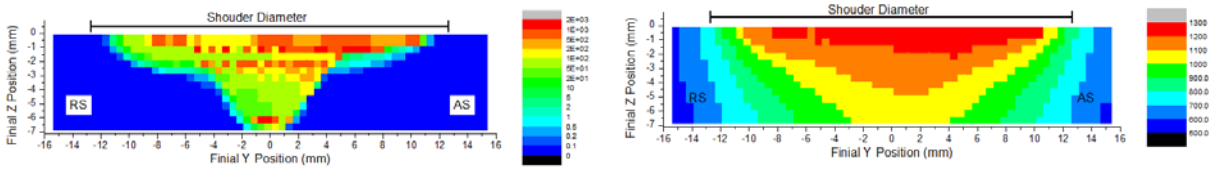

(a) Strain distribution. *(b) Peak temperature distribution.*

Figure 11. Plastic strain and peak temperature distribution at a cross section in FSW

Conclusions

1. Although FSW is a solid state low heat input joining technology, it still caused grain structures and strengthening precipitates growth inside the stir zone with parameters applied in this study. Further investigation is needed to suppress the grain and precipitates grown by adjusting FSW conditions and parameters.
2. The HAZ of a RAFM steel FSW joint is the weakest point to resist high temperature creep, and that of the stir zone is the strongest, even better than the base metals.
3. The 3D thermal – mechanical coupled computer modeling provides excellent information for fundamental understanding of the FSW process.

Future Work

We have successfully completed this project.

3.1 DEVELOPMENT OF SiC JOINING TECHNOLOGIES FOR FUSION: PRE-IRRADIATION EXPERIMENT —T. Koyanagi, J.O. Kiggans, and Y. Katoh (Oak Ridge National laboratory), T. Hinoki (Kyoto University, Japan), M. Ferraris (Politecnico di Torino, Italy), C.H. Henager (Pacific Northwest National Laboratory), C.A. Lewinsohn (Ceramatec Inc.), S. Grasso (Queen Mary University of London)

OBJECTIVE

The objective of this work is the development of an irradiation tolerant joining technology for fusion. This report presents mechanical property and microstructure data of various silicon carbide (SiC) joints in the unirradiated condition.

SUMMARY

Various SiC joints were prepared using diffusion bonding with active titanium and molybdenum inserts, pressurized and pressureless transient eutectic-phase (TEP) sintering, pressurized and pressureless reaction-formed Ti-Si-C MAX-phase bonding, $CaO–Al_2O_3$ (CA) glass ceramics, and Al-Si-C-O braze. Torsional shear strength, fracture behavior, and microstructural of the bonding layer were evaluated in the unirradiated condition. These results are being used as the basis to understand neutron irradiation effects on mechanical properties and microstructures of the SiC joints.

PROGRESS AND STATUS

Introduction

The development of SiC joints that retain adequate mechanical and functional properties in the anticipated service conditions is a critical step toward establishment of advanced SiC composite technology for fusion structural components [1]. Neutron irradiation is among the most critical factor for the fusion blanket components under the service operations. For the purpose of determining the effects on neutron irradiation at fusion-relevant temperatures on strength and microstructures of SiC joints, candidate SiC joints were irradiated in the High Flux Isotope Reactor at 500 and 800°C up to 5 dpa and evaluated by torsional shear tests and microstructural observations. The results show that the effect of irradiation on joint strength was insignificant for all the joints such as titanium diffusion bonding, Ti–Si–C MAX-phase joining, calcia–alumina glass–ceramic joining, and transient eutectic-phase SiC joining [1].
For further development of SiC joining technology, this work is being extended to different irradiation conditions (higher irradiation temperatures or higher neutron fluences) and different types of the joints. This report presents results of pre-irradiation experiments, baseline information on the SiC joints to be used for the irradiation experiments including data for torsional shear tests, microstructural observations, and phase identifications. The post-irradiation experiments on the SiC joints are in progress at ORNL.

Joining Procedure and the Microstructure

The various SiC joints were prepared at Oak Ridge National Laboratory or by outside collaborators, using diffusion bonding with the active titanium and molybdenum inserts, pressurized transient eutectic-phase (TEP) joining using slurry and green tape, pressureless TEP joining, reaction-formed Ti-Si-C MAX-phase bonding with pressure-less sintering, hot-pressing, or spark plasma sintering (SPS), CA glass ceramics joining, and Al-Si-C-O braze-based joining, as summarized in Table 1. High-purity chemical vapor deposited (CVD) SiC was used for substrate material for all the joints.

Table 1. SiC joints prepared in this work.

Method of joining	Joint alias	Main phases present in joint layer	Material provider
Ti diffusion	Ti dif	Ti_3SiC_2, TiC_x	ORNL
Mo diffusion	Mo dif	$Mo_{4.8}Si_3C_{0.6}$, Mo_2C	ORNL
Pressurized TEP using slurry	TEPs	SiC, Y-Al-Zr-O	Kyoto Univ.
Pressurized TEP using green tape	TEPt	SiC, Y-Al-Zr-O	Kyoto Univ.
Pressureless TEP	PL TEP	SiC, Y-Al-O	ORNL
Pressure-less Ti-Si-C MAX-phase	PL MAX	SiC, Ti_3SiC_2	ORNL
Ti-Si-C MAX-phase hot pressing (I)*	HP MAX(I)	SiC, Ti_3SiC_2	PNNL
Ti-Si-C MAX-phase hot pressing (II)*	HP MAX(II)	SiC, Ti_3SiC_2	PNNL
Ti-Si-C MAX-phase SPS	SPS MAX	Ti base phases	Queen Mary Univ.
Calcia-Alumina glass	CA glass	Ca-Al Oxides	Politecnico di Torino
Al-Si-C-O braze-based joining	Braze	Al-C-O, Al-Si-C-O and Al-O phases	Ceramatec

* The main difference between HP MAX (I) and (II) is joint thickness.

(1) Titanium diffusion-bonded SiC
Pure titanium foil (25 μm thick, 99.94% pure, Alfa-Aesar, Ward Hill, MA) was used for diffusion bonding. The Ti foil joints were fabricated at ORNL. The joining of SiC/metal/SiC sandwiches was accomplished by hot-pressing at 1500°C, for 1 h, in vacuum, under a uniaxial pressure of 17 MPa. Estimated partial pressure of oxygen impurity in the furnace was ~0.6 Pa. To reduce oxygen partial pressure in the furnace, titanium powder was used as the oxygen getter. Reduction of oxidation during joining is a key for Ti foil joint to increase the joint strength and to reduce the processing defect at the joint layer [2].
The joint microstructure was reported in our previous work [2]. The joint thickness was ~40 μm. The joint layer exhibited Ti_3SiC_2 phase near the joint interface and mixed structure of Ti_3SiC_2 and TiC_x at the center of the joint layer. The joint layer contained micro-cracks as a pre-existing defect.

(2) Molybdenum diffusion-bonded SiC
Pure molybdenum foil (25 μm thick, 99.95% pure, Alfa-Aesar, Ward Hill, MA) was used for Mo diffusion bonding. The Mo foil joints were fabricated at ORNL. The joining of SiC/metal/SiC sandwiches was accomplished by hot-pressing at 1500°C, for 1 h, in flowing Ar-4% H_2 atmosphere, under a uniaxial pressure of 20 MPa. Estimated partial pressure of oxygen impurity in the furnace was ~0.02 Pa. During the hot-pressing, the presence of both hydrogen and titanium powder facilitated effective oxygen gettering.
The joint microstructure was also reported in our previous work [2]. Mo foil-joined SiC had a layered structure of $Mo_{4.8}Si_3C_{0.6}$ near the joint interface and Mo_2C phases at the center of the joint layer. The joint contained cracks roughly perpendicular to the joint boundary in the as-processed condition. The joint thickness was ~35 μm.

(3) SiC joints formed by pressurized TEP method using SiC-based slurry and green tape

Two types of TEP joining were prepared in this work: the joining using mixed powder slurry (TEPs) and the joining with a commercial green tape (TEPt). Both joints were fabricated at Kyoto University in Japan.

To make the slurry for the TEPs joining, SiC nano-phase powder (average diameters ~30 nm), and Al_2O_3 powder, Y_2O_3 powder were dispersed in ethanol. The total amount of oxide additives was 6 wt%. The powder mixture was prepared by milling with ZrC balls. For the fabrication of TEPs joint, the slurry was sandwiched by CVD SiC plates, and then dried at ~80°C. After that, the TEPs joint was formed by hot-pressing at 1850°C, for 1 h, in an Ar atmosphere, under a pressure of 10 MPa.

The feedstock of the green tape for the TEPt joint was same as that of the TEPs slurry except for the additional use of organic binder. The green tape was provided by in Gunze ltd. in Japan. The joining of SiC/green tape/SiC sandwiches was accomplished by hot-pressing. The hot-pressing conditions were same as those for the TEPs joint.

Cross-sectional backscattered electron image of the TEPs and TEPt joint was shown in Figure 1. The joint thickness was ~80 μm for TEPs joint and ~150 μm for TEPt joint. The TEPs joint layer appeared to be highly dense. On the other hand, the TEPt joint was partially deboned due to the presence of large (~50 to ~100 μm) pores (The image is not presented here). In addition, lineal segregation of the secondary phases was observed in the bonding layer, which was not present in the TEPs joint.

The composition of the secondary phases in the bonding layers was examined using SEM-EDS analysis (Figure 2 for TEPs joint and Figure 3 for TEPt joint). Yttrium, aluminum, and oxygen, which were in sintering additives, were clearly detected as elements of secondary phases in both joints. This is commonly observed in TEP sintered SiC [3]. In addition, the secondary phases contained zirconium as impurity. This may be come from ZrC as ball milling media during processing. Note that TEP joints which showed excellent irradiation tolerance in previous work did not contain Zr impurity [1].

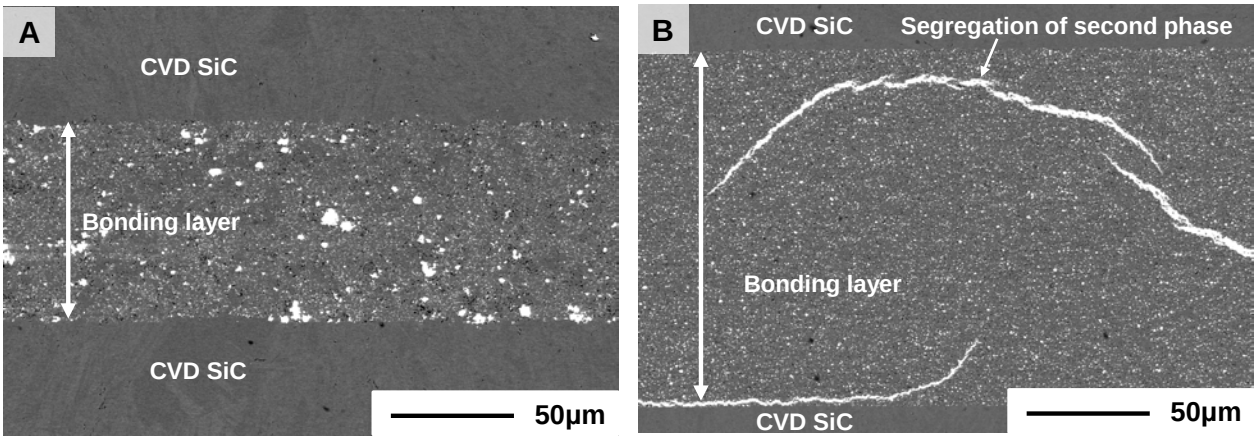

Figure 1. Cross-sectional backscattered electron images of (A) TEPs and (B) TEPt joints.

(4) Pressure-less TEP SiC joint

Pressureless (PL) TEP joint was prepared at ORNL. The joint was formed using the powder mixtures consisting of SiC nano-powder (average diameters ~30 nm), and sintering additives (Al_2O_3 powder and Y_2O_3 powder), with organic agents. The total amount of the oxide additives was 6 wt.%. The total amount of the organic agents was ~3.5 wt.%. The PL TEP joints were formed by sandwiching mixed powder between CVD SiC plates followed by cold-pressing at ~10 MPa in graphite die to partially densify the powder. The sandwiched materials were then heat-treated at 1875^{o}C for 1 h in a flowing argon atmosphere in the graphite. Very small amount of pressure (~0.1 MPa) was applied during heating to hold the specimen in furnace. The detail of the processing condition can be found elsewhere [4].

The microstructure of the bonding layer was reported in previous work [5]. The bonding layer contains some amount of porosity and secondary phases. The secondary phases were analyzed by SEM-EDS as

shown in Figure 4. The mapping shows that large part of secondary phases is a Y-Al oxide material. The impurity element such as Zr was not observed in this joint.

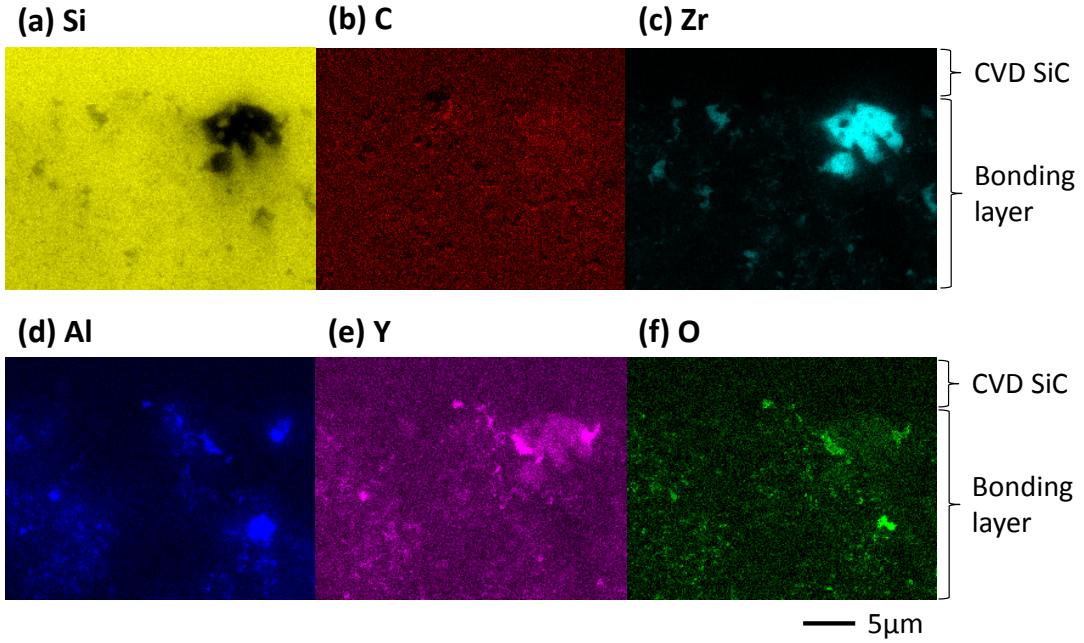

Figure 2. SEM-EDS maps for (a) Si, (b) C, (c) Zr, (d) Al, (e) Y, and (f) O for TEPs joint.

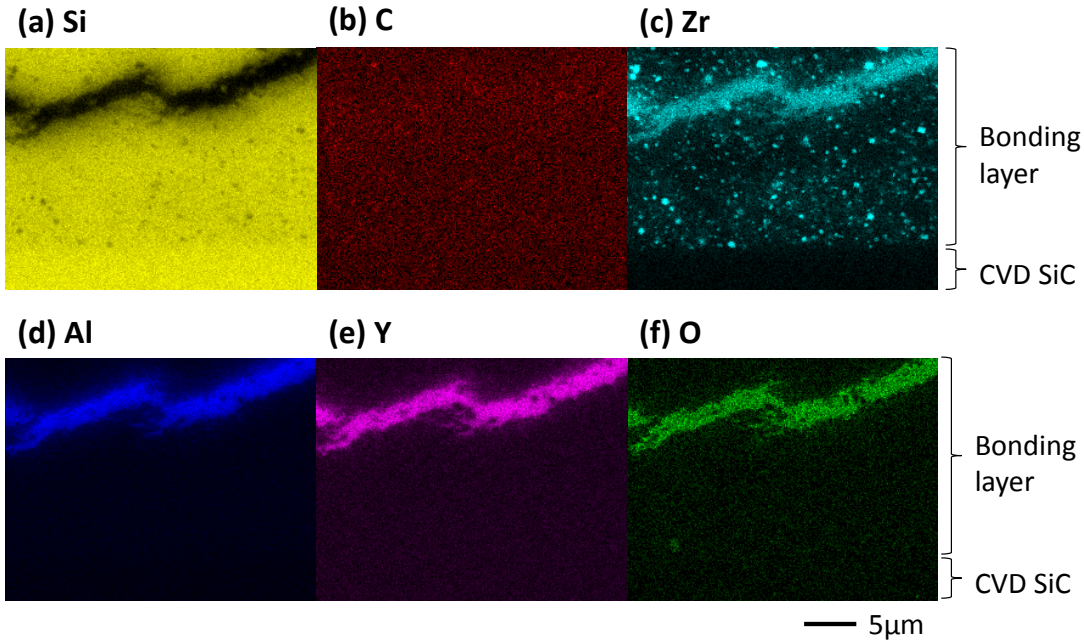

Figure 3. SEM-EDS maps for (a) Si, (b) C, (c) Zr, (d) Al, (e) Y, and (f) O for TEPt joint.

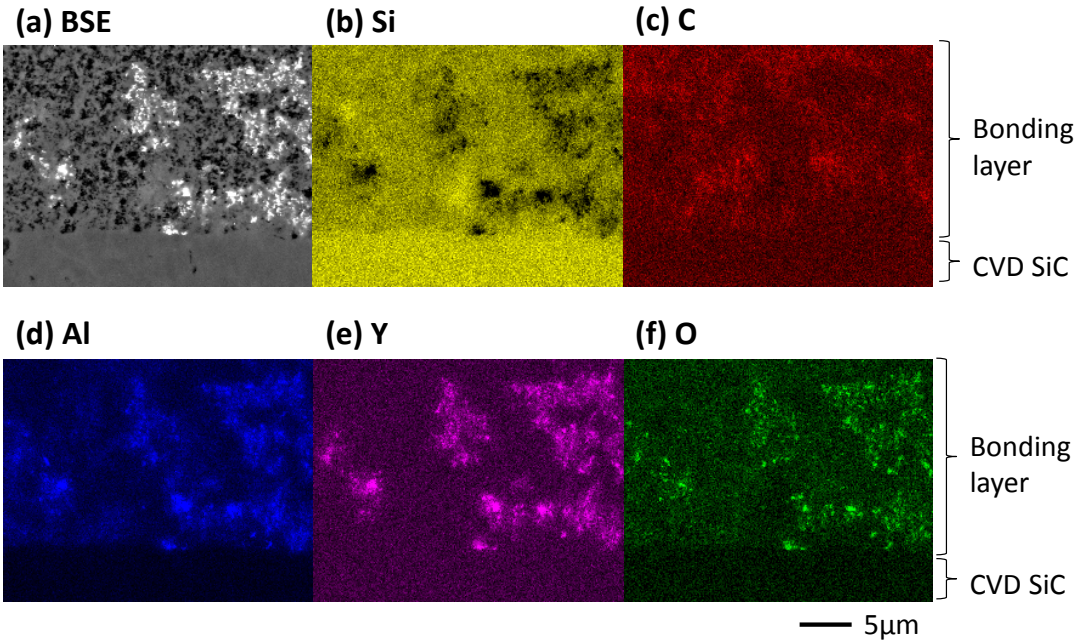

Figure 4 SEM-EDS maps for (a) backscattering electron, (b) Si, (c) C, (d) Al, (e) Y and (f) O, and for PL TEP joint.

(5) Pressureless Ti-Si-C MAX-phase bonded SiC

For PL MAX phase bonding, a set of joining agent materials were purchased from Hyper-Therm High Temperature Composites, Inc. (currently Rolls-Royce High Temperature Composites, Inc., Huntington Beach, CA). Ti-Si-C phase-based joints of CVD SiC were produced at ORNL based on a pressure-less slurry process per the Hyper-Therm formula. Details of the raw materials and the process conditions are proprietary.

The microstructure of the joint was reported in previous work [5]. The joint layer appeared to be dense, and the joint thickness was about 150 μm. The bonded zone consisted of SiC grains and Ti-Si-C phase. The Ti-Si-C phases were expected to be mainly Ti_3SiC_2, and the small amount of Ti-C and Si rich Ti-Si-C phases. The dominant processing defect in the joint layer was crack roughly perpendicular to the joint boundary.

(6) Ti-Si-C MAX-phase jointed SiC by hot-pressing

Two types of Ti-Si-C MAX-phase jointed SiC were prepared at PNNL (HP MAX(I) and (II) hereafter). The HP MAX(I) joint was used for the previous irradiation experiments [1]. The bonding layer was prepared using a tape casting method that includes organic binders and plasticizers together with a mixture of TiC and silicon powder, followed by hot-pressing SiC/bonding layer/SiC sandwich at ~1400°C.

Cross-section backscattering electron images of HP MAX(I) and (II) are shown in

Figure 5. Appearance of the bonding layer is very similar between them, except for the joint thickness. The thickness was approximately 15 to 20 μm for HP MAX(I) and less than 10 μm for HP MAX(II). SEM-EDS analysis revealed that the bonding layer manly consisted of two phases: SiC and Ti-Si-C phases. In addition to those phases, small amount of Fe impurity was contained in both joints, which might be attributed to the impurity of the starting powder.

X-ray diffraction (XRD) patterns of the HP MAX(I) and (II) joints are shown in Figure 6. Both types of joints contain SiC and Ti_3SiC_2 phase in the bonding area. Based on SEM-EDS and XRD results, the main phase in the HP MAX joints are Ti_3SiC_2 and SiC.

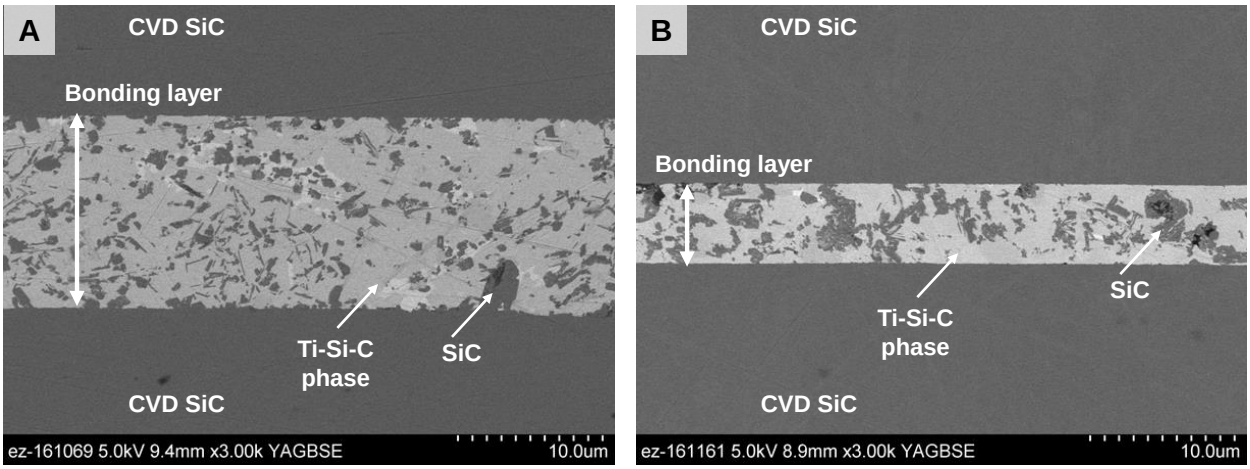

Figure 5 Cross-sectional backscattered electron images of (A) HP MAX(I) and (B) HP MAX(II) joints.

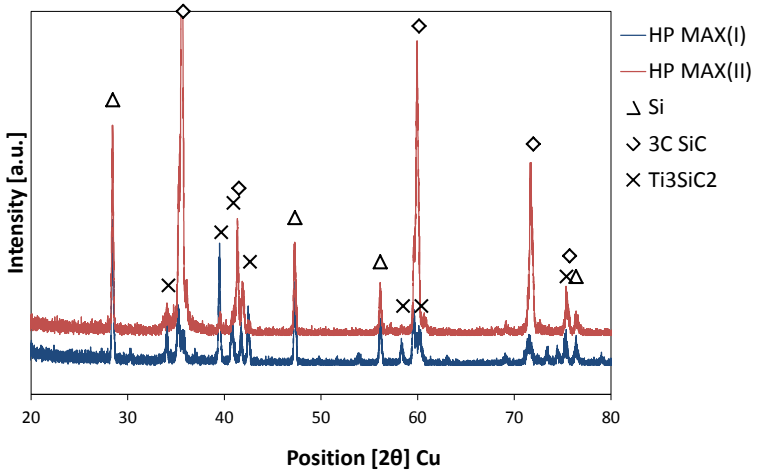

Figure 6 XRD patterns of HP MAX(I) and (II) joints. Silicon powder is used for an internal standard which was not contained in the joint.

(7) Calcia-Alumina glass ceramic bonded SiC

Calcia-Alumina glass-ceramic (CA glass) joint was prepared at Politecnico di Torino in Italy. The joint specimens are same as those used in previous irradiation experiments [1]. The joint phase was reportedly a mixture of $Ca_3Al_2O_6$ and $Ca_{12}Al_{14}O_{33}$ [6]. Details of processing condition and microstructure of the bonding layer can be found in references [1, 6].

(8)Ti reaction bonding by SPS

Additional Ti based SiC joint was formed by SPS with titanium foil as intermediate joining material at Queen Mary University of London. The joint is referred to as SPS MAX. During joining, constant force of 15 kN was applied on hourglass shape CVD SiC/Ti foil/CVD SiC sandwiches, which is used for torsion shear tests. Heating rate was 50°C/minute from 450 to 1700°C, and dwelling temperature was 1700°C for 5 minutes. Cooling condition was 50 °C /minute from 1700 to 450°C. The joining atmosphere was vacuum (5 Pa). Titanium foil with 30 um thickness (Ti000300 grade, Purity:99.6+%, Goodfellow) was used for this joining.

(9)Al-Si-C-O brazed SiC joint

The brazed CVD SiC joint was prepared using Al-Si-C-O system by Ceramatec, Inc. in Utah. The starting materials of the brazing filler metal and the processing conditions are proprietary. The joint thickness was very thin (~3 μm) as shown in Figure 7. The brazed area consisted of complex phases; Al-C-O (phase 1 in Figure 7 (A)), Al-Si-C-O (phase 2 in Figure 7 (A)), Al-O, and Si rich phases were detected by SEM-EDS analysis. In addition, a few micron-sized pores also existed in the bonding layer.

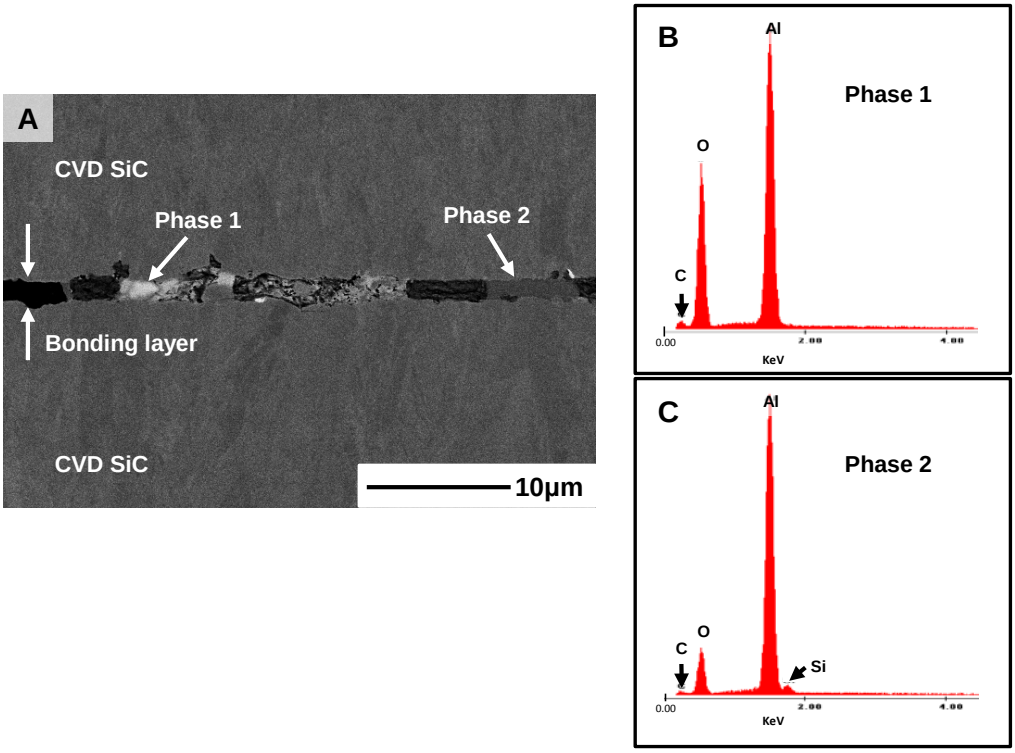

Figure 7. Cross-sectional backscattered electron image of the Al-Si-C-O braze-based joint (A). EDS spectrums of phase 1 and 2 indicated in image A are shown in image B and C, respectively.

Mechanical property of SiC joints

Shear strength of the joint test specimens was evaluated by the torsional shear testing of hourglass-type specimens that had specifically been designed and established for neutron irradiation studies [1]. Detail of the test method can be found elsewhere [4]. Two types of specimen geometries were used in this work; type 6SQ-4D specimen [1] was used for the TEPt, TEPs, and PL TEP joints, and type 6SQ-5D specimen [1] was for the other joints.

Results of pre-irradiation torsion tests on various SiC joints are summarized in Figure 8. The graph shows individual testing result. Three to ten specimens were tested for each joint. All the joints except for TEPs joint exhibited primary a shear strength of 50 to 150 MPa. Relatively high shear strengths of 250 to 350 MPa were obtained from TEPs joints. The typical fracture appearances of the joints are shown in Figure 9. The Ti diff, Mo diff, TEPs, PL TEP, PL MAX, SPS MAX, and Braze joints failed within SiC substrate as shown in Figure 9A, which is typical for the robust joints. It is difficult to identify the location of the crack initiation for these joints, because the neck part of the specimen was shattered into pieces during the test. The TEPt joints exhibited the substrate failure or failure at partially joint interface (Figure 9 (C)). The HP MAX(I) joints mostly failed at the joint plane (Figure 9B). The MAX(II) and CA glass joints completely or partially failed at the joint plane or partially at the joint plan. The differential strength value and the fracture appearance were observed among PL MAX, HP MAX(I) and (II), and SPS MAX joints, though those joints contained SiC and Ti-Si-C phases in the bonding area. The torsional shear strength evaluated in this work may be affected by not only the bonding strength but also

residual stress, surface condition, and differential elastic modulus between bonding layer and SiC substrate.

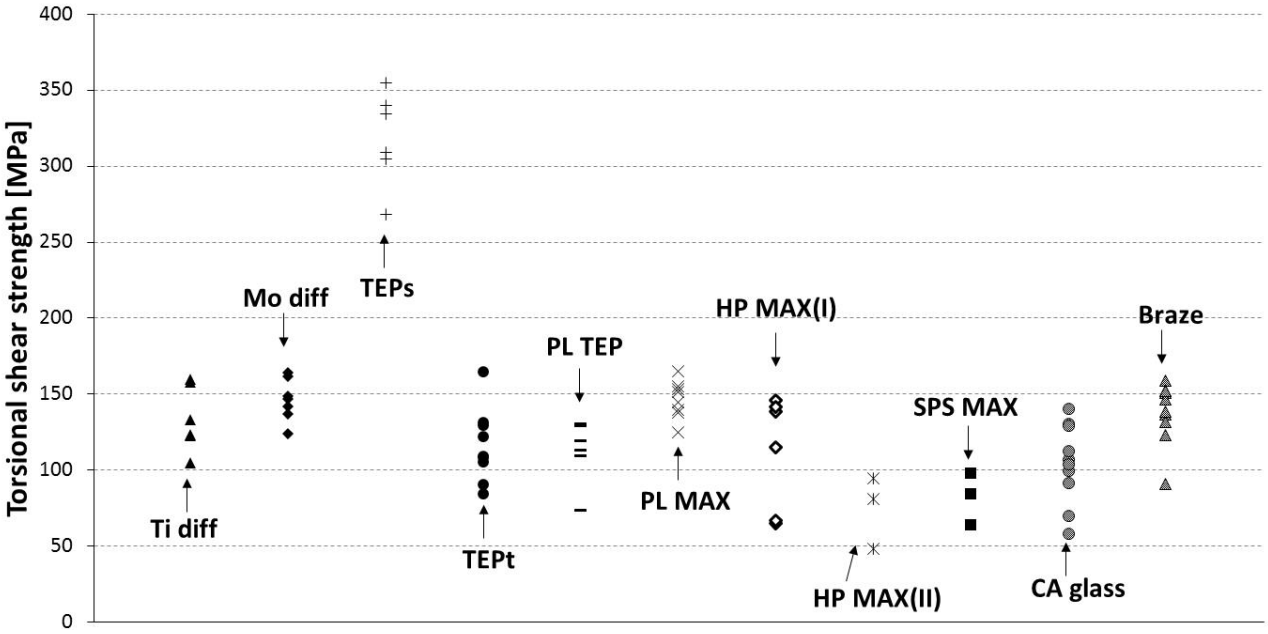

Figure 8. Shear strength of various SiC joints tested in unirradiated condition. The specimen ID is listed in Table 1.

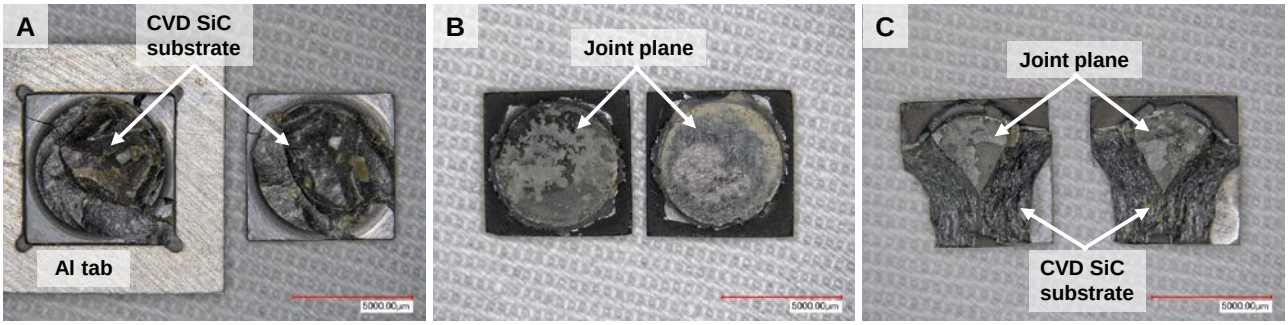

Figure 9. Typical fracture appearance of torsion tested specimens: (A) failure in CVD SiC substrate, (B) failure at joint plane, and (C) failure partially at joint plane.

Acknowledgements

This work was supported by Office of Fusion Energy Sciences under contract DE-C05-00OR22725 with UT-Battelle, LLC. The authors gratefully acknowledge Mr. Joseph Fellows (Ceramatec Inc.) for preparing braze joints.

References

[1] Y. Katoh, L. L. Snead, T. Cheng, C. Shih, W. D. Lewis, T. Koyanagi, T. Hinoki, C. H. Henager Jr., and M. Ferraris, J. Nucl. Mater., 448 (2014) 497–511.
[2] T. Koyanagi, J. Kiggans, C. Shih, Y. Katoh, Ceram. Eng. Sci. Proc., 35 (2015) 151–160–.
[3] T. Koyanagi, S. Kondo, T. Hinoki, Ceram. Eng. Sci. Proc. 32 (2011) 53–62.

[4] T. Koyanagi, J. Kiggans, C. Shih, Y. Katoh, Fusion Reactor Materials Program Report, DOE/ER-0313/56, 94–102.
[5] T. Koyanagi, J. Kiggans, C. Shih, Y. Katoh, Fusion Reactor Materials Program Report, DOE/ER-0313/55, 11–22.
[6] M. Ferraris, M. Salvo, C. Isola, M. Appendino Montorsi, A. Kohyama, J. Nucl. Mater. 258–263 (1998) 1546–1550.

3.2 LOW ACTIVATION JOINING OF SiC/SiC COMPOSITES FOR FUSION APPLICATIONS: MODELING MINIATURE TORSION TESTS WITH ELASTIC AND ELASTIC-PLASTIC MODELS — C.H. Henager, Jr., B.N. Nguyen, and R.J. Kurtz; (Pacific Northwest National Laboratory, Richland, WA, USA); M. Ferraris, (Politecnico di Torino, Torino, Italy); Y. Katoh, (Oak Ridge National Laboratory, Oak Ridge, TN, USA)

OBJECTIVE

Mechanics damage models have been developed to match torsion experiments involving elastic and elastic-plastic materials and to help formulate a path forward with joint testing and analysis for SiC materials in nuclear environments. This report extends the analysis from the last reporting cycle by including plots of stress fields and strain energy density fields and by limiting the model to shear damage.

SUMMARY

The international fusion community designed miniature torsion specimens for joint testing and irradiation in test reactors with limited irradiation volumes since SiC and SiC-composites used in fission or fusion environments require joining methods for assembling systems. Torsion specimens fail out-of-plane when joints are strong and when elastic moduli are comparable to SiC, which causes difficulties in determining shear strengths for many joints or for comparing unirradiated and irradiated joints. A finite element damage model was developed to treat elastic joints such as SiC/Ti_3SiC_2+SiC and elastic-plastic joints such as SiC/epoxy and steel/epoxy. The model uses constitutive shear data and is validated using epoxy joint data. The elastic model indicates fracture is likely to occur within the joined pieces to cause out-of-plane failures for miniature torsion specimens when a certain modulus and strength ratio between the joint material and the joined material exists. Lower modulus epoxy joints always fail in plane and provide good model validation.

PROGRESS AND STATUS

Introduction

The international fusion materials community is currently irradiating several joint types and compositions in the HFIR reactor at ORNL [1]. PNNL is working with Politecnico di Torino (POLITO) and ORNL using miniature torsion specimens (hourglass samples) that have been specifically designed for pre- and post-irradiation joint shear strength testing [2]. Many of the joints fail out-of-plane, or in the base CVD-SiC material, during torsion testing, but some do not. To elucidate how and where cracks can initiate and propagate in the torsion joint specimens, finite element analyses of these specimens subjected to torsion were performed using a continuum damage mechanics (CDM) model previously developed at PNNL for elastic materials for which any nonlinearity in stress/strain response is due solely to damage and not to other irreversible processes such as plasticity [3]. The CDM model was implemented in the ABAQUS® finite element code via user subroutines. Comparative analyses of the torsion joints using ABAQUS® and the damage model were conducted considering typical mechanical properties in shear of CVD-SiC and different mechanical behaviors of the joint material using assumed shear stress/strain responses up to failure. Since SiC/epoxy and steel/epoxy joints were used to validate the miniature torsion specimen design, a CDM elastic-plastic model is included.

Model Formulation

Approach

This section summarizes the damage model and method for predicting crack initiation and propagation [3-5] in the joined CVD-SiC or steel material together with a thin joint region consisting of either Ti_3SiC_2/SiC of varying modulus and strength or a hypothetical brittle epoxy and an elastic-plastic epoxy. Considering damage in an elastic and damageable material, for which any nonlinearity in stress/strain response is due solely to damage and not to other irreversible processes, can be described by a scalar variable, D, that can be related to the microcrack density or microcrack volume fraction, or simply a parameter to phenomenologically quantify the level of damage accumulation in the material [4]. Damage affects the material stiffness according to a stiffness reduction law. Using the concepts of thermodynamics of continuous media [4, 6], a thermodynamic potential is defined to derive the constitutive relations and the thermodynamic force associated with the damage variable. This damage model uses the density of the

elastic deformation energy as the thermodynamic potential that provides a coupling between damage and elasticity. A damage criterion dependent on a damage threshold function is defined and the damage evolution law is obtained. Damage evolves with the deformation according to the damage evolution law until a critical (saturation) state at which $D=D_{cr}$ $(0<D_{cr}<1)$ and failure occurs. D_{cr} is small for brittle materials, and this is the case for ceramic materials studied in this work. In this work, failure at damage saturation ($D=D_{cr}$) leading to crack initiation and propagation is modeled by a vanishing finite element technique [7] that reduces the stiffness and stresses of the failed element to zero [3, 8].

We choose to implement the damage model for brittle ceramics in shear loading (Figure 1a). In this case, a flaw under Mode III loading experiences some damage accumulation prior to critical crack growth due to frictional forces on the crack faces and a non-linear shear stress-strain curve results [9]. Furthermore, it is understood that this problem can be addressed using multiaxial loading considerations if a known flaw distribution was available [9-14], but that this is not practicable here. Rather, the damage model approach is used in a phenomenological sense to address the effects of load sharing in this complex joined system. The thermodynamic and CDM approach adopted is phenomenological. It does not describe the detailed frictional sliding of crack ligaments but the magnitude and effect of shear damage on the material response are *phenomenologically* captured by the damage variable, *D,* driven by the associated thermodynamic force, *F*(*D*), and the damage evolution law.

As discussed in Refs. [15, 16] miniature torsion joints were made at POLITO using Araldite AV119 epoxy between CVD-SiC and a 316-grade stainless steel. The epoxy was cured for 1 h at 130°C [15]. The torsion tests for these samples were performed in the same manner as all the other torsion testing. In addition, simple compression tests were performed [16] on cylinders of cured AV119 epoxy to establish the mechanical properties of this toughened adhesive material [17, 18]. Materials such as 316SS and AV119 epoxy exhibit pronounced nonlinear behaviors controlled by plasticity and damage. Therefore, an elastic-plastic damage description is used in this work to model the nonlinear responses of these materials to monotonic loading up to failure [19]. This elastic-plastic damage model was implemented in ABAQUS via user subroutines to describe the constitutive behaviors of the AV119 joint [18] and of the joined 316SS material [20] in the ABAQUS analyses of torsion specimens. Figs. 1b-c show the uniaxial stress/strain curves of 316SS and AV119 captured by this elastic-plastic damage model.

RESULTS

Model Results

The damage models are implemented in ABAQUS® as a finite element analysis of the miniature torsion joint specimen. In order to investigate specimen failure for different types of joints, different material properties of the joints were considered and are reflected through the assumed shear stress/strain responses up to failure in the damage models. In addition, typical mechanical properties of CVD-SiC and nominal steel (316SS) as the joined halves in the experimentally observed range were assumed. Figure 1 and Table 1 present the mechanical properties assumed in this parametric study. There are 5 different behaviors (denoted by case study numbers 1 through 5) considered for the Ti_3SiC_2/SiC composite joint differentiated by their calculated modulus and assumed failure strength. In addition, a similar analysis was performed for two epoxy joined CVD-SiC and steel specimens. The damage variable value at saturation was taken to be 0.2 for all the ceramics while it was considered to be 0.4 for the brittle epoxy (case 6) leading to an epoxy strength of 120 MPa and failure strain of 0.02 and 0.48 for an elastic-plastic epoxy (AV119, case 7) with a strength of 80 MPa at 0.05 failure strain [15, 16, 18].

Damage analyses were conducted for all the torsion joint specimens made of the simulated materials listed in Table 1, which are based on the calculated modulus values for the various joints with differing amounts of porosity. The predicted failure patterns for all the studied elastic cases are gathered in Figure 2. Computed stress and strain fields, along with the strain energy density field, for Case 1 are shown in Figure 3 to illustrate fields that are not related to the damage model. Cases 1 and 5 for the Ti_3SiC_2/SiC joint represent the extreme cases for the most dense joint in Case 1 and the least dense joint in Case 5. The failure location changes from within the CVD-SiC joined materials (Case 1) to within the joint plane (Case 5). Cases 2 and 3 represent Ti_3SiC_2/SiC joints made at 30 MPa and 20 MPa, respectively, which are increasingly less stiff than the joined CVD SiC. For both of these cases, failure is predicted to initiate in the joint but then develop into the SiC sample resulting in out-of-plan failure. Case 4 for the 10 MPa

Ti_3SiC_2/SiC joint is now only about 1/3 as stiff as the CDV-SiC and the simulation indicates a mixture of failure within the joint and within the sample. Experimentally, these 10 MPa joints sometimes fail within the joint and sometimes within the CVD-SiC. Case 5 is predicted to fail within the joint and experiments confirm this failure mode. The brittle epoxy joint (Case 6) also always exhibits in-plane failure.

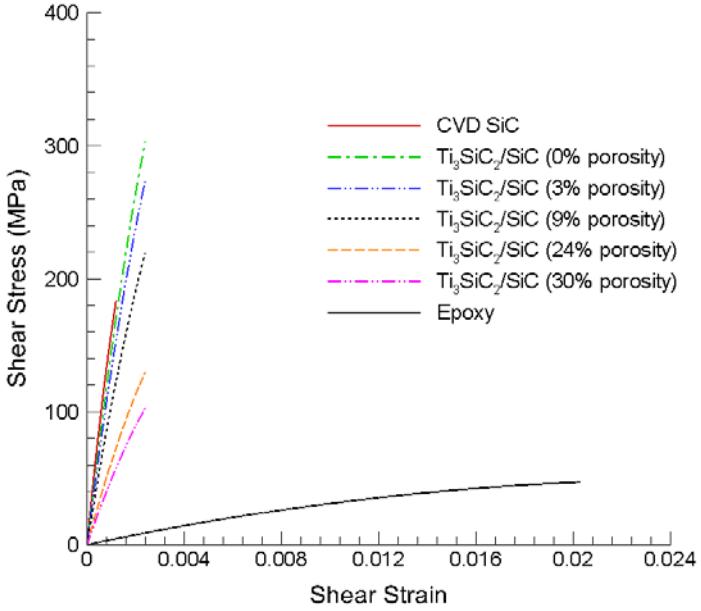

(a)

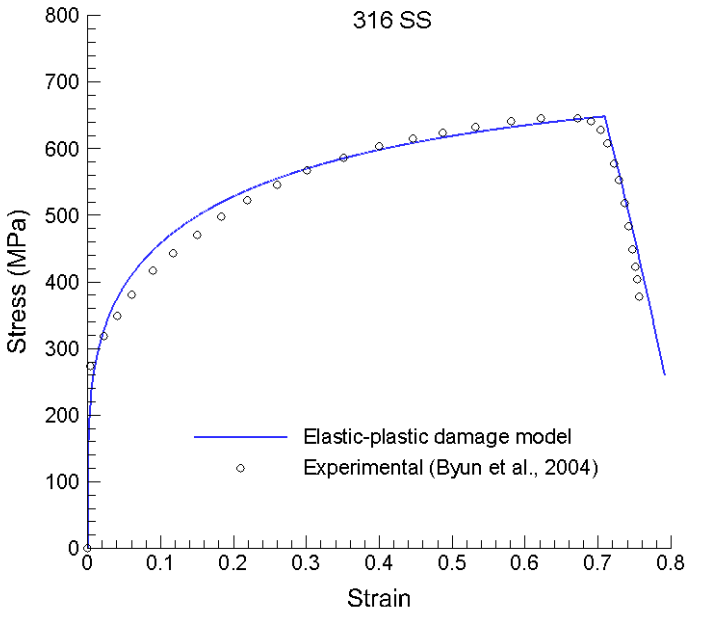

(b)

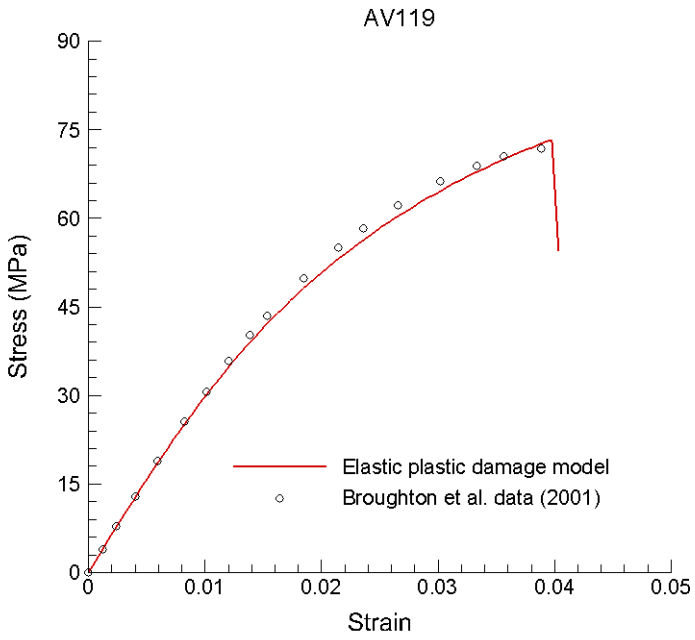

(c)

Figure 1. Shear and uniaxial stress/strain responses considered for (a) an elastic damage model for CVD-SiC and different types of joint material, including a brittle epoxy, (b) an elastic-plastic damage model for 316SS [20] and (c) an elastic-plastic damage model for AV119 epoxy [18]. See Tables 1 and 2 for model parameters.

Table 1. Mechanical properties of the CVD-SiC and joint material assumed for the analysis.

Material	Case Study No.	Shear Modulus (GPa)	Poisson Ratio	Shear Strength (MPa)	Failure Strain in shear	Damage Variable Critical Value
CVD-SiC	–	192	0.2	184	1.2×10^{-3}	0.2
Ti_3SiC_2+SiC (0% porosity)	1	158	0.2	304	2.4×10^{-3}	0.2
Ti_3SiC_2+SiC (3% porosity)	2	143	0.2	274	2.4×10^{-3}	0.2
Ti_3SiC_2+SiC (9% porosity)	3	115	0.2	220	2.4×10^{-3}	0.2
Ti_3SiC_2+SiC (24% porosity)	4	68	0.2	130	2.4×10^{-3}	0.2
Ti_3SiC_2+SiC (30% porosity)	5	54	0.2	103	2.4×10^{-3}	0.2
Epoxy (Brittle)	6	3.8	0.3	47	2.0×10^{-2}	0.4

Table 2. Parameters of the elastic-plastic models identified for 316SS and AV119.

Materials	E (MPa)	σ_0 (MPa)	v	n	$\bar{\varepsilon}_p^D$	$\bar{\varepsilon}_p^R$	D_c
316SS	193000	150	0.3	4.3	0.02	0.42	0.7
AV119	3200	110	0.34	3	0	0.01	0.45

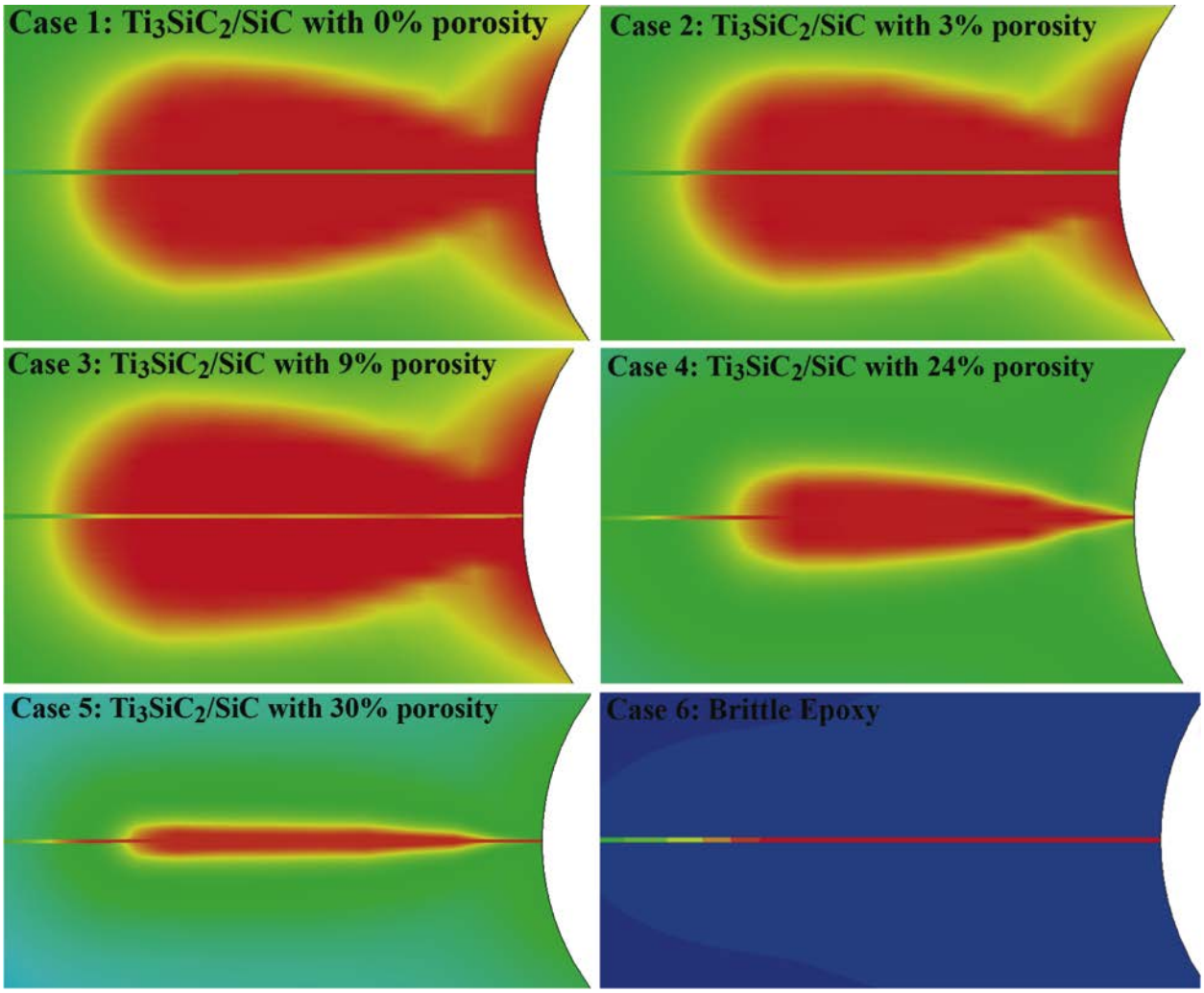

Figure 2. Predicted fracture patterns (red regions) using an elastic damage model for the torsion joint specimens made of different joint materials with mechanical properties listed in Table 1. Cases 1, 2, and 3 fail within the CVD-SiC base material (out-of-plane), while case 4 sometimes fails within the joint. Case 5 always fails in the joint region. Case 6 shows results from the brittle epoxy simulation, which also fails within the joint without exception.

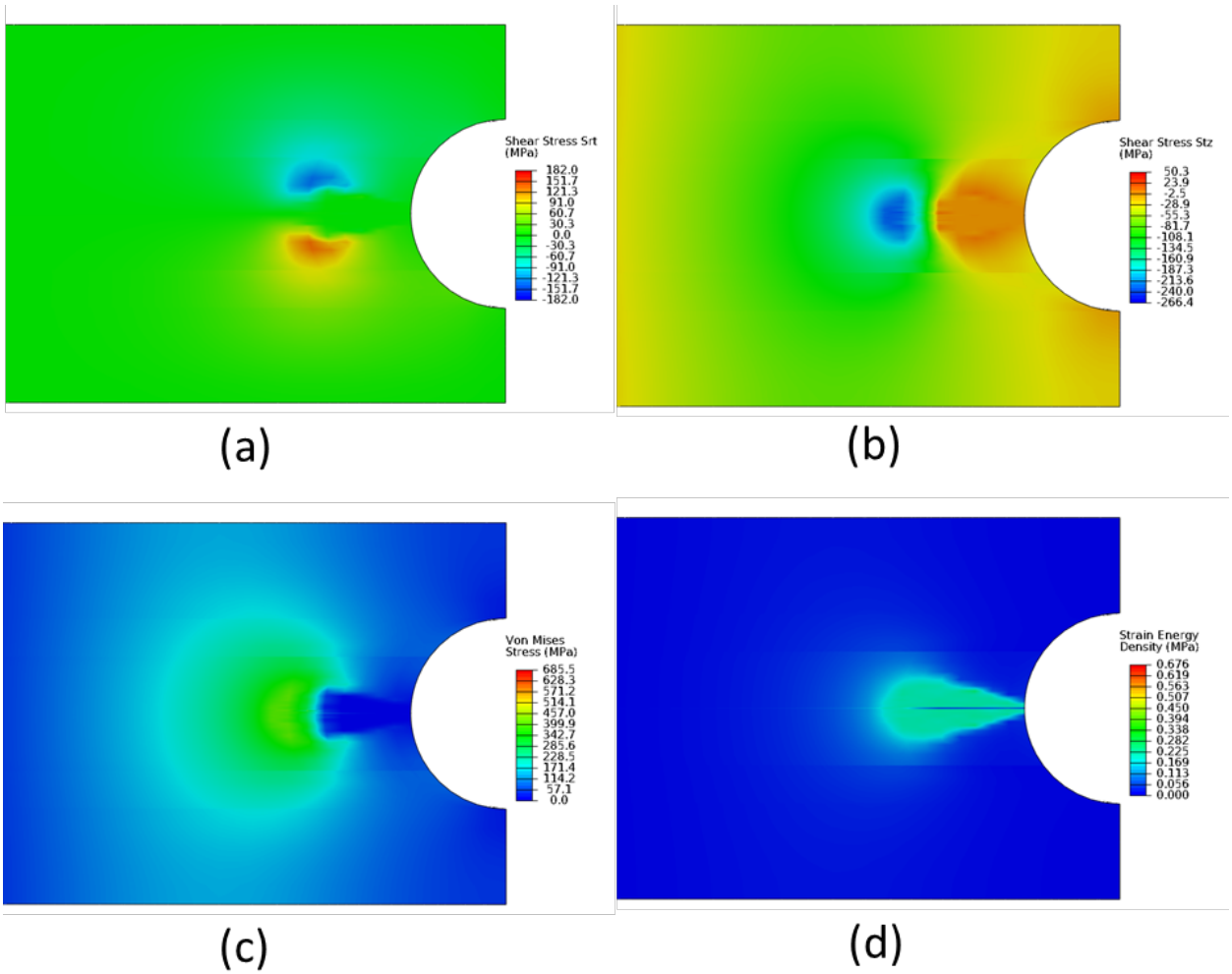

Figure 3. Contours of (a) shear stress τ_{rt}, (b) shear stress τ_{tz}, (c) equivalent Von Mises stress, and (d) strain energy density causing damage and fracture of Case 1 torsion joint specimen.

As recognized by Ferraris et al. [16] the toughened adhesive epoxy AV119 is not a brittle material but behaves as an elastic-plastic material and, therefore, must be treated accordingly. Figures 1b-c and Table 2 together with the elastic-plastic damage model provide the necessary tools to address this issue. In addition to using an elastic-plastic response, the joint thickness in the model was modified to more closely simulate the work performed in Torino. Figure 4 shows the predicted failure locations for a 50-μm thick AV119 joint between CVD-SiC and 316SS. The CVD-SiC is treated elastically as before but in this case the AV119 and 316SS are treated using the elastic-plastic model developed here. The model results validate what the torsion testing observed, namely, that the torsion specimens fracture in the plane of the joint when bonded using AV119 adhesive epoxy regardless of the specimen material.

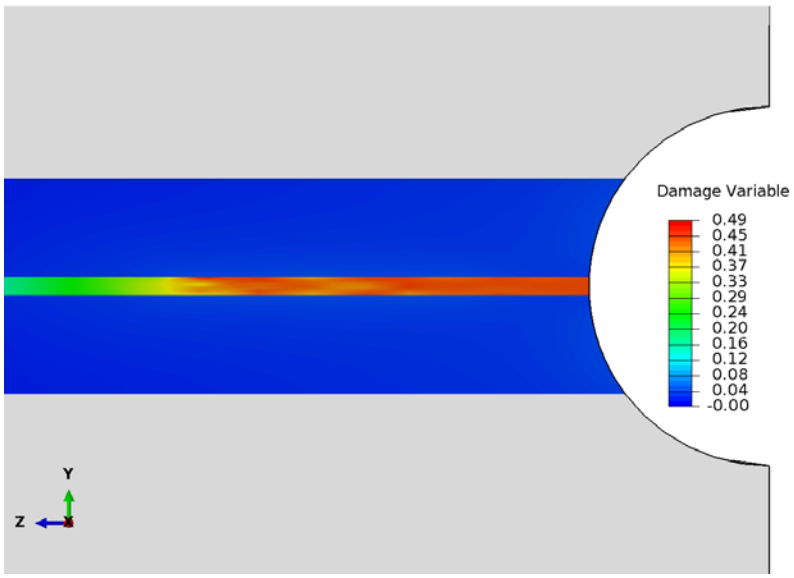

(a)

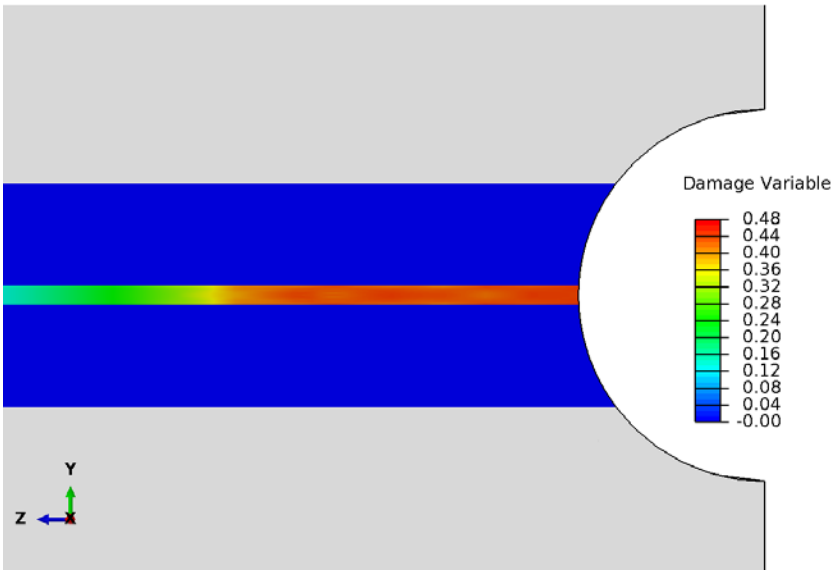

(b)

Figure 4. Predicted fracture patterns using an elastic-plastic damage model for the AV119 adhesive epoxy and for 316SS. Shown in (a) is the predicted fracture for CVD-SiC joined with AV119 where the epoxy is elastic-plastic and the SiC is elastic. Shown in (b) is the case for both materials obeying the elastic-plastic damage model for 316SS joined with AV119 epoxy. In all cases the failure occurs within the epoxy joint.

Discussion

Model Predictions and Comparisons

The damage models were created to help understand the fracture results from the THG specimens that exhibited non-planar fracture that was not truly reflective of joint properties. Rather, the literature refers to this data as “torsional shear resistance” of the THG [1, 2, 21-24] when the THG specimen fails in the base material, or out-of-plane. The critical part of the damage models was to be able to simulate the stress-

strain curves for the constitutive materials; otherwise the models would not be reasonable. The shear stress-strain curves shown in Figure 1a using the data in Table 1 capture the material elastic constants as well as the failure strengths and are reasonable assumptions. In addition, the stress-strain responses computed by the elastic-plastic damage model shown in Figures 1b and c correctly capture the stress-strain behavior of both the 316SS steel and AV119 epoxy. The accuracy of the THG damage modeling is predicated on the accuracy of the individual constituent's stress-strain data and, even though this model data is not completely precise, the results from carefully applying the model are expected to show the desired effects.

The models, both the elastic damage and elastic-plastic damage approaches, capture the key observations, namely that there is a transition from planar to non-planar fracture over a range of elastic moduli and strength values. High strength and high moduli materials are predicted to fail out-of-plane and within the base THG material, whereas low modulus materials fail in the plane of the joint. Intuitively, it is anticipated that low modulus epoxy will behave differently compared to high modulus Ti_3SiC_2+SiC or CA glass-ceramic in terms of load sharing with the CVD-SiC base material. In fact, one thought (*gedanken*) experiment is to imagine the entire miniature torsion specimen machined from a single piece of CVD-SiC and then to predict where it will fail. Probabilistic brittle fracture mechanics predicts that it will fail somewhere in the specimen that contains a combination of the largest flaw and the highest tensile/shear stresses, which will not necessarily coincide with the central plane of the torsion specimen. Thus, a high strength, high modulus joint may not fail in the plane of the joint either. As shown in Figs. 2 and 3 load sharing with the CVD-SiC forces a majority of the damage for high modulus joints to occur within the base CVD-SiC material and failure is predicted to occur out-of-plane of the joint. However, this load sharing is a function of the constitutive behavior (i.e., modulus, stress-strain response, etc.) differences between the joint and base THG material. The model predicts a high degree of load sharing and CVD-SiC damage for a joint modulus greater than about 200 GPa and a minimal amount of load sharing with highly localized (planar) fracture for moduli 100 GPa and lower (Figure 2). This is in good agreement with the observed experimental data for the THG joints tested at POLITO (Figure 5).

Figure 5a shows the computed maximum shear stresses for all the cases studied in this work. The maximum shear stress is highest (104 MPa) for the specimen with the Ti_3SiC_2+SiC stiffest and strongest joints, cases 1, 2, and 3. Cases 4 and 5 have shear strengths that are smaller than this and, in the simulation, reflect the shear strength of the joint. In addition, the predicted failure strengths in shear shown in Figure 5a correlate with measurements from ORNL and POLITO [1, 21]. The ORNL data for the unirradiated Ti_3SiC_2+SiC joints indicated a torsional shear resistance value of 117 MPa ± 10 MPa, which agrees with the model prediction of 104 MPa [1]. It is noted that this predicted strength value follows from the CVD-SiC damage model determined from the *assumed* CVD-SiC mechanical properties. Thus, the model predicts that the torsion test will fail in the CVD-SiC material and that the torsional shear resistance of the sample will be 104 MPa because that is the predicted shear strength of the CVD-SiC simulated here. Note that the NITE materials tested in Ref. [1] fail at higher shear strengths compared to the CVD-SiC and this is attributed to the higher shear strength of the NITE SiC. However, the main point is that for certain material combinations the THG test will fail at the shear strength limit of the base material and will not provide information regarding the shear strength of the joint material.

The epoxy joined data from POLITO is more complex. Results indicate a shear fracture strength of 36 MPa, which agrees with the model prediction of about 38 MPa[1] for the brittle epoxy material (Case 6 and Figure 5a). In this case, where the epoxy modulus is only a fraction of the CVD-SiC or 316SS the fracture path is in the plane of the joint in the epoxy material and provides a true shear stress value. However, since AV119 toughened adhesive epoxy is not a linear elastic brittle material, the elastic damage model is not appropriate and an elastic-plastic damage model was developed based on mechanical property data for AV119 and 316SS as discussed. This model predicts a shear failure strength of 28 MPa for a 50-µm thick joint region of AV119 (Figs. 5a and 5b), which is less than the POLITO calculated value of 36 MPa but is in agreement with the measured asymmetric 4-point bending for epoxy-joined SiC [16]. However, Ferraris et al. also report a value of 66 MPa ± 10 MPa for AV119-joined THG CVD-SiC specimens where the shear strength is calculated using $\tau = k\frac{16\,T}{\pi d^3}$, where *T* is the applied torque and *d* is the minimum

[1] Personal Communication from Prof. M. Ferraris of Politecnico di Torino. They used AV119 Epoxy with an elastic modulus of 2.8 GPa and Poisson ratio of 0.4. They obtained accurate, in-plane shear failures for all tests and a shear strength of 36 MPa ± 8 MPa.

radius at the fillet of the miniature torsion specimen, and *k* was set to 1. However, as discussed in Timoshenko and Goodier [25] this equation is only strictly valid for linear elastic homogeneous bodies, not for elastically dissimilar bodies, and *k* for the miniature torsion specimen is not equal to 1. In addition, applying this equation for elastic-plastic materials is inappropriate as discussed in Ref. [16]; rather it is suggested that this value be reduced and a value of 36 MPa is suggested as a more accurate value, which is in general agreement with the FE model results presented here of 28 MPa. This model prediction is based solely on the accuracy of the assumed mechanical properties of AV119 adhesive epoxy taken from Ref. [18], however the strength of AV119 depends on the curing time and temperature, etc., so that the value determined by the elastic-plastic model here might differ from AV119 experimental data.

Data Interpretation and Torsion Test Future

Since the model predicts that high strength, high modulus joints will likely not fail so as to provide a true shear strength for the joints then an obvious point of discussion is what to make of the miniature torsion test? First, the THG specimen is ideal for small-volume, in-reactor experiments and provides a vehicle for obtaining valuable microstructural evolution data for experimental joints. The THG specimen can still provide microstructural evolution leading to differential strains, environmental exposures, and radiation damage. This became clear in the HFIR data recently obtained at ORNL [1]. In that respect, the miniature THG specimen is a successful design.

Second, changes in joint strength or moduli due to radiation damage can be revealed during post-irradiation joint testing. The Ti_3SiC_2+SiC joints survived after 800˚C (1073 K) and 5 dpa but the torsion failure location changed from CVD-SiC base material failure to in-plane joint failure as noted in Ref. [1]. This suggests that a major change occurred in the joined specimens and post-irradiation microscopy revealed interface cracking and microcracking within the joint material. This is thought to be due to either thermal expansion or swelling mismatches between the joint material and the CVD-SiC and/or within the dual-phase joint material. Thus, both shear strength and shear failure location can be used to help understand joining for fusion materials. The model can guide experimental data interpretation by allowing various parameters to be controlled and varied. Many of these parameters can be independently quantified so that the model can be refined as needed.

The torsion shear test is an example of a seemingly simple mechanical test that is, in reality, a complex multiaxial loading problem and methods exist to address these problems in terms of strengths and failure probabilities [9-14]. For future reference, if flaw distributions were known for CVD-SiC and for the joint materials, plus flaws at the joint/CVD-SiC interface, then a true multiaxial, probabilistic solution to the THG specimen could be implemented. However, such an approach is outside of the scope of this study and would be extremely challenging to implement since determining the actual flaw distributions would be a difficult task. Still, the transition from out-of-plane, base CVD-SiC failure to in-plane joint failures that was observed in the post-irradiation testing of these joints most likely indicates a change in the joint flaw distribution due to the irradiation exposure. Significantly, new flaws were observed in post-irradiation SEM examinations of these joints [1].

Finally, it is noted that for a THG specimen previously subjected to neutron irradiation, the experimentally determined irradiated elastic properties can be used to compute the initial elastic stiffness of the irradiated material, and knowing thermal expansion coefficients, thermal stresses can be computed that represent the residual stresses before any mechanical actions (i.e., applied torsion loading). Exactly the same kind of FE analysis of the THG specimen can be applied to elucidate how important the contribution of residual stresses is on the onset of cracking, crack propagation, and shear strength of the irradiated THG specimen. This manuscript does not address the effects of residual stress or the effects of neutron damage, such as differential swelling leading to irradiation-induced stresses, even though it is anticipated that these will be significant, since at this time these effects are not known with certainty for any of these joined material combinations. This level of detail can certainly be implemented in the model presented here but will be reserved for a future study.

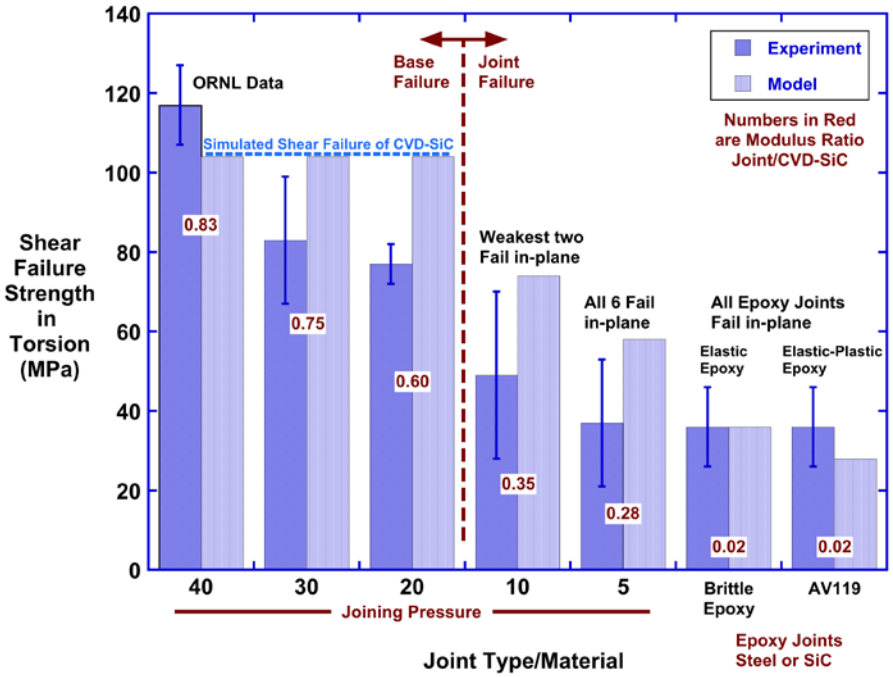

(a)

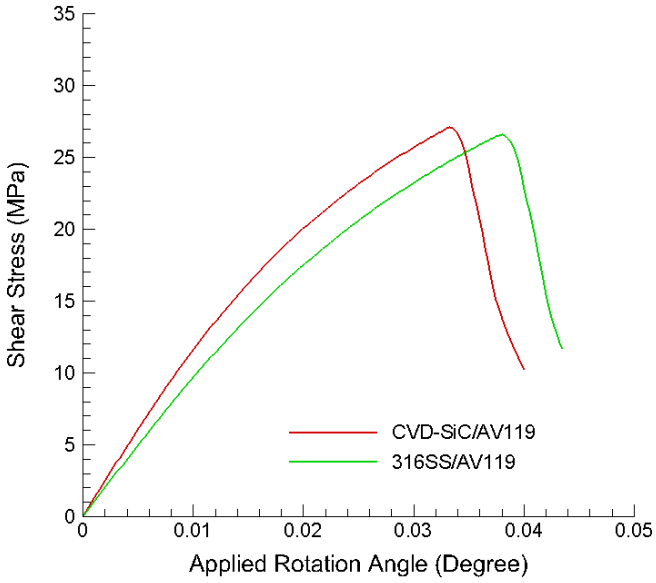

Figure 5. Shown in (a) is the predicted maximum shear stress at fracture for all damage model simulations together with experimental data. Shown in (b) is the predicted evolution of the maximum in-plane shear stresses with applied rotation angle for the elastic-plastic AV119 cases from Figure 4.

Future Work

The in-reactor irradiation results from ORNL display a failure mechanism that is not included in the model yet, namely, the failure of the joint/CVD-SiC interface. Both the Ti_3SiC_2+SiC joints and the CA glass-ceramic joints exhibited interface fractures located at the joint/CVD-SiC interface. The model assumes a

strongly bonded interface between the joint and CVD-SiC and no evolution of that bond is treated in the FE model. Future model implementations will treat the interface as a separate material region with an identifiable strength.

Acknowledgements

This research was supported by Office of Fusion Energy Sciences, U.S. Department of Energy (DOE) under Contract DE-AC05-76RL01830.

References

[1] Katoh, Y., L.L. Snead, T. Cheng, C. Shih, W.D. Lewis, T. Koyanagi, T. Hinoki, C.H. Henager Jr, and M. Ferraris, J. Nucl. Mater., (2014), 448(1-3), 497-511.
[2] Jung, H.-C., T. Hinoki, Y. Katoh, and A. Kohyama, J. Nucl. Mater., (2011), 417(1-3), 383-386.
[3] Nguyen, B.N., B.J. Koeppel, S. Ahzi, M.A. Khaleel, and P. Singh, J. Am. Ceram. Soc., (2006), 89(4), 1358-1368.
[4] Lemaitre, J. and J.L. Chaboche, Journal de Mecanique Appliquee, (1978), 2(3), 317-65.
[5] C. H. Henager, J., B.N. Nguyen, R.J. Kurtz, T. Roosendaal, B. Borlaug, M. Ferraris, A. Ventrella, and Y. Katoh, in Fusion Reactor Materials Program Semiannual Progress Reports, Vol. 56, F. Wiffen, R. Godfrey, and B. Waddell, Editors,(2014), ORNL: Oak Ridge, TN, p. 79-93.
[6] Maugin, G.A., The Thermomechanics of Plasticity and Fracture. (1992), Cambridge, UK: Cambridge University Press.
[7] Tvergaard, V., Int. J. Fract., (1986), 31(3), 183-209.
[8] Nguyen, B.N., V. Kunc, J.H. Phelps, C.L. Tucker Iii, and S.K. Bapanapalli, in 23rd Technical Conference of the American Society for Composites (2008), September 9, 2008 - September 11, 2008, Memphis, TN, United states: DEStech Publications Inc.
[9] Chao, L.-Y. and D.K. Shetty, J. Am. Ceram. Soc., (1990), 73(7), 1917-1921.
[10] Nemeth, N.N., Int. J. Fract., (2014), 185(1-2), 97-114.
[11] Fett, T., D. Munz, and G. Thun, J. Am. Ceram. Soc., (2003), 86(8), 1427-1429.
[12] Suresh, S., C.F. Shih, A. Morrone, and N.P. O'Dowd, J. Am. Ceram. Soc., (1990), 73(5), 1257-1267.
[13] Lamon, J., J. Am. Ceram. Soc., (1990), 73(8), 2204-2212.
[14] Priddle, E.K., Journal of Strain Analysis, (1969), 4(2), 81-87.
[15] Ferraris, M., M. Salvo, V. Casalegno, M. Avalle, and A. Ventrella, Int. J. Appl. Ceram. Technol., (2012), 9(4), 795-807.
[16] Ferraris, M., A. Ventrella, M. Salvo, and D. Gross, Int. J. Appl. Ceram. Technol., (2014), 11(2), 394-401.
[17] Xu, B., "Fracture Mechanisms and Failure Criteria of Adhesive Joints and Toughened Epoxy Adhesives," in School of Engineering and Materials Science. (2010), Queen Mary, University of London: University of London, p. 225.
[18] Broughton, W.R., L.E. Crocker, and J.M. Urquhart, "Strength of Adhesive Joints: A Parametric Study," (2001), T. National Physical Laboratory, Middlesex, TW11 0LW, UK, NPL Materials Centre, National Physical Laboratory, Teddington, Middlesex, TW11 0LW, UK, p. 41.
[19] C. H. Henager, J., B.N. Nguyen, R.J. Kurtz, T. Roosendaal, B. Borlaug, M. Ferraris, A. Ventrella, and Y. Katoh, in Fusion Reactor Materials Program Semiannual Progress Reports, Vol. 57, F. Wiffen, R. Godfrey, and B. Waddell, Editors, (2014), ORNL: Oak Ridge, TN, p. 74-84.
[20] Byun, T.S., N. Hashimoto, and K. Farrell, Acta Mater., (2004), 52(13), 3889-3899.
[21] Ferraris, M., A. Ventrella, M. Salvo, Y. Katoh, and D. Gross, Int. J. Appl. Ceram. Technol., (2014), in press.
[22] Hinoki, T., Y. Katoh, L.L. Snead, H.-C. Jung, K. Ozawa, H. Katsui, Z.-H. Zhong, S. Kondo, Y.-H. Park, C. Shih, C.M. Parish, R.A. Meisner, and A. Hasegawa, Mater. Trans., (2013), 54(4), 472-476.
[23] Ferraris, M., M. Salvo, S. Rizzo, V. Casalegno, S. Han, A. Ventrella, T. Hinoki, and Y. Katoh, Int. J. Appl. Ceram. Technol., (2012), 9(4), 786-794.
[24] Ferraris, M., M. Salvo, V. Casalegno, S. Han, Y. Katoh, H.C. Jung, T. Hinoki, and A. Kohyama, J. Nucl. Mater., (2011), 417(1-3), 379-82.
[25] Timoshenko, S.P. and J.N. Goodier, Theory of Elasticity, Third ed. Engineering Societies Monographs. (1970), New York: McGraw Hill.

3.3 PROGRESS IN CHARACTERIZATION OF PRECIPITATES AND DEFECT STRUCTURES IN Mg^+ ION IMPLANTED CUBIC SILICON CARBIDE

— W. Jiang, J. Zhang, Z. Zhu, T. J. Roosendaal, S. Y. Hu, C. H. Henager, Jr., R. J. Kurtz (Pacific Northwest National Laboratory), and Y. Wang (Los Alamos National Laboratory)

OBJECTIVE

This study aims at characterizing precipitates and defect structures in Mg^+ ion implanted and high-temperature annealed cubic silicon carbide (3C-SiC).

SUMMARY

This report describes the progress of our current experimental effort on Mg^+ ion implanted 3C-SiC. Following our initial study [1] that suggests possible formation of Mg_2Si and MgC_2 precipitates as well as tetrahedral voids in $^{24}Mg^+$ ion implanted 3C-SiC, we have designed specific experiments to confirm the results and examine the inclusions and defects. Relatively low fluence (5.0×10^{15} $^{24}Mg^+/cm^2$) implantation in 3C-SiC was performed to reduce defect concentrations and isolate individual defect features for characterization. In addition, $^{25}Mg^+$ isotope was implanted in 3C-SiC to the same previously applied ion fluence (9.6×10^{16} ions/cm^2) for atom probe tomography (APT) study of precipitates. Each set of the samples was annealed at 1573 K for 2, 6 and 12 h, respectively. The depth profiles of the implanted Mg were measured using secondary ion mass spectrometry (SIMS) before and after the annealing steps. The samples are currently being analyzed using transmission electron microscopy (TEM) and APT.

PROGRESS AND STATUS

Introduction

Cubic silicon carbide has been a candidate material for a number of applications in fusion reactor designs [2,3]. Upon exposure to high-energy neutrons, silicon carbide undergoes transmutation reactions with magnesium as the major metallic transmutant, as predicted by Sawan, *et al*. [4]. The impact of the transmutants and irradiation induced defects on SiC structural modifications and property degradation is currently unknown. Our previous scanning transmission electron microscopy (STEM) study [1] suggests that precipitates of cubic Mg_2Si and tetragonal MgC_2 as well as tetrahedral voids of ~5 nm in size are likely formed in 3C-SiC implanted to 9.6×10^{16} $^{24}Mg^+/cm^2$ at 673 K and subsequently annealed at 1573 K for 12 h. As the defect concentration was too high and the defect features could not be spatially resolved by TEM, the conventional under- and over-focus imaging technique could not be used to confirm the defect nature. Likewise, we cannot ascertain whether the observed bright-contrast triangular shape in the STEM image is associated with stacking fault tetrahedra (SFTs). To increase the probability of generating isolated defect features, samples were implanted to an order of magnitude lower in ion fluence (5.0×10^{15} $^{24}Mg^+/cm^2$) at 673 K. The low-dose samples have been annealed at 1573 K and are currently being examined to study defect structures, including possible tetrahedral voids, stacking fault tetrahedra, and Mg nucleation site using atomic-level resolution aberration-corrected TEM.

In addition, the precipitates of cubic Mg_2Si and tetragonal MgC_2 were not observed directly, but derived from fast Fourier transformation (FFT) of a high-resolution STEM image [1]. APT was attempted to confirm and better characterize the precipitates, but element ^{24}Mg and atomic cluster C_2 could not be resolved in the mass spectra. To solve the technical issues, ^{25}Mg isotope was obtained and $^{25}Mg^+$ ion implantation (9.6×10^{16} $^{25}Mg^+/cm^2$ at 673 K) was performed. The implanted 3C-SiC samples have been annealed at 1073 and 1573 K and are being analyzed using APT. The 1073 K annealed sample is intended for analysis without involving voids in the crystal structure. Reported here are some of the initial data, including x-ray diffraction (XRD) pole figures for the 3C-SiC film before ion implantation and the depth profiles of the implanted Mg by SIMS before and after the thermal annealing steps.

Experimental Procedure

Single crystal (001)-oriented 3C-SiC films (~2 μm in thickness) on Si (001) substrates used in this study were characterized using XRD pole figures. Scans were performed for 3C-SiC (111) and (220) poles at 2θ = 35.597° and 59.978°, respectively. The samples were implanted 7° off the surface normal with 200 keV $^{25}Mg^{+}$ ions at 673 K to a high fluence of 9.6×10^{16} ions/cm^2. The ion fluence corresponds to maxima of ~6 at.% ^{25}Mg at 280 nm and 54 dpa at 220 nm according to SRIM simulation [5], as shown in Figure 1. The isotope ^{25}Mg was obtained from National Isotope Development Center (NIDC) at Oak Ridge and the implantation was performed at Los Alamos National Laboratory (LANL). Additional implantation was also performed at LANL using 200 keV $^{24}Mg^{+}$ ions to a lower fluence of 5×10^{15} ions/cm^2 at the same elevated temperature. The implanted sample was cleaved into smaller pieces (5 mm × 5 mm) for different thermal annealing conditions. Each set of the low and higher dose samples was thermally annealed at 1573 K for 2, 6 and 12 h in flowing Ar gas, respectively. Additional annealing of the $^{25}Mg^{+}$ ion implanted sample was also performed at 1073 K for 12 h to prevent void formation due to vacancy clustering in the structure. To minimize surface oxidation, the samples were placed inside a chimney of Ta metallic foil to reduce the oxygen partial pressure. The Mg depth profiles in the SiC samples were measured before and after the annealing steps using time-of-flight SIMS (ToF-SIMS) with 2 keV O_2^{+} ions as sputtering beam and 25 keV Bi^{+} ions as analyzing beam. The depth scale was calibrated by measuring the crater depth with a Veeco Dektak 150 stylus profilometer.

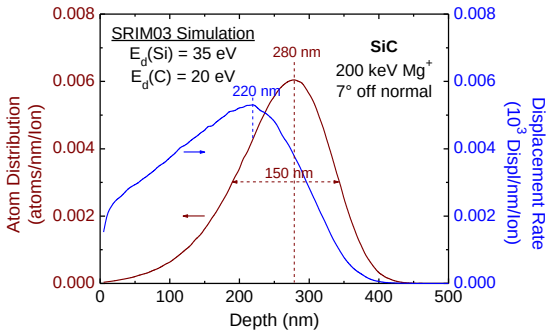

Figure 1. Depth profiles of Mg implants and atomic displacement rate in Mg^{+} ion implanted SiC from SRIM simulation.

Results and Discussion

The 3C-SiC films on Si substrates used in this study were analyzed using XRD pole figures before ion implantation. The data are shown in Figure 2, along with a stereographic display of poles from simulation. The data clearly show four symmetric 3C-SiC (111) and (220) [equivalent to (110)] poles, respectively, suggesting that the film is a single crystal with a nearly on-axis (001) cut. Additional symmetric scans of the sample (data not shown) indicate that the crystal has high monocrystalline quality without presence of any secondary phases.

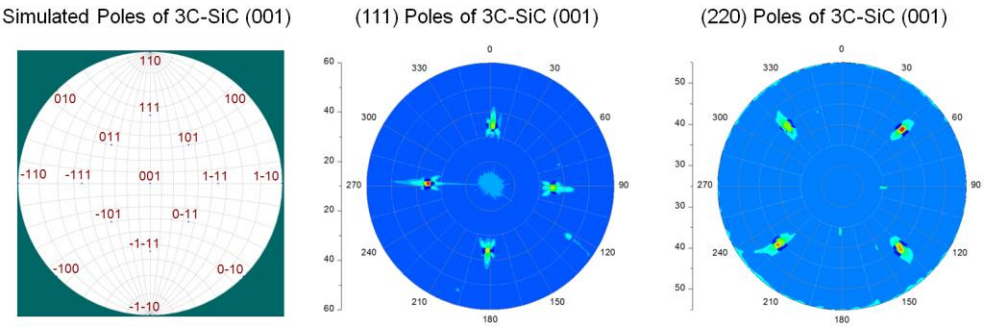

Figure 2. Comparison of simulated poles of (001) oriented 3C-SiC with the experimental data for (111) and (220) poles of an as-grown 3C-SiC film on Si (001).

Prior to annealing of the ion implanted samples, an as-grown 3C-SiC was furnace annealed for a test inside a Ta chimney at 1573 K under Ar gas flow. ToF-SIMS was used to measure the oxygen concentration for assessment of surface oxidation. The data are shown in Figure 3. Oxidation from the surface to a depth of ~10 nm was observed after the annealing for 12 h, but more extensive surface oxidation beyond the depth did not occur. This annealing condition was applied for the Mg^+ ion implanted 3C-SiC.

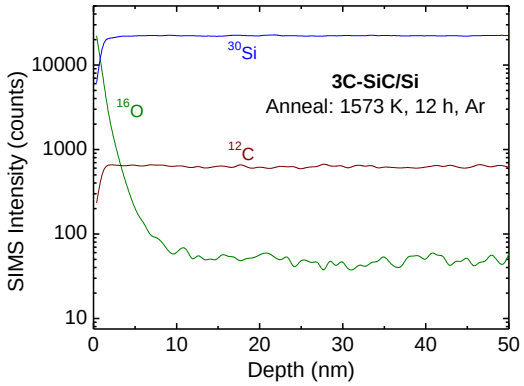

Figure 3. ToF-SIMS depth profiles of ^{16}O, ^{30}Si and ^{12}C in an as-grown single crystal 3C-SiC film on Si annealed at 1573 K in Ar gas.

The normalized SIMS depth profiles of the implanted Mg in 3C-SiC are shown in Figure 4. The normalization follows $I'_{Mg}(i) = 100I_{Mg}(i)/[w\Sigma I_{Mg}(j)]$, where $I_{Mg}(i)$ is the Mg intensity at channel number i and w is the channel width. This normalization procedure does not alter full width at half maximum (FWHM) of the peak, but allows for all the ToF-SIMS data measured under different conditions (dwelling time of sputtering beam, beam current, etc.) to be plotted in one figure for comparison. In Figure 4(a), the peak maximum of the ^{24}Mg profile in the as-implanted 3C-SiC is located at ~240 nm with FWHM of ~145 nm, which is consistent with our previous observation [1], but slightly shallower than the SRIM prediction (Figure 1). Similarly, the profile peak for ^{25}Mg in Figure 4(b) is also at ~240 nm with a slightly larger FWHM of ~160 nm. There is no significant difference in the ^{24}Mg and ^{25}Mg profiles, as expected. According to Figure 4, annealing at 1573 K for 2, 6 and 12 h does not lead to a peak position shift or a noticeable change in the shape of the Mg depth profiles, indicating that there is no significant Mg diffusion during the thermal annealing. The small deviation shown for the $^{25}Mg^+$ ion implanted and 6 h annealed

sample may be due to the uncertainty in the depth calibration. It should be noted that this non-diffusion behavior is not the same as that observed in a previous study [1], where Mg diffused into the bulk of a 3C-SiC single crystal after annealing at 1573 K for 12 h. Possible reasons include some difference in the

actual sample temperature during the thermal annealing in the two cases because significant Mg diffusion in single crystal SiC starts to occur between 1473 and 1573 K [1].

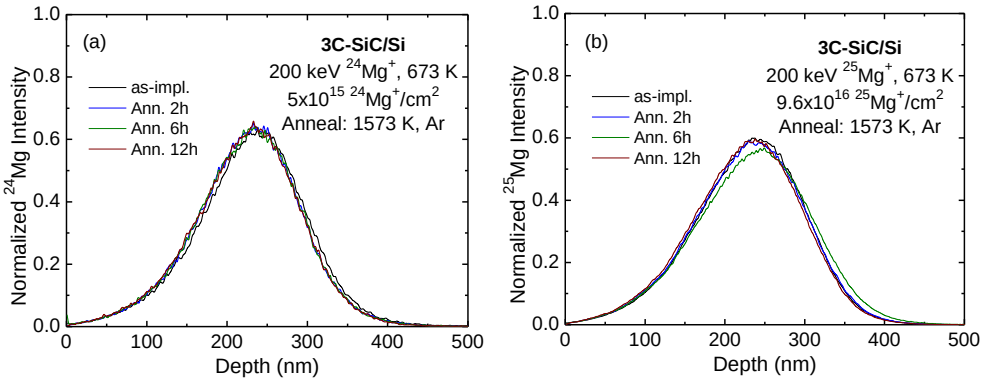

Figure 4. ToF-SIMS depth profiles of (a) ^{24}Mg and (b) ^{25}Mg in single crystal 3C-SiC films on Si before and after furnace annealing at 1573 K for 2, 6 and 12 h, respectively, in Ar gas.

At 1573 K, implantation induced vacancies in 3C-SiC are mobile and vacancy clustering is expected to occur during the thermal annealing. Although long-range diffusion of the implanted Mg in 3C-SiC does not occur, short-range migration of Mg is possible, which can lead to precipitation of secondary phases. In fact, preliminary APT data (not shown) have suggested formation of precipitates that contain ^{25}Mg in the 12 h annealed sample. This study is focused on the formation and growth of possible voids and precipitates as a function of annealing duration at 1573 K as well as the dependence of the precipitate characteristics on annealing temperature. We will report the results when the data are available.

Acknowledgements

This research was supported by Office of Fusion Energy Sciences, U.S. Department of Energy (DOE) under Contract DE-AC05-76RL01830. Ion implantation was performed at Ion Beam Materials Laboratory through a partial support from Center for Integrated Nanotechnologies (CINT), a DOE nanoscience user facility jointly operated by Los Alamos and Sandia National Laboratories. SIMS and XRD were performed under a general user proposal at the Environmental Molecular Sciences Laboratory (EMSL), a national scientific user facility located at PNNL. Isotope ^{25}Mg used in this research was supplied by DOE Office of Science Isotope Program in the Office of Nuclear Physics.

References

[1] W. Jiang, H. J. Jung, L. Kovarik, Z. Wang, T. J. Roosendaal, Z. Zhu, D. J. Edwards, S. Y. Hu, C. H. Henager, Jr., R. J. Kurtz, and Y. Wang, J. Nucl. Mater. 458 (2015) 146.
[2] A. R. Raffray, R. Jones, G Aiello, M. Billone, L. Giancarli, H. Golfier, A. Hasegawa, Y. Katoh, A. Kohyama, S. Nishio, B. Riccardi, and M. S. Tillack, Fusion Eng. Des. 55 (2001) 55.
[3] C. P. C. Wong, M. Abdou, M. Dagher, Y. Katoh, R. J. Kurtz, S. Malang, E. P. Marriott, B. J. Merrill, K. Messadek, N. B. Morley, M. E. Sawan, S. Sharafat, S. Smolentsev, D. K. Sze, S. Willms, A. Ying, and M. Z. Youssef, Fusion Eng. Des. 85 (2010) 1129.
[4] M. E. Sawan, Y. Katoh, and L. L. Snead, J. Nucl. Mater. 442 (2013) S370.
[5] J. F. Ziegler, J. P. Biearsack, and U. Littmark, The stopping and Range of Ions in Solids (Pergamon Press, New York,) (1985); available from: http://www.SRIM.org/.

4.1 RECENT PROGRESS IN THE FABRICATION AND CHARACTERIZATION OF DUCTILE-PHASE-TOUGHENED TUNGSTEN LAMINATES FOR PLASMA-FACING MATERIALS — K. H. Cunningham, G. R. Odette, K. Fields, D. Gragg, T. Yamamoto, and F. W. Zok (University of California, Santa Barbara)

OBJECTIVE

The objective of this study is to develop ductile-phase-toughened tungsten composites as candidates for plasma-facing components in future fusion reactors.

SUMMARY

A promising approach to increasing the fracture toughness of W-alloys is ductile-phase toughening (DPT). A ductile reinforcement in a brittle matrix increases toughness primarily by crack bridging. A W-Cu laminate was fabricated, and fracture resistance curves (R-curves) were calculated via precracked three-point bend testing. An analytical model of crack bridging was used to estimate the parameter space of useful toughening reinforcements for rolled W plate. Work began on extending the model framework to calculate the bridging stress-displacement function (bridging law) of a ductile reinforcement from test load-displacement data.

PROGRESS AND STATUS

Introduction

Background information and previous progress have been discussed in earlier semi-annual reports [1-4].

Experimental Procedure

Brazed W-Cu Laminate Fracture Testing

As described in the previous report, W plates were brazed with layers of Cu to form a laminate. The layup consisted of five lapped 0.85x50x50-mm W plates stacked with four alternating 75-μm Cu foils. The W plates were aligned using the rolling direction. One of the outer plates was rotated 90° from the others, as will be discussed later. Notched three-point bend bars were EDM-cut from the laminate with dimensions 21x4.65x2.125 mm, with a nominal notch depth of 0.93 mm. Specimens were separated into “edge” and “face” categories, for which the direction of crack propagation was normal to the edge or face of the ductile laminate layers, respectively. Specimens were labeled “L” or “T” with respect to the rolling direction of the W plates they contained, indicating if the crack propagation direction was parallel (L) or perpendicular (T) to the rolling direction. Specimens were also fabricated with a mixture of L and T plates, called L+T. The average W toughness and standard deviations were 13.06±2.34 and 20.90±0.45 MPa $m^{0.5}$ in the L and T directions, respectively [4].

Laminate specimens were precracked by compression-compression fatigue in the span direction as described previously for monolithic W bars [4]. Precracks were grown to an approximate target depth of a/w=0.3. Three-point bend specimens with a 20.5-mm span were tested at a crosshead displacement rate of 0.05 mm/min on an MTS load frame. A microscope mounted on the load frame was used to observe the increments of crack growth for correlation with the load-displacement data. The load (P) and displacement (D) at each increment of measured crack length (a) was used to calculate the fracture toughness corresponding to the arrested crack length following ASTM E399-12. This gives rise to a resistance [K_R(da)] curve, associated with crack bridging by the ductile layer. The crack shape at the end of each test was marked by oxidizing the W surface at 400°C in air.

Large-Scale Crack Bridging Code

The previous report discussed a large scale bridging (LSB) code we are developing with emphasis on comparing the predicted post-peak load-displacement (P-D) values to a previous model [1-7]. Our code for calculating R-curves and the pre-peak portion of load-displacement (P-D) curves was used to estimate the range of useful values for each of four parameters that describe the stress-displacement function of a ductile reinforcement ($\sigma(u)$, the bridging law) given by the flexibly parameterized Equation 1. As illustrated in Figure 1, these parameters are: the peak load (σ_{max}), the peak-load displacement (u_1), a post-peak shape exponent (n), and the failure displacement (u_2). The combination of parameters examined is shown in Table 1.

$$\sigma(u) = \frac{\sigma_{max}}{2}\left(1-\frac{u-u_1}{u_2-u_1}\right)^n + \frac{\sigma_{max}}{2}\left(1-\left(\frac{u-u_1}{u_2-u_1}\right)^{1/n}\right), u_1 < u < u_2 \quad [1]$$

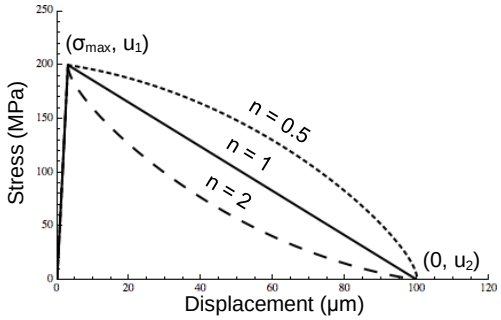

Figure 1. Example bridging stress-displacement function. The function is defined by four parameters, and assumes linear elastic behavior approaching the peak load. Examples of the effect of n on the post-peak shape are given.

Table 1. Values used for each parameter in parametric study. The resulting data set contains 256 associated R-curves and P-D curves to allow for a quantitative comparison of reinforcements for a W-matrix composite.

σ_{max} (MPa)	100	200	300	400
u_1 (μm)	1	3	5	7
n	0.3	1	3	9
u_2 (μm)	50	150	250	350

We also began work on developing an "inverse" code to estimate the ductile reinforcement $\sigma(u)$ using P-D data. The inverse code requires the same elastic constant and matrix toughness as the LSB code [4]. In principle it can extract all 4 $\sigma(u)$ parameters. However the failure displacement of the ductile reinforcements, u_2, usually can be obtained from measurements on the broken specimens, hence this was fixed in this exercise. The basic algorithm is as follows:

- Store the R-curve data points as an interpolated function.
- Estimate the elastic portion of the bridging law:
  - Guess low values for σ_{max} and u_1 (1 MPa and 0.1 μm).
  - Model a very short crack extension to ensure that the opening displacement is less than u_1.
  - Run the LSB model to calculate the crack shape u(x), crack-face stress distribution σ(x), and K_R using the interpolation function.
  - Calculate the ratio of the measured increase in fracture resistance to the calculated increase in fracture resistance, $(K_{R,test} - K_I)/(K_{R,calc} - K_I)$, where K_I is the known toughness of the matrix.
  - Multiply σ_{max} by the K ratio to update the estimated value, and iterate until σ_{max} converges.
  - Save the (σ_{max}, u_1) point, then increase the u_1 guess by a small amount and repeat.

- End the iterative process when the convergent σ_{max} value begins to decrease between iterations.

- Estimate the post-peak shape:
  - Guess a value for n (1 is simplest).
  - Model K_R(da) using the first measured K_R point after crack initiation in the test data.
  - Follow the same procedure as above, except dividing n by the K ratio with each iteration.
  - Manually choose an appropriate n value based on the resulting plot of n versus a.

Results

Brazed W-Cu Laminate Fracture Testing

No face-orientation composite was tested because the compression-compression precracking method caused shear failure at the W-Cu interfaces. Edge-orientation fracture was characterized by varying increments of unstable crack growth followed by crack arrest (pop-ins) due to the Cu reinforcement, as illustrated in Figure 2 from an L+T oriented specimen. A representative fracture surface image of a heat-tinted sample is shown in Figure 3 from the same L+T specimen. Precrack fronts had a concave or flat shape instead of the usual convex "thumbnail" shape, and in the mixed orientation the crack propagated to a greater depth in the L-oriented versus T-oriented plates. This is qualitatively consistent with the anisotropic toughness of the W matrix, as the rolled plate is tougher in the T direction than the L direction by a factor of about 1.6 [4].

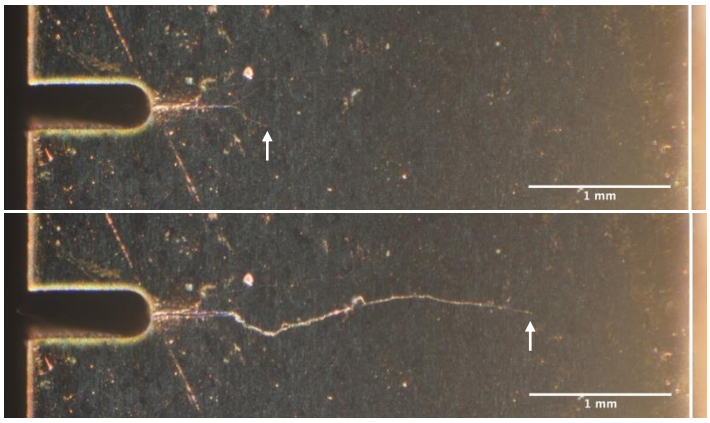

Figure 2. Comparison of two successive images from three-point bend testing on W-Cu laminate (specimen O3-2). The crack at a/w=0.36 (top) grows unstably to a/w=0.76 (bottom) before being arrested by the Cu reinforcement. Arrows indicate the crack tip in each image, and the vertical line at right indicates the edge of the specimen.

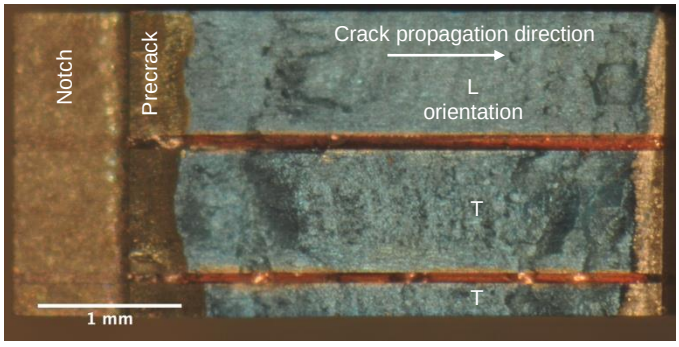

Figure 3. Fracture surface of W-Cu laminate bend bar (O3-2). Blue coloration on W layers is from heat tinting to observe the final crack length in different W plates. Crack is longer in L-oriented plate than in T

plates. Dark contrast in blue test crack region is from surface features; L plate has relatively flat fracture surface while T plates are rough.

A representative P-D curve along with the corresponding R-curve is shown in Figure 4, illustrating the load drops associated with unstable crack growth as well as the loads used to calculate each point in the R-curve. A summary of all calculated R-curves is given in Figure 5 as a set of plots grouping tests by orientation (L, T, or L+T). The T orientation showed greater increases in toughness with crack extension than the L orientation, but had less stable crack growth. For the mixed orientation, in which one of the three W plates was a different orientation than the other two (one L and two T, or vice versa), had a small initial increment of higher R-curve slope than the L orientation, but plateaued around a/w=0.5, and reached a maximum K_R between those for the L and T orientations at very large a/w. Again, this behavior simply reflects the differences in the T and L matrix toughness. These data do not show a significant difference in R-curve behavior between areas of the laminate containing 2L+1T versus 1L+2T plates.

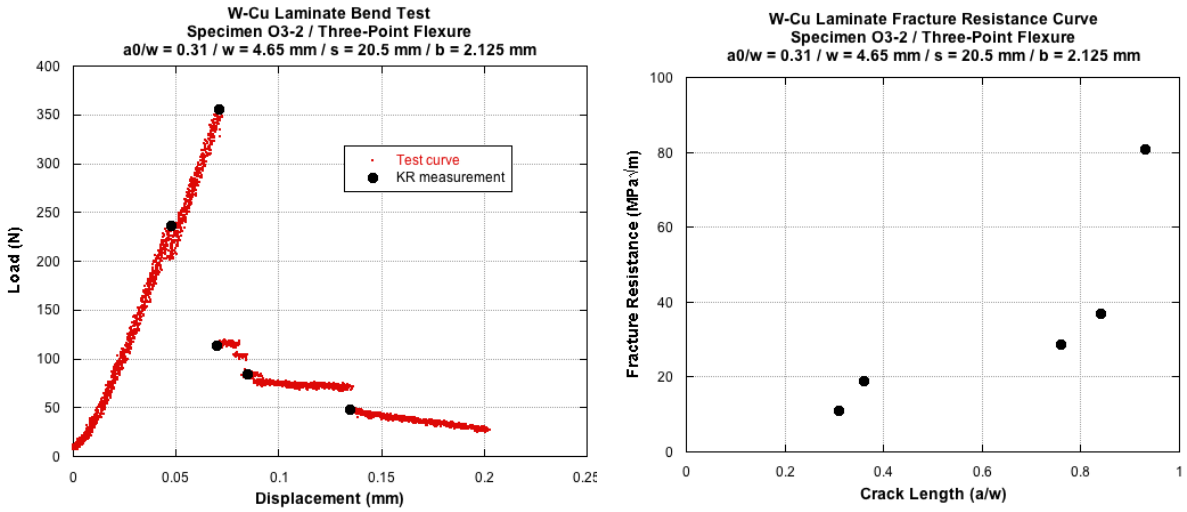

Figure 4. P-D curve (left) and R-curve (right) for W-Cu laminate bend specimen O3-2. Black points on P-D curve indicate the maximum load at each measured crack length used to calculate K_R. Significant load drops were observed corresponding to unstable crack growth and subsequent crack arrest.

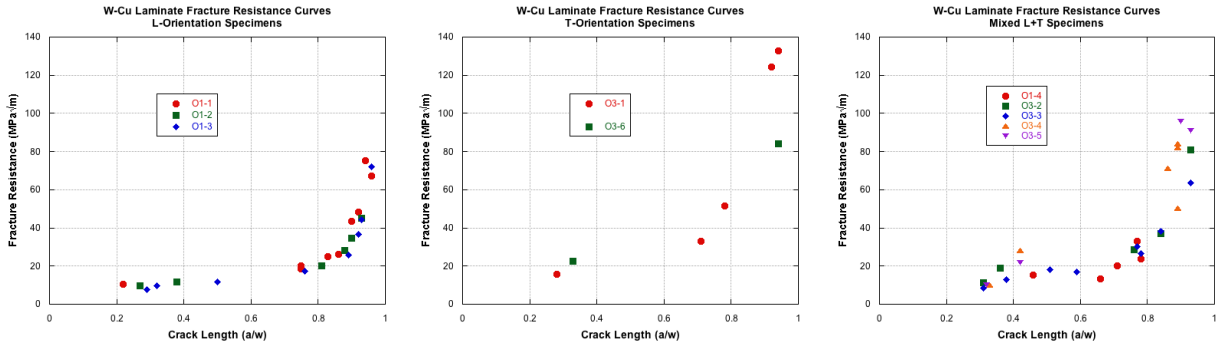

Figure 5. Comparison of R-curves for W-Cu laminate in different orientations. Plots are grouped by laminate orientation: specimens with only L-orientation W plates (left), only T-orientation plates (center), or a mix of L and T plates (right). The T orientation has higher initiation toughness as expected, as well as a greater increase in fracture resistance with crack growth. The L orientation shows more stable crack growth, evidenced by the greater number of points per test. In the mixed orientation, initiation toughness appears controlled by the L orientation, with the subsequent R-curve shape a mixed character of L and T.

Since the K_R curves show significant toughness increases only at large a/w, one might conclude that the small amount (< 8% by volume) of relatively weak (annealed Cu) and thin reinforcement had little beneficial effects on the fracture resistance of the composite versus the monolithic W. Indeed this is the case if the metric is the relative engineering strength of the composite. However, crack arrest and increments of quasi-stable growth are observed, providing some degree of engineering ductility in the composite that is entirely absent in the monolithic W plate. Therefore, a composite with a higher volume fraction of stronger reinforcing phase, with an optimized thickness, would be expected to perform significantly better. To this end, we used our crack bridging model to guide the fabrication of an improved composite.

Large-Scale Crack Bridging Code

A parametric study of reinforcement $\sigma(u)$ was used to evaluate the effects of the controlling parameters individually and in combination as illustrated in Figure 6. Here the P-D curves are normalized by the corresponding loads and displacements at elastic fracture of the brittle matrix, P' and D', respectively.

σ_{max} (MPa)	u_1 (μm)	n	u_2 (μm)	P-D Curves [P/P' vs. D/D']	R-Curves [K_R (MPa) vs. a/w]
100 200 300 400	1	0.3	350	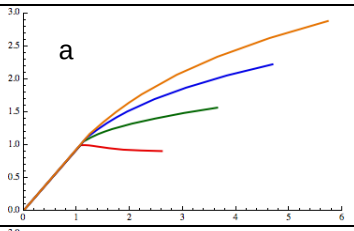	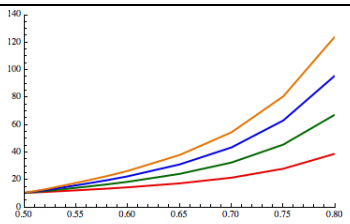
400	1 3 5 7	0.3	350	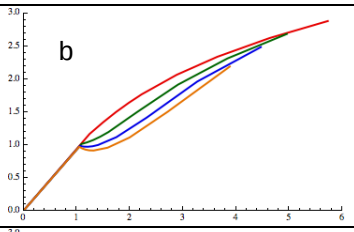	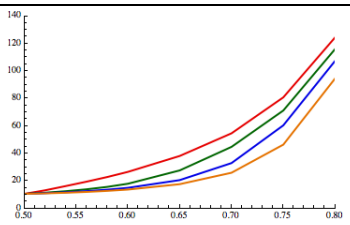
400	1	0.3 1 3 9	350	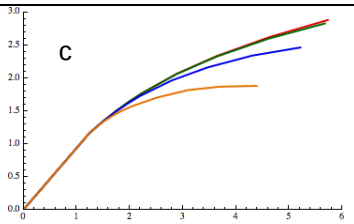	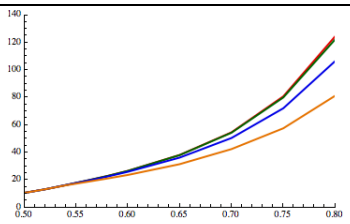
400	1	9	50 150 250 350	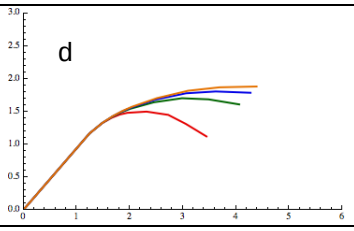	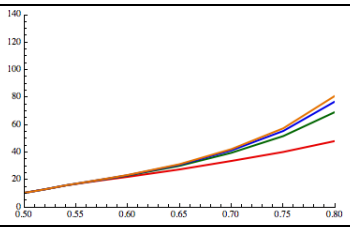

Figure 6. Parametric study summary. In each row of values and plots, one parameter is varied and the resulting P-D curves and R-curves are shown. Load and displacement values are normalized by the load capacity (P') and displacement (D') at fracture, respectively, of the unreinforced tungsten matrix. The mechanical behavior of the composite is more sensitive to σ_{max} and u_1 than to n and u_2.

For a desirable, and expected, low value of u_1, the P-D and K_R(da/w) curves increase with increasing σ_{max}, resulting in a desirable increase in P_{max}, accompanied by increasing D or ductility (Figure 6a). The

detrimental effect of increasing u_1 is also revealed in the P-D curves (Figure 6b). Both increasing the convex shape of the bridging law (Figure 6c) and, to a lesser extent, increasing u_2 (Figure 6d) increase the composite strength and ductility P-D curves.

It must be emphasized that while these effects can be qualitatively anticipated, they all represent LSB effects for a growing bridging zone that cannot be quantitatively predicted based on "intuition" or simple energy-based concepts. Such mistaken and misleading thinking is unfortunately all too common. The engineering performance capabilities of a DPT composite are reflected in the normalized P-D curves with values of P/P' and D/D' greater than 1, which is the limit for the elastically brittle monolithic matrix material. It is also worth noting that it is the initial slope of the K_R(da) curve that controls the crack growth initiation P-D and any subsequent stable crack growth for any expected practical initial crack length.

It is generally not possible to directly measure σ(u) curves for embedded reinforcements since this depends on details like debonding and triaxial stresses in matrix cracks that are blunted in the ductile phase. However, as noted above they can be inversely extracted from P-D data [6,7]. The estimation strategy for σ_{max} and u_1 successfully reconstructed the elastic loading portion of the bridging law in cases where the true u_1 value was 5 μm or less. Assuming that u_2 is a measurable quantity, the estimate for n also converges to the correct value for intermediate values of a/w as illustrated in Figure 7. The estimation algorithm described can be used to estimate a relatively narrow range of σ(u) parameters, but this is still work in progress.

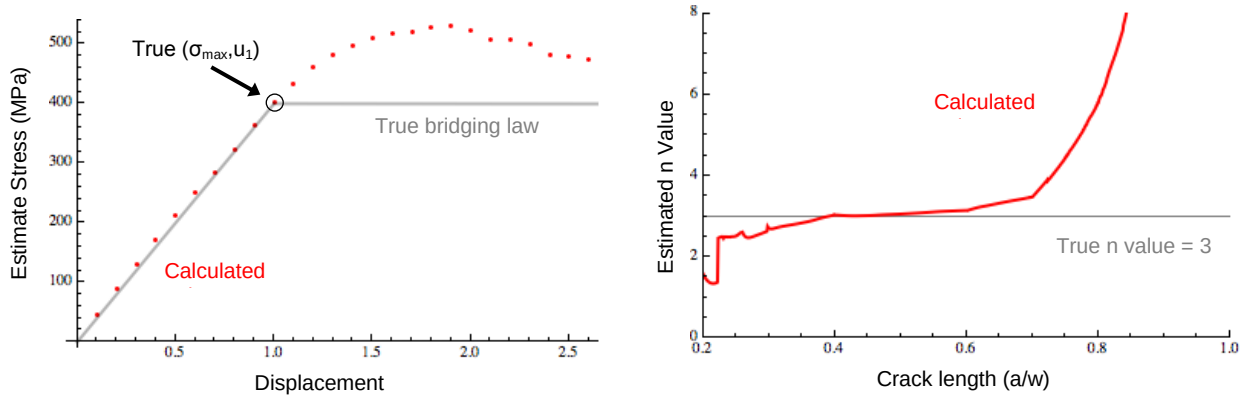

Figure 7. Summary of bridging law estimation from simulated test data. Left: estimate of (σ_{max},u_1) point shown against a close-up view of the true bridging law. Calculated values track well with the true elastic slope of the bridging law. Without knowing the true bridging law that was used to construct the R-curve that the estimate uses, it is difficult to determine the true point, even though it has been estimated quite accurately. Right: estimate of n parameter shown as the values calculated at a variety of crack lengths. The plateau around a/w=0.45 is the correct estimate of the true n value, but as with (σ_{max},u_1) it is difficult to choose an exact value from the estimates alone.

Ongoing and Future Work

The large-scale bridging model will be finalized with respect to the calculation of P-D and K_R(da) curves for a given σ(u), and the "inverse" calculation of σ(u) from given P-D data.

References

[1] K. H. Cunningham, K. Fields, D. Gragg, F. W. Zok, C. H. Henager, Jr, R. J. Kurtz, and T. Roosendaal, Recent Progress in the Development of Ductile-Phase Toughened Tungsten for Plasma-Facing Materials, in DOE/ER-0313/54 - Volume 54, Semiannual Progress Report, June 30, 2013. 2013, US DOE: ORNL, TN.

[2] C. H. Henager, Jr, R. J. Kurtz, T. J. Roosendaal, B. A. Borlaug, G. R. Odette, K. H. Cunningham, K. Fields, D. Gragg, and F. W. Zok, Recent Progress in the Development of Ductile-Phase Toughened Tungsten for Plasma-Facing Materials, in DOE/ER-0313/55 - Volume 55, Semiannual Progress Report, Dec. 31, 2013. 2013, US DOE: ORNL, TN.
[3] K. H. Cunningham, G. R. Odette, K. Fields, D. Gragg, F. W. Zok, C. H. Henager, Jr., R. J. Kurtz, T. J. Roosendaal, and B. A. Borlaug, Recent Progress in the Fabrication and Characterization of Ductile-Phase-Toughened Tungsten Composites For Plasma-Facing Materials, in DOE/ER-0313/56 - Volume 56, Semiannual Progress Report, Jun. 30, 2014. 2014, US DOE: ORNL, TN.
[4] K. H. Cunningham, G. R. Odette, K. Fields, D. Gragg, T. Yamamoto, F. W. Zok, C. H. Henager, Jr., R. J. Kurtz, T. J. Roosendaal, and B. A. Borlaug, Recent Progress in the Fabrication and Characterization of Ductile-Phase-Toughened Tungsten Laminates For Plasma-Facing Materials, in DOE/ER-0313/57 - Volume 57, Semiannual Progress Report, Dec. 31, 2014. 2014, US DOE: ORNL, TN.
[5] G. R. Odette, B. L. Chao, J. W. Sheckherd, and G. E. Lucas. Acta Metall. Mater. 40-9 (1992) 2381-2389.
[6] G. R. Odette and B. L. Chao, unpublished notes.
[7] J. A. Heathcote. Ph.D. Dissertation, University of California, Santa Barbara, 1996.

4.2 RECENT PROGRESS IN THE DEVELOPMENT OF DUCTILE-PHASE TOUGHENED TUNGSTEN FOR PLASMA-FACING MATERIALS: W-Ni-Fe COMPOSITES – C. H. Henager, Jr., E. L. Stevens, R. J. Kurtz, T. J. Roosendaal, E. A. Nyberg, C. A. Lavender (Pacific Northwest National Laboratory), G. R. Odette, K. H. Cunningham, and F. W. Zok (University of California, Santa Barbara)

OBJECTIVE

The objective of this study is to fabricate, test, and characterize a lamellar W-Ni-Fe composite based on tungsten heavy metal alloys suitable for model material development for fusion reactor studies of ductile-phase toughening. The lamellar structure will be obtained by hot-rolling the as-sintered W-Ni-Fe composite.

SUMMARY

A promising approach to increasing fracture toughness and decreasing the DBTT of a W-alloy is by ductile-phase toughening (DPT) [1-3]. In this method, a ductile phase is included in a brittle matrix to prevent fracture propagation by crack bridging or crack deflection. Liquid-phase sintered W-Ni-Fe alloys consisting of nearly spherical W-particles embedded within a Ni-Fe-W ductile matrix are being manipulated by hot-rolling to create lamellar W/Fe-Ni-W composites with anisotropic fracture properties. The rolled W-Ni-Fe alloy becomes a lamellar alloy consisting of W lamellae separated by ductile-phase regions. The W-rich lamellae are strong but brittle, while the ductile-phase metallic regions have a thin, plate-like morphology to provide a ductile bridging region. This rolled material is oriented with the W-rich lamellae parallel to principal stresses so that surface cracking is normal to the ductile-phase bridging regions.

PROGRESS AND STATUS

Background

Tungsten (W) and W-alloys are the solid materials of choice for plasma-facing components (PFCs) of future fusion reactors, such as the International Thermonuclear Experimental Reactor (ITER) and Demonstration Power Plant (DEMO), due to their high melting point, strength at high temperatures, high thermal conductivity, low coefficient of thermal expansion, and low sputtering yield [4-8]. However, W and most W-alloys exhibit low fracture toughness and a high ductile-brittle transition temperature (DBTT) that would render them as brittle materials during reactor operations [4, 6, 9]. The DBTT for unirradiated W-alloys typically ranges from 573K to 1273K (300 to 1000˚C) and in a reactor environment radiation hardening would further elevate this range [6, 10, 11]. W-alloys toughened by engineered reinforcement architectures, such as ductile-phase toughening (DPT), are strong candidates for PFCs. In DPT, a ductile phase is included in a brittle matrix to prevent fracture propagation. The principles of DPT are illustrated in Figure 1, which shows an actual and schematic illustration of ductile bridging ligaments stretching across an open crack in a brittle matrix material, such as W [12, 13].

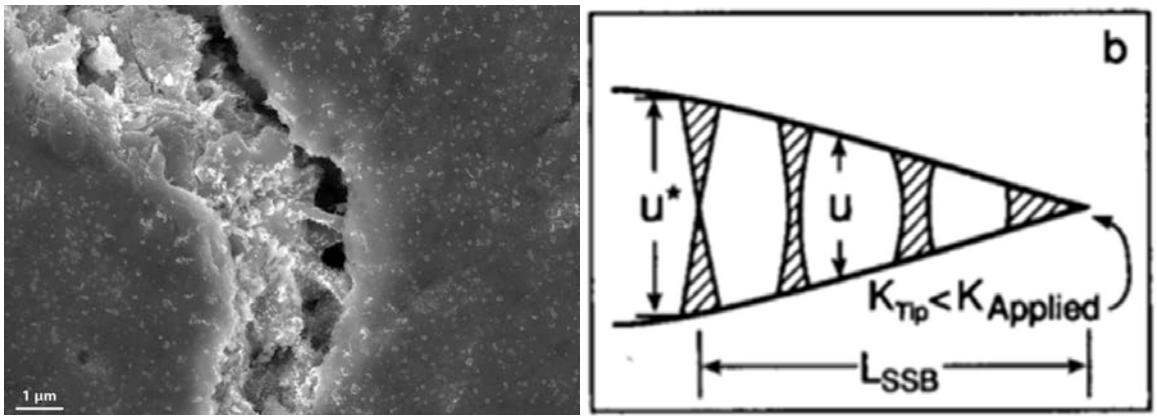

Figure 1. (a) SEM image of W-Cu fracture where the ductile phase (Cu) is effectively bridging the crack. (b) A steady-state bridging zone shown schematically in 2D [13].

Experimental

W-Ni-Fe alloys, purchased as green bodies consisting of W-7%Ni-3%Fe[1], were prepared for testing using hot-rolling to provide a range of lamellar microstructures with anisotropic fracture behavior. The starting alloy shown in Figure 2 is formed using liquid phase sintering methods and exhibits an isotropic structure consisting of W-spheroidal particles embedded in a Fe-Ni-W matrix. The W-particles are very close to 100% W. The matrix, basically a Ni-based superalloy, is 52.2-56.9% Ni, 25.8-29.3% W, and 13.8-21.6% Fe by wt%.

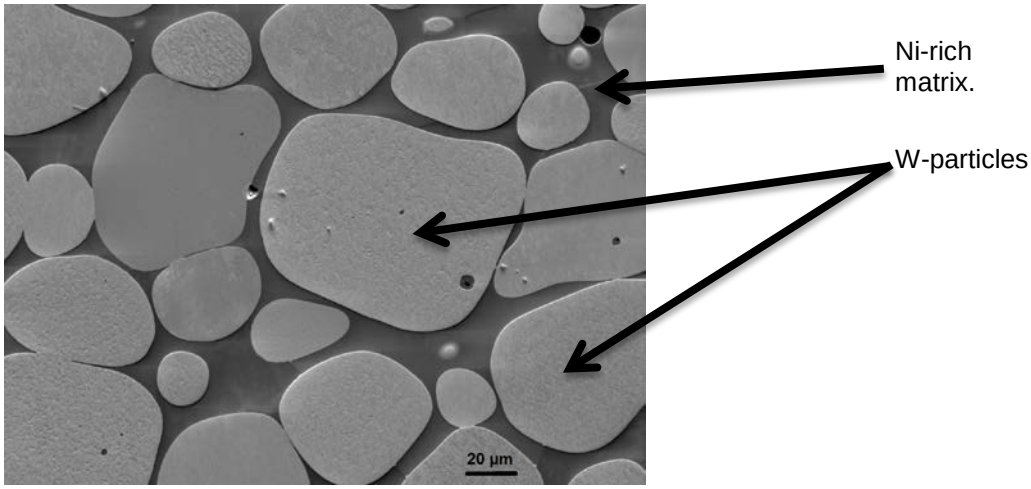

Figure 2. W-Ni-Fe alloy showing W-particles and Ni-rich ductile matrix.

These alloys were hot-rolled to three different reduction percentages, in two series of hot-roll/annealing sequences. The first rolling sequence was performed at 1150˚C for two passes with 5% reduction per rolling pass after the initial sintering. Then the alloys are rolled at 900˚C in 11% reduction passes to 62% reduction and 74% reduction. After three passes the materials are annealed at 900˚C for 1 hour in Ar-H (50:50) atmosphere. The second rolling sequence was similar but was started using a thicker plate and rolled to 87% reduction. Following this reduction samples were then hydrogen de-gassed at 900˚C in

[1] Mi-Tech Metals, Indianapolis, IN, USA.

vacuum. Figure 3 shows SEM images of the as-rolled materials at different reduction percentages. Note that only the 87% reduced material resembles a lamellar structure with highly elongated W-particles.

Four-point single-edge notched bend (SENB) specimens measuring 25.4 mm x 1.75 mm x 4.0 mm were cut from pieces with total reductions of 62%, 74%, and 87% (labeled R62, R74, and R87, respectively). The notch depth, a, was set at 0.45 a/W, where W was 4.0 mm. Three samples from each reduction amount were tested at room temperature using 0.2 mm/min displacement rate until failure in an Instron 5500 test frame equipped with a 4-point bend mid-point displacement transducer. Representative load-displacement curves for each are shown in Figure 4**.** Note that the hydrogen de-gassing treatment increased the fracture resistance of the 87% reduction material but decreased that for the 62% and 74%. The reasons for this difference in response are not yet understood, but it was expected that hydrogen de-gassing would improve the overall fracture resistance by increasing the toughness of the Ni-rich matrix phase. That appeared to be the case for the 87% reduction material.

Each tested sample was then polished and examined with optical and scanning electron microscopy. Crack morphology and propagation path were evaluated by visual inspection of the micrographs, shown in Figures 5 and 6. It was observed that there were significant differences between the 62% and 74% crack morphologies compared to the 87% reduced materials in the form of additional crack deflection and crack tortuosity. Figure 6 reveals that near the crack-tip differences are more pronounced but that all the rolled samples exhibit crack bridging toughening with fracture through the W-particles.

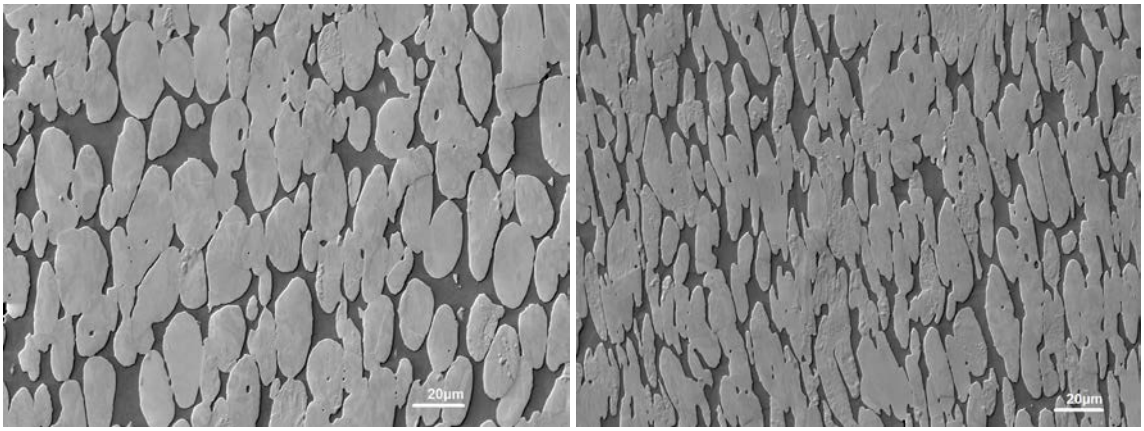

(a) 62% (b) 74%

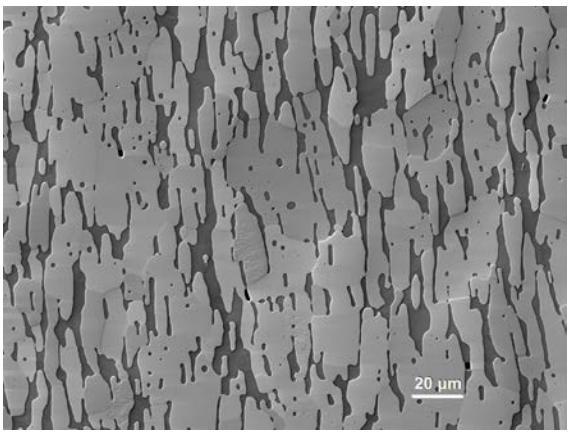

(c) 87%

Figure 3. SEM images of hot-rolled W-Ni-Fe alloy with (a) 62%, (b) 74%, and (c) 87% reductions, respectively. These rolled materials were tested with the specimens oriented so that crack growth was horizontal (right to left) in the image.

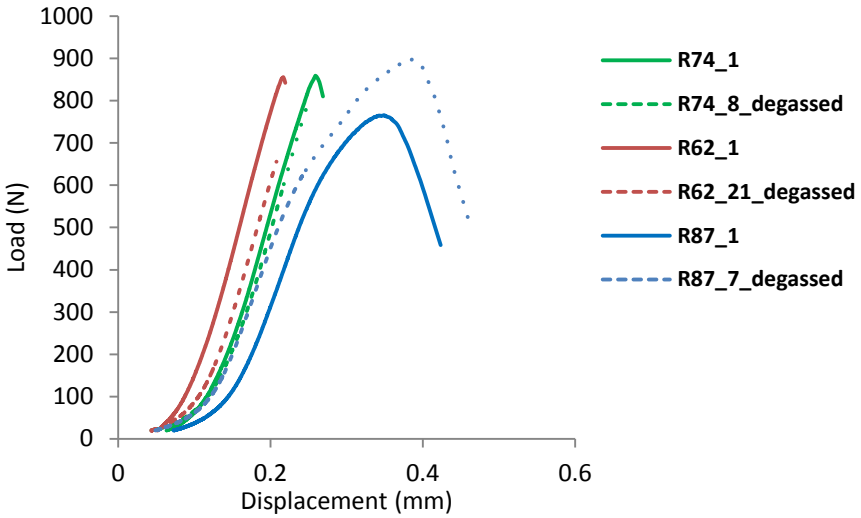

Figure 4. Representative load-displacement curves for R62, R74, and R87 4-point SENB specimens before and after hydrogen de-gassing.

Interaction of the growing crack with W-particle crystallography was assessed using electron backscatter diffraction (EBSD) as shown in Figure 7. Some particles fractured along grain boundaries, while others fractured through grains via transgranular cleavage. The EBSD data showed that the majority of the W-particles are single grains but that some appear to be polycrystalline. The images suggest that polycrystalline W-particles are formed by agglomeration of single crystal particles during the rolling operation. An EDS phase mapped image shows that cracks deflect between the W-particles (red) and the Ni-rich matrix phase (blue) and that many of the cracks stop within the Ni-rich phase. Figure 8 is a higher magnification image of a crack in a tested W-Ni-Fe sample that shows a flat cleavage face of a W-particle (A) and the more ductile-like fracture surface of the Ni-rich matrix phase (B). A series of crack-tip bridges along with crack debonding are shown in Figure 9 for the 87% reduction material. Crack bridging is accompanied by crack deflection due to significant debonding between the brittle W-particles and the ductile Ni-rich matrix phase. The formation of crack-tip debonding is critical to the formation of crack-tip bridges.

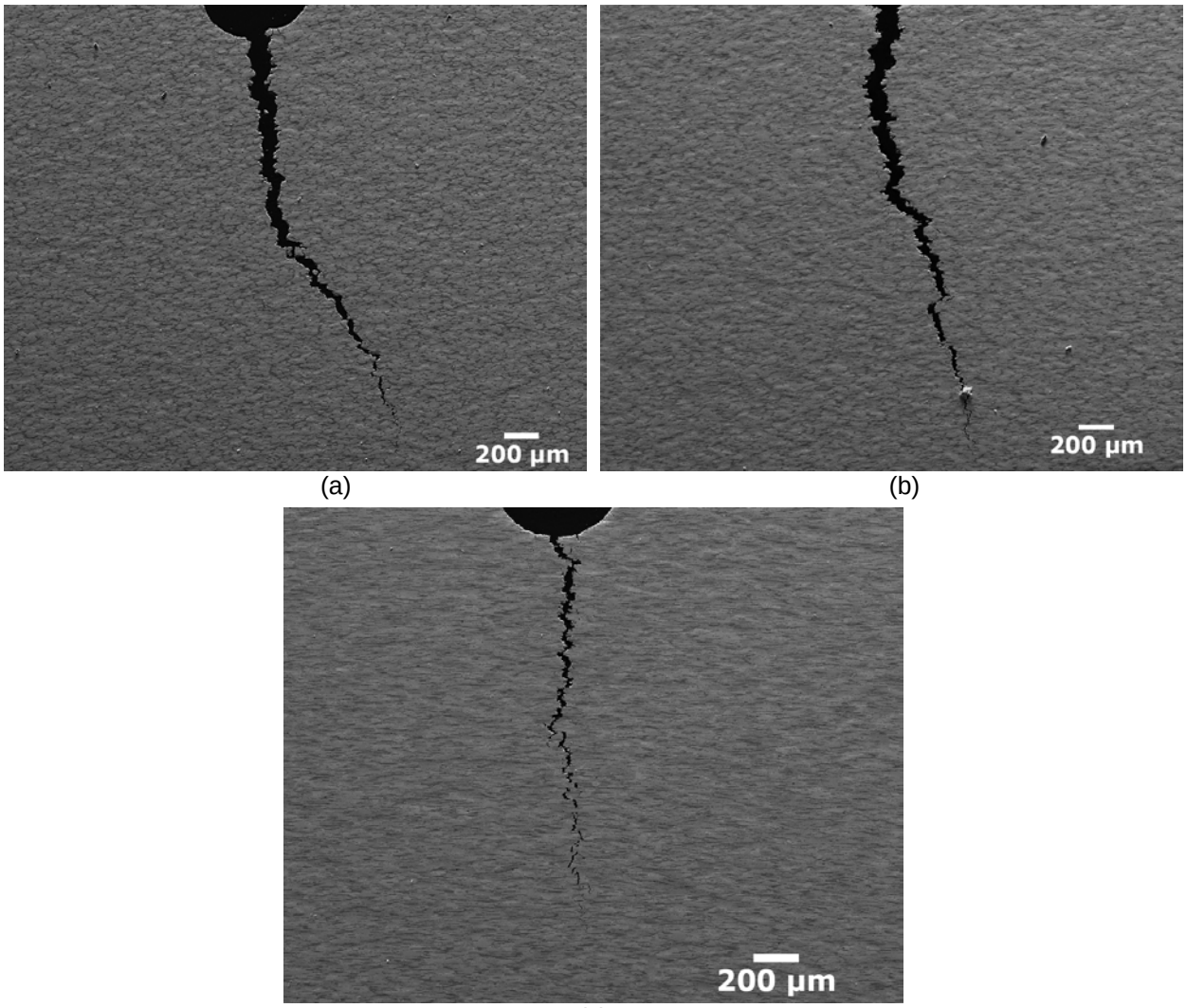

Figure 5. Scanning electron (secondary image) micrographs of crack morphologies observed in SENB specimens tested in 4-point bending at 0.2 mm/min at ambient temperature. Shown in (a) is 62%, (b) 74%, and (c) 87% hot-rolled reduction prior to hydrogen degassing. These samples correspond to the load-displacement curves shown in Figure 3 above. Note the crack path deflection seen in the 87% rolled sample is more pronounced compared to 62% and 74% reductions. This is better seen in the higher magnification images shown in Figure 6 below.

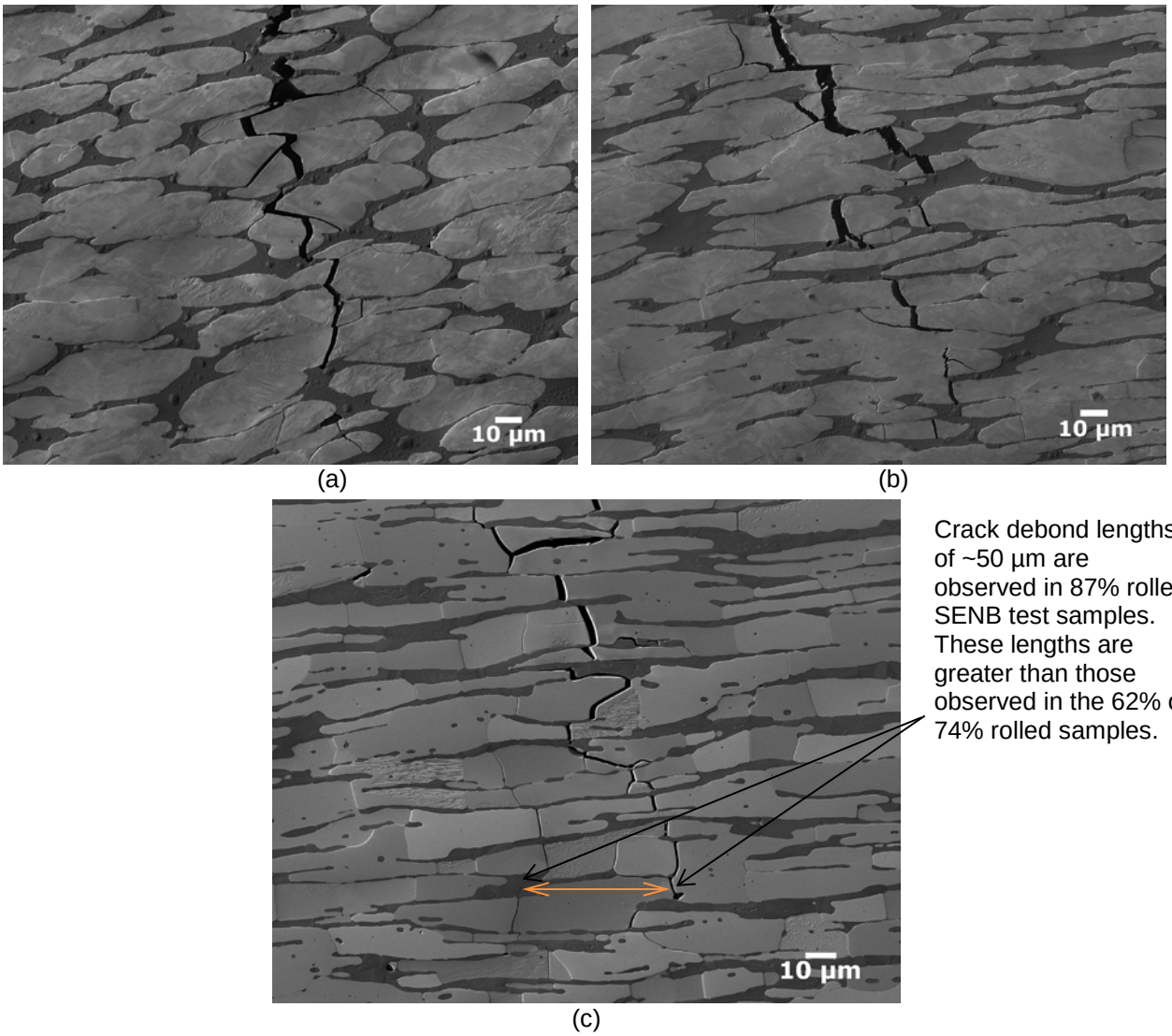

Figure 6. SEM micrographs of crack-tip morphologies taken at 500x showing crack deflection, crack bridging, and crack nucleation in all rolled samples as in (a) 62%, (b) 74%, and (c) 87%. Crack deflection is more pronounced in the 87% reduced sample but is observed in all rolled materials. Measured crack debond lengths (the length between parallel cracks) approaches 50 µm for the 87% rolled material.

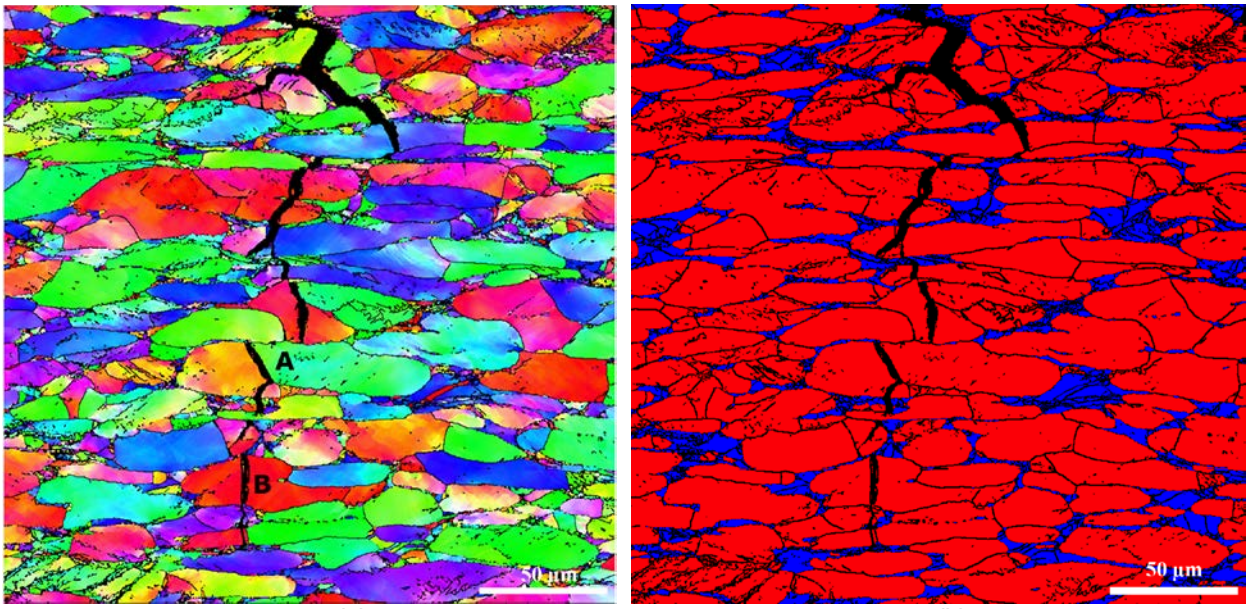

(a) (b)

Figure 7. (a) SEM EBSD inverse pole figure along the z-direction for a 62% reduction sample, showing intergranular cracking (A) and transgranular cleavage (B). This behavior was observed also in the 74% and 87% reduction samples. Shown in (b) is an EDS phase map of the image in (a) with W shown in red and the ductile Ni-rich matrix phase shown in blue. This figure highlights the crack bridging and deflection occurring at the phase boundaries in this rolled composite.

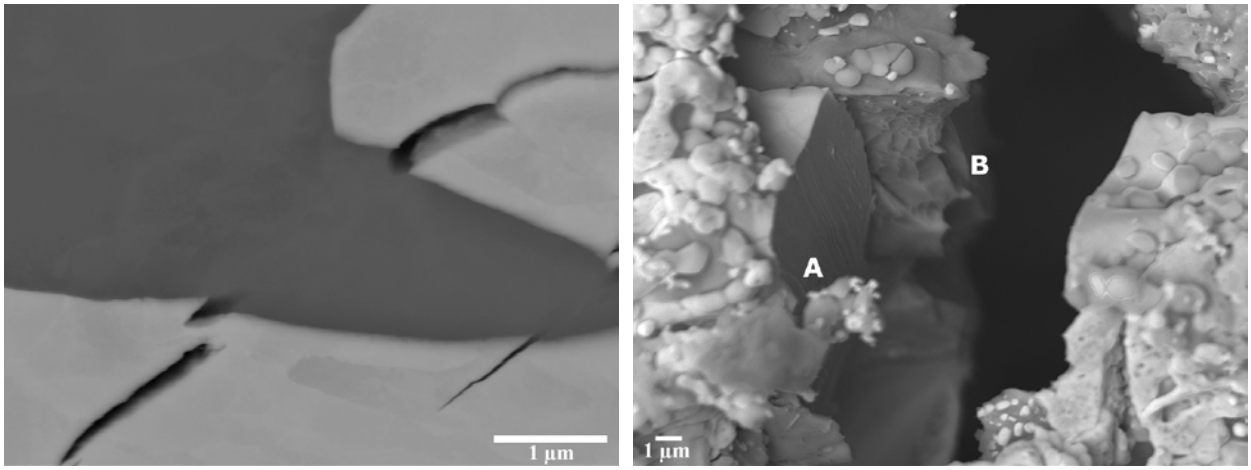

(a) (b)

Figure 8. (a) SEM backscatter image showing matrix phase (dark) bridging a crack in W-particles. Shown in (b) is an SEM image inside a crack in one of the tested composites showing transgranular cleavage fracture of W-particle in A and a more ductile tearing fracture of the Ni-rich phase in B.

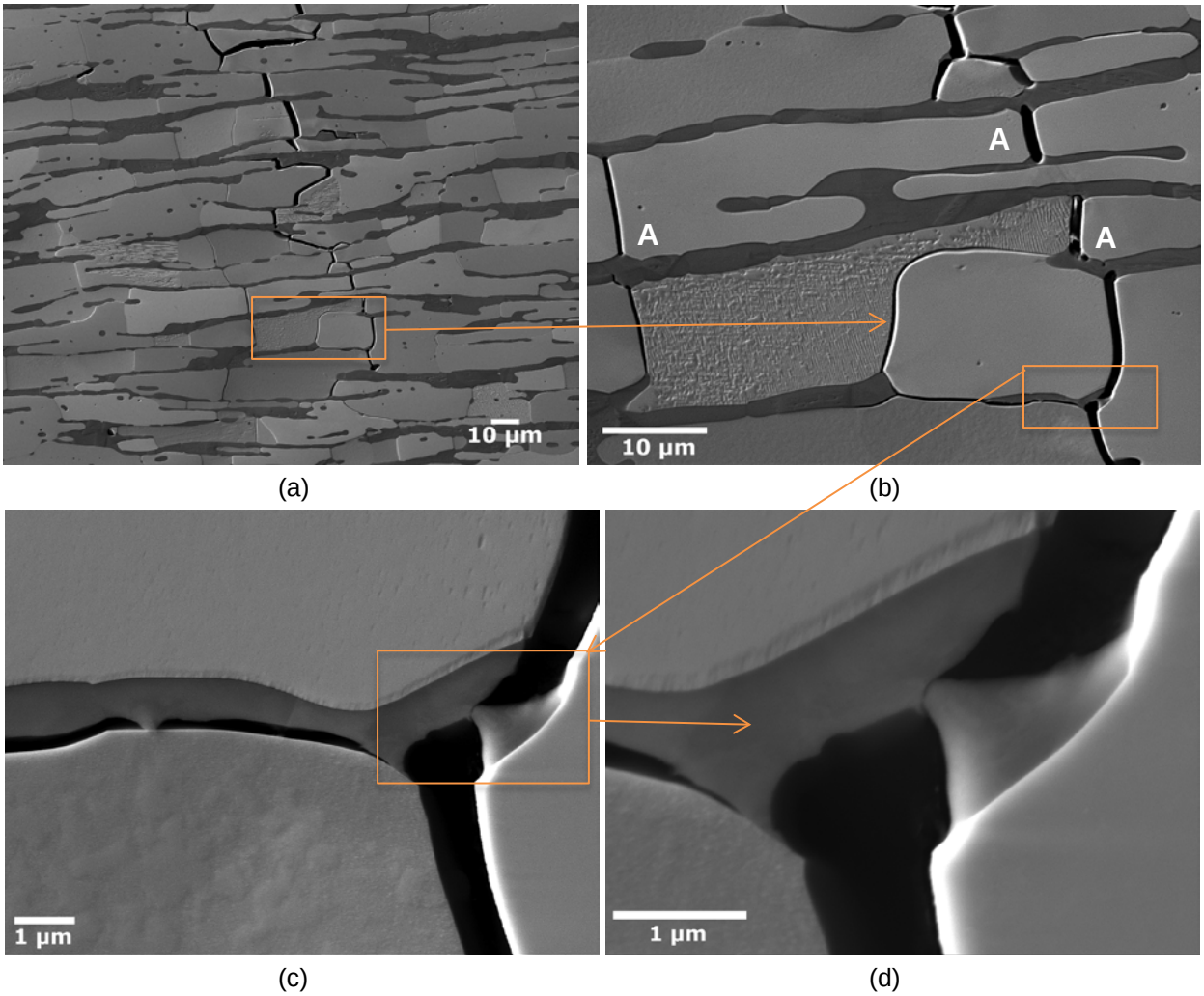

Figure 9. A sequence of SEM images of increasing magnification for the 87% rolled and tested sample. Shown in (a) is a 500x image of the crack-tip region with the image in (b) showing the debonding associated with the crack deflection. The image shown in (c) highlights several Ni-rich bridges that are formed along the debond. The image in (d) is at 27kx and shows a partially intact bridge region. Areas marked with A in (b) illustrate cracks in the W-particles that are blunted in the Ni-rich matrix layers.

Discussion

In contrast to the W-Cu alloys that consist of Cu-particles embedded within a pure W-matrix, these W-Ni-Fe alloys consist of W-particles embedded within a Ni-Fe-W matrix phase. This material can be hot-rolled to produce nearly pure W-lamellae embedded within a lamellar Ni-rich ductile phase that behaves like a dual-phase composite, i.e. a ductile-phase composite. The as-sintered starting alloy fractures almost entirely within the Ni-rich matrix phase and, therefore, does not engage the W-phase as desired. The rolled alloys, in contrast, fracture by transgranular cleavage (mostly) in the highly elongated W-particles and ductile tearing of the Ni-rich phase that occupies the space between the pancake-shaped rolled W-particles. The cracking is accompanied by significant debonding, crack deflection, and crack bridging in all of the rolled alloys tested here. This initial work has shown that 87% reduction by hot rolling performs better than rolled reductions of 62% or 74% in terms of graceful failure as indicated by the load-displacement curves shown in Figure 4. Micrographs confirm the formation of a suitable lamellar structure at the rolling reduction amount of 87%. This lamellar structure behaved in a more ductile manner in 4-point SENB testing than the 62% and 74% reduction samples.

The observation of toughness improvement with increased rolling reduction appears to be a type of threshold that occurs when the W-particles reach a certain eccentricity. The 4-point SENB testing

suggests that a critical threshold occurs between 74% and 87% rolling reduction such that a significant increase in crack deflection begins to occur during crack propagation in the 87% rolled material (see Figure 5c). If this is the case, then increases in crack debonding lengths act to increase the volume of ductile-phase regions that interact with the crack and result in a more effective crack-bridging zone. This appears to be the case as shown in Figure 6c. This will have to be more completely verified and validated by further testing, additional characterization, and modeling.

The SEM EBSD and EDS phase mapping analysis in Figure 7 shows that W-particles fracture both through grains as transgranular cleavage cracks as well as intergranularly. However, most W-particles in the observed area consisted of single grains, which necessarily precluded grain boundary cracking. An image of a transgranular cleavage crack face is seen in Figure 8. It might be the case that W-particle interfaces are from two W-particles agglomerating during the hot-rolling operation. Research in these alloys by others indicates that transgranular cleavage is preferred over intergranular fracture or decohesion [14]. The presence of cleavage cracking indicates a high degree of bonding between the ductile matrix phase and the W-particles, whereas the intergranular strength of these alloys is thought to be rather low due to impurities. Maximum ductility, or toughness, of deformed W-Ni-Fe alloys is observed when there is a good combination of W-particle cleavage and ductile-phase rupture [14].

Future Work

Further testing and microscopy are planned to explore the crack deflection hypothesis discussed above. Additional testing, advanced characterization, and quantitative metallography are planned. A bridging model and an FE model are being explored for microstructural modeling of the SENB data. Exploration of alternative alloy compositions that reduce the amount of Ni in the alloy to alleviate neutron activation concerns will follow successful fracture testing and model validation.

References

[1] Deve, H.E., A.G. Evans, G.R. Odette, R. Mehrabian, M.L. Emiliani, and R.J. Hecht, "Ductile reinforcement toughening of -TiAl: effects of debonding and ductility," Acta metallurgica et materialia, (1990), 38(8), 1491-502.

[2] Erdogan, F. and P.F. Joseph, "Toughening of ceramics through crack bridging by ductile particles," Journal of the American Ceramic Society, (1989), 72(2), 262-270.

[3] Sigl, L.S., P.A. Mataga, B.J. Dalgleish, R.M. McMeeking, and A.G. Evans, "On the Toughness of Brittle Materials Reinforced with a Ductile Phase," Acta Metallurgica, (1988), 36(4), 945-953.

[4] Rieth, M., J.L. Boutard, S.L. Dudarev, T. Ahlgren, S. Antusch, N. Baluc, M.F. Barthe, C.S. Becquart, L. Ciupinski, J.B. Correia, C. Domain, J. Fikar, E. Fortuna, C.C. Fu, E. Gaganidze, T.L. Galan, C. Garcia-Rosales, B. Gludovatz, H. Greuner, K. Heinola, N. Holstein, N. Juslin, F. Koch, W. Krauss, K.J. Kurzydlowski, J. Linke, C. Linsmeier, N. Luzginova, H. Maier, M.S. Martinez, J.M. Missiaen, M. Muhammed, A. Munoz, M. Muzyk, K. Nordlund, D. Nguyen-Manh, P. Norajitra, J. Opschoor, G. Pintsuk, R. Pippan, G. Ritz, L. Romaner, D. Rupp, R. Schaublin, J. Schlosser, I. Uytdenhouwen, J.G. Van Der Laan, L. Veleva, L. Ventelon, S. Wahlberg, F. Willaime, S. Wurster, and M.A. Yar, "Review on the EFDA programme on tungsten materials technology and science," Journal of Nuclear Materials, (2011), 417, 463-467.

[5] Pitts, R.A., A. Kukushkin, A. Loarte, A. Martin, M. Merola, C.E. Kessel, V. Komarov, and M. Shimada, "Status and physics basis of the ITER divertor," Physica Scripta Volume T, (2009), 2009(T138), 014001 (10 pp.).

[6] Mertens, P., T. Hirai, M. Knaup, O. Neubauer, V. Philipps, J. Rapp, V. Riccardo, S. Sadakov, B. Schweer, A. Terra, I. Uytdenhouwen, and U. Samm, "A bulk tungsten divertor row for the outer strike point in JET," Fusion Engineering and Design, (2009), 84(7-11), 1289-93.

[7] Gervash, A., R. Giniyatulin, T. Ihli, W. Krauss, A. Makhankov, I. Mazul, P. Norajitra, and N. Yablokov, "Fabrication of a He-cooled divertor module for DEMO reactor," Journal of Nuclear Materials, (2007), 367-370 B(SPEC. ISS.), 1472-1475.

[8] Merola, M., W. Danner, and M. Pick, "EU RD on divertor components," Fusion Engineering and Design, (2005), 75-79(SUPPL.), 325-331.

[9] Mertens, P., V. Philipps, G. Pintsuk, V. Riccardo, U. Samm, V. Thompson, and I. Uytdenhouwen, "Clamping of solid tungsten components for the bulk W divertor row in JET-precautionary design for a brittle material," Physica Scripta Volume T, (2009), (T138), 014032 (5 pp.).
[10] Gludovatz, B., S. Wurster, A. Hoffmann, and R. Pippan, "Fracture toughness of polycrystalline tungsten alloys," International Journal of Refractory Metals and Hard Materials, (2010), 28(6), 674-8.
[11] Zinkle, S.J. and N.M. Ghoniem, "Operating temperature windows for fusion reactor structural materials," Fusion Engineering and Design, (2000), 51-52, 55-71.
[12] Venkateswara Rao, K.T., G.R. Odette, and R.O. Ritchie, "Ductile-reinforcement toughening in -TiAl intermetallic-matrix composites: effects on fracture toughness and fatigue-crack propagation resistance," Acta Metallurgica et Materialia, (1994), 42(3), 893-911.
[13] Odette, G.R., B.L. Chao, J.W. Sheckherd, and G.E. Lucas, "Ductile phase toughening mechanisms in a TiAl-TiNb laminate composite," Acta metallurgica et materialia, (1992), 40(9), 2381-9.
[14] Ostolaza Zamora, K.M., J.G. Sevillano, and M. Fuentes Pérez, "Fracture toughness of W heavy metal alloys," Materials Science and Engineering: A, (1992), 157(2), 151-160.

4.3 PROCESS IMPROVEMENTS FOR PREPARATION OF NANO-W SPECIMENS FOR MECHANICAL TESTING AND TESTING UNDER PLASMA ENVIRONMENTS— C. Ren and Zak Fang, Department of Metallurgical Engineering, University of Utah, 135 S. 1460 E. Room 412, Salt Lake City, UT 84112

OBJECTIVE

The objective of this work is to improve the fabrication process to minimize the grain growth while maximize sintered density. The nano-W specimens will be used to evaluate the mechanical properties and hydrogen permeation under plasma exposure conditions.

SUMMARY

In the last reporting period, the problem of sample cracking during sintering was resolved by implementing the novel multi-step pelletizing and compaction process (MPC). The ongoing work in this report period is focused on improving the sintered density of nano-W specimens. To accomplish this objective, a systemic study on the effect of sintering temperature, sintering atmosphere, sintering time and reduction temperature on the densification behavior of nano-W materials has been performed.

PROGRESS and STATUS

Introduction

For fusion reactor applications, the stability of the mechanical properties of plasma facing materials before and after irradiation is highly desired. Among various candidate materials, tungsten alloys is promising due to its superior mechanical properties with excellent thermal behaviors. [1-2]. In our previous work, we have developed processing method for making nano-W with grain size near 100 nm. [3-4]. However, when making large samples thye showed lateral and radial cracks after processing. In the last reporting periods, this cracking problem has been eliminated by introducing a novel multi-step pelletizing and compaction process (MPC). [5] The first set of specimens has been sent to our collaborator at Sandia National Laboratory (Dr. Buchenauer, Hydrogen & Metallurgy Science Department) for hydrogen permeation tests.

To further improve the mechanical properties and thermal behaviors of this material, the minimization of grain size and maximization of density of the sintered nano-W material is highly desired. Based on the last report, Ti-based additives work as pinning spots of grain boundary migration during sintering process which serves to minimize the grain growth of nano-W material. [5] The study further suggested that nano-W material with Ti additive has superior densification behavior than the material with TiC additive. The density of sintered nano-W increases as the sintering temperature increases. Based on these results, Ti has been selected as the additive for the further studies.

In this period, work to minimize grain size and increase relative density of sintered nano-W materials has been continued. The research work is mainly focused on the effects of processing parameters on the grain size and density of nano-W materials. The studied parameters include reduction temperature, sintering time, sintering temperature and sintering atmosphere. All of these parameters have been considered as factors that have significant effects on the densification of nano-W.

Experimental Procedures

Green part preparation

Commercial tungsten powders with particle size of about 100 nm and titanium hydride powders with particle size about 45 μm were milled using the customer designed high energy high pressure planetary mill (HEPM). The raw powders and 1 mm diameter tungsten carbide balls with ball to powder ratio of 4:1 were loaded in to the milling canister and then the canister was filled with mixed liquid of heptane and ethanol. The powders were milled for 6 hours and dried in evaporating dishes for 3 days. The dried tungsten powders were compacted to discs shape samples by the MPC process.

Low temperature sintering

A low temperature step was performed for 3 h to reduce the oxidized W powders and minimize its effect on sintering. The sintering steps were carried out at high temperature (above 1000 ºC) under hydrogen or argon atmosphere using a tube furnace. In this period of work, the reduction temperatures range is from 650 to 850 ºC, the sintering temperatures range is from 1000 to 1300 ºC and the sinter time range is from 1 to 16 h.

Characterizations

After sintering, the densities of samples were measured by Archimedes method. The fractured surface microstructures of sintered samples were examined by Scanning Electron Microscope (SEM). The surface areas of samples were characterized by Brunauer-Emmett-Teller (BET) surface area analysis method.

Results

Effect of sintering temperature, atmosphere and time

Ar and H_2 atmospheres and seven sintering temperatures range from 1000 to 1300 ˚C have been selected for comparison. The samples were prepared using MPC process, then low temperature reduced at 700 ˚C in H_2 for 3 h and high temperature sintered at the selected temperature with selected atmosphere for 1 h. Figure 1 shows the comparison of the effect of H_2 and Ar atmosphere on the densification of W - 1% Ti materials at different sintering temperatures.

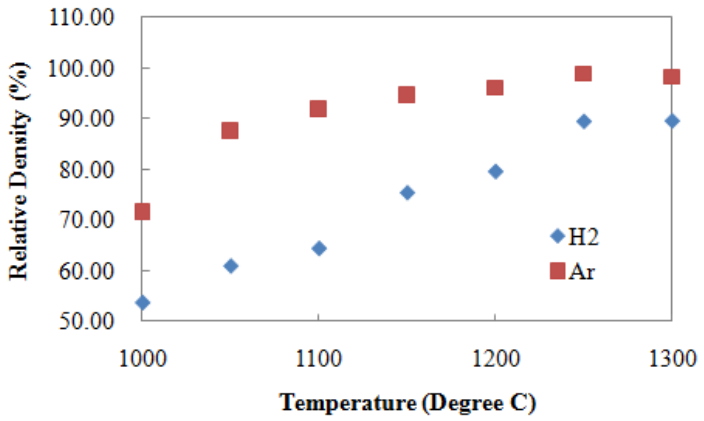

Figure 1. Comparison of W – 1% Ti sintered densities with Ar or H_2 atmosphere.

Similar to the data reported previously, the results demonstrate that the density of sintered W-1% Ti increases as the sintering temperature increases from 1000 to 1300 ˚C. Samples sintered in Ar atmosphere have higher relative densities than the samples sintered in H_2 atmosphere. This difference decreases as the temperature increases. The sample sintered at 1300 ˚C with Ar atmosphere has a density of 18.2 g/cc (relative density ~ 98.3%) which is the highest we obtained from this set of data.

To obtain better understand on the effect of atmosphere, a similar set of experiments were performed on the pure W samples. Figure 2 shows the comparison of the effect of H_2 and Ar atmosphere on the densification of pure W samples.

The results on pure nano-W has similar trend as the W – 1% Ti samples. Ar atmosphere sintering provides higher density than the H_2 atmosphere. The difference decreases as the temperature increases. The pure nano-W sample reaches a maximum density of 18.92 g/cc with 1300 ˚C sintering temperature and Ar atmosphere. Based on the result, this behavior arise from the interaction between W and H_2 gas. However, further study is required to obtaining better understanding.

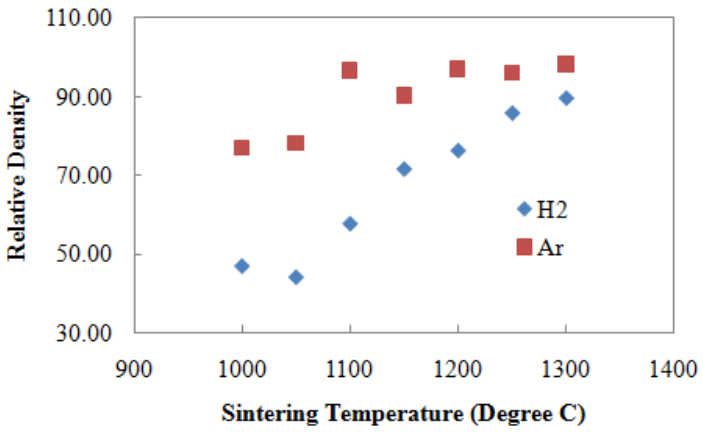

Figure 2. Comparison of W sintered densities with Ar or H_2 atmosphere.

Although high relative density is required for the structure material applications, a small grain size is also highly desired for the fusion reactor materials. Based on our study, a relative high sintering temperature (1300 ˚C) is required to reach the desired relative density. However, high sintering temperature leads to rapid growth in grain size which may decreases the mechanical property of nano-W. To investigate a potential solution to this problem, a study on the effect of sintering time on the densification of nano-W at relatively low sintering temperature has been performed. Figure 3 shows the relative density of nano-W samples sintered at 1100 ˚C in Ar atmosphere for 1 to 16 h.

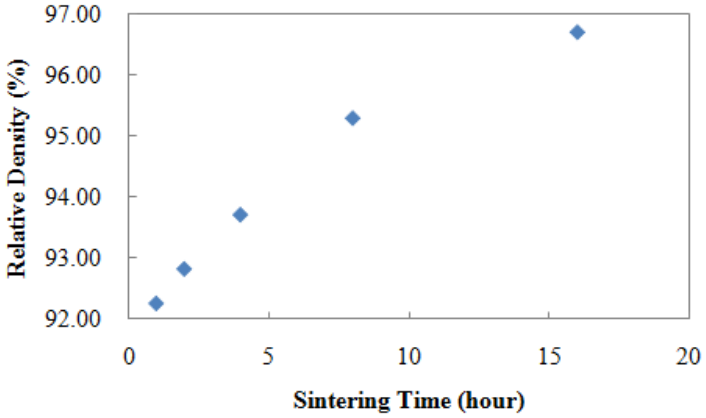

Figure 3. Effect of sintering time on densification of nano-W

As the sintering time increases from 1 to 16 h, the relative density of sintered nano-W increases from 17.1 g/cc (92.3%) to 17.9 g/cc (96.7%). This is about the same density as we obtained from high temperature sintered sample. However, a smaller grain size could be expected as the significant decrease in the kinetic of grain growth caused by the 200 ˚C decrease in sintering temperature.

Effect of reduction temperature

The effect of reduction temperature has been studied in the temperature range from 650 ˚C to 850 ˚C. After reduction, all of the samples were sintered in Ar at 1050 ˚C for 2 h and 1300 ˚C for 1 h. Figure 4 shows the results of the relative density of nano W – 1% Ti samples as a function of reduction temperature.

The result indicates the density of sintered W – 1% Ti first increases as the reduction temperature increases from 650 to 750˚C and then decreases as the temperature further increases to 850 ˚C. The W – 1% Ti sample reaches its maximum density at 700 or 750 ˚C.

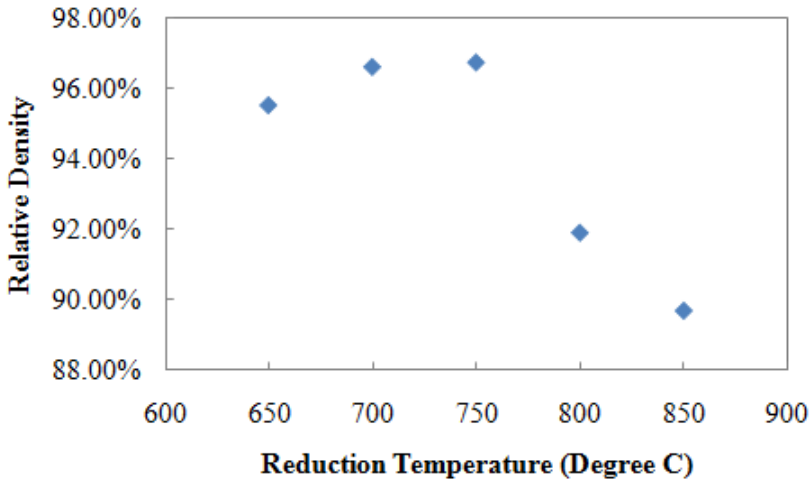

Figure 4. Comparison of W – 1% Ti sintered densities with different reduction temperatures.

To have better understanding on the effect of reduction temperature on the sintered density, similar experiments were performed on the pure nano-W materials. Figure 5 shows the comparison of the effect of reduction temperature on the densification of pure nano-W materials.

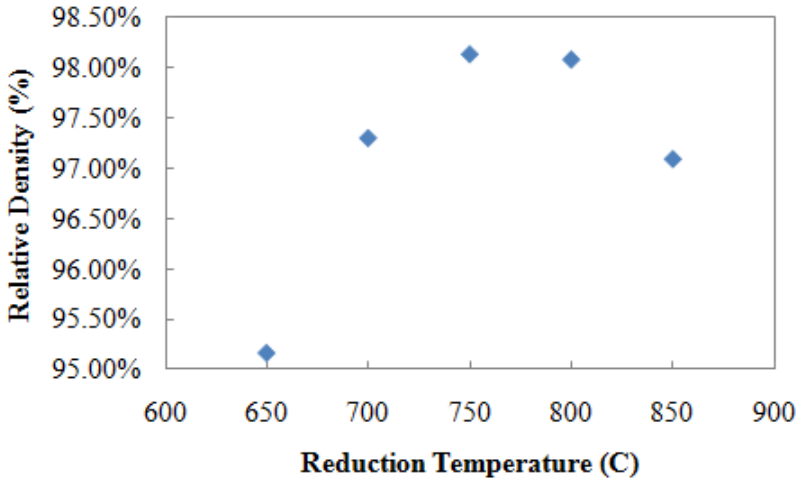

Figure 5. Comparison of W sintered densities with different reduction temperatures.

Pure nano-W has similar behavior as the W – 1% Ti material. As reduction temperature increases, the sintered density first increases and then decreases. Therefore, this behavior is also related to the W to H_2 reaction.

To minimized the potential effect of sintering on this reduction behavior, a set of pure nano-W samples were reduced at 650 to 850 ˚C and then directly cool down to room temperature without sintering step. Figure 6 shows the relative densities and surface area analysis results of these samples.

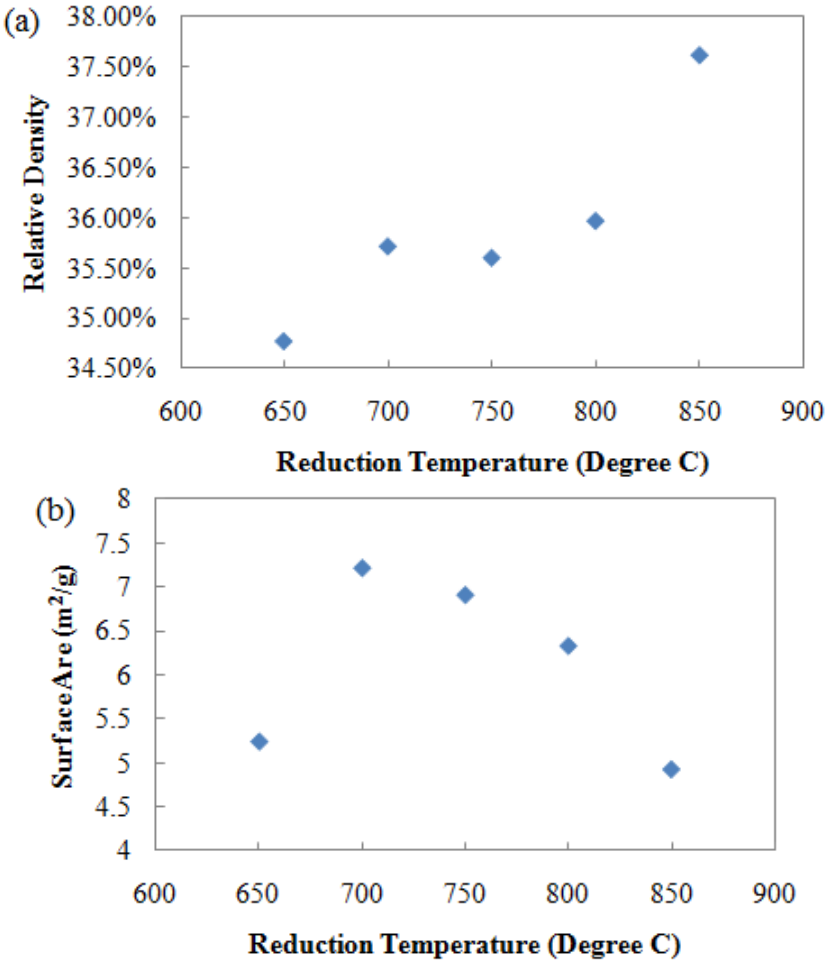

Figure 6. (a) Comparison of pure W densities after reduction at different temperatures.
(b) Comparison of pure W surface areas after reduction at different temperatures.

As shown in the figure, the relative density of reduced sample increases as the reduction temperature increases. The surface area density first increases as the reduction temperature increases from 650 to 700 ˚C which indicates a particle refinement effect. Above 700 ˚C, the surface area starts to decreases as a result of particle growth inside the sample. The surface analysis result has the similar trend as the sintered density data. As a result of the high activity of nano-sized W powders, pre-sintering effect may presents as the reduction temperature increases above 700 ˚C. This pre-sintering effect increases both the density and the grain size of the W samples. Figure 7 shows a microstructure comparison of samples reduced at 700 ˚C and 850 ˚C.

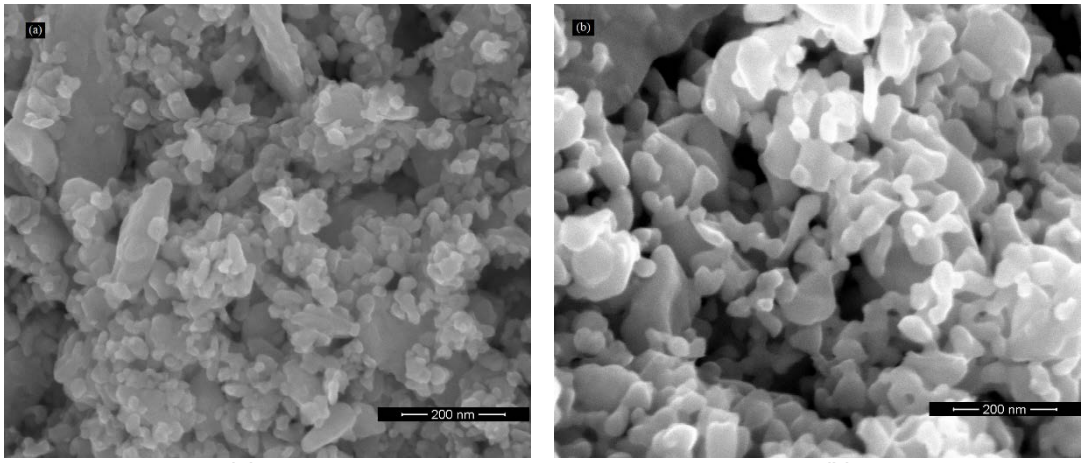

(a) (b)

Figure 7. Microstructure of pure nano-W samples reduced at (a) 700 ˚C and (b) 850 ˚C.

A clear difference could be observed on these two images, the particles reduced at 850 ˚C has smoother surface and necking starts to form between the particles. Based on the sintering theory, this pre-sintering step decreases the activity of nano particles and introduces necking which impendent further sintering process. Based on the result, 700 or 750 ˚C is the optimized reduction temperature which ensure the sufficient reduction of oxidize and limits the pre-sintering effect.

Future Work

Samples will be prepared with the optimized sintering process to obtain maximized relative density and minimized grain size. Further evaluation of mechanical properties and hydrogen permeation behavior will be performed.

Reference

[1] M. Rieth, et al, J. Nucl. Mater. 432 (2011) 482-500.
[2] M. Jain, et al, Int. J. Powder Metall. 42 (2006) 53.
[3] X. Wang, Z. Fang. Fusion Materials Semiannual Report DOE/ER-0313/53 (2013) 40.
[4] X. Wang, Z. Fang. Fusion Materials Semiannual Report DOE/ER-0313/54 (2013) 108.
[5] C. Ren, Z. Fang. Fusion Materials Semiannual Report DOE/ER-0313/55 (2015).

4.4 FABRICATION OF FUNCTIONALLY GRADED TUNGSTEN STEEL LAMINATE - L. M. Garrison (Oak Ridge National Laboratory)

OBJECTIVE

The objective of this project is to create a functionally graded tungsten-steel laminate composite for use in plasma facing components in fusion reactors.

SUMMARY

Tungsten foils in thicknesses 250, 100, and 25 µm and grade 92 steel foils in nominal thicknesses 250, 100, and 76 µm were obtained. The foils were alternately stacked within a stainless steel container and then hot rolled at 1000°C to approximately 80% reduction of the original height to induce bonding. The composite was analyzed with EDS to reveal the elemental composition at the tungsten-steel interfaces. Tungsten foils were electropolished to reveal the grains for EBSD analysis. Samples of the tungsten and steel foils were tensile tested. An initial test was done with select foil samples utilizing digital image correlation to monitor the deformation.

PROGRESS AND STATUS

Introduction

For the plasma-facing components of fusion reactors, tungsten will be the interface between the plasma and the underlying structural component because tungsten has a low sputtering yield, high melting temperature, and relatively high thermal conductivity. However, because tungsten is brittle and has low fracture toughness, it is impractical to fabricate the entire plasma-facing component out of tungsten. Current divertor designs utilize various methods to bond the tungsten surface layer to the underlying structural part of the component that contains the cooling channels, but for future divertors where the operating temperature will be higher, more robust solutions are needed. Advanced steels are being developed for structural components in future fusion reactors. Unfortunately, tungsten and steel have vastly different coefficients of thermal expansion, so a direct joint would be subjected to intense thermal stresses. A tungsten-steel functionally graded material would ideally both improve the fracture toughness as compared to tungsten alone as well as reduce the thermal stresses between the tungsten and steel parts of the plasma-facing component.

Results

Interface analysis

A cross section sample of the rolled composite material was polished for scanning electron microscope (SEM) analysis. The microstructure in the region of the composite that was initially composed of the thinnest tungsten foils and thickest steel foils was examined with the backscatter detector in the SEM (Figure 1a). Four regions are labeled in Figure 1a. Region 1 was the tungsten foil layer and does not contain iron, but does show some Cr from the steel has diffused into the tungsten. Some grains in the tungsten layer are elongated up to 10 µm in the rolling direction. Region 2 is a tungsten rich layer on the order of 1.5 µm thick that contains voids in the range of 0.3-1.6 µm. Comparing Figure 1a and 1b it can be seen that some tungsten has diffused into Region 3, but the boundary between Region 3 and 4 is sharp, where Region 4 is the closest area to the original steel composition.

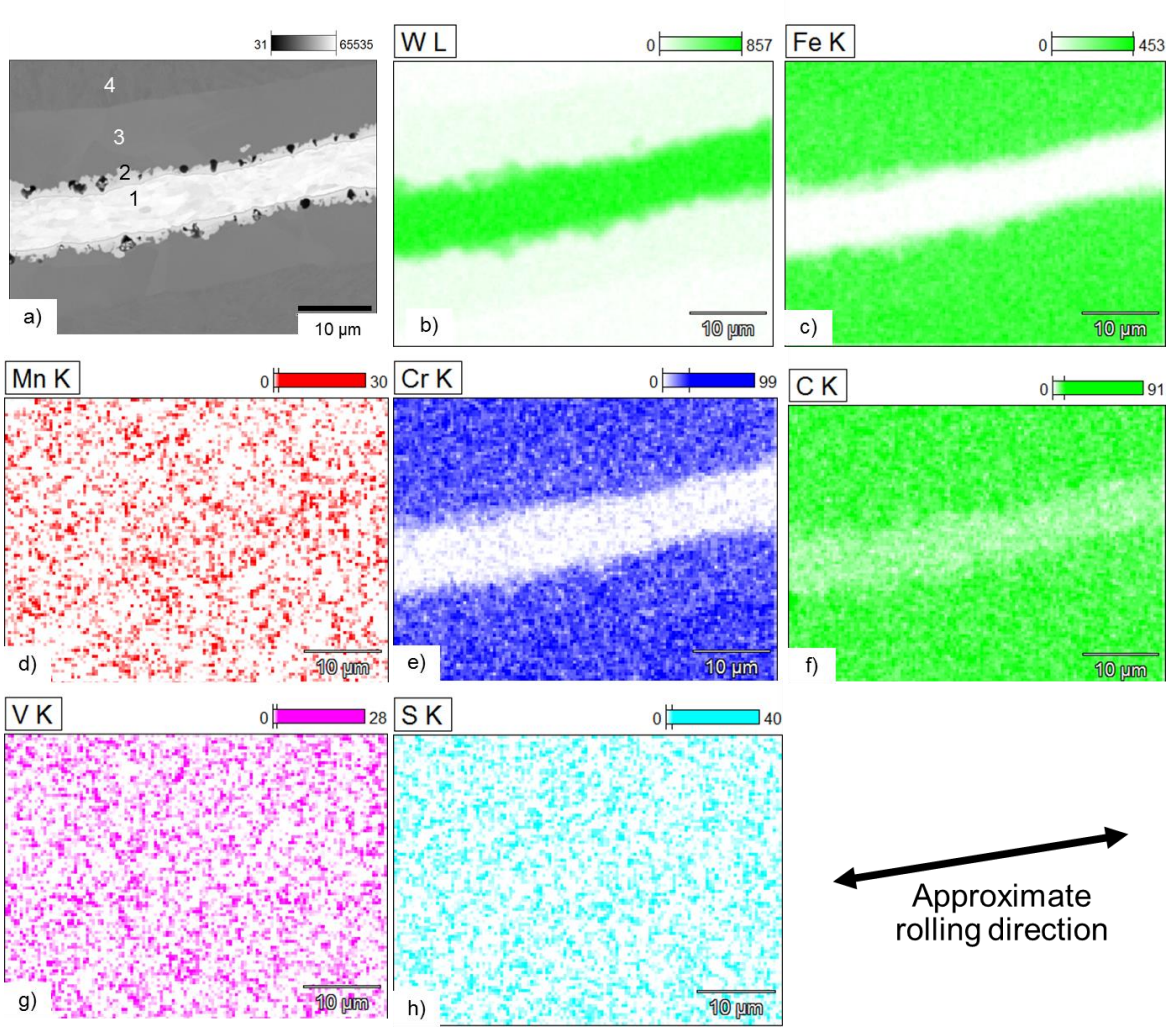

Figure 1. a) Backscatter electron image of the cross section of the tungsten steel composite. b)-h) x-ray analysis of elemental distribution in the selected region of the composite.

The maps in Figure 1 are qualitative, so to gain more information, quantitative line scans were performed on selected regions. In the SEM image in Figure 2 the tungsten layers have bright contrast and the steel layers have darker contrast.

A region near the left in Figure 2 was analyzed and the results are presented in Figure 3. The line scan goes from the steel phase, through the intermetallic region, into the pure tungsten region, and through to the steel zone on the opposite side. The signal from the trace alloying elements in the steel, Mo, Mn, and V, is multiplied by 100 in all the following profiles for better comparison. It can be seen that the Mo is enriched near the W layer, but all the other alloying elements in the steel are depleted near the W layer. A region composed of thicker tungsten and steel layers, near the right side in Figure 2, is analyzed in Figure 4. The same behavior observed in the thin tungsten region is seen near the thick tungsten region.

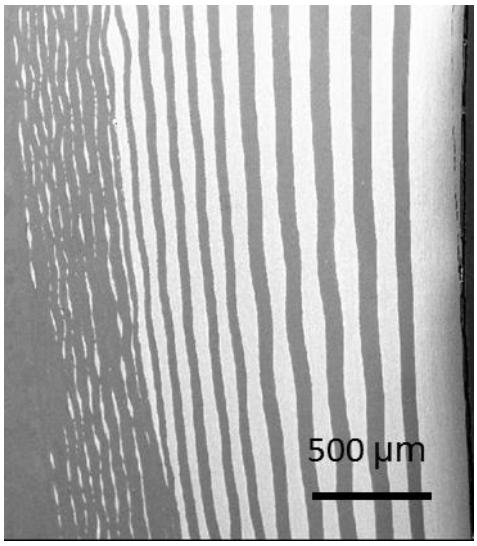

Figure 2. A cross-section of the tungsten-steel composite after fabrication.

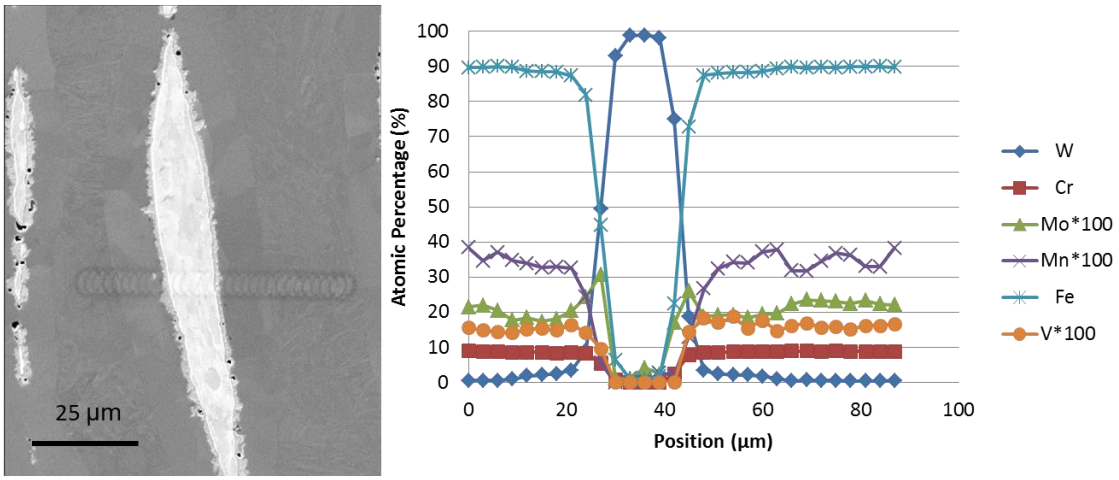

Figure 3. Quantitative line scan of a thin tungsten layer in the tungsten-steel composite.

As seen in Figure 1a and in both Figure 3Figure 4, two separate microstructure layers can be seen between the base tungsten and the base steel zones (Regions 2 and 3 in Figure 1), but their elemental composition cannot be differentiated. A more detailed scan is shown in Figure 5. It reveals that the thin, porous layer near the tungsten is composed of near equal amounts of tungsten and iron. Based on the atomic percentages, it is likely that this layer is a W_6Fe_7 phase. Moving into the more iron rich intermetallic phase, the tungsten percentage quickly drops to 10-20%. In this detailed view it is more clearly seen that Mo enriches closer to the W layer, while Cr, Mn, and V deplete closer to the W layer.

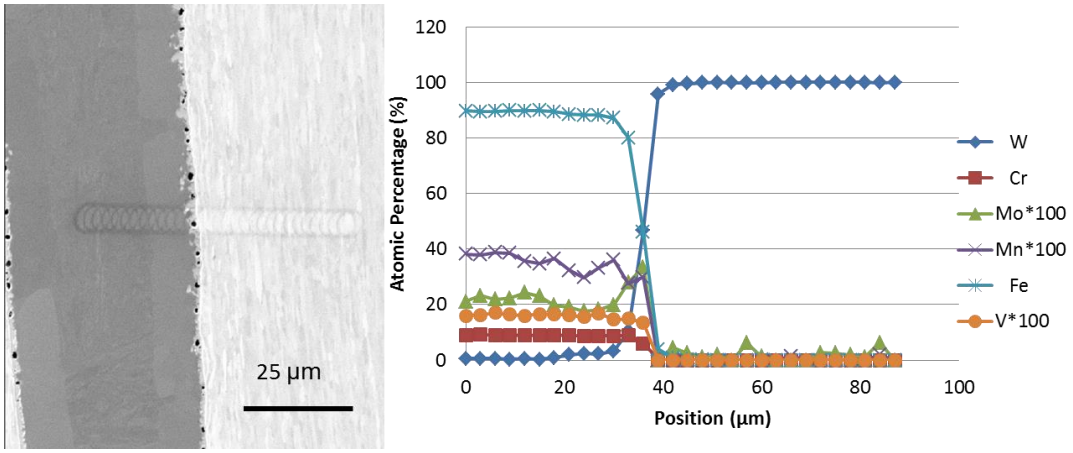

Figure 4. Quantitative line scan of a thick tungsten layer in the tungsten-steel composite.

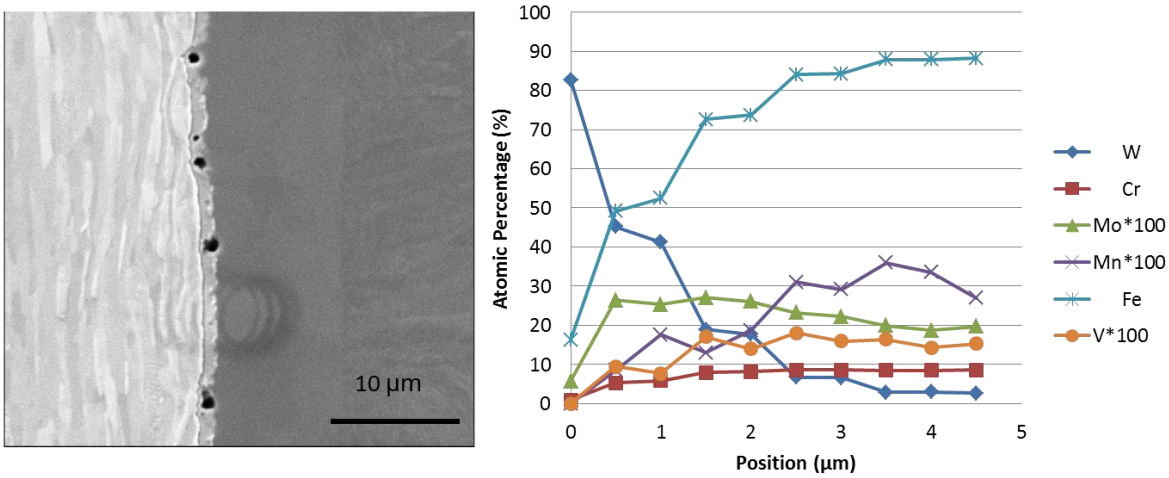

Figure 5. Detailed line scan to identify the composition of the intermetallic phases between the tungsten and steel layers.

Tensile tests

To tensile test the foils, specialized grips were designed and fabricated. Standard tensile grips for SSJ-3 style samples rely on pressure exerted on the shoulder of the sample to keep it in place during the tensile test. For foil samples, the standard method does not work because the sample shoulder can bend or deform, allowing the sample to slip out of the grips. The grips for foil samples were designed with an extra piece that can be screwed in place to provide pressure to the tabs rather than the shoulder of the samples (Figure 6). Initial tests with the new grips confirmed that the grips are able to hold the sample in place during the tensile test. The grips were fabricated from Inconel 718 with titanium screws to allow future high temperature tensile tests.

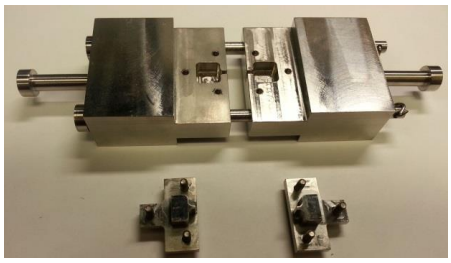

Figure 6. Tensile grips for foil samples with inserts to apply pressure to tab sections of samples.

Tensile samples were cut using EDM from all three tungsten thicknesses and the thicker two steel materials. The tensile samples were cut with the tensile direction (a) parallel, (b) perpendicular, and (c) at 45 degrees to the rolling direction. The data for the 25 µm tungsten foil samples has the most spread and may not be truly representative of the material properties because several of the samples fractured in two places (Figure 7). For the 100 and 250 µm tungsten samples, the expected trend is clear. The samples cut parallel to the rolling direction have the highest strength, the samples cut perpendicular to the rolling direction have the least ductility, and the samples cut at 45 degrees show some ductility but lower ultimate strength than the parallel samples (Figure 7). Because no strain gauge could be placed on the foil samples without impacting the test results, the tensile frame motion was recorded to estimate the elongation of the samples. Therefore the x-axis values plotted in Figure 7 and Figure **8** include the sample deformation as well as the machine compliance and are calculated as

(crosshead displacement)/(original gauge length)*100% (1)

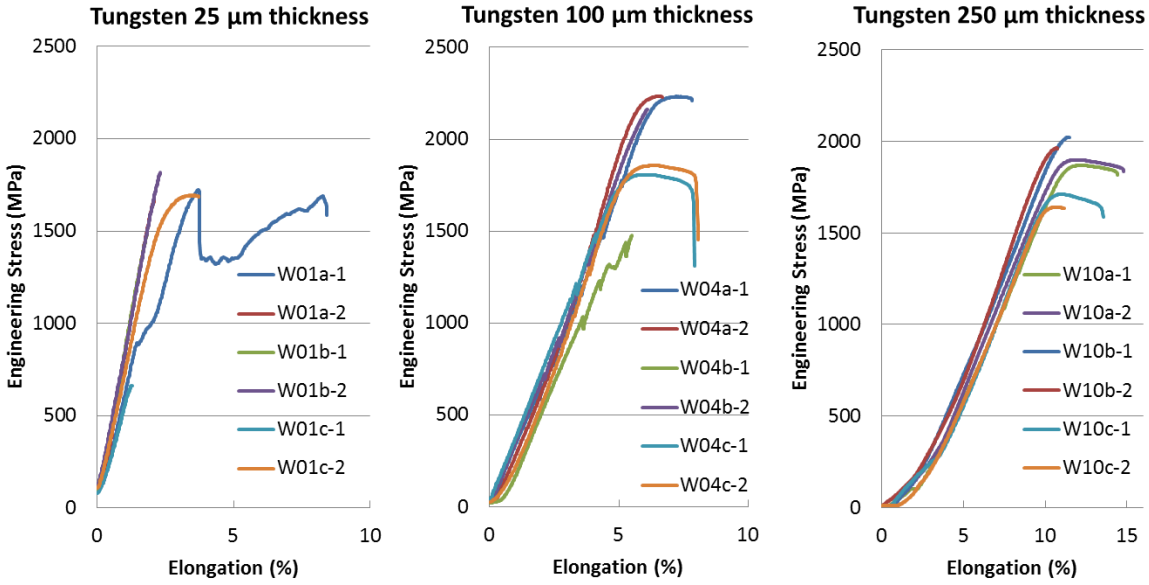

Figure 7. Tungsten foils tensile test results at room temperature. Sample labels including “a” were cut with the tensile direction parallel to the rolling direction, “b” perpendicular, and “c” at 45 degrees. Values on the x-axis are calculated from the crosshead displacement.

For the 100 µm thickness steel foils, the samples cut perpendicular to the rolling direction exhibited less ductility than the other direction samples (Figure 8). However, the ultimate strengths of all of the samples are similar. The trend of tensile behavior with comparison to rolling direction is unclear for the 250 µm steel foil samples (Figure 8).

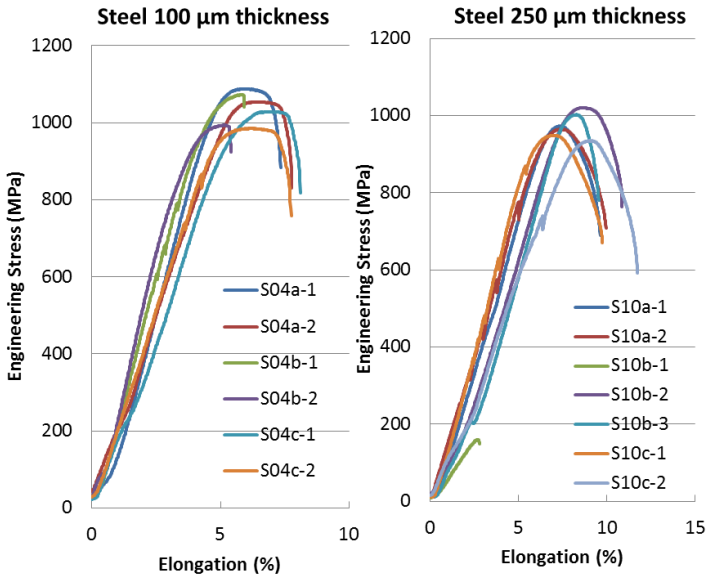

Figure 8. Steel foils tensile test results at room temperature. Sample labels including "a" were cut with the tensile direction parallel to the rolling direction, "b" perpendicular, and "c" at 45 degrees. Values on the x-axis are calculated from the crosshead displacement.

Digital image correlation

Because strain gauges cannot be attached to the foil samples, digital image correlation (DIC) was investigated to potentially give more information about the sample deformation during the tensile test. Two steel samples 250 µm thick, two tungsten samples 250 µm thick, and one tungsten sample 25 µm thick were used in an initial test of the DIC system. When tested with the special grips, too much of the gauge section was blocked by the grips, so no useful DIC information was collected. Additionally, for the tungsten samples, little to no deformation was observed before fracture. The steel samples were thick enough to be tested without the additional inserts in the grips, which allowed the entire gauge section to be viewed. The data from the steel tests is being analyzed. To utilize the DIC method for the thinner foils will require modifying the grips to allow the camera to view more of the gauge section.

Metallography

Previous efforts to mechanically polish the foil samples have been unsuccessful, so as an alternative, electropolishing was performed on tungsten samples 250 and 100 µm thick. The electropolishing used a 2 wt. % solution of KOH. The samples were dipped in the solution for 20 seconds at each of three voltages: 20, 25, 30 V. The electropolishing was more successful at revealing the grains than previous mechanical polishing attempts (Figure 9). The electropolish was not uniform over the whole sample surface, so some areas can be found where the grains are not as clearly revealed. Also, the electropolishing leaves behind an artifact of small raised areas on the tungsten surface. The rolling direction is approximately vertical on the page in Figure 9, the direction along which the grains are elongated.

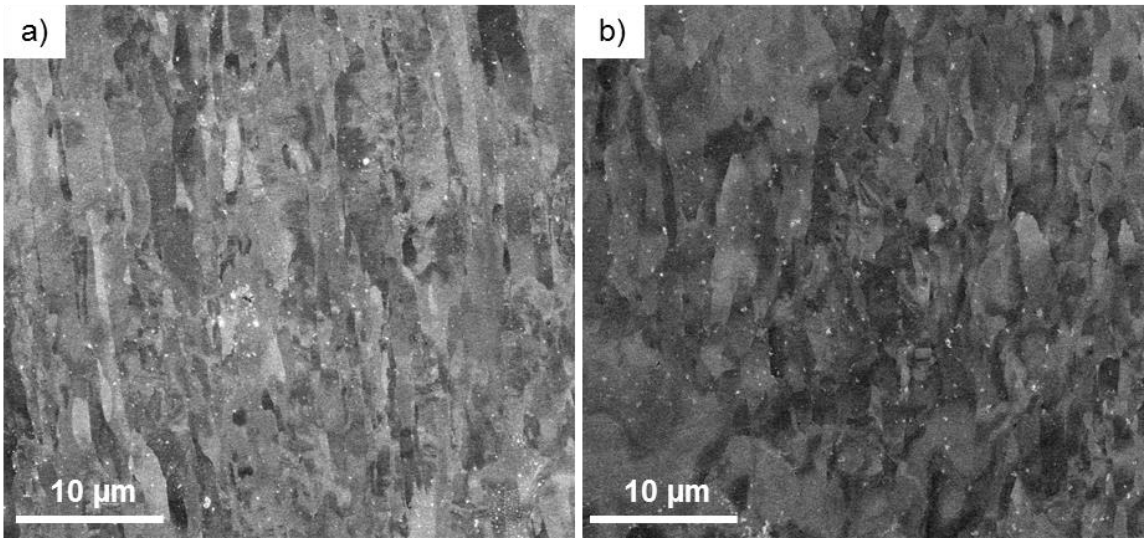

Figure 9. Tungsten foils imaged in SEM after electropolishing. a) W foil 100 µm thick b) W foil 250 µm thick

After electropolishing, the tungsten foils were imaged with Electron Backscatter Diffraction (EBSD) to reveal the grain orientations. For both samples the EBSD data was taken with a 0.2 µm step size and no clean-up operations were performed on the data. For the tungsten foil 100 µm thick (Figure 10) the texture along the (001) to (111) edge of the inverse pole figure is clearly visible. For the tungsten foil 250 µm thick (Figure 11) the texture is not as distinct as for the 100 µm thick foil but has some concentration of grains with orientations between (001) and (101). For both samples, strain can be observed in the EBSD images by the spectrum of colors present in each grain.

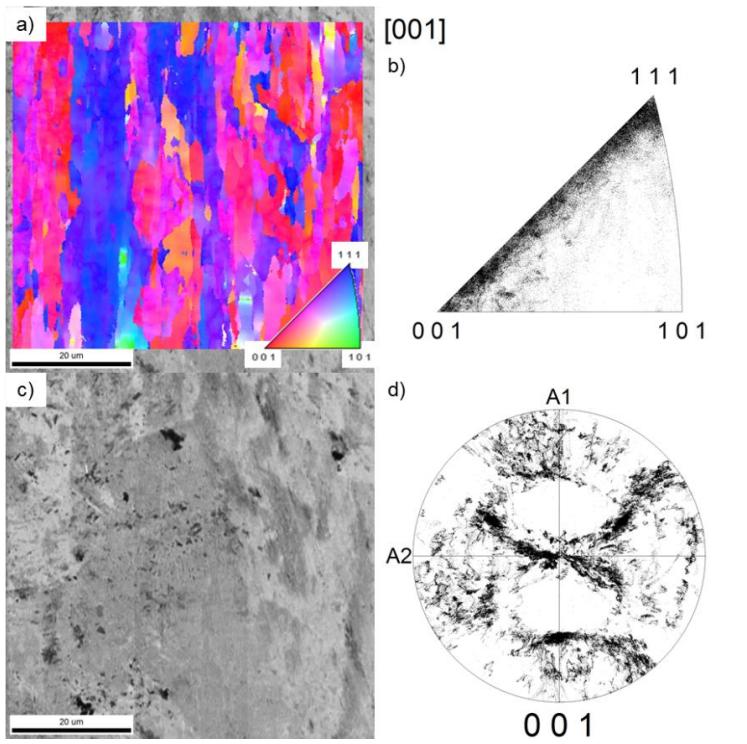

Figure 10. Tungsten foil 100 µm thick after electropolishing. a) grain map b) inverse pole figure showing the texture c) SEM image of analyzed zone d) pole figure of grain orientations.

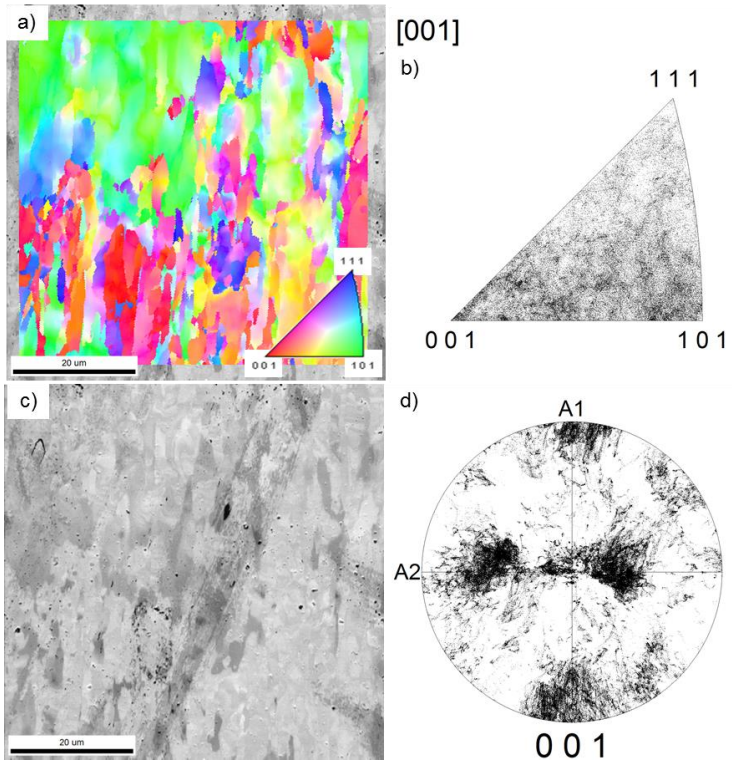

Figure 11. Tungsten foil 250 µm thick after electropolishing. a) grain map b) inverse pole figure c) SEM image of analyzed zone d) pole figure of grain orientations.

4.5 DEFECT EVOLUTION IN NEUTRON-IRRADIATED SINGLE CRYSTALLINE TUNGSTEN – X. Hu, T. Koyanagi, Y. Katoh (Oak Ridge National Laboratory), M. Fukuda (Tohoku University), B.D. Wirth, L.L. Snead (University of Tennessee, Knoxville)

OBJECTIVE

The objective of this work is to investigate the microstructural defect evolution and the resulting mechanical property changes in neutron irradiated single crystalline tungsten to facilitate the development of plasma-facing materials for fusion reactors.

SUMMARY

High purity <110> single crystalline tungsten samples were examined by positron annihilation spectroscopy following low temperature and low dose neutron irradiation and subsequent isochronal annealing. The results were used to determine microstructural and defect evolutions, thus, identifying the annealing mechanisms. The one-hour isochronal annealing was performed on two specimens neutron-irradiated to very low (0.006) and low (0.03) dpa at ~90°C. Following annealing at 400, 500, 650, 800, 1000, 1150, and 1300°C, *ex-situ* characterization of vacancy defects used positron lifetime spectroscopy and coincidence Doppler broadening (CDB). Vacancy cluster size distributions showed significant damage recovery around 1000°C, consistent with Stage III below 400°C and Stage V temperature around 1000°C. CDB results confirmed the trend of the vacancy defect evolution and S-W plots confirmed a single type of vacancy clusters. This microstructure information is consistent with the measured hardness changes.

PROGRESS AND STATUS

Introduction

Numerous studies have explored the recovery processes of radiation-induced damage in tungsten. Residual electrical resistivity was commonly used as an index of the damage present in materials for the damage recovery study, resulting in the identification of the temperatures and activation energies for different annealing stages. Early studies on neutron-irradiated tungsten [1-5] demonstrated five damage recovery stages by using resistivity measurement. Stage I occurs below −170°C, attributing to the migration of self-interstitials. Stage II, covering a broad temperature regime, −170~350°C, results from the thermal activation of interstitials from traps with activation energies from 0.25 to 1.7 eV. Stage III (~ 0.15 T_m/350°C), Stage IV (~ 0.22 Tm/640°C), and Stage V (0.31 Tm/970°C) were also identified. To date, the physical mechanisms governing the damage recovery in these five stages are still controversial. In this work, single crystalline tungsten samples following low dose and low temperature neutron irradiation were investigated to explore the radiation damage evolution at different annealing stages and to link them with the observed microstructure and the hardness at different annealing conditions.

Experiment

Neutron irradiation of the specimens was carried out in the flux trap facility in HFIR at a temperature of 90 ± 10°C. The two specimens studied here, 1W05 and 1W25, were irradiated to fast neutron fluences of 2×10^{23} and 1×10^{24} n/m^2 (E>0.1 MeV) equivalent to displacement damage levels of ~0.006 dpa and ~0.03 dpa, respectively. Following the isochronal annealing for one hour at 400, 500, 650, 800, 1000, 1150, and 1300°C, *ex-situ* characterization of vacancy defects was performed using positron annihilation spectroscopy (PAS). Micro-hardness tests were also conducted after each annealing step using a micro-Vickers indentor at a load of 1.96 N.

Results

Positron Annihilation Lifetime Spectroscopy

Subsequent to each annealing step, PAS measurement was conducted. To illustrate directly the influence of annealing temperature on the measured positron lifetime data, the normalized spectra obtained for specimens 1W05 and 1W25 at seven annealing conditions together with the as-received and as-irradiated conditions are shown in Figure 1. The annealing processes of 1W05 and 1W25 involve some common features. Clearly, the long lifetime components of the spectra become more intense after irradiation. The spectra for the annealing temperatures 400, 500, 650, and 800°C are difficult to distinguish, but have more significant long lifetime components compared to the as-irradiated samples. Subsequently, the lifetime spectra start to shift to the shorter lifetimes after the 1000°C anneal, closer to the spectra of unirradiated samples. This shows qualitatively that the density and the size of the vacancy clusters evolve during the isochronal annealing process.

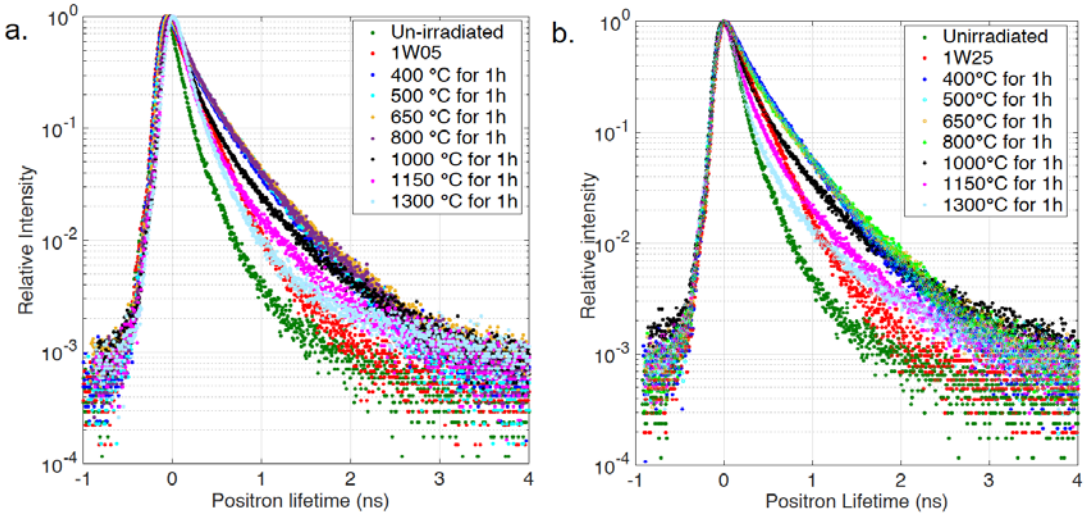

Figure 1. Positron lifetime spectra for annealed tungsten (a) 1W05 and (b) 1W25. Spectra for un-irradiated and as-irradiated tungsten samples are also shown for comparison.

In the present study, the measured positron lifetime spectra for tungsten could be resolved into three lifetime components by applying the trapping model. The results of the analysis are shown in Figure 2. τ_1 and I_1 indicate the lifetime and relative intensity of the positrons annihilated in the bulk lattice. The two long lifetimes, τ_2 and τ_3 and their associated intensity I_2 and I_3 arise from the positrons trapped in the 3D vacancy clusters. For the un-irradiated samples, the presence of single vacancies and nano-voids were observed but in relatively small fractions (23% and 7%, respectively). τ_2 increased to ~230 ps for both 1W05 and 1W25 subject to neutron irradiation, equivalent to a complex containing 2~3 vacancies, along with a significant increase in intensity, indicating that a large amount of small vacancy clusters were induced by neutron irradiation. In contrast, the τ_3 had a small increase and the change for I_3 was negligible. The higher does level of 1W25 implied a larger mean positron lifetime in comparison with 1W05, as shown in Figures 2(a) and (c).

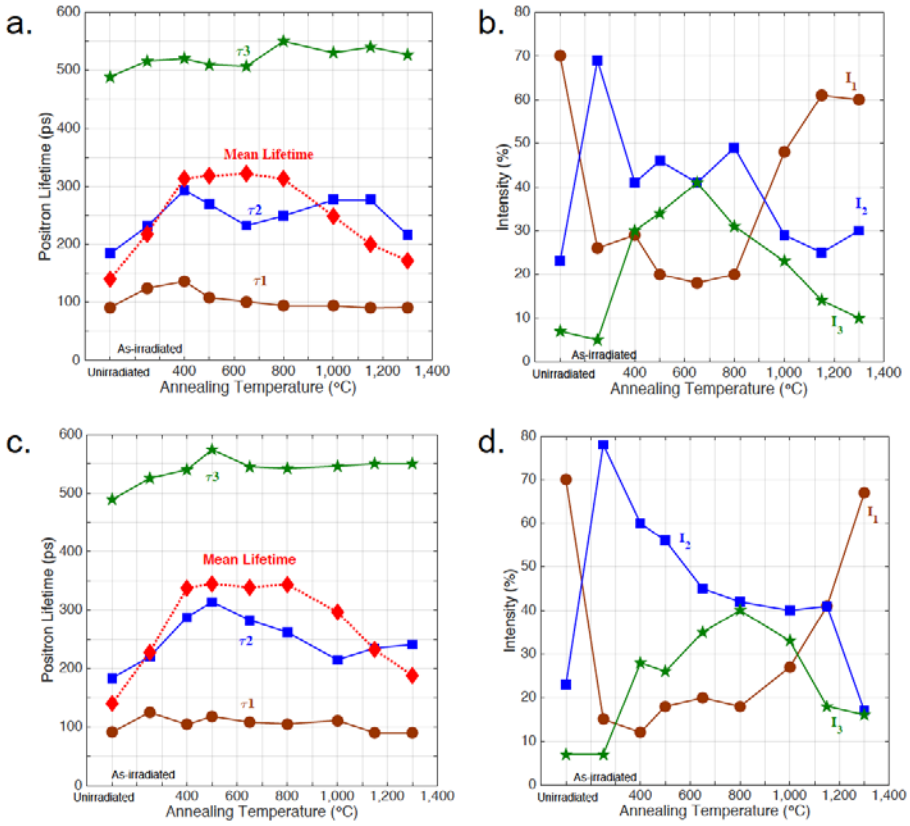

Figure 2. Positron lifetimes (a, c) and their intensities (b, d) as functions of annealing conditions for 1W05 (a, b) and 1W25 (c, d). The dashed lines in (a) and (c) indicates the mean lifetimes for these two samples at different annealing stages.

The changes of the PAS parameters in different temperature ranges reflect the microstructural defect evolutions during annealing. As shown in Figure 2(a) and (c), the mean positron lifetime showed a quite similar trend for both samples and provided a rough identification of different annealing stages. After annealing at 400°C, the mean lifetime increased and then kept at a constant value up to 800°C annealing. Subsequently, it started to drop after being annealed at 1000°C, when the emission of single vacancy from thermal dissociation of large vacancy clusters and the annihilation of mobile vacancy clusters at sinks were becoming significant.

The analysis of two longer exponents yielded more detailed microstructural information as following. The presence of τ_2 and τ_3 demonstrated the presence of small vacancy clusters and nano-voids. The lifetime, $\tau_2 \sim 200 - 314\ ps$, is equivalent to average cavity sizes of ~1−9 vacancies and the longest lifetime of ~550 ps is associated with voids containing more than 40 vacancies. After annealing at 400°C for both samples, τ_2 is increasing, indicating the growth of small vacancy clusters due to the mobile single vacancy, which is consistent with the previous definition of Stage III (~0.15 T_m/350°C) [3]. In the anneal stages of 400−650°C for 1W05 and 400−800°C for 1W25, although the mean lifetime had negligible change, I_2, the intensity of τ_2, which is corresponding to the number density of small vacancy clusters, decreased, while the number density of voids increased. In this stage, the growth of voids is at the expense of small vacancy clusters. The strong coarsening of the nano-void population implied the stage IV, 650−800°C, caused by the migration and coalescence of the existing vacancy clusters. In the annealing stages above 800°C for 1W05 and above 1000°C for 1W25, the significant vacancy dissociation from nano-voids and voids yielded a strong reduction of the populations of these defects, named as Stage V. When the annealing temperature increased above stage V, I_3 dropped abruptly while I_2 had a general decrease trend. After the 1300°C annealing, the impurity stabilized vacancy clusters

contributed to the observation of I_2 [4]. The significant drop of void population at this stage was likely induced by coarsening of the void population due to Ostwald ripening or the dissociation of the voids [6, 7].

Coincidence Doppler Broadening

Positrons injected into materials eventually annihilate with electrons, producing predominantly two gamma rays travelling in approximately opposite directions, necessitated by energy-momentum conservations during annihilation. The total energy of the annihilation gamma rays is given by $2m_0c^2 - E_B$, where m_0c^2 is the electron rest mass energy and E_B is the electron binding energy. Since there is a net center of mass energy associated with the annihilating positron-electron pair, the total energy will not split equally for the two gamma rays. One gamma ray is upshifted and the other is downshifted. The energy shift of each photon is given by

$$\Delta E=\frac{1}{2}p_L c=\frac{1}{2}\theta_L m_0 c^2 \quad (1)$$

where ΔE is the photon energy difference from the nominal value, p_L is the corresponding longitudinal momentum shift along the direction of gamma ray emission, in atomic unit (1 a.u.=7.28 mrad×m_0c), θ_L is the angular deviation of the photons from 180°. Since p_L has element specific spectral distributions that correspond to the momentum distributions of the annihilation electrons, analysis of the orbital electron momentum spectrum (OEMS) provides information on the defects. The OEMS is typically represented as the fraction of annihilations at each momentum interval as a function of p_L, normalized by a standard spectrum. It is more convenient to represent OEMS data in so called *S−W* plots. The S is a fraction of low-momentum annihilation defined by specified p_L region, which in this study is $p_L \leq 0.382\ a.u.$, and W is the corresponding high-momentum annihilation fraction, defined as $1.0\ a.u. \leq p_L \leq 4.0\ a.u.$. A particular microstructure produces a point on a *S−W* plot. *S−W* correlation plots are useful in detecting the change in the nature of the positron trapping defects, since the slope of the plot is a fingerprint of a specific vacancy.

Figure 3 shows the $n(p_L)/n_W(p_L)$ OEMS obtained as a function of annealing temperature for 1W05 and 1W25. The basic principle to understand this plot is that damaged materials gave rise to the enhancement of the low momentum fraction due to the higher possibility of being annihilated by valence electrons for positrons. As shown in Figure 3, the increase of low momentum part and decrease of high momentum part indicated that intense damage was induced in tungsten subject to neutron irradiation for both samples. The OEMS curves for annealing processes at the temperatures lower than 1000°C overlapped without obvious changes, while the low momentum parts were enhanced and high momentum parts were weakened in comparison with the as-irradiated conditions. The subsequent high temperature annealing (1000°C, 1150°C, and 1300°C) promoted damage recovery, driving the OEMS curves close to the non-irradiated W.

S-W plots could be obtained from the OEMS plots based on the definition of different momentum windows for S and W, shown in Figure 4. Each data point in Figure 4 refers to one specific microstructure following the corresponding annealing process. Larger low momentum fraction and smaller high momentum fraction refers to the more damaged microstructure. It is apparent that the pathways of the data points are consistent with the materials responses to annealing shown in the normalized OEMS plots. Significant damage recovery was observed after annealing at 1000°C for both 1W05 and 1W25. The circled S-W data points in Figure 4 indicated that the overall microstructure had insignificant evolution at the annealing stages lower than 1000°C. As can be seen from Figure 4, the linear relationship between S and W demonstrated only one type of vacancy-type defects dominated in both 1W05 and 1W25 following different annealing conditions. The identical slope for these two samples implies that transmutation elements produced by neutron irradiation are negligible for such small dose level. The dominant positron trapping sites are solely W-vacancy clusters for both 1W05 and 1W25.

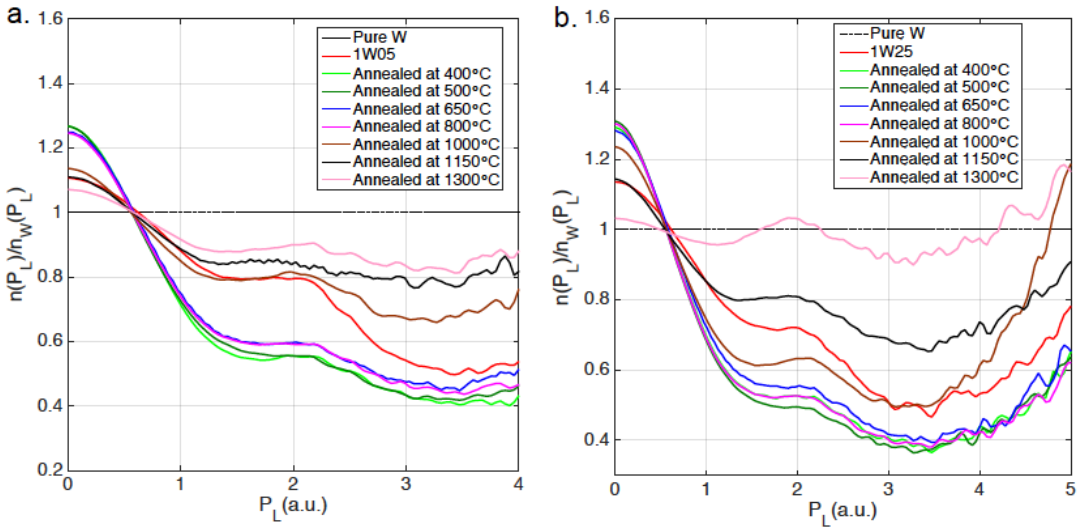

Figure 3. Normalized OEMS of 1W05 and 1W25 in different annealing conditions. The correspondingly normalized curves for as-received and as-irradiated conditions are also shown for comparison.

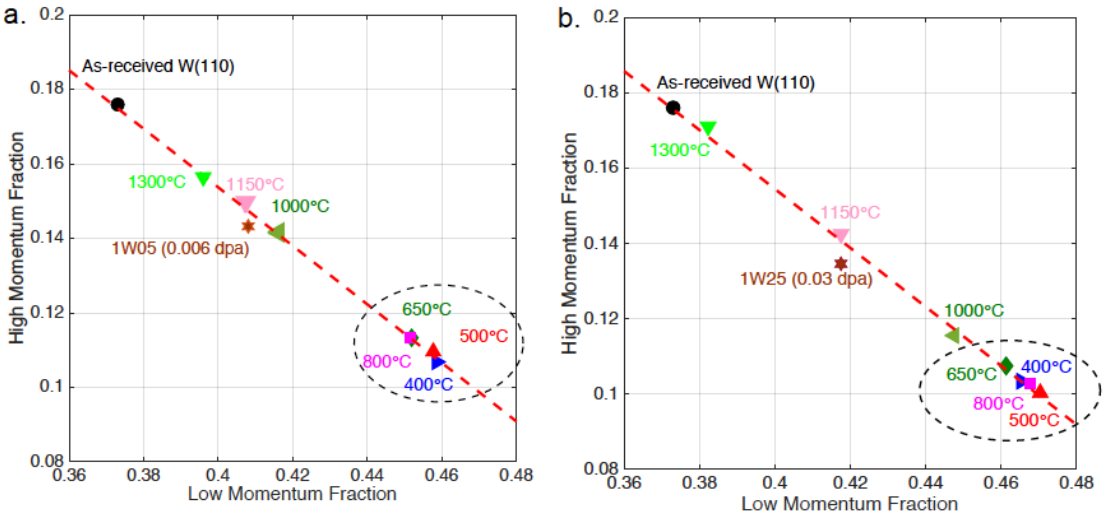

Figure 4. S-W plots for (a) 1W05 and (b) 1W25 during the annealing process. Positron annihilation fraction in the high momentum region ($\mathbf{1.0}\ \boldsymbol{a.u.} \leq \boldsymbol{p_L} \leq \mathbf{4.0}\ \boldsymbol{a.u.}$) versus the low momentum region ($\boldsymbol{p_L} \leq \mathbf{0.382}\ \boldsymbol{a.u.}$). The dashed lines are drawn to guide eyes.

Mechanical Property Characterization

In response to the defect damages inside tungsten, its mechanical properties are expected to change during the annealing processes. Embrittlement is one of the most significant degradation phenomena for tungsten exposed to irradiation and impacts the tungsten's service life and performance in the application of PFM. During the annealing process, microstructures of the studied samples evolve, and the corresponding mechanical property change occurs. Hardness of the studied samples, as a factor contributing to irradiation embrittlement, was determined by micro-Vickers testing following each annealing condition, as shown in Figure 5. Overall, significant hardening was observed after annealing stages at temperatures below 800°C while softening occurred for the annealing stages with temperatures

higher than 1000°C. Similar to the tensile tests, the observed hardness change could be linked to the microstructure evolution. It is known that the hardness (H_v) is roughly proportional to the yield stress (τ_y), [8], therefore,

$$\Delta H_V \propto \Delta\tau_y \propto \alpha(Nd)^{1/2}. \quad (2)$$

While the interstitial clusters are obstacle to the mobile dislocations, the hardness is dominated by the vacancy defects due to the facts that the concentration of interstitial clusters is by several orders of magnitude lower than that of vacancy defects as well as that vacancy clusters are much stronger obstacles [9].

Hardness of both samples increased after neutron exposure in Figure 5. The absolute increase values of hardness for 1W05 and 1W25 were quite close with a slightly higher value for 1W25. The increase of defect population observed in PALS also showed a similar tendency. This observation indicated that although the irradiation dose of 1W25 is five times of that of 1W05, the resulting displacement damage is not proportional to the radiation level.

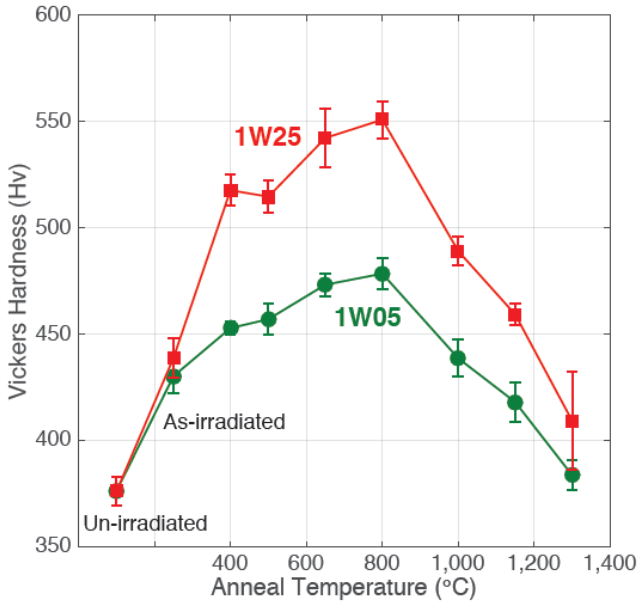

Figure 5. Vickers hardness for 1W05 and 1W25 following different annealing conditions. The hardness values for un-irradiated and as-irradiated samples are also shown for comparison.

As shown in Figure 5, significant hardening was observed after annealing stages at temperatures below 800°C, although the overall concentration of vacancy clusters decreased. It is noted that the consequential hardness results from the collective contributions of all kinds of defects involved. Eq. 21 implies that the competition of strength factor, defect size and concentration determines the hardness. When temperature was lower than 800°C, the concentration of small vacancy clusters (i.e., monovacancy) reduced dramatically, the intermediate vacancy clusters had insignificant changes, and large vacancy clusters (i.e., cavity) has an obvious trend to grow for both samples. It is known that the strength factor of vacancy defects is a function of defect size [9]. The strength factor of big cavities could be several orders higher than that of a monovacancy. The annealing hardening observed in Figure 5 was ascribed mainly to the growth of cavities, resulting from the mobility of single vacancy and small vacancy clusters. Starting from the 1000°C annealing, sample softening showed up due to the significant damage recovery. The growth of big cavities was suppressed by the dissociation process driven by high temperatures. Therefore, the reduction of defect population gave rise to the softening. Note that the measured hardness of both samples following the 1300°C anneal was still higher than that of un-irradiated tungsten samples, which indicated that radiation-induced damage was not completely recovered, consistent with the PAS results.

References

[1] Thompson, M.W., The damage and recovery of neutron irradiated tungsten. Philosophical Magazine, 1960. 5(51): p. 278-296.

[2] Keys, L.K., J.P. Smith, and J. Moteff, High-Temperature Recovery of Tungsten after Neutron Irradiation. Physical Review, 1968. 176(3): p. 851-856.

[3] Keys, L.K. and J. Moteff, Neutron irradaition and defect recovery of tungsten. Journal of Nuclear Materials, 1970. 34: p. 260-280.

[4] Kim, Y.-W. and J.M. Galligan, Radiation damage and stage III defect annealing in thermal neutron irradiated tungsten. Acta Matallurgica, 1978. 26: p. 379-390.

[5] Kim, Y.-W. and J.M. Galligan, An annealing study of thermal neutron irradiated tungsten. Journal of Nuclear Materials, 1978. 69&70: p. 680-682.

[6] Eldrup, M. and B.N. Singh, Study of defect annealing behavior in neutron irradiated Cu and Fe using positron annihilation and electrical conductivity. Journal of Nuclear Materials, 2000. 276: p. 269-277.

[7] Eldrup, M. and B.N. Singh, Accumulation of point defects and their complexes in irradiated metals as studied by the use of positron annihilation spectroscopy – a brief review. Journal of Nuclear Materials, 2003. 323(2-3): p. 346-353.

[8] Busby, J.T., M.C. Hash, and G.S. Was, The relationship between hardness and yield stress in irradiated austenitic and ferritic steels. Journal of Nuclear Materials, 2005. 336(2-3): p. 267-278.

[9] Hu, X., et al., Modeling of irradiation hardening of iron after low-dose and low-temperature neutron irradiation. Modelling and Simulation in Materials Science and Engineering, 2014. 22(6): p. 065002.

4.6 NEUTRON IRRADIATION EFFECTS IN TUNGSTEN — L.M. Garrison, P. Edmondson, N.A.P. Kiran Kumar, T. Colling, M. McAlister, L. Snead, T. S. Byun, D. Lewis (Oak Ridge National Laboratory), and M. Fukuda (Tohoku University, Japan)

OBJECTIVE

The objective of this work is to evaluate the effects of neutron irradiation on the mechanical properties and microstructure of tungsten-based materials to aid in developing plasma-facing materials for fusion reactors.

SUMMARY

A total of 440 samples were irradiated in HFIR at temperatures from 70 to 900°C and fast neutron fluences of 0.01 to 20 $\times 10^{25}$ n/m^2 at E>0.1 MeV. Types of tungsten irradiated in this study were [110] single crystal tungsten, [100] single crystal tungsten, wrought tungsten foils, annealed tungsten foils, and tungsten-copper laminates. Analysis of room temperature tensile test data of the single crystal samples reveals that ultimate strength decreases at less than 1 dpa. The copper tungsten laminate tensile tests were completed and fracture analysis is underway. Atom probe analysis of a single crystal tungsten sample irradiated to 2.2 dpa at approximately 750°C revealed rod-like, ribbon-like, and clusters-shaped Os and Re rich precipitates. Tungsten foils irradiated to 2.2 and 3.8 dpa are being prepared for TEM analysis.

PROGRESS AND STATUS

Mechanical Properties

The hardness data previously reported was re-analyzed by grouping the samples based on their irradiation temperature (Figure 1). For these tungsten samples, the conversion 1×10^{25} n/m^2 (E>0.1 MeV) ≈ 0.32 dpa was used. For both the [100] and [110] samples, the hardness increases with increasing dose, but there is no clear trend with increasing irradiation temperature.

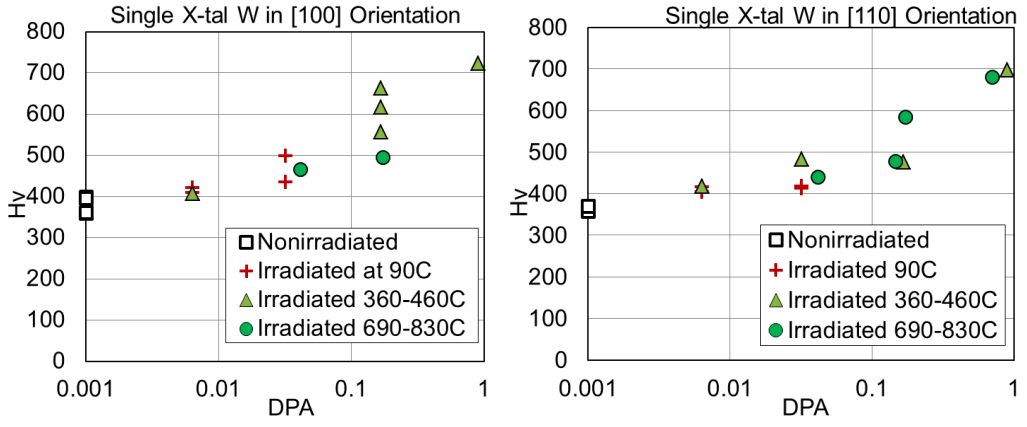

Figure 1. Hardness (Hv) of single crystal tungsten irradiated up to 1 dpa.

Strain gauges were not used during the tensile tests, so the crosshead motion was used to estimate the deformation of the samples. The x-axis for the tensile data is elongation calculated as

(crosshead displacement)/(original gauge length)*100% (1)

Both the [100] and [110] orientation unirradiated tensile samples exhibited non-zero ductility starting at 300°C test temperature (Figure 2Figure 3). For the [110] sample unirradiated and tested at room temperature, the fracture occurred alomg a diagonal across the gauge section with little to no deformation

near the fracture surface (Figure 2a). At the highest test temperature of 650°C there is significant deformation and elongation in the gauge section (Figure 2b). The deformation occurred along the same diagonal as the fracture at room temperature.

For the [100] unirradiated samples, the room temperature fracture occurred perpendicular to the [100] axis of the tensile bar (Figure 3a). Starting at 300°C the [100] samples experienced ductile fracture. The sample tested at the highest temperature of 650°C had significant elongation (Figure 3b).

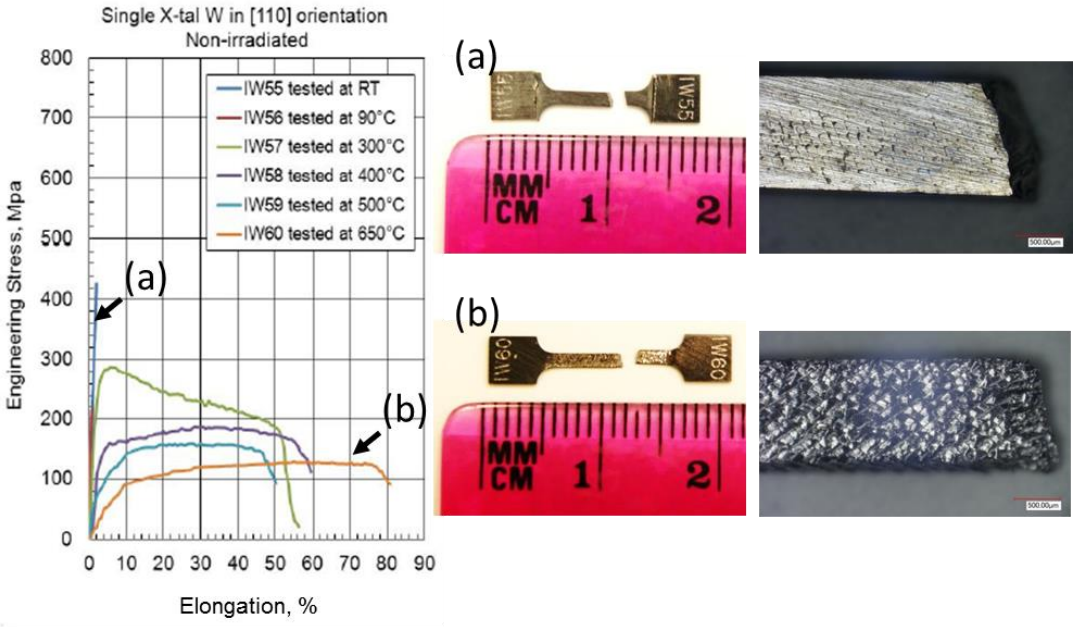

Figure 2. Unirradiated [110] tungsten tensile tested from room temperature to 650°C. (a) no significant deformation is observed on the sample tested at room temperature. (b) the sample tested at 650°C shows significant deformation before fracture.

After irradiation to 0.03 dpa at 90°C, both the [100] and [110] samples still exhibited tensile ductility starting at 300°C test temperature. However, the elongation of the [110] sample tested at 300°C is significantly greater than the [100] sample at the same conditions.

The ultimate tensile strengths of single crystal tungsten samples irradiated at higher temperatures and tensile tested at room temperature are plotted in Figure 5. The fracture behavior of all of these samples was brittle with no plastic deformation observed. At low dpa, the ultimate strength increases as compared to the unirradiated sample strengths. However, as the dpa increases further, starting near ~0.1 dpa, the ultimate strengths decreased.

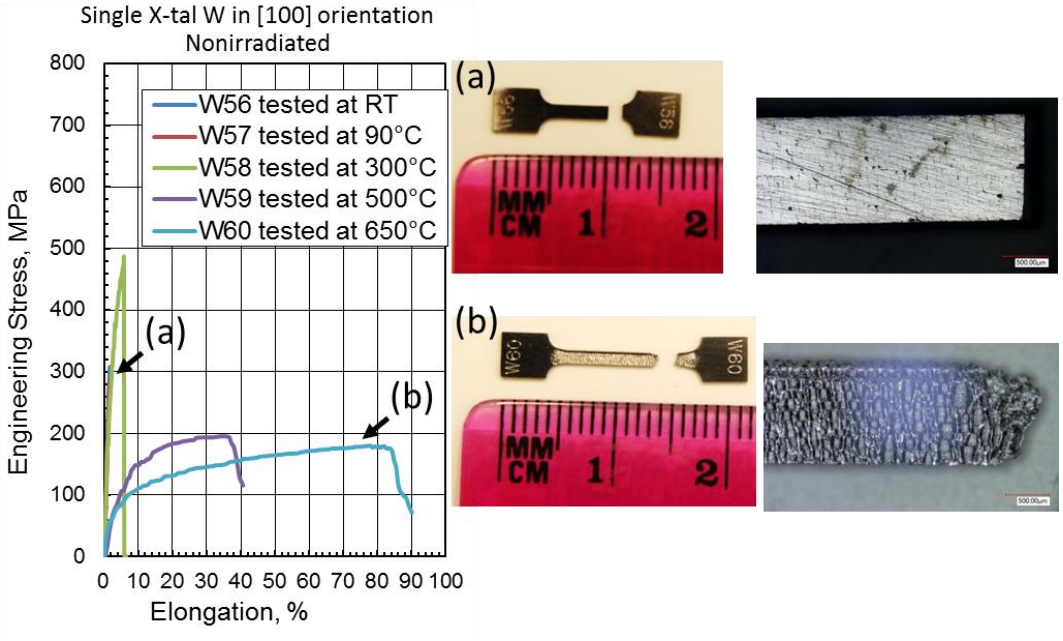

Figure 3. Unirradiated [100] tungsten tensile tested from room temperature to 650°C. (a) no significant deformation is observed on the sample tested at room temperature and the fracture is perpendicular to the tensile axis. (b) the sample tested at 650°C shows significant deformation before fracture.

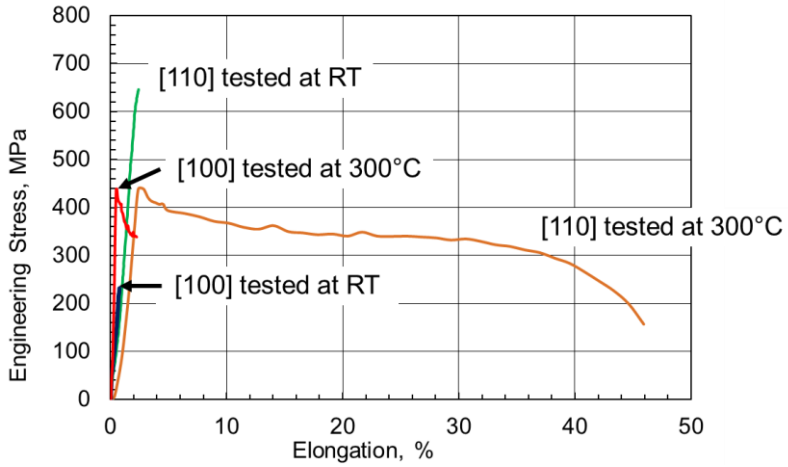

Figure 4. Single crystal tungsten tensile behavior for material irradiated to 0.03 dpa at 90°C.

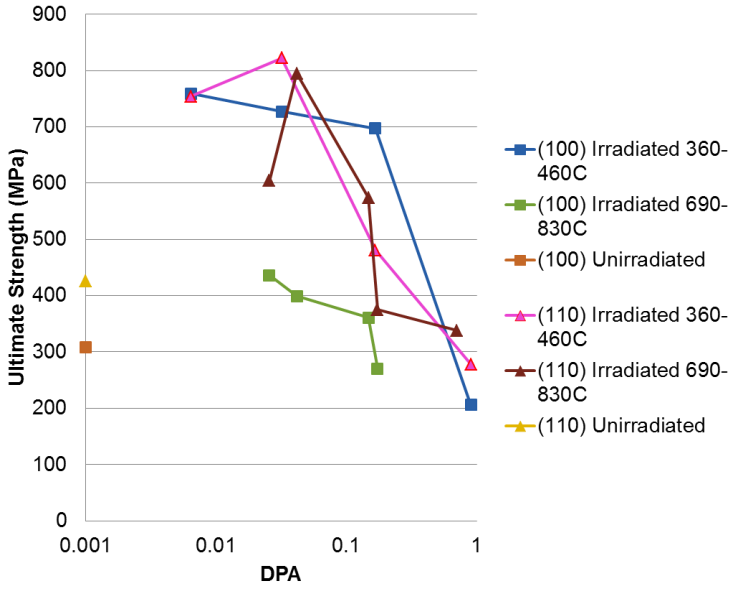

Figure 5. Room temperature ultimate tensile strength of irradiated single crystal tungsten.

Copper-Tungsten Laminates

Tensile tests have been conducted on the copper-tungsten laminate composites. To remove artifacts in the data from the machine compliance, the elastic section of each curve was removed to isolate the plastic deformation section, as in the example in Figure 6. Then, each of the resulting tensile curves was analyzed and evaluated for yield strength, ultimate tensile strength, ultimate elongation, and total elongation (Table 1. **Tensile properties of Cu-W laminate composites.**).

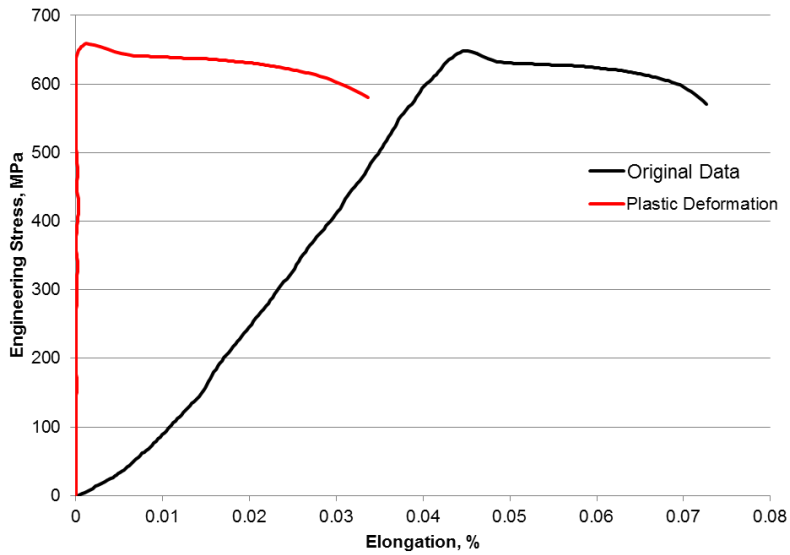

Figure 6. Engineering stress vs. elongation of unirradiated Cu-W laminate composite sample SW36 tested at 650°C.

Table 1. Tensile properties of Cu-W laminate composites.

Specimen Identification	*HFIR Rabbit Capsule*	*Irradiation Temp. (°C)*	*Fast Fluence 10^{25}n/m^2 (E>0.1 MeV)*	*Test Temp (°C)*	*Yield Stress (MPa)*	*Ultimate Tensile Stress (MPa)*	*Uniform Elon-gation (%)*	*Total Elon-gation (%)*
SW40	*unirradiated*	*unirradiated*	*unirradiated*	*22*	*896*	*916*	*0.75*	*15.5*
SW06	*TB-300-1*	*414*	*0.02*	*22*	*1128*	*1131*	*0.22*	*3.7*
SW05	*TB-300-1*	*414*	*0.02*	*22*	*1054*	*1073*	*0.42*	*7.5*
SW07	*TB-300-2*	*448*	*0.1*	*22*	*Brittle Fracture*	*728*	*0*	*0.05*
SW17	*TB-300-3*	*420*	*0.52*	*22*	*1134*	*1139*	*0.09*	*1.4*
SW01	*T9G-11*	*452*	*2.82*	*22*	*Brittle Fracture*	*366*	*0*	*0.01*
SW40	*unirradiated*	*unirradiated*	*unirradiated*	*22*	*896*	*916*	*0.75*	*15.5*
SW12	*TB-500-1*	*751*	*0.08*	*22*	*Brittle Fracture*	*622*	*0*	*0.02*
SW13	*TB-500-2*	*667*	*0.54*	*22*	*Brittle Fracture*	*1033*	*0.08*	*0.08*
SW16	*T9C-14*	*706*	*2.2*	*22*	*Brittle Fracture*	*1245*	*0*	*0.03*
SW15	*T9C-14*	*706*	*2.2*	*22*	*Brittle Fracture*	*1104*	*0*	*0.04*
SW19	*TB-500-3*	*633*	*9*	*22*	*Brittle Fracture*	*691*	*0.1*	*0.15*
SW40	*unirradiated*	*unirradiated*	*unirradiated*	*22*	*896*	*916*	*0.75*	*15.5*
SW23	*TB-650-1*	*776*	*0.13*	*22*	*1141*	*1141*	*0.2*	*1.04*
SW25	*TB-650-2*	*759*	*0.46*	*22*	*Brittle Fracture*	*1244*	*0.15*	*0.15*
SW39	*unirradiated*	*unirradiated*	*unirradiated*	*300*	*457*	*575*	*3.93*	*16.7*
SW38	*unirradiated*	*unirradiated*	*unirradiated*	*400*	*434*	*548*	*4.18*	*12.2*
SW37	*unirradiated*	*unirradiated*	*unirradiated*	*500*	*358*	*448*	*2.15*	*9.8*
SW36	*unirradiated*	*unirradiated*	*unirradiated*	*650*	*318*	*408*	*3.04*	*7.8*
SW08	*TB-300-2*	*448*	*0.1*	*300*	*733*	*741*	*0.41*	*9*
SW18	*TB-300-3*	*420*	*0.52*	*300*	*909*	*909*	*0.2*	*1.3*
SW11	*TB-500-1*	*751*	*0.08*	*750*	*479*	*484*	*0.47*	*4.9*
SW14	*TB-500-2*	*667*	*0.54*	*670*	*Brittle Fracture*	*703*	*0.17*	*0.17*
SW24	*TB-650-1*	*776*	*0.13*	*780*	*496*	*522*	*0.56*	*3.9*
SW26	*TB-650-2*	*759*	*0.46*	*650*	*659*	*661*	*0.17*	*3.4*

SEM and optical microscope images are being taken of the samples, starting with the unirradiated, control samples. Unirradiated laminate sample SW36 tested at 650°C (Figure 7) did not develop any of the surface features in the gauge section that the unirradiated single crystal tungsten samples did when tested at the same temperature (Figure 2Figure 3). From the top view in Figure 7 the pull out of the copper layer is just visible on the right half of the sample.

Figure 7. Optical image of unirradiated Cu-W laminate sample SW36 tensile tested at 650°C.

The optical image of the fracture surface of SW36 (Figure 8), shows that the copper layers partially pulled away from the tungsten layers. The copper layers plastic deformation is observed as the central ridge each formed, while the surface of the tungsten layers is rough and not peaked. While the optical image provides color to help distinguish the layers, the drawbacks are the limited resolution and difficulty with glare on metal samples. In contrast, the SEM gives more detail on the surface structure, but in this case does not give distinct elemental contrast between the tungsten and copper layers (Figure 9). The optical and SEM imaging of the tensile samples will continue so that the modes of failure can be investigated.

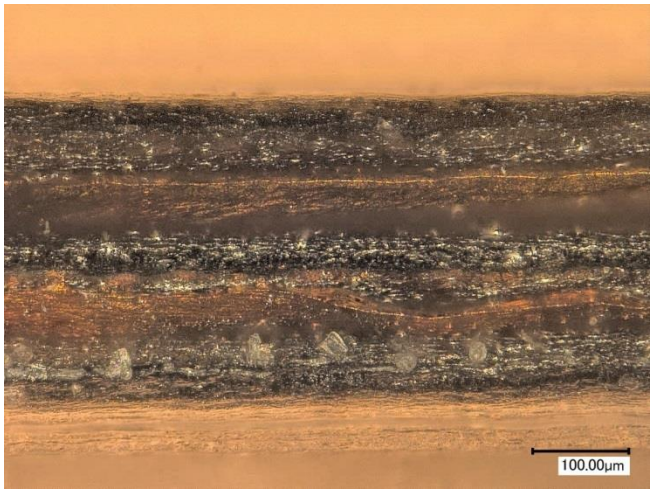

Figure 8. Optical image of fracture surface of SW36 tensile tested at 650°C.

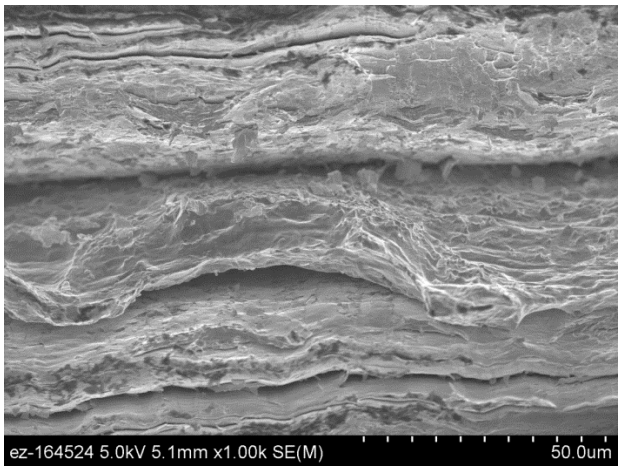

Figure 9. SEM image of unirradiated sample SW37 tested at 500°C.

Important characteristics of a material for fusion applications are its ductility and fracture toughness. Shear punch testing is a well-known technique for characterizing ductility that has several advantages for irradiated tungsten samples. The method uses only small amounts of material, so is suitable for irradiated samples, and is not sensitive to edge machining defects, which is beneficial for a brittle material such as tungsten. Initial investigations have begun with this technique for the copper-tungsten laminate samples.

Microstructure Analysis—Atom Probe

The ORNL-CNMS Cameca Instruments Local Electrode Atom Probe (LEAP) was used to identify and characterize the second phase precipitates formed during the irradiation of single crystal (011), nominally pure tungsten to doses up to 2.2 displacements per atom (dpa) at a temperature of approximately 750 °C.

For the 0.16 dpa irradiated specimen, the recorded time-of-flight spectra indicated that the tungsten had undergone some neutron-induced transmutation, with the primary transmutation products being Os and Re resulting in a bulk composition of W-0.4Os-0.7Re (at.%). The atomic reconstruction of the atom probe data shows the presence of fusiform-shaped Re- and Os-rich clusters (Figure 10a). The average composition of these clusters was found to be W-2.8Os-7.4Re (at.%), with a small spread in compositions, as shown in Figure 10b.

The neutron-induced transmutation in the sample irradiated to 2.2 dpa resulted in a bulk composition of W-7.5Os-5.2Re (at.%). Again, precipitates rich in Os and Re are formed under irradiation, Figure 11a. These precipitates have morphologies that could be broadly classified as rod-like, ribbon-like, rod- and ribbon-like, and clusters. The compositions of these individual precipitates in addition to the bulk and average compositions (W-20.2Os-15.9Re) are shown in Figure 11b. All precipitates, with the exception of 2, lie within the sigma phase composition boundary regardless of the morphology.

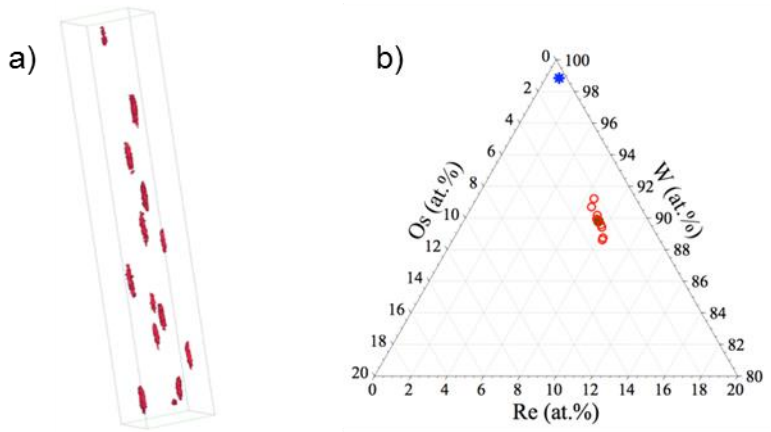

Figure 10. a) Concentration isosurface (ReOs - 20%) from the irradiated tungsten sample. Reconstruction volume is 350 x 60 x 60 nm. b) Ternary diagram showing the composition of individual clusters in the 0.16 dpa irradiated sample. The blue asterisk is the average bulk composition.

There are two points of interest that should be noted regarding the shape and orientation of the precipitates: first, the shape (fusiform, and rod- and ribbon-like) of the neutron irradiated precipitates are vastly different to those formed during self-ion irradiation of a W-1Os-1Re (at.%) alloy in which spherical clusters were formed after irradiations to 33 dpa (1). Second, the precipitates all appear to be crystallographically aligned. Electron backscatter diffraction was used to determine the crystal orientation along the *z*-axis of the atom maps (the long axis of the atom probe needle analyzed). This revealed that the direction of analysis was along the (111) crystal orientation, indicating that there may be some form of preferred diffusion of the solutes along this orientation.

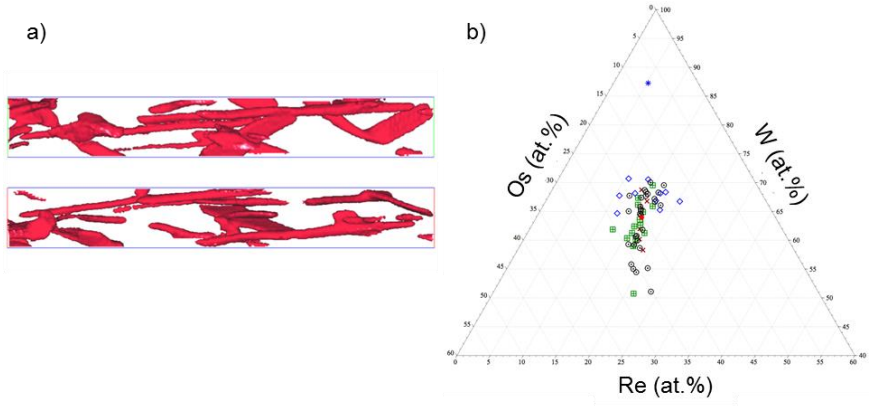

Figure 11. a) Concentration isosurface (ReOs - 20%) from the irradiated tungsten sample. Reconstruction volume is 250 x 35 x 35 nm. b)Ternary diagram showing the composition of individual precipitates (ppt's) found in the irradiated tungsten sample. The blue asterisk is the average bulk composition; red circle is the average ppt composition; the black circles are ribbon-like ppt's; green squares are rod-like ppt's; dark red crosses are rod- and ribbon-like ppt's; and blue diamonds are cluster ppt's.

Microstructure Analysis—TEM

A new set of polycrystalline tungsten specimens exposed to higher neutron doses was selected for further microstructural examination (Table 2). The purpose of selecting these tungsten specimens is to better understand the irradiation-induced transmuted phases and their orientation relation with the tungsten matrix. Selected specimens were mechanically polished in order to remove the oxide layer from the metal surface. A focused ion beam (FIB) system with Ga^+ ion beam was used to prepare TEM specimens. In order to minimized the unwanted damage caused by Ga^+ ions on the TEM specimen, very low energy of 2 kV and 27 pA was used during the final thinning process. The TEM sample preparation and examination is ongoing.

Table 2. Pure tungsten polycrystalline specimens selected for TEM examination.

Sample ID	Target Irradiation Temp (ºC)	Fluence ($x10^{25}$ n/m^2)	dpa	FIB – TEM specimen preparation
OW158	650	7	2.2	Finished
OW125	500	12	3.8	Finished
OW159	650	12	3.8	
AW170	650	12	3.8	
AW134	500	12	3.8	
AW165	650	7	2.2	
OW097	300	7	2.2	
AW098	300	7	2.2	

References

[1] A. Xu *et al*, Acta Mater. **87** (2015) 121

4.7 ALLOYING AND NEUTRON IRRADIATION EFFECTS IN TUNGSTEN-RHENIUM — L. M. Garrison (Oak Ridge National Laboratory)

OBJECTIVE

The objective of this project is to gain a fundamental understanding of the changes to mechanical and thermal behavior of tungsten that are caused by neutron irradiation and rhenium additions.

SUMMARY

Five alloys of tungsten with different rhenium additions as well as one pure tungsten control material were fabricated by arc melting. After arc melting, the samples were hot-rolled to approximately 80% reduction to improve the microstructure. The distribution of rhenium in one of the alloys was investigated with EDS. Samples for mechanical testing, thermal testing, and neutron irradiation are being prepared from these alloys.

PROGRESS AND STATUS

Introduction

Tungsten transmutes to rhenium during neutron irradiation. The behavior of the transmuted rhenium and its influence on the thermal and mechanical properties of tungsten needs to be better understood. The atoms displaced by the neutron irradiation also create defects that can change the thermal and mechanical properties of tungsten. To isolate and understand the influence of the rhenium versus the influence of the neutron damage, tungsten alloyed with varying amounts of rhenium will be evaluated before and after irradiation.

Results

The alloy compositions that were fabricated by arc-melting are listed in Table 1. After the initial arc-melting, the materials were brittle and had internal cracks and voids which made them difficult to machine. To improve the microstructure, the materials were hot-rolled at 1200°C to approximately 80% reduction. During hot rolling, the materials were encased in molybdenum boxes. The molybdenum outer layer was then chemically dissolved from the sample materials.

Table 1. W-Re alloy compositions.

Alloy number	Initial Re wt.%
Alloy 1	0.03
Alloy 2	0.17
Alloy 3	0.83
Alloy 4	3.4
Alloy 5	17.7
Alloy 6	0.0

After rolling, the appearance of Alloy 3 with large flat grains is representative of all the materials except Alloy 5 which contains significantly more rhenium than the other alloys (Figure 1). Alloy 5 was not able to be rolled as thin as the other alloys and has smaller grains visible on the exterior than the other alloys.

Figure 1. Alloy 3, left, and Alloy 5, right, after rolling.

Alloy 4 with nominally 3.4% Re was analyzed with EDS to determine the distribution of Re in the sample. The qualitative map in Figure 2 shows the Re is present in the sample in concentrated areas rather than evenly distributed throughout. However, no second phase was identified with the EDS analysis.

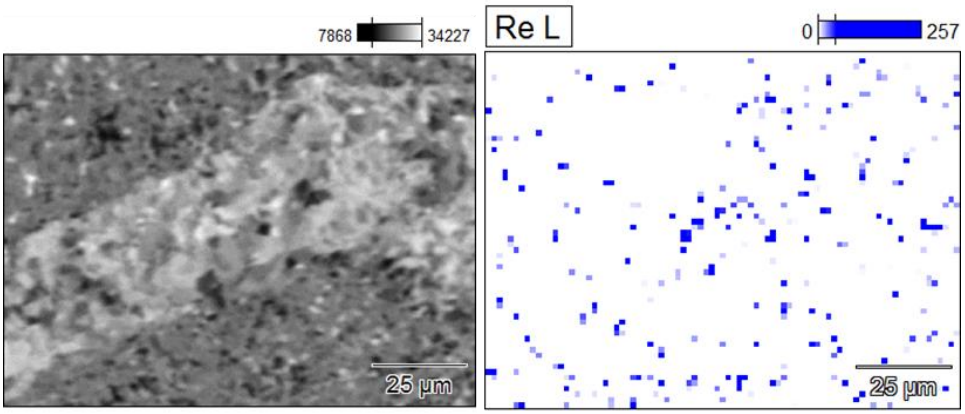

Figure 2. EDS qualitative elemental map of the W-3.4% Re sample showing the rhenium distribution.

4.8 HIGH-HEAT FLUX TESTING OF LOW-LEVEL IRRADIATED MATERIALS USING PLASMA ARC LAMPS — A.S. Sabau, Y. Katoh, and Sarma Gorti (Oak Ridge National Laboratory)

OBJECTIVE

The objective of this work, part of the PHENIX collaboration with Japan, is testing of irradiated candidate divertor component materials and mock-up divertor components under high-heat flux conditions using Plasma Arc Lamps (PAL).

SUMMARY

In this reporting period, a simplified thermo-mechanical model was developed and implemented in ABAQUS™ in order to understand the deformation and residual stresses in the samples tested under high-heat flux. The results of the thermo-mechanical model simulations indicated that W/F82H specimens tested at high-heat fluxes expected in fusion power devices would deform plastically and undergo complex deformation states. The numerical simulation results for the stress levels and pattern of deformation are essential to the understanding of the property degradation and damage mechanisms during HHFT.

PROGRESS AND STATUS

Effort was conducted in three main areas: (a) analysis of data acquired during HHFT of five W-F82H specimens, (b) development of a simplified model for heat transfer during HHFT in order to estimate the thermal gradient through the specimen, and (c) development of a simplified thermo-mechanical model in ABAQUS for the simulation of the state of stress and deformation during HHFT.

First, the temperature data for the high-heat flux testing of five specimens, which was conducted in collaboration with Dr. Kazutoshi Tokunaga of Kyushu University, Japan in Dec. 2014, as part of the PHENIX program, were analyzed to formulate models for temperature evolution during HHFT. It was found that the average heat flux per cycle for each of the five specimens was above 210 W/cm^2 and did not vary significantly: 292.35, 253.52, 297.93, 297.24, and 295.21 W/cm^2, respectively. The main variables in the high-heat flux testing were the number of cycles at high heat flux and average cycle duration (Table 1).

Table 1. Main variables during HHFT.

Specimen	[2]No. Cycles	[2]Average cycle time [s]	Cycle duration [s]	Max. Heat Flux [W/cm^2]	Total heat input from PAL [MJ/cm^2]	Total heat input [MJ/cm^2]	Total time at high-heat flux [s]
1	119	12	10-15	300	0.476	0.418	1,428
2	172	8	7-10	210-278	0.369	0.349	1,375
3	226	4.73	4-5	300	0.338	0.318	1,069
[1]4	100	14.8	10-16	300	0.456	0.44	1,480
[1]5	54	13	10-15	300-323	0.242	0.207	702

[1] Specimen diameter 6 mm. Diameter was 10mm for specimens 1, 2, and 3.
[2] Number of cycles at heat fluxes above 210 W/cm^2.

Second, based on the analysis of the experimental data, several simplified modeling approaches were proposed in order to understand the deformation and residual stresses in the samples tested under high-heat flux. The specimen was bolted directly onto a Cu cooling rod to attain the lowest temperature on the back surface of the specimen and thus enabling the highest thermal gradient in the specimen (Figure 1a). As armor materials, such as W, are much stiffer than Cu, during HHFT, the specimen deformation would be imprinted into the Cu contacting surface. Thus, to ensure a reproducible contact between the armor specimen and Cu rod, a Cu washer was placed between the armor specimen and Cu rod. The

availability of accurate temperature data on the back surface of the Cu washer was essential to the development of the simplified thermal model. The accurate temperature measured on the back surface of the Cu washer was considered a known, an input quantity. This assumption enabled the calculation of the heat flux removed on the back surface of the Cu washer by water-cooling within the Cu rod. The simplified model heat transfer model eliminated the need for complex Computational Fluid Dynamics (CFD) simulation of the water flows and the coupling of CFD and stress analysis. In this model, the thermal contact conduction (TCC) between the F82H and Cu washer is an unknown as the only the top surface temperature could not be measured.

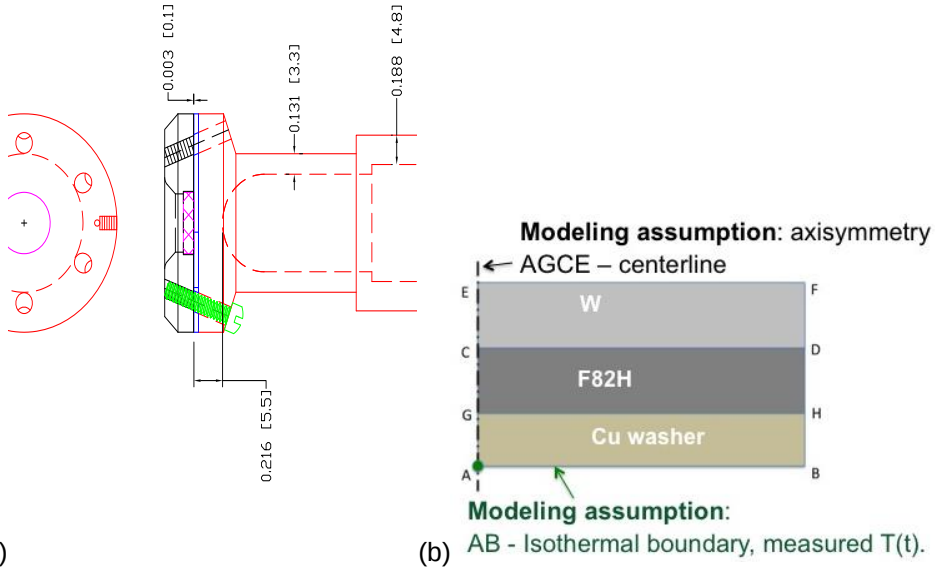

Figure 1. Illustrations of the: (a) final design for the bolting fixture and cooling rod, and (b) main assumptions used to simply the thermal model during HHFT and actual model geometrical.

Third, in order to understand the deformation and residual stresses in the samples tested under high-heat flux, a coupled thermal and mechanical analysis is sought. Temperature-dependent mechanical properties for the materials involved were obtained in preparation for numerical simulations. Inelastic properties, including hardening properties, were obtained from open literature for F82H steel and Cu materials. From the stress-strain curves for F82H, the data for the hardening model was obtained. Thermomechanical models for the simulations of entire HHFT were implemented in the ABAQUS™ software.

Finally, the numerical simulation results were conducted for sample S5. The actual high-temperature cycles for specimen S5 are shown in Table 2. The duration from the end of each cycle to the onset of the next high-heat flux cycle was approximately 70-100s. The main modeling assumptions are illustrated in Figure 1 and Figure 2 and include: (1) modeling of the specimen (W-F82H) and Cu washer below it, (2) isothermal boundary condition at the back surface of the Cu washer, as prescribed by the actual measured temperature during HHFT, and (3) a rigid body clamp, i.e., keeping the distance between the clamp surface to the back-side of the Cu washer constant.

Table 2. High-heat flux cycles experienced by specimen S5.

Cycles	Heat Flux [MW/m^2]	Duration [s]
1-6	0.987	10
7-12	1.194	10
13-18	1.41	10
19-24	1.41	12
25-30	1.41	15
31-36	1.41	20
37-42	1.5	10

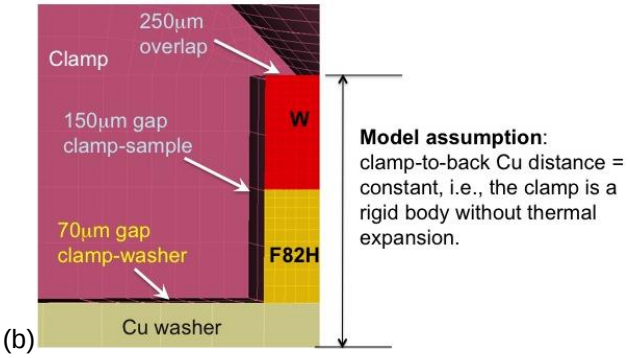

(b)

Figure 2. Illustrations of the clamping detail and rigid body assumption of the clamping fixture.

For the last HHFT cycle, the calculated temperatures at the top surface of W, top and back surfaces of F82H, and top of Cu washer are shown in Figure 2. The results presented were for thermal contact conduction (TCC) per unit area (between the F82H and Cu washer) of 5,000 and 7,000 [W/m^{2}K].

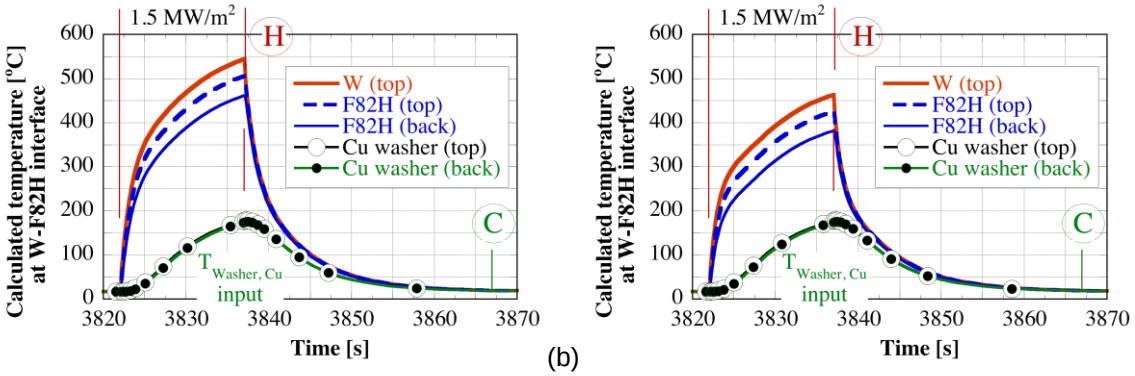

(a) (b)

Figure 3. Calculated temperature evolution during cycle 42 for thermal contact conduction per unit area between the F82H and Cu washer of (a) 5,000 and (b) 7,000 [W/m^{2}K]. The temperature on the back-surface of the Cu washer was used as input.

Based on the temperature and mechanical properties, the following variables were calculated: specimen deformation, plastic deformation, and build-up of residual stresses during HHFT. The results for the Von Mises stress [Pa] is shown at two instances for cycle 42, as indicated by letters H and C in Figure 3. At

these instances, the specimen is at high temperature (Hot), i.e., right at the end of the HHF, and at room temperature (Cold), respectively. The stresses are shown on a deformed mesh in order to illustrate the changes in the specimen geometry during HHFT, with the deformation scale indicated in figures. Figure 4 and Figure 5 contain the data for the case when TCC would be 5,000 and 7,000 [W/m^{2}K], respectively. Although the specimen S5 was 6 mm, simulation data was also obtained for 10 mm specimens. The following observations can be made with respect to the stress and deformation results:

- At high temperatures, the specimens bulge *downward* at its center, as it is resting on the clamp at its outer edges,
- At room temperature, before clamp removal, the specimens bulge *upward* at its center,
- Predicted residual stresses after cooling are higher for the 6 mm than those for the 10 mm specimens.
- The maximum stress is predicted to occur in the steel, at the steel-W interface. The location of maximum stress is (a) at the edge of the steel for the 6 mm specimens, and (b) within the steel for the 10 mm specimens.

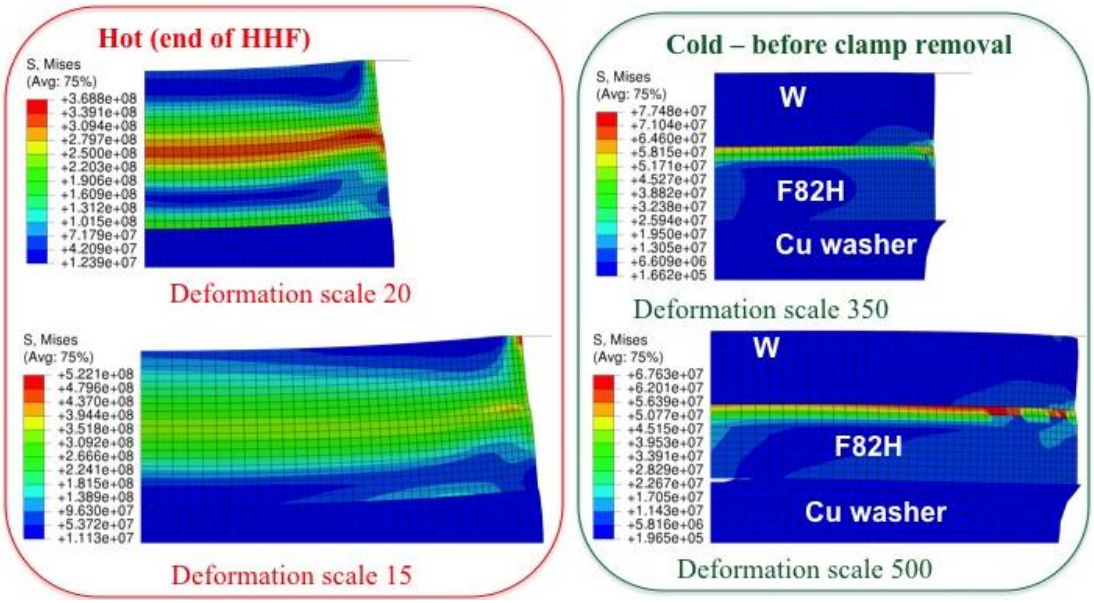

Figure 4. Von Mises stress results when specimen is at high temperature (Hot), i.e., right at the end of the HHF, and at room temperature (Cold) for 6 mm specimens (top line of figures) and 10 mm specimens (the last line of figures) for the case when TCC per unit area F82H-Cu was 5,000 [W/m^{2}K].

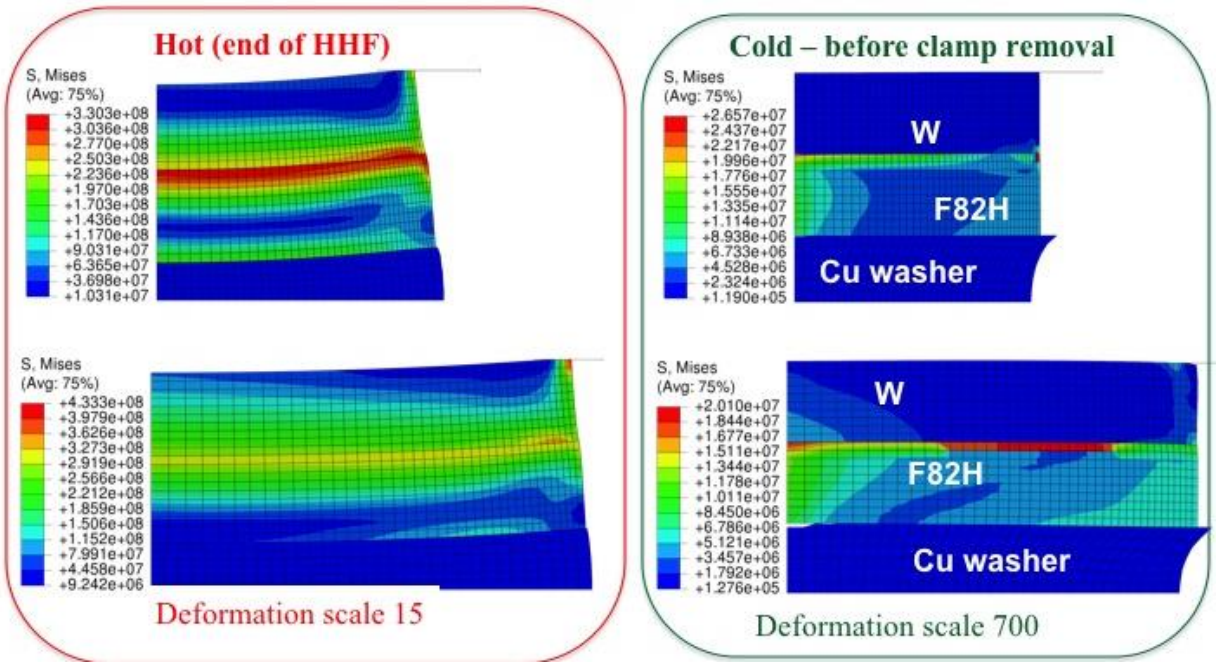

Figure 5. Von Mises stress [Pa] results when specimen is at high temperature (Hot), i.e., right at the end of the HHF, and at room temperature (Cold) for 6 mm specimens (top line of figures) and 10 mm specimens (the last line of figures) for the case when TCC per unit area F82H-Cu was 7,000 [W/m^{2}K].

5.1 IRRADIATION RESPONSE OF NEXT GENERATION HIGH TEMPERATURE SUPERCONDUCTOR TAPES — K.J. Leonard, F.A. List III, A.M. Williams, J.W. Geringer and T. Aytug (Oak Ridge National Laboratory)

OBJECTIVE

The goal of this work is to evaluate the irradiation response of the newest generation of coated conductors based on rare earth doping of $YBa_2Cu_3O_{7-x}$ (YBCO) high temperature superconductors. The materials under investigation represent different methods for enhanced flux pinning for improved performance under externally applied magnetic fields. Response of these tapes to neutron irradiation is examined.

SUMMARY

Post-irradiation electrical characterization of two high temperature superconducting tapes (HTS) was performed. The Zr-(Gd,Y)$Ba_2Cu_3O_7$ and (Dy,Y)$Ba_2Cu_3O_7$ tapes are commercially available from SuperPower and American Superconductor, respectively, and are part of a new generation of conductors which utilize nanoparticles and correlated defect structures within the films to produce tapes capable of use under higher applied magnetic fields than earlier $YBa_2Cu_3O_7$ (YBCO) tapes. The results of neutron exposures between $6.54x10^{17}$ and $1.12x10^{19}$ n/cm^2 (E>0.1MeV) at irradiation temperatures of 75-80°C, show losses in critical current (I_c) in tests under applied fields up to 0.5 Tesla at 77 K. Increases in I_c loss with dose occurs gradually in the (Dy,Y)$Ba_2Cu_3O_7$ conductor, but is rapid in the Zr-(Gd,Y)$Ba_2Cu_3O_7$ with transport current unable to be measure at fluences above $6.54x10^{17}$ n/cm^2.

PROGRESS AND STATUS

Introduction

Ion irradiation, 5 MeV Ni and 25 MeV Au, response of the $GdBa_2Cu_3O_7$, Zr-(Gd,Y)$Ba_2Cu_3O_7$ and (Dy,Y)$Ba_2Cu_3O_7$ tapes were previously investigated. While, predominantly within the electronic stopping regime, the ion irradiation conditions studied of these HTS tapes was within a lower electronic to nuclear stopping ratio (S_e/S_n) as compared to earlier studies. This revealed that their was a significant sensitivity of YBCO based conductors on electronic stopping effects, but also offered a promising evaluation that the rare-earth and nano-particle doped conductors may perform well under neutron irradiation.

Based on the preliminary results from ion irradiation studies, work on the $GdBa_2Cu_3O_7$ tapes produced from SuperPower was not continued. This was due to the greater sensitivity of this material to ion irradiation compared to the Dy and Zr-doped conductors. While performance was improved over conventional YBCO films, under irradiation the Gd_2O_3 nanoparticles present within the $GdBa_2Cu_3O_7$ films (which in addition to stacking-fault and intergrowth gives the conductor improved in-field performance) begin to dissolve with increasing irradiation fluence.

The evaluation of the electrical properties and the corresponding microstructural evolution of the Zr-(Gd,Y)$Ba_2Cu_3O_7$ and (Dy,Y)$Ba_2Cu_3O_7$ tapes under neutron irradiation were further explored.

Experimental Procedure

Neutron irradiation capsules were designed and prepared for High Flux Isotope Reactor (HFIR) exposures using the hydraulic port facility. The irradiation capsules (Figure 1) utilize a square internal cross-section rabbit design loaded with internal packets containing samples (Figure 2).

Additional samples of thermoelectric (TE) materials were also included in two of the four-irradiation capsules as part of a separately funded project. Each internal packet contains samples of one type of HTS sample or the TE materials. High purity aluminum bars provide mechanical support for the flexible HTS tapes, with the tapes and bars over-wrapped with high purity aluminum foil to form a packet. The HTS samples within the wrapped packet are placed against the internal wall of the irradiation capsule.

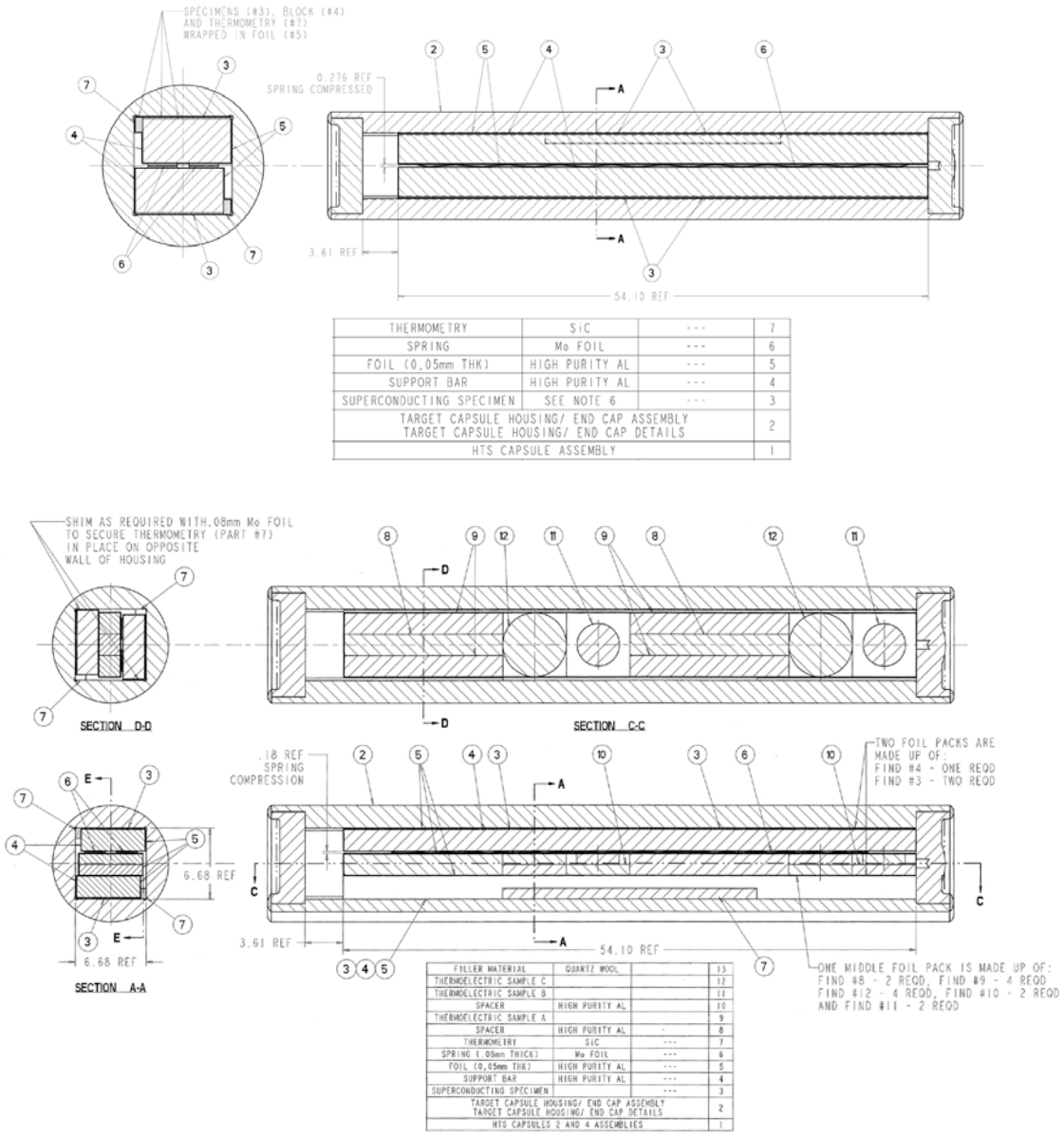

THERMOMETRY	SiC	---	7
SPRING	Mo FOIL	---	6
FOIL (0,05mm THK)	HIGH PURITY AL	---	5
SUPPORT BAR	HIGH PURITY AL	---	4
SUPERCONDUCTING SPECIMEN	SEE NOTE 6	---	3
TARGET CAPSULE HOUSING/ END CAP ASSEMBLY TARGET CAPSULE HOUSING/ END CAP DETAILS			2
HTS CAPSULE ASSEMBLY			1

FILLER MATERIAL	QUARTZ WOOL		13
THERMOELECTRIC SAMPLE C			12
THERMOELECTRIC SAMPLE B			11
SPACER	HIGH PURITY AL		10
THERMOELECTRIC SAMPLE A			9
SPACER	HIGH PURITY AL	-	8
THERMOMETRY	SiC	---	7
SPRING (.08mm THICK)	Mo FOIL	---	6
FOIL (0,05mm THK)	HIGH PURITY AL	---	5
SUPPORT BAR	HIGH PURITY AL	---	4
SUPERCONDUCTING SPECIMEN		---	3
TARGET CAPSULE HOUSING/ END CAP ASSEMBLY TARGET CAPSULE HOUSING/ END CAP DETAILS			2
HTS CAPSULES 2 AND 4 ASSEMBLIES			1

Figure 1. Schematic of the internal sample placement for the HFIR irradiation capsules containing HTS samples only (top) and those containing both HTS and TE samples (bottom).

Estimated irradiation temperatures near 75-80°C. SiC thermometry contained within the capsules remains to be evaluated. The targeted fluences were $5x10^{17}$, 10^{18}, $5x10^{18}$ and 10^{19} n/cm^2 (E>0.1 MeV). The TE sample packets were included in the 10^{18} and 10^{19} n/cm^2 fluence capsules. Examples of the two capsule configurations are shown in Figures 1 and 2. For the capsules containing the TE sample packets, the thicknesses of the HTS support bars are reduced in order to accommodate a middle packet containing the TE materials. In both irradiation capsule-loading schemes, Mo-springs are inserted between the sample packets to hold the packets up against the internal wall of the irradiation capsules. This ensures the lowest possible irradiation temperature for the HTS materials. SiC thermometry is included in the capsules in various positions. The irradiations were performed during HFIR cycle 456, in October 2014. The actual fluences based on the recorded time within the core and position for the four capsules during the irradiation resulted in fluences of $6.54x10^{17}$, $1.30x10^{18}$, $7.00x10^{18}$ and $1.12x10^{19}$ n/cm^2 (E>0.1MeV).

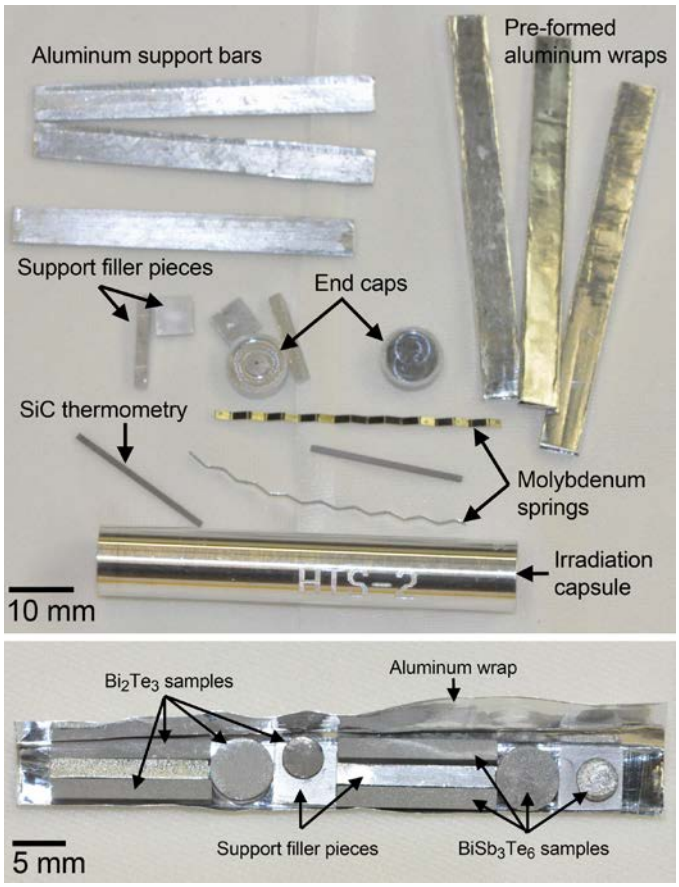

Figure 2. Internal components of the HTS-2 capsule (1.05×10^{18} n/cm^2) containing HTS and TE samples. The HTS samples (not shown) are placed on the long aluminum support bars and then wrapped in the pre-formed aluminum sheet. The lower image shows the configuration of the TE samples included in two of the irradiation capsules.

The high purity aluminum packets containing the HTS samples were unloaded from the rabbit capsules in January 2015. The capsules were dry cut at the Irradiated Materials Examination and Testing (IMET) facility. The packets were then removed from the irradiation capsules and placed in paper tubes containing desiccant and loaded into shielded containers with additional desiccant and sealed in plastic bags. Final sample unloading from the packets was performed in the Low Activation Materials Development and Analysis (LAMDA) laboratory at ORNL. Due to high removable contamination levels of Sb-124 on the high dose HTS packets, produced from a degraded $BiSb_3Te_6$ thermoelectric sample in the adjacent packet, the high dose HTS packets cannot be safely disassembled until October 2015 when activity levels degrade to manageable levels. However, as will be shown, degradation in the HTS samples from neutron irradiation occurs below 1.12×10^{19} n/cm^2.

Field-oriented dependence of the critical current (I_c) at 0.5 Tesla and 77 K was tested for the irradiated HTS samples as well as I_c versus field for applied fields parallel to the ab plane of the films up to 1 Tesla. Before the irradiation, all the YBCO films were patterned into a strip configuration (removing the silver "shunt" overlayer in the process) with silver contact pads and a 1-mm-long bridge with a width of either 1.00 mm or 0.200 mm, using a focused-electron-beam scribing system. Prior to post-irradiation electrical testing a strip of indium was applied to the silver pads at pressed copper injection areas of the probe contact points, which limited the electrical contact resistance to between ~ 10^{-6} and 10^{-4} Ω.

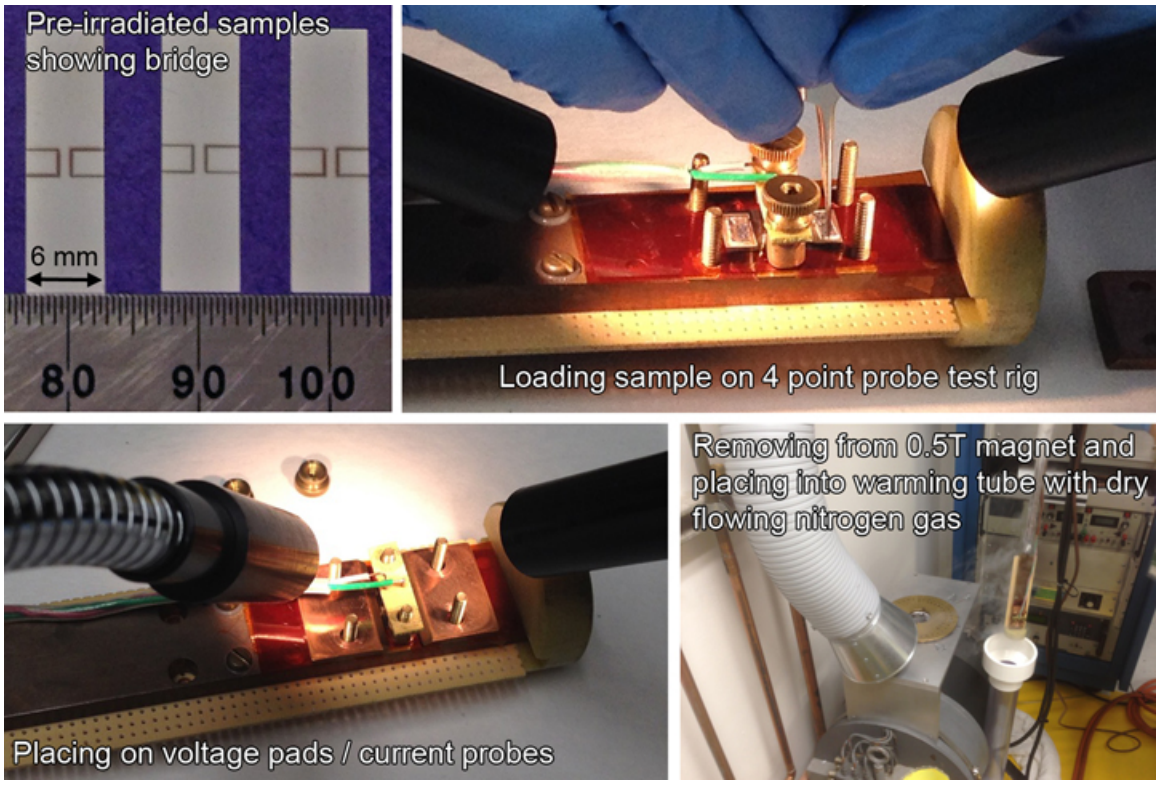

Figure 3. Various illustrated stages during testing of the neutron irradiated HTS samples.

Results and Discussion

Two tapes each of the Zr-(Gd,Y)$Ba_2Cu_3O_7$ and (Dy,Y)$Ba_2Cu_3O_7$ materials (Zr-YBCO and DyBCO from herein), were tested for the $6.54x10^{17}$, $1.30x10^{18}$ and $7.00x10^{18}$ n/cm^2 (E>0.1MeV) irradiation conditions. The results for each irradiated tape was compared to the pre-irradiation characterization data. Very little difference was observed between the pre-irradiated electrical property data for the samples of a given material type. The post-irradiation data was also consistent between the two HTS samples of a given materials type for each irradiation condition. Therefore, repeatability in the experiment was found to be good with no extraneous results.

A summary of the data for the DyBCO tapes is presented in Figure 4, which shows the pre- and post-irradiation angular dependence of I_c at 0.5T and 77 K and I_c as a function of applied magnetic field (□=90° at 77K).

The DyBCO tapes showed a gradual loss in transport current with irradiation dose. While testing of the $1.12x10^{19}$ n/cm^2 dose samples could not be completed as previous discussed, transport currents are expected to be even lower and may not be able to be effectively measured. Loss in the I_c curve as a function of applied field may cross the pre-irradiation values at fields much greater than those tested, as was observed in the samples ion irradiated in previous tests [1,2]. The loss in the I_c with dose is likely attributed to defect generation within the 123-structured matrix of the film. This is most likely in the form of amorphous regions initiating at fluences lower than that of those conditions tested, with the amorphous regions growing and eventually restricting current flow. Based on the consistency in the shape of the angular dependence curves, it is not expected that a significant change has occurred to the size, shape and distribution of the nanoparticle Dy_2O_3 particles within the conductor film.

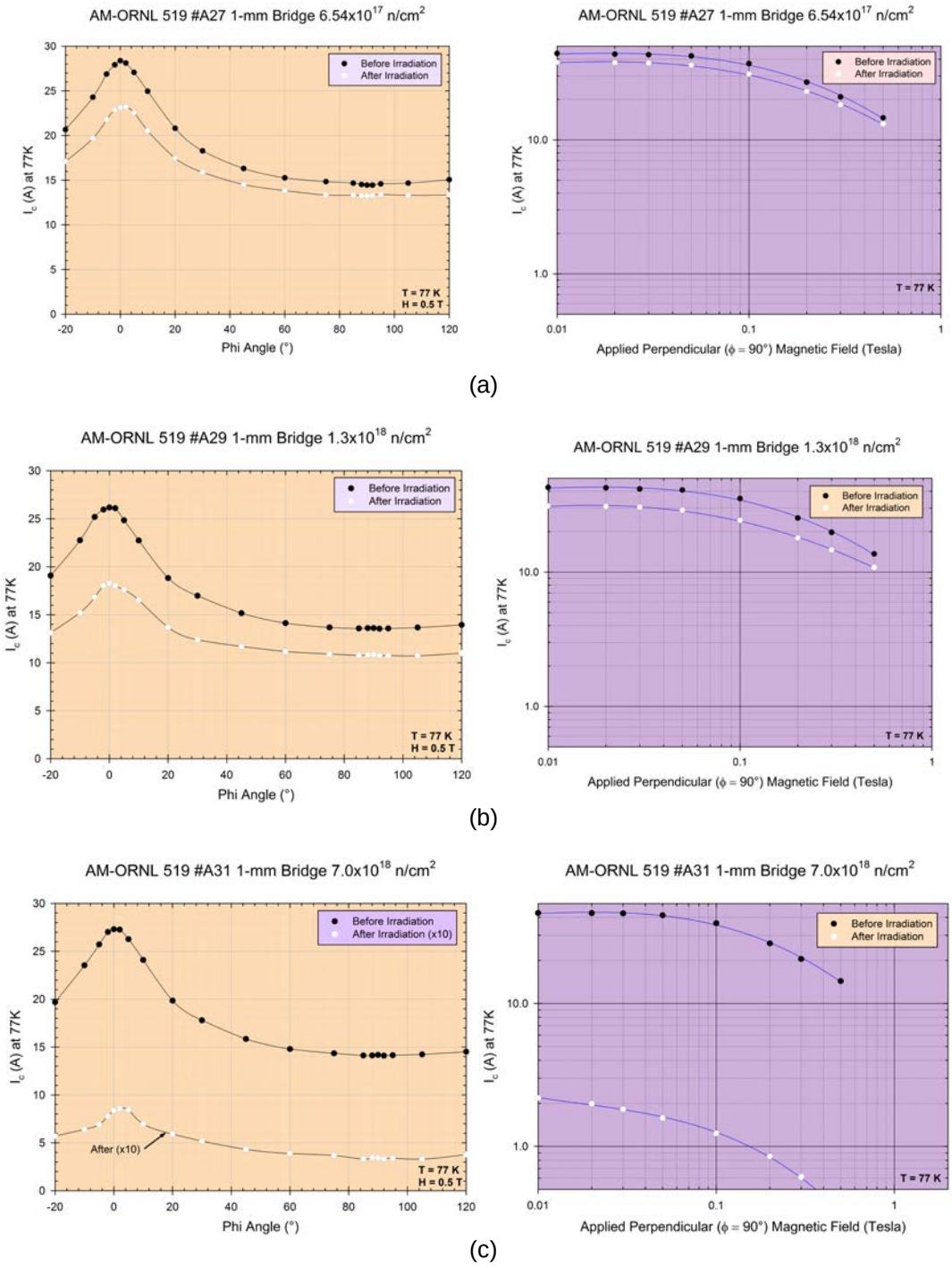

Figure 4. Pre- and post-irradiation values of I_c as a function of applied field direction and magnitude up to 0.5 Tesla, tested at 77 K for the $(Dy,Y)Ba_2Cu_3O_7$ conductor. (a) $6.54x10^{17}$, (b) $1.30x10^{18}$ and (c) $7.00x10^{18}$ n/cm^2 (E>0.1MeV).

The post-irradiation data for the Zr-YBCO could only be measured for the $6.5x10^{17}$ n/cm^2 irradiated material, as transport currents for the higher dose samples were below detection level of the instrumentation used in the lab. The data for the two Zr-YBCO samples from the HTS-1 capsule are shown in Figure 5. The shape of the angular field dependence curves for the Zr-YBCO samples suggests

a significant change in the distribution of the $BaZrO_3$ nanoparticles within the conductor. The I_c loss near ϕ=90° measurement, suggests the loss of c-axis nanoparticle alignment within the material.

Improvements in flux pinning through irradiation-induced defect creation has been seen in YBCO through ion [1-6], proton [7-8], electron [9-12], and neutron [13-23] irradiation. Increases in critical current density (J_c) have been generally measured following neutron irradiation to fluences > $1x10^{16}$ n/cm^2 (E>0.1 MeV) and peak around 0.6-$1x10^{18}$ n/cm^2. Increases in the irradiated J_c over unirradiated values $\left(J_c^{irrad}/J_c^{unirr}\right)$ are between 2 to 4 times for YBCO irradiated to $4.4x10^{21}$ n/m^2 (E>0.1 MeV) for measurements between 50 and 77 K [18]. By comparison, increased critical current values of Nb_3Sn are approximately 1.5 times unirradiated values following 14 MeV neutron irradiation to $1.78x10^{17}$ n/cm^2 [24]. The decreased sensitivity of J_c is in-part due to the larger coherency length (ξ) of Nb_3Sn than YBCO (3 nm versus 1.5 nm at 0 K [25]), which reduces the net effect of the elementary pinning force of the defects.

The lack of improvement in transport properties of the neutron irradiated conductors of this study, may be due to several factors, some of which are currently being examined. However, improvements in I_c may have occurred at fluences below that which was tested. A fluence of ~ $5x10^{17}$ n/cm^2 is the lowest achievable using the HFIR hydraulic port facility without increased uncertainties related to accurate recording of dwell time within the core due to the high nominal flux (1-$2x10^{15}$ n/cm^{2}s). Other port locations can provide lower flux conditions, but increases complexity of the experiment as well as costs. The magnitude increase in J_c following irradiation is also highly sample dependent, with variations in literature data attributed to sample defect conditions prior to irradiation [19] or to secondary phases present in the YBCO [23]. For effective flux pinning, the defect size must be around the coherency length, which is dependent on temperature [4]. The small coherence length in YBCO, makes point defects effective at pinning of vortices [25]. Small pre-irradiation defects may not contribute to pinning at higher test temperatures (near 77 K), while larger defects are efficient pinning sites at higher temperatures and lower fields [18]. Therefore, effective pinning from neutron induced defects or changes to pre-existing defects may not be observed even within the lower exposure doses due to the higher post-irradiation characterization temperatures used in this study. Furthermore, the presence of non-conducting nanoparticles that are intentionally added to improve in-field transport properties of the conductors may result a more rapid reduction in the viable superconducting pathway for current as radiation-induced amorphization of the conductor occurs with dose.

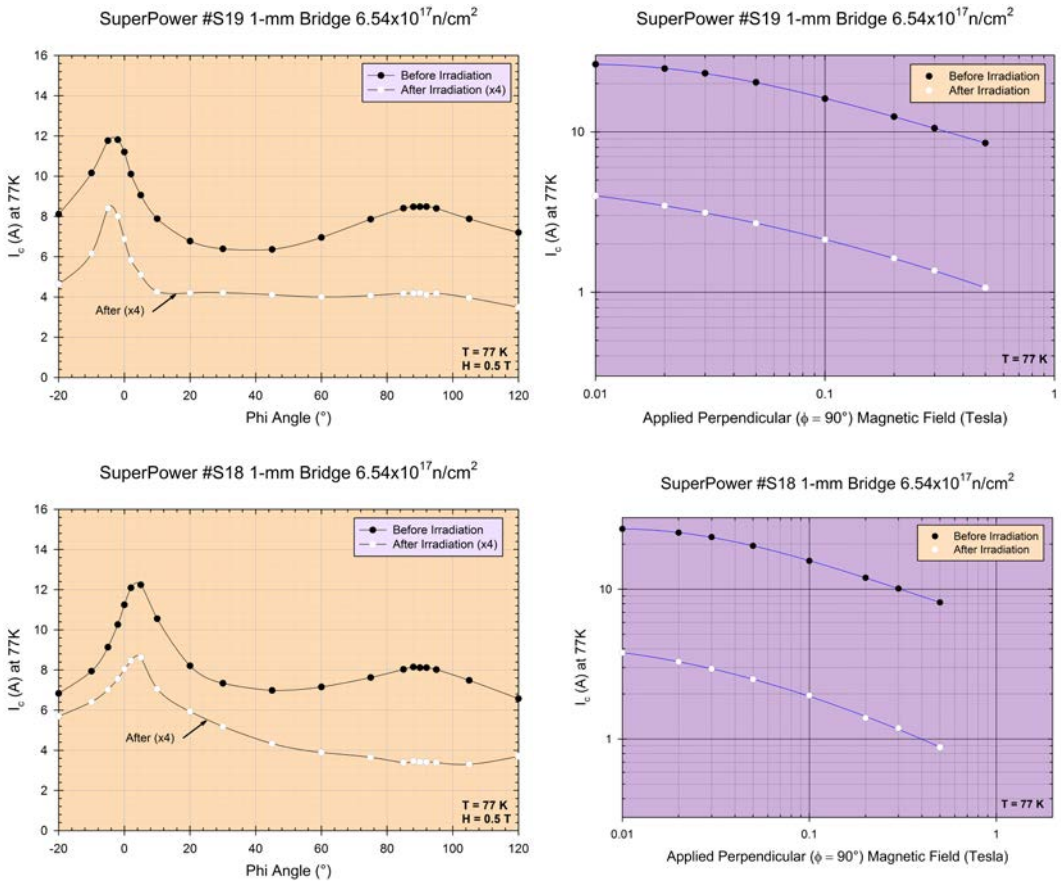

Figure 5. Pre- and post-irradiation values of I_c as a function of applied field direction and magnitude up to 0.5 Tesla, tested at 77 K for the two Zr-(Gd,Y)$Ba_2Cu_3O_7$ conductors exposed to $6.54x10^{17}$ n/cm^2 (E>0.1MeV). Transport currents were too low to be effectively measured for neutron exposures to higher fluence.

Future Plans

The next step in analyzing the neutron irradiated Zr-(Gd,Y)$Ba_2Cu_3O_7$ and (Dy,Y)$Ba_2Cu_3O_7$ tapes will involve microstructural characterization. Transmission electron microscopy specimens have been prepared through focused ion beam milling of the two HTS materials exposed to $6.5x10^{17}$ n/cm^2. The higher dose materials will also be examined. Further analysis of the ion irradiated samples from previous work is also planned for the final comparison of microstructural evolution under irradiation.

References

[1] K.J. Leonard, T. Aytug, A.A. Gapud, F.A. List III, N.T. Greenwood, Y. Zhang, A.G. Perez-Bergquist, W.J. Weber and M.W. Rupich, "Irradiation Response of Next Generation High Temperature Superconductors for Fusion Energy Applications", *Fusion Sci. and Techn.,* 66, 1 (2014) 57.

[2] A.A. Gapud, N.T. Greenwood, J.A. Alexander, A. Khan, K.J. Leonard, T. Aytug, F.A. List III, M. Rupich and Y. Zhang, "Irradiation of Commercial, High T_c Superconducting Tape for Potential Fusion Applications: Electromagnetic Transport Properties", *J. Nucl. Mater*. 462 (2015) 108.

[3] J.R. Liu, J. Kulik, Y.J. Zhao and W.K. Chu, *Nucl. Instr. and Meth. In Phys. Res. Section B,* 80, 2 (1993) 1255-1258.

[4] L. Civale, *Superconductor Sci. and Techn.,* 10, 7A (1997) A11-A28.

[5] T. Sueyoshi, et al., *Physica C*, 424, 3-4 (2005) 153-158.
[6] N.M. Strickland, et al., in Adv. Mater. and Nanotechnology, AIP Conference Proceedings, 1151, eds. S.C. Hendy and I.W.M. Brown, (2009) 82-85.
[7] T.J. Shaw, J. Clarke, R.B. vanDover, L.F. Schneemeyer and A.E. White, *Physical Rev B*, 54, 21 (1996) 15411-15416.
[8] Y.L. Zhao, W.K. Chu, M.F. Dais, J.C. Wolfe, S.C. Deshmukh, D.J. Economou, A. McGuire, *Physica C*, 184, 1-3 (1991) 144-148.
[9] P.H. Hor, et al, *Physica C*, 185, 4 (1991) 2311-2312.
[10] M.H. Abdullah and K. Shiraishi, *Solid State Communications*, 86, 2 (1993) 109-112.
[11] J.Y. Lin, M. Gurvitch, S.K. Tolpygo, A. Bourdillon, S.Y. Hou and J.M. Philips, *Physical Review B*, 54, 18 (1996) 12717-12720.
[12] R. Rangel, D.H. Galvan, G.A. Hirata, E. Adem, F. Marales, M.B. Maple, *Supercond. Sci. Techn*., 12, 5 (999) 264-269.
[13] H.W. Weber, *Physica C*, 185-189 (1991) 309-314.
[14] P.X. Zhang, et al., *Physica C*, 282-287 (1997) 1607-1608.
[15] F. Vasiliu, V. Sandu, P. Nita, S. Popa, E. Cimpoiasu, and M.C. Bunescu, *Physica C*, 303 (1998) 209-219.
[16] D.V. Kulikov, Y.V. Trushin, F.M. Sauerzopf, M. Zehetmayer and H.W. Weber, *Physica C*, 355 (2001) 245-250.
[17] U. Topal, H. Sozeri, and H. Yavuz, *Physica C*, 408-410 (2004) 636-637.
[18] U. Topal, L. Dorosinskii and H. Sozeri, *Physica C*, 407 (2004) 49-54.
[19] V. Sandu, S. Popa, E. Sandu, D. DiGioacchino, and P. Tripodi, J*. of Optoelectronics and Adv. Materials*, 8, 1 (2006) 391-395.
[20] S. Shojaei, R. Khoda-Bakhsh and H. Sedgi, *J. Supercond. Nov. Magn*, 24 (2008) 387-390.
[21] R. Fuger, M. Esterer, H.W. Weber, *IEEE Trans. on Appl. Supercond*., 19, 3 (2009) 1532-1535.
[22] M. Chudy, R. Fuger, M. Eisterer and H.W. Weber, *IEEE Trans. on Appl. Supercond*., 21, 3 (2011) 3162-3165.
[23] J. Veternikova, M Chudy, V. Slugen, M. Eisterer, H.W. Weber, S. Sojak, M. Petriska, R. Hinca, J. Degmova, and V. Sabelova, *J. Fusion Energ*., published on-line June 9, 2011.
[24] A. Nishimura, T. Takeuchi, S. Nishijima, G. Nishijima, T. Shikama, K. Ochiai, and N. Koizumi, *Fusion Eng. and Design*, 84 (2009) 1425-1428.
[25] D. Larbalestier, A. Gurevich, D.M. Feldmann and A. Polyanski, *Nature*, 414 (2001) 368-377.

6.1 LIQUID METAL COMPATIBILITY — S. J. Pawel (Oak Ridge National Laboratory)

OBJECTIVE

The objective of this task is to identify potential structural materials having sufficient compatibility with flowing Pb-Li eutectic that the maximum metal temperature for operation can be increased to improve overall system efficiency.

SUMMARY

Operation of the first thermal convection loop (TCL) using dispersion strengthened FeCrAl (Kanthal APMT) tubing and specimens utilized commercially pure eutectic Pb-17at%Li, and both the peak temperature (550˚C) and temperature gradient (116˚C) were maintained without interruption for 1000 h. The previous report documented limited but somewhat irregular weight change of loop specimens as a function of exposure temperature, with the observation that a pre-oxidation process substantially improved compatibility with the Pb-Li over the exposure period. Further, post-exposure mechanical property data indicated a large increase in strength with concomitant loss of ductility for APMT specimens exposed at or below about 475-500˚C in the TCL. In this reporting period, analysis of TCL specimen cross sections for composition gradients and follow-up tests to examine mechanical properties of APMT exposed for 1000 h in argon (rather than Pb-Li) is documented.

PROGRESS AND STATUS

Introduction

Currently, the maximum allowable wall temperature for the dual coolant lead-lithium (DCLL) blanket concept is set at 475˚C based primarily on corrosion limitations of the structural containment materials. To increase overall system efficiency, potential structural materials are being sought with a combination of high strength and creep resistance with simultaneous resistance to dissolution in eutectic Pb-Li at temperatures > 500˚C. Preliminary research using static capsule exposures has indicated that dispersion strengthened FeCrAl (Kanthal APMT) may be resistant to dissolution in eutectic Pb-Li at temperatures in the range of 600-800˚C, at least in part due to the stability of an Al-rich oxide film.

Kanthal APMT is an iron-based alloy produced by a powder metallurgy process and generically contains about 21% Cr, 3% Mo, 0.2% Cu, and 5% Al. This alloy does not possess the physical/mechanical properties required for fusion materials service and is not being considered as a candidate alloy, but it is available in tubing and several other forms necessary to fabricate a thermal convection loop (TCL) and was evaluated in the experiment described here as a surrogate for more appropriate materials under development but not yet readily available. While previous compatibility data for APMT in static capsules containing Pb-Li are encouraging, corrosion data in a flowing system must be generated to analyze the potential for issues associated with thermal gradient mass transfer – that is, relatively high dissolution in hotter portions of the flow system with concomitant deposition in the colder portions – which has been known to disrupt heat transfer and even plug flow paths completely in some temperature gradient/material combinations. Thus, TCLs are being incorporated as the follow-on step to capsule testing for evaluation of liquid metal compatibility.

Results

Cross-section element maps developed via energy-dispersive x-ray (EDX) analysis for two specimens exposed in the hot leg are shown in Figure 1. The maps reveal the qualitative concentration of the indicated element corresponding to the analysis area, which is shown in the upper left in each set of six photos (denoted “SE” for secondary electron image). The relative concentration of each element is suggested by the relative black/white intensity in the photograph, with relatively bright white indicating higher concentrations and lesser amounts indicated by darker shading.

One specimen – exposed at 474.5˚C near the bottom of the hot leg – represents the results for all the specimens that received the pre-exposure oxidation treatment (8 h at 1050˚C in air) intended to form a continuous alumina film. The weight loss for this particular specimen was very low which, with only rare exception for specimens exposed up to the peak temperature of 550˚C, was the trend observed for all specimens receiving the pre-oxidation treatment. As suggested by Figure 1, this specimen retains an aluminum oxide film over most of the surface, which is shown by the very high concentration of Al and O on the surface in a band (bright white) about 1-2 μm thick. Note that Cr – a typical component of passive films on many grades of stainless steels – is not present in the oxide film in significant amounts, and that there is no apparent composition gradient in the oxide film (indicating Pb or Li penetration or loss of Al) or in the parent metal below the oxide film (which would indicate selective leaching of primary alloy elements into the Pb-Li). Specimens exposed at other positions (temperatures) around the TCL exhibited identical patterns, although the continuity of the alumina film became more irregular as the exposure temperature increased, with the result that at the highest exposure temperatures, very little if any alumina film remained on the specimen surface.

The other specimen in Figure 1 – exposed at 538˚C with no oxidation treatment prior to exposure – exhibited a weight loss ~ 50 times that of the previously mentioned pre-oxidized specimen. The element maps (grey scale detection sensitivity not identical to that for the other specimen) indicate essentially a surface free of Cr- or Al-oxides and considerably more roughness than the pre-oxidized counterparts. The latter observation is consistent with irregular initiation of the dissolution process common to many alloys exposed to liquid metal environments. Even in the absence of a protective alumina film and with considerably higher weight loss than the pre-oxidized specimen, the element maps do not indicate composition gradients in the base metal at/near the specimen surface, which suggests uniform dissolution in Pb-Li.

Taken together, these results – in particular, the relative absence of the alumina film for pre-oxidized specimens exposed at the highest TCL temperatures – suggest that the alumina film on the APMT specimens is not completely stable in Pb-Li and perhaps dissolves slowly in Pb-Li with extended exposure time. That the film dissolves slowly is indicated by the large difference in weight losses for specimens with and without the pre-exposure oxidation treatment and the relative lack of surface roughness on originally pre-filmed specimens for which the film has apparently dissolved. No trace of another compound (for example, lithium aluminate) was found on the post-exposure specimens, suggesting either that any such compound formation is soluble or that the post-test cleaning procedure confounds detection of such a compound. That even the highest weight loss among these pre-oxidized specimens was only 2.2 mg/cm^2 (for the pre-oxidized specimen exposed at 512˚C; not at the highest loop temperature of 550˚C) corresponds to an average wastage rate of only ~ 25 μm/y suggests that the oxide film is relatively protective for extended periods and perhaps could be rendered even more protective via composition changes or alternate heat treatments.

Previous analysis of the APMT specimens exposed within the TCL revealed a substantial increase in tensile strength with a concomitant decrease in ductility for specimens exposed at or below about 490˚C; specimens exposed at higher temperatures revealed mechanical properties unchanged from the as-received material (with or without a pre-oxidation treatment). Post-exposure weight change data and metallographic examination of selected samples indicated very little interaction between APMT and Pb-Li at these temperatures, suggesting the cause of the change in mechanical properties was related to time-at-temperature effects as opposed to compatibility effects (for example, penetration of Pb or Li contributing to a precipitate within the APMT). To further consider this possibility, an experiment was conducted to examine potential mechanical property changes as a result of time-at-temperature in argon for comparison with the Pb-Li exposures. The results are summarized in Figure 2. Clearly, the change in mechanical properties with extended time-at-temperature below about 490˚C is independent of compatibility with Pb-Li, and appears consistent with something akin to “475˚C embrittlement” observed within some grades of stainless steels, which involves precipitation of brittle Cr- and/or Mo-rich phases throughout the structure. Selected specimens are being prepared for TEM examination to identify the constituent(s) responsible for this mechanical property anomaly.

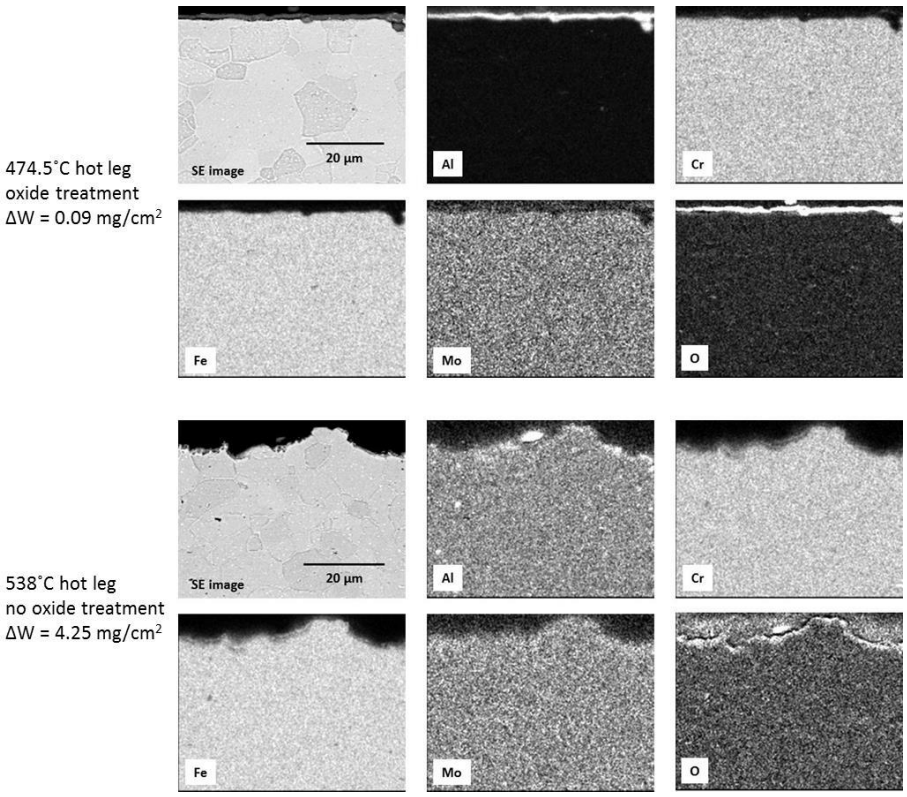

Figure 1. Element maps for major constituents of APMT made from specimens exposed in the hot leg of the TCL. Top series of photos (two rows of three) is for a specimen receiving the pre-oxidation treatment and subsequently exposed at 474.5˚C within the TCL; bottom series of photos (corresponding two rows of three) is for a specimen without the pre-exposure oxidation treatment exposed at 538˚C. Relative abundance of the specified element is indicated by relative light coloration; relative absence of the element indicated by relative darkness on the map.

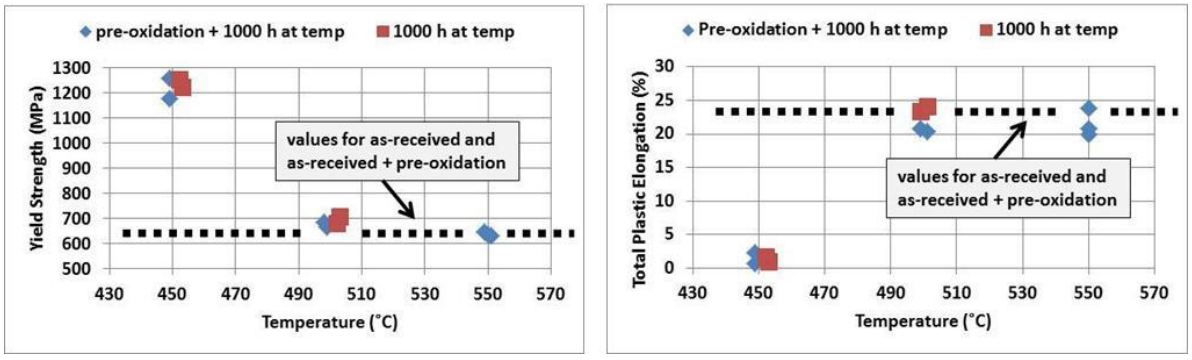

Figure 2. Room temperature yield strength (left) and total plastic elongation (right) for APMT specimens heat treated in argon for 1000 h at the indicated temperatures. [Actual treatment temperatures were 450, 500, and 550˚C; data staggered slightly on plot for ease of visualization.] The pre-oxidation treatment indicated was 8 h in air at 1050˚C, and in selected cases this treatment was performed prior to the subsequent heat treatment for 1000 h in argon. Tensile tests performed at room temperature following exposure in the TCL.

Future plans include completion of the fabrication process for two additional APMT thermal convection loops with attendant specimens and components. It is anticipated that the next TCL will be operated similarly to the prior experiment (1000 h duration, ~ 116˚C temperature gradient) except that all temperatures around the loop will be raised by 50˚C.

7.1 MORPHOLOGY AND MECHANICAL PROPERTIES OF COMMERCIAL $M_{n+1}AX_n$ PHASES UNDER NEUTRON IRRADIATION — C.Ang, A. Campbell, N. Cetiner, C. Silva, C. Shih, Y. Katoh, S.J. Zinkle (Oak Ridge National Laboratory, USA), T. Toyama, T. Shikama (Tohoku University, Japan)

OBJECTIVE

$M_{n+1}AX_n$ (MAX) phases are potential candidates for future nuclear applications due to their potentially unique radiation tolerance. The present work evaluates the effects of neutron irradiation on selected MAX phase materials at moderate (~2, 6 and 10 dpa) radiation doses.

SUMMARY

MAX phases ternary nitrides and carbides were previously characterized (DOE/ER-0313/55). These nominally "Ti_3SiC_2" and "Ti_2AlC" compositions were irradiated to 2 x 10^{25} n/m^2 (E > 0.1 MeV), ~ 2 dpa (SiC). Both materials (referred to as Ti-Si-C and Ti-Al-C) had impurities, including ~6 wt% uncarburized $Al_{11}Ti_5$ and $TiSi_2$ This report covers specimens in Capsules 1, 4 and 7 irradiated at target temperatures of 400, 700 and 1000°C. Mechanical properties of Ti-Al-C were severely degraded at low irradiation temperatures due to grain boundary microcracks attributed to anisotropic swelling. Ti-Si-C consistently maintained moderate strength. Electrical resistivity suggested that metallic Si and Al layers were disrupted at 400°C by point defect accumulation, which recovered in the irradiation temperature interval 400 to 700°C. Ti-Al-C mechanical properties recovered at ~700°C. Young's modulus appeared unaffected. Swelling was more consistent in Ti-Si-C. Conclusions from XRD data were limited, particularly for Ti-Al-C material.

PROGRESS AND STATUS

Introduction

The promise of hybrid metal-ceramic materials from $M_{n+1}AX_n$ (MAX) phases is of interest to engineering ceramics, particularly given the attractive reports of a reversible slip-based deformation mechanism, implying that catastrophic failure associated with brittle fracture could be mitigated or nullified.[1] The lamellar atomic structure of metallic "A-layer" metal atoms alternating between crystalline "MX" ceramic unit cells yield good machinability, thermal and electrical conductivity in addition to high temperature strength and possible ductility. The alternating layers represent an ultra-high density of nanoscale interfaces that may function as natural sinks for mitigating defect accumulation that is responsible for degradation of materials under irradiation.[2] Both Ti-Al-C and Ti-Si-C specimens were irradiated at the High Flux Isotope Reactor (HFIR) during 2013. After a period of cooling, investigation of mechanical properties (swelling, elastic modulus, fracture strength), morphology (microcracking, changes in interfaces) and microstructure (irradiation-induced defects, lattice expansion, phase changes) commenced. The acquired materials were adequate as a first screening to assess whether these MAX phases were suitable for further development.

Experimental Procedures

For details, see DOE/ER-0313/55.

Results

Irradiation temperature

The irradiation temperature was determined by SiC temperature monitors (TMs) inserted in the capsules. The technique identified the change in instantaneous coefficient of thermal expansion (CTE) once heating annealed the irradiation induced defects.[3] The SiC TMs in Capsules 1, 4 and 7 respectively reached irradiation temperatures 370°C (643K), 620°C (893K) and 640°C (910K). These temperatures were then correlated to individual specimens using thermal modeling using ANSYS 12.0. This can be seen in Figure 1.

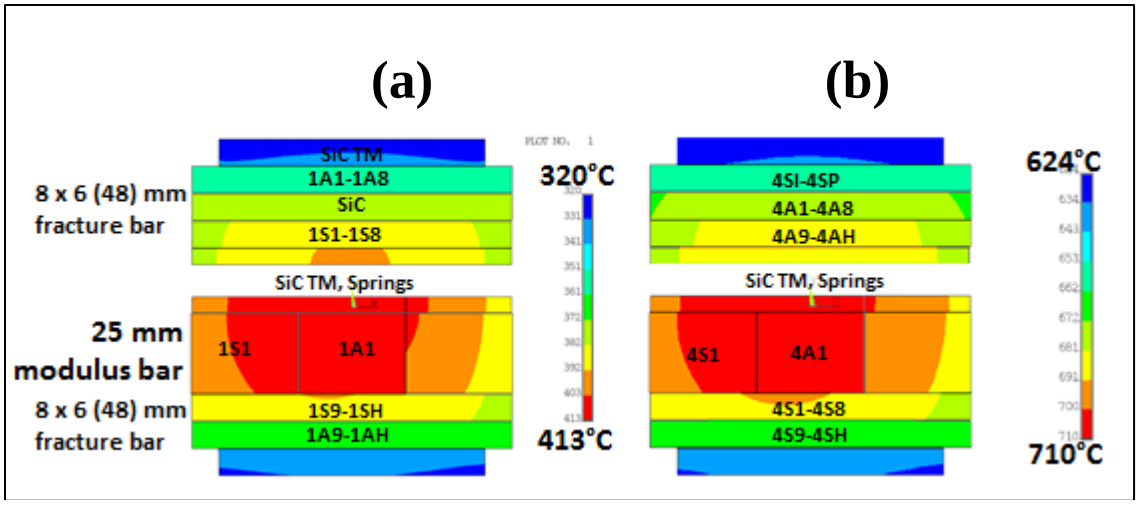

Figure 1. Specimen configuration for **(a)** Capsule 1 and **(b)** Capsule 4. Overlayed is a 2D thermal modelling showing respective temperature distributions as viewed from the end of the capsule where the modulus bars were inserted.

For convenience, the same color map was used for both Capsules 4 and 7. Since the intervals in color mapping in Figure 1 were ~10°C, and the TMs are deconvoluted to ±15°C, a value of ±25°C was used as the range of possible error for the irradiation temperature in parenthesis.

Scanning electron microscopy (SEM)

Figure 2(a) and (b) show the morphology of the as-received material after machining, polished to 40 nm OP-S. A Back-Scatter Electron (BSE) detector was used to show Z-atomic contrast to assist limited phase identification. In (a), the Ti-Al-C grains were anisotropic and up to 50 μm in length due to preferential a-axis growth. Due to an incomplete reaction, material contained an estimated Ti_3AlC_2 (43 wt%) Ti_2AlC (34 wt%) $Ti_5Al_2C_3$ (16 wt%) by XRD. These phases are indistinguishable by SEM, however, attempts to select grains using Electron Back Scatter Diffraction (EBSD) are currently in progress. In Figure 2(b), the Ti-Si-C shows an identical morphology but has a finer grain size and dispersed intergranular particles and TiC is observed as the brighter, equiaxed, dispersed intergranular particles. An alumina intergranular phase was also noted in the report, and can be seen by the bright contrast and low contact angle. This is likely from contamination of milling media. In both materials, an intermetallic Ti_5Al_{11} (6.4 wt%) or $TiSi_2$ (5.7 wt%) phase was observed. For further details, see DOE/ER-0313/55.

Recovered specimens from Capsules 1, 4 and 7 were polished to 1 μm finish. Figure 2(c) shows the neutron irradiated Ti-Al-C material, with an irradiation temperature (see Figure 1(a)) of 401(25)°C. Extensive transgranular and minor intergranular cracking through the material was observed. Figure 2(d) shows that Ti-Si-C irradiated at a temperature of 435(25)°C showed no differences in morphology. Microscopy is continuing.

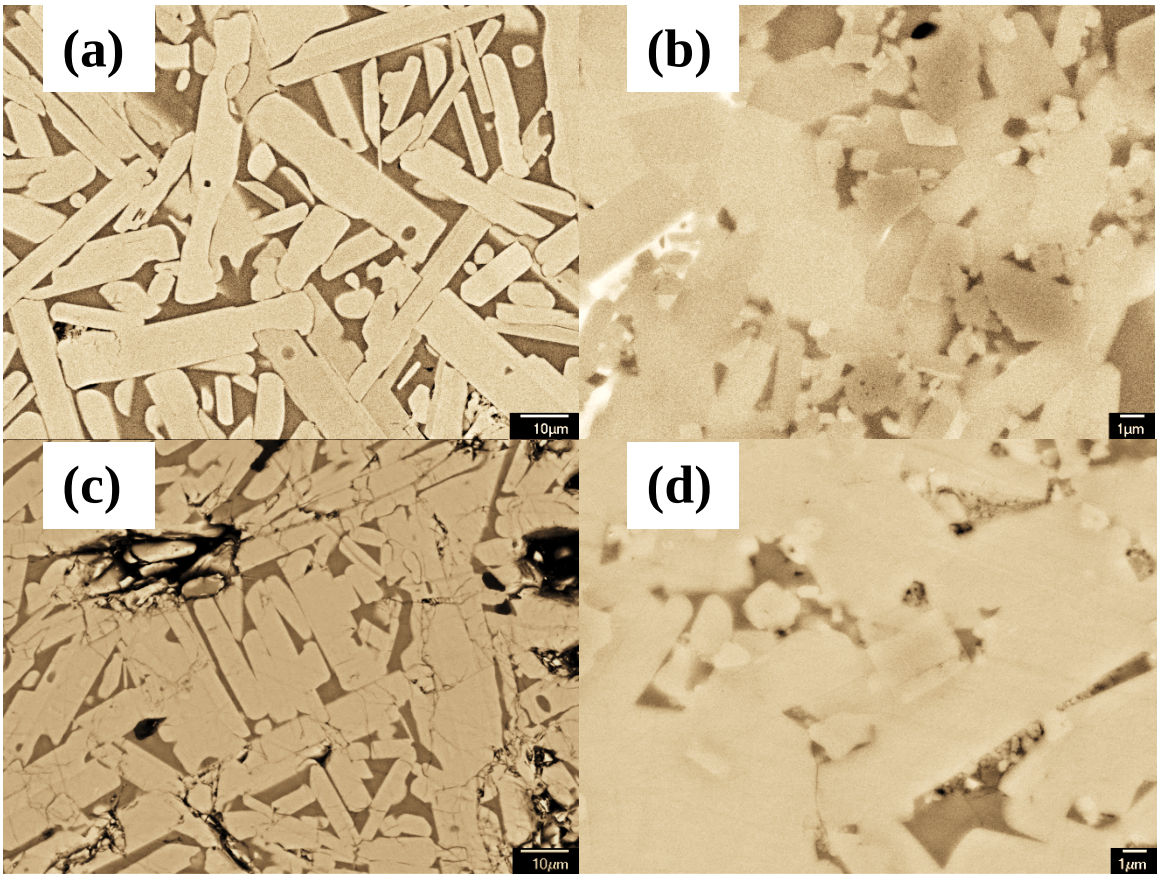

Figure 2. (a) SEM image of as-machined and polished Ti-Al-C (b) Ti-Si-C. Post-irradiation SEM images of (c) Ti-Al-C and (d) Ti-Si-C.

Swelling and density

Figure 3(a) shows the volumetric swelling measured from the modulus bars. It can be deduced that Ti-Si-C swelling of 0.8%, 0.9% and 1.5% for Capsules 1, 4 and 7 is more consistent than Ti-Al-C, which experienced variations in volumetric swelling from 4.0%, -0.4% and 1.65% at the respective temperatures. In Ti-Al-C material, the increase of 2% swelling from Capsule 4 (705°C) to Capsule 7 (725°C) may be caused by errors in swelling measurement or phase transformation during irradiation. Figure 3(b) shows the density measurements of the samples, which were in agreement with the swelling in Figure 3(a). Archimedes density on specimens using ASTM B962 used a proprietary 3M Fluorinet Liquid FC-43 as the suspension and immersion medium. The only anomalous result was Ti-Al-C Capsule 1, where the increase in volumetric swelling is accompanied by an *increase* in density, followed by a return to as-received values.

In Ti-Si-C, the trend of decreasing density was consistent with increasing volumetric swelling. Interestingly, Figure 3 shows that at ~700°C irradiation temperature, both materials show a decrease in density and increase in swelling. Further density measurements are to follow.

Phase analysis (XRD)

Rietveld analysis of XRD data was conducted using GSAS™ and CrystalDiffract™ Suite. Crystallite size and strain were calculated by Williamson-Hall method. The refinement was adequate for Ti-Si-C. The major phase of Ti_3SiC_2 (ICSD-180419) was identified in all samples, with a minor phase identified as TiC (ICSD-5910091). There were minor peaks in the XRD patterns that were not properly identified. The quantity of Ti_3SiC_2 decreases after irradiation by ~10 wt% relative to the TiC phase. The TiC unit cell expands isotropically; in Ti_3SiC_2 an expansion of the crystal structure occurs via a proportional elongation

of the c-axis by 1.0% and corresponding shrinkage of the a-axis. At higher irradiation temperatures, the TiC content and lattice parameters of both phases return to as received values.

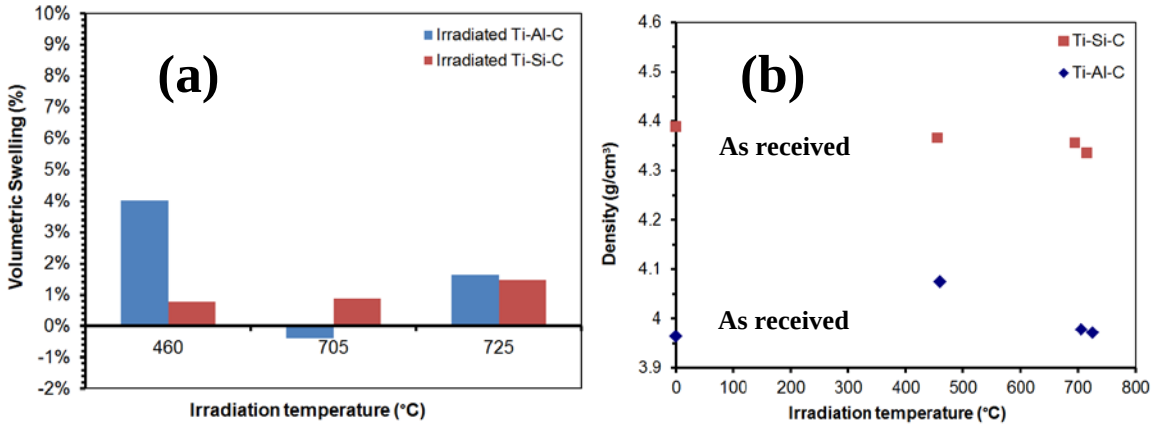

Figure 3. (a) Volumetric swelling on MAX phase materials compared to specimen original dimensions **(b)** Density of specimens after irradiation (compared to "As received").

The analysis of Ti-Al-C material should be considered qualitative. Ti_2AlC and Ti_3AlC_2 possess identical space groups, resulting in peak overlap. By selecting to model with Ti_3AlC_2, it obviously ignores Ti_2AlC and $Ti_5Al_2C_3$ in the pattern fitting. It has been reported that TiC was found upon decomposition of Ti_3AlC_2 and Ti_2AlC materials under low neutron doses, indicating that the absence of Al layer results in de-twinning to a Ti-C material; additional work by Patel et al suggests that a Ti_3C_2 structure forms but no ICSD database file exists to fit a Rietveld model.[4, 5] The relative weight of Ti_3AlC_2 (or more precisely the "MAX phases") decreases by 5 wt% after irradiation and TiC content increased. An expansion of the crystal structure occurs via a proportional elongation of the c-axis by 1.0% and shrinkage of the a-axis after irradiation in Capsule 1. This is significantly less than ~1.7% reported by Tallman et al for Ti_3AlC_2 at a lower neutron dose of 0.1 dpa, but recall that Ti_2AlC c-axis expansion was ~1%[4]. Given the composition of the Ti-Al-C material, these values are reasonable. In cross-referencing Figure 3(a), this indicates the majority of the swelling is from microcracks. In both materials, low temperature irradiation yielded a drop in crystallite size, MAX phase content and increase in microstrain; at higher irradiation temperatures, microstrain values decreased and MAX phase content increased.

Electrical resistivity

Electrical resistivity ($\times 10^{-7}$ Ωm) values for as-received materials were 4.8 and 2.7 for Ti-Al-C and Ti-Si-C respectively. Room temperature resistivity increased after irradiation in Capsule 1 to a high value of 56 for Ti-Al-C and 9.3 for Ti-Si-C. The results are plotted in Figure 4.

Since electrical conductivity is primarily from the metal "A" layers in the MAX phase, this is suggestive of defects in the Si/Al layer. When compared to phase pure materials from Drexel University, it appears from Figure 4(a) that for Ti-Al-C, the 211 phase maintains electrical conductivity better than the 312 phase after irradiation.[4]

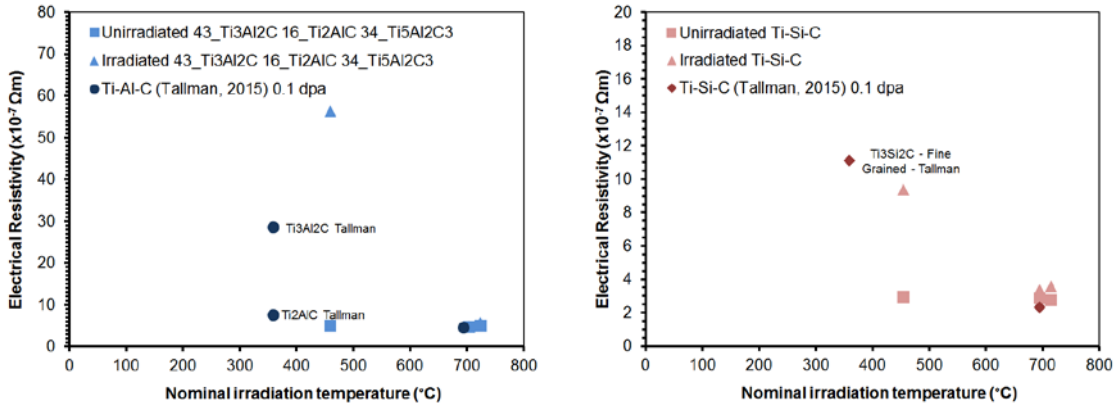

Figure 4. Electrical resistivity data for **(a)** Ti-Al-C material and **(b)** Ti-Si-C (nominally Ti_3SiC_2) compared with published data.[4] FG Ti_3SiC_2 is equivalent to ORNL Ti-Si-C.

Mechanical properties

The Dynamic Young's (E_y) modulus was measured for individual specimens. The average values across all as-machined specimens was 313.4(6.2) GPa for Ti-Si-C and 250.8(6.5) GPa for Ti-Al-C. The six specimens with their pre- and post-irradiation conditions are shown in Figure 5(a) and (b). The Capsule 1, 4 and 7 temperatures for the modulus bars were respectively 460(25), 705(25) and 725(25)°C. For the Ti-Al-C in Capsule 1, the E_y dropped from 241±3.2 GPa to 202±2.2 GPa. After irradiation in Capsule 4, the pre-irradiated value of 254 GPa matched the post-irradiation value of 257±1.0 GPa. With only a slight increase in irradiation temperature in Capsule 7, modulus abruptly decreased from 285 GPa to 214±0.2 GPa.

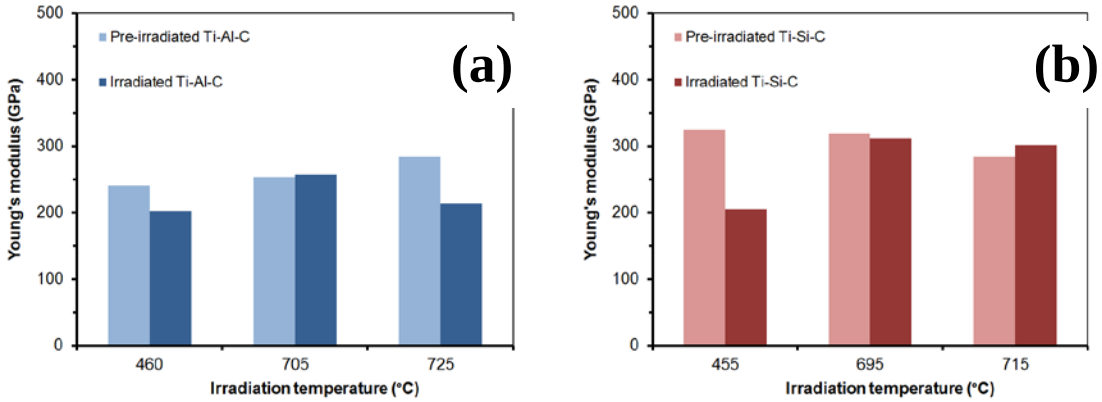

Figure 5. Elastic modulus individual 25 mm modulus bars of **(a)** Ti-Al-C **(b)** Ti-Si-C before and after irradiation at ~2 dpa.

In Ti-Si-C material (Figure 5(b)), irradiation in Capsule 1 reduced the modulus from 325 GPa to 205(6) GPa. In Capsule 4, the specimen appeared unaffected, with a pre-irradiated value of 319 GPa and 312(1) GPa. Finally, after Capsule 7 conditions, the modulus increased slightly from 285 GPa to 302(0.8) GPa.

Equibiaxial ring-on-ring fracture strength was measured according to ASTM C1499 using multipurpose square discs at room temperature. Table 1 shows the results. After irradiation in Capsule 1, Ti-Al-C tested at room temperature showed a loss of equibiaxial flexural strength as shown in Table 1, from 308(16) MPa on 31 specimens to 28(5) MPa based on the two selected specimens. Tests on single specimens recovered from Capsules 4 and 7 at the higher irradiation temperature shows that strength is maintained

at ~300 MPa. Ti-Si-C shows a small decrease in strength after irradiation in Capsule 1 and recovers to unirradiated values in Capsules 4 and 7.

Table 1. Room temperature ring-on-ring fracture strength after irradiation at 2 dpa.

Material/ID	Corrected irradiation T (°C)	F (N)	t (mm)	σ_f (MPa)
Ti-Si-C (31 tests)	As purchased	-	-	444.8 (29.5)
Ti-Si-C 1S7, 1S8	370+67 = 437(25)°C	115	0.484	302 (6.0)
Ti-Si-C 4S2	620+62 = 682(25)°C	128	0.511	302.1
Ti-Si-C 7S8	640+66 = 706(25)°C	171	0.572	322.2
Ti-Al-C (31 tests)	As purchased	-	-	307.8 (15.8)
Ti-Al-C 1A7,1A8	370+46 = 416(20)°C	12.0	0.511	28 (5.3)
Ti-Al-C 4AA	620+62 = 682(25)°C	121	0.497	302.5
Ti-Al-C 7AH	640+53 = 693(25)°C	150	0.558	297.0

The key result was that the microcracking observed in Ti-Al-C at Capsule 1 results in a substantial loss of strength since cracking prevents continuous load transfer, apart from mechanical interlocking between anisotropic grains.

Conclusions

$M_{n+1}AX_n$ (MAX) phase materials exhibited reduced electrical conductivity and materials properties after irradiation, although defects responsible for these effects appeared to balance against dynamic interstitial migration between 460°C and 700°C. In Ti-Al-C, low temperature irradiation leads to accumulation of point defects, which appear to be removal of Al on the A-layer and reduction in electrical conductivity. This results in smaller crystallite size and increased microstrain, calculated to lead to ~ 1% anisotropic elongation of the unit cell c-axis, resulting in grain boundary cracks that contribute to substantial swelling and absence of mechanical strength. At higher irradiation temperatures, recovery of mechanical properties occurs. In Ti-Si-C, the same process appears to displace the Si on the A-layers, leading to reduced electrical conductivity, increased microstrain and reduced crystallite size, but no microcracking is observed. A minor reduction in strength of Ti-Si-C occurs and both materials maintain moderate strength at higher irradiation conditions. Microscopy and compilation of properties of $M_{n+1}AX_n$ (MAX) materials will continue. Additionally, specimens from irradiations to ~6 and ~10 dpa are waiting for activity decay (cooling) before evaluation.

Acknowledgements

The authors would like to thank Patricia Tedder, Brian Eckhart, Bill Comings, Jordan Couch, Michael McAllister and Felipe Mora. Particular thanks to Kenny Curtis for contamination control and activated materials handling. Research was sponsored by the Office of Fusion Energy Sciences, U.S. Department of Energy, under contract DE-AC05-00OR22725 with UT-Battelle, LLC.

References

[1] 1. M. W. Barsoum, T. Zhen, S. R. Kalidindi, M. Radovic, and A. Murugaiah, "Fully reversible, dislocation-based compressive deformation of Ti3SiC2 to 1 GPa," *Nat Mater,* 2[2] 107-11 (2003).

[2] 2. S. J. Zinkle and L. L. Snead, "Designing Radiation Resistance in Materials for Fusion Energy," *Annual Review of Materials Research,* 44[1] 241-67 (2014).

[3] 3. A. A. Campbell, W. D. Porter, Y. Katoh, and L. L. Snead, "Method for Analyzing Passive Silicon Carbide Thermometry with a Continuous Dilatometer to Determine Irradiation Temperature," *submitted to Journal of Nuclear Materials* (2015).

[4] 4. D. J. Tallman, E. N. Hoffman, E. a. N. Caspi, B. L. Garcia-Diaz, G. Kohse, R. L. Sindelar, and M. W. Barsoum, "Effect of neutron irradiation on select MAX phases," *Acta Mater.,* 85[0] 132-43 (2015).

[5] 5. M. K. Patel, D. J. Tallman, J. A. Valdez, J. Aguiar, O. Anderoglu, M. Tang, J. Griggs, E. G. Fu, Y. Q. Wang, and M. W. Barsoum, "Effect of helium irradiation on Ti3AlC2 at 500 degrees C," *Scr. Mater.,* 77 1-4 (2014).

7.2 ION IRRADIATION CHARACTERIZATION STUDIES OF MAX PHASE CERAMICS – D.W. Clark[1], S.J. Zinkle[1,2], M.K. Patel[1], C.M. Parish[2] ([1]University of Tennessee, Knoxville, [2]Oak Ridge National Laboratory)

OBJECTIVE

This report presents results of research aimed to characterize the radiation resistance of three leading-candidate MAX Phase materials using ion beam irradiation techniques.

SUMMARY

Ti_3AlC_2, Ti_2AlC and Ti_3SiC_2 MAX phase ceramics were irradiated with 5.8 MeV Ni ions to midrange doses of 10 and 30 dpa at 400 and 700°C. In all cases, the materials remain fully crystalline. X-ray diffraction and nanoindentation show anisotropic swelling and hardening in all materials, with Ti_3AlC_2 and Ti_2AlC exhibiting more pronounced property changes than Ti_3SiC_2. In all three materials there is little damage dependence on dose (suggesting saturation of radiation damage at levels below 10 dpa) and significantly less retained damage at higher temperatures. SEM surface analysis showed significant grain boundary cracking in the aluminum based MAX phase irradiated at 400°C. Ti_3AlC_2 and Ti_2AlC do not appear to be suitable for irradiation applications near 400°C whereas the Ti_3SiC_2 is overall more damage tolerant.

PROGRESS AND STATUS

Introduction

A promising but as yet unproven class of material known as MAX Phase Ceramics (or simply MAX Phases) represents a relatively new class of solids best described as *thermodynamically stable nanolaminates*. MAX Phases are a family of layered compounds with chemical formula $M_{n+1}AX_n$, where M is an early transition metal, A is an element from the IIIA or IVA groups, X is carbon or nitrogen, and *n = 1, 2*, or *3* [1-5]. The atomic stacking is based on a layered hexagonal close packed (HCP) crystal structure with alternating layers of close-packed M-atoms and X-atoms filling octahedral sites (comprising a formula identical to those found in the rock salt structure of MX binaries), and layers of pure A-group elements. Due to their unique crystal structure, MAX phases combine many attractive properties of both ceramics and metals. These properties include high temperature stability, high stiffness, good electrical and thermal conductivity, fracture toughness, thermal shock resistance, and machinability [1-5]. Certain MAX phases also promise good oxidation resistance and chemical compatibility [6]. While most of these materials physical properties have been documented, studies exploring the radiation properties the MAX phases have only recently begun.

Although radiation response mechanisms of the MAX phase ceramics are still relatively unexplored, some preliminary knowledge can be drawn from low dose, low temperature irradiation experiments that have been completed to date. The first and most basic conclusion is that the MAX phases are expected to follow physical and mechanical property change trends similar to those seen in traditional HCP ceramics. Secondly, previous experiments suggest that the MAX phases are generally resistant to amorphization up to relatively high doses (~25 dpa) following irradiation between 25°C and 500°C. This has been confirmed using selected area electron diffraction (SAED) and transmission electron microscopy (TEM) imaging techniques in Ti_3SiC_2 and Ti_3AlC_2 at ~25 dpa [4], and using SAED, TEM, x-ray diffraction (XRD), and nanoindentation for Ti_3SiC_2 at lower damage levels (~5 dpa) for multiple irradiation conditions between RT and 500°C. Based on these studies, amorphization is not expected to be an issue at relevant fusion reactor temperatures of ~300-1000 C [1, 7-14]. Additionally, there is no evidence of void formation in Ti_3SiC_2 and Ti_3AlC_2 up to 500°C and ~25 dpa [12], suggesting that vacancies are immobile below 500°C (or else void nucleation and growth is strongly suppressed). These two factors hint that 25°C and 500°C in MAX phases correspond to temperatures above recovery Stage I (onset for interstitial motion) and below recovery Stage III (onset for vacancy motion), respectively [15, 16]. Finally, X-ray diffraction, TEM and nanoindentation results suggest that the MAX phases have a positive correlation between temperature and radiation damage recovery. This is manifest in the decrease in crystalline lattice disorder and defects observed at higher irradiation temperature conditions by XRD and TEM [7, 9-

11, 17], as well as a pronounced decrease in nanoindentation hardness at higher irradiation temperatures [8, 14], again suggesting mobile interstitials and immobile vacancies ("point defect swelling" regime). Hence, it is hypothesized that the MAX phases may have substantial radiation resistance up to relatively high damage levels between 25 and 500˚C or higher.

Experimental Procedure

The MAX phase bulk samples used in this experiment were synthesized and provided by Darin Tallman at Drexel University; a detailed explanation of the synthesis and processing conditions is discussed elsewhere [18, 19]. The bulk samples were subsequently sectioned, cut into ~3 mm diameter disks, ground to ~0.6 mm, and polished using diamond lapping film and colloidal silica suspension on polishing cloth. After the final polishing, the 3 mm diameter disk samples had a nominal final thickness of 0.55 mm. The samples were irradiated to midrange doses of 10 and 30 displacements per atom, at temperatures of 400 and 700˚C, at the Texas A&M Accelerator Laboratory using 5.8 MeV Ni^{++} ions. The correlation between ion fluence and displacements per atom was determined using SRIM 2013, recommendations from Stoller [20], and an assumed atomic displacement energy of 30 eV. A graphic of normalized displacements per atom (dpa) versus ion penetration depth for all three materials can be seen in Figure 1, with the selected area for post-irradiation analysis defined by the red box. A list of irradiation conditions and corresponding fluences for the four batches can be seen in Table 1.

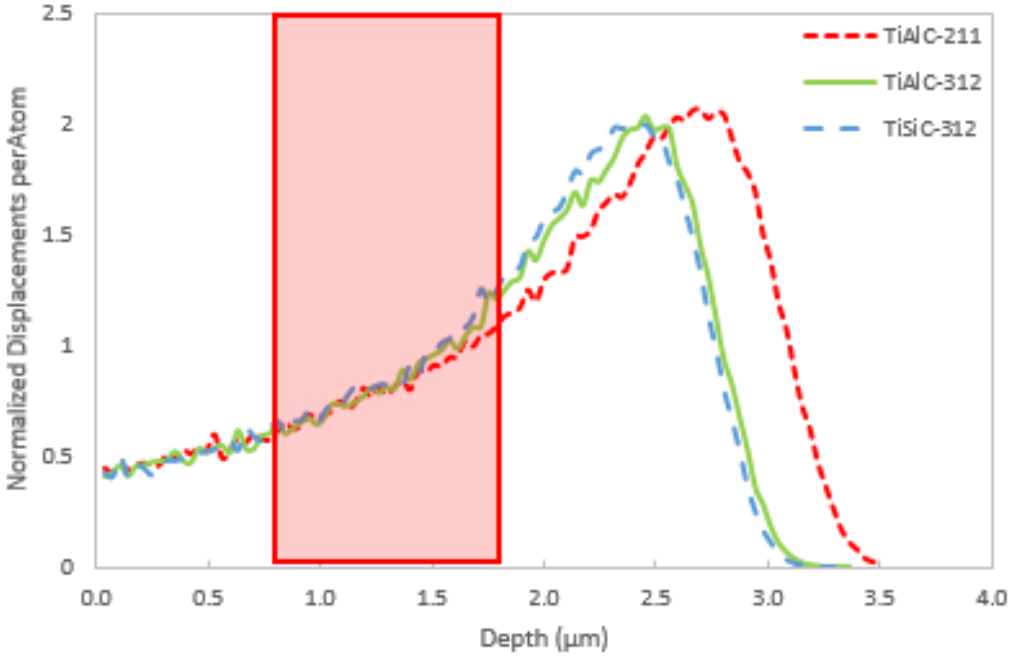

Figure 1. Normalized damage versus depth profiles for 5.8 MeV Ni^{4+} ions MAX phase ceramics.

Table 1 List of irradiation conditions and corresponding fluences.

Midrange Dose (dpa)	Fluence (ion/cm^2)	Temp. (°C)
10	2.43E+16	400
10	2.43E+16	700
30	7.30E+16	400
30	7.30E+16	700

Following irradiation, small scale analysis techniques were used to analyze the ~1.5-3 μm deep, thin film irradiated region. These techniques included grazing incidence X-ray diffraction, nanoindentation, scanning electron microscopy (SEM) and TEM.

To determine lattice parameter swelling, a GXRD capable X'Pert/PANalytical XRD machine was used to analyze the irradiated MAX phase samples. Due to the small irradiated sample size and aperture constraints, samples were mounted on single crystal silicon to provide a nearly zero background plate test environment. The incident beam angle, ω, was calculated using the computer program HighScore Plus to achieve an approximate maximum beam depth of 1.5 μm, which corresponds to the depth for the nominal midrange dose. In order to analyze diffraction patterns, the computer programs CMPR and Highscore Plus were used to find peak positions and match ICSD crystal patterns respectively [21, 22].

An Agilent nanoindenter with a Berkovich diamond indenter tip was used to examine the change of hardness and elastic modulus of the irradiated surface region. The indents were completed using a constant load rate of 500 μN/s (continuous stiffness mode) and preformed up to a depth 1100 nm. Optimized indentation positions were manually chosen using an optical microscope attached to the instrument. The areas considered optimized were those that appeared to be optically pristine and devoid of flaws, including scratches, pull-out, secondary phases, contamination, etc. To avoid the effect of strain fields, the distance between indents, large scratches, and sample edges was at least 50 μm. Approximately twenty indents were made per sample to obtain a good statistical average. Hardness and elastic modulus were then determined as functions of indentation depth using the software associated with indenter [23]. When analyzing the nanoindentation data, it was crucial to determine the transition point between the irradiated and substrate regions. This transition depth was determined by plotting the square of the hardness versus inverse indent depth, as recommended in the Nix-Gao Model [24]. This transition depth was determined to be approximately 400 nm. In order to minimize errors associated with low indentation depths and obtain good statistics, hardness and elastic modulus changes were calculated across all indents averaged from a 200-400 nm indentation depth.

Typical surface analysis was conducted using secondary electron detection mode in a Zeiss Gemini Scanning Electron Microscope to examine the effect of irradiation and nanoindentation on sample surfaces.

TEM cross-sectional foils were prepared using a FEI V400ACE Focused Ion Beam to create samples that were approximately 15 μm long by 10 μm deep with a viewing thickness of approximately 50-100 nm. The final polish on these samples were done using a 2 kV, 8 pA probe to help eliminate any residual damage/amorphous regions created during initial milling. An FEI Tecnai Transmission Electron Microscope was used to image defects in select samples. For the initial analysis, a traditional two-beam condition was used with a beam direction of approximately $\langle 11\bar{2}0 \rangle$, as determined by electron diffraction and Kikuchi patterns. This allowed for imaging along the approximate diffraction vectors (*g*) of $\langle 0001 \rangle$ and $\langle 1\bar{1}00 \rangle / \langle 01\bar{1}0 \rangle$, corresponding to the characteristic basal and prismatic directions of the HCP crystal structure. As no large voids were observed in the traditional two-beam imaging condition, under- and over-focus imaging was used to search for the existence of any small voids in the materials [25, 26].

Results

Figures 2, 3, and 4 show as-irradiated sample surfaces at the four irradiation conditions for Ti_3AlC_2, Ti_2AlC, and Ti_3SiC_2 respectively. From Figs. 2 and 3, it can be seen that both of the aluminum based MAX phases show significant surface cracking at both doses following irradiation at 400˚C, while no significant cracking was observed at both doses following irradiation at 700˚C. In contrast, the surface images of the silicon based MAX phase shown in Figure 6.3 show no significant surface cracking at either the low or high temperature irradiation conditions for either dose.

The Ti_3AlC_2 30 dpa -700˚C (Figure 2(d)) sample had significant contamination build up on the surface of the sample, believed to be hydrocarbon formation caused from outgassing of silver paste used to fasten the sample to the substrate for the ion irradiations. Cross section analysis showed that the contaminant film was 100-200 nm at its thickest. This surface contamination is believed to be responsible for slight difference between the Ti_3AlC_2 10 dpa -700˚C and 30 dpa -700˚C diffraction patterns and the unexpected decrease in hardness of the Ti_3AlC_2 30 dpa -700˚C data point discussed later in this section.

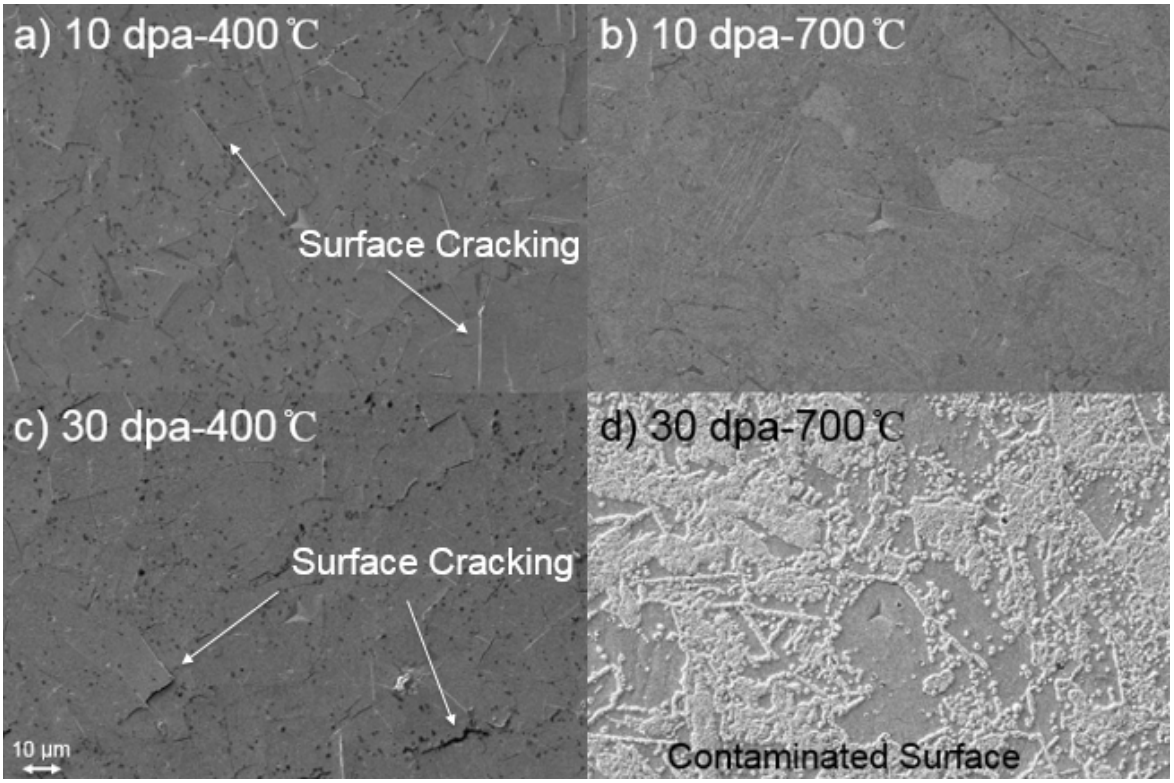

Figure 2 SEM surface imaging on Ni ion irradiated Ti_3AlC_2 for (a) 10 dpa-400˚C, (b) 10 dpa -700˚C, (c) 30 dpa-400˚C, and (d) 30 dpa-700˚C irradiation conditions.

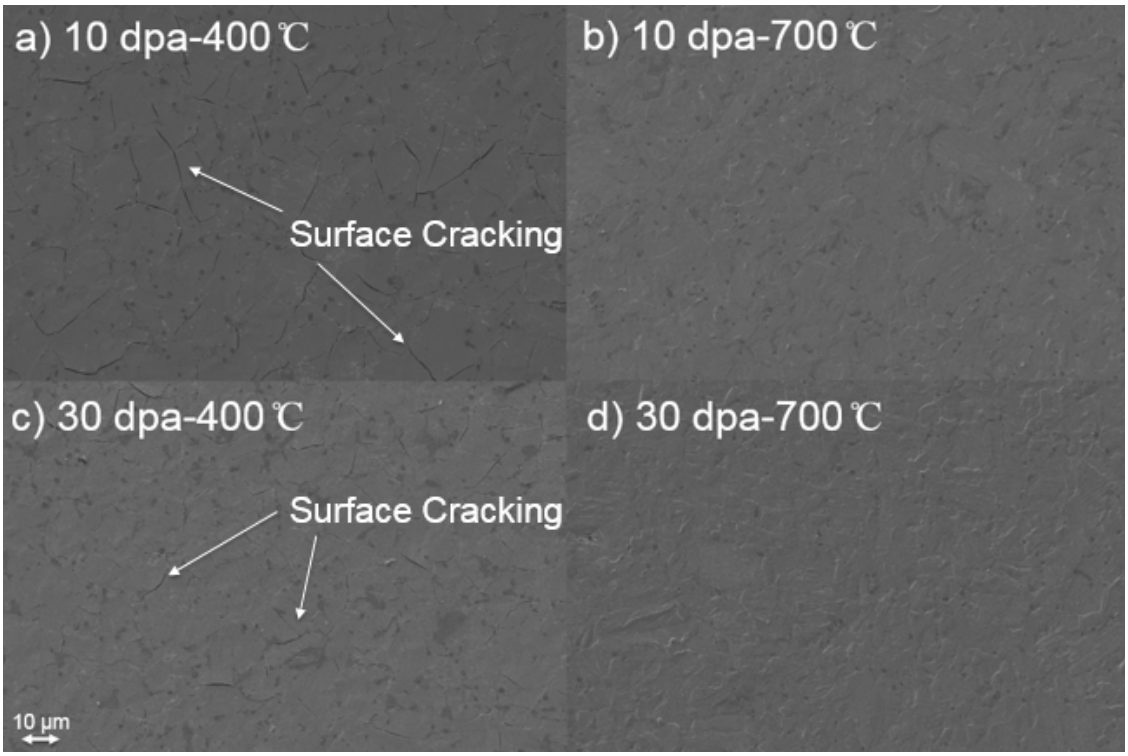

Figure 3 SEM surface imaging on Ni ion irradiated Ti_2AlC for (a) 10 dpa-400˚C, (b) 10 dpa-700˚C, (c) 30 dpa-400˚C, and (d) 30 dpa-700˚C irradiation conditions.

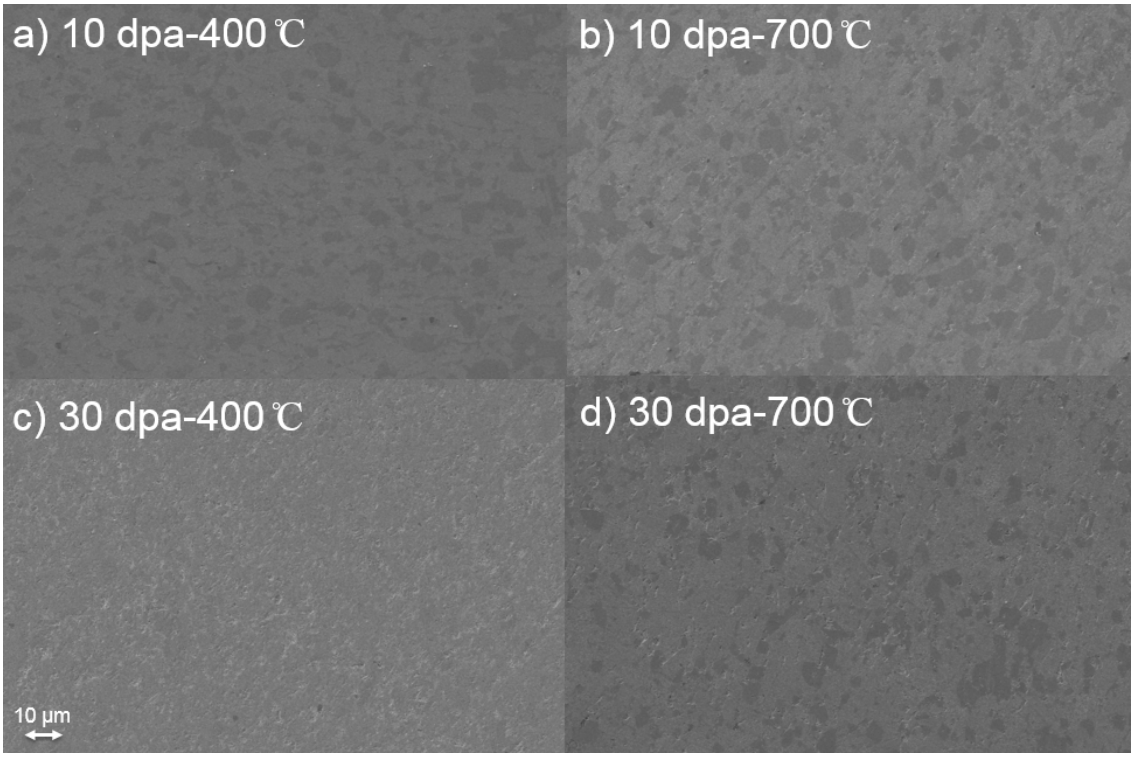

Figure 4 SEM surface imaging on Ni ion irradiated Ti_3SiC_2 for (a) 10 dpa-400˚C, (b) 10 dpa-700˚C, (c) 30 dpa-400˚C, and (d) 30 dpa-700˚C irradiation conditions.

The degree of surface cracking was quantified for the irradiated samples to determine if there was any discernable dependence of cracking on material composition, dose, or temperature. Randomly oriented lines were drawn across surface images. The number of crack intersections were counted for a large number of lines and divided by the total line length to provide a quantitative measure of the cracked grain boundary area per unit volume (S_v) using the formula S_v=2N where N is the average number of cracked grain boundary intersections per unit length of randomly drawn surface lines [27]. This crack density parameter does not take into account other crack features that might have an impact on structural integrity, such as average crack length, but was used to quantify overall cracking severity. The measured S_v values for samples irradiated at 400˚C are summarized in Table 2. As can be seen, there is no discernable difference in the linear crack densities between the same aluminum MAX phase materials at different doses at 400˚C, though the Ti_2AlC does appear to have a slightly higher crack density than the Ti_3AlC_2. As noted earlier, surface cracking was not observed in Ti_3SiC_2 for either dose at 400˚C, and no surface cracking was observed in any of the three materials irradiated at either dose at 700˚C.

Table 2 Irradiation-induced surface cracking per unit volume in Ti_3AlC_2 and Ti_2AlC irradiated at 400˚C.

Condition	S_v (1/μm)	Std. Dev.
Ti_3AlC_2-10 dpa-400˚C	1.52E-01	9.72E-03
Ti_3AlC_2-20 dpa-400˚C	1.49E-01	8.25E-03
Ti_2AlC-10 dpa-400˚C	2.13E-01	1.33E-02
Ti_2AlC-30 dpa-400˚C	1.97E-01	1.63E-02

The GXRD patterns for irradiated Ti_3AlC_2 at low dose (10 dpa) and high dose (30 dpa) can be seen in Figure 5, where (a, d) denotes low temperature (400˚C), (b, e) high temperature (700˚C), and (c, f) pristine conditions. The graphics are presented such that, going from bottom to top, it can be seen there is a significant temperature dependence on the disruption of the diffraction patterns. It can also be seen in Figure 5 that there is very little variation in the irradiated diffraction patterns with increasing dose from 10 dpa to 30 dpa, with the sole exception of the high dose, high temperature (30 dpa-700˚C) sample that was believed to have an artifact associated with surface contamination accrued during the irradiation. Additionally, the deduced lattice parameter changes for all four irradiation conditions yielded virtually identical results for samples irradiated at the same temperature but different doses. For these reasons, and in order to save time and cost, the remaining two materials, Ti_2AlC and Ti_3SiC_2, were only analyzed using GXRD at the high dose condition (30 dpa), with only the high dose Ti_3AlC_2 patterns being used for comparison. The GXRD patterns for Ti_2AlC and Ti_3SiC_2 at (a) 30 dpa-700˚C, (b) 30 dpa-700˚C, and (c) pristine conditions are shown in Figs. 7 and 8 respectively.

Editor's note: There is no Figure 6 in this section.

In all cases, the ion irradiation resulted in augmentation of the diffraction pattern through reduction of the peak heights, broadening, and shifting of the peak locations. In all three materials, there is significantly less disruption of the diffraction pattern at the 30 dpa-700˚C condition then at the 30 dpa-400˚C condition. Consequently, there are only slight differences in the pristine and 30 dpa-700˚C diffraction patterns for all three materials, with the Ti_3AlC_2 30 dpa-700˚C sample exhibiting the most change. Further examinations of the diffraction patterns shows that the Ti_3SiC_2 irradiated samples appear to show the least disturbance due to irradiation, with very little peak shift and only slight peak reduction and broadening. Consequently, only minor diffraction peaks are lost for this material at the 30 dpa-400˚C condition. In stark contrast, both aluminum based MAX phases appear to have suffered significant damage at the 30 dpa-400˚C irradiation. Only the largest diffraction peaks are still visible in Ti_2AlC and both the both aluminum MAX phases exhibit peaks that are not prevalent in the pristine samples, suggesting large shifts and/or emergence of new peaks.

Manipulation of the ICSD diffraction pattern peak positions to match the observed data using Highscore Plus yielded nominal lattice parameter changes for each material. A summary of these calculated values can be seen in Table 3.

In all three MAX phases, there was a pronounced increase in the c-LP at the 30 dpa-400˚C irradiation condition, with a less significant increase of the c-LP in the Ti_3AlC_2 and only minimal change for the Ti_2AlC, and Ti_3SiC_2 at the 30 dpa-700˚C irradiation condition. At the 30 dpa-400˚C condition, the Ti_2AlC exhibited the highest c-LP swelling, with an increase from 13.41(5) Å to 13.74(8) Å, an increase of approximately 2.46%. The Ti_3SiC_2 exhibited the least amount of c-LP swelling for irradiation at 400˚C, with an increase of 17.65(4) Å to 17.72(6) Å, corresponding to a relative increase of approximately 0.40%. For the 30 dpa-400˚C irradiation condition, Ti_3AlC_2 fell in between with an increase of 18.54(6) Å to 18.74(9) Å, or 1.08%. For the 30 dpa-700˚C condition, only the Ti_3AlC_2 exhibited lattice parameter swelling, which was limited to 0.38%, from 18.54(6) Å to 18.61(3) Å. Both the Ti_2AlC, and Ti_3SiC_2 exhibited slight contraction from pristine c-LP values at the 30 dpa-700˚C condition.

With respect to the a-LP, both aluminum MAX phases exhibit a slight a-LP reduction at the 30 dpa-400˚C condition with minimal change at the 30 dpa-700˚C condition, while the silicon based MAX phase exhibits a slight a-LP increase at both irradiation conditions. The Ti_2AlC shows the most a-LP contraction at the 30 dpa-400˚C irradiation condition, decreasing from 3.061(8) Å to 3.04(1) Å, a change of 0.69%. The Ti_3AlC_2 exhibits a less exaggerated reduction, going from 3.0735(7) Å to 3.065(5) Å, a 0.28% change at the 30 dpa-400˚C condition. Both aluminum MAX phases exhibit only slight change at the 30 dpa-700˚C irradiation condition (absolute change of 0.2% or less). The silicon base MAX phase exhibits a slight increase in the a-LP at both the 30 dpa-400˚C and 30 dpa-700˚C irradiation conditions, going from 3.059(4) Å to 3.069(3) Å and 3.067(3) Å, a 0.33% and 0.26% respective increase. A plot of both the relative (a) c-LP and (b) a-LP shifts post irradiation can be seen in Figure 9. It should be noted that large differences in c-axis and a-axis swelling can produce pronounced strains at randomly oriented grain boundaries and can result in grain boundary cracking depending on the magnitude of anisotropic swelling and material parameters.

Table 3. Irradiation-induced structural changes in Ti_3AlC_2, Ti_2AlC, and Ti_3SiC_2 for irradiation up to 30 dpa at 400˚C and at 700˚C.

Condition	a-LP (Å)	Δa-LP (%)	c-LP (Å)	Δc-LP (%)
Ti_3AlC_2-Pristine	3.0735(7)	-	18.54(6)	-
Ti_3AlC_2-10 dpa-400˚C	3.068(6)	-0.18	18.74(7)	1.08
Ti_3AlC_2-10 dpa-700˚C	3.070(1)	-0.11	18.60(1)	0.32
Ti_3AlC_2-30 dpa-400˚C	3.065(5)	-0.28	18.74(9)	1.08
Ti_3AlC_2-30 dpa-700˚C	3.076(3)	0.08	18.61(3)	0.38
Ti_2AlC-Pristine	3.061(8)	-	13.41(5)	-
Ti_2AlC-30 dpa-400˚C	3.04(1)	-0.69	13.74(8)	2.46
Ti_2AlC-30 dpa-700˚C	3.055(7)	-0.20	13.38(5)	-0.22
Ti_3SiC_2-Pristine	3.059(4)	-	17.65(4)	-
Ti_3SiC_2-30 dpa-400˚C	3.069(3)	0.33	17.72(6)	0.40
Ti_3SiC_2-30 dpa-700˚C	3.067(3)	0.26	17.61(3)	-0.23

Numbers in parentheses represent one standard deviation of the last significant digit.

In order to obtain a quantitative estimation of the critical differential strain required for grain boundary cracking, the analytical technique developed by Clarke et al. in their 1964 studies on grain boundary cracking in BeO was used [28]. Their analysis considered the misfit strain introduced at grain boundaries from anisotropic lattice expansion that led to grain boundary cracking. Spontaneous cracking is predicted to occur for misfit strains above a critical value given by Eq. (5), where the critical differential strain (ε) is related to the grain boundary surface energy in the absence of anisotropic strain (γ), the elastic modulus (E), and the average grain diameter ($2l$).

$$\varepsilon \sim \left(\frac{24\,\gamma}{El}\right)^{\frac{1}{2}} \qquad (5)$$

The grain diameters were measured for each of the materials by Darin Tallman at Drexel University [17] and were independently confirmed using Electron Back Scattering diffraction in the present study. The nominal average grain diameter for Ti_3AlC_2, Ti_2AlC, and Ti_3SiC_2 were determined to be 16(6), 10(4), and 8(3) μm respectively. The elastic moduli are given in Table 1 and the grain boundary surface energy was assumed to be 1.5 N/m, a typical value for Al_2O_3. A comparison of the calculated critical differential strain and the experimental differential strains for the three materials irradiated at the two temperature conditions can be seen in Table 6. As can be seen, only the low temperature irradiated aluminum base MAX phase samples experienced differential swelling sufficient to induce grain boundary cracking (an order of magnitude larger than the predicted critical value), supporting the conclusion that anisotropic swelling is the cause of grain boundary cracking in the 400˚C irradiated aluminum MAX phases.

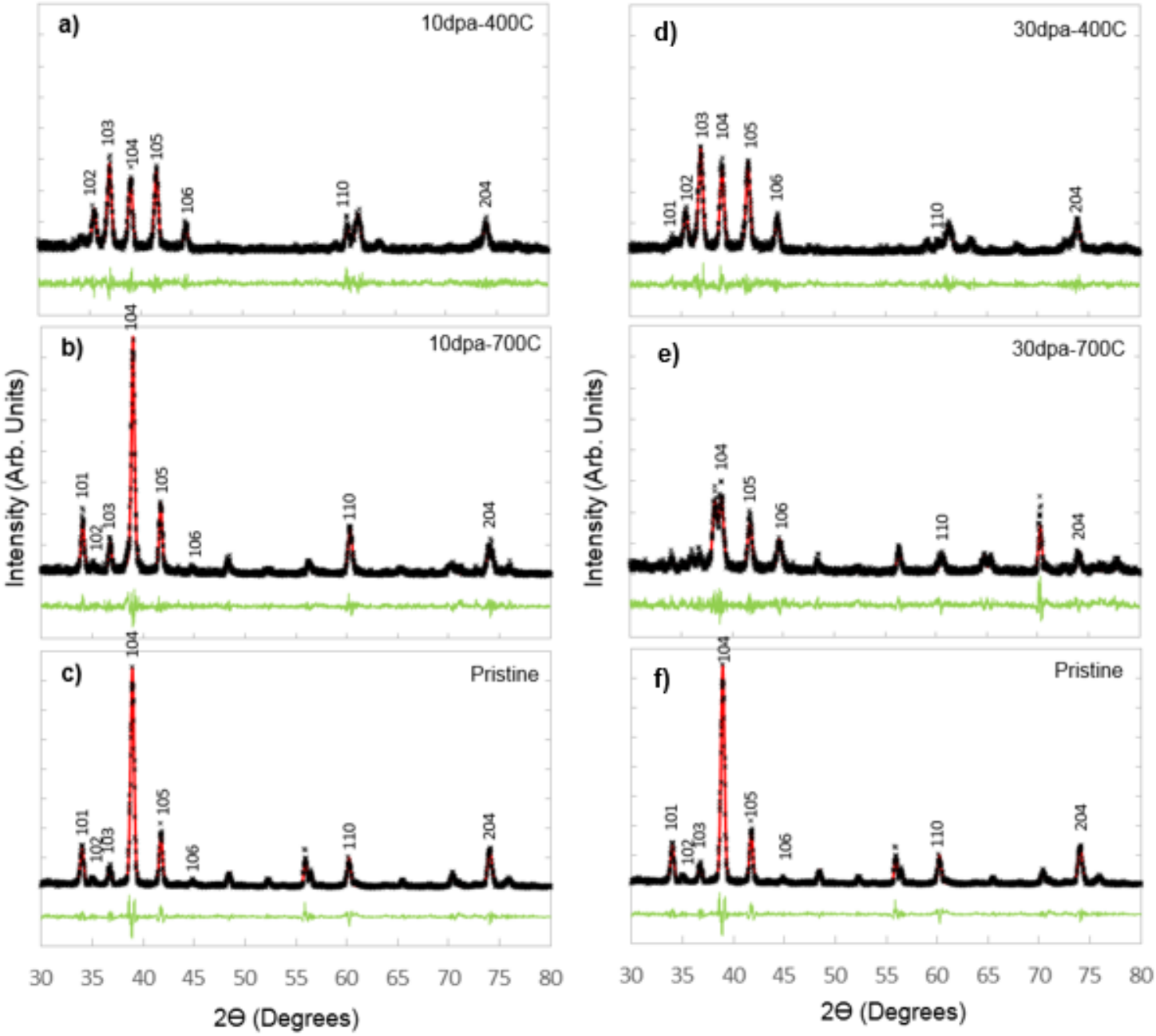

Figure 5 GXRD data of Ti_3AlC_2 irradiated to a midrange dose of 10 dpa using 5.8 MeV Ni ions at (a) 10 dpa-400˚C, (b) 10 dpa-700˚C, (d) 30 dpa-400˚C, (e) 30 dpa-700˚C, and (c&f) Pristine Ti_3AlC_2. Black data points, solid red lines, and solid green lines represent the observed data, calculated model, and the difference between the two respectively.

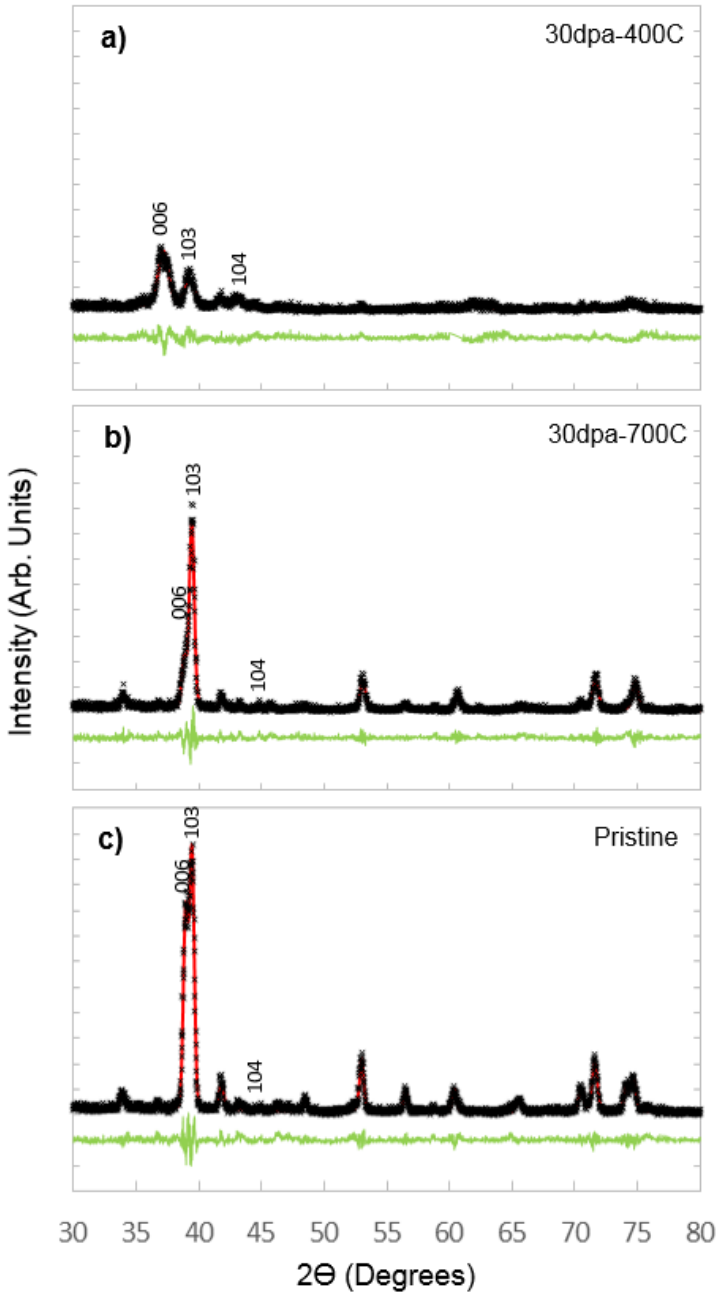

Figure 6 GXRD data of Ti_2AlC irradiated to a midrange dose of 30 dpa using 5.8 MeV Ni ions at (a) 30 dpa-400˚C, (b) 30 dpa-700˚C, and (c) Pristine Ti_2AlC. Black data points, solid red lines, and solid green lines represent the observed data, calculated model, and the difference between the two respectively.

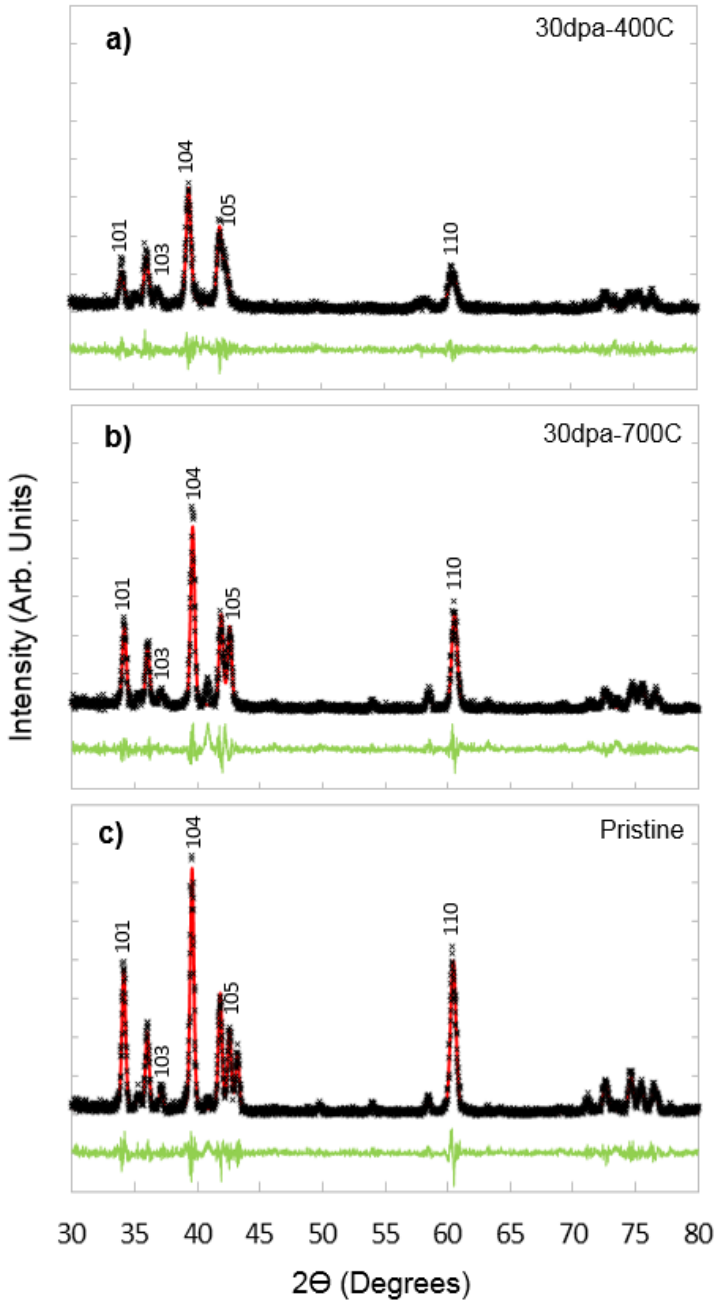

Figure 7 GXRD data of Ti_3SiC_2 irradiated to a midrange dose of 30 dpa using 5.8 MeV Ni ions at (a) 30 dpa-400˚C, (b) 30 dpa-700˚C, and (c) Pristine Ti_3SiC_2. Black data points, solid red lines, and solid green lines represent the observed data, calculated model, and the difference between the two respectively.

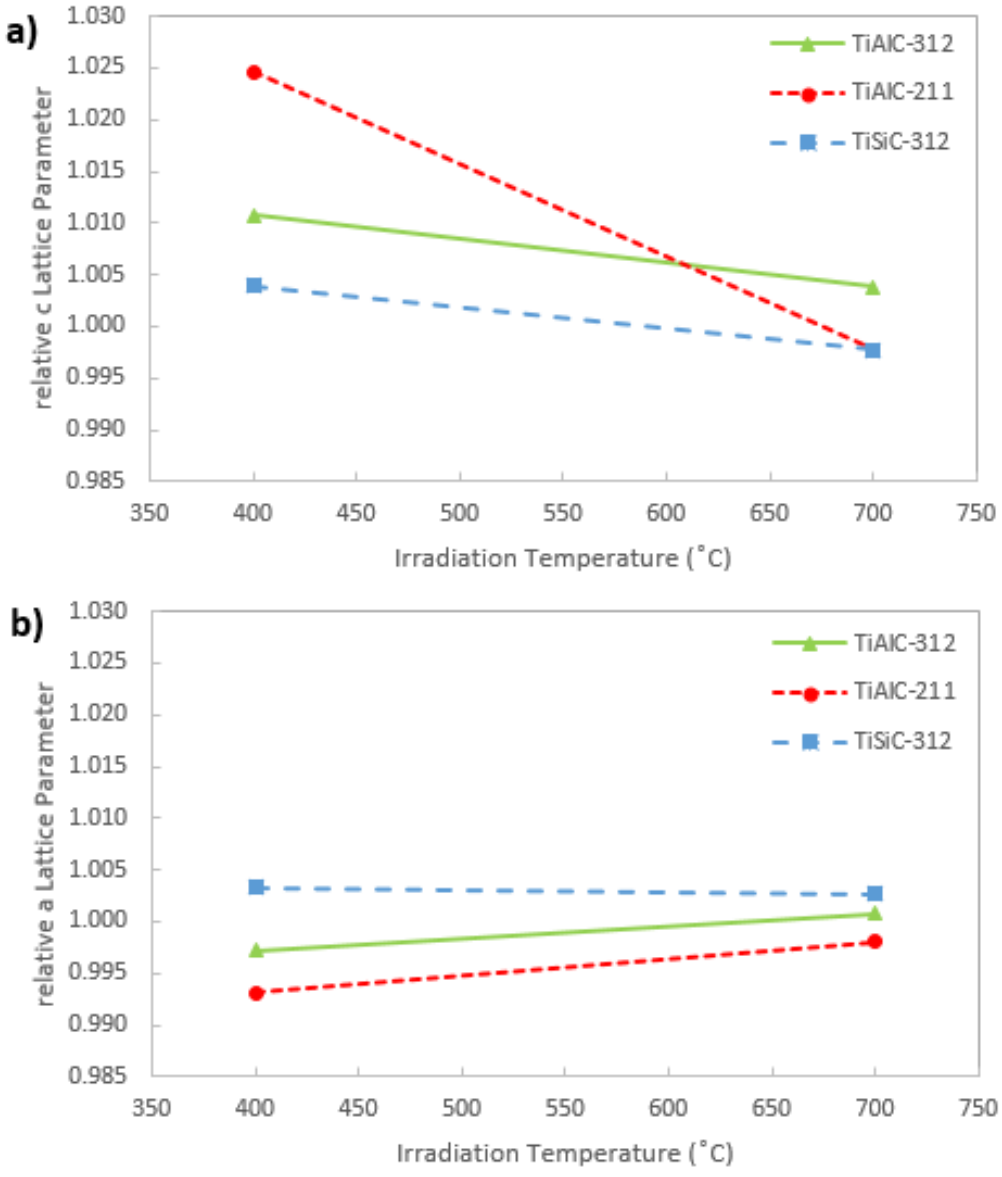

Figure 8 Temperature dependent relative lattice parameter shifts at 30 dpa midrange dose for (a) c-LP and (b) a-LP.

Table 4 Comparison of experimental differential strain to estimated critical differential strain required for grain boundary cracking.

Sample	ε at 400˚C	ε at 700˚C	ε critical
Ti_3AlC_2	1.36E-02	2.96E-03	3.89E-03
Ti_2AlC	3.15E-02	2.77E-04	5.10E-03
Ti_3SiC_2	6.97E-04	4.88E-03	5.14E-03

The evolution of hardness as a function of irradiation dose averaged over 200-400 nm for the three MAX phase materials can be seen at (a) 400˚C and (b) 700℃ in Figure 10. It can be seen that for all three materials at both 400˚C and 700℃, there is significant increase in hardness from the pristine samples to the irradiated samples, due to radiation induced defects. Of the three materials, Ti_3AlC_2 exhibits the most radiation hardening up to a maximum of approximately 1.9x for the low temperature irradiations and 1.6x for high temperature irradiations. In comparison, Ti_3SiC_2 exhibits the least amount of hardening at both the low and high temperature irradiation conditions with a maximum of approximately 1.4x and 1.2x respectively. The Ti_2AlC falls in between the other materials with a maximum relative hardening of approximately 1.6x at the low temperature condition and 1.4x at the high temperature condition. Additionally, it can be seen that there is little variation in hardness from samples irradiated at to a midrange dose of 10 dpa and those irradiated to a midrange dose of 30 dpa, for both irradiation temperatures. This suggests a saturation effect in the radiation induced hardening has occurred for a dose of 10 dpa and higher. As noted for the GXRD results in the previous section, the surface contamination of the 30 dpa- 700˚C was believed to have induced significant error on the nanoindentation results associated with this sample. As such, as dose increases from 10 to 30 dpa for Ti_3AlC_2 at the 700˚C irradiation temperature, the relative hardness of an uncontaminated sample is expected to stay constant, as is consistent with radiation hardness saturation, rather than the significant decrease as observed in the experimental data.

The effect of irradiation temperature on hardness for all three materials at a midrange dose of (a) 10 dpa and (b) 30 dpa can be seen in Figure 11. From this figure, it becomes apparent that there is significantly less hardening at an irradiation temperature of 700℃ than at an irradiation temperature of 400˚C for all three materials. This suggest a positive correlation between irradiation temperature and radiation induced hardness.

The evolution of the relative elastic modulus of the three materials as a function of irradiation dose averaged over 200-400 nm can be seen in Figure 12 for (a) 400˚C and (b) 700˚C, and as a function of irradiation temperature in Figure 13 for (a) 10 dpa midrange dose and (b) 30 dpa midrange dose. For irradiated materials there is expected to be a slight change in the elastic modulus that saturates after relatively small amounts of damage, similar to irradiation induced hardness. Upon examination, it appears that all of the irradiated samples follow this trend, with the majority of samples experiencing a slight elastic modulus increase of approximately 10%. The exception to this trend are the low temperature irradiations of the aluminum MAX phases, in which Ti_3AlC_2 exhibited little to no change in elastic modulus and Ti_2AlC exhibited a slight decrease in elastic modulus of about 6%. This behavior is indicative of a radiation induced effect not found in other samples.

SEM examination was used following indentation hardness testing to observe the surface features associated with nanoindentation. Imaging the surface indents, it was seen that for the 400˚C irradiated aluminum MAX phase surfaces (those that experienced cracking), the indenter produced significant corner cracking. For the un-cracked aluminum and all the silicon based MAX phase surfaces, the indentation did not induce corner cracking and features analogous to that of indentation on pristine MAX phase, such as slip bands/delamination and push-out, are observed [29]. Figures 14, 15, and 16 show

indents in surfaces irradiated at the (a) 10 dpa-400˚C and (b) 10 dpa-700˚C conditions in Ti_3AlC_2, Ti_2AlC, and Ti_3SiC_2 respectively.

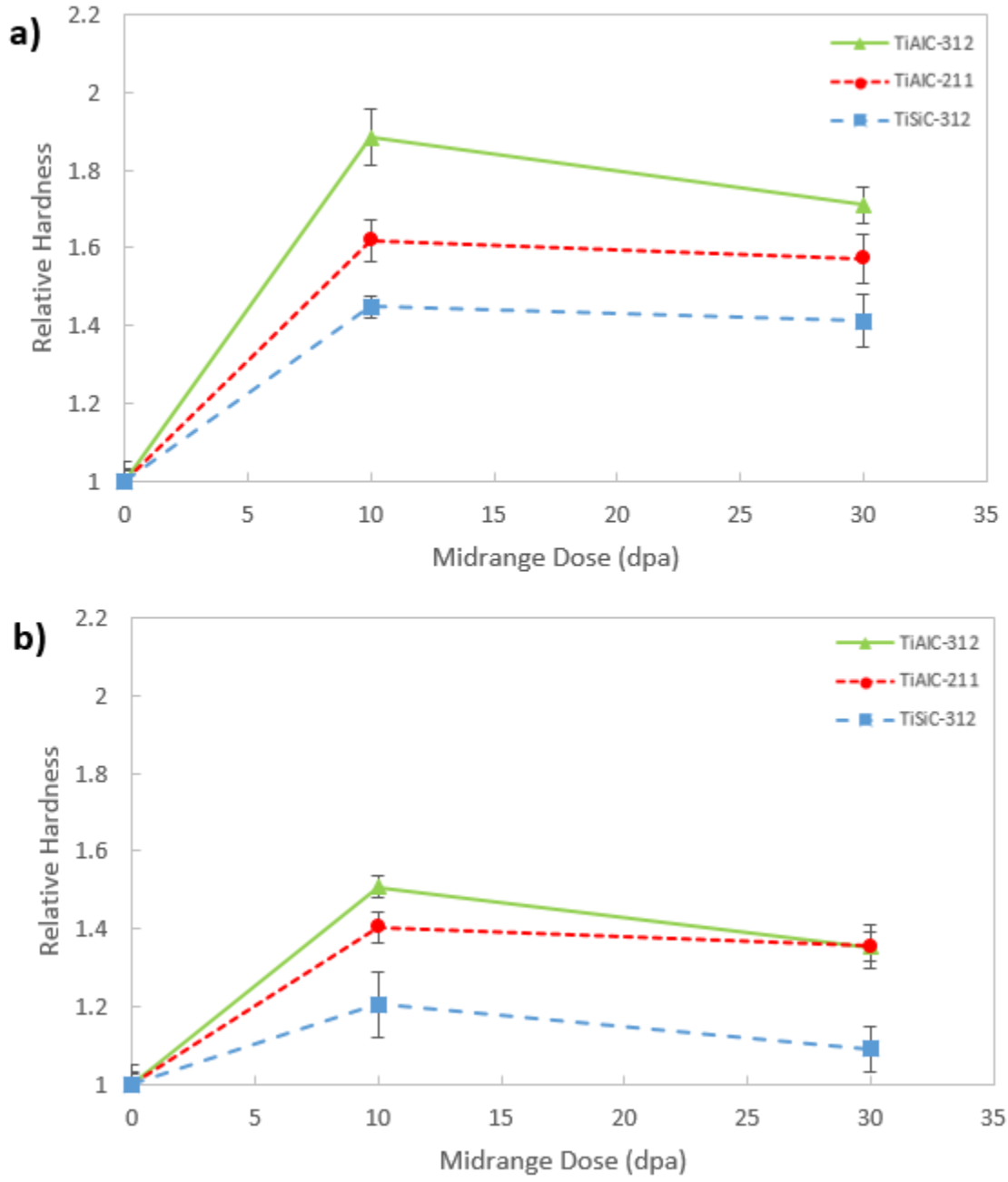

Figure 9 Normalized hardness dose dependence in irradiated Ti_3AlC_2, Ti_2AlC, and Ti_3SiC_2 by 5.8 MeV Ni ions at (a) 400˚C and (b) 700℃.

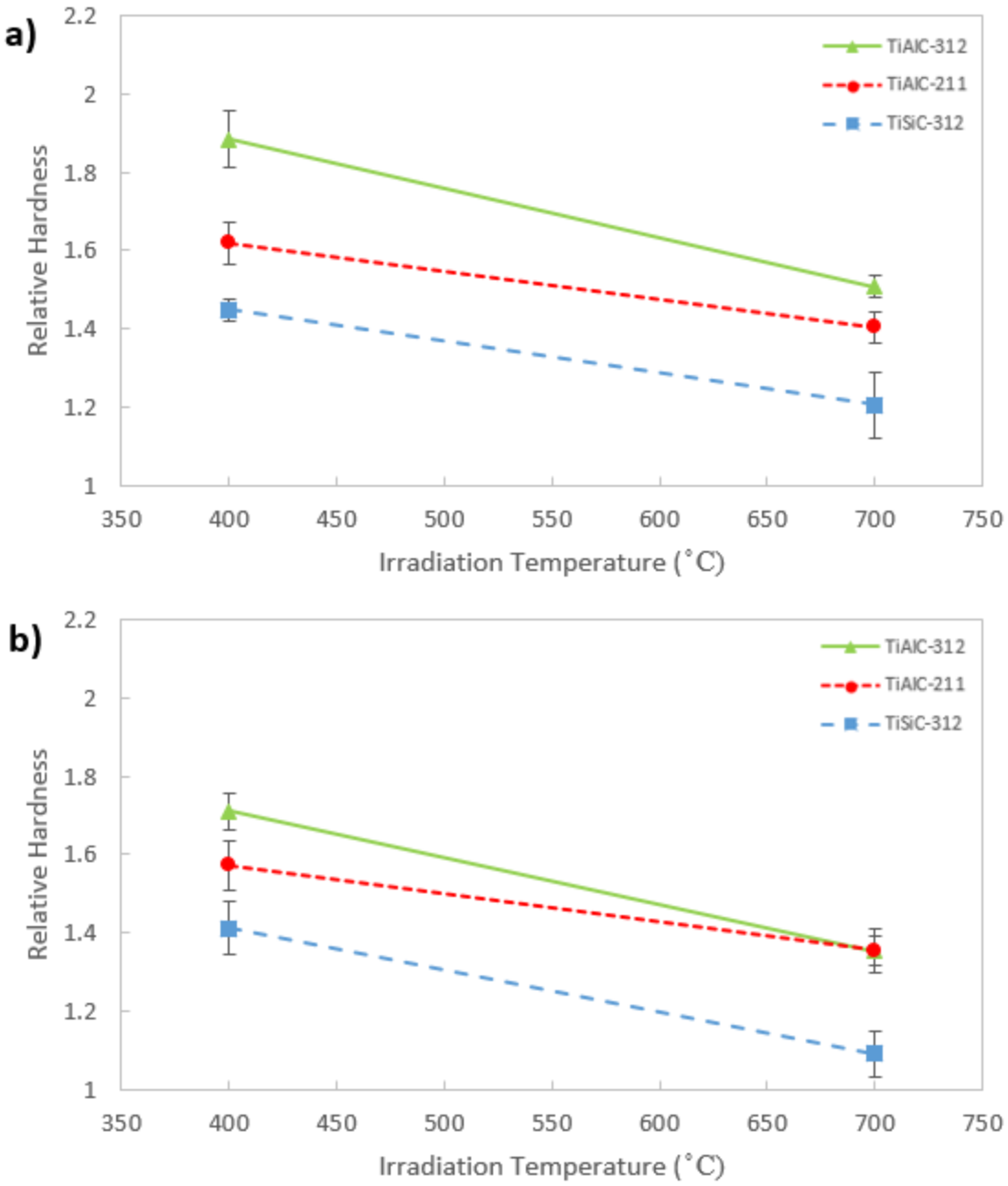

Figure 10 Normalized hardness temperature dependence in irradiated Ti_3AlC_2, Ti_2AlC, and Ti_3SiC_2 by 5.8 MeV Ni ions at midrange doses of (a) 10 dpa and (b) 30 dpa.

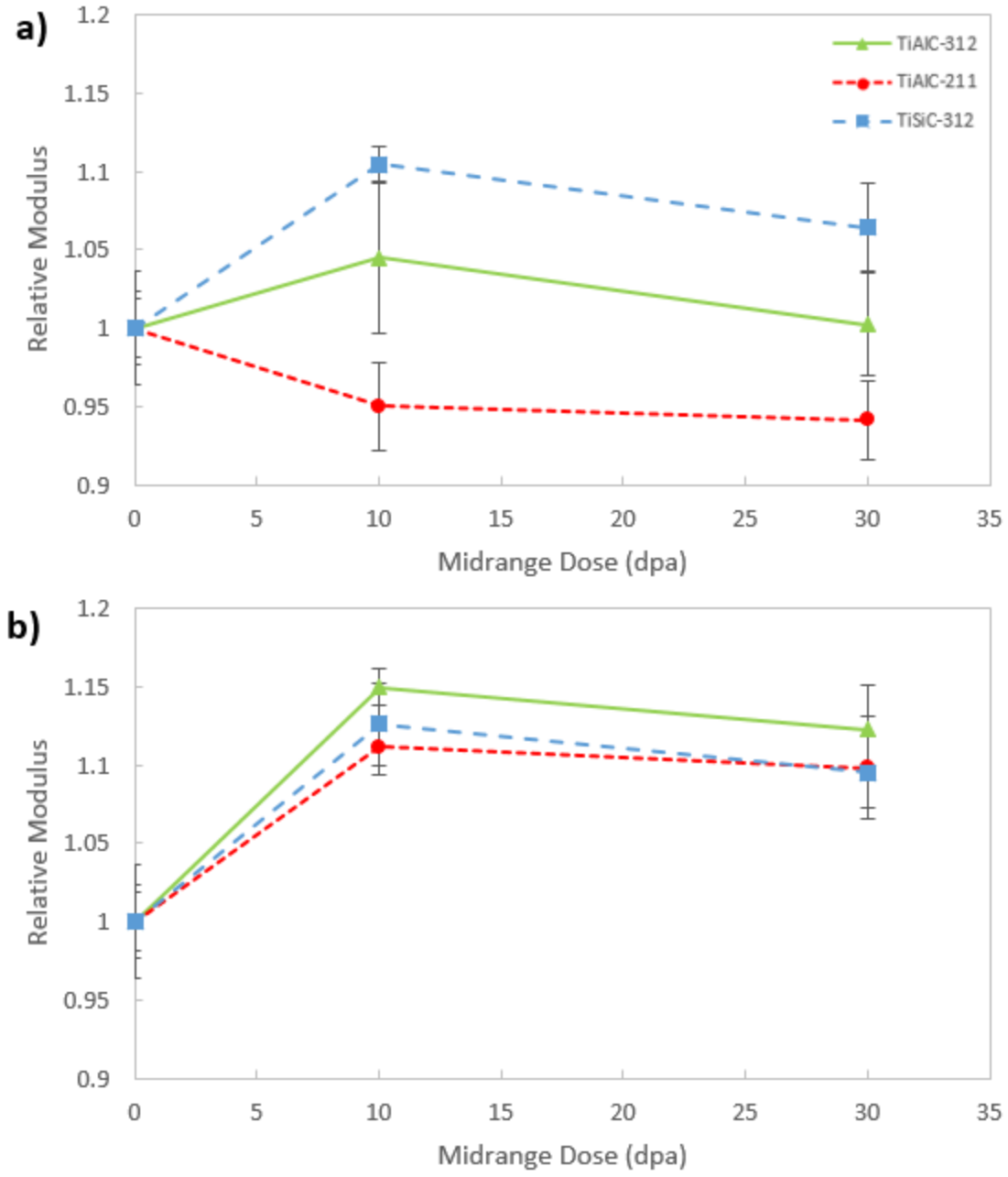

Figure 11 Normalized elastic modulus dose dependence in irradiated Ti_3AlC_2, Ti_2AlC, and Ti_3SiC_2 by 5.8 MeV Ni ions at (a) 400˚C and (b) 700˚C.

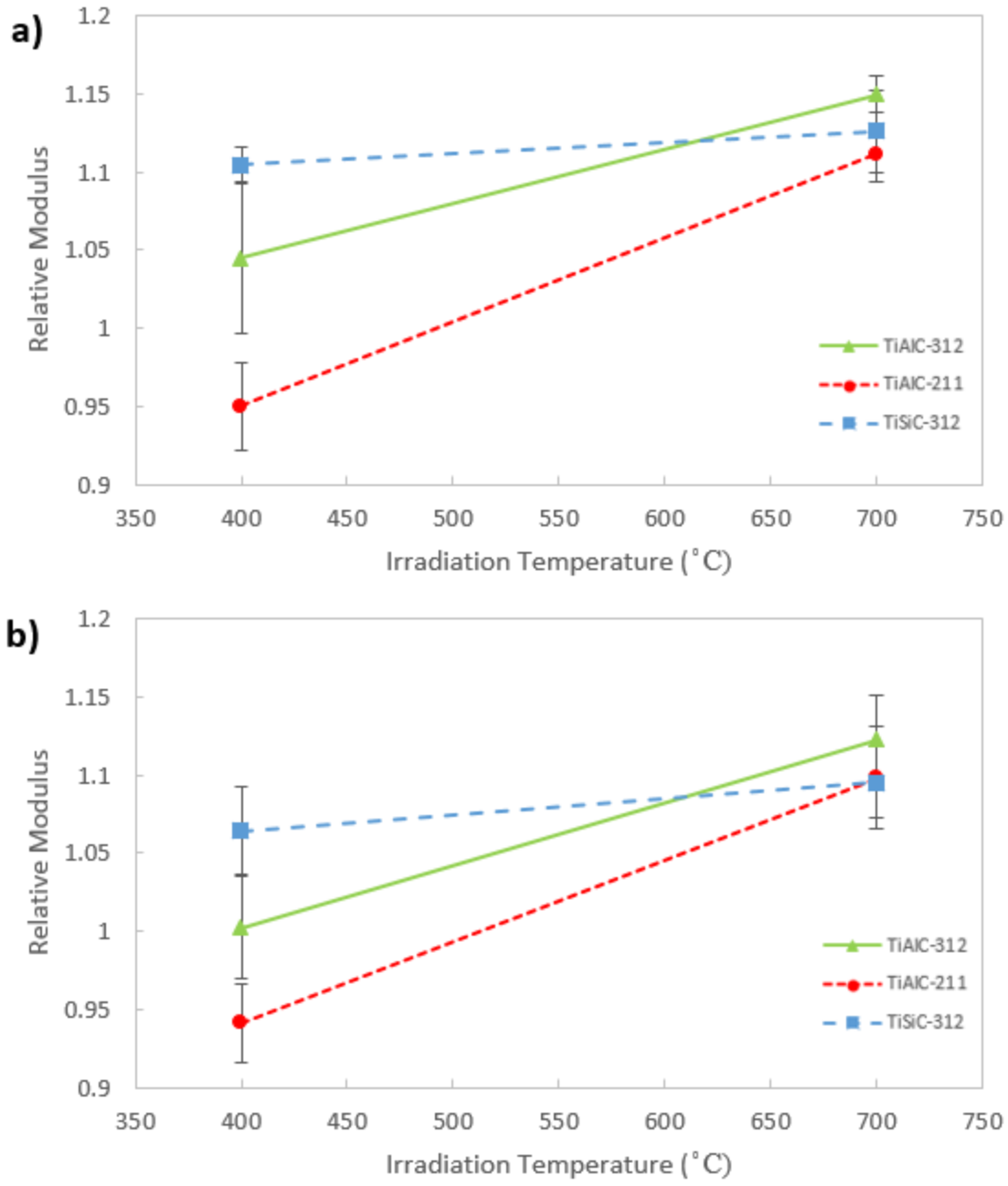

Figure 12 Normalized elastic modulus temperature dependence in irradiated Ti_3AlC_2, Ti_2AlC, and Ti_3SiC_2 by 5.8 MeV Ni ions at midrange doses of (a) 10 dpa and (b) 30 dpa.

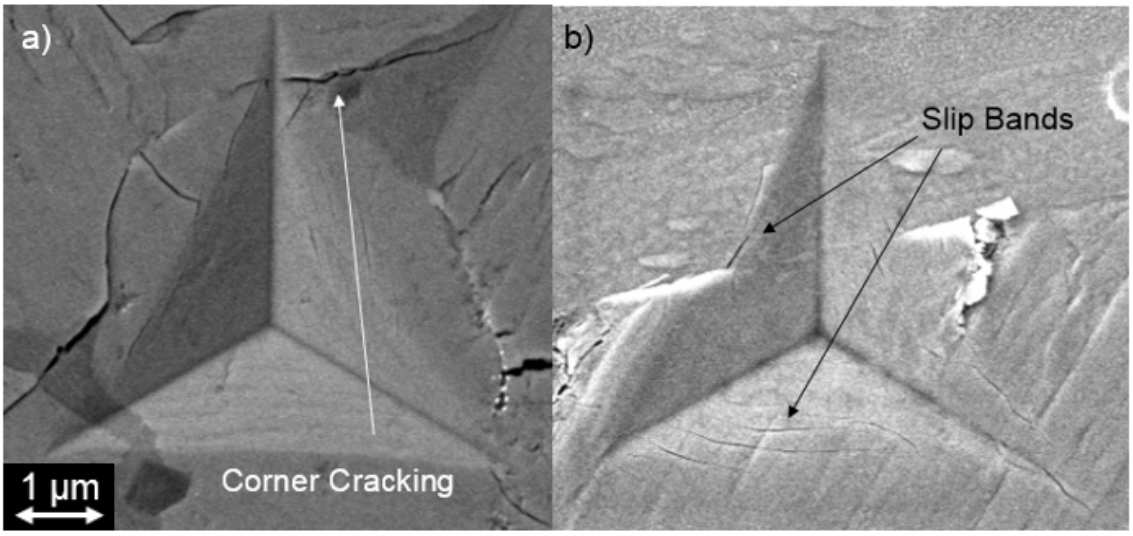

Figure 13 SEM morphology of indents on (a) 10 dpa-400˚C, and (b) 10 dpa-700˚C Ni ion irradiated Ti_3AlC_2.

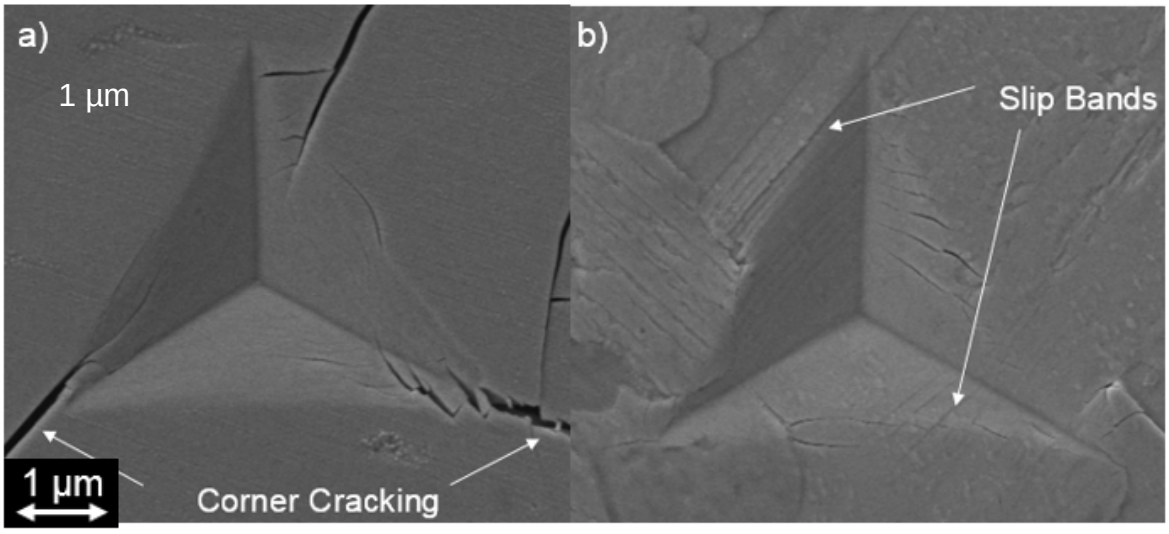

Figure 14 SEM morphology of indents on (a) 10 dpa-400˚C, and (b) 10 dpa-700˚C Ni ion irradiated Ti_2AlC.

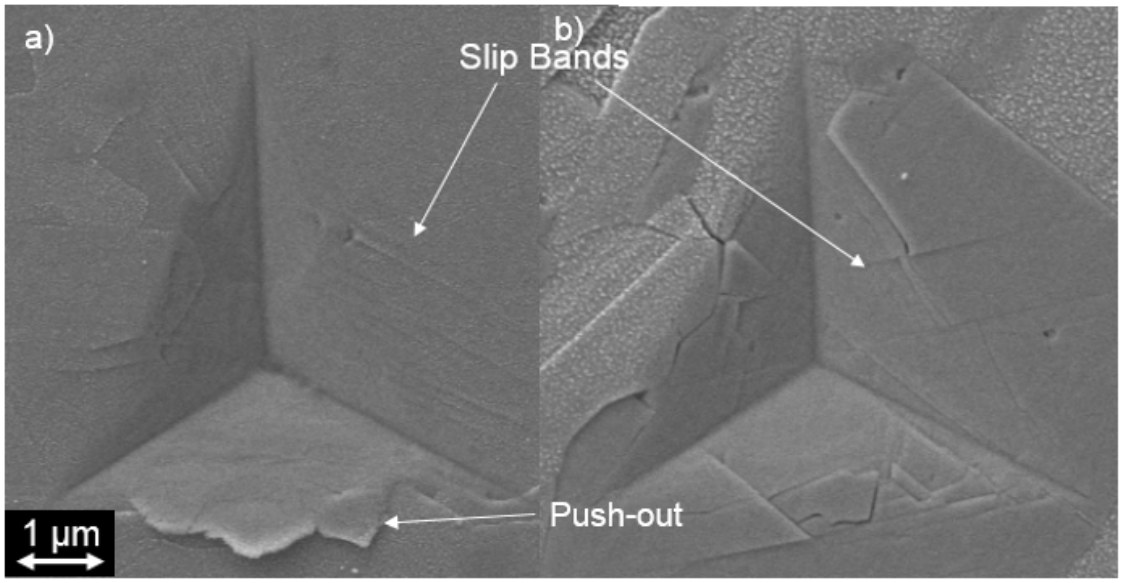

Figure 15 SEM morphology of indents on (a) 10 dpa-400˚C, and (b) 10 dpa-700˚C Ni ion irradiated Ti_3SiC_2.

TEM cross section analysis was used to examine microstructural defects in select samples. The samples chosen were those that were thought to be most relevant to the questions raised by the previous SEM surface, XRD, and nanoindentation analysis, the most important of which are why are the aluminum based MAX phases cracking at the 400˚C irradiation conditions and not cracking following 700˚C irradiation, as well as are vacancies sufficiently mobile to produce observable cavity formation in either the aluminum or silicon based MAX phase at 700˚C. Assuming that both the aluminum MAX phases would exhibit qualitatively similar microstructural evolution under irradiation (due to their qualitatively similar response in terms of lattice parameter changes, hardening, and surface cracking propensity), the samples deemed as highest priority for TEM analysis were Ti_3AlC_2 30 dpa-400˚C, Ti_3AlC_2 30 dpa-700˚C, and Ti_3SiC_2 30 dpa-700˚C.

A low-magnification TEM micrograph of the Ti_3AlC_2 30 dpa-400˚C cross-section foil and SAED results for the underlying unirradiated region (2) can be seen in Figure 17. The green arrow represents the direction of ion irradiation, which penetrated to a depth of approximately 3 μm, as displayed by the white line denoting the separation of the irradiated area and non-irradiated bulk. This is consistent with SRIM ion penetration depth calculations provided above. SAED was performed on the unirradiated region (2), well beyond the range of the ions (displayed as an inset in the upper right of Figure 17), in order to determine both the phase and orientation of the grain. Comparing experimental and ICSD diffraction pattern spacing, the grain was confirmed to be the nominal Ti_3AlC_2 phase and the beam direction was determined to be ~$\langle 11\bar{2}0 \rangle$. This low magnification analysis was completed again for both the 30 dpa-700˚C Ti_3AlC_2 and Ti_3SiC_2 samples.

Subsequently, standard two-beam conditions were used to obtain bright field and dark field images using the $\langle 0001 \rangle$ (basal) and $\langle 1\bar{1}00 \rangle$ (prism) diffraction vectors for both the unirradiated (2) and irradiated (1) regions of Ti_3AlC_2 irradiated to 30 dpa at 400˚C, as shown in Figs. 18 and 19 respectively. It is important to note that the irradiated region (1) was analyzed at a depth of ~1.5 μm, corresponding to the nominal midrange dose of 30 dpa. As can be seen in both the $\langle 0001 \rangle$ and $\langle 1\bar{1}00 \rangle$ g vectors in Figure 18, a low density of large defect clusters typical of unirradiated materials exist in the pristine region. On the contrary, for both g vectors in the 400˚C irradiated region shown in Figure 19, there is a large density of "black spots" or small defect clusters, with a distinct lack of voids (the latter was confirmed using under- and over-focusing techniques). The very high density of defect clusters visible in these images suggest a saturation of interstitial point defect clusters in the irradiated area induced through nuclear displacements.

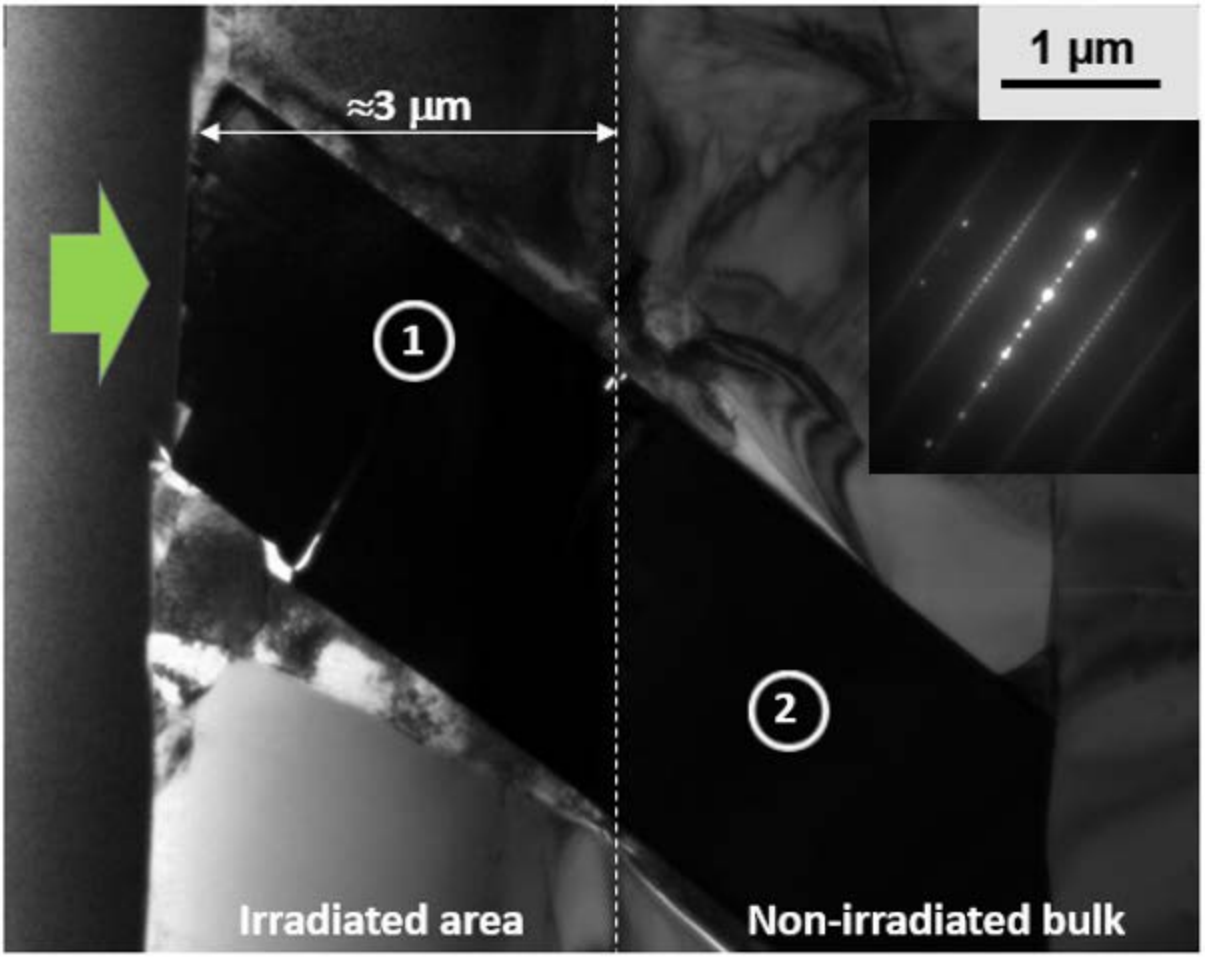

Figure 16 Cross-sectional TEM micrograph of the full Ti_3AlC_2 foil irradiated to 30 dpa at 400˚C using 5.8 MeV Ni ions, with ion direction denoted by the green arrow. The dashed white line denotes the transition depth between the ion irradiated area and the non-irradiated bulk. Region 1 denotes the selected area for ion radiation damage characterization and Region 2 denotes the selected area for pristine crystal characterization. SAED pattern for the pristine crystal can be seen in the upper right-hand corner.

Standard two-beam conditions were also used to obtain bright field and dark field images for $\langle 0001 \rangle$ (basal) and $\langle 1\bar{1}00 \rangle$ (prism) diffraction vector directions for Ti_3AlC_2 and Ti_3SiC_2 irradiated to a midrange dose of 30 dpa at 700˚C, shown in Figs 20 and 21. Again, under- and over-focus showed a distinct lack of voids, suggesting that vacancy mobility is limited in both the aluminum and silicon based MAX phase at 700˚C (or else void nucleation and growth is otherwise inhibited). However, contrary to the 400˚C irradiated Ti_2AlC, the irradiated microstructures did not contain a large density of small, point defects, but instead consisted of a lower density of large defect clusters for both the $\langle 0001 \rangle$ and $\langle 1\bar{1}00 \rangle$ diffraction vectors. In the Ti_3AlC_2, these grouped defect clusters appeared to form a hatched or diamond pattern for g=$\langle 0001 \rangle$ and a striped pattern for g=$\langle 0001 \rangle$ $\langle 1\bar{1}00 \rangle$. Upon inspection, the defects appear to be comprised of smaller basal defects that coalesce in a stacking sequence at $\pm$ 35 degree angles from the basil direction. The fact that these defects can also be seen for the prism zone axis suggest a prismatic component as well. Full characterization of these defect clusters is needed before any definitive conclusions as to their nature can be draw, but the general features of significantly coarser defect cluster microstructure suggest a higher mobility of interstitial defects at this higher irradiation temperature.

Similar to the 700˚C irradiated Ti_3AlC_2, the Ti_3SiC_2 irradiated microstructure did not contain a large density of small, point defects, but instead consisted of a lower density of larger defect clusters at both

the basal and prism viewing zone axis. However, these grouped defects did not form similar self-organized patterns seen in the Ti_3AlC_2, but instead exhibited what appears to be large stacking faults along the basal plane and dislocation loops along the prism axis. Again, full characterization of these defect clusters is still needed before any definitive conclusions as to their nature can be draw, but the general irradiation damage seen in Ti_3SiC_2 appears to be less pronounced than that observed in Ti_3AlC_2, and is consistent with previous results.

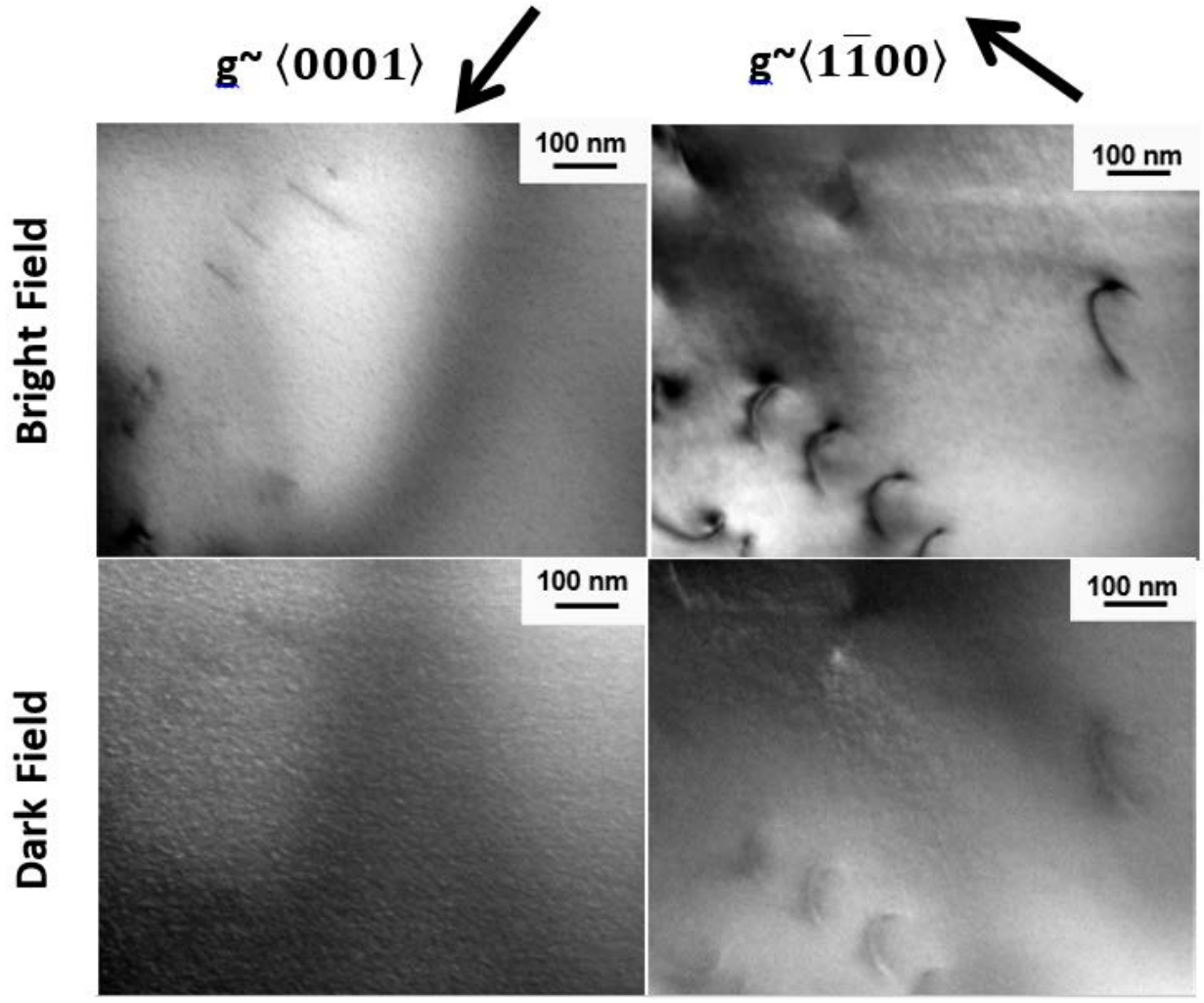

Figure 17 High magnification bright field and dark field cross-sectional TEM micrographs of pristine Ti_3AlC_2 (region 2). The basal and prism diffraction vector directions are indicated by $\langle 0001 \rangle$ and $\langle 1\bar{1}00 \rangle$ respectively.

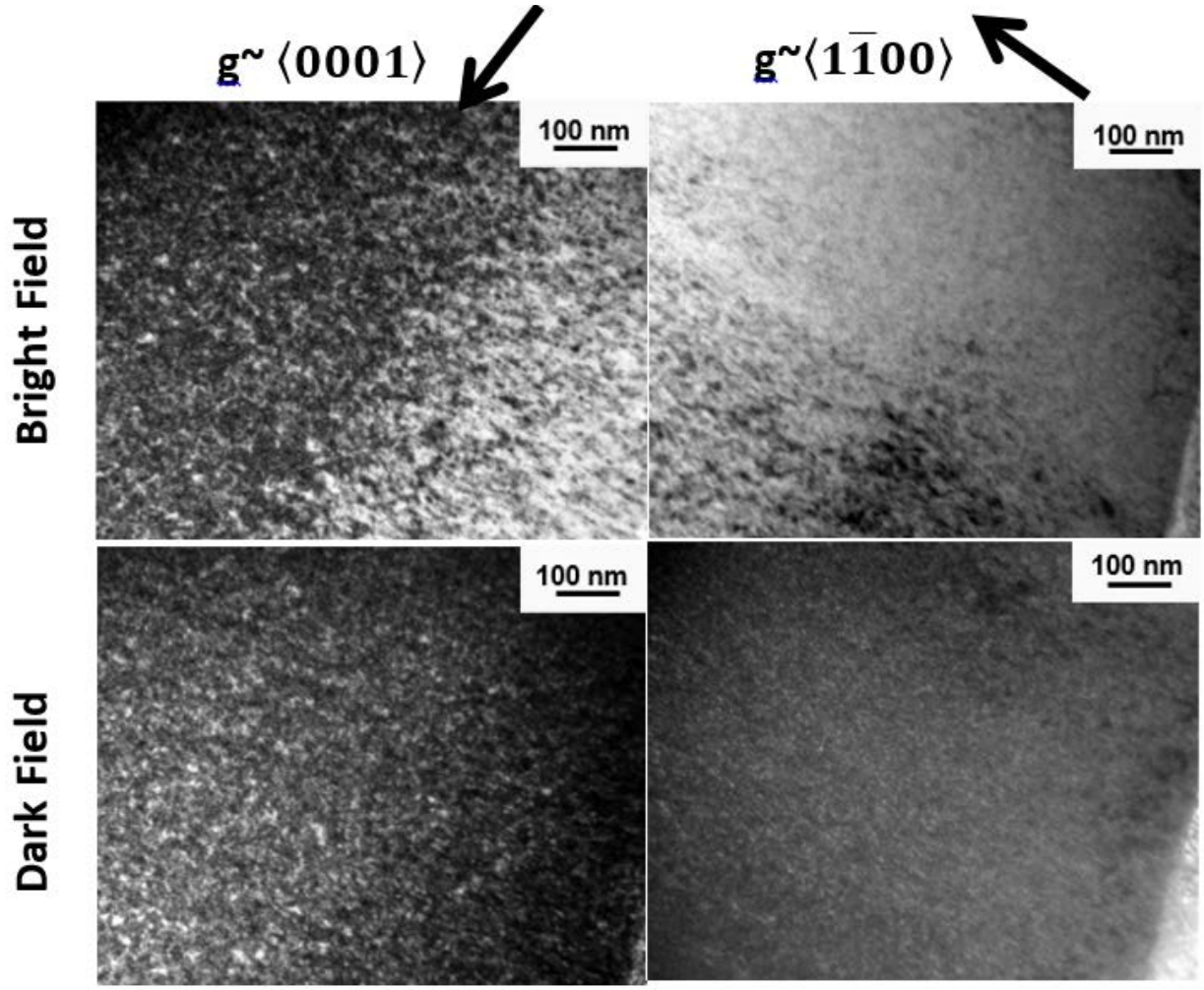

Figure 18 High magnification bright field and dark field cross-sectional TEM micrographs of 5.8 MeV Ni ions irradiated Ti_3AlC_2 to a midrange dose of 30 dpa at a temperature of 400˚C. The basal and prism diffraction vector directions are indicated by ⟨0001⟩ and ⟨1$\bar{1}$00⟩ respectively.

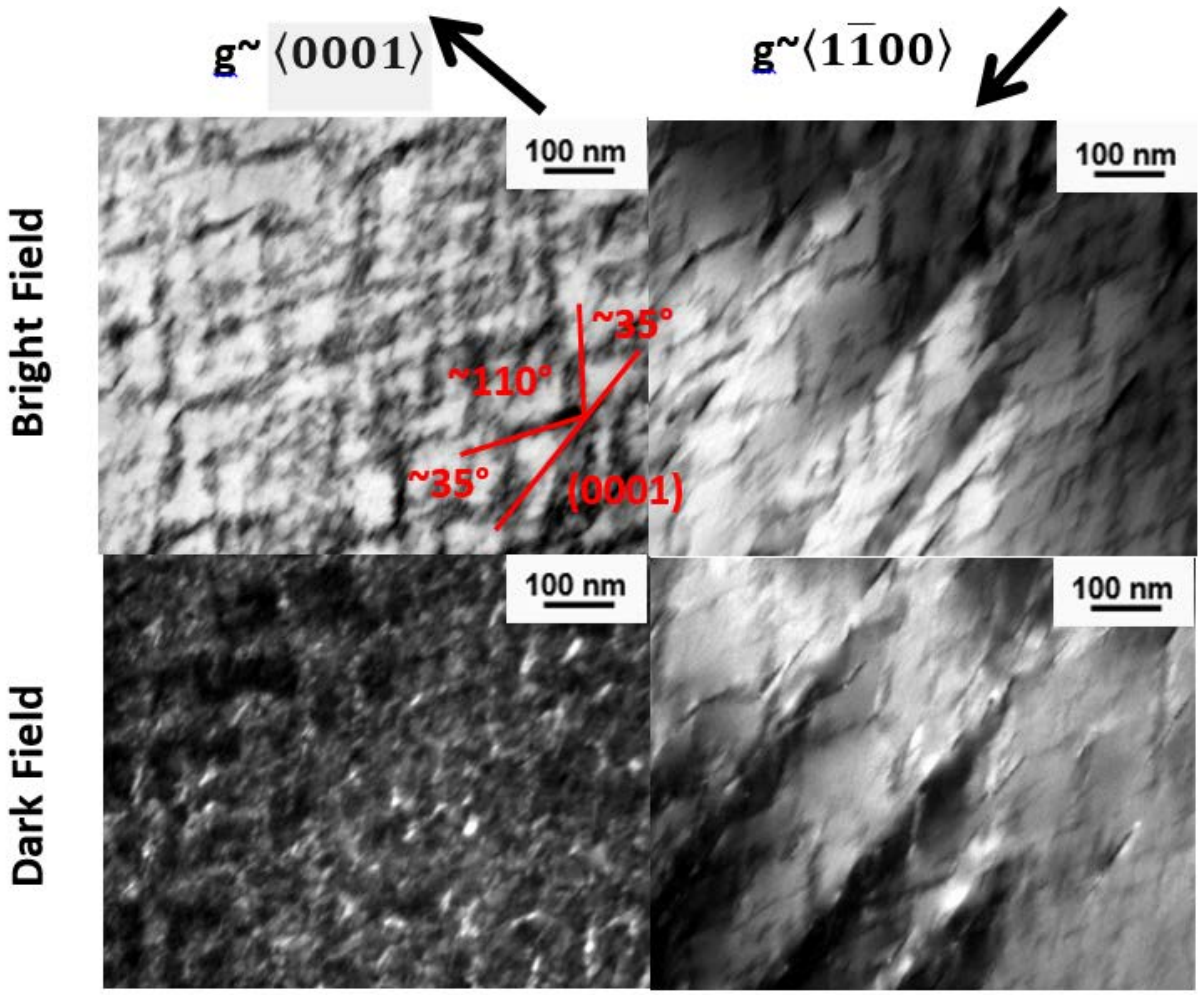

Figure 19 High magnification bright field and dark fieldcross-sectional TEM micrographs of 5.8 MeV Ni ions irradiated Ti_3AlC_2 to a midrange dose of 30 dpa at a temperature of 700˚C. The diffraction vectors are indicated by $\langle 0001 \rangle$ and $\langle 1\bar{1}00 \rangle$ respectively. The red marking show the estimated stacking sequence of small defects with respect to the basal plane.

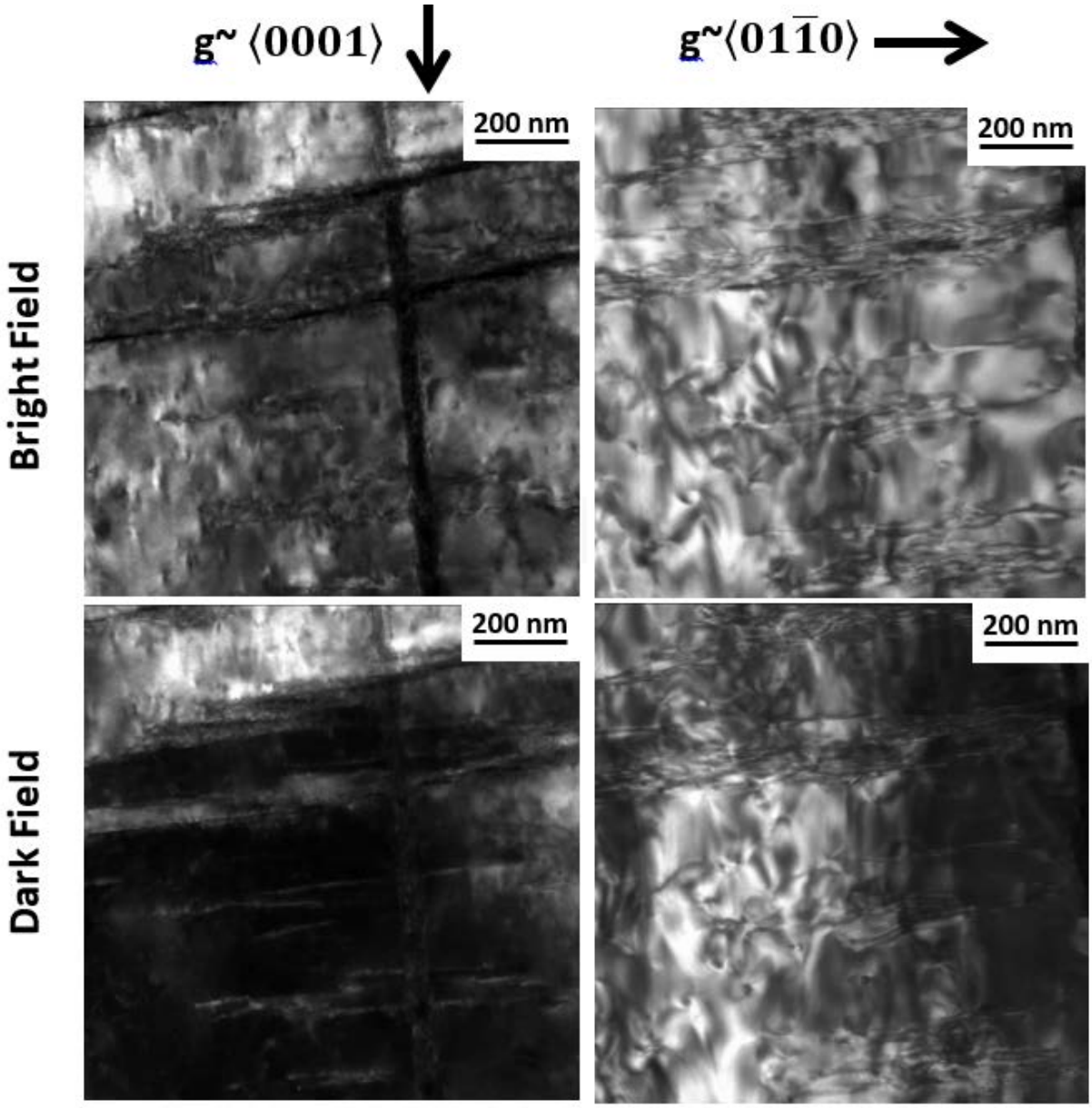

Figure 20 High magnification bright field and dark field cross-sectional TEM micrographs of 5.8 MeV Ni ions irradiated Ti_3SiC_2 to a midrange dose of 30 dpa at a temperature of 700°C. The diffraction vectors are indicated by $\langle 0001 \rangle$ and $\langle 01\bar{1}0 \rangle$ respectively.

Discussion

The GXRD patterns collected from the ion irradiated MAX phase samples revealed a distortion of lattice parameters (LPs) under ion irradiation for all three compositions. For Ti_3AlC_2, four samples at both irradiation doses and temperatures were explored, reveling a lack of lattice parameter dilation on irradiation dose, suggesting radiation damage saturation at damage levels below 10 dpa. Contrary to the weak dose dependence, lattice dilation had a significant dependence on irradiation temperature. For all three materials, the low temperature irradiations produced the largest deviations in both the c-LP and a-LP, with all three materials experiencing an increase or swelling of their c-LP. Ti_2AlC exhibited the largest increase in c-LP, subsequently followed by Ti_3AlC_2 and lastly by Ti_3SiC_2. For a-LP at the low

temperatures, both the aluminum MAX phases showed a decrease in a-LP while the silicon MAX phase showed a slight increase in a-LP. Again, the Ti_2AlC showed the largest deviation from pristine, with both the Ti_3AlC_2 and Ti_3SiC_2 had very similar magnitudes of deviation, if with opposite signs. For most samples, irradiation at high temperatures resulted in only slight variation of LPs from their pristine values, with the exception being high temperature irradiated Ti_3AlC_2, in which there was still noticeable, though not nearly as severe, c-LP swelling. Overall, the c-LP showed more distinct deviation from pristine samples than the a-LP for all three materials at the low temperature irradiations. The results obtained from GXRD show that anisotropic swelling is the underlying cause for grain boundary cracking in the 400˚C irradiated aluminum MAX phases. The significant swelling at lower irradiation temperatures, and the subsequent decrease of swelling as irradiation temperature is increased, are consistent with what is typically observed in irradiated materials in the "point defect swelling" regime where interstitials are mobile but vacancies are immobile [15, 16]. Furthermore, the lack of dose dependence in lattice parameter swelling suggests that defect saturation is reach at some displacement level beneath the minimum 10 dpa dose analyzed in this research, again congruent with the "point defect swelling" regime, which saturates at low doses ('~0.1-1 dpa) and agrees with previous ion irradiation experiments [9-11, 17].

The increase in hardness in the irradiated MAX phases could not be attributed to oxide formation or dramatic chemical change at the sample surface, and as such, must be directly related to the formation of irradiation defects, as previously reported in other ceramics [30-33] .Furthermore, this increase in hardness is consistent with the conclusion that the materials are not being amorphized, as that would have led to a drop, rather than increase in hardness [31]. The lack of hardness change between doses at both the low temperature and high temperature irradiation conditions suggest that radiation induced hardness reaches a saturation point somewhere below the Ni ion fluence level associated with the 10 dpa midrange dose at both 400˚C and 700˚C. Additionally, the progressive recovery of induced hardness with increasing irradiation temperature suggests radiation defect recombination/annealing for all three materials. The present results are consistent with the general evolution of radiation induced hardness in the "point defect swelling" regime corresponding to temperatures between recovery Stage I (onset of interstitial migration) and recovery Stage III (onset of vacancy migration), wherein hardness is more prominent at lower irradiation temperatures and saturates after small doses [15, 16]. Additionally, it is congruent with previous nanoindentation results on MAX phase ceramics [8, 14]. In terms of elastic modulus, the majority of samples underwent a slight increase, with the exceptions being the low temperature irradiation aluminum based MAX phases, which instead underwent a slight decrease in elastic modulus. This effect has been seen in other ceramics where, after low doses, the pinning of dislocations lead to material strengthening and an increase in elastic modulus [34]. Following the SEM observations, it can be concluded that the outlying samples that experienced a decrease in elastic modulus were in fact the ones suffering from grain boundary/surface cracking, which was believed to be the direct cause for the decrease in elastic modulus. One last topic related to indentation is with respect to the damage tolerance properties of the MAX phases. Vickers or Berkovich indentation in brittle solids traditionally result in sharp cracks emanating from the corners of the indent, which is indicative of low toughness. In pristine MAX phases, instead of crack formation at corners, one typically observes delaminations or slip bands, kinking of individual grains, grain push-outs and pull-outs around the area of indentations [29].

SEM examination of indentations showed that no cracks were induced during indentation in the silicon base MAX phase at any of the four irradiation conditions or in the high temperature irradiated aluminum based MAX phases. It is far from conclusive, but the presence of characteristic sliding features in the materials that did not exhibit corner cracking shows that the MAX phases are still able to confine localized mechanical damage and are reasonably damage tolerant at those conditions, albeit to what extent is still unknown. This can be attributed to the preservation of the typical layered structure of the MAX phases, and agrees with the GXRD results wherein the most heavily disordered structures appeared to be those of the aluminum MAX phases at the low irradiation temperatures. Due to the fact that indentation induced pronounced corner cracking in the low temperature irradiated aluminum MAX phases, it can be suggested that irradiation at these conditions for these materials affected the microstructure in such a way as to decrease the damage tolerance.

The presented TEM micrographs exhibit several key features that further support the results discussed above. The appearance of a standard crystalline SAED pattern in the irradiated 30 dpa-400˚C irradiated

Ti_3AlC_2, which is arguably one of the most damaged materials confirms that crystallinity is indeed maintained in all three materials at all irradiation conditions. The high density of small defect clusters in the 30 dpa-400˚C irradiated Ti_3AlC_2 sample implies interstitials are sufficiently mobile to create small defect clusters while the lack of voids up to a dose of 30 dpa implies immobile vacancies at this temperature. This suggests that at 400˚C all three MAX phase are between recovery Stage I and Stage III, or the so called "point-defect swelling regime.

The micrographs of 30 dpa-700˚C irradiated Ti_3AlC_2 appear to show large, grouped clusters of small basal plane defects that coalesce at $\pm$ 35 degree step angles. This is analogous to "rafting" of small defect clusters that has been previously observed in other metallic materials, such as BBC iron, tungsten, and molybdenum [35], and full identification of these defect clusters will require more extensive imaging analysis. In any case, it is clear that the defect clusters are more distinct and with a lower density, leading to the conclusion that interstitials are more mobile than those at the 400˚C irradiation condition. The lack of voids implies that vacancies are still immobile at the 700˚C irradiation condition.

The micrographs of 30 dpa-700˚C irradiated Ti_3SiC_2 coincide with the results shown for Ti_3AlC_2 irradiated at the same condition in that they show larger, better defined defect clusters with a lower density. Again, these larger defects coupled with the lack of voids implies that interstitials have significantly higher mobility than vacancies at the 700˚C irradiation conditions in Ti_3SiC_2. The lack of "rafting" in the Ti_3SiC_2 could be indicative of fundamental differences in radiation response between the aluminum and silicon based MAX phase. However, full identification of these defect clusters through extensive imaging analysis is required before any conclusion can be drawn.

Overall, the micrographs of 30 dpa-700˚C irradiated Ti_3AlC_2 and Ti_3SiC_2, depicting larger, more fully formed defects with a lack of voids suggests that all materials are between recovery Stage I and Stage III at 700˚C. This region is defined by high interstitial mobility, which allows them to coalesce to form large defect structures, and the lack of void formation suggests that Stage III recovery, or vacancy mobility, has not been reached. This microstructural evidence suggests that the point defect swelling regime extends between at least 400 and 700˚C and explains why there is significantly more swelling at lower irradiation temperatures in all three materials. Additionally, these results agree with several studies that suggest amorphization (which occurs for irradiation temperatures below recovery Stage I) during irradiation of MAX phase ceramics is possible only for irradiation temperatures well below room temperature and that voids do not form below 900˚C [7-13, 17].

Concluding Summary

The family of layered carbides and nitrides known as MAX phase ceramics combine many attractive properties of both ceramics and metals due to their nanolaminate crystal structure and are promising potential candidates for application in fusion reactors. This report summarizes experimental results on the effects of energetic heavy ion irradiations on polycrystalline samples of two titanium aluminum carbides (Ti_3AlC_2, Ti_2AlC) and one titanium silicon carbide (Ti_3SiC_2). The irradiation conditions consisted of midrange ion doses between 10 and 30 displacements per atom at temperatures of 400 and 700^{o}C, conditions relevant to application in fusion reactors, and a relatively un-explored regime for MAX phase materials. Following irradiation, a comprehensive analysis of radiation response properties was compiled using X-ray diffraction, nanoindentation, scanning electron microcopy, and transmission electron microscopy. In all cases, the materials remain fully crystalline though atomic collisions induce significant damage and disorder into the layered crystalline lattice. X-ray diffraction and nanoindentation show this damage is manifest in anisotropic swelling and hardening at all conditions and in all materials, with the aluminum based MAX phase exhibiting more pronounced property changes than their silicon counterpart. In all three materials there is little damage dependence on dose (suggesting saturation of radiation damage at levels below 10 displacements per atom) and a high correlation between residual damage and irradiation temperature (with significantly less damage at higher temperatures) suggesting radiation defect annealing. SEM surface analysis showed significant grain boundary cracking and loss of damage tolerance properties in the aluminum based MAX phase irradiated at the low temperature condition. TEM analysis of selected samples suggest that interstitials are mobile while vacancies are immobile and that all three MAX phase are in the so-called "point defect swelling" regime between 400 and 700^{o}C. All results are generally consistent with previous work involving traditional and MAX phase ceramics.

Results show that the aluminum MAX phase is not suitable for application in irradiation environments near 400^{o}C whereas the silicon MAX phase is overall more damage tolerant.

References

[1] 1. Barsoum, M.W., *The Mn+1 AXn Phases and their Properties*, in *Ceramics Science and Technology*. 2010, Wiley-VCH Verlag GmbH & Co. KGaA. p. 299-347.

[2] 2. Barsoum, M.W., *The MN+1AXN phases: A new class of solids: Thermodynamically stable nanolaminates.* Progress in Solid State Chemistry, 2000. **28**(1–4): p. 201-281.

[3] 3. Barsoum, M.W. and M. Radovic, *Elastic and Mechanical Properties of the MAX Phases*, in *Annual Review of Materials Research, Vol 41*, D.R. Clarke and P. Fratzl, Editors. 2011. p. 195-227.

[4] 4. Radovic, M. and M.W. Barsoum, *MAX phases: Bridging the gap between metals and ceramics.* American Ceramics Society Bulletin, 2013. **92**(3): p. 20-27.

[5] 5. Radovic, M., et al., *On the elastic properties and mechanical damping of Ti3SiC2, Ti3GeC2, Ti3Si0.5Al0.5C2 and Ti2AlC in the 300-1573 K temperature range.* Acta Materialia, 2006. **54**(10): p. 2757-2767.

[6] 6. Tallman, D.J., B. Anasori, and M.W. Barsoum, *A critical review of the oxidation of Ti2AlC, Ti3AlC2 and Cr2AlC in Air.* Materials Research Letters, 2013. **1**(3): p. 115-125.

[7] 7. Bugnet, M., et al., *Contribution of core-loss fine structures to the characterization of ion irradiation damages in the nanolaminated ceramic Ti3AlC2.* Acta Materialia, 2013. **61**(19): p. 7348-7363.

[8] 8. Liu, X.M., et al., *Nanoindentation investigation of heavy ion irradiated Ti-3(Si,Al)C-2.* Journal of Nuclear Materials, 2010. **401**(1-3): p. 149-153.

[9] 9. Liu, X.M., et al., *XRD investigation of ion irradiated Ti3Si0.90Al0.10C2.* Nuclear Instruments & Methods in Physics Research Section B-Beam Interactions with Materials and Atoms, 2010. **268**(5): p. 506-512.

[10] 10. Nappe, J.C., et al., *Microstructural changes induced by low energy heavy ion irradiation in titanium silicon carbide.* Journal of the European Ceramic Society, 2011. **31**(8): p. 1503-1511.

[11] 11. Nappe, J.C., et al., *Structural changes induced by heavy ion irradiation in titanium silicon carbide.* Journal of Nuclear Materials, 2011. **409**(1): p. 53-61.

[12] 12. Whittle, K.R., et al., *Radiation tolerance of M(n+1)AX(n) phases, Ti3AlC2 and Ti3SiC2.* Acta Materialia, 2010. **58**(13): p. 4362-4368.

[13] 13. Zhang, L., et al., *Damage tolerance of Ti3SiC2 to high energy iodine irradiation.* Applied Surface Science, 2012. **258**(17): p. 6281-6287.

[14] 14. Marion, L. and I. Monnet, *Saturation of irradiation damage in (Ti,Zr)(3)(Si,Al)C-2 compounds.* Journal of Nuclear Materials, 2013. **433**(1-3): p. 534-537.

[15] 15. Was, G.S. and SpringerLink (Online service), *Fundamentals of Radiation Materials Science Metals and Alloys*. 2007, Springer-Verlag GmbH.,: Berlin Heidelberg.

[16] 16. Zinkle, S.J., *Radiation-Induced Effects on Microstructure*. Comprehensive Nuclear Materials, Vol 1: Basic Aspects of Radiation Effects in Solids/Basic Aspects of Multi-Scale Modeling, ed. R.J.M. Konings. 2012. 65-98.

[17] 17. Tallman, D.J., et al., *Effect of neutron irradiation on select MAX phases.* Acta Materialia, 2015. **85**: p. 132-143.

[18] 18. Barsoum, M.W. and T. ElRaghy, *Synthesis and characterization of a remarkable ceramic: Ti3SiC2.* Journal of the American Ceramic Society, 1996. **79**(7): p. 1953-1956.

[19] 19. Eklund, P., et al., *The Mn+1AXn phases: Materials science and thin-film processing.* Thin Solid Films, 2010. **518**(8): p. 1851-1878.

[20] 20. Stoller, R.E., et al., *On the use of SRIM for computing radiation damage exposure.* Nuclear Instruments & Methods in Physics Research Section B-Beam Interactions with Materials and Atoms, 2013. **310**: p. 75-80.

[21] 21. Toby, B., *CMPR - a powder diffraction toolkit.* Journal of Applied Crystallography, 2005. **38**(6): p. 1040-1041.

[22] 22. *HighScore & HighScore Plus Quick Start Guide*. August 2013; 2nd:[Available from: www.PANalytical.com.

[23] 23. Oliver, W.C. and G.M. Pharr, *An improved technique for determining hardness and elastic modulus using load and displacement sensing indentation experiments.* Journal of Materials Research, 1992. **7**(06): p. 1564-1583.

[24] 24. Nix, W.D. and H. Gao, *Indentation size effects in crystalline materials: A law for strain gradient plasticity.* Journal of the Mechanics and Physics of Solids, 1998. **46**(3): p. 411-425.
[25] 25. Jenkins, L. and A. Kirk, *Characterisation of Radiation Damage by Transmission Electron Microscopy*. 2000: Taylor & Francis.
[26] 26. Jenkins, M.L., *CHARACTERIZATION OF RADIATION-DAMAGE MICROSTRUCTURES BY TEM.* Journal of Nuclear Materials, 1994. **216**: p. 124-156.
[27] 27. DeHoff, R.T., F.N. Rhines, and U.o. Florida, *Quantitative microscopy*. 1968: McGraw-Hill.
[28] 28. Clarke, F.J.P., R.S. Wilks, and D.H. Bowen, *Mechanisms of irradiation-induced growth and cracking in beryllia.* Journal of Nuclear Materials, 1964. **14**: p. 205-207.
[29] 29. El-Raghy, T., et al., *Damage Mechanisms around Hardness Indentations in Ti3SiC2.* Journal of the American Ceramic Society, 1997. **80**(2): p. 513-516.
[30] 30. Iseki, T., et al., *HARDENING BY POINT-DEFECTS IN NEUTRON-IRRADIATED ALN AND SIC.* Journal of Nuclear Science and Technology, 1993. **30**(1): p. 68-77.
[31] 31. Snead, L.L., et al., *Amorphization of SiC under ion and neutron irradiation.* Nuclear Instruments & Methods in Physics Research Section B-Beam Interactions with Materials and Atoms, 1998. **141**(1-4): p. 123-132.
[32] 32. Suematsu, H., et al., *POINT-DEFECT HARDENING IN MGO.3AL2O3.* Journal of the American Ceramic Society, 1992. **75**(7): p. 1742-1747.
[33] 33. Yang, Y., et al., *Microstructure and mechanical properties of proton irradiated zirconium carbide.* Journal of Nuclear Materials, 2008. **378**(3): p. 341-348.
[34] 34. Snead, L.L. and S.J. Zinkle, *Use of beryllium and beryllium oxide in space reactors*, in *Space Technology and Applications International Forum-Staif 2005*, M.S. ElGenk, Editor. 2005. p. 768-775.
[35] 35. Zinkle, S.J. and B.N. Singh, *Microstructure of neutron-irradiated iron before and after tensile deformation.* Journal of Nuclear Materials, 2006. **351**(1-3): p. 269-284.

7.3 EFFECTS OF ION AND NEUTRON IRRADIATION ON BAM-11 BULK METALLIC GLASS — J. Brechtl[2], N.A.P Kiran Kumar[1], H. Bei[1], and S. J. Zinkle[1,2] (*[1]Oak Ridge National Laboratory, [2]University of Tennessee)*

OBJECTIVE

The goal of this project is to study ion and neutron irradiation effects in BAM-11 bulk metallic glass alloy to determine its viability as a candidate for structural applications in high-radiation fusion environments.

SUMMARY

Bulk metallic glasses are candidates for fusion reactor structural components due in part to their good mechanical properties and near net shape fabrication potential. Metallic glasses might also exhibit good radiation resistance as their amorphous structure prohibits the formation of Frenkel defects, and subsequent voids and dislocation loops. Mechanical properties of $Zr_{52.5}Cu_{17.9}Ni_{14.6}Al_{10}Ti_5$ bulk metallic glass (BAM-11) irradiated with fission neutrons to 0.1 and 1 dpa at ~90°C show a slight increase in the Vickers hardness (roughly ~7, ~10% for 0.1, 1 dpa respectively). Using a Nix-Gao method it was found that the nano-indentation hardness increased by about ~0.4% and ~66% for samples irradiated to 0.1 and 1 dpa. The dynamic Young's modulus in the sample irradiated to 0.1 dpa was ~5% less than the control sample, and the nano-indentation Young's modulus at 0.1, 1 dpa was approximately 1.4%, 0.9% less than the control specimen. The density of BAM-11 decreased roughly ~0.4% for both 0.1 and 1 dpa. The results suggest that the irradiation-induced damage begins to saturate at doses between 0.1 and 1 dpa.

PROGRESS AND STATUS

Introduction

The formation of the first metallic glass of $Au_{75}Si_{25}$ was reported by Duwez at Caltech, USA, in 1960 [1]. More recently, bulk metallic glasses have been proposed as a candidate for use in radiation environments due to their lack of crystalline structure, which prohibit the formation of Frenkel pairs and dislocation loops [2] and might lead to superior resistance to radiation-induced property degradation. Bulk metallic glasses also exhibit exceptional hardness, high strength and corrosion resistance [3].

Another factor which may make amorphous metals desirable is their potentially high helium permeability due to their large free atomic volume and lack of grain boundaries which can act as helium traps [4]. The trapping of helium at defects is very important in irradiated materials since it can lead to embrittlement and swelling. Furthermore, there is some evidence that the amount of retained displacement damage can be significantly less in amorphous materials [5,6]. Recent studies also show that metallic glasses may be resistant to cavity swelling, and hence possibly tritium retention, as compared to crystalline materials, which would make them appealing for fusion energy applications [6, 7]

For this study the neutron irradiation effects on the mechanical properties of bulk metallic glass BAM-11 (composition: $Zr_{52.5}Cu_{17.9}Ni_{14.6}Al_{10}Ti_5$) were investigated. Specimens were irradiated with fission neutrons to 0.1 and 1 dpa at ~90°C.

Experimental Procedures

A $Zr_{52.5}Cu_{17.9}Ni_{14.6}Al_{10}Ti_5$ alloy (BAM-11) was fabricated by arc melting in an argon atmosphere using a mixture of base metals with the following purities: 99.5% Zr, 99.99% Cu, 99.99% Ni, 99.99% Al, and 99.99% Ti. The alloy was then remelted and drop cast in a Zr-gettered helium atmosphere. Specimens were then prepared from the as-cast rods by electrical discharge machining. Table 1 shows the experimental matrix for the current project which includes the testing property, the measurement condition, and the specimen dimension. Samples were encased in a perforated rabbit irradiation capsule which allowed the coolant water to directly contact the samples. Furthermore, the BAM-11 samples were wrapped in aluminum foil to minimize any potential corrosion or contamination.

After encapsulation, BAM-11 specimens were irradiated with fission neutrons at the ORNL High Flux Isotope Reactor (HFIR) in hydraulic tube 2 (HT-2). Here the samples were exposed to neutron fluences of 1.40 X 10^{20} n/cm^2 and 1.35 X 10^{21} n/cm^2 (E>0.1 MeV) in a perforated hydraulic rabbit capsule. Using a conversion factor of ~0.8 dpa per 10^{21}n/cm^2, the neutron doses in the BAM-11 were approximately 0.1 dpa and 1 dpa [8]. The specimens were wrapped in aluminum foil and the external surface of the wrapped specimens was directly exposed to the reactor coolant water at ~60^{o}C. After consideration of internal nuclear heating effects in the samples, the estimated average sample temperature is ~90 ^{o}C.

Table 1. Testing matrix for control samples and after irradiation to 0.1 and 1 dpa at ~ 90^{o}C.

Testing Property	Measurement Condition	Specimen Dimensions
Bulk Hardness (Hv)	At Room Temperature	3 x 2 x 14 mm Ø 3 x 0.4 mm
Nano-indentation Hardness (GPa)	At Room Temperature	3 x 2 x 14 mm Ø 3 x 0.4 mm
Dynamic Young's Modulus (GPa)	At Room Temperature	3 x 2 x 27 mm
Density (g/cm^3)	At Room Temperature	3 x 2 x 27 mm 3 x 2 x 14 mm

Bulk hardness measurements were performed at room temperature using a Buehler Micromet 3 hardness indenter equipped with a Vickers indenter tip. The tests were performed using a 500 g load with a dwell time of 15 s for all indents. Five indents were taken on each specimen to a depth of ~6.5 μm and spaced 500 μm apart. For this experiment both a bend test bar and a transmission electron microscopy (TEM) disk were used. Prior to indentation, both specimens were surface polished with 1 micron diamond lapping film. With respect to the bend test bar, all indents were made on the end regions of the specimen, well away from the center region of the specimen so that later flexural strength tests are not influenced.

Nano-indentation hardness and Young's modulus measurements were performed at room temperature using an Agilent G200 Nano-indenter with a Berkovich diamond indenter tip. Like the Vicker's hardness tests, the samples consisted of a bend test bar and a TEM disk. All the tests were performed in continuous stiffness measurement mode with a constant loading rate $\dot{P}/P = 0.05\text{s}^{-1}$. In total, 20 indents were made where hardness was measured as a function of depth from the point of contact of the nanoindenter with the surface to a depth of about 800 nm. The hardness data below a depth of ~300 nm from the specimen surface was discarded due to large data scatter associated with surface roughness. Hardness was calculated using the Oliver and Pharr method [9, 10]. The area function of the tip in addition to the machine stiffness for the nanoindenter was calibrated by indenting on a standard fused silica sample [2, 11].

Dynamic elastic modulus measurements were performed using the Resonant Frequency and Damping Analyzer (RFDA) from Integrated Material Control Engineering (IMCE). Here two nodes were set up perpendicular to the length and are located 0.224 times the length in from the ends of the specimen. For the experiment the center of the sample was struck. The resultant vibration propagates through the sample where it is absorbed by a transducer located at the end of the sample. The transducer converts the energy of the vibration into a signal which may be analyzed by an oscilloscope.

Density measurements were performed at room temperature using an immersion density instrument, which consists of an ultra-sensitive balance, the Satorius ME215S, a density kit, and a high-precision

digital thermometer. Samples were immersed in a 3M Fluorinert™ Liquid FC-43 which has high density, low surface tension, low thermal expansion, low vapor pressure and low water/air solubility. Each specimen was measured three times and the density was determined using Archimedes principle.

Mechanical Properties

Vickers hardness values of the neutron irradiated BMG specimens are shown in Figure 1. There was a modest increase of ~7% and ~10% at neutron doses (~90 ^{o}C) of 0.1, 1 dpa respectively. Furthermore, the hardness appears to approach saturation for doses above approximately 0.1 dpa. This result is further supported by an earlier study conducted by Perez-Bergquist et al. which irradiated BAM-11 alloy with 3 MeV Ni^{+} ions to doses of 1, 10 dpa [12]. They found that the irradiation induced change in the hardness of the BMG did not change markedly between doses of ~1 and 10 dpa.

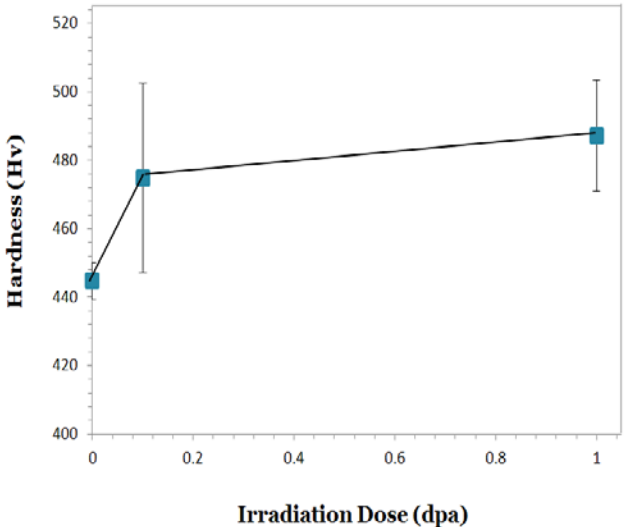

Figure 1. Bulk hardness of neutron irradiated bulk metallic glass samples as a function of irradiation dose.

Nano-indentation hardness was measured as a function of depth from the point of contact of the nano-indenter with the surface to a depth of about 800 nm. The hardness data below a depth of ~300 nm from the specimen surface was discarded due to large data scatter associated with surface roughness. The depth-dependence hardness values of the neutron irradiated BMG specimens are shown in Figure 2. A pronounced depth dependence was measured for the nanoindentation hardness, particularly for the unirradiated and 0.1 dpa irradiated samples. At 800 nm, there was a decrease in the nano-indentation hardness of about ~6% and ~12% from the unirradiated state was observed in the specimens irradiated to 0.1 dpa and 1 dpa.

The as-measured nanoindentation hardness softening implied by Figure 2 is unexpected since the nano-indentation hardness should have a similar trend to the bulk Vickers hardness. It is notable in Figure 2 that the nanoindentation hardness exhibits a pronounced depth dependence. Since the nano-indentation hardness is performed at relatively shallow depths compared to the bulk Vickers hardness measurements (<1 microns vs. ~6.5 microns), the discrepancy between the two hardness tests could be a result of surface effects due to machining or mechanical polishing effects, or a near-surface composition gradient due to chemical inhomogeneity or near-surface radiation induced solute segregation.

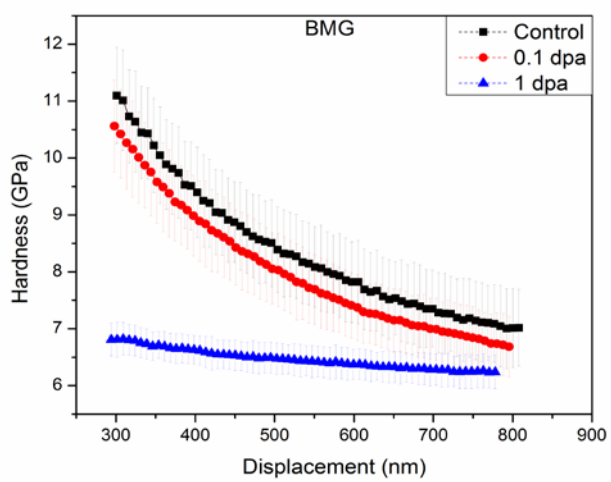

Figure 2. Nano-indentation hardness as a function of indenter depth in the irradiated and control BAM-11 specimens.

In order to make a quantitative comparison of the nano-indentation hardness results with the bulk hardness, the Nix-Gao model was used to evaluate possible near-surface layer with a different hardness than the bulk, and to obtain an extrapolated value of the bulk hardness [13]. For this method, the square of the nano-indentation hardness was plotted vs. the reciprocal of the indentation depth. Samples with uniform hardness should exhibit a linear relationship in this type of plot. To determine the extrapolated bulk hardness H_0, a line was fit to the data and extrapolated towards the ordinate axis. The hardness H_0 occurs where the abscissa equals zero and corresponds with the hardness at an arbitrarily large depth in the material. Due to the deviation away from linear behavior, only the data at a depth >400 nm was used to determine the extrapolated bulk hardness H_0. The extrapolated bulk hardness for each irradiation condition can be seen in Figure 3 below.

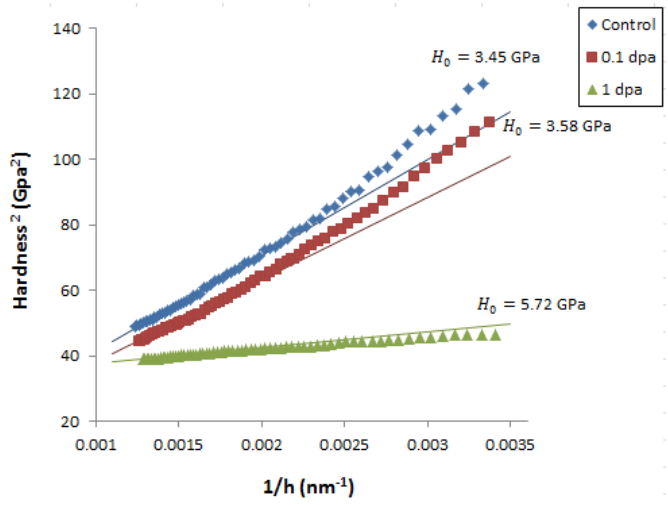

Figure 3. Hardness squared vs. the inverse of the nano-indentation depth.

The hardness results for the hardness H_0 vs. irradiation dose can be seen in Figure 4 below. As can be observed in the graph, the hardness results for the Nix-Gao model exhibits a similar qualitative trend as the Vicker's bulk hardness in the material (Figure 1). In particular, the extrapolated bulk hardness derived from a Nix-Gao analysis indicates an increase of ~0.4%, ~66% after irradiation to 0.1 and 1 dpa, respectively as compared to the unirradiated specimen. The results suggest that there may be a surface

modification which affects the surface hardness of the BAM-11 alloy which may require further investigation, including nanoindentation to deeper depths.

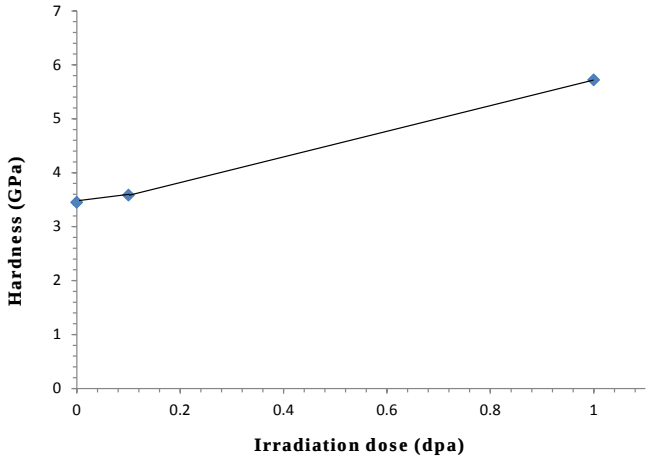

Figure 4. Nix-Gao extrapolated bulk hardness vs. irradiation dose.

The Young's modulus vs. nano-indentation depth can be seen in Figure 5 below. As can be seen, the elastic modulus decreases with increasing depth, resembling the trend for nano-indentation hardness. At 800 nm, the data indicates a slight decrease of ~1.4% and ~0.9% after irradiation to 0.1 and 1 dpa, respectively as compared to the unirradiated specimen

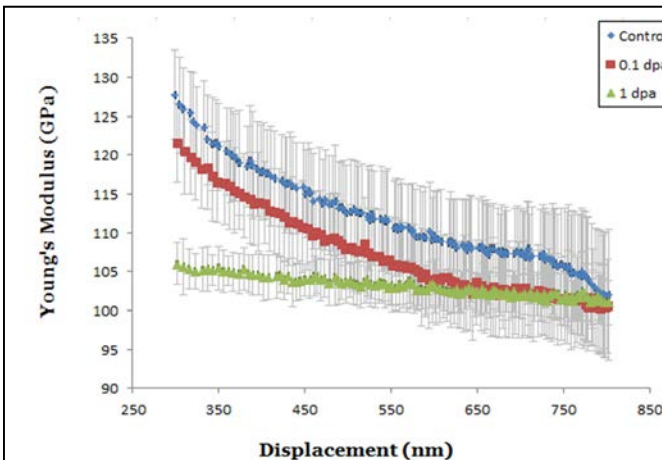

Figure 5. Young's modulus vs. nano-indentation depth.

The dynamic Young's modulus for the control and sample irradiated to 0.1 dpa can be seen in Table 2 below. There was a decrease of ~5% in the dynamic Young's modulus of the specimens irradiated to 0.1 dpa at 90°C as compared to the control sample.

An experiment conducted by Perez-Bergquist et al., which involved the Ni^{+} ion irradiation of the same BAM-11 bulk metallic glass at room temperature and 200 ^{0}C, observed different responses in the nano-indentation hardness and Young's modulus [2]. Specifically, it was found that samples irradiated at room temperature exhibited a clear drop in hardness and elastic modulus while samples irradiated at 200 ^{0}C did not experience significant changes in hardness and saw only small changes in Young's modulus.

Table 2. Average dynamic Young's modulus of unirradiated and irradiated BMG specimens.

BMG	Control	0.1 dpa – 90°C
Average Dynamic Young's Modulus (GPa)	79.4	75.7
Std. Dev of Dynamic Young's Modulus (GPa)	0.7	1.8

However, the results of the Vicker's bulk hardness and the Nix-Gao analysis for nano-indentation hardness indicate that bulk metallic glasses exhibit increased hardness when exposed to neutron irradiation up to doses in the range of 0.1 and 1 dpa. The moderate quantitative discrepancies between the Nix-Gao extrapolation and the Vicker's hardness results require further investigation.

The measured densities for the control and irradiated specimens are listed in Table 3. A decrease in density was found in the irradiated samples as compared to the control specimens. Here the specimens exhibited ~0.4% decrease in density at both irradiation doses. Moreover, the density at 1 dpa was slightly greater than the density at 0.1 dpa. The slight change in density is likely associated with the irradiation induced rearrangement of short range atomic bonding which results in greater atomic spacing.

Previous studies have also found neutron irradiation induced microstructural changes in metallic glasses. For example, a study conducted by Gupta et al. found that thermal neutron irradiation of iron based metallic glass to low doses increased the short range order which was accompanied by a relief in the random internal stresses of the as received specimens [14]. In contrast to the above studies, the study by Perez-Bergquist et al. found no significant microstructure changes of BAM-11 after exposure to Ni^{+} ion irradiated BAM-11 [2]. This discrepancy between experimental results of ion and neutron irradiation warrants further research on the radiation response of BAM-11 amorphous alloy.

Table 3. Measured density of unirradiated and irradiated BMG specimens

Condition	Specimen weight (g)		Density of specimen (g/cm^3)
	In Air	In Fluid	
Control	0.98818	0.70871	6.66046
0.1 dpa	1.06142	0.76024	6.63491
1 dpa	1.06797	0.76475	6.63520

In summary, there were relatively slight irradiation induced changes in the bulk hardness, nano-indentation hardness, density and dynamic Young's modulus for the given dose regime. For the first three tests, the exhibited change did not differ significantly between the samples tested at 0.1 and 1 dpa. This result signifies that a saturation of irradiation damage may be occurring in BAM-11 within the examined dose regime.

Conclusions

After irradiation with fission neutrons to dose levels of 0.1 and 1 dpa at ~90 ^{o}C, the BAM-11 bulk metallic glass specimens were found to exhibit slight decreases in both the dynamic and nanoindentation Young's modulus. Specifically there was a drop of 5% for the dynamic Young's modulus at 0.1 dpa while for the nano-indentation Young's modulus there was a drop of 1.4% and 0.9% for 0.1 and 1 dpa respectively. The density was found to drop by 0.4% for both irradiation conditions, which suggests BAM-11 is susceptible to a slight neutron induced densification. In terms of hardness, there was an 7-10% increase in the bulk hardness and a 0.4%, 66% increase in the nano-indentation hardness based on a Nix-Gao extrapolation of the data. In addition, damage approaching a dose of approximately 1 dpa exhibits an apparent saturation based on the results of the density and bulk Vickers hardness tests.

In summary, the material response of BAM-11 following fission neutron irradiation indicates that the alloy exhibits good resistance to pronounced structural and property changes during low dose neutron irradiation near room temperature. However, further studies of the bulk metallic glass are needed to fully understand the effects of neutron irradiation on the material. These studies include Transmission Electron Microscopy (TEM) and Extended X-ray Absorption Fine Structure (EXAFS) to explore nanoscale changes to microstructure, if any. Future experiments may include neutron irradiation to doses of ~10 dpa and ion irradiation to doses greater than 10 dpa to examine whether BAM-11 exhibits a true saturation effect.

References

[1] W. Klement, R.H. Wilens, and P. Duwez, Nature, 187 (1960) 869-870.
[2] A. G. Perez-Bergquist, H. Bei, K. J. Leonard, Y. Zhang, S. J. Zinkle,. Intermetallics 53 (2014) 62-66.
[3] A. Inoue, Acta Materialia, 48 (2000) 279-306.
[4] W.J. Weber, R.C. Ewing, C.A. Angell, G.W. Arnold, A.N.Cormack, J.M. Delaye, D.L. Griscom, L.W. Hobbs, A.Navrotsky, D.L. Price, A.M. Stoneham, and M.C. Weinberg, J. Mater. Res. 12 (1997) 1946 ‐ 1978.
[5] W.J. Weber, R.C. Ewing, C.A. Angell, G.W. Arnold, A.N. Cormack, J.M. Delaye, D.L. Griscom, L.W. Hobbs, A. Navrotsky, D.L. Price, A.M. Stoneham, and M.C. Weinberg, J. Mater. Res.12 (1997) 1946-
1978.
[6] A. G. Perez-Bergquist, H. Bei, Y. Zhang, and S.J. Zinkle, Fusion Materials Semiannual Progress Report for Period Ending December 31, 2013, DOE/ER-0313/26, U. S. Department of Energy, 154.
[7] X. Mei, B. Wang, C. Dong, F. Gong, Y. Wang, and Z. Wang, Nucl. Instrum. Methods Phys. Res. B
307(2013) 11-15.
[8] L.L. Snead, J. Nucl. Mater., 326 (2004) 114-124.
[9] W.C. Oliver and G.M. Pharr, J. Mater. Res. 7 (1992) 1564-1583.
[10] W.C. Oliver and G.M. Pharr, J. Mater. Res. 19 (2004) 3-20.
[11] W. Li, H. Bei, Y. Tong, W. Dmowski, and Y.F. Gao, Appl. Phys. Lett. 103 (2013) 171910.
[12] A. G. Perez-Bergquist, J. Brechtl, H. Bei, Y. Zhang, and S. J. Zinkle, Fusion Materials Semiannual Progress Report for Period Ending June 30, 2014, DOE/ER- 0313/56, U.S. Department of Energy, 184.
[13] W.D. Nix and H. Gao, J. Mech. Phys. Solids, 46, (1998) 411-425.
[14] A. Gupta and S. Habibi, Mat. Sci. and Engineering A134 (1991), 992-995.

7.4 EXPLORATION OF THE RADIATION RESISTANCE OF HIGH ENTROPY ALLOYS — C. Li, S.J. Zinkle (University of Tennessee), N.A.P. Kiran Kumar, H. Bei (ORNL)

OBJECTIVE

The goal of this project is exploring the basic radiation resistance of high entropy alloys (HEAs) that may have the potential for very good resistance to radiation-induced property degradation.

SUMMARY

This report summarizes the experimental characterization of neutron and ion irradiated 27%Fe-27%Mn-28%Ni-18%Cr HEA. Samples have been neutron irradiated at ~70˚C from 0.1 dpa to 1 dpa, and ion irradiated with 5.8 MeV Ni ions at temperatures ranging from 400˚C to 700˚C and midrange doses from 0.1 dpa to 10 dpa. Post irradiation examination of the neutron irradiated samples found a large increase of hardness after 0.1 dpa, whereas there was only a mild increase from 0.1dpa to 1dpa. Similar trend was observed with the change of yield strength and electrical resistivity. The stress-strain curves of the neutron irradiated specimens are in agreement with the typical behavior of 304, 316 and 347 austenitic stainless steels, but the large yield drop and reduction of work hardening rate seems to be unique to HEA. Ion irradiations at higher temperatures showed evidence of sluggish diffusion with almost no solute depletion or enrichment at grain boundaries. Voids were also not observed at any irradiation condition, suggests that this type of HEA is fairly stable under high temperature radiation.

PROGRESS AND STATUS

Introduction

HEAs consist of four or more elements with nearly equimolar ratios, giving rise to high configurational entropy. HEAs can be either face centered cubic (f.c.c) or body centered cubic (b.c.c) phases without formation of brittle phases that frequently observed in conventional simple intermetallic alloys[1-5]. Due to their superior mechanical properties, HEAs have potential application as a structural material in advanced nuclear energy systems. However, little is known about their stability under neutron or ion irradiation. It is hypothesized that the high configurational entropy might modify point defect (solute and radiation-induced point defects) diffusion, recombination and agglomeration processes.

Austenitic steels are widely used in current nuclear fission reactors and are proposed for advanced fission reactors and fusion reactor first-wall structures such as ITER[6]. However, they don't appear to show sufficient radiation resistance required for the extended operation of current fission reactors or advanced reactor concepts. Of all the radiation degradation phenomena in Fe-based austenitic steels, void swelling and radiation-induced segregation (RIS) are two extremely significant challenges.

In the current study, a novel 27%Fe-27%Mn-28%Ni-18%Cr single phase f.c.c HEA has been characterized after ion and neutron irradiation. The objective of this study is to examine the change of mechanical properties and microstructure of this HEA after irradiation over a wide range of irradiation temperatures.

Experimental Procedure

Many of the high entropy alloys studied to date contain Co, making them unfavorable for nuclear applications due to neutron activation. In the present study, a novel 27%Fe-27%Mn-28%Ni-18%Cr high entropy alloy has been synthesized. The material was prepared by arc-melting by mixing constituent metals of high purity. The cast bar was then homogenized at 1200°C for 48 h, cold rolled and recrystallized at 900°C for 4hr in a vacuum furnace to obtain fully recrystallized microstructure.
For neutron irradiation, samples were irradiated at ~70 ˚C from 0.1 dpa to 1 dpa in the High Flux Isotope Reactor (HFIR). Six SS3J tensile specimens (overall length 25 mm, thickness 0.76mm, gage length 7.6 mm and gage width 1.5 mm) and three TEM disks were prepared for each irradiation condition. For ion irradiation, six TEM disks were mechanically polished down to 1 micron diamond lapping film and shipped

to the Texas A&M University- Radiation effects facility for ion irradiation at the conditions summarized in Table 1. However, due to poor vacuum in the specimen chamber, all the irradiated specimens exhibit a surface contamination layer following irradiation (due in part to outgassing from the silver paste used to attach the specimens to the target holder, and also due to a vacuum leak during the irradiations). The contamination layer formed on the sample surface was relatively non-uniform and the thickness ranged from ~100 nm in 400°C to ~200nm in 700°C. Nanoindentation tests were not performed on the ion irradiated samples as the non-uniform contamination layer will influence the determination of specimen contact area, which may cause errors for the measurement of hardness and modulus. Ion irradiation doses were computed by SRIM following the recommendations of Stoller (40 eV displacement energy, quick Kinchin-Pease option).[7] The calculated ion range is ~1.9 micron and mid-range dose is evaluated at a depth of ~1 micron.

Table 1. Summary of ion irradiation conditions for the high entropy alloy.

Material	Ion irradiation (mid-range dose, ~5.8MeV Ni ions)
HEA (Fe-28%Ni-27%Mn-18%Cr)	1dpa, 500°C
	1dpa, 600°C
	10dpa, 400°C
	10dpa, 500°C
	10dpa, 600°C
	10dpa, 700°C

All the post-irradiation examinations of the neutron irradiated samples were conduced at room temperature. Bulk hardness was measured by a hardness indenter equipped with a Vickers indenter tip. The load and dwell time were set at 500 grams and 10s. Five indents were made on two TEM disks irradiated to 0.1dpa and 1dpa, respectively. Nanohardness was also measured on the same two TEM disks (after light mechanical polishing of the surfaces with 1 micron diamond lapping film) using a Nano Indenter G200, manufactured by Agilent Technologies, with Berkovich diamond indenter. All tests were performed in continuous stiffness measurement mode with a constant load rate $\dot{P}/P = 0.05\ s^{-1}$. Nanohardness was measured as a function of depth from the point of contact to a depth of about 1000nm. Hardness data below a depth of ~ 300nm from the surface was discarded due to large data scatter associated with surface roughness. 25 indents were made for each specimen to obtain sufficient statistics for the evaluation of average and error.

Tensile testing was conducted using three SS3J specimens (one control specimen, one 0.1dpa and one 1dpa) on a screw-driven mechanical test frame, with a nominal strain rate of $0.0003s^{-1}$. Anomalous strain in the load vs. crosshead displacement data due to machine compliance effects was corrected to show the right stress-strain relationship. The correction was done by assuming that irradiation induces minimum change of elastic modulus, and that Young's modulus is the same for both irradiated and unirradiated samples. Electrical resistivity was measured using a four-point probe technique on five 0.1 dpa and six 1 dpa SS3J tensile specimens. 100 mA current was used through the outer contact near the tab region of the specimen, and the voltage drop between the inner contacts of the specimen's gage section was measured and converted to resistivity based on measurements of the individual sample gage dimensions. For each specimen, five measurements were taken first, and the specimen was then flipped over to make another five measurements to minimize the effect of voltage fluctuation and sample orientation effects.

For the ion irradiated samples, cross-section transmission electron microscopy (TEM) specimens from the irradiated samples were prepared using a focus ion beam (FIB) (FEI Quanta 3D 200i) system with Ga+ ions. The ion energy at the main thinning step is 30keV, and during the later stages of thinning the energy was progressively reduced to 8, 5 and 2 keV with the final thinning at a foil thickness of ~100 nm

performed with a current of 27 pA. In order to minimize the unwanted FIB damage caused by Ga+ ions, a low voltage argon ion polishing system (Fischione NanoMill-model 1040) was subsequently used for creating high quality TEM specimens. A very low voltage and current of 900 eV and 90 pA were used on the TEM specimen during the final thinning. As a final step, a Fischione Plasma Cleaner (Model 1020) was used to remove carbonaceous contamination from the TEM specimen. A Philips CM200 FEG (field emission gun) TEM/scanning transmission electron microscope (STEM) that produces a probe of 1.4 nm at 200-kV operating voltage was used to examine the changes of microchemistry at the grain boundaries in the irradiated samples.

Results and Discussion

The hardness of HEA following neutron irradiation near 70°C increased rapidly at lower dose (0.1 dpa), but the hardness increase slowed down at higher dose (1 dpa). Compared with the unirradiated sample, the bulk hardness of neutron irradiated HEA increased by 80% after 0.1 dpa and by ~120% after 1 dpa (Figure 1). Figure 2 shows the corresponding nanohardness measurement data on the neutron irradiated samples and Figure 3 shows a linear fit of hardness squared as a function of the inverse of indentation depth according to the Nix-Gao model[8] that was used to verify uniform hardness versus depth for the unirradiated and neutron irradiated samples. The R-square values are very close to 1 for all three fitting curves, verifying depth-independent hardness. The nanohardness measurement for neutron irradiated samples showed ~ 70% increase for the 0.1dpa sample and ~80% increase after 1dpa at an indent depth of ~800nm, which was comparable to the bulk Vickers hardness measurement (at an indentation depth ~ 8 to 12 microns, depending on sample hardness). On the other hand, by extrapolation of the Nix-Gao fit in Figure 3, the hardness at infinite depth can be obtained from the intercepts of the curves. The extrapolation showed ~250% hardness increase for 0.1 dpa and ~270% increase for 1 dpa, both higher than the bulk Vickers hardness results.

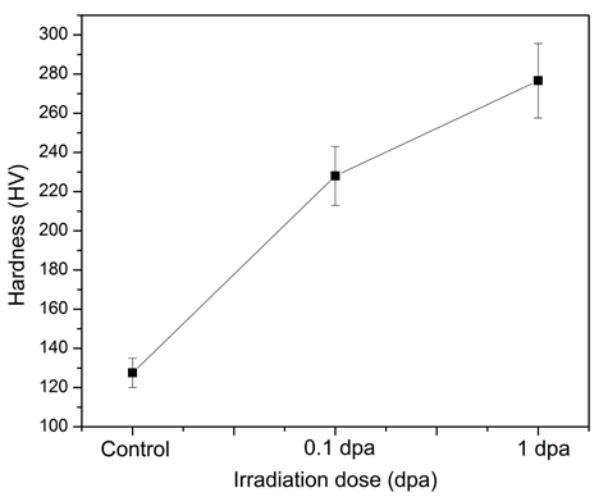

Figure 1. Bulk hardness of neutron irradiated samples as a function of dose

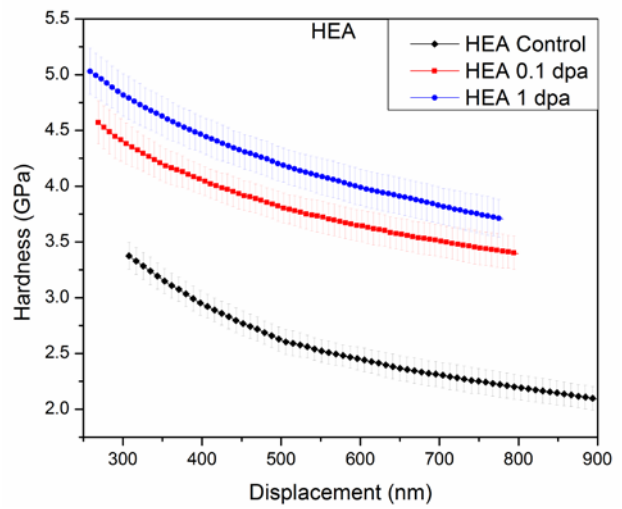

Figure 2. Nanoindentation hardness as a function of depth for samples irradiated by neutrons at 70°C from 0.1 dpa to 1 dpa

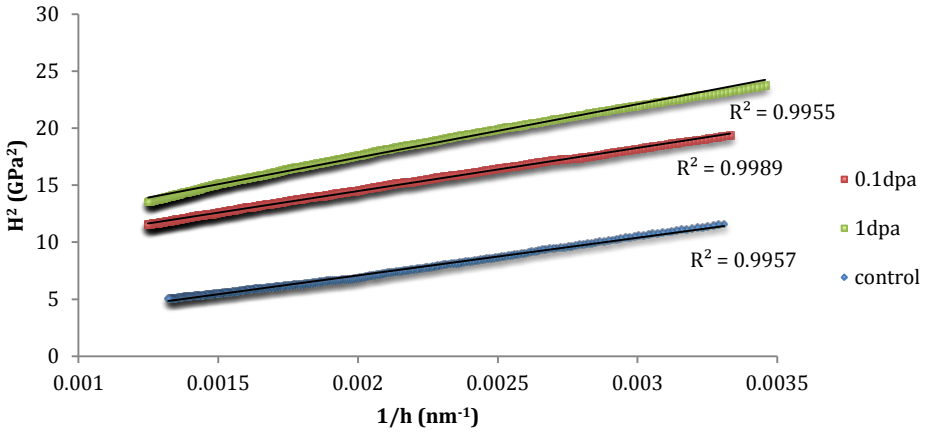

Figure 3. Nix-Gao fit of the nanohardness data, with R-square values below showing the quality of the linear fit

The electrical resistivity of the neutron irradiated samples also increased with irradiation dose (Figure 4). Resistivity increased by ~16% from 0 dpa to 0.1 dpa, but increased only a little (~1% from 0.1 dpa to 1 dpa) with further irradiation dose. For the irradiated alloys, change of electrical resistivity can be caused by precipitate dissolution/formation, phase change, ordering/disordering and defect creation[9], along with nuclear transmutation effects. In the present experiment, the material studied is single phase, and the irradiation is conducted at relatively low dose and at room temperature. Thus, the increase of resistivity should be dominated by production of radiation induced defects. The rapid resistivity increase suggests a large increase in radiation defects from 0 to 0.1 dpa, while the less rapid change of resistivity from 0.1 to 1 dpa indicates slower increase in radiation defects at higher dose regime.

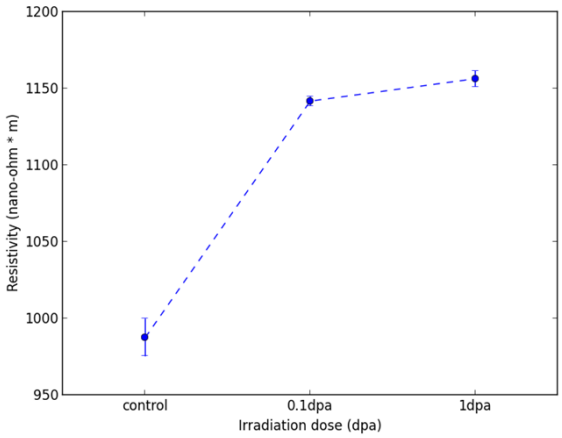

Figure 4. Electrical Resistivity of neutron irradiated samples as a function of dose

Representative stress/strain curves of neutron irradiated high entropy alloy tensile specimens, given in Figure 5, shows similar behavior as typical austenitic 304, 316 and 347 stainless steel[10, 11]. At lower dose, yield strength increases substantially while ductility suffers relatively mild loss. At higher dose, loss of ductility is more significant, but the elongation is still uniform and shows no sign of prompt plastic instability.

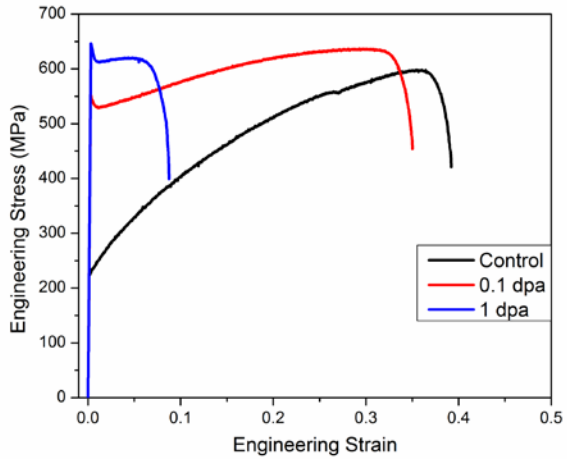

Figure 5. Stress-strain behavior of neutron irradiated tensile samples at different doses

Both irradiated samples exhibit yield drops, and the magnitude of the yield drop increases with dose. The magnitude of yield drop, however, seems to be larger than that of a typical stainless steel. For HEA, the yield drop is ~24 MPa at 0.1 dpa and ~34 MPa at 1 dpa. For 316 stainless steel, the yield drop is ~4MPa at 0.1 dpa and ~16MPa at 0.78 dpa[11].

Both HEA and conventional austenitic alloys exhibit reduction of work hardening with increasing dose, which indicates that neutron irradiation alters the work hardening behavior. However, the magnitude of reduction for HEA is more significant. At 1 dpa, the work hardening regime is almost flat, and the difference between ultimate tensile strength and lower yielding point is only ~8 MPa. The upper yield point is even higher than ultimate tensile strength. This is atypical for austenitic Fe-based alloy (304, 316 and 347) because work hardening can still be observed at relatively high dose[10, 11]. Since plastic deformation is characterized by the interaction of dislocation and pre-existing solute/radiation induced defects (in the

case of austenitic steels, microtwinning is also involved), the differences in yield drop and work hardening magnitude suggest different defect microstructures, or different interaction mode after irradiation.

Since both yield strength and hardness are connected to the plastic properties, change in yield strength should correlate with that of hardness[12]. Previous experimental studies have shown linear correlation between Vickers hardness and yield strength and this correlation is independent of material composition[13]. In this study, the increasing trend of yield strength and hardness also shows good agreement, qualitatively. Yield strength rapidly increases by ~140% from 0 to 0.1 dpa, but the increasing trend slows down and only increases by ~180% from 0 to 1 dpa. This agrees with the trends from Vickers hardness and nanoindentation hardness measurement, showing good consistency between different experiments.

Microstructural examination

Figure 6 shows the over and under focused TEM micrographs of HEA specimen irradiated at 700°C and 10 dpa. The search for void swelling was performed in the midrange damage regions in order to minimize void swelling suppression effects associated with injected ions or the irradiated sample surface. In contrast to conventional Fe-Ni-Cr alloys, HEA shows no pronounced void swelling at any of the ion irradiation conditions in this study. The fact that no voids are found in current HEA after irradiation to midrange doses of 10 dpa at 400-700^{o}C indicates that the HEA has better swelling resistance than conventional austenitic FeCrNi or FeCrMn alloys, which exhibit significant void formation after 10 dpa in this temperature range[14].

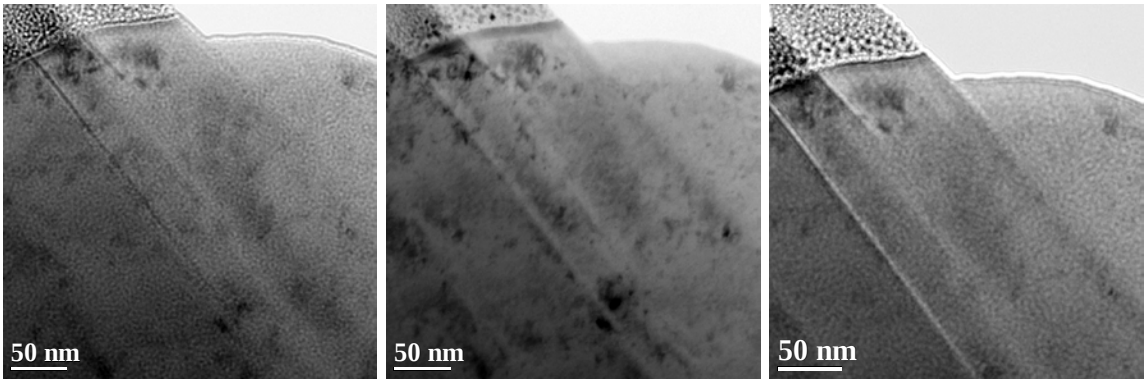

Figure 6. Bright field TEM image series from HEA alloy a) over-focus, b) focus c) under-focus, showing that no voids are observed in the specimen irradiated at 700°C, 10 dpa.

Figure 7 shows the scanning transmission electron microscopy (STEM) micrographs of the samples exposed to different ion irradiation conditions. Samples at any irradiation condition do not show any measurable segregation detectable by STEM/EDS measurements. Figure 7d shows the STEM line profile performed across the grain boundary of 600°C-10dpa specimen, where no variation in composition is observed. This lack of radiation-induced solute segregation (RIS) is in marked contrast to the behavior observed in FeCrNi and FeCrMn austenitic alloys, where Cr and Mn depletion and Ni enrichment have been observed in numerous prior studies[15]. It is assumed that the two main factors that influence the RIS behavior in the current alloy are the composition and high configurational entropy. In high entropy alloys the contribution of configuration entropy in reduction of total Gibbs free energy will be high only when the alloy microstructure is single-phase. Buildup of large local defect concentrations during irradiation can introduce noticeable changes in stability of phases. There would be no RIS if all the vacancies and interstitials created during irradiation are recombined close to where they are created. No measurable segregation in the current HEA suggests that the vacancy-interstitial recombination is high and/or the mobility of vacancies are sluggish even at a relatively high irradiation temperature of 700°C. However, lack of thermodynamic and kinetic databases on HEAs restricts the deeper understanding of their segregation behavior. Nevertheless, it can be clearly concluded that, compared to conventional austenitic

FeCrNi or FeCrMn alloys, a significant difference in radiation response in HEAs at higher irradiation temperatures is observed.

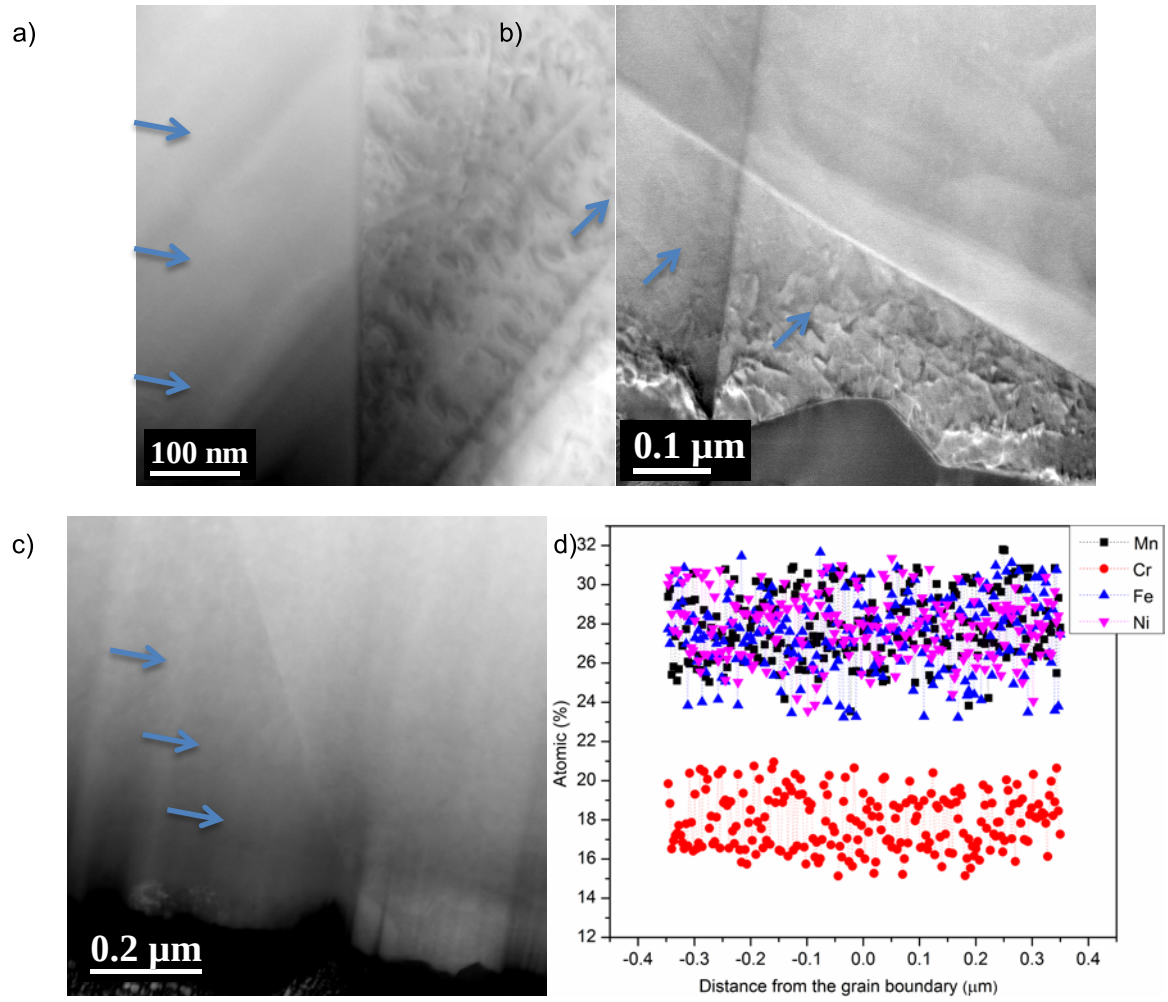

Figure 7. a), b) STEM micrographs showing grain boundaries of 700°C-10dpa specimen, c) STEM micrograph showing grain boundary of 400°C-10 dpa specimen d) STEM/EDS grain boundary composition profile of 600°C-10 dpa specimen.

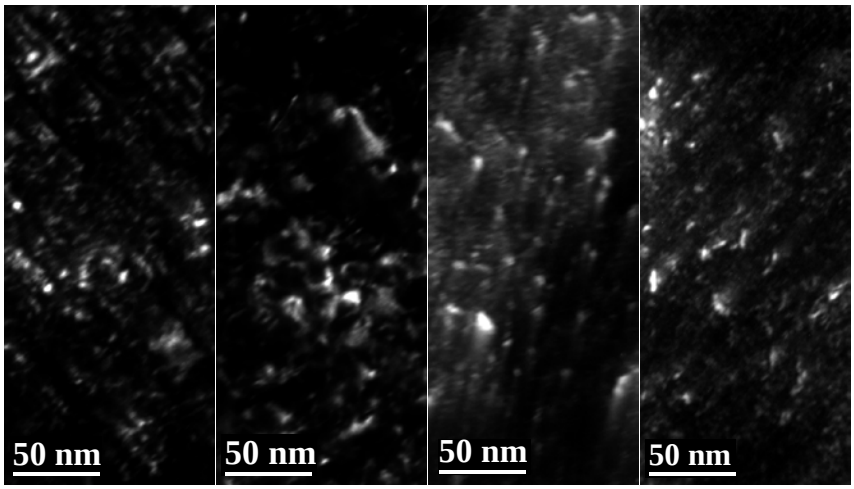

Figure 8. Dislocation loops in weak beam dark field (WBDF) images of 10 dpa irradiated specimens at temperatures a) 400°C, b) 500°C, c) 600°C, d) 700°C.

Figure 8 shows weak-beam dark field images of ion irradiated HEA specimens. Dislocation loops dominate the defect microstructure at all irradiation conditions. Fine scale dislocation loops with diameters ranging from 1 to 10 nm can be seen in the micrographs. Table 2 summarizes the average loop size and loop density variation in HEA with irradiation dose and temperature. A qualitative trend of increase in loop size and decrease in loop density is observed with increasing irradiation temperature. However the increase in dislocation loop size with increasing temperature is not very substantial (from 4 to 5.5 nm as temperature is increased from 400 to 700°C). Loop density appears to nearly saturate after exposure to a dose of 1 dpa at 500°C. Although the uncertainty in loop density measurement is a factor to be considered, it should be noted that the concentration of point defects retained in HEAs in visible defect clusters is around 10^{21}-10^{22} m^{-3}, i.e., about 7 orders of magnitude less than the integrated concentration of point defects produced by the irradiations. The observed defect cluster densities of irradiated HEAs are significantly higher than the reported dislocation loop densities of many Fe-Cr-Ni alloys irradiated under similar conditions, and the corresponding loop sizes for the HEA specimens are smaller than reported for Fe-Cr-Ni alloys[16]. Slight variation in defect density could be due to the fact that some authors separated the black spots and dislocation loops, where in the current study both black spots and dislocation loop are treated as dislocations loops. In addition, if the imaging of loops is done in a thick foil regions (>150 nm), lower loop density is observed due to poor contrast of small (~2 nm) loops and overlap effects. In this study, all the observations were made in relatively thin foils (thickness of 60-80nm). Relatively constant defect density was also observed for high temperature irradiated specimen. Usually, the increase in irradiation temperature results in decrease in loop density and an increase in loop diameter due to increase in diffusion rate of solute interstitial and vacancies. However, the nearly constant dislocation loop density (only a factor of 5 decrease between 400 and 700°C) and limited increase in loop size (17% increase in size between 400 and 700°C) in the ion irradiated HEA specimens suggest that the diffusion kinetics in HEAs is more sluggish than conventional Fe-Ni-Cr alloys. The possibility of relatively low solute diffusivity in HEA alloys is supported by the recent study on Co-Cr-Fe-Mn-Ni high entropy alloy, where it was shown that the HEA showed larger fluctuation in lattice potential sites, which resulted in the presence of abundant low-energy lattice potential sites that would thereby lower the diffusion kinetics of solute atoms[17]. In addition, the smaller loop size in HEA suggest that only a small fraction of the produced point defects are eventually trapped in the loops and recombination of vacancies and interstitials is the dominant recovery process in the HEAs.

Table 2. Summary of microstructural observations in HEAs after ion irradiation

Temperature (°C)	Dose (dpa)	Mean loop diameter (nm)	Loop Density (m^{-3})
400	10	4.66	1.89×10^{22}
500	1	4.13	7.13×10^{21}
500	10	4.32	9.35×10^{21}
600	10	5.21	6.68×10^{21}
700	10	5.45	4.33×10^{21}

References

[1] 1. C. Y. Hsu, J. W. Yeh, S. K. Chen and T. T. Shun, Metallurgical and Materials Transactions a-Physical Metallurgy and Materials Science 35A (5), 1465-1469 (2004).
[2] 2. J. W. Yeh, S. K. Chen, J. Y. Gan, S. J. Lin, T. S. Chin, T. T. Shun, C. H. Tsau and S. Y. Chang, Metallurgical and Materials Transactions a-Physical Metallurgy and Materials Science 35A (8), 2533-2536 (2004).
[3] 3. C. J. Tong, Y. L. Chen, S. K. Chen, J. W. Yeh, T. T. Shun, C. H. Tsau, S. J. Lin and S. Y. Chang, Metallurgical and Materials Transactions a-Physical Metallurgy and Materials Science 36A (4), 881-893 (2005).
[4] 4. Y. J. Zhou, Y. Zhang, Y. L. Wang and G. L. Chen, Applied Physics Letters 90 (18), 3 (2007).
[5] 5. C. M. Lin and H. L. Tsai, Journal of Alloys and Compounds 489 (1), 30-35 (2010).
[6] 6. S. J. Zinkle and G. S. Was, Acta Materialia 61 (3), 735-758 (2013).
[7] 7. R. E. Stoller, M. B. Toloczko, G. S. Was, A. G. Certain, S. Dwaraknath and F. A. Garner, Nuclear Instruments & Methods in Physics Research Section B-Beam Interactions with Materials and Atoms 310, 75-80 (2013).
[8] 8. W. D. Nix and H. J. Gao, Journal of the Mechanics and Physics of Solids 46 (3), 411-425 (1998).
[9] 9. C. Dimitrov, M. D. C. Belo and O. Dimitrov, Journal of Physics F-Metal Physics 10 (8), 1653-1664 (1980).
[10] 10. H. R. Higgy and F. H. Hammad, Journal of Nuclear Materials 55 (2), 177-186 (1975).
[11] 11. K. Farrell, T. S. Byun and N. Hashimoto, Journal of Nuclear Materials 335 (3), 471-486 (2004).
[12] 12. D. Tabor, British Journal of Applied Physics 7 (5), 159-166 (1956).
[13] 13. J. T. Busby, M. C. Hash and G. S. Was, Journal of Nuclear Materials 336 (2-3), 267-278 (2005).
[14] 14. F. A. Garner, H. R. Brager, D. S. Gelles and J. M. McCarthy, Journal of Nuclear Materials 148 (3), 294-301 (1987).
[15] 15. E. A. Kenik, Journal of Nuclear Materials 205, 317-323 (1993).
[16] 16. S. J. Zinkle, P. J. Maziasz and R. E. Stoller, Journal of Nuclear Materials 206 (2-3), 266-286 (1993).
[17] 17. K. Y. Tsai, M. H. Tsai and J. W. Yeh, Acta Materialia 61 (13), 4887-4897 (2013).

7.5 DERIVATION OF TRUE STRESS-TRUE STRAIN CONSTITUTIVE LAWS FOR IRRADIATED FERRITIC STEELS -T. Yamamoto, G. R. Odette, S. Li (University of California Santa Barbara), S. Maloy, T. Saleh (Los Alamos National Laboratory)

OBJECTIVE

The objective of this study is to derive true stress-stain constitutive [$\sigma(\varepsilon)$] laws for irradiated candidate fusion reactor structural materials.

SUMMARY

In previous studies we developed a self-consistent approach to derive true stress-stain constitutive [$\sigma(\varepsilon)$] laws for 8Cr-2W tempered martensitic steel, F82H, encompassing a range of unirradiated and irradiated conditions [1]. In this report, five 8-12Cr tempered martensitic steels and one 14Cr oxide dispersion strengthened alloy, that were side-by-side irradiated to 6.5 dpa at 295°C in the Advanced Test Reactor (ATR), were analyzed. The approach is based on simultaneous measurements and finite element method (FEM) simulations of engineering stress-strain s(e) curves, that are consistent with a unique $\sigma(\varepsilon)$ law. In the irradiated condition, the $\sigma(\varepsilon)$ fall into categories of: strain softening, nearly perfectly plastic and strain hardening. Increases in the average $\sigma(\varepsilon)$ in the range of 0-10% strain are smaller than the corresponding increases in the yield stress and vary more from alloy to alloy.

PROGRESS AND STATUS

Introduction

Deformation controlled failure of a structure is mediated by the interaction of a number of intrinsic properties, including constitutive properties and plasticity laws, as well as extrinsic factors, such as geometry and loading conditions. Standard tensile tests directly provide data for engineering stress and strain, s(e), defined in the usual way: s given by load divided by the initial cross section area and e by the change in gauge length divided by its original length. Tensile properties are usually simply characterized by the engineering yield stress $s_y \approx \sigma_y$, the ultimate stress (s_{uts}), the uniform elongation (e_u) at the onset of necking, the total elongation (e_t) and the reduction in area (RA), both at specimen rupture. Note, the so-called ductility and post yield stress measures are not true material properties, since they depend on the deformed body cross-section shape and dimensions. It is trivial to convert s(e) to $\sigma\ \varepsilon$) up to the point of necking using the relation of $\sigma\ (\ \varepsilon\ )$ = s(e)(1+e) and ε = ln(1+e). However, due to typically very low e_u after irradiation, tensile test s(e) that undergo nearly immediate necking cannot directly provide post-yielding $\sigma(\varepsilon)$. Plastic strains increase rapidly to high values in the necked region undergoing large geometry changes (LGC), where continued deformation occurs under complex tri-axial stress states. The $\sigma(\varepsilon)$ derived from tensile tests are assumed to represent effective stress and strain that can be used under arbitrary multi-axial loading conditions. Modeling plastic deformation also requires a proper description of the governing flow potential (like J_2 flow theory) and associated flow-hardening rules. As described below, s(e) curves can be used to derive $\sigma(\varepsilon)$ up to large ε by iterative FEM calculations. The FEM meshing is shown in Figure 1.

Approach

The post yield total flow stress can be decomposed into the yield stress and a strain hardening component as:

$$\sigma(\varepsilon,\dot{\varepsilon},T)=\sigma_y(\dot{\varepsilon},T)+\sigma_{pl}(\varepsilon,\dot{\varepsilon},T) \quad (1)$$

Or more simply for a given $\dot{\varepsilon}$ and T:

$$\sigma(\varepsilon)=\sigma_y+\sigma_{pl}(\varepsilon) \quad (2)$$

Experimental s(e) data was directly converted to $\sigma(\varepsilon)$ up to the necking instability strain (or uniform elongation), ε_u. The strain hardening $d\sigma/d\varepsilon$ (= $d\sigma_{pl}/d\varepsilon$) derived from the $\sigma(\varepsilon)$ at $\varepsilon \leq \varepsilon_u$ was fitted to modified Voce-Mecking model [2], that describes the change in dislocation density (ρ) as the competition of dislocation storage with increasing strain and annihilation rates controlled by ρ. The model can be rewritten in terms of the strain hardening, σ_{pl}, using the dislocation to hardening relation, $\sigma_{pl} = M\alpha\mu b\sqrt{\rho}$, where M is Taylor factor, α is the strength factor, μ is shear modulus and b is Burgers vector as:

$$d\sigma_{pl}/d\varepsilon = P_1/\sigma_{pl} - P_2\sigma_{pl} = P_1/(\sigma_t - \sigma_o) - P_2(\sigma_t - \sigma_o) \quad (3)$$

Integration of Eq. 3 with a boundary condition of $\sigma(\varepsilon_o) = \sigma_o$ gives the following function form that saturates at $\sigma_{pl,sat} = (P_1/P_2)^{1/2}$ or $\sigma_{t,sat} = \sigma_o + (P_1/P_2)^{1/2}$.

$$\sigma_{pl} = \sqrt{\frac{P_1 - \left(P_1 - P_2\sigma_o^2\right)\exp(-2P_2(\varepsilon_p - \varepsilon_o)}{P_2}} \quad (4)$$

The fitted P_1, P_2, and σ_o were used to extrapolate $\sigma(\varepsilon)$ up to a steady state saturation at $d\sigma/d\varepsilon = 0$. The fitted model was used to perform the finite element (FE) simulations of the tests using the ABAQUS 6.11.2 software package with a three-dimensional mesh, consisting of ≈ 1400 brick elements that, as shown in Figure 1, models 1/8 of a tensile specimen gauge section. In most cases the initial $\sigma(\varepsilon)$ model that fits best to the experimental data up to the necking does not work to simulate post-necking behavior. So the input $\sigma(\varepsilon)$ was iteratively adjusted until the FE engineering s(e) prediction matched the experimental curve. A proper $\sigma_{s,sat}$ often worked in unirradiated condition. However, in many cases for the irradiated condition it did not. In these cases the simulated s(e) is persistently higher than experimental value, even taking σ_{sat} as low as ≈ $\sigma(\varepsilon_u)$ at the point of necking. This signals that strain softening needs to be considered.

Assuming that softening occurs due to defect free bands formed as a result of moving dislocations interacting with irradiation induced defects, which presumably are dislocation loops, a part of the irradiation induced increase of yield stress is recovered as a function of plastic strain, ε_{pl} as:

$$\sigma_y = \sigma_y - \sigma_{ssat}\left\{1 - \exp\left(-K\varepsilon_{pl}\right)\right\} \quad (5)$$

Here $\sigma_{s,sat}$ and K are both fitting parameters for the maximum and rate constant of softening, respectively. Figure 2 shows an example of fitted $\sigma_y(\varepsilon)$ function along with total $\sigma(\varepsilon)$ and $\sigma_{pl}(\varepsilon)$. Two competing effects of hardening in $\sigma_{pl}(\varepsilon)$ and softening in $\sigma_y(\varepsilon)$ create peaking $\sigma(\varepsilon)$ right after the necking.

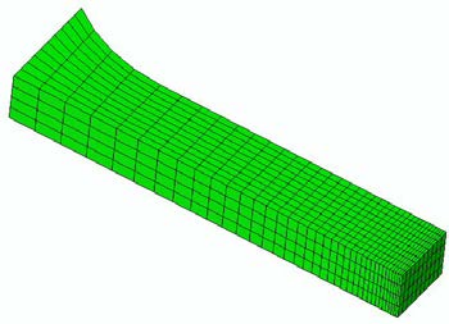

Figure 1. An example of 3D model used in a finite element method simulation of tensile tests.

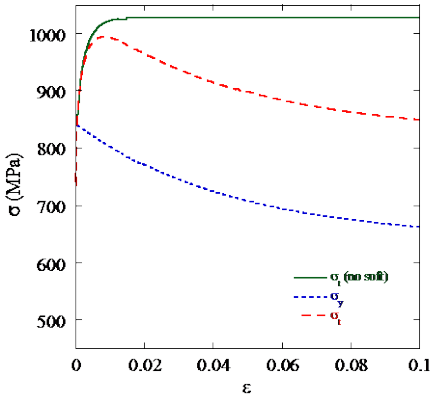

Figure 2. An example of hardening-softening constitutive models.

Our method to deriving $\sigma(\varepsilon)$ also includes quantifying large geometry changes (LGC) and deformation-flow (micro to macro) patterns of strain distribution (SD) for a wide variety of test geometries. This allows access to high stains and provides additional constraints on $\sigma(\varepsilon)$. For tensile specimens LGC is characterized by the evolution of the necked region geometry. Measured necking geometries were compared with corresponding simulations in FEM models in order to confirm the consistency of the $\sigma(\varepsilon)$.

Experimental details

The post-irradiation examination results reported here are from a large, multipurpose University of California Santa Barbara led irradiation program carried out in the Advanced Test Reactor (ATR) at the Idaho National Laboratory (INL), as part of the ATR Nuclear Science Users Facility (NSUF) Program [3]. One of many purposes of the UCSB ATR-1 experiment was to irradiate a large number of candidate structural alloys "side by side", at nearly identical temperatures and dpa, so that relatively direct comparisons of changes in their microstructures (not discussed here) and mechanical properties could be made, without many of the usual confounding factors encountered in analyzing results from different irradiations. Here we focus on five 8-12Cr TMS and one ODS alloy. The TMS include: HT-9 (H9), T91, F82H-IAEA (F2), NF616 (N6) and Eurofer97 (E9), where the (X#) notation indicates the compact alloy identification code used here. The measured alloy compositions and the TMS normalized and tempered heat treatments are summarized in Table 1. This MA957 ODS alloy was processed by ball milling Y_2O_3 and elemental powders, followed by consolidation via hot extrusion at ≈ 1100°C [4].

The irradiation was carried out in the A10 position in the ATR over a range of nominal temperatures from ≈ 290 to 750°C, and displacement damage doses from ≈ 1.7 to 6.5 dpa. A large number and wide range of specimen types (1375 in total) were contained in 32 UCSB designed sub-packets that optimized gas gap temperature control and minimized the corresponding specimen temperature uncertainties in the un-instrumented drop-in the ATR A10 position test train. The as-run fluxes and fluences were calculated by the MCNP code, and varied over the 110 cm length of the 10 mm ID capsule, with a mid-core peak of flux ≈ $2.3\text{x}10^{14}$ n/cm^2-s (E > 1 MeV), corresponding to ≈ $3.5\text{x}10^{-7}$ dpa/s, and a fluence ≈ $4\text{x}10^{21}$ n/cm^2/s. The temperatures were determined by detailed finite element thermal analyses conducted independently by both UCSB and INL. Further details on the UCSB ATR-1 experiment are described elsewhere [3]. The average irradiation conditions for the tensile specimens were ≈ 296°C and 6.5 dpa.

The tensile tests were carried out in the LANL CMR hot cells, on an Instron 5567 screw driven test machine, at a strain rate of $5\text{x}10^{-4}$/s at both ≈ 25°C and 300°C, using sub-size SSJ2 type specimens with gauge dimensions of 5 mm length, 1.2 mm width and 0.5 mm thickness. The specimens were shoulder loaded to provide good alignment in tension. The elevated temperature tensile tests were performed in an inert argon atmosphere. In general, two irradiated tests were carried out at 25°C, but only one test was conducted at 300°C. The redundant s(e) curves at 25°C were very similar in all cases. The raw digitized load and load point displacement data were converted to nominal engineering stress-strain s(e) curves, that were subsequently used for the derivation of the $\sigma(\varepsilon)$.

Table 1. Alloy Composition (wt.%) and Heat Treatments

Alloy	C	Cr	Mn	Ni	Si	Mo	Nb	V	W	O	N	P	Y_2O_3	Al/Cu/Co/Ti	Fe
HT-9	.201	12.49	.41	.60	.28	1.07	<.002	.29	.52	.002	.001	.007	<.0005	.015	Bal
Eurofer97	.117	8.69	.47	.024	.056	.005	<.002	.20	.82	.003	.023	.004	.002	.009	Bal
F82H	.093	7.89	.16	.026	.12	.005	<.002	.16	1.21	.003	.008	.004	.002	.002	Bal
NF616	.108	9.71	.46	.064	.056	.47	.043	.20	1.22	.003	.060	.007	.001	.003	Bal
T91	.052	9.22	.46	.18	.24	.96	.063	.24	.013	.002	.057	.016	.001	.009	Bal
MA 957	0.02	13.57	0.07	0.10	0.03	0.30	<0.002	--	--	0.22	---	0.004	0.25	1.1	Bal

Heat Treatments: HT9- 1040°C-1hr./air cool, 760°C 1hr./air cool; T91- 1040°C-1hr./air cool, 760°C 1hr./air cool; F82H IAEA-1040°C-40min./air cool, 750°C 1hr./air cool; Eurofer97- 980°C-27min./air cool, 760°C 90min./air cool; NF616- Hot Rolled at 1025°C/air cool; 750°C-2hr./air cool

Results and Discussion

The iterative FE method described above was used to extract true stress-true strain constitutive laws, $\sigma(\varepsilon)$, from engineering s(e) curves. Figure 3 shows the results for both unirradiated and irradiated conditions on

a consistent e or ε-scale up to 50%. Figures 3a - l summarize the results of the analysis for the six alloys in this study at 25°C (3a-f) and 300°C (3g-l), respectively. Each plot for a specific alloy shows the unirradiated (blue) and irradiated (red) s(e) curves (heavy dashed lines) along with the corresponding derived σ(ε) curves (heavy dotted lines) and the converged FEM prediction of the s(e) curve (light solid line). Figure 4 shows limited comparisons of FEM predicted reduction of area (RA) at an onset for fracture, while Figure 5 shows a few examples of shape comparisons. More specifically FEM geometry was evaluated at the corresponding strain that a rapid drop in experimental s(e) is observed. This may cause some differences that are associated with early damage development that ultimately leads to fracture. In the future more direct comparisons will include continuous monitoring of the LGC in the neck and strain-mapping by digital image correlation. As shown by the red regions in the FEM cross sectional images in Figure 5, the center of the neck thins more than at the corners of the rectangular simulation section. The LGC pattern is also observed experimentally. The average of the center and corner thicknesses was used to calculate these RA, and compared to experiment when both thicknesses measurements were available. However in some tests only a side view was measured to evaluate corner thickness. The shrinkage at the corner is often more pronounced in the experiments than in the FEM simulations, probably due to the assumption of ideally sharp starting corners, while in reality they have a finite radius that enhances the actual thickness reduction. Better approaches to LGC evaluation will also be pursued in the future work. Nevertheless, the LGC comparisons between the FEM models and experimental observations are very encouraging. In most cases differences are only a few percent; larger differences are associated with limited LGC measurements. Hence, the LGC results provide a first order validation of the FEM simulation.

The derived σ(ε) have some common classes of behavior. The unirradiated alloys continuously strain harden, albeit at various rates. However, following irradiation the σ(ε) fall into one of three general categories:

- i) Strain softening up to $\varepsilon \approx$ 10-20%, followed by an approximately saturated constant, perfectly plastic σ(ε).
- ii) A small increment of strain hardening, followed by an approximately saturated constant, perfectly plastic σ(ε).
- Iii) Continuous strain hardening.

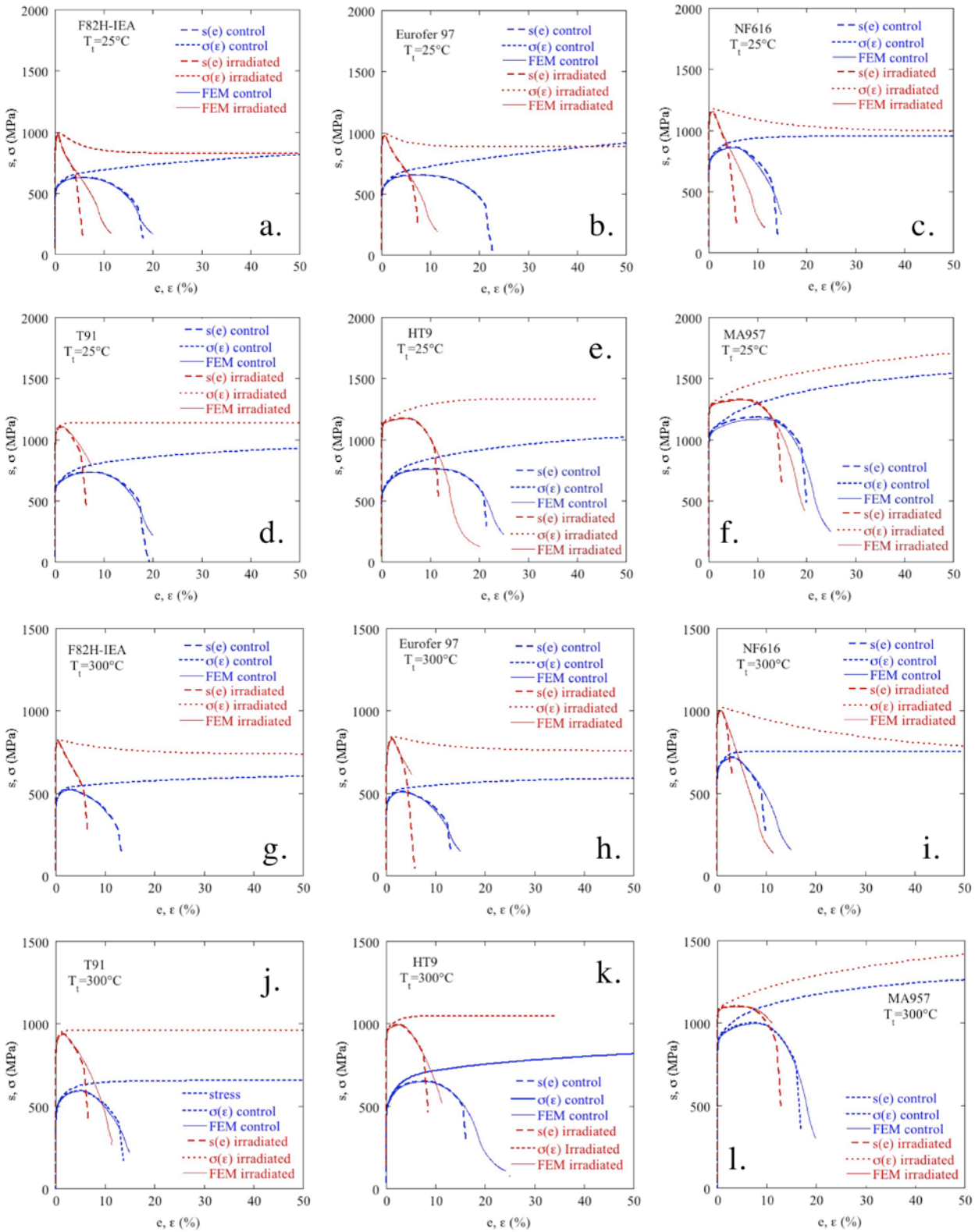

Figure 3. Experimental vs simulated s(e) curves along with derived σ(ε)□models for irradiated and unirradiated materials tested at 25°C (a-f) and 300°C (g-l).

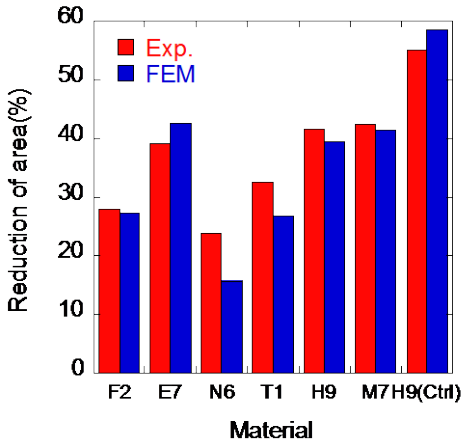

Figure 4. Comparison of the reduction of area at the fracture onset in FEM with that of fractured specimens in the tests.

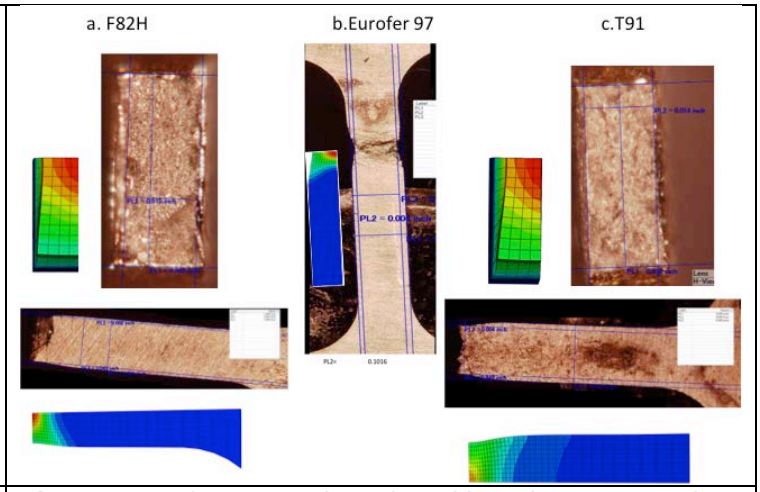

Figure 5. A few examples of necking shape comparison between FEM and experiments.

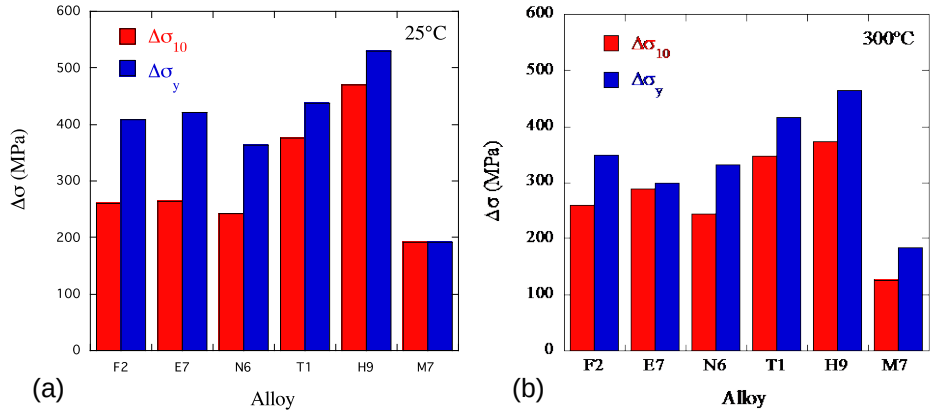

Figure 6. Changes in the average flow stress between 0 and 10% strain ($\Delta\sigma_{10}$) and the corresponding $\Delta\sigma_y$ for tests at: a) 25°C; b) 300°C.

For irradiated condition tests at 25°C, type i behavior is observed for F2, E9 and N6, type ii for T1 and type iii for H9 and M7. At 300°C the pattern is similar, but N6 continues to slowly soften up to 50% and the H9 displays type ii behavior. For tests at 25°C the FH, E7 and N6 irradiated $\sigma(\varepsilon)_i$ approach the unirradiated $\sigma(\varepsilon)_u$ at $\varepsilon \approx 50\%$, while the $\sigma(\varepsilon)_i$ remains higher for T1, H9 and M7. In the case of the 300°C tests, the $\sigma(\varepsilon)_i$ remain significantly higher than the $\sigma(\varepsilon)_u$ over the entire strain range examined. Note that we have previously carried out a similar analysis of F2 tensile test data from High Flux Isotope Reactor irradiations [1,5]. In the dose range of ≈ 4.9 to 18 dpa at ≈ 300°C and for strains up to 50%, one case showed strain softening, while another was closer to perfectly plastic with slight strain hardening following a nearly perfectly plastic low strain increment with slight softening. However, in a third case, significant, continuous strain hardening was observed after a small increment of perfectly plastic flow. And in all three cases at more than 7 dpa, strain hardening was found at even higher strains. Possible effects of high levels of He, produced in a spallation proton irradiation on $\sigma(\varepsilon)_i$ were also observed. The reasons for the similarities and differences between these previous and current results will be explored in future research.

As noted previously, the plastic strain range between 0 and 10% is especially important since this probably represents a practical structural limit and since this plastic strain range plays a dominant role in both hardness and fracture toughness [6,7]. Figure 6a and b compare the σ_y and the average flow stress between 0 and 10% ε ($\Delta\sigma_{10}$) for all the alloys at both 25 and 300°C, respectively. In general the changes in $\Delta\sigma_{10}$ are less than $\Delta\sigma_y$, with the largest differences for F2, E7 and N6 at 25°C. On average, $\Delta\sigma_{10} \approx 0.78\ \Delta\sigma_y$ at both test temperatures.

Conclusions

The true stress-true strain σ(ε) laws of five 8-12Cr tempered martensitic steels and one 14Cr oxide dispersion strengthened alloy, that were side-by side irradiated to 6.5 dpa at 295°C in the Advanced Test Reactor (ATR), were derived from tensile test results at 25 and 300°C, using iterative FE simulations of engineering s(e) curves.

The main results and conclusions include:

- For the irradiated alloys, the derived σ(ε) curves fall into categories of: strain softening, nearly perfectly plastic and strain hardening.
- Large geometry changes in necking behavior are also consistent between FEM simulation and experimental observation, while further study on more detailed shapes are planned in the future studies.
  Differences in the average σ(ε) increases in the range of 0-10% strain are smaller than the corresponding $\Delta\sigma_y$, and vary more from alloy to alloy. This has important implications to irradiated properties like fracture toughness.

Future Work

In addition to a wide range of applications of the σ(ε) laws derivation method, future research will be directed at understanding the differences in constitutive laws between the materials as well as the effects of irradiation.

Acknowledgements

The work at UCSB was funded by a DOE NEUP (NU-11-3150) and Office of Fusion Energy Science (DE-FG03-94ER54275) grants. The work at LANL was funded under the Advanced Fuels Campaign of the Department of Energy (DOE) Fuel Cycle Research and Development Program. The UCSB ATR-1 irradiations were carried out as part of the National Scientific Users Facility program, with the assistance of a large number of outstanding engineers. The help of Colin Knight in arranging shipment of the specimens from INL to LANL is greatly appreciated. Special thanks also go to UCSB staff members Doug Klingensmith and David Gragg who played the key roles in building the experiment and former PhD student, Dr. Nicholas Cunningham, who carried out the thermal design analysis.

References

[1] T. Yamamoto, G.R. Odette, Y. Wu, Fusion Materials Semi-annual Progress Report for Period Ending December 31, 2011, DOE/ER-0311/51, US Department of Energy, 78.
[2] P. Spatig, G. R. Odette, G. E. Lucas, M. Victoria, J. Nucl. Mater. 307-311 (2002) 536.
[3] G.R. Odette, T. Yamamoto, B. Sams, D. Klingensmith, N. Cunningham, G. Waches, J.I. Cole, P.E. Murrey, “Summary of the USCB Advanced Test Reactor National Scientific Users Facility Irradiation Experiment,” DOE/ER-0313/46 (2009) 79.
[4] G.R. Odette, M.J. Alinger, B.D. Wirth, Recent developments in irradiation-resistant steels, Annual Review of Materials Research, Annual Reviews, Palo Alto, 2008, pp. 471-503.
[5] T. Yamamoto, G.R. Odette, M.A. Sokolov, Journal of Nuclear Materials, 417 (2011) 115-119.
[6] G.R. Odette, M.Y. He, T. Yamamoto, Journal of Nuclear Materials, 367 (2007) 561-567.
[7] M.Y. He, G.R. Odette, T. Yamamoto, D. Klingensmith, J. Nucl. Mater. 367 (2007) 556-560.

7.6 A NEW APPROACH TO FRACTURE MECHANICS USING VOLTERRA DISLOCATIONS, WITH APPLICATIONS TO THERMO-MECHANICAL FRACTURE — A. Sheng, G. Po, N.M. Ghoniem (University of California, Los Angeles)

OJBECTIVE

This report presents a dislocation-based technique for fracture modeling that is capable of simulating complex crack systems, particularly those under thermo-mechanical loads. The main application for fusion energy is in the design of Plasma-Facing components, especially those made of tungsten, where fracture and plasticity control the mechanical behavior during plasma transients.

SUMMARY

Complex fracture phenomena involving multiple interacting cracks in three-dimensional geometries have proven difficult to model computationally. This may be a result of the way cracks are typically conceptualized - as a disruption to an otherwise perfect continuum. As a result, existing fracture-modeling methods are generally limited to simple geometries containing a small number of cracks. The mechanical response of the first wall/blanket and divertor systems to plasma transients will inevitably involve analysis of multiple interacting cracks in 3-D geometries. We present here a different strategy for fracture modeling in which cracks are represented by distributions of discrete Volterra dislocations. This new approach overcomes many of the computational difficulties of state-of-the art fracture mechanics based on the Finite Element method.

PROGRESS AND STATUS

Introduction

Fracture is an everyday occurrence with consequences that can range from inconvenient to catastrophic and incredibly costly. As the complexity and performance requirements of modern engineering applications grow, the ability to accurately model and predict failure becomes increasingly valuable and necessary. The similarity between the elastic fields of cracks and linear distributions of dislocations has been recognized for some time [1, 2]. A fracture modeling technique exploiting this resemblance is presented and shown to be a promising alternative to existing methods.

The method outlined herein is an extension of the Parametric Dislocation Dynamics (PDD) method developed by Ghoniem et al. [3] to investigate crystal plasticity. In PDD simulations, discrete crystal dislocations are represented by parametric space curves, and their collective interactions in 3-D is completely resolved [3, 4, 5]. This allows us to model cracks with complex shapes and their mutual interactions, since a crack may be considered a distribution of dislocations on the crack plane. Examples of crack problems in 3D finite geometry will be given to illustrate the utility of the proposed method. Additionally, an example of crack propagation is shown in 2D.

Volterra Dislocation-Based Fracture Mechanics

A loaded crack can be completely described by a distribution of dislocations with suitable Burger's vectors $\boldsymbol{b}$. The crack tip, which is fixed prior to propagation, determines the size and shape of the crack and is represented by a fixed dislocation loop conforming to the same contour. Enclosed by this loop is a series of additional loops that are free to expand and contract according to the applied load, their mutual interactions, as well as their interactions with the crack-tip loop.

The classical Griffith-Inglis crack in an elastic body may be subjected to three different load configurations, referred to as modes I, II, and III. Cracks under mode-I and mode-II loading consist of climb-edge and glide-edge dislocations respectively, while mode-III cracks consist of screw dislocation distributions. The configurational force that drives the motion of these dislocations is given by the Peach-Koehler formula. For a 2D crack under mixed mode-I and mode-II loading, dislocations are driven along the crack line by the Peach-Koehler force components shown in Figure 1.

When tractions are applied to an elastic body, forces cannot be transferred across crack surfaces. Dislocation velocities are proportional to the Peach-Koehler force so that when in mechanical equilibrium the stress on each dislocation is zero, satisfying this traction-free crack surface condition.

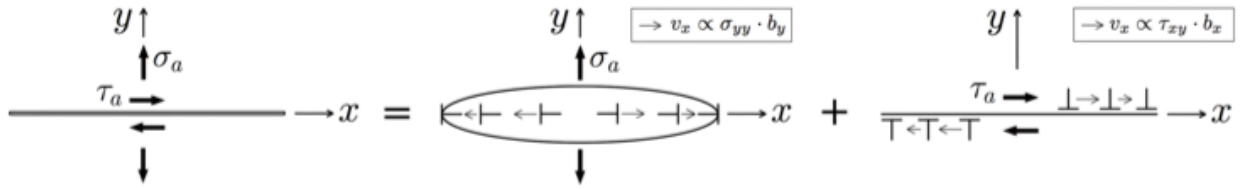

Figure 1. 2D mixed mode-I and mode-II crack

The fixed crack-tip dislocation experiences an unbalanced Peach-Koehler force as a result of the dislocation pileup. It can be shown that this unbalanced configurational force is equivalent to the J-integral described in classical fracture mechanics. The stress-intensity factor for each fracture mode can then be calculated using the relationship:

$$K_I = \sqrt{J_I E}\,, \quad K_{II} = \sqrt{J_{II} E}\,, \quad K_{III} = \sqrt{2 J_{III} \mu} \qquad (1)$$

The number of distributed dislocations and the magnitude of their Burger's vectors have a close relationship with the crack opening displacement (COD). Analytical expressions for the COD of numerous crack problems have been found using LEFM. In cases where the COD is available from these results, the Burgers vector magnitude is exactly the ratio of the COD to the number of dislocation dipoles or loops. For cases in which the COD is not known exactly, an estimate can be made based on the observation that the ratio of the COD to the crack length is proportional to the ratio of the applied load to the shear modulus. Note that as the number of dislocations in the distribution increases, the resolution of the approximate crack opening shape improves as shown in Figure 2 for a 2D mode-I crack in an infinite body.

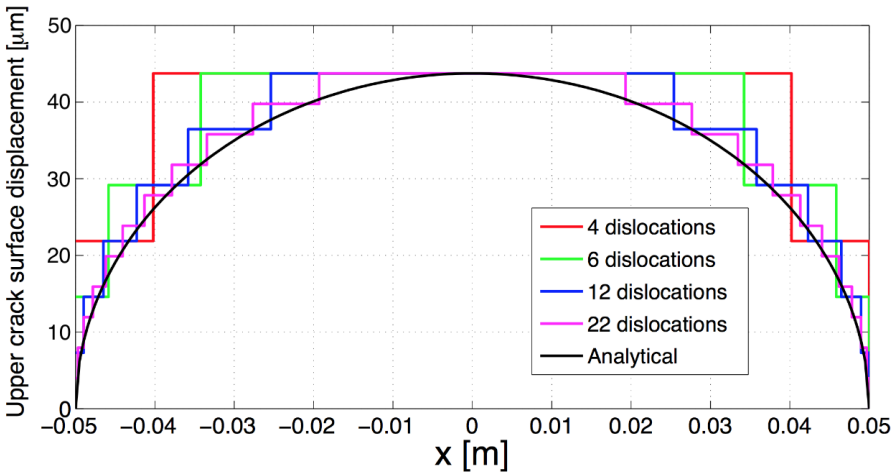

Figure 2. Mode I crack profile with increasing number of dislocations

Applying Dislocation Dynamics to Model Fracture

A fixed dislocation loop following the same contour as the crack tip is used to specify the crack size and shape. A dislocation loop is placed inside this fixed loop and allowed to equilibrate under the applied load. Once the free dislocation has reached its equilibrium position, a new loop is seeded inside the previous one, and the system is again allowed to equilibrate. This process is repeated until a newly seeded dislocation immediately begins to collapse (i.e. the applied load is no longer sufficient to drive the expansion of the seeded dislocation), as depicted with dislocation dipoles for a 2D mode-I crack in Figure 3.

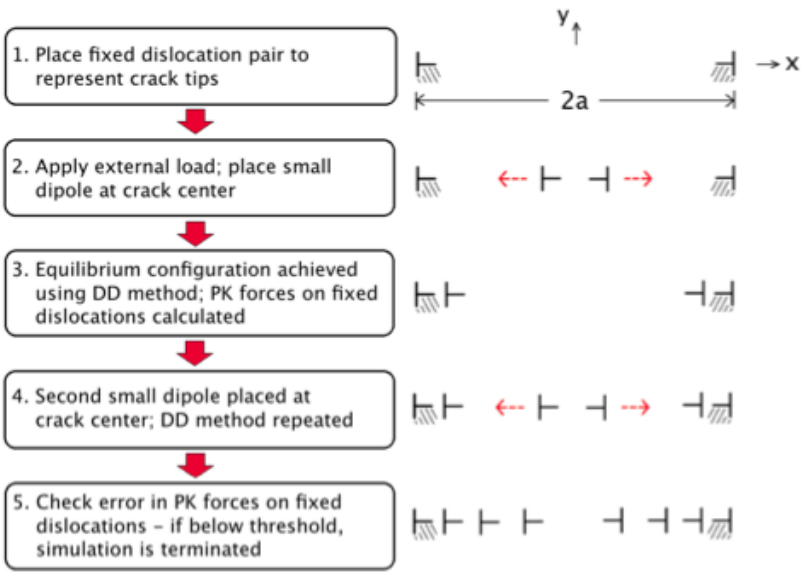

Figure 3. DD crack modeling procedure

For a crack in an infinite body, this procedure is sufficient for determining the stress intensity factor *K*. An additional procedure is required for a crack in a finite body, where the influence of the boundaries on the elastic field of the crack must be accounted for. In addition to the traction-free crack surfaces, the free boundaries of the finite domain must also be free of traction. To satisfy this condition, an additional step that will henceforth be referred to as the boundary correction procedure must be performed.

Based on a technique developed by van der Giessen and Needleman to calculate the elastic fields of dislocations in finite bodies [6], the boundary correction procedure utilizes the superposition principal to decompose the finite-body crack problem into two separate elastic problems. The first consists of a dislocation distribution in an infinite body – the same problem as described above. Calculating the dislocation stresses on virtual surfaces in the infinite body that match the free surfaces of the finite body, one finds that the stresses are non-zero and thus the traction-free boundary condition is not satisfied. The second problem consists of the finite body without the crack, with tractions applied to the surfaces that are the opposite of those calculated on the virtual boundary in the infinite body problem. The boundary correction procedure is illustrated for a 2D mode-I crack in Figure 4.

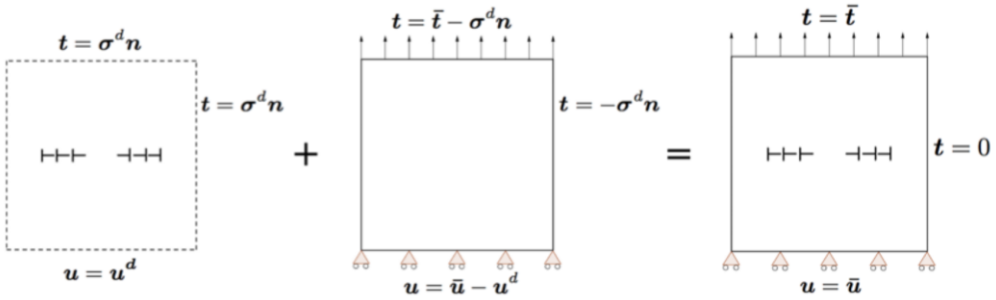

Figure 4. Boundary correction procedure for finite-body cracks

Examples

Mode-I Penny Crack in Infinite Body

For this example, a penny crack in an infinite body was modeled. The crack radius is *a* = 500 nm and a uniform stress of 100 MPa is applied in the mode-I loading direction as shown in Figure 5a. The dislocation loops used to model the crack are represented by parametric space curves in the PDD method. Results of the PDD fracture method are presented in Figure 5b for a number of dislocation loops ranging from two to eight loops. The shear modulus used is G = 80 GPa and the Poisson's ratio taken to be v = 0.3 to represent a generic material.

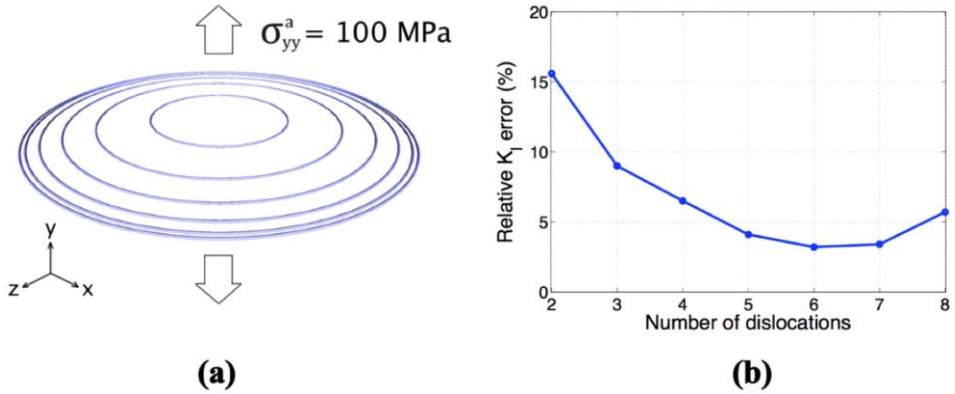

(a) **(b)**

Figure 5. (a) Iso-displacement contours for a penny crack (b) Relative error in K_I given by PDD simulation, as compared to analytical solution [7].

Mode-I Penny Crack in Cylinder

A penny crack with a radius of *a* = 500 nm is placed in the center of a cylinder of radius *b*. The bottom face of the cylinder is held fixed, and a traction of 100 MPa is applied uniformly to the top face as shown in Figure 6.

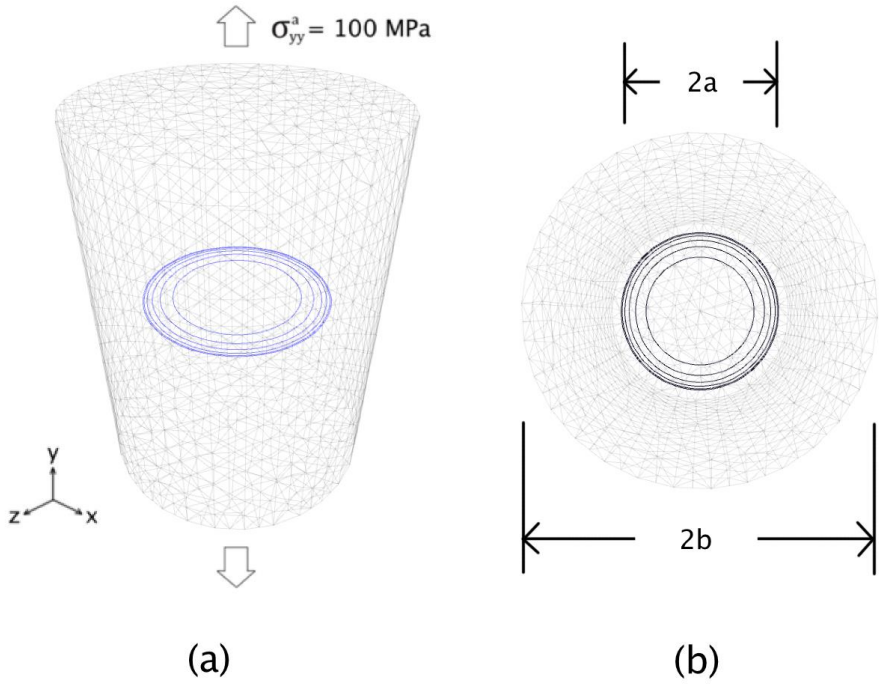

Figure 6. (a) Iso-displacement contours for a penny crack in a cylinder (b) Top-view of penny crack in cylinder

Results from the PDD crack simulation are given in Figure 7 for a range of cylinder radii.

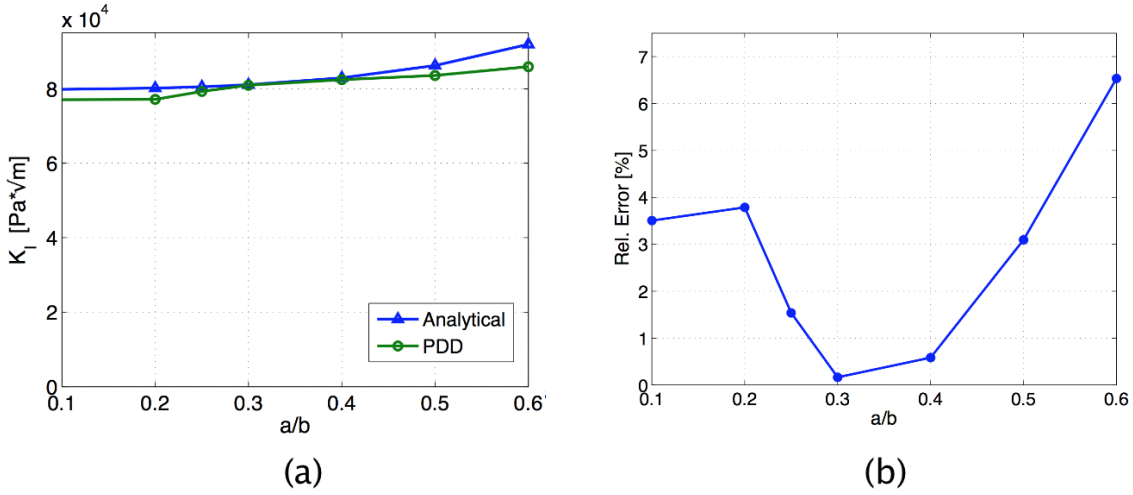

Figure 7. (a) Penny crack SIF vs. a/b (b) Relative SIF error. The analytical solution is obtained from reference [7]

Mode-I Penny Crack in Rectangular Pillar

A penny crack with a radius of 500 nm is placed in the center of a rectangular pillar with a width of 1500 nm, a thickness of 1050 nm, and a height of 2000 nm. A traction of 100 MPa is applied to the top face in the mode-I loading direction as shown in Figure 8a. Note that because the crack shape does not conform to that of the boundary, the crack dislocation loops take on the elliptical contour shown in Figure

8b due to the non-axisymmetric boundary effect. Note that the dislocations are more tightly compacted at $\theta = 90°$ compared to at $\theta = 0°$ due to the increased severity of the boundary effect.

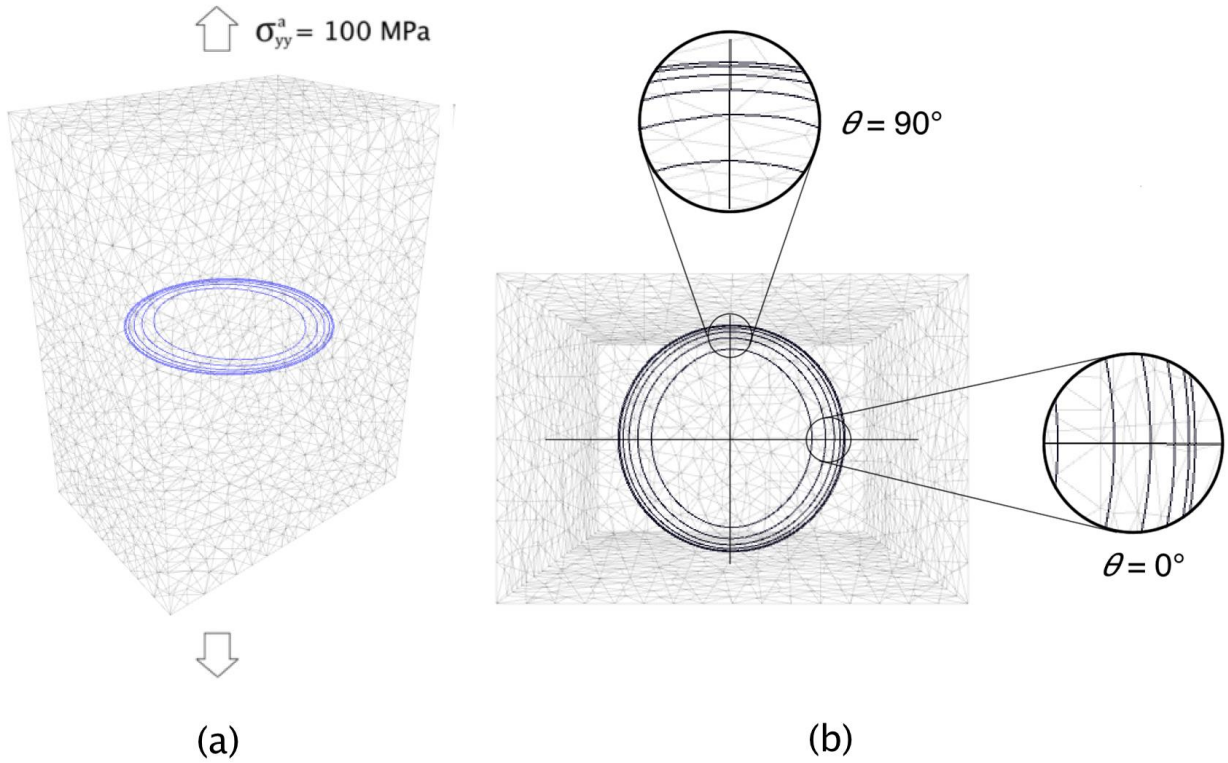

Figure 8. (a) Iso-displacement contours for a penny crack in a rectangular pillar (b) Top view of penny crack in a rectangular pillar

This boundary effect is further illustrated in the K_I results from the PDD simulation shown in Figure 9, which are plotted against the angular position θ.

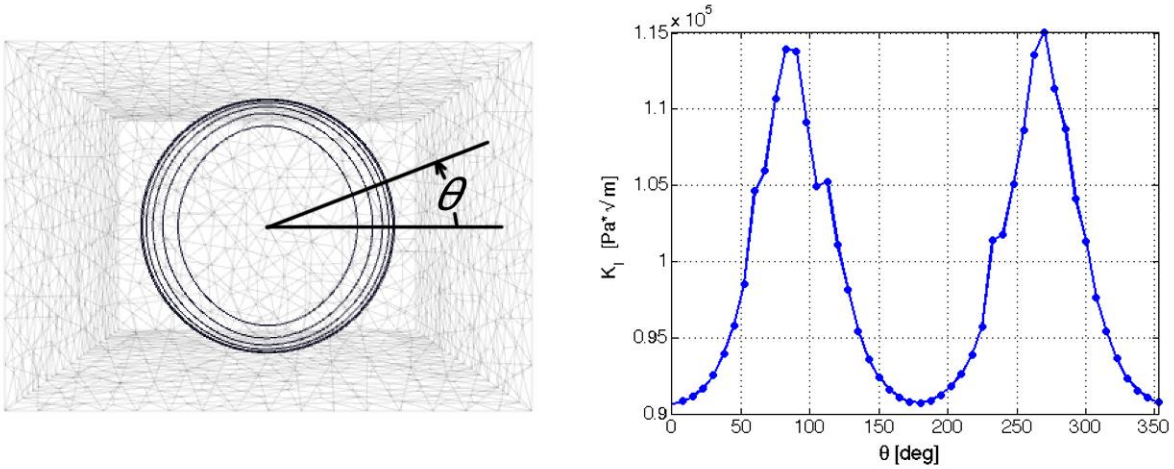

Figure 9. Stress Intensity Factor K_I vs. angular position θ for penny crack in rectangular pillar

Mode-I 2D Crack Propagation in Finite Plate

A simple 2D crack propagation example is presented in which a 50.8 × 50.8 mm square plate containing a 20 mm long center crack represented by a distribution of three dipoles is subjected to a "fixed grips" loading condition. A prescribed vertical displacement of 0.25 mm is applied to the upper and lower surfaces of the plate at successive time steps, m, as shown below in Figure 10.

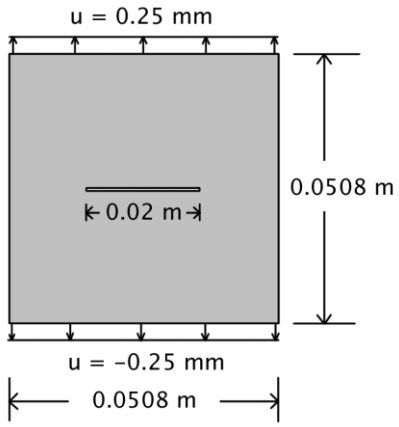

Figure 10. 2D plate containing a center crack under fixed-grips loading

To represent a generic material, the fracture toughness used is 130 MPa√m. Under the prescribed loading conditions, the stress intensity factors at the crack tips are found to exceed the fracture toughness. This initiates the crack propagation process. For each time step *m*, the crack tip is shifted a distance proportional to the Peach-Koehler force acting on the crack-tip dislocation and a new equilibrium configuration is solved for using the average stress along the crack line.

Under the fixed-grips loading condition, crack growth results in a relaxation of the material which decreases the stress intensity factor despite the increased crack length. This procedure is repeated until the calculated stress-intensity factor drops below the fracture toughness of the material (final K_I = 126 MPa√m). Figure 11 shows the crack as it increases in length over a period of time. Figure 12 shows the y-component stress field of the crack at the time steps corresponding to those shown in Figure 11.

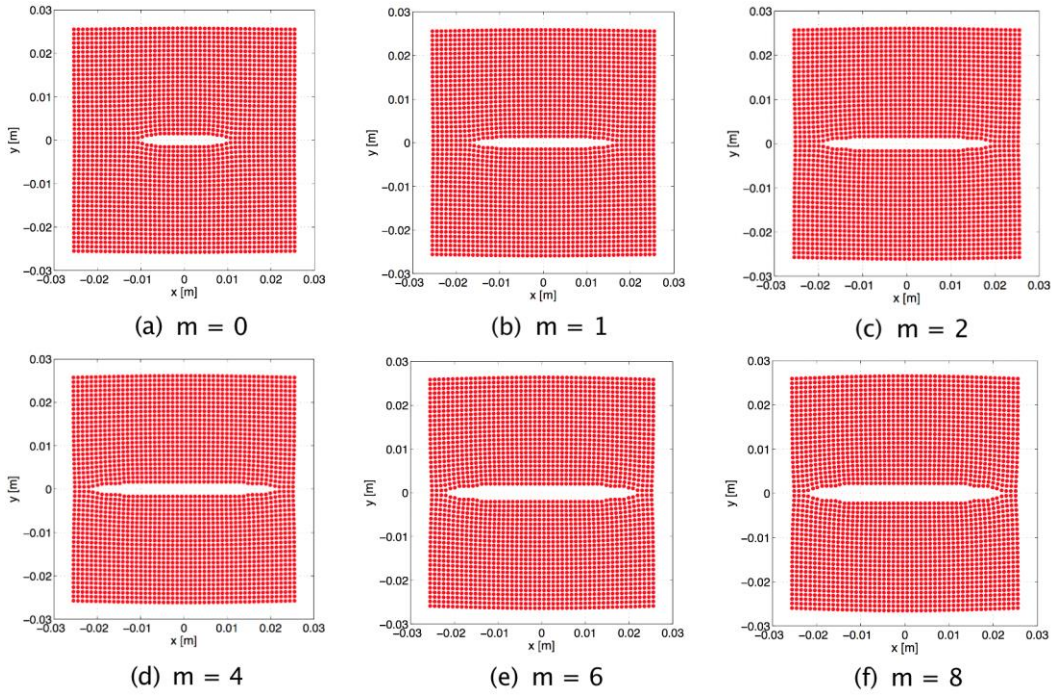

Figure 11. The displacement field associated with a propagating crack in finite geometry. (a) Initial crack length followed by (b-e) Crack size at different time steps, each with a displacement of 0.25 mm at the upper boundary. (f) Final crack length

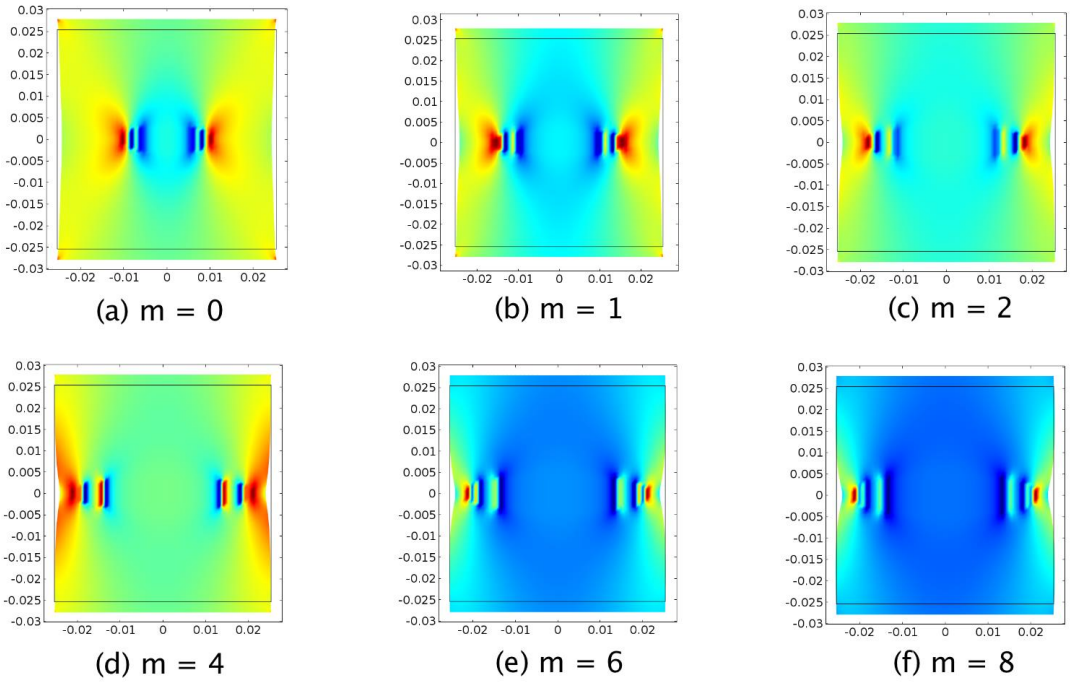

Figure 12. σ_y stress component for (a) Initial crack length followed by (b-e) Crack at different time steps (f) final crack length

Conclusions and Future Research

We have demonstrated the computational viability of the Volterra dislocation-based fracture mechanics method for solution of several fracture problems that have been traditionally challenging. These are: (1) 3-D cracks in infinite and finite geometry; (2) 2-D Mixed-mode cracks in finite geometry; and (3) a propagating crack in finite geometry. Future extensions and applications will be in the following areas: (1) single cracks in 3-D geometry in FW/B and PFC materials during plasma transients; (2) multiple interacting cracks in thermally shocked and mechanically loaded components.

References

[1] J. D. Eshelby, F. C. Frank, and F. R. N. Nabarro, *The London, Edinburgh, and Dublin Philosophical Magazine and Journal of Science*, **42 (327)** (1951), 351.
[2] J. Weertman, in Dislocation Based Fracture Mechanics, *World Scientific*, 1996, 33.
[3] N. M. Ghoniem, S. H. Tong, and L. Z. Sun, *Physical Review B* **61 (2)** (2000), 913.
[4] R. J. Amodeo and N. M. Ghoniem, *Physical Review B* **41 (10)** (1990), 6958.
[5] G. Po and N.M. Ghoniem, *JMPS* **66** (2014), 103.
[6] E. van der Giessen and A. Needleman, *Modelling Simul. Mater. Sci. Eng.* **3** (1995), 689.
[7] H. Tada, P. C. Paris, and G. R. Irwin, in The analysis of cracks handbook, *Del Research Corp.*, 1973, 24.1-28.1.

8.1 PROPERTIES OF VACANCY COMPLEXES WITH H AND He IN TUNGSTEN FROM FIRST PRINCIPLES - G.D. Samolyuk*, Y.N. Osetsky, and R.E. Stoller (Oak Ridge National Laboratory)

OBJECTIVE

Tungsten and its alloys are the primary candidate materials for plasma facing components in fusion reactors. The material is exposed to high-energy neutrons and high fluxes of helium and hydrogen atoms. He and H atoms, being very mobile in the defect-free material bulk, strongly affect the microstructure evolution, mainly through changing the stability of vacancy-type defects. We are studying the properties of single vacancy interactions with hydrogen in W using a first principles approach (density functional method, DFT). We also will calculate interaction of vacancies in complexes of up to six vacancies and their interaction with H/He atoms. The binding energies obtained will be used in mean-field type modeling of deuterium/helium implantation in tungsten with the purpose of comparison with experimental observations.

SUMMARY

It was demonstrated that the formation energy of both single vacancy and six vacancies clusters, the largest cluster investigated in current research, converges for model cells containing 250 atoms. This size is therefore enough to reproduce interaction and formation energy for both H and He atoms. A He atom is strongly attracted to the vacancy with binding energy of 4.6 eV. The di-vacancy clusters are unstable in first nearest (1NN) and second nearest neighbors (2NN) positions and weakly attract each other at 3NN positions. The introduction of H/He stabilizes di-vacancies. The compact 6 vacancies cluster is stable with binding energy of 2 eV

PROGRESS AND STATUS

As an initial effort we analyzed the existing scientific literature on the subject. The analysis demonstrates that there exist contradictions in even such simple value as di-vacancy interactions results. Thus we started our research from the calculation of properties of single vacancy.

All calculations have been done using the plane-wave basis set and PAW pseudo-potential for W with semi core p-states in the valence band, as it realized in VASP package. The Perdew, Burke, and Ernzerhof exchange-correlation function was used. The Brillouin zone summations were carried out over a 4×4×4 BZ grid for modeling cell containing 6x6x6 cubic unit cells (432 atoms) and the grid was increased to keep the same k-pint density in the modeling cell of smaller size. The plane wave energy cut off was 360 eV. The atomic structure was optimized until the forces to all atoms dropped below 0.001 Ry/A.

In the Figure 1 the result for properties of a single vacancy as a function of modeling cell size is presented. The results shown in blue color correspond to case of constant lattice parameter of perfect structure; in the second case, shown in red, the lattice parameter was recalculated to keep constant volume per atoms value.

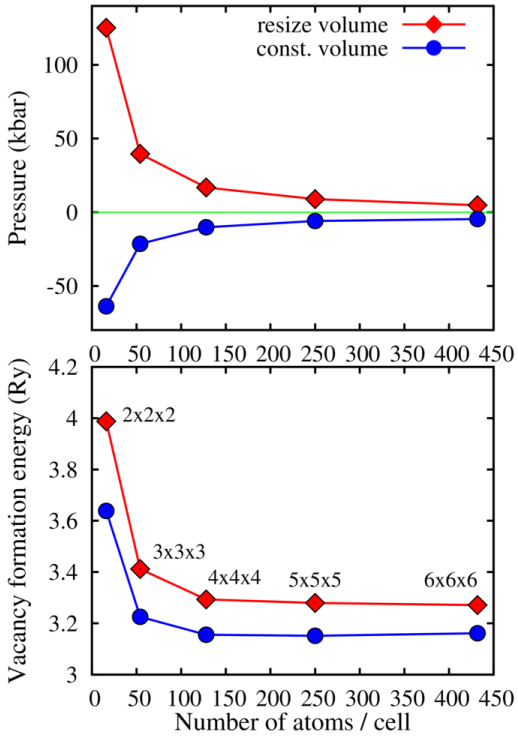

Figure 1. The total pressure and vacancy formation energy as a function of modeling cell size. Two type of calculations results are presented. In the first one shown by red line with diamonds the volume per atom was kept constant. Whereas, by the blue line with circles - the constant modeling cell size results are presented.

As it can be seen, binding energy has converged for 4x4x4 modeling cell containing 128 atoms, however to keep pressure in the system close to zero 5x5x5 modeling cell containing 250 atoms is necessary. The comparison with existing results is presented in Table 1.

Table 1. Single vacancy formation energy, in eV, as a function of modeling cell size together with existing results.

N_{at}	Current	[1]	[2]	[3]
54	3.23	3.23		
128	3.16		3.56	3.17
250	3.15			
432	3.16			

The results obtained are in good agreement with results of existing DFT calculations except formation energy obtained in reference [2], which is in contradiction with all available data.

Interstitial H/He atoms occupy tetrahedral positions in perfect W. The difference between energies of interstitial in tetrahedral and octahedral positions is equal to -0.37 and -0.25 eV for H and He respectively. These energy differences are in agreement with results obtained in Ref. [4].

In the presence of a vacancy, H/He occupy distorted octahedral position shown in Figure 2 as a grey color sphere.

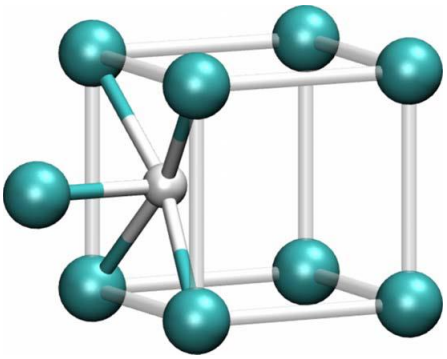

Figure 2. Distorted octahedral position occupied by H/He atom shown by light color sphere in the presence of a vacancy.

While the vacancy formation energy has converged in the super cell of the size 128 atoms (see Figure 1), to preserve total pressure in the system close to zero we need system of the size 452 atoms. The modeling in smaller size model cells has been done for comparison with existing results and to test the convergence. The presence of He atoms, according to our results, increases the total pressure by 1 kbar. It points out that the presence of He in one of the vacancies should lead to binding of H/He with a vacancy and increase the di-vacancy binding energy. The binding energy of one He atom with vacancy is equal to 4.64 eV, which is in agreement with previous results, 4.5 eV obtained in the 4x4x4 modeling cell [4].

In agreement with result obtained for the smaller modeling cell (250 atoms), two vacancies placed in the nearest (1NN) and next-nearest (2NN) neighbors positions repulse each other. The binding energies are equal to -0.11 and -0.46 eV respectively (see Table 2). The interaction between vacancies in third nearest (3NN) neighbor's position is attractive and binding energy is equal to 0.05 eV.

Table 2. Di-vacancy binding energy in eV.

N_{at}	432	128	54 [1]	128 [2]	128 [3]
1NN	-0.11	-0.16	-0.03	0.41	-0.16
2NN	-0.46	-0.48	-0.47	0.19	-0.47
3NN	0.05				0.13

The presence of H atom changes 1NN and 2NN di-vacancy interaction to attraction with binding energy equal to 1.51 and 1.42 eV of 1NN and 1NN respectively.

Table 3. Di-vacancy binding energy in presence of H atom in one of vacancies in eV.

N_{at}	432	128	128 [3]
1NN	1.51	1.30	1.80
2NN	1.42	1.38	2.15

In the presence of a He atom the di-vacancy binding energy changes to 0.13 eV, i.e. interaction is slightly attractive.

Similar to other materials, in tungsten the large size vacancy cluster started to be stable. Thus, binding energy for 6 vacancies, shown in Figure 3, is equal to 2.02 eV in 6x6x6 modeling cell (1.98 in 5x5x5 and 1.89 eV in 4x4x4).

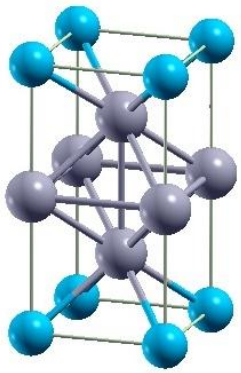

Figure 3. Six vacancies cluster.

Literature

[1] L. Ventelon, F. Willaime, C.-C. Fu, M. Heran, I. Ginoux, JNM 425 (2012) 16

[2] P. M. Derlet, D. Nguyen-Manh, and S. L. Dudarev, PRB 76 (2007) 54107

[3] D. Kato, H. Iwakiri, K. Morishita, JNM 417 (2011) 1115

[4] Becquart C S and Domain C JNM. (2009) 386

8.2 STRENGTHENING DUE TO RADIATION INDUCED OBSTACLES IN FE AND FERRITIC ALLOYS.

— Yu. N. Osetskiy and R. E. Stoller (Oak Ridge National Laboratory)

OBJECTIVE

The purpose of this research is to understand atomic level strengthening mechanisms in materials with radiation induced localized microstructures such as voids, gas-filled bubbles, secondary phase precipitates and oxide particles. These microstructures work as obstacles to dislocation motion and cause radiation induced hardening and embrittlement. Currently, we are investigating the map of mechanisms depending on the obstacle type and size.

SUMMARY

Irradiation of structural alloys by neutrons and ions lead to formation of a high density of nanoscale objects such as secondary phase precipitates, voids and gas-filled bubbles. These objects are obstacles for dislocation motion and cause wanted or unwanted changes in mechanical properties. In order to predict materials behavior these obstacles must be characterized as well as their individual strength to be estimated. The only technique that allows this at the scale of nanometers is classical molecular dynamics (MD). In this work we modeled vacancy voids, He-filled bubbles, Cu precipitates and rigid inclusions in bcc-Fe matrix. At the current stage of the research we investigated ½<111>{110} edge dislocation. During its motion this dislocation cannot change its glide plane (cross-slip) to avoid interaction with obstacles and therefore produces maximum strengthening effect. The results obtained in this research will be used to improve theoretical prediction of mechanical properties changes.

PROGRESS AND STATUS

We now have finished modeling obstacles of up to 7 nm in diameter and continue with 8 nm obstacles. This demands larger modeling crystals, $>8x10^6$ atoms. Unlike small obstacles, <4 nm, which show individual mechanisms with different hardness, large obstacles are strong and according to the dislocation line shape that adopts a long dipole of screw dislocations the mechanism is assumed to be the Orowan-type. However, as our modeling has demonstrated, the classical Orowan mechanism [1] i.e. with formation of a sheared dislocation loops around the obstacle is applicable only to rigid obstacles. Other obstacles demonstrate the shear mechanism with a similar strength. This can be seen in Figure1 where a comparison of critical resolved shear stress (CRSS) is presented for different obstacles of different size. Rigid obstacles are found to be the strongest. The dependence of their strength is also exceptionally strong within the range studied as can be seen in Figure2 where the comparison of atomistic modeling of rigid obstacles from 1 to 7 nm in diameter at 300K (circles) with theoretical estimation from [2,3] (lines) is presented.

Our data demonstrate that obstacles of a few nanometers in diameter have individual dependence of their strength versus their size. This is especially important for the irradiation conditions for the majority of obstacles is typically small, within a few nanometers. Our calculations provide parameters for the prediction of mechanical properties change due to irradiation. This work was already started within the corresponding task. Within the current task we now are finalizing investigation of the interaction geometry effect for large obstacles. The main issue is if a simple usage of mean defect size is appropriate for strengthening estimation. We have already some evidences that interaction between an obstacle and a dislocation gliding above and below its equator can be strongly asymmetric for some obstacles. In this case a simple usage of dispersed barrier hardening model [4] with a mean obstacle size can be inaccurate especially for small obstacles.

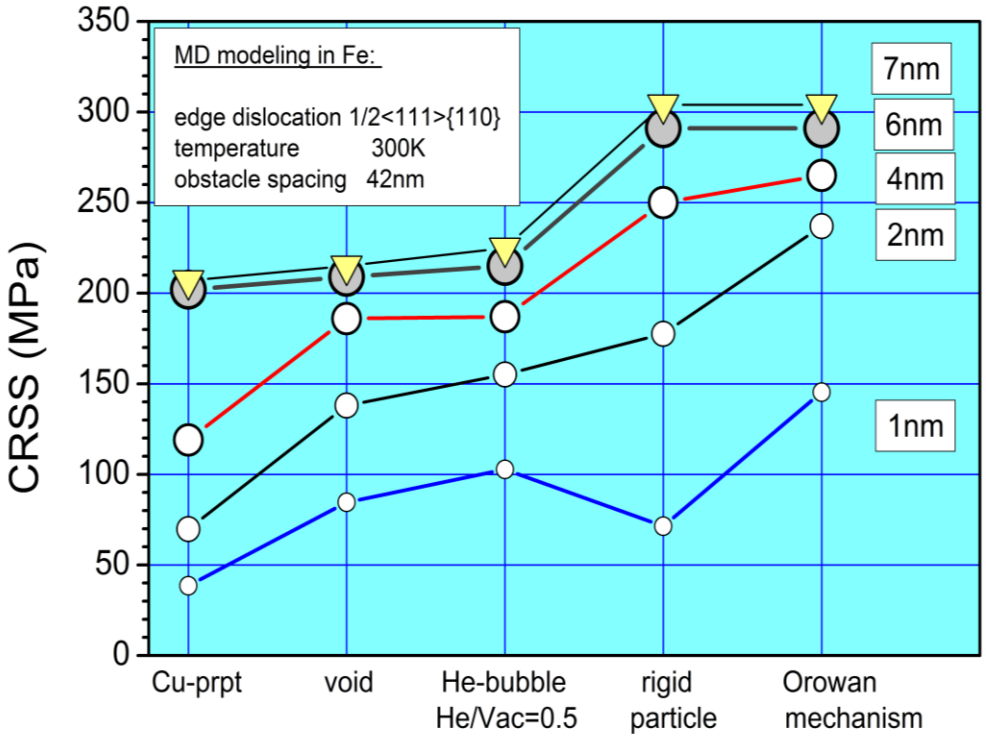

Figure 1. Critical resolved shear stress for different obstacles of different size obtained by molecular dynamics modeling at 300K.

Future Studies

1.Development of the enhanced dispersed barrier hardening model able to include dislocation obstacles interaction mechanisms revealed in atomic-scale modeling.

2. Extension of modeling program to screw dislocation to cover all possible interactions.

3. Extension of modeling program to dislocation-type obstacles such as dislocation loops. So far dislocation loops are threated in the same way as inclusions however their interaction with dislocations is quite different and this must be taken into account.

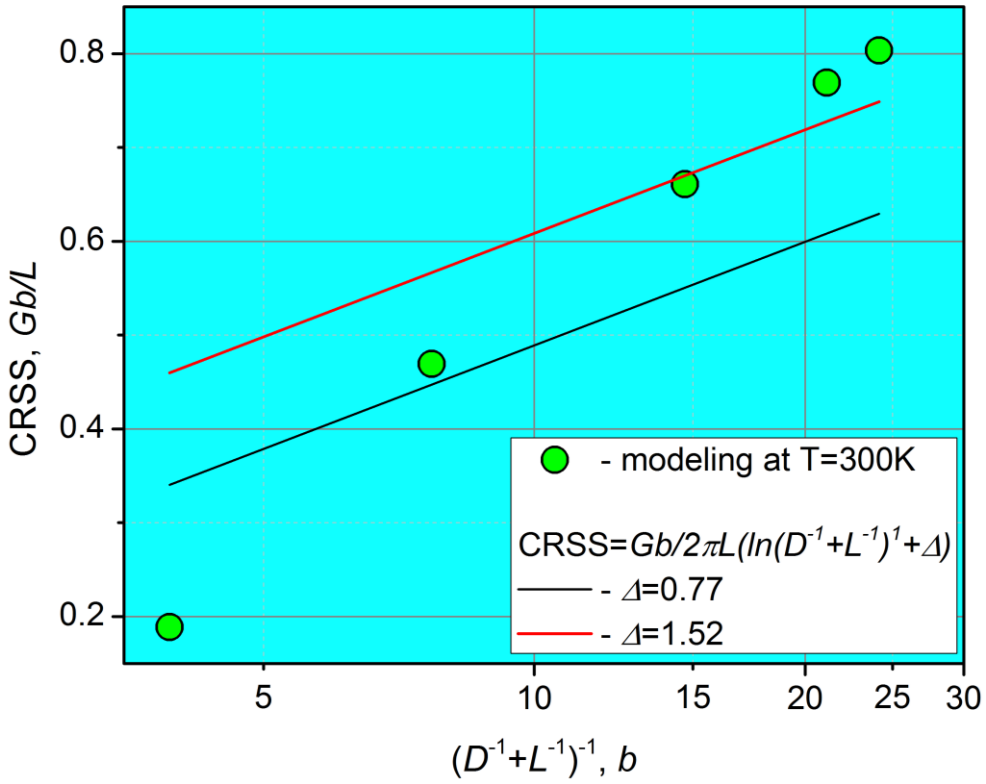

Figure 2. Critical resolved shear stress in reduced units as a function of harmonic mean of an obstacle diameter, *D*, and spacing between them along the dislocation line. Circle - rigid inclusions simulated in current work, lines are dependences obtained in dislocation dynamic modeling for Orowan mechanism (black line) and void (red line) in [1,2].

References

[1] Orowan E., A type of plastic deformation new in metals, *Nature,* 1942, vol.149, p.643.
[2] Bacon, D. J., Kocks, U. F., and Scattergood, R. O., 1973, *Phil. Mag.,* 28, 1241.
[3] Scattergood, R. O., and Bacon, D. J., 1982, *Acta metall.,* 30, 1665.
[4] Seeger A., Proc. 2nd UN Int. Conf. on Peaceful Uses of Atomic Energy (Geneva, Switzerland, September 1958), 1058, vol.6, p.250.

8.3 OBJECT KINETIC MONTE CARLO SIMULATIONS OF RADIATION DAMAGE IN BULK TUNGSTEN

G. Nandipati, W. Setyawan, H. L. Heinisch, K. J. Roche, R. J. Kurtz (Pacific Northwest National Laboratory) and B. D. Wirth (University of Tennessee)

OBJECTIVE

The objective of this work is to study the damage accumulation in pure crystalline bulk tungsten (W) during irradiation using the object kinetic Monte Carlo (OKMC) method.

SUMMARY

We used our recently developed lattice based OKMC code; *KSOME* [1] to carry out simulations of radiation damage in bulk W. We study the effect of dimensionality of self-interstitial atom (SIA) diffusion, i.e. 1D versus 3D, on the defect accumulation during irradiation with a primary knock-on atom (PKA) energy of 100 keV at 300 K for dose rates of 10^{-5} and 10^{-6} dpa/s. As expected 3D SIA diffusion significantly reduces damage accumulation due to increased probability of recombination events. In addition, dose rate, over the limited range examined here, appears to have no effect in both cases of SIA diffusion.

PROGRESS AND STATUS

Results

Simulation conditions used in the present simulations are exactly the same as reported in Ref. [2]. Figure 1 shows the total number of vacancies and vacancy clusters and average vacancy clusters for 1D and 3D SIA cluster diffusion as a function of the dose at 300 K in W irradiated with 100 keV cascades at the dose rates of 10^{-5} dpa/s and 10^{-6} dpa/s. In both cases of SIA cluster diffusion, there is no effect of dose rate on the densities of vacancies and vacancy clusters, or on the average vacancy cluster size (see Figure 1(a-c)) This behavior is not surprising because of the fact that SIA clusters diffuse very fast and are quickly absorbed at grain boundaries and vacancies are immobile at 300 K, and all this occurs in a very short time interval. This time-interval is very small when compared to the time-interval between two cascade insertions for the dose rates studied in this report. To see any effect of dose rate, the cascade insertion rate has to be faster than the damage evolution. In addition, the average vacancy cluster size does not appear to change with dose for both cases of SIA cluster diffusion (see Figure 1(c)). As expected, due to the higher probability for recombination events, the number density of vacancies for 3D SIA diffusion is lower by an order of magnitude when compared to 1D SIA diffusion. Surprisingly, the average vacancy cluster size of the 3D SIA diffusion case is slightly larger than for 1D SIA diffusion. From Figure 1(a), the number density of vacancies appears to grow linearly for 3D SIA diffusion with a growth rate (slope) of 13,660 vacancies/dpa, while for 1D SIA diffusion it appears to grow as $DPA^{0.21}$, a power law growth rate.

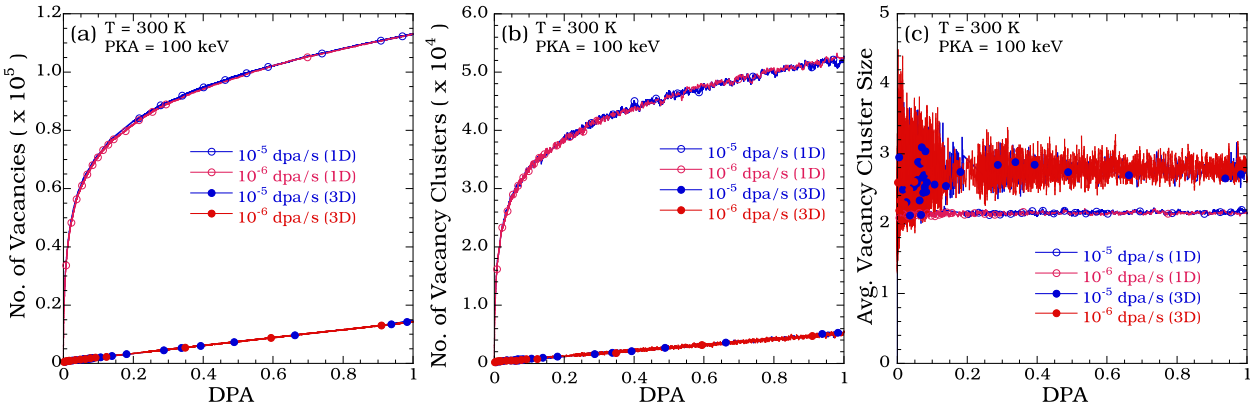

Figure 1. Comparison of damage accumulation at 300 K when SIA clusters diffuse in 1D and 3D at dose rate of 10^{-5} and 10^{-6} dpa/s using 100 keV cascades. (a) number density of vacancies (b) number density of vacancy clusters (c) average vacancy cluster size.

Figure 2 shows snap shots of the vacancy cluster distributions at 1 dpa. The radius of each sphere in a snap shot is scaled by the vacancy cluster size as $(\text{cluster size})^{1/3}$. To aid the visualization the radius of each sphere is increased by 5 times. The coloring scheme for each sphere is based on the increased radius. It can be seen from Figure 2 that the scale runs from 5 to 26.39, which corresponds to vacancy cluster sizes from ranging from 1 to 147 vacancies. Both for 1D and 3D SIA diffusion, most of the vacancies exist as mono-vacancies. As expected, Figs 1 and 2 show that 3D SIA diffusion significantly inhibits damage accumulation.

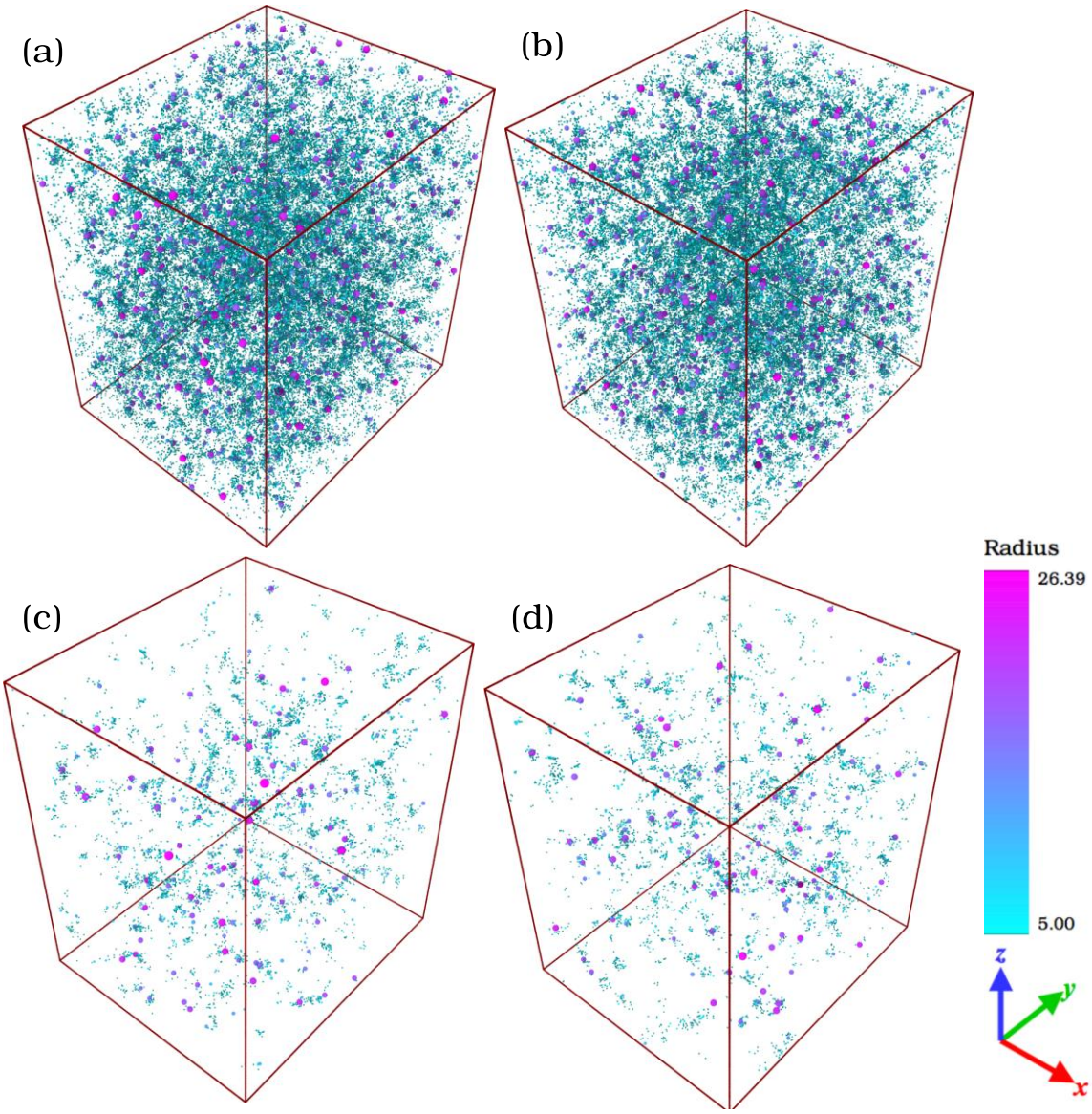

Figure 2. Snap shots of vacancy cluster microstructure at a dose of 1dpa at 300 K. (a) 10^{-5} dpa/s, SIAs diffuse 1D (b) 10^{-6} dpa/s, SIAs diffuse 1D (c) 10^{-5} dpa/s, SIAs diffuse 3D (d) 10^{-6} dpa/s, SIAs diffuse 3D (Radius = 5 x (vacancy cluster size)$^{1/3}$)

Future Work

We are carrying out further simulations to understand defect accumulation at various dose rates, PKA energies, temperatures, simulation cell and grain size, and also at different PKA spectrums. In addition we also intend to carry out sensitivity studies to understand the effect of kinetic parameters and, SIA and vacancy clustering.

Acknowledgement

All computations were performed either on HOPPER or CARVER at National Energy Research Scientific Computing Center (NERSC) and Argonne National Lab, MCS Workstations.

References

[1] G. Nandipati *et al* Semiannual Progress Report DOE/ER-0313/54, Jun (2013), 179-183
[2] G. Nandipati *et al* Semiannual Progress Report DOE/ER-0313/57, Dec (2014), 160-165

8.4 QUANTUM CALCULATIONS OF ENERGETICS OF RHENIUM CLUSTERS IN TUNGSTEN —

W. Setyawan, G. Nandipati, K. J. Roche, R. J. Kurtz (Pacific Northwest National Laboratory), and B. D. Wirth (University of Tennessee)

OBJECTIVE

The objective of this research is to explore the binding properties of small clusters of Re and intrinsic point defects in W. The results will be used to inform kinetic Monte Carlo simulations of radiation damage accumulation containing transmutant Re. In addition, the energetics and the forces will be used to develop an interatomic potential for the Re-W system.

SUMMARY

Density functional theory was employed to explore the energetic properties of clusters up to size 2 of Re in W. While WW<111> is the most stable intrinsic dumbbell, ReW<110> is more stable than ReW<111>. However, when they are trapped by a substitutional Re (Re_s), ReW<111> becomes more stable than ReW<110>. In this case, the most stable configuration forms a ReWRe crowdion with the W atom between the Re atoms. Simulations of a ReW[111] (dumbbell's vector is from Re to W) approaching a Re_s along [111] indicate that the binding energy decreases from 0.83 eV at the first nearest neighbor (NN1) to 0.10 eV at NN3 and ~0 at NN4. In addition, while ReW<111> and ReW<110> are stable near a Re_s at NN1, the ReW<100> instantaneously rotates toward ReW<111>.

PROGRESS AND STATUS

Method

VASP [1, 2] software was used to perform the quantum calculations within the density functional theory (DFT) framework. Core electrons are modeled with accurate projector-augmented-wave pseudopotentials [2]. Electrons at 6s and 5d states are treated as valence electrons for both W and Re. Perdew-Burke-Ernzerhof formulations [3] were employed for the exchange-correlation functionals. We used 250 eV as the energy cutoff for the plane waves. Defect energies were calculated using cubic 5x5x5 supercells of tungsten's bcc conventional unit cell. A Monkhorst-Pack grid of 3x3x3 was used to sample the k-points in the Brillouin zone [4]. The coordinates of atoms and the dimensions of the simulation cell were fully relaxed with a force tolerance of 0.025 eV/Å and an external pressure tolerance of 0.5 kbar. At the end of the relaxations, a static calculation was performed to eliminate errors due to basis incompleteness associated with changes in the simulation cell.

Results

Table 1 shows the formation energy of single point defects obtained in our calculations. The tungsten <111> dumbbell (WW<111>) is the most stable configuration for intrinsic dumbbells. The formation energy, E_f, of WW<111> is 9.97 eV. WW<110> is approximately 0.27 eV less stable than WW<111>. For ReW split dumbbells, ReW<110> is the most stable, E_f = 9.29 eV, which is also more stable than a WW<111>. However, ReW<111> is only 0.03 eV less stable than ReW<110>. Note that 0.03 eV is well above the total energy change in the last two ionic relaxations of < 1 meV. The effect of periodic images is negligible as will be demonstrated later. However, 0.03 eV may not be significant at high-temperature applications, especially if the rotation barrier between ReW<111> and ReW<110> is low. Nevertheless, it remains to be seen whether ReW<110> will still be more stable than ReW<111> in the presence of a substitutional Re (Re_s).

To explore the interaction between two point defects, we develop a utility code to enumerate all possible configurations and to reduce those configurations to a set of non-equivalent configurations. Figure 1 shows the numbering of the lattice sites that is used to generate the configurations. Sites 1, 2, 6, 7, 26, 27, 31, and 32 are the first nearest neighbors of site 126. Sites 7, 27, 31, 33, 37, and 57 are the second nearest neighbors of site 32. Sites 127, 131, 133, 137, 151, 153, 161, 163, 177, 181, 183, and 187 are the third nearest neighbors of site 157.

Table 1. Formation energy, E_f, of single point defects in tungsten calculated with 5x5x5 supercell of tungsten's bcc convectional unit cell.

Point defect	E_f (eV)
Vacancy	3.30
W <111> dumbbell	9.97
W <110> dumbbell	10.24
W <100> dumbbell	11.99
Substitutional Re	0.17
ReW <111> dumbbell	9.32
ReW <110> dumbbell	9.29
ReW <100> dumbbell	11.28

First, we explore the binding between Re_s and ReW<111> and between Re_s and ReW<110> at the first nearest neighbor (NN1) distance. There are four unique configurations for the former, and three unique configurations for the latter. Note that the vector from Re to W in the dumbbell is taken as the direction of the dumbbell. The binding energies (E_b) are summarized in Table 2. As usual, a positive value indicates attraction. While some of the calculations are still running, it appears that ReW<111> (E_b = 0.83 eV) becomes more stable than ReW<110> (E_b = 0.53 eV) when it is trapped by a Re_s at NN1 distance. With Re_s at site 126, the most stable configuration is ReW[111] at site 1, forming a ReWRe crowdion. Exploration of the binding energies at NN2 distance is underway. While ReW<111> and ReW<110> are stable near Re_s at NN1, ReW<100> instantaneously transforms into ReW<111>.

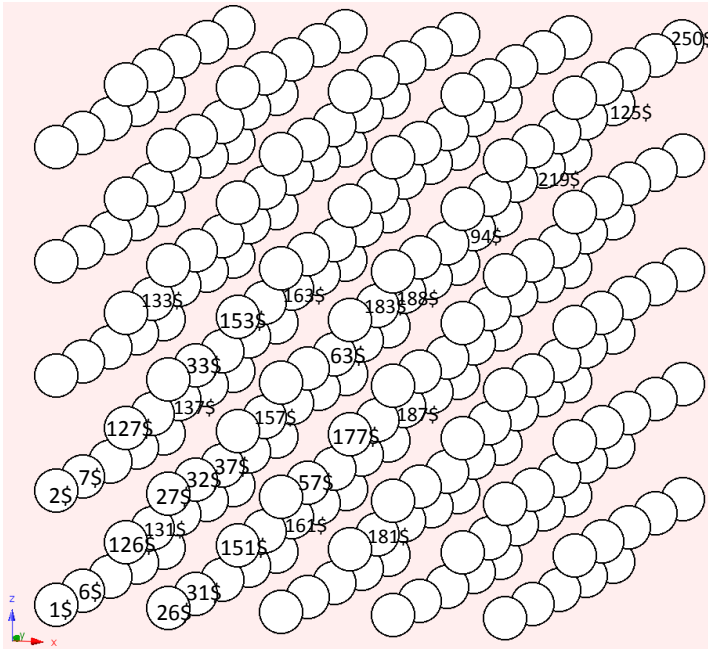

Figure 1. Numbering of lattice sites in the 5x5x5 supercell. Sites 1, 2, 6, 7, 26, 27, 31, and 32 are the first nearest neighbors of site 126. Sites 7, 27, 31, 33, 37, and 57 are the second nearest neighbors of site 32. Sites 127, 131, 133, 137, 151, 153, 161, 163, 177, 181, 183, and 187 are the third nearest neighbors of site 157.

Table 2. Binding energy, E_b, between a substitutional Re and a ReW<111> or a ReW<110> dumbbell. The i and j denotes the location of the first and second point defect, respectively, and corresponds to the numbering of sites as shown in Figure 1. The vector from the Re to the W atom in the dumbbell is taken as the direction of the dumbbell. R indicates that full relaxation has not been reached (simulations still in progress).

Substitutional Re	ReW<111>	E_b (eV)
i-126	j-1 [111] j-1 [11-1] j-1 [1-1-1] j-1 [-1-1-1]	0.83 0.54 R 0.45 R 0.60 R
Substitutional Re	ReW<111>	E_b (eV)
i-126	j-1 [110] j-1 [1-10] j-1 [-1-10]	0.53 -0.03 R 0.47 R

To estimate the range of the interaction between the Re_s and a ReW<111>, we separate them along a specific direction, [111], up to the fifth neighbor (the maximum distance allowed with the 5x5x5 supercell). At this moment, two permutations of the dumbbell vector have been completed, namely ReW[111] and ReW[-1-1-1]. For the ReW[111], the dumbbell approaches the Re_s along [111]. The E_b decreases from 0.83 eV at NN1 to 0.10 eV at NN3 and ~0 at NN4. While for the ReW[-1-1-1], it approaches the Re_s along [-1-1-1]. The E_b decreases from 0.60 eV at NN1 to 0.01 eV at NN3 and ~0 at NN4. The results are summarized in Table 3. These results also indicate that the effect of periodic images is negligible.

Table 3. Binding energy, E_b, between a substitutional Re and a ReW[111] or a ReW[-1-1-1] dumbbell separated along [111]. NNn denotes that they are separated at the n-th nearest neighbor along [111]. The i and j denotes the location of the first and second point defect as shown in Figure 1. The vector from the Re to the W atom in the dumbbell is taken as the direction of the dumbbell.

Substitutional Re	ReW[111]	E_b (eV)
i-126	j-1 NN1 j-250 NN2 j-125 NN3 j-219 NN4 j-94 NN5	0.83 0.61 0.10 ~0 ~0
Substitutional Re	ReW[-1-1-1]	E_b (eV)
i-126	j-32 NN1 j-157 NN2 j-63 NN3 j-188 NN4	0.60 0.13 0.01 ~0

Next, we explore the binding between two dumbbells, namely two ReW<111>, two ReW<110>, and between ReW<111> and ReW<110>. Table 4 -Table 6 summarize the enumeration of the non-equivalent configurations for these dumbbells separated up to NN2. Most of the calculations are still underway as indicated by missing entries.

Table 4. Non-equivalent configurations between two ReW<111> separated at the first (top panel) and second (bottom panel) nearest neighbor distance. Site-i and site-j indicates the location of the first and second dumbbell, respectively. The numbering of the sites is shown in Figure 1. R indicates that full relaxation has not been reached.

Configuration	First dumbbell	Second dumbbell	E_b (eV)
1	i-126 [111]	j-1 [111]	2.10
2	i-126 [111]	j-1 [11-1]	5.50 R
3	i-126 [111]	j-1 [1-1-1]	5.62 R
4	i-126 [111]	j-1 [-1-1-1]	1.47
5	i-126 [111]	j-2 [111]	6.35 R
6	i-126 [111]	j-2 [11-1]	5.66 R
7	i-126 [111]	j-2 [1-11]	5.74 R
8	i-126 [111]	j-2 [1-1-1]	4.67 R
9	i-126 [111]	j-2 [-1-1-1]	6.23 R
10	i-126 [111]	j-7 [11-1]	5.12 R
11	i-126 [111]	j-7 [1-1-1]	5.83 R
12	i-126 [111]	j-7 [-1-1-1]	6.44 R
13	i-126 [111]	j-32 [-1-1-1]	2.63
1	i-32 [111]	j-7 [111]	
2	i-32 [111]	j-7 [11-1]	
3	i-32 [111]	j-7 [-111]	
4	i-32 [111]	j-7 [1-1-1]	
5	i-32 [111]	j-7 [-11-1]	
6	i-32 [111]	j-7 [-1-1-1]	
7	i-32 [111]	j-33 [11-1]	
8	i-32 [111]	j-33 [1-1-1]	
9	i-32 [111]	j-33 [-1-1-1]	

Table 5. Non-equivalent configurations between two ReW<110> separated at the first (top panel) and second (bottom panel) nearest neighbor distance. Site-i and site-j indicates the location of the first and second dumbbell, respectively. The numbering of the sites is shown in Figure 1. R indicates that full relaxation has not been reached.

Configuration	First dumbbell	Second dumbbell	E_b (eV)
1	i-126 [110]	j-1 [110]	6.12 R
2	i-126 [110]	j-1 [1-10]	5.65 R
3	i-126 [110]	j-1 [-1-10]	5.98 R
4	i-126 [110]	j-1 [101]	3.85 R
5	i-126 [110]	j-1 [10-1]	5.36 R
6	i-126 [110]	j-1 [-101]	5.35 R
7	i-126 [110]	j-1 [-10-1]	3.61 R
8	i-126 [110]	j-6 [110]	6.02 R
9	i-126 [110]	j-6 [1-10]	5.78 R
10	i-126 [110]	j-6 [-1-10]	6.05 R
11	i-126 [110]	j-6 [101]	5.41 R
12	i-126 [110]	j-6 [10-1]	5.61 R
13	i-126 [110]	j-6 [-101]	5.62 R
14	i-126 [110]	j-6 [0-11]	5.38 R
15	i-126 [110]	j-31 [-1-10]	6.16 R
16	i-126 [110]	j-31 [-101]	3.68 R
1	i-32 [110]	j-7 [110]	
2	i-32 [110]	j-7 [1-10]	
3	i-32 [110]	j-7 [-110]	
4	i-32 [110]	j-7 [-1-10]	
5	i-32 [110]	j-7 [101]	
6	i-32 [110]	j-7 [-101]	
7	i-32 [110]	j-7 [011]	
8	i-32 [110]	j-7 [0-11]	
9	i-32 [110]	j-31 [110]	
10	i-32 [110]	j-31 [1-10]	
11	i-32 [110]	j-31 [-1-10]	
12	i-32 [110]	j-31 [101]	
13	i-32 [110]	j-31 [-101]	
14	i-32 [110]	j-37 [1-10]	
15	i-32 [110]	j-37 [-1-10]	
16	i-32 [110]	j-37 [0-11]	

Table 6. Non-equivalent configurations between ReW<111> and ReW<110> separated at the first (top panel) and second (bottom panel) nearest neighbor distance. Site-i and site-j indicates the location of the first and second dumbbell, respectively. The numbering of the sites is shown in Figure 1.

Configuration	First dumbbell	Second dumbbell	E_b (eV)
1	i-126 [111]	j-1 [110]	
2	i-126 [111]	j-1 [1-10]	
3	i-126 [111]	j-1 [-1-10]	
4	i-126 [111]	j-2 [110]	
5	i-126 [111]	j-2 [1-10]	
6	i-126 [111]	j-2 [-1-10]	
7	i-126 [111]	j-2 [101]	
8	i-126 [111]	j-2 [10-1]	
9	i-126 [111]	j-2 [-101]	
10	i-126 [111]	j-2 [-10-1]	
11	i-126 [111]	j-7 [110]	
12	i-126 [111]	j-7 [1-10]	
13	i-126 [111]	j-7 [-110]	
14	i-126 [111]	j-7 [-1-10]	
15	i-126 [111]	j-7 [011]	
16	i-126 [111]	j-7 [01-1]	
17	i-126 [111]	j-7 [0-1-1]	
18	i-126 [111]	j-32 [110]	
19	i-126 [111]	j-32 [1-10]	
20	i-126 [111]	j-32 [-1-10]	
1	i-32 [111]	j-7 [110]	
2	i-32 [111]	j-7 [1-10]	
3	i-32 [111]	j-7 [-110]	
4	i-32 [111]	j-7 [-1-10]	
5	i-32 [111]	j-7 [011]	
6	i-32 [111]	j-7 [01-1]	
7	i-32 [111]	j-7 [0-1-1]	
8	i-32 [111]	j-33 [110]	
9	i-32 [111]	j-33 [1-10]	
10	i-32 [111]	j-33 [-1-10]	
11	i-32 [111]	j-33 [101]	
12	i-32 [111]	j-33 [10-1]	
13	i-32 [111]	j-33 [-101]	
14	i-32 [111]	j-33 [-10-1]	

This research has been supported by the U.S. Department of Energy, Office of Science, and Office of Fusion Energy Sciences (DE-AC06-76RL0-1830).

References

[1] P. E. Blöchl, Phys. Rev. B 50 (1994) 17953.
[2] G. Kresse and D. Joubert, Phys. Rev. B 59 (1999) 1758.
[3] J. P. Perdew, K. Burke and M. Ernzerhof, Phys. Rev. Lett. 77 (1996) 3865.
[4] H. J. Monkhorst and J. D. Pack, Phys. Rev. B 13 (1976) 5188.

8.5 DISPLACEMENT CASCADE SIMULATION IN TUNGSTEN UP TO 200 KEV OF DAMAGE ENERGY AT 300, 1025, AND 2050 K — W. Setyawan, G. Nandipati, K. Roche, R. J. Kurtz (Pacific Northwest National Laboratory) and B. D. Wirth (University of Tennessee, Knoxville)

OBJECTIVE

The objective of this research is to support the prediction of irradiation damage properties of bulk tungsten-based materials using computational methods. In particular, to provide distributions of primary defects as inputs for kinetic Monte Carlo simulations of damage evolution and accumulation in tungsten.

SUMMARY

We generated a molecular dynamics database of primary defects that adequately covers the range of tungsten recoil energy imparted by 14-MeV neutrons. During this semi annual period, cascades at 150 and 200 keV at 300 and 1025 K were simulated. Overall, we included damage energy up to 200 keV at 300 and 1025 K, and up to 100 keV at 2050 K. We report the number of surviving Frenkel pairs (N_F) and the size distribution of defect clusters. The slope of the N_F curve versus cascade damage energy (E_{MD}), on a log-log scale, changes at a transition energy (μ). For E_{MD} > μ, the cascade forms interconnected damage regions that facilitate the formation of large clusters of defects. At 300 K and E_{MD} = 200 keV, the largest size of interstitial cluster and vacancy cluster is 266 and 335, respectively. Similarly, at 1025 K and E_{MD} = 200 keV, the largest size of interstitial cluster and vacancy cluster is 296 and 338, respectively. At 2050 K, large interstitial clusters also routinely form, but practically no large vacancy clusters do.

PROGRESS AND STATUS

Simulation details

The molecular dynamics (MD) simulations were performed using LAMMPS software [1]. For the W-W interaction, the Finnis-Sinclair potential developed by Ackland and Thetford [2] was taken, in which the short-range part was then modified to harden the repulsion [3]. Modification was also done at distances relevant to self-interstitial configurations to improve defect formation energies. Before a displacement cascade was initiated, the system was thermalized in the *NPT* ensemble for 50 ps with a Nosé-Hoover thermostat to generate a canonical distribution of positions and velocities at the intended temperature. Subsequently, a primary-knock-on atom (PKA) was randomly chosen near the center of the simulation box and assigned an initial velocity with a random direction. Periodic boundaries were employed. The simulation was discarded if an atom crossed the boundaries. Electronic losses were not considered. Therefore, the PKA energy corresponds to the cascade damage energy (E_{MD}). The details of the simulations for cascades up to 100 keV can be found in [4]. Cascades at 150 and 200 keV at 300 and 1025 K were simulated using the following procedure. *NVE* ensemble was used throughout the cascade simulations, except for atoms within two lattice units of the boundaries (border atoms). A Nosé-Hoover thermostat with a time constant of 50 fs was applied to these border atoms to model the heat conduction out of the box. The simulations were followed up to 75 ps (default setting), or beyond 75 ps in a few cases, to ensure that the number of surviving Frenkel pairs (N_F) remained constant for at least 25 ps. Wigner-Seitz cell analysis was employed to detect the defects. Self-interstitial (SIA) clustering was searched with connectivity up to the third nearest-neighbor distance (NN3), while NN4 was used for detecting vacancy clusters, as suggested in [5].

Updated Results

The calculated melting temperature of the empirical potential is T_m = 4100 ± 50 K [3], compared to the experimental value of 3695 K. The displacement threshold energy, averaged over all directions, was calculated to be E_d = 122.6 ± 4.4 eV [4]. Table 1 summarizes the size of simulation box (L), the number of simulations (N_r), N_F, and the standard deviation (STD) of N_F for all damage energies that we have explored. In Table 1, the first horizontal line between 0.3 and 0.5 keV indicates the approximate energy above which N_F > 1. The second horizontal line between 30 and 40 keV for 300 and 1025 K, and between

20 and 30 keV for 2050 K, indicates the approximate energy in which the morphology of the cascade changes from single supersonic shock (SS) to interacting multiple supersonic shocks (iMS) [4].

Table 1. List of cascade damage energies (E_{MD}), simulation cells (cubes with side length L), number of simulations (N_r), and number of surviving Frenkel pairs (N_F) with the standard deviation (STD). The lattice constants (a) at 300, 1025, and 2050 K are 3.167, 3.184, and 3.216 Å, respectively. The displacement threshold energy, averaged over all directions, is E_d = 122.6 eV.

E_{MD}	E_{MD}/E_d	L	300 K			1025 K			2050 K		
(keV)		(a)	N_r	N_F	STD	N_r	N_F	STD	N_r	N_F	STD
0.1	0.82	15	40	0.45	0.5	40	0.30	0.5	40	0.45	0.5
0.15	1.22	15	40	0.55	0.5	40	0.33	0.5	40	0.45	0.5
0.2	1.63	15	40	0.58	0.5	40	0.38	0.5	40	0.60	0.5
0.3	2.45	15	40	0.85	0.6	40	0.80	0.6	40	0.63	0.6
0.5	4.08	20	20	1.4	0.7	20	1.3	0.6	20	1.1	0.7
0.75	6.12	20	20	1.8	1.0	20	1.4	1.1	20	1.6	0.9
1	8.16	30	20	2.2	1.0	20	1.8	0.8	20	1.7	1.3
1.5	12.2	30	20	3.1	1.2	20	2.4	1.6	20	2.4	0.8
2	16.3	30	20	3.9	1.7	20	2.6	1.5	20	2.7	1.3
3	24.5	30	20	4.7	1.8	20	4.4	1.5	20	3.5	2.0
5	40.8	40	20	7.1	2.3	20	5.2	2.0	20	5.8	2.1
7.5	61.2	40	20	9.7	3.3	20	7.0	2.2	20	5.8	2.0
10	81.6	50	20	12.0	2.8	15	9.3	2.5	15	9.3	1.3
15	122.4	50	20	15.0	3.5	15	13.6	3.7	15	10.9	3.0
20	163.1	64	20	21.2	5.1	15	18.0	3.5	15	15.1	5.0
30	244.7	64	20	27.2	5.5	15	22.4	6.0	15	21.7	5.9
40	326.3	64	15	34. 7	7.0	15	31.7	7.4	15	32.5	4.9
50	407.8	80	15	49.9	11.0	15	43.2	9.7	15	39.3	8.4
60	489.4	80	15	60.9	20.8	15	52.9	12.0	15	53.4	17.7
75	611.8	100	15	81.5	20.4	15	80.9	29.9	15	77.1	28.9
100	815.7	120	20	116	35.3	20	111	29.3	20	107	29.5
150	1223	160	10	226	109	-	-	-	-	-	-
150	1223	180	-	-	-	10	200	91.3	-	-	-
200	1631	180	10	315	81	-	-	-	-	-	-
200	1631	200	-	-	-	10	320	131	-	-	-

Figure 1 shows the updated plots of N_F versus E_{MD}. The data points are fitted with a bilinear curve by using a linear-least-square minimization on a log-log scale. The resulting empirical formulas of N_F as a function of E_{MD} are shown in Figure 1. The kink in the bilinear fit is defined as the transition energy (μ) corresponding to a SS → iMS morphological transition. The transition occurs at 37, 31, and 25 keV for cascades at 300, 1025, and 2050 K, respectively. The new cascade data at 150 and 200 keV follow the trend of the data above μ. Future studies may include higher energies to explore the possibility that another transition of cascade morphology might occur.

Clustering data of the defects are summarized in Table 2Table 4. Evidently, large clusters of size 30 or more, and even of size 200 or more, form for E_{MD} > μ. The defect distribution for E_{MD} > μ is significantly different from that for E_{MD} < μ. Therefore, properly including primary defects from cascades below and above the transition energy is suggested in kinetic Monte Carlo simulations of damage accumulation in tungsten.

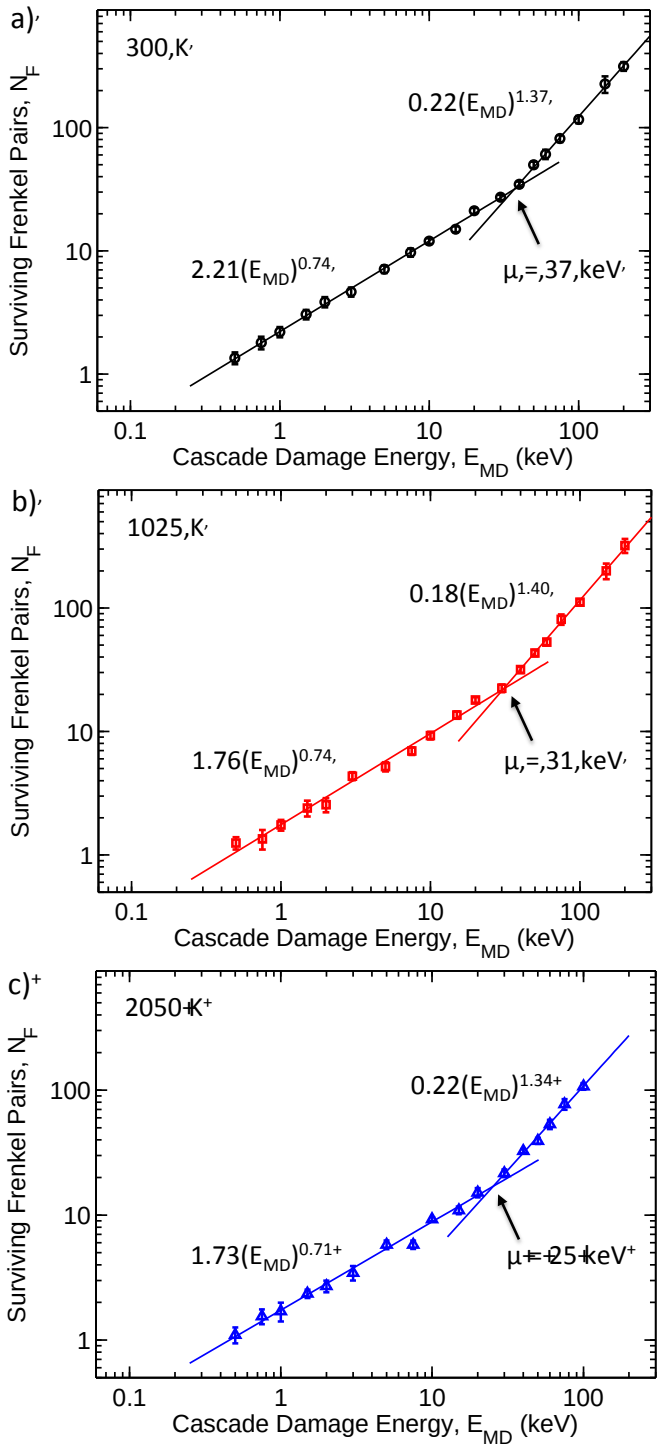

Figure 1. Number of surviving Frenkel pairs as a function of cascade damage energy. A bilinear curve is employed to fit the data. The kink in the curve is defined as the transition energy (μ).

Table 2. Counting data of SIA clusters (top panel) with connectivity up to NN3 and vacancy clusters (bottom panel) up to NN4 at 300 K. E_{MD} denotes the cascade damage energy. N_r denotes the number of simulations.

E_{MD} (keV)	N_r	Number of clusters (C_j) listed in order, starting from cluster of size S_j = 1, 2, 3 …, or given in C_j/S_j format.
1	20	38 3 0 0 0
1.5	20	48 5 1 0 0
2	20	58 5 3 0 0
3	20	54 8 2 3 1
5	20	102 12 2 1 0 1/6
7.5	20	114 14 7 5 1 1/6
10	20	137 29 4 1 4 0 1 0 0 0
15	20	158 31 8 7 3 1 1 0 0 0
20	20	220 31 10 6 3 2 2 1 1 0 1/12 1/16
30	20	263 38 9 7 3 2 5 1 1 2 1/11 1/12 1/13 1/14
40	15	255 35 15 7 2 1 1 3 0 1 2 1 0 0 1 1/16
50	15	276 34 7 7 7 3 0 3 4 1 0 0 2 0 1 1/18 1/21 2/23 2/24 1/27 1/32
60	15	326 50 8 6 5 5 2 3 2 0 1 1 1 0 0 1 0 0 0 0 1/21 1/22 1/23 1/25 1/27 1/31 1/36 1/41 1/50
75	15	391 60 20 7 7 8 6 2 1 5 2 1 0 0 1 0 0 1 0 1 1/24 1/26 1/27 1/37 2/38 1/45 1/46 1/56
100	20	666 74 27 18 10 11 3 3 4 3 4 2 1 1 2 2 2 1 0 2 1 1 3 0 0 0 1 1 0 2 1/33 1/38 1/40 1/41 1/57 2/61 2/63 2/65 1/70
150	10	408 65 19 11 10 5 5 3 3 1 1 1 1 2 1 1 0 1 0 1 1 0 0 0 1 0 1 1 2 2 1/31 1/39 1/40 1/45 1/50 1/71 1/72 1/83 1/91 1/97 1/110 1/115 1/250
200	10	513 55 33 13 7 7 4 2 4 2 3 1 1 0 0 1 2 3 1 0 1 1 0 0 0 1 0 0 2 1 1/31 1/35 1/36 1/38 1/39 1/48 1/51 1/56 1/61 1/64 1/65 1/70 1/72 1/76 1/83 1/87 1/138 2/170 1/195 1/266
1	20	16 6 4 1 0
1.5	20	22 6 5 3 0
2	20	32 7 4 1 0 1/7 1/8
3	20	41 6 4 3 2 1/6
5	20	55 12 4 4 3 2/6 1/8
7.5	20	80 16 11 1 3 3/6 1/12
10	20	95 16 11 3 3 5 2 0 1 0
15	20	138 25 3 8 3 2 3 0 0 0 1/11 1/12
20	20	188 33 21 5 5 1 3 0 0 2 1/14
30	20	254 54 15 7 3 1 4 2 1 0 1/16 1/19
40	15	273 46 13 8 4 1 0 2 0 1 0 1 0 0 0 1/20
50	15	267 50 13 6 6 2 3 3 2 3 0 0 0 1 0 1/18 1/22 1/29 1/30 1/34 1/37
60	15	348 50 19 7 6 1 0 1 2 1 0 0 1 2 0 0 0 0 0 0 1/29 1/43 1/51 1/70 1/74
75	15	449 75 24 11 5 2 2 1 0 1 1 4 0 0 0 1 1 0 0 0 1/21 1/27 1/34 1/35 1/38 1/51 1/57 1/84
100	20	706 120 40 23 10 6 4 2 3 3 2 1 3 1 0 2 0 0 1 0 1 0 0 1 0 0 0 0 0 0 1/60 1/86 1/87 1/91 1/104 1/105 1/114 1/153
150	10	596 84 33 13 9 7 3 2 0 2 0 0 1 0 0 1 0 1 0 0 0 0 0 0 0 1 0 0 0 0 1/51 1/66 1/111 1/140 1/172 1/193 1/397
200	10	720 146 38 18 13 10 2 2 3 0 0 2 0 0 1 0 0 0 1 0 0 1 0 0 0 1 0 0 0 0 1/32 1/39 3/41 1/92 1/122 1/127 1/130 1/142 1/163 1/167 1/188 1/335

Table 3. Counting data of SIA clusters (top panel) with connectivity up to NN3 and vacancy clusters (bottom panel) up to NN4 at 1025 K. E_{MD} denotes the cascade damage energy. N_r denotes the number of simulations.

E_{MD} (keV)	N_r	Number of clusters (C_j) listed in order, starting from cluster of size S_j = 1, 2, 3 …, or given in C_j/S_j format.
1	20	28 2 1 0 0
1.5	20	39 2 0 0 1
2	20	44 2 1 0 0
3	20	62 5 2 1 1
5	20	80 7 1 0 0 1/7
7.5	20	90 10 5 1 2
10	15	100 14 1 2 0 0 0 0 0 0
15	15	115 13 4 2 1 2 0 2 0 1
20	15	143 22 5 2 1 4 3 0 0 1
30	15	148 21 9 4 7 2 2 1 0 1 1/11 1/13
40	15	186 23 15 6 1 6 1 1 1 0 1 0 0 1 1 1/20 1/22 1/26
50	15	228 40 9 4 3 3 0 2 2 2 0 1 1 1 0 1/20 2/22 1/31 1/35 1/41
60	15	240 40 9 3 1 4 0 3 2 2 1 2 0 0 0 1 1 1 0 3 2/22 1/24 2/27 1/28 1/47
75	15	292 47 15 8 4 4 1 2 4 1 4 0 1 0 2 2 0 0 1 1 1/23 2/25 1/26 1/27 1/47 1/51 1/56 1/57 1/68 1/75
100	20	513 76 28 13 3 2 9 3 1 2 2 5 2 1 6 1 1 2 1 0 0 4 0 1 1 2 1 0 1 0 2/32 1/37 1/41 1/44 1/52 1/54 1/59 1/71 1/72 1/73 1/77 1/97
150	10	313 60 11 9 3 6 3 4 3 2 0 0 2 1 4 0 2 1 0 0 1 1 0 0 1 0 0 0 0 1 2/31 1/34 2/43 1/48 1/53 1/56 1/57 1/67 1/76 1/77 1/79 1/97 1/104 1/201
200	10	384 69 31 11 2 7 3 2 2 2 1 4 4 1 1 2 1 2 0 1 1 1 2 1 0 0 1 0 1 0 2/31 1/32 1/33 1/37 1/40 1/44 1/45 1/52 1/58 1/59 1/67 1/69 2/75 1/90 1/91 1/106 1/124 1/128 1/155 1/267 1/296
1	20	12 10 1 0 0
1.5	20	20 8 2 0 0 1/6
2	20	20 10 1 2 0
3	20	46 7 3 3 0 1/6
5	20	53 12 3 2 2
7.5	20	72 20 3 2 2
10	15	83 20 4 1 0 0 0 0 0 0
15	15	96 31 8 1 1 1 1 0 0 0
20	15	137 31 7 1 5 1 1 1 0 0
30	15	177 43 7 7 2 1 0 1 0 0
40	15	268 41 4 7 1 1 1 0 2 1 0 1 1 1 0
50	15	300 45 17 6 2 2 4 2 1 2 1 0 1 0 0 1/18 1/21 1/25
60	15	407 66 20 7 5 3 2 4 2 0 0 0 0 0 0 0 0 0 1 0 1/41
75	15	451 88 21 8 4 0 3 0 4 0 0 1 0 1 2 0 2 0 0 0 1/21 1/46 1/56 1/82 1/120
100	20	838 141 34 15 13 2 1 5 3 0 1 0 0 1 1 0 0 0 1 1 1 0 0 0 1 1 0 1 0 0 1/42 1/58 1/73 1/74 2/83 1/88 1/117
150	10	650 90 25 13 3 5 3 1 4 0 0 1 1 0 0 0 0 0 1 0 0 0 0 0 0 0 0 0 0 1/32 1/35 1/36 1/42 1/124 1/160 1/197 1/263
200	10	892 153 38 29 11 5 4 2 1 2 3 2 1 0 0 0 0 0 1 0 1 0 0 0 1 1 1 0 0 0 1/38 1/39 1/57 1/77 1/90 1/132 1/165 1/169 1/326 1/338

Table 4. Counting data of SIA clusters (top panel) with connectivity up to NN3 and vacancy clusters (bottom panel) up to NN4 at 2050 K. E_{MD} denotes the cascade damage energy. N_r denotes the number of simulations.

E_{MD} (keV)	N_r	Number of clusters (C_j) listed in order, starting from cluster of size S_j = 1, 2, 3 …, or given in C_j/S_j format.
1	20	30 2 0 0 0
1.5	20	30 7 1 0 0
2	20	48 3 0 0 0
3	20	44 8 1 0 0 1/6
5	20	82 11 4 0 0
7.5	20	83 7 5 1 0
10	15	56 10 2 3 1 3 2 1 0 0
15	15	65 16 4 2 1 2 1 1 0 0 1/15
20	15	90 18 3 1 2 4 3 0 1 0 1/11 1/13
30	15	124 11 6 4 2 2 1 1 2 0 1/12 3/13 1/15 1/24
40	15	154 20 9 6 3 4 2 2 1 1 3 3 1 0 2 1/16 1/27
50	15	140 21 6 5 3 1 0 0 0 1 1 1 0 1 0 1/17 3/19 1/20 2/21 2/30 1/32 1/36 1/37
60	15	184 24 11 2 3 5 3 0 0 1 2 0 0 1 0 2 1 0 0 0 1/22 1/23 1/24 1/29 1/31 1/42 1/47 1/69 1/80
75	15	137 23 6 1 1 2 1 1 0 0 0 1 1 1 0 1 1 1 0 2 1/24 1/26 1/27 1/29 2/31 1/36 1/41 1/47 1/56 2/58 1/64 1/75 1/79 1/108
100	20	301 46 11 5 6 2 2 4 0 1 1 0 1 3 4 3 0 1 2 1 2 1 0 0 1 2 0 1 1 1 1/31 3/32 1/35 1/36 1/43 2/44 1/53 1/54 2/59 1/63 1/66 1/71 1/72 1/81 1/92 1/126
1	20	22 4 0 1 0
1.5	20	34 5 1 0 0
2	20	37 7 1 0 0
3	20	43 7 1 1 1
5	20	68 14 4 2 0
7.5	20	88 8 4 0 0
10	15	94 7 7 1 0 1 0 0 0 0
15	15	137 9 3 0 0 0 0 0 0 0
20	15	169 20 2 3 0 0 0 0 0 0
30	15	249 29 4 0 0 1 0 0 0 0
40	15	359 37 7 4 2 0 0 1 0 0 0 0 0 0 0
50	15	441 46 15 3 0 0 0 0 0 0 0 0 0 0 0
60	15	558 68 15 3 2 2 1 1 0 0 0 0 1 0 0 0 0 0 0 0
75	15	706 99 14 11 5 2 1 0 1 1 0 0 0 0 0 0 0 1 0 0 0 1/27 1/60
100	20	1339 146 35 16 11 6 3 0 1 4 2 0 0 2 1 0 0 0 0 0 0 0 1 0 0 0 0 0 0 0 1/38 1/60

References

[1] S. Plimpton, J. Comp. Phys. 117 (1995) 1.
[2] G.J. Ackland and T. Thetford, Phil. Mag. A 56 (1987) 15.
[3] N. Juslin and B.D. Wirth, J. of Nuc. Mat. 432 (2013) 61.
[4] W. Setyawan, A.P. Selby, N. Juslin, R.E. Stoller, B.D. Wirth and R.J. Kurtz, J. Phys: Cond. Matt. 27 (2015) 225402.
[5] W. Setyawan, G. Nandipati, K.J. Roche, H.L. Heinisch, B.D. Wirth and R.J. Kurtz, J. Nuc. Mat. 462 (2015) 329.

8.6 EFFECTS OF TEMPERATURE ON THE FLOW STRESS AND POST-YIELDING HARDENING OF TUNGSTEN MICROPILLARS

— Y.N. Cui, G. Po, N.M. Ghoniem (University of California, Los Angeles)

OBJECTIVE

This work is aimed at developing an effective simulation method to capture the mechanical response and microstructure features of BCC crystals; revealing the underlying dislocation mechanisms of temperature dependent plastic behavior and the small size effects on these mechanisms.

SUMMARY

A powerful simulation method is developed to reveal the BCC crystal plastic deformation mechanisms. The obtained simulation results are shown to be consistent with available experimental results. In addition, a systematic study is carried out to reveal the new features and mechanisms of plastic flow in tungsten micropillars as a function of temperature.

PROGRESS AND STATUS

Introduction

Tungsten offers great potential for applications in magnetic fusion energy devices. As a representative BCC crystal, the plastic behavior of bulk tungsten is strongly temperature sensitive. A number of experiments have demonstrated that the flow stress sharply decreases at high temperatures[1]. At the same time, at submicron scales, limited sample size usually contributes to new features of the plastic behavior, such as the widely observed size effect of flow stress and strain bursts [2]. An interesting question is whether the temperature effect on the flow stress and post-yielding behavior will be influenced by the small sample size. The relationship between size dependence of plastic deformation and the underlying dislocation mechanisms is also of great interest. Investigations on these problems will shed light not only on our understanding BCC submicron plasticity, but will also provide guidance on improving the mechanical properties of tungsten devices through alloying and material processing.

Simulation Set-up

Dislocation Dynamics (DD) simulations, as a powerful approach to reveal the mechanical response and deformation mechanisms, is used here to investigate this problem [3]. An atomistically informed dislocation mobility law for BCC crystal is developed, which can capture both the twinning/anti-twinning and the tension/compression asymmetries. A series of DD simulations are carried out on [001]-oriented W micropillars subjected to uniaxial tension loading under temperatures ranging from 150 K to 900 K.

Results

To validate simulation results, the calculated 0.2% yield strength for W micropillars with diameters ranging from 200 nm to 800 nm at room temperature is first compared with experimental data [2]. Good agreement can be observed, as shown in **Figure 1**. In addition, many experimental observations are well reproduced, such as the tension-compression asymmetry.

Then, a systematic study is carried out to reveal the influence of temperature on the plastic deformation of W micropillars. In the following, only the simulation results for a micropillar with 500 nm diameter are given here as an example. Comprehensive results will be detailed in a separate publication. Figure 2 presents typical engineering stress-strain relationships. For each temperature, the results with three different initial dislocation configurations are given. Even though the results exhibit significant stochastic signature of plastic flow, the temperature effect on the flow stress can still be observed, which is qualitatively similar to that in bulk BCC crystals. Moreover, there is no pronounced strain hardening for the considered strain range.

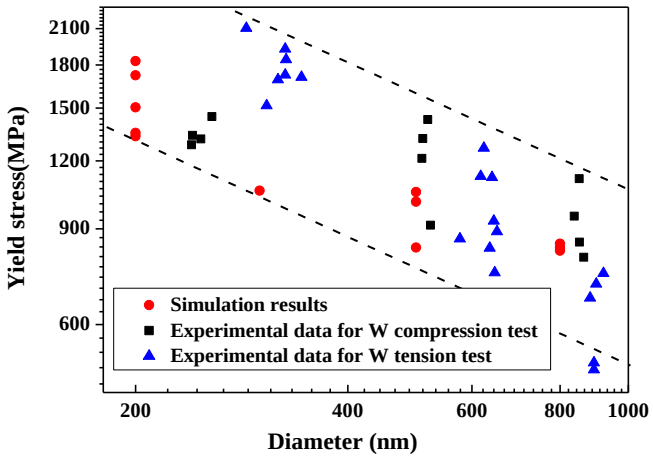

Figure 1. Comparison of the 0.2% offset yield stress for W micropillars between experimental data [2] and the present simulation results at room temperature.

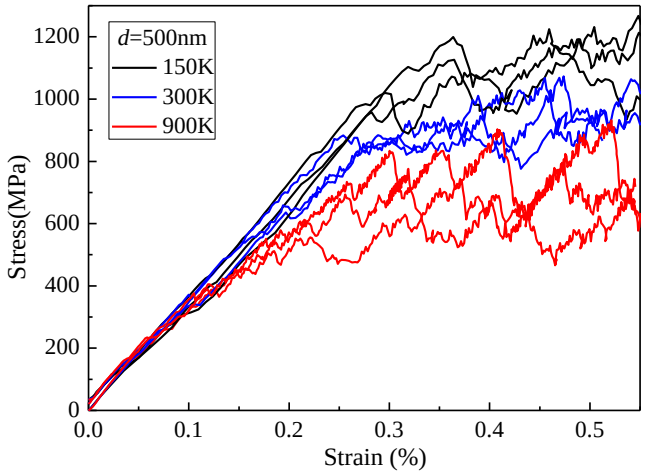

Figure 2. Stress-strain relationships during tension tests of tungsten micropillars with diameter 500 nm at different temperatures.

In order to gain insight into the underlying dislocation mechanisms, close examination of the dislocation configuration evolution is carried out. Two typical dislocation configurations are given in Figure 3. As expected, only at low temperatures, long screw dislocations can be observed due to their low mobility. When the temperature is higher than the athermal temperature (800 K), however, dislocation lines are curved, and mainly have mixed screw-edge character. In addition, single arm sources (SAS) also exhibits different features, as the temperature is raised. At low temperatures, the SAS operates mainly by the bowing out of the mixed part of the dislocation. After it interacts with the free surface, a long screw dislocation will be left inside the pillar. In Figure 4 (d-f), the evolution of the dislocation segment GH reflects this process. This is very similar to the experimental observation in Fe [4]. By way of contrast, in the case of high temperature, the SAS acts similar to half of a Frank-Read source, just like in an FCC micropillar.

The pinning points of these SAS are generally formed by dislocation junctions or jogs. In a BCC crystal, another kind of pinning point is also widely observed. This is the cross kink (see Figure 3) pinning point, which is caused by the cross slip of a screw segment of the dislocation. At low stress, such cross kink has only a short lifetime, because of the quick annihilation at the surface. However, at high stresses, cross kinks can further cause dislocation self-multiplication. As shown in Figure 4 (a-c), a cross kink ABC is first formed with the dislocation segment AB on the (011) slip plane, and segment BC on the slip plane. Under

the combined effects of the applied stress and the dislocation interaction stress, the nearly edge part of the dislocation bows out, as indicated by the arrows in Figure 4(b), until some dislocation segment annihilates from the free surface. Note that the dislocation segment near point B in Figure 4(c) is not very smooth, because cross slip occurs when the dislocation glides close to the free surface. Such kind of surface cross slip is also observed by Rao and Hussein et al. [5, 6] in FCC crystal. Moreover, this self-multiplication process shown in Figure 4(a-c) is also consistent with previous Molecular dynamic and dislocation dynamic simulation results [7].

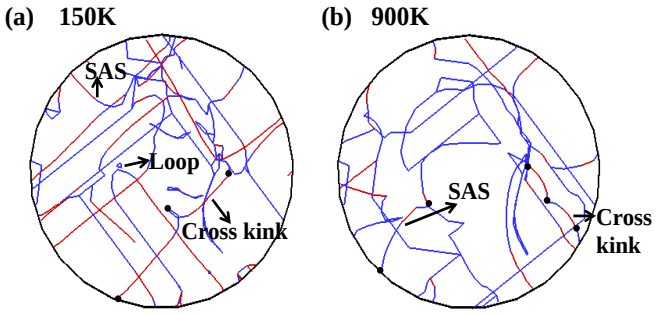

Figure 3. Dislocation configurations at different temperatures: (a) T=150 K and (b) T=900 K, respectively from the top view. Screw dislocations are indicated in red, while mixed dislocations are in blue.

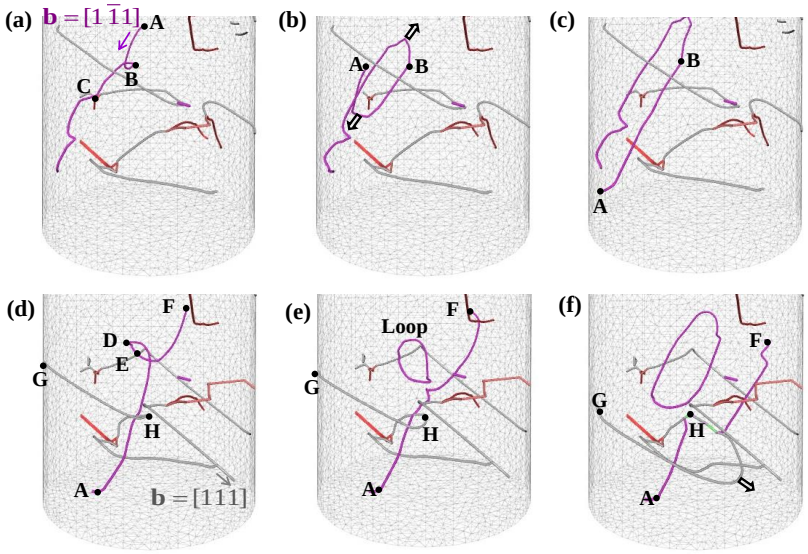

Figure 4. Snapshots of dislocation configurations showing the dislocation self-multiplication process in a W micropillar at 150 K, when the engineering strain is between 0.42% and 0.47%. Hollow arrows indicate the dislocation motion direction. Different colors in the figure are used to represent different burgers vectors, grey=(111), purple= $(1\bar{1}1)$, orange= $(11\bar{1})$, red= $(1\bar{1}\bar{1})$

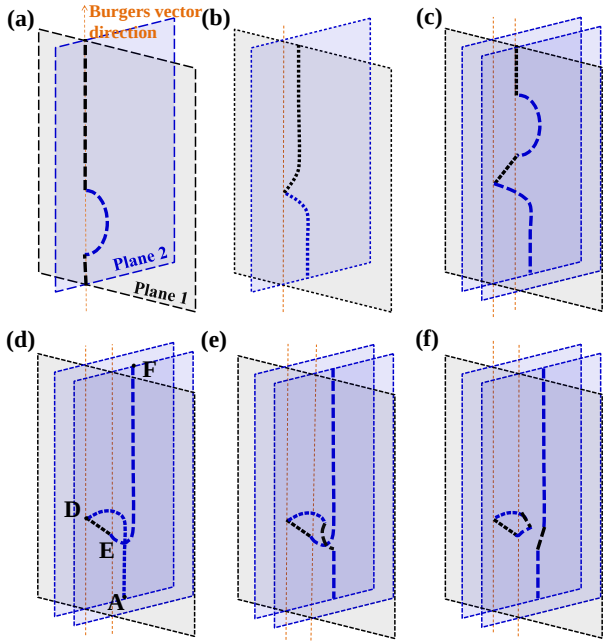

Figure 5. Schematic showing the dislocation loop formation mechanism by multiple crosses slip. The thick lines represent dislocation lines, whose colors indicate their slip planes as indicated in (a).

Interestingly, a new kind of self-multiplication mechanism is also revealed in our simulations as shown in Figure 4(d-f). The dislocation multiplies through forming a large dislocation loop. Figure 5 further schematically shows the formation process of the dislocation loop. After some amount of deformation, many relatively long screw dislocations are left in the BCC crystal. After one dislocation segment cross slips, a cross kink can be formed as shown in Figure 5(b). Then, another cross slip occurs because of the complex internal stress field induced by other dislocations. The upper-side mixed part of the dislocation in Figure 5(c) quickly bows out and forms the dislocation configuration, as shown in Figure 5(d), which exactly corresponds to the dislocation segment ADEF in Figure 4(d). Here, the dislocation segments DE and AD belong to two parallel slip planes, while segment DE belongs to the (011) slip plane. After another cross slip occurs, as shown in Figure 5(e), a dislocation loop is generated. Note that when the formed dislocation loop is small, it does not expand under the instantaneous stress level, as shown in Figure 3(b). This dislocation loop formation mechanism can also explain the reason why many dislocation loops and debris are experimentally observed in deformed BCC crystal.

References

[1] Argon AS, Maloof SR. Plastic deformation of tungsten single crystals at low temperatures. Acta Metallurgica 1966;14:1449-62.
[2] Kim J-Y, Jang D, Greer JR. Tensile and compressive behavior of tungsten, molybdenum, tantalum and niobium at the nanoscale. Acta Materialia 2010;58:2355-63.
[3] Po G, Mohamed M, Crosby T, Erel C, El-Azab A, Ghoniem N. Recent Progress in Discrete Dislocation Dynamics and Its Applications to Micro Plasticity. JOM 2014;66:2108-20.
[4] Caillard D. Kinetics of dislocations in pure Fe. Part I. In situ straining experiments at room temperature. Acta Materialia 2010;58:3493-503.
[5] Rao S, Dimiduk D, Parthasarathy T, Uchic M, Woodward C. Atomistic simulations of surface cross-slip nucleation in face-centered cubic nickel and copper. Acta Materialia 2013;61:2500-8.
[6] Hussein AM, Rao SI, Uchic MD, Dimiduk DM, El-Awady JA. Microstructurally based cross-slip mechanisms and their effects on dislocation microstructure evolution in fcc crystals. Acta Materialia 2015;85:180-90.
[7] Weinberger CR, Cai W. Surface-controlled dislocation multiplication in metal micropillars. Proceedings of the National Academy of Sciences 2008;105:14304-7.

8.7 MODELING MICROSTRUCTURAL EVOLUTION IN NEUTRON IRRADIATED TUNGSTEN — X. Hu, Y. Katoh (Oak Ridge National Laboratory), D. Xu, L.L. Snead, B.D. Wirth (University of Tennessee, Knoxville)

OBJECTIVE

The objective of this project is to develop a self-consistent cluster dynamics model based on diffusion-reaction rate theory to simulate the microstructural evolution of tungsten subject to neutron irradiation, thereby, to aid in understanding the degradation mechanism of tungsten and developing practical plasma facing materials.

SUMMARY

A diffusion-reaction cluster dynamics model based on rate theory was applied to depict the distribution of vacancy and interstitial clusters in tungsten following low temperature (90°C) and low dose (0.03 dpa) neutron irradiation. For experimental data to validate the developed model, *ex situ* characterization of vacancy defects using positron lifetime spectroscopy (PLS) was performed following one-hour anneals at 400, 500, 650, 800, 1000, 1150, and 1300°C for the high purity (110) single crystalline tungsten. TEM observations on tungsten after selected anneal conditions were also performed to determine the dislocation loop population. The data from microstructural observation were then used to validate the developed model as well as the kinetics and energetics parameters describing defect interactions in tungsten obtained from atomistic simulations.

PROGRESS AND STATUS

Introduction

Tungsten plasma facing components (PFCs) in fusion reactors will experience an extreme environment including high temperature and thermal flux, intense radiation, and significant cyclic thermal stress loading. Significant defect accumulations and the resulting degradation of thermo-mechanical properties are expected for tungsten during and after exposure to intense radiation. The combined effects of radiation damage and heat load in tungsten must be understood through a coordinated experimental and modeling approach due to a lack of fusion-relevant testing capability [1]. The effect of irradiation on materials' microstructure and properties is an inherently multiscale phenomenon [2], requiring the close integration of various modeling methods. In a recent review paper [3], Wirth et al. summarized their recent modeling efforts to closely integrate the modeling results with high-resolution experimental characterization of the evolving radiation-damaged microstructure. In order to compare with experimental data directly, it is common to model the neutron irradiation process by using a mean field diffusion-reaction cluster dynamics model, which involves the use of energetics and kinetics parameters obtained from atomistic simulations, such as DFT, MD, and yields the defect cluster population [3] [4] .

Model Description

Free vacancies and self-interstitial atoms (SIAs), as well as spherical vacancy clusters and SIA clusters in the form of planar, prismatic dislocation loops, are continuously generated and evolve in pure tungsten under neutron irradiation [5] [6], therefore, only intrinsic defects and their clusters are considered in this model. Given that the energy transfer cross section of energetic neutrons is very small (~10^{-24} cm^2), the defect generation and evolution are assumed to be homogeneous and no spatial dependence will be considered here. Therefore, the concentration of each cluster is only a function of time, and ordinary differential equations are employed to depict the defect evolution. The generic form to describe the evolution of a cluster is

$$\frac{dC_i}{dt} = f'\ P_i + G\_T + G\_E - A\_T - A\_E \qquad (1)$$

where C_i refers to the volumetric concentration (in 1/m^3) of the i-th cluster, f is neutron flux (in neutron/m^2/sec), P_i is the production 'probability' of the i-th cluster by neutron irradiation, *G* refers to the collective generation rates, *A* indicates the collective annihilation rates, *T* refers to generation or annihilation by trapping events, and *E* refers to generation or annihilation by emission events. The detailed construction of the coupled system of ODEs can be found in References [3] [4] .The mathematical expressions for the binary interactions can also be found in these two references.

The external source of intrinsic point defects and the corresponding clusters is the neutron irradiation induced collision cascade occurring inside the tungsten. A recent systematic MD study of cascade in tungsten [7] clearly showed that energetic PKAs directly produce small interstitial and vacancy clusters rather than isolated Frenkel pairs. Therefore, intra-cascade cluster production was used to determine the defect production probability, same as the work presented in [4]. PKA spectrum in tungsten neutron-irradiated in HFIR was calculated by using SPECTER, the results of which are shown in Figure 1.

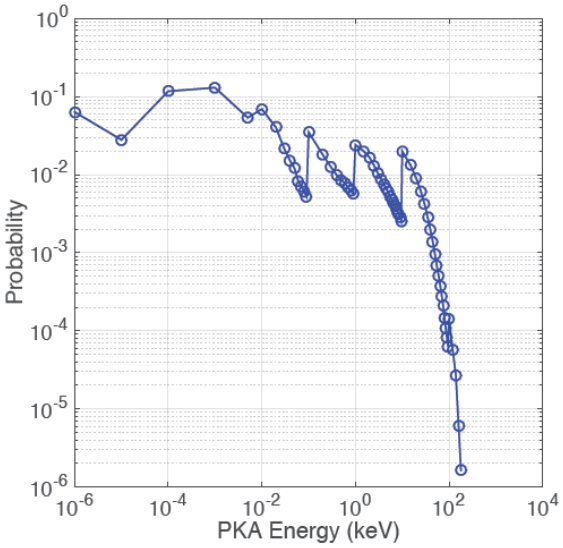

Figure 1. PKA spectrum in neutron irradiated tungsten in HFIR.

The surviving Frenkel pairs from the displacement cascade induced by the PKAs with different energies were calculated based on the empirical expressions summarized in [7], in the form of

$$N_F = \begin{cases} 0.49 \times \left(\frac{E_{PKA}}{E_d}\right)^{0.74} & \text{if } E_{PKA} < 35 \text{ keV} \\ 0.02 \times \left(\frac{E_{PKA}}{E_d}\right)^{1.30} & \text{if } E_{PKA} \geq 35 \text{ keV} \end{cases} \quad (2)$$

Consequently, the survived point defects in the cascade were partitioned into small clusters according to the clustering fractions obtained from [7]. The numbers of clusters produced by all PKA energies were then multiplied by the corresponding probabilities shown in Figure 1. The resulting cluster production 'probability' in unit of 1/PKA is listed in Table 1.

Table 1. Intra-cascade defect cluster production rate

Vacancy cluster size	Production Probability (1/PKA)	Production rate (1/cm^3/s)	Interstitial cluster size	Production Probability (1/PKA)	Production rate (1/cm^3/s)
1	1.03E+00	5.116E+15	1	1.31E+00	1.48E+15
2	1.73E-01	8.620E+14	2	1.74E-01	1.96E+14
3	8.36E-02	4.164E+14	3	4.66E-02	5.26E+13
4	3.82E-02	1.904E+14	4	3.02E-02	3.40E+13
5	2.39E-02	1.188E+14	5	1.53E-02	1.73E+13
6	1.58E-02	7.876E+13	6	6.50E-03	7.34E+12
7	1.01E-02	5.033E+13	7	5.93E-03	6.69E+12
8	4.38E-03	2.182E+13	8	2.58E-03	2.92E+12
9	1.82E-03	9.040E+12	9	1.86E-03	2.10E+12
10	2.30E-03	1.147E+13	10	1.36E-03	1.54E+12
11	8.02E-04	3.995E+12	11	1.08E-03	1.22E+12
12	2.02E-03	1.007E+13	12	1.56E-03	1.76E+12
13	1.22E-04	6.075E+11	13	6.87E-04	7.75E+11
14	1.07E-03	5.334E+12	14	3.90E-04	4.41E+11
16	4.47E-04	2.226E+12	15	4.18E-04	4.72E+11
17	4.43E-05	2.206E+11	16	1.14E-03	1.28E+12
18	1.08E-04	5.357E+11	17	2.66E-05	3.00E+10
19	3.90E-04	1.940E+12	18	1.65E-04	1.86E+11
20	2.40E-04	1.197E+12	20	7.11E-05	8.02E+10
21	5.77E-05	2.872E+11	21	2.03E-04	2.29E+11
22	1.08E-04	5.365E+11	22	9.55E-05	1.08E+11
24	1.33E-05	6.630E+10	23	3.37E-04	3.81E+11
27	4.44E-05	2.209E+11	24	2.60E-04	2.93E+11
29	1.90E-04	9.453E+11	25	8.21E-05	9.26E+10
30	1.08E-04	5.370E+11	26	4.44E-05	5.01E+10
34	1.52E-04	7.572E+11	27	2.47E-04	2.79E+11
35	4.43E-05	2.204E+11	28	1.33E-05	1.50E+10
37	1.08E-04	5.365E+11	30	2.67E-05	3.01E+10
38	4.44E-05	2.208E+11	31	8.22E-05	9.27E+10
43	8.21E-05	4.087E+11	32	1.08E-04	1.21E+11
51	1.26E-04	6.295E+11	33	1.33E-05	1.51E+10
57	4.43E-05	2.206E+11	36	8.20E-05	9.25E+10
60	1.33E-05	6.642E+10	37	4.44E-05	5.01E+10
70	8.21E-05	4.087E+11	38	1.02E-04	1.15E+11
74	8.21E-05	4.089E+11	40	1.33E-05	1.50E+10
84	4.43E-05	2.207E+11	41	9.54E-05	1.08E+11
86	1.33E-05	6.620E+10	45	4.43E-05	5.00E+10
87	1.33E-05	6.635E+10	46	4.43E-05	5.00E+10
91	1.33E-05	6.632E+10	50	8.21E-05	9.26E+10
104	1.33E-05	6.635E+10	56	4.43E-05	5.00E+10
105	1.33E-05	6.632E+10	57	1.33E-05	1.50E+10
114	1.33E-05	6.635E+10	61	2.66E-05	3.00E+10
153	1.33E-05	6.630E+10	63	2.66E-05	3.00E+10
			65	2.67E-05	3.01E+10
			70	1.33E-05	1.50E+10

Now it is necessary to determine the cluster production rate with respect to a specific neutron flux. This requires the PKA production rate be specified. From SPECTER calculations, the displacement cross section of the neutron irradiation was also obtained, which enabled the computation of the total displacement rate (R_d) in tungsten, as defined in Eq. (3),

$$R_d\left[\frac{1}{cm^3 \cdot s}\right] = f\left[\frac{1}{cm^2 \cdot s}\right] s_d\left[cm^2\right] N\left[\frac{1}{cm^3}\right], \quad (3)$$

where $\phi=3.5\times10^{15}$ $[\frac{\text{neutron}}{\text{cm}^2}/\text{s}]$, $\sigma_d=51.229$ barn, and $N=6.3\times10^{22}$ atoms/cm^3. The displacement cross section for tungsten under neutron irradiation in HFIR has a low value due to the incorporation of thermal neutrons in the neutron flux energy spectrum, which in general do not cause direct displacements through elastic scattering.

Fortunately, there is another way to calculate the displacement rate, as defined in Eq. (4),

$$R_d\left[\frac{1}{cm^3\cdot s}\right] = I\left[\frac{PKA}{cm^3\cdot s}\right]P_d\left[\frac{displacements}{PKA}\right], \quad (4)$$

where the displacements per PKA can be computed based on the MD database (P_d=2.27 disp./PKA).

Combining Eqs. (3) and (4) yielded the PKA production rate, 1.12×10^{15} PKA/cm^3/s. Thus, the intra-cascade cluster production probabilities can be obtained by multiplying the values in the second and fifth columns of Table 1 with PKA production rate in the tungsten subject to neutron irradiation at HFIR.

In the present model, all interstitial loops and only single vacancy are considered mobile. Diffusion coefficients of mobile species are required to describe the binary interactions of the binding process of two species (at least one is mobile). Table 2 listed the set of mobility data chosen on empirical basis by considering various studies.

Table 2. Mobility set for interstitial clusters and single vacancy for the modeling of neutron irradiated W

Clusters	V	I_1-I_{10}	I_{11}-I_{20}	I_{21}-I_{30}	I_{31}-I_{40}	I_{41}-I_{50}	$I_{>=51}$
Migration E (eV)	1.30	0.23	0.53	0.63	0.73	0.83	1.35
D_0 (nm^2/s)	1.77×10^{12}				$8.77\times10^{10}/n^{0.5}$		

For the dissociation process of big defect clusters, the emission of single vacancy and SIA is more energetically preferable. The binding energies of single V and SIA to the V and interstitial clusters [8] are shown in Figure 2.

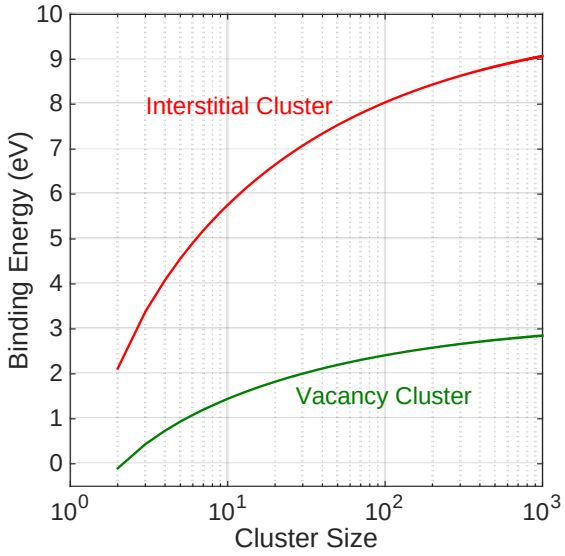

Figure 2. Binding energies of single V and SIA to V and interstitial clusters

Results

ORNL is conducting intense research activities to characterize the microstructure of tungsten neutron-irradiated at HFIR and the resulting mechanical property degradation. 1W25, experiencing low dose (0.03 dpa) and low temperature (90°C) neutron irradiation, was chosen to validate the developed model. Following the cluster dynamics model described above, the vacancy and interstitial cluster population could be predicted, as shown in Figure 3. It can be seen that interstitials undergo significant clustering

even at low doses and low temperature, while vacancies do not, which reflects that the interstitials are much more mobile than vacancies, as shown in Table 2.

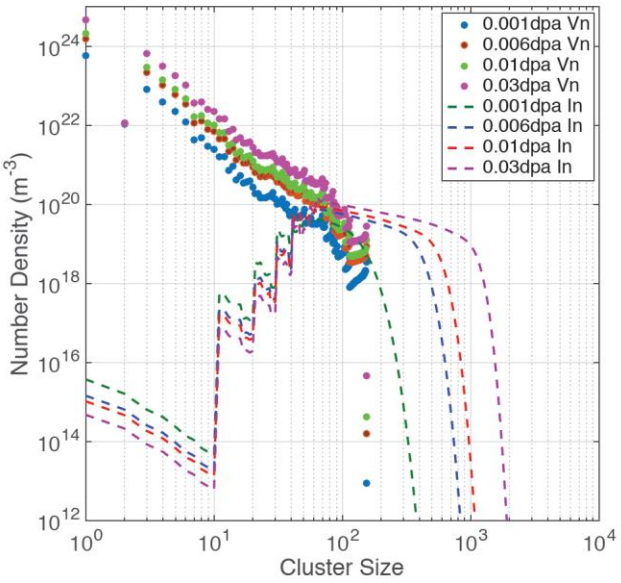

Figure 3. Model predicted volumetric density of interstitial and vacancy clusters plotted as a function of cluster size (n, # of point defects in the cluster) at 90°C.

The validation of model predicted interstitial dislocation loop was realized by comparing with TEM observations. Average dislocation density and size were obtained from TEM. Then a straightforward calculations based on Figure 3 was performed to acquire the information to be compared with TEM. The comparison of experimental data and modeling predictions was shown in Figure 4. It is apparent that the modeling results had a good agreement with the TEM observation for the as-irradiated 1W25 in terms of the interstitial dislocation loops.

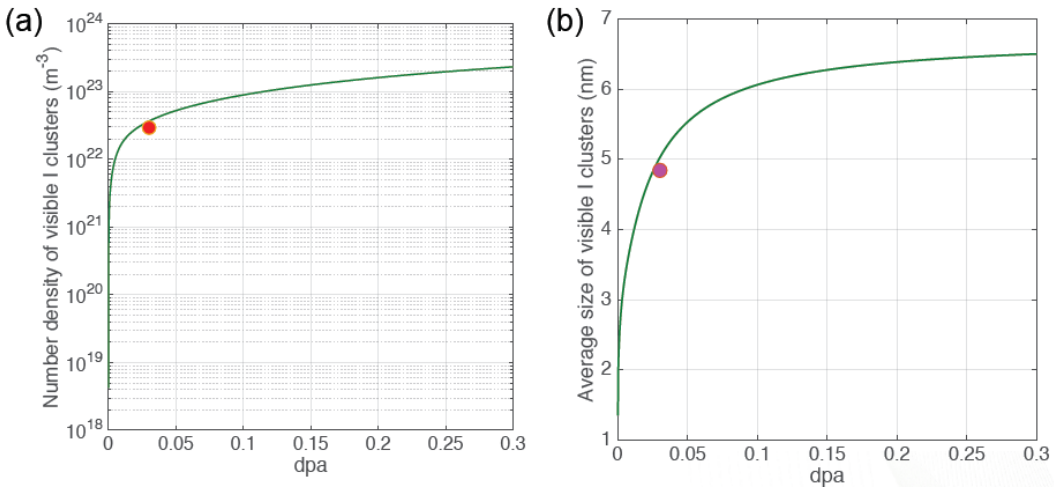

Figure 4. Model prediction of (a) interstitial dislocation loop density and (b) average size of the visible dislocation loop with a TEM resolution of 1.5 nm, as compared to the TEM observations.

In addition to the interstitial dislocation loop, the model predicted vacancy cluster population could be validated by the PAS results. Learning from a recent PAS work on neutron irradiated tungsten, the total vacancy concentration of 1W25 is in the order of 10^{24} m^{-3}, which is consistent with the modeling result,

6.2×10^{24} m^{-3}. Moreover, the PAS also provides the vacancy distribution in a rough way. A straightforward comparison is shown in Figure 5.

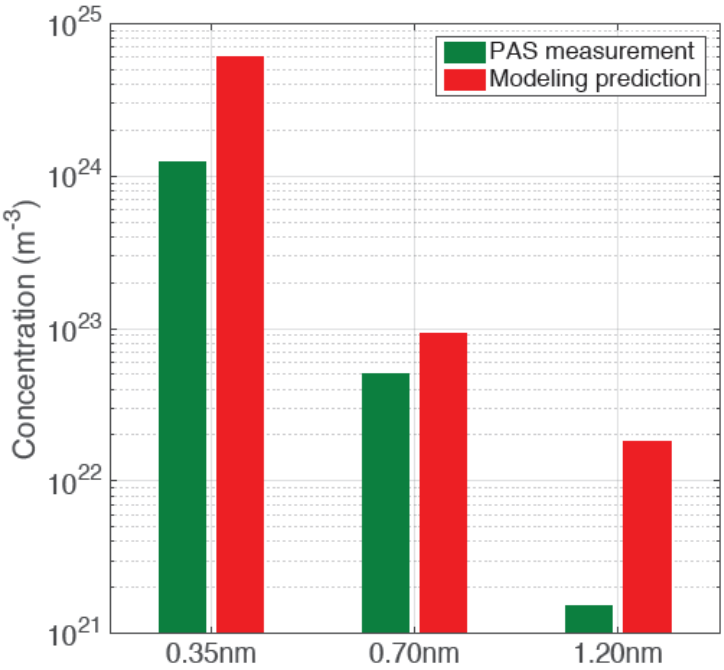

Figure 5. Comparison of modeling prediction and experimental measurements of size distribution of vacancy clusters in as-irradiated 1W25.

There was only one experimental data for both interstitial dislocation loop and vacancy cluster to validate the developed model, which is definitely not sufficient. A recent annealing study of neutron irradiated single crystalline tungsten enabled a more systematic comparison between the PAS results and the modeling results. Following one hour anneals at 400, 500, 650, 800, 1000, 1150, and 1300°C for 1W25, *ex situ* characterization of vacancy defects used positron lifetime spectroscopy, which gave a rough estimation of the vacancy defect population at different annealing stages. The cluster dynamics model was then applied to simulate the corresponding annealing stages. The currently available modeling results are shown in Figure 6.

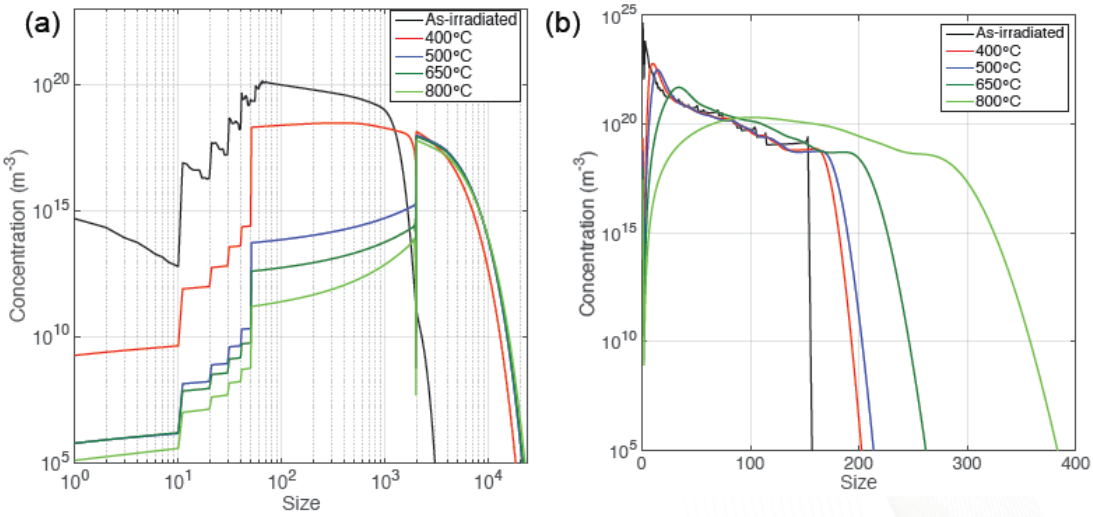

Figure 6. Modeling results of (a) interstitial dislocation loop and (b) vacancy defect cluster at different annealing stages together with the as-irradiated condition.

It is shown in Figure 6(a) that the mobile interstitial dislocation loops decreased with the increasing annealing temperature. After annealed at 400°C for one hour, the loops expanded to larger regime due to the strong combination of the mobile clusters. However, the 500, 650, and 800°C anneals didn't push this process further due to continuously decreasing concentrations of the mobile clusters. With respect to the vacancy cluster, anneals at 400 and 500°C didn't change the distribution dramatically. Starting from 650°C, the vacancy defect cluster moved to larger space and the case of 800°C was more significant.

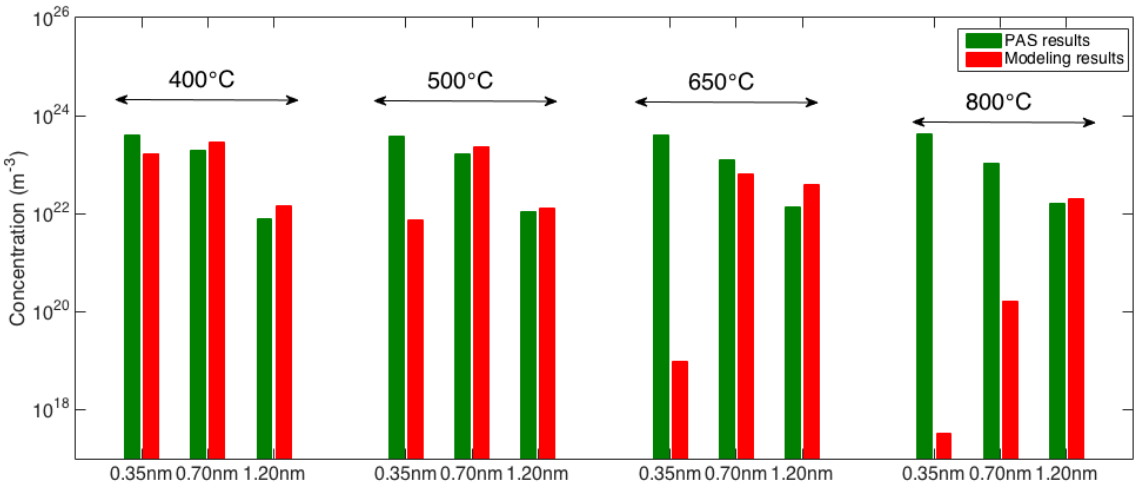

Figure 7. Comparison of the vacancy cluster population obtained from modeling (Red bars) and PAS measurements (Green bars) at different annealing stages.

The vacancy defect population obtained by employing positron annihilation lifetime spectroscopy enabled the validation of the modeling predictions as shown in Figure 7. The modeling predictions of the intermediate and larger voids had a good agreement with the experimentally obtained results. However, the model didn't successfully reproduce the small vacancy cluster evolution when the annealing temperature was higher than 500°C. The small vacancy cluster population obtained from PAS measurement didn't not change obviously, due to the presence of impurity-stabilized vacancy clusters, which was not explicitly included in the model. More work is needed to address the discrepancy between modeling and experimental data.

Planned Work

Up to date, the annealing stages at 400, 500, 650, and 800°C have been simulated by applying the developed cluster dynamics model. The modeling of the remaining three annealing stages, 1000, 1150, and 1300°C, are being performed. Meanwhile, the validation of the vacancy defect cluster was performed by comparing with the PAS measurements for the completed modeling work. In addition, the information of interstitial dislocation loops from TEM observations is necessary to validate the model predictions.

References

[1] Wirth, B.D., et al., Fusion materials modeling: Challenges and opportunities. MRS Bulletin, 2011. 36(03): p. 216-222.

[2] Wirth, B.D., et al., Multiscale modeling of radiation damage in Fe-based alloys in the fusion environment. Journal of Nuclear Materials, 2004. 329-333: p. 103-111.

[3] Wirth, B.D., et al., Modeling defect cluster evolution in irradiated structural materials: Focus on comparing to high-resolution experimental characterization studies. Journal of Materials Research, 2015: p. 1-16.

[4] Hu, X., et al., Modeling of irradiation hardening of iron after low-dose and low-temperature neutron irradiation. Modelling and Simulation in Materials Science and Engineering, 2014. 22(6): p. 065002.
[5] Nandipati, G., et al., Displacement cascades and defect annealing in tungsten, Part III: The sensitivity of cascade annealing in tungsten to the values of kinetic parameters. Journal of Nuclear Materials, 2015.
[6] Ogorodnikova, O.V. and V. Gann, Simulation of neutron-induced damage in tungsten by irradiation with energetic self-ions. Journal of Nuclear Materials, 2015. 460: p. 60-71.
[7] Setyawan, W., et al., Displacement cascades and defects annealing in tungsten, Part I: Defect database from molecular dynamics simulations. Journal of Nuclear Materials, 2014.
[8] Becquart, C.S., et al., Microstructural evolution of irradiated tungsten: Ab initio parameterisation of an OKMC model. Journal of Nuclear Materials, 2010. 403(1-3): p. 75-88.

8.8. Unraveling the temperature dependence of the yield strength in single-crystal tungsten using atomistically-informed crystal plasticity calculations

David Cereceda, Jaime Marian

[a]*Department of Materials Science and Engineering, University of California Los Angeles, Los Angeles, CA 90095, USA*

Abstract

We use a physically-based crystal plasticity model to predict the yield strength of body-centered cubic (bcc) tungsten single crystals subjected to uniaxial loading. Our model captures the thermally-activated character of screw dislocation motion and full non-Schmid effects, both of which are known to play a critical role in bcc plasticity. The model uses atomistic calculations as the sole source of constitutive information, with no parameter fitting of any kind to experimental data. Our results are in excellent agreement with experimental measurements of the yield stress as a function of temperature for a number of loading orientations. The validated methodology is then employed to calculate the temperature and strain-rate dependence of the yield strength for 231 crystallographic orientations within the standard stereographic triangle. We extract the strain-rate sensitivity of W crystals at different temperatures, and finish with the calculation of yield surfaces under biaxial loading conditions that can be used to define effective yield criteria for engineering design models.

Keywords: Bcc crystal plasticity, Yield stress, Non-Schmid effects, Screw dislocations, Single crystal tungsten, Uniaxial/biaxial loading

1. Background and motivation

The plastic behavior of body-centered cubic (bcc) single crystals at low to medium homologous temperatures is governed by the motion of $\frac{1}{2}\langle 111\rangle$ screw dislocations on close-packed crystallographic planes. There are two particularities that make bcc metals unique in relation to their deformation characteristics. The first one is the thermally-activated nature of screw dislocation glide, a consequence of the compact (non-planar) structure of the dislocation core at the atomistic level [1–4]. This feature is also responsible for the high intrinsic friction stresses reported in the literature for bcc metals and their alloys [4; 5]. The second is the breakdown of the standard geometric projection rule for the resolved shear stress (RSS) from the total stress tensor known as *Schmid law* [6]. This is owed to both specific crystallographic properties of the bcc lattice structure as well as to the coupling between the dislocation core and non-glide components of the stress tensor, which –to the best of our understanding– is unique to bcc crystals [7–11]. These anomalies have been the subject of much research and discussion going back to the 1960's [12–15], both experimentally and –more recently– using computational atomistic models.

In regards to the first point above, at low stresses slip proceeds via the thermally activated nucleation of steps on the dislocation line, known as *kink pairs*, and their subsequent sideward relaxation. For a constant strain rate, this gives rise to the characteristic temperature dependence of the flow stress in bcc single crystals, which has been observed for all refractory metals and is considered to be a principal signature of their plastic response [10; 16–20]. The flow stress is considered to be composed of thermal and athermal contributions, with the latter depending on temperature only as the elastic moduli. Dislocation glide is thought to occur on $\{110\}$, $\{112\}$, and even $\{123\}$ planes, depending on temperature and stress, over a periodic energy landscape known as the *Peierls* potential U_P. The connection between the experimentally measured flow stress and this periodic energy potential is via the critical stress for which U_P

vanishes at zero temperature, known as the Peierls stress σ_P. Theoretically then, the flow stress at very low temperatures ($\leqslant$ 25 K) is thought to represent the macroscopic equivalent of σ_P as the temperature approaches 0 K. σ_P can thus be unequivocally defined and has been the object of considerable numerical work since the first atomistic models were devised by Vitek and co-workers starting in the 1970s [21].

For their part, non-Schmid effects were detected in tests done in the 1930's by Taylor in the wake of his seminal works on plastic flow and strain hardening [22–24]. Subsequent observations and measurements [25–31], and a rigorous theoretical formulation of the problem [9–11; 32–36] have established non-Schmid behavior as a principal tenet of bcc plasticity that must be accounted for in order to understand bcc plastic flow. In terms of phenomenology, the two essential aspects to bear in mind are (i) that the resolved shear stress is not independent of the sign of the stress in glide planes of the $\langle 111 \rangle$ zone (the so-called *twinning/anti-twinning* asymmetry), and (ii) that non-glide components of the stress tensor –*i.e.* those which are perpendicular to the Burgers vector– play a role on the magnitude and sign of the RSS on the glide plane of interest.

Areas where we do not have a complete understanding of bcc plastic picture include the value of the flow stress at near zero absolute temperatures, the meaning of the so-called *knee* temperature, and the onset of athermal flow. In the last two decades, computer simulation has unquestionably emerged as discipline capable of shedding light on these processes on a similar footing with experiments, providing physically-substantiated explanations across a range of temporal and spatial scales. These include the use and application of density-functional theory methods [37–41], semi empirical atomistic calculations and molecular dynamics calculations [42–45], kinetic Monte Carlo [46–50], and crystal plasticity (CP)[51–53], to name but a few. In general, while there is no doubt that the intricacies associated with $\frac{1}{2}\langle 111 \rangle$ screw dislocation glide –including its thermally activated nature and deviations from Schmid law– cannot but be resolved using methods capable of atomistic resolution, one must recognize that, at the same time, flow is a phenomenon potentially involving statistically-significant amounts of dislocations and –as such– cannot be captured resorting to atomistic calculations only.

Modeling thermally-activated flow and non-Schmid effects in bcc systems has been the subject of much work, starting in the 1980s and, particularly, in recent times. Different authors have considered different subsets of the $\{110\}$, $\{112\}$, and $\{123\}$ families of glide planes, without [54–65] and with non-Schmid effects [66–76]. Of particular interest are some recent simulations where the flow rule is directly formulated on the basis of screw dislocation properties in Fe [68; 70; 72; 73; 76; 77], Ta [67; 71; 74; 75], Mo [69; 71; 75; 77], W [66; 69; 71; 74; 75], and Nb [75; 77]. These works also include non-Schmid effects following the model proposed by Vitek and Bassani [32; 34; 35; 51]. However, albeit very useful for certain applications, all these works resort to (i) a partial consideration of non-Schmid effects, and (ii) some kind or another of parameter fitting with experimental data, which prevents their use in regions of the parameter space outside the range of fitting and does not link the effective (*macroscopic*) response to exclusively fundamental material properties and features.

In this work, we provide a unified computational methodology consisting of rate-dependent crystal plasticity calculations parameterized entirely and exclusively to atomistic calculations. We show that a full description of non-Schmid effects, together with the state of the art in terms of our understanding of thermally-activated screw dislocation motion, suffices to capture the experimentally measured temperature dependence of the flow stress in tungsten. This is achieved in a fully classical framework, without the need for quantum effects recently invoked to explain the long standing discrepancy observed between the experimentally-measured flow stress below 25 K and calculated values of the Peierls stress [78]. Our methodology also captures the athermal limit of W to within 5% of the experimental value. We emphasize that this agreement is reached without fitting to any experimental data, all the parameterization is done from first principles atomistic calculations.

Our paper is organized as follows. After this introduction, we provide an overview of the CP method in Section 2.2. This is followed by Sections 2.3.1 and 2.3.2, where the formulation of the dislocation mobility law and the implementation of non-Schmid effects are presented, including a detailed description of the parameterization procedure employed. The results are given in Section 3, which includes: (i) the validation exercise, with special focus on uniaxial tests as a function of temperature for several loading orientations;

(ii) the calculation of temperature and strain rate dependence of the yield strength for uniaxial tensile tests as a function of orientation; and (iii) yield surfaces under biaxial loading conditions as a function of temperature. We finalize in Section 4 with a brief discussion and the conclusions.

2. Computational methods

2.1. Flow kinematics

[79] have presented a detailed review of the kinematic and constitutive aspects of crystal plasticity and here we simply provide a brief overview of the fundamental theory. The kinematics for elasto-plastic behavior is defined within the finite deformation framework. The material deformation involves both a reversible lattice response to externally imposed loads or displacements (elastic), and a permanent deformation (irreversible shape change) that remains after all external constraints cease to be applied (plastic). Consequently, crystal plasticity formulations rely on the definition of three reference systems: (i) a fixed coordinate system that represents a laboratory (undeformed) frame of reference, (ii) a current (also known as *material*) frame of reference that represents the global (deformed) shape of the material, and (iii) a *lattice* coordinate system that represents distortions of the underlying crystal structure of the deformed body. Although reference system (i) is used for mathematical convenience, the distinction between (ii) and (iii) is necessary to calculate internal stresses, which arise from distortions defined with respect to a crystallographic frame of reference, as global shape changes may not necessarily have a one-to-one correspondence to internal lattice distortions [79; 80].

Mathematically, each point $\boldsymbol{X}$ in the reference configuration may be mapped to its image in the current configuration $\boldsymbol{x}$ by means of a linear transformation represented by the *deformation gradient* tensor $\boldsymbol{F}$, defined as:

$$\boldsymbol{F} = \frac{\partial \boldsymbol{x}}{\partial \boldsymbol{X}} \tag{1}$$

In general, $\boldsymbol{F}$ is not a symmetric tensor. However, invariance requirementsmake it more desirable to work with symmetric measures of strain. One such measure is the so-called *Lagrangian* strain:

$$\boldsymbol{E} = \frac{1}{2}\left(\boldsymbol{C} - \boldsymbol{I}\right) = \frac{1}{2}\left(\boldsymbol{F}^T\boldsymbol{F} - \boldsymbol{I}\right) \tag{2}$$

which refers the deformation of the solid to the reference configuration ($\boldsymbol{I}$ is the identity tensor). In the above equation, $\boldsymbol{C}$ is the so-called *right Cauchy-Green* tensor.

Following [81], the total deformation gradient $\boldsymbol{F}$ can be multiplicatively decomposed into an elastic, $\boldsymbol{F}_e$, and a plastic, $\boldsymbol{F}_p$, part[1], *i.e.*:

$$\boldsymbol{F} = \boldsymbol{F}_e\boldsymbol{F}_p \tag{3}$$

whence

$$\boldsymbol{F}_e = \boldsymbol{F}\boldsymbol{F}_p^{-1} \Leftrightarrow \boldsymbol{F}_p = \boldsymbol{F}_e^{-1}\boldsymbol{F}$$

This is schematically shown in Figure 1, where the relationship between the reference, intermediate, and current configurations is provided. To close the CP model, we take the time rate in eq. (1), which results in:

$$\boldsymbol{L} = \dot{\boldsymbol{F}}\boldsymbol{F}^{-1} = \dot{\boldsymbol{F}}_e\boldsymbol{F}_e^{-1} + \boldsymbol{F}_e\left(\dot{\boldsymbol{F}}_p\boldsymbol{F}_p^{-1}\right)\boldsymbol{F}_e^{-1} = \boldsymbol{L}_e + \boldsymbol{F}_e\boldsymbol{L}_p\boldsymbol{F}_e^{-1} \tag{4}$$

where $\boldsymbol{L}_p$ is the plastic velocity gradient, which is evaluated in the intermediate configuration and must therefore be mapped into the current configuration by $\boldsymbol{F}_e$. Constitutive information enters the CP model via $\boldsymbol{L}_p$, which is described in the following section.

The above finite-deformation kinematic frameworkis implemented into the Düsseldorf Advanced Materials Simulation Kit (DAMASK), which is the tool employed in this work to carry out of the calculations. DAMASK is a flexible and hierarchically structured model of material point behavior for the solution of elastoplastic boundary value problems along with damage and thermal physics [84].

[1] It must be noted that other decompositions are also admissible [82]. The reader is referred to the work by [83] for a discussion on the uniqueness and validity of the multiplicative decomposition.

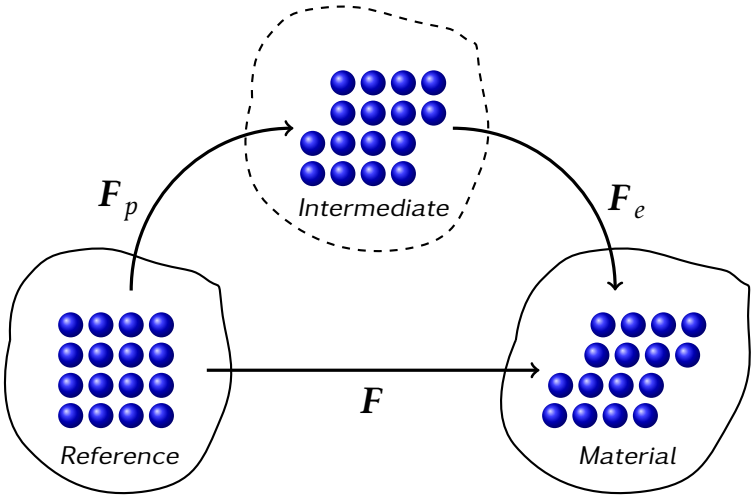

Figure 1: Multiplicative decomposition of the deformation gradient $\boldsymbol{F}$.

2.2. Solution procedure and constitutive model

A *Hookean* constitutive response is assumed such that the stress depends linearly on the elastic strain via the anisotropic elastic stiffness tensor $\mathbb{C}$. Both the stress and strain measures that are used internally are formulated in terms of material coordinates. For the stress, we use the *second Piola-Kirchhoff* stress measure $\boldsymbol{S}$, defined as:

$$\boldsymbol{S} = \mathbb{C} : \boldsymbol{E}_e = \frac{\mathbb{C}}{2}\left(\boldsymbol{F}_e^T \boldsymbol{F}_e - \boldsymbol{I}\right) \tag{5}$$

where $\boldsymbol{E_e}$ is the (elastic) *Green-Lagrange* strain tensor. $\boldsymbol{S}$ and $\boldsymbol{E}_e$ are both symmetric material tensors, and thus $\mathbb{C}$ is itself symmetric such that a general $3\times3\times3\times3$ tensor can be written as a 6×6 matrix. For cubic lattices, $\mathbb{C}$ can be reduced by symmetry to only the three independent elastic constants $\mathbb{C}_{11}$, $\mathbb{C}_{12}$, and $\mathbb{C}_{44}$.

The stress $\boldsymbol{S}$ acts as the driving force for the plastic velocity gradient $\boldsymbol{L}_p$. $\boldsymbol{L}_p$ depends on the underlying microstructure via a set of state variables ξ defined by the plasticity model employed:

$$\boldsymbol{L}_p = f(\boldsymbol{S}, \xi, \ldots) \tag{6}$$

$\boldsymbol{L}_p$ controls the evolution of the plastic deformation gradient:

$$\dot{\boldsymbol{F}}_p = \boldsymbol{L}_p \boldsymbol{F}_p \tag{7}$$

The set of nonlinear eqs. (3) and (5) to (7) must be solved iteratively, which in DAMASK is done by using an integration algorithm based on the implicit scheme originally proposed by [85]. The linear system is solved iteratively using the Newton-Raphson technique and, once convergence is achieved, the plastic deformation gradient is obtained using the Euler backward update. In this integration scheme described above, the primary variable to solve for is the plastic velocity gradient. However, one may devise schemes where the primary variables are the stress, the plastic or elastic deformation gradient, the internal variables or a combination thereof. Such schemes may be chosen on the basis of computational efficiency [86].

Constitutive information for the plastic regime enters the CP model via eq. (6), where the dependencies of the flow rule on each of the state variables are established. It is here where the plastic deformation modes are defined, their geometric particularities, as well as specifics associated with the crystal structure under study. The CP model must also include evolution equations for the state variables ξ:

$$\dot{\xi} = g(\boldsymbol{S}, \xi, \ldots) \tag{8}$$

where the details again depend on the model selected. In DAMASK, various integration schemes for the state update exist [84]. Then, two integration schemes are performed staggered: eqs. (3) to (7) are solved

at a fixed plastic state, followed by a state update. This procedure is iteratively repeated until a converged solution is achieved within the given tolerances. More details about the implementation of this technique in the code are given by [85]. In general then, the stress in the CP model can be considered a response function of the position $\boldsymbol{r}$, the deformation state $\boldsymbol{F}$, the set of state variables ξ, and a set of boundary conditions, *i.e.*

$$\boldsymbol{S} = f(\boldsymbol{r}, \boldsymbol{F}, \xi, \ldots) \tag{9}$$

In these calculations we are interested in simulating engineering stress-strain tests, and –consequently– it is helpful to express the results in the reference coordinate frame. For the stress, we use the *first* Piola-Kirchhoff measure defined as:

$$\boldsymbol{P} = \boldsymbol{F}_e \boldsymbol{S}$$

Note that, although in general $\boldsymbol{P}$ is not symmetric, for uniaxial tension tests $\boldsymbol{P}$ is a symmetric tensor on account of $\boldsymbol{F}_e$ being symmetric. For the strain, we use the *Biot* tensor:

$$\boldsymbol{B} = \boldsymbol{U} - \boldsymbol{I} = \sqrt{\boldsymbol{F}^T \boldsymbol{F}} - \boldsymbol{I}$$

where $\boldsymbol{U}$ is the *right stretch* tensor[2]. The stress-strain curves shown throughout this paper are obtained by tracking the evolution of P_{zz} and B_{zz}, where z is designated as the loading direction. For uniaxial loading simulations, $\dot{\boldsymbol{F}} \equiv \dot{\boldsymbol{F}}^T$ and thus $\dot{\boldsymbol{C}} = \dot{\boldsymbol{F}} \approx \dot{\boldsymbol{B}}$. We refer to the deformation rate represented by $\dot{F}_{zz}$ generically as $\dot{\varepsilon}$ in the remainder of this paper.

2.3. The flow rule

In the present CP calculations it is assumed that all the plastic deformation is due to dislocation slip. Then, the plastic velocity gradient can be written as:

$$\boldsymbol{L}_p = \sum_{\alpha} \boldsymbol{P}_{\mathrm{S}}^{\alpha} \dot{\gamma}^{\alpha} \tag{10}$$

where $\dot{\gamma}^{\alpha}$ is the slip rate on slip system α, and $\boldsymbol{P}_{\mathrm{S}}^{\alpha}$ is a geometric projection tensor that will be defined later. The slip rate is calculated from Orowan's equation:

$$\dot{\gamma}^{\alpha} = b \rho^{\alpha} v_s(\tau^{\alpha}, T) \tag{11}$$

where $b = a_0 \sqrt{3}/2$ is the modulus of the Burgers vector, a_0 is the lattice parameter, T the absolute temperature, ρ^{α} is the (mobile) screw dislocation density in slip system α, and $v_s(\tau^{\alpha}, T)$ is the screw dislocation velocity. The present formulation of the flow rule belongs to the class of *non-associated, rate-dependent* CP models [87].

The two characteristics that are particular to bcc plasticity are the thermally-activated nature of screw dislocation motion, which makes it the rate-controlling process during plastic deformation, and the existence of non-Schmid effects, *i.e.* deviations from the geometric projection law for the resolved shear stress. Both of these physical processes have been known for several decades, and have been carefully analyzed experimentally (cf. Section 1). If our intent is to predict the temperature dependence of the flow stress in bcc metals, accurate physical descriptions of both of them must be incorporated into our CP model. This is the subject of the following sections. As we shall see, non-Schmid effects establish the form of the projection tensor $\boldsymbol{P}_{\mathrm{tot}}^{\alpha}$, while the velocity $v_s(\tau^{\alpha}, T)$ captures the thermally activated character of dislocation motion. We make tungsten the object of our study for a number reasons presented in previous works [50; 88][3].

[2] $\boldsymbol{U}$ emerges from the so-called *polar* decomposition: $\boldsymbol{F} = \boldsymbol{R}\boldsymbol{U}$, where $\boldsymbol{R}$ is a matrix the represents rigid rotation, and $\boldsymbol{U}$ is a pure stretch. Plasticity-induced crystal rotations are very important and give rise to crystallographic texture evolution in deformed crystals. However, only yielding is of concern here, and thus $\boldsymbol{U}$ is the component of interest.

[3] W is an elastic isotropic metal, which simplifies the constitutive plastic formulation.

2.3.1. Screw dislocation mobility law

Except at high homologous temperatures and strain rates, screw dislocation motion is the rate-limiting step in bcc crystal deformation. Although recent dislocation dynamics simulations in α-Fe challenge the notion that the dislocation density is monolithic across the entire temperature range [89–92], it is reasonable to assume a dominance of screw dislocations in the temperature and strain rate regimes considered in this work ($0 < T/T_m < 0.2$ and $\dot{\varepsilon} \approx 10^{-4}$ s^{-1}). In the thermally activated regime, screw dislocation motion proceeds via the nucleation of kink-pairs and their subsequent lateral relaxation. In the regime of interest here, kink relaxation is a significantly faster process than kink-pair nucleation, and it can thus be assumed that no new kink-pairs will be nucleated while lateral kink motion is underway [50]. Such assumption leads to the following expression for the total time, t_t, required for a kink pair to form and sweep a rectilinear screw dislocation segment of length λ^α lying on a given slip plane:

$$t_t = t_n + t_k = J(\tau^\alpha, T)^{-1} + \frac{\lambda^\alpha - w}{2v_k(\tau^\alpha, T)} \tag{12}$$

where t_n is the mean time to nucleate a kink pair, t_k is the time needed for a kink to sweep half a segment length, J is the kink-pair nucleation rate, w is the kink-pair separation, and v_k is the kink velocity. The kink-pair nucleation rate follows an Arrhenius formulation [50]:

$$J(\tau^\alpha, T) = \frac{\nu_0(\lambda^\alpha - w)}{b} \exp\left(-\frac{\Delta H_{kp}(\tau^\alpha)}{kT}\right) \tag{13}$$

where ν_0 is an attempt frequency, ΔH_{kp} is the activation enthalpy of a kink pair at stress τ^α, and k is Boltzmann's constant. For its part, the kink velocity can be expressed as [93; 94]:

$$v_k(\tau^\alpha, T) = \frac{b\tau^\alpha}{B(T)} \tag{14}$$

where B is friction coefficient typically assumed to be linearly dependent on temperature. However, calculations made to obtain the value of B for the interatomic potential employed in this work, have yielded no temperature dependence, and here B is simply a constant [95] . The dislocation velocity can be obtained after operating with eqs. (13) and (14) as:

$$v_s = \frac{h}{t_t} = \frac{h}{t_n + t_k} = \frac{2bh\tau^\alpha \nu_0(\lambda^\alpha - w)\exp\left(-\frac{\Delta H_{kp}}{kT}\right)}{2b^2\tau^\alpha + \nu_0 B(\lambda^\alpha - w)^2 \exp\left(-\frac{\Delta H_{kp}}{kT}\right)} \tag{15}$$

where $h = a_0\sqrt{6}/3$ is the distance between two consecutive Peierls valleys. We note that at low temperatures, or when $t_k \ll t_n$, the second term in the denominator vanishes and one recovers the standard diffusive velocity expression commonly used in crystal plasticity and dislocation dynamics:

$$v_s = \nu_0 h \frac{(\lambda^\alpha - w)}{b} \exp\left(-\frac{\Delta H_{kp}(\tau^\alpha)}{kT}\right)$$

The parameterization of eq. (15) is a critical step that establishes a physical connection with the scales where kink-pairs are resolved as atomistic entities. This is the first essential piece of physics required to achieve predictive capabilities. We have devoted much effort in past works to calculate the necessary parameters from fundamental models based on semiempirical interatomic potentials [50; 88]. The list of parameters employed in this work and their associated values and units are given in Table 1. The physical meaning of some of these parameters is best expressed in pictorial form. Figure 2 shows a schematic diagram of the topology of a kink pair lying on the Peierls energy substrate. The figure highlights the physical meaning of each parameter listed in the table. In addition to the references provided earlier, a detailed description of the protocols used to calculate all the adjustable parameters in our formulation is provided by [96].

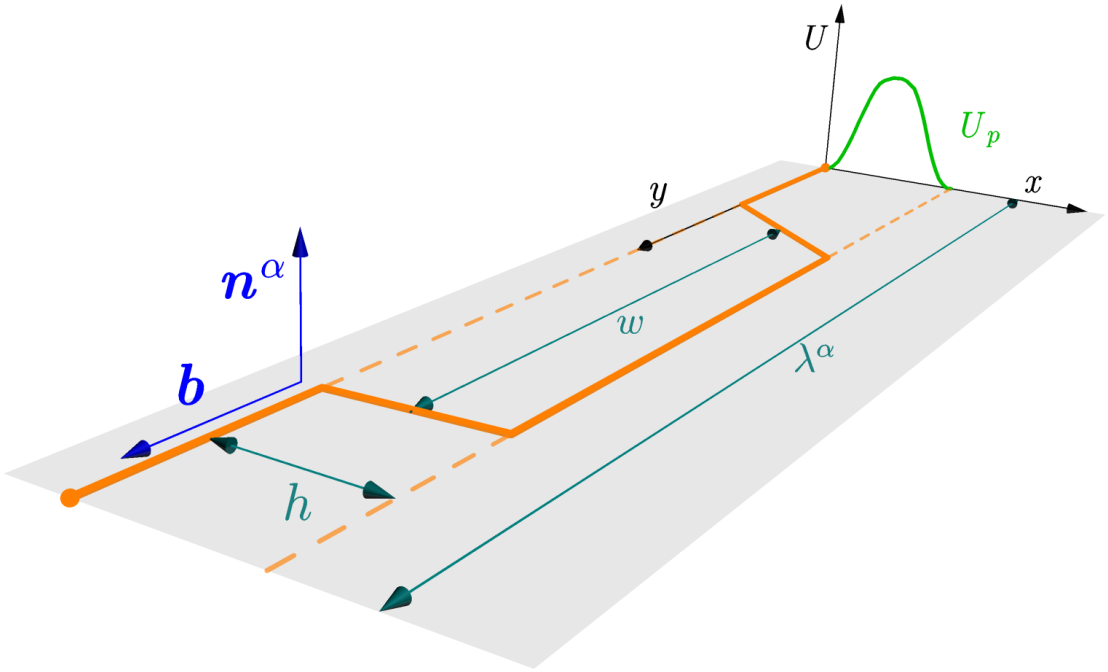

Figure 2: Schematic depiction of a kink pair on a screw segment of length λ lying on a slip plane $\boldsymbol{n}^\alpha$ (of the $\{110\}$ family). The vertical axis represents the potential energy, with the Peierls potential clearly marked. The dashed line represents the initial equilibrium line position.

At this stage, it is worth to introduce a note about the available slip systems (which establish the running indices of α. [50] have shown that in W an elementary glide on a $\{112\}$ plane is a composite of two elementary steps on alternate $\{110\}$ planes. Judging by these results, we conclude that glide on any given plane is achieved by way of sequential $\{110\}$ jumps, which constitutes the basis to simulate plastic yielding in the foregoing Sections. This is consistent with recent atomistic simulations [88] and experiments [97–100] and limits the number of available slip systems in our study to 12 (listed in Appendix A). We note that this model of slip for W is not necessarily suggestive of what may happen in other bcc crystals [101].

2.3.2. Projection tensor and non-Schmid effects

The tensor $\boldsymbol{P}_{\mathrm{S}}^{\alpha}$ introduced in eq. (10) represents the Schmid (geometric) projection of the strain rate contribution from a slip system defined by the plane normal $\boldsymbol{n}^\alpha$ and slip direction $\boldsymbol{m}^\alpha$ (both unit vectors). However, as pointed out above, $\boldsymbol{P}_{\mathrm{S}}^{\alpha}$ does not capture the full panoply of non-Schmid effects needed to calculate the value of the resolved shear stress on that slip system, τ^α. For this, we introduce a total projection tensor $\boldsymbol{P}_{\mathrm{tot}}^{\alpha}$ such that:

$$\tau^\alpha = \boldsymbol{P}_{\mathrm{tot}}^{\alpha} : \boldsymbol{\sigma} = \left(\boldsymbol{P}_{\mathrm{S}}^{\alpha} + \boldsymbol{P}_{\mathrm{T/AT}}^{\alpha} + \boldsymbol{P}_{\mathrm{ng}}^{\alpha}\right) : \boldsymbol{\sigma} \tag{16}$$

where

$$\boldsymbol{P}_{\mathrm{S}}^{\alpha} = \boldsymbol{m}^\alpha \otimes \boldsymbol{n}^\alpha \tag{17}$$

is the Schmid tensor, with

$$\boldsymbol{\sigma} = J^{-1}\boldsymbol{F}\boldsymbol{S}\boldsymbol{F}^T$$

the *Cauchy* (true) stress and $J = \det(\boldsymbol{F})$ the *Jacobian*. The tensors

$$\boldsymbol{P}^{\alpha}_{\mathrm{T/AT}} = a_1 \boldsymbol{m}^{\alpha} \otimes \boldsymbol{n}^{\alpha}_1 \tag{18}$$

$$\boldsymbol{P}^{\alpha}_{\mathrm{ng}} = a_2 \left(\boldsymbol{n}^{\alpha} \times \boldsymbol{m}^{\alpha}\right) \otimes \boldsymbol{n}^{\alpha} + a_3 \left(\boldsymbol{n}^{\alpha}_1 \times \boldsymbol{m}^{\alpha}\right) \otimes \boldsymbol{n}^{\alpha}_1 \tag{19}$$

are non-Schmid tensors representing respectively the twinning/anti-twinning asymmetry (T/AT) and the effects due to non-glide stress components. a_1, a_2, and a_3 are material-dependent constants that must also be calculated and added to our parameterization database. The vector $\boldsymbol{n}^{\alpha}_1$ forms an angle of -60° with the reference slip plane defined by $\boldsymbol{n}^{\alpha}$, and changes sign with the direction of slip on each glide plane [68].

The present non-Schmid formulation was originally developed by Vitek and expanded by others, and has been successfully used to propose yielding criteria adapted to finite element and crystal plasticity calculations in a number of cases [69; 102; 103]. The reader is referred to these works for more details but it is worth pointing out that the methodology that these authors have proposed is not unique, and that other rigorous implementations of non-Schmid effects could equally be devised. For the purposes of this section, suffice it to say that the particularities of the screw dislocation core and the bcc lattice structure result in deviations from a purely geometric projection. These deviations originate, respectively, from a geometric asymmetry between the twinning and anti-twinning directions of the $\langle 111 \rangle$ zone –from which a_1 is first calculated–, and from the effect that nonglide components (termed generically 'σ') of the local stress tensor have on the critical resolved shear stress, from which a_2 and a_3 are obtained. Atomistic calculations specifically designed to calculate the non-Schmid critical stress τ_c^{χ} as a function of the angle χ between the maximum resolved shear stress (MRSS) plane were performed according to the geometry shown schematically in Figure 3. The Figure shows the mapping between the atomistic box and the crystallography of the $[111]$ zone. Following the sign convention used in the Figure, the stress tensor applied is:

$$\begin{pmatrix} -\sigma & 0 & 0 \\ 0 & \sigma & \tau \\ 0 & \tau & 0 \end{pmatrix} \tag{20}$$

which activates axial (nonglide) stress components while maintainign zero pressure. τ_c^{χ} is expressed as a combination of the contributions displayed in Fig. 3:

$$\tau_c^{\chi} = \frac{\tau_c^{*} + \sigma \left(a_2 \sin(2\chi) + a_3 \sin\left(2\chi + \frac{\pi}{6}\right)\right)}{\cos\chi + a_1 \cos\left(\chi + \frac{\pi}{3}\right)} \tag{21}$$

where τ_c^{*} is a fitting constant that represents the Peierls stress. The details of these atomistic calculations are provided in Appendix B. The results for τ_c^{χ} are shown in Figure 4 as a function of χ and σ, with τ_c^{*}, a_1, a_2, and a_3 given in Table 1. It is worth noting that the relation between τ_c^{χ} and σ has been established for tensile nonglide stresses only ($\sigma > 0$), for consistency with the linear dependence used in the work of Vitek and collaborators [34; 35] that has been used in other crystal plasticity works [68]. However, nothing precludes the use of nonlinear fitting functions that capture both the tensile and compressive regimes simultaneously (cf. Appendix B). It is worth noting that [35] obtained values of $a_1 = 0$, $a_2 = 0.56$, and $a_3 = 0.75$ using a bond-order potential, substantially far from our values for those parameters.

By way of example, we calculate the maximum projection factor M for directions in the standard stereographic triangle using the fully parameterized projection tensor:

$$M = (\boldsymbol{l} \otimes \boldsymbol{l}) : \boldsymbol{P}_{\mathrm{tot}} = (\boldsymbol{l} \otimes \boldsymbol{l}) : (\boldsymbol{P}^{\alpha}_{\mathrm{S}} + \boldsymbol{P}^{\alpha}_{\mathrm{T/AT}} + \boldsymbol{P}^{\alpha}_{\mathrm{ng}}) \tag{22}$$

where $\boldsymbol{l}$ is the loading direction, which is obtained by visiting each of the nodes resulting from the discretization of the standard triangle area into a uniform grid consisting of 231 points. The results for tension ($\sigma > 0$) are shown in Figure 5. It is clear than non-Schmid effects –particularly the impact of nonglide components– are critical to calculate the RSS on a given slip system. We find that from a maximum nominal value of $M = 0.5$ for the standard Schmid law ($\boldsymbol{P}^{\mathrm{max}}_{\mathrm{S}}$) there is a twofold amplification when

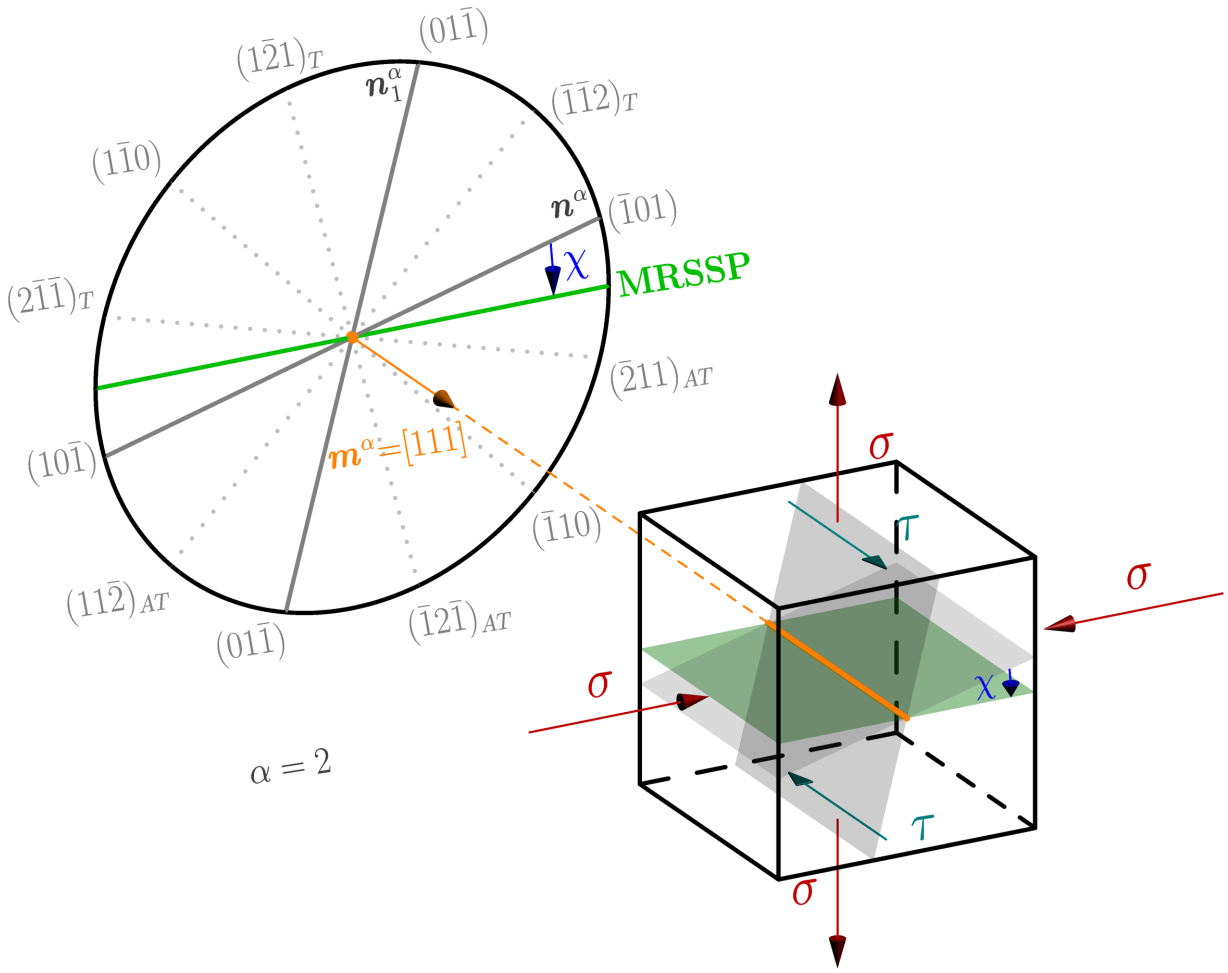

Figure 3: Crystallographic diagram of the [111] zone in the bcc lattice with each {110} and {112} clearly labeled. The picture also shows a mapping of the [111] zone to a schematic atomistic box containing a screw dislocation subjected to shear and nonglide stresses according to Vitek's convention. This setup is used to calculate the critical RSS using atomistic calculations (cf. Appendix B). The glide $\boldsymbol{n}^\alpha$, auxiliary ${\boldsymbol{n}_1}^\alpha$ and MRSS planes are labeled in each case. A $[\bar{1}01]$ glide plane corresponds to $\alpha = 2$ in our CP calculations.

the twinning/anti-twinning asymmetry is considered ($\boldsymbol{P}^{\max}_{\mathrm{S}} + \boldsymbol{P}^{\max}_{\mathrm{T/AT}}$), and an astonishing fourfold increase when nonglide effects are also included ($\boldsymbol{P}^{\max}_{\mathrm{S}} + \boldsymbol{P}^{\max}_{\mathrm{T/AT}} + \boldsymbol{P}^{\max}_{\mathrm{ng}}$). As we shall see in Section 3.2, this has extraordinary importance when comparing CP calculations to experimental measurements.

2.4. Dislocation density evolution model

To close the model, one needs to provide an evolution law for the dislocation density in Orowan's equation 11. There are numerous density evolution models proposed in the literature, each with a specific domain of applicability [61; 104–107]. In this work we are mainly interested in yielding, *i.e.* the elastic-to-plastic transition before dislocation-based slip takes on a dominant role in the constitutive model. We use the model presented by [108], in which the mobile dislocation density on slip system α evolves in time according to:

$$\dot{\rho}^\alpha = \dot{\rho}^\alpha_{\mathrm{mult}} + \dot{\rho}^\alpha_{\mathrm{ann}} \tag{23}$$

The evolution model is initialized by the dislocation density at $t = 0$, ρ^α_0. In eq. (23), $\dot{\rho}^\alpha_{\mathrm{mult}}$ and $\dot{\rho}^\alpha_{\mathrm{ann}}$ represent the dislocation multiplication and dislocation annihilation rate terms, respectively. In this model, both $\dot{\rho}^\alpha_{\mathrm{mult}}$

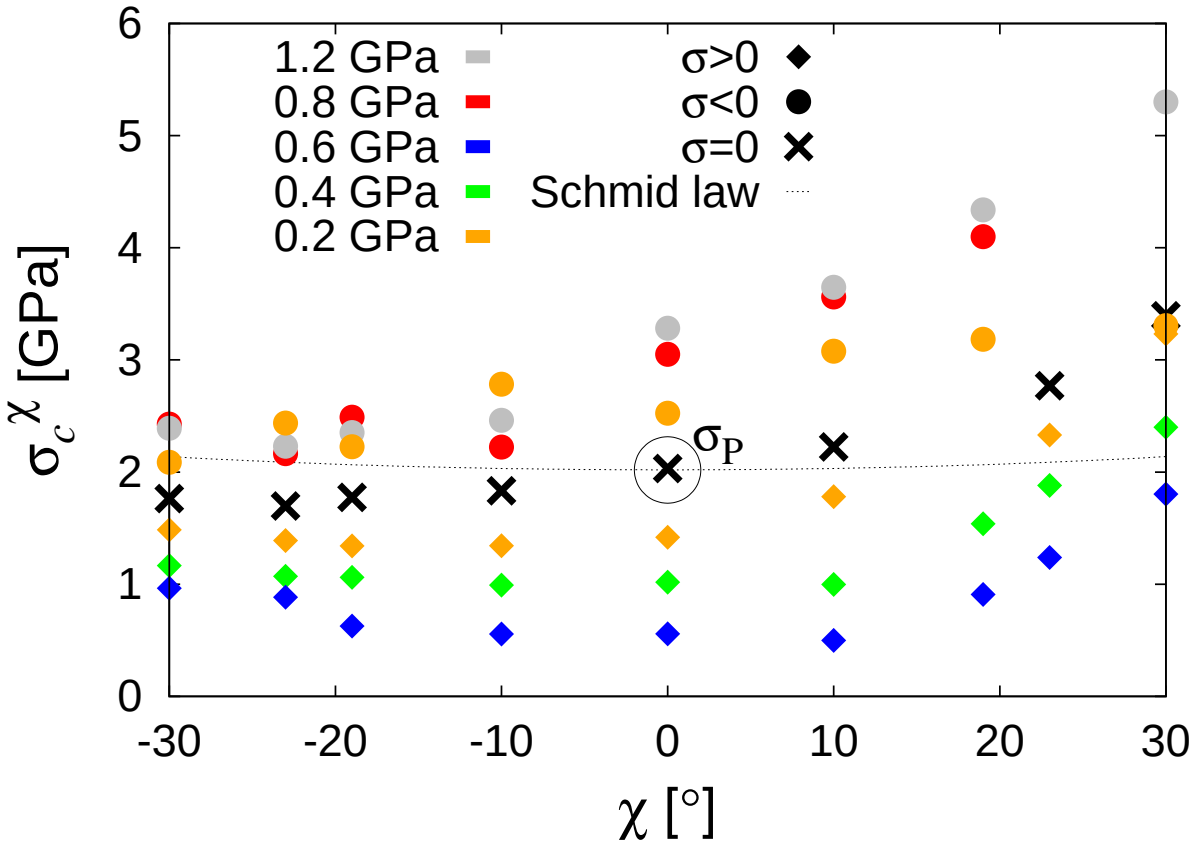

Figure 4: Critical resolved shear stress as a function of the angle χ between the MRSS and glide planes and the value of the nonglide stress component σ with the sign convention according to Fig. 3. The value of the Peierls stress $\sigma_P = 2.03$ GPa is circled.

and $\dot{\rho}^{\alpha}_{\text{ann}}$ are directly proportional to the plastic strain rate. Dislocation multiplication is treated as being proportional to the inverse mean free path of the dislocations, λ_{α}:

$$\dot{\rho}^{\alpha}_{\text{mult}} = \frac{|\dot{\gamma}^{\alpha}|}{b\lambda^{\alpha}} \tag{24}$$

which is defined as a function of the grain size d_g, the *forest* dislocation density ρ^{α}_f, and a hardening constant c:

$$\frac{1}{\lambda^{\alpha}} = \frac{1}{d_g} + \frac{\sqrt{\rho^{\alpha}_f}}{c} \tag{25}$$

Here, c and d_g are set, respectively, to one and to an arbitrarily high value such that the term controlling the dislocation mean free path is:

$$\lambda^{\alpha} \approx \left(\sqrt{\rho^{\alpha}_f}\right)^{-1}$$

The forest dislocation density is calculated as [79]:

$$\rho^{\alpha}_f = \sum_{\beta} \rho^{\beta} |\boldsymbol{n}^{\alpha} \cdot \boldsymbol{m}^{\beta}| \tag{26}$$

Note that, in general, the mean free path as defined in eq. (25) need not be equal to the effective dislocation segment length (in fact, it can be up to several orders of magnitude different [109]). However, our

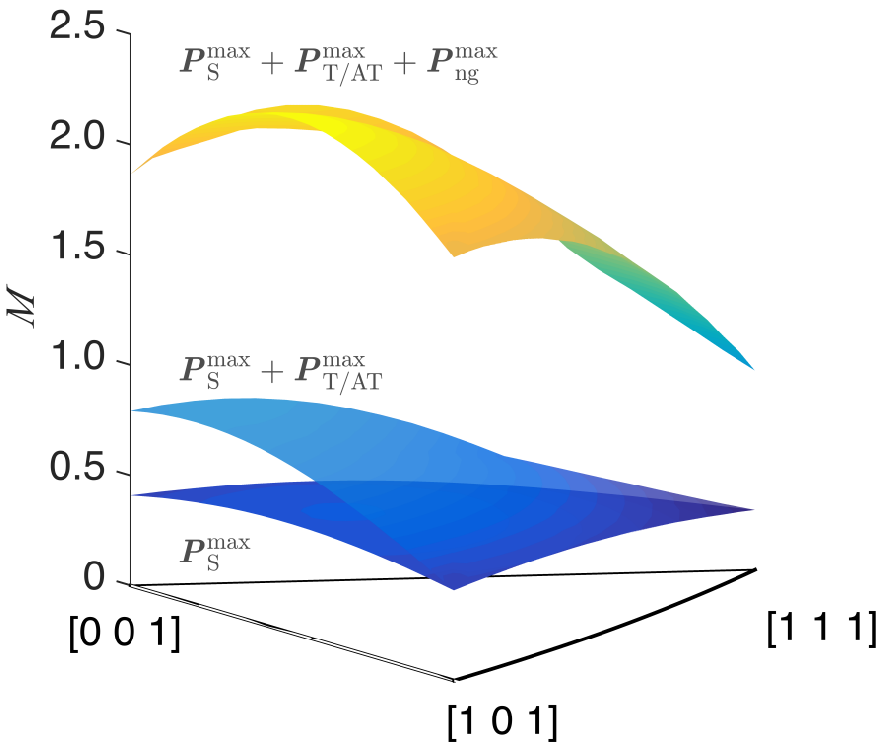

Figure 5: Projection factor according to eq. (22) for 231 directions within the standard triangle. The contributions of each of therms in eq. (16) are broken down for comparison.

model is designed with well-annealed, high-purity single W crystals in mind, with low initial dislocation densities and no impurities or obstacles other than dislocations themselves. Under this assumption, the use eq. (25) can be justified in this case [61; 91].

For its part, dislocation annihilation occurs spontaneously when dipoles approach to within a spacing of d_{edge}:

$$\dot{\rho}^{\alpha}_{\text{ann}} = -\frac{2d_{\text{edge}}}{b}\rho^{\alpha}|\dot{\gamma}^{\alpha}| \tag{27}$$

Equations (23) through (27) form the basis of the *Kocks-Mecking* family of dislocation density evolution models [104]. These models offer two interesting connections with the broader CP formulation employed here. First, a relation between the dislocation density evolution model and Section 2.3.1 is established by way of the dislocation mean free path λ^{α}, which determines the available segment length in the dislocation mobility function (eq. (15)). In this fashion, the dislocation velocity –and, through it, the plastic strain rate– is self-consistently linked to the microstructure changes predicted by the model. Second, by virtue of the existence of latent and self-hardening, the model provides a correction to the available RSS for dislocation motion in eq. (15) of the following form:

$$\tau'^{\alpha} = \tau^{\alpha} - \tau_h = \boldsymbol{P}^{\alpha}_{\text{tot}} : \boldsymbol{\sigma} - \mu b \sqrt{\sum_{\alpha'} \xi_{\alpha\alpha'}\rho^{\alpha'}} \tag{28}$$

where τ_h is the hardening stress and $\xi_{\alpha\alpha'}$ are the coefficients of the interaction matrix, which characterizes the interaction strength between slip systems α and α' as a result of six possible independent interactions [110; 111]: self, coplanar, collinear, mixed-asymmetrical junction (orthogonal), mixed-symmetrical junction (glissile) and edge junction (sessile) [112]. The values of $\xi_{\alpha\alpha'}$ employed here are given in Table 2, and were obtained from dislocation dynamics simulations of isotropic elastic bcc Fe under uniaxial deformation[4] [113]. The correspondence between each coefficient and each slip system considered in this work is given in Appendix A. τ'^{α} replaces τ^{α} in eqs. (12) to (15), although, as mentioned earlier, this pertains mainly to the plastic flow regime and –as such– is not expected to have a significant bearing on our calculations of σ_y.

Table 1: List of parameters and functional dependences for fitting the CP model. All of these parameters have been obtained using dedicated atomistic calculations. The parameter s represents the normalized shear stress: $s = \frac{\tau'^{\alpha}}{\sigma_P}$ (cf. eq. (28)).

parameter	value or function	units
a_0	3.143	Å
b	2.72	Å
h	$a_0\sqrt{6}/3$	Å
$\mathbb{C}_{11}$	523	GPa
$\mathbb{C}_{12}$	202	GPa
$\mathbb{C}_{44}$	161	GPa
ν_0	9.1×10^{11}	s^{-1}
σ_P	2.03	GPa
B	8.3×10^{-5}	Pa·s
$\Delta H(s;T)$	$\Delta H_0\,(1-s^p)^q$	eV
ΔH_0	1.63	eV
p	0.86	-
q	1.69	-
w	11	b
σ_c^{χ}	$\frac{\tau_c^* + \sigma(a_2\sin(2\chi) + a_3\sin(2\chi+\pi/6))}{\cos\chi + a_1\cos(\pi/3+\chi)}$	GPa
a_1	0.938	-
a_2	0.71	-
a_3	4.43	-
τ_c^*	2.92	GPa
c	1	-
d_g	2.72	Å
d_{edge}	2.72	Å

Table 2: Values of $\xi_{\alpha\alpha'}$ for latent hardening in bcc crystals (from [113]).

self	coplanar	collinear	orthogonal	glissile	sessile
0.009	0.009	0.72	0.05	0.09	0.06

[4] Although the $\xi_{\alpha\alpha'}$ coefficients were calculated for bcc Fe and not W, the results are equally applicable because Fe was treated as isotropic elastic –as is W– and the interaction matrix coefficients are non-dimensional and independent of the value of the plastic constants considered.

3. Results

In this Section we present results of uniaxial and biaxial tensile test simulations to explore the dependence of the yield strength on loading direction, temperature and strain rate. First, however, a robust and consistent yield criterion must be defined to extract the yield stress from the raw output data from DAMASK.

3.1. Yield criterion

In metals, where dislocation flow is not a singular event but a diffuse continuous process, it is generally accepted that the definition of yield point[5] is not unique. Perhaps as the result of these conceptual indetermination, modern usage has evolved into that of an arbitrary rule, the 0.2% strain offset rule for obtaining the yield stress of metals. For materials having nonlinear elastic behavior, there are not even arbitrary rules, only individual preferences and proclivities in defining yield when a given amount of strain has been reached. It is quite apparent then that to define robust yield criteria it is necessary that they be implemented and supported by consistent and meaningful definitions in terms of the stress-strain behavior. This is often difficult when the transition from the elastic to the inelastic regimes is obscured in the global picture of deformation. However, in the present calculations we effectively possess an arbitrary degree of data resolution and can define an unambiguous mathematical criterion.

The preferred method for defining the elastic limit of a ductile material is to compute the second derivative of the stress-strain curve, referred to generically as $\sigma(\varepsilon)$, and identify the location of the inflection point [114]. The yield point then corresponds to the strain, ε_y, for which $\left|\frac{d^2\sigma}{d\varepsilon^2}\right|$ is maximum. Mathematically:

$$\sigma_y = \sigma(\varepsilon_y),\ \varepsilon_y := \varepsilon \mid \max\left|\frac{d^2\sigma}{d\varepsilon^2}\right| \tag{29}$$

For ductile metals, the location of the maximum of the second derivative represents the point at which dislocation-mediated flow is the major contribution to $\boldsymbol{L}$ (cf. Section 2.1). However, this condition works surprisingly well for other materials such as glassy polymers, where flow might be caused by molecular rearrangement and damage at both the molecular and macroscopic scales [115].

To illustrate the accuracy of the second-derivative method, we plot in Figure 6 the first and second derivative of a stress-strain curve corresponding to a $[101]$ uniaxial tensile test of a W single crystal under representative initial conditions. Recall from Section 2.2 that the stress and strain metrics of choice are $\boldsymbol{P}$ and $\boldsymbol{B}$, and so we plot $\frac{dP_{zz}}{dB_{zz}}$ and $\frac{d^2P_{zz}}{dB_{zz}^2}$ specifically. The inflection point –marked by a vertical dashed line in the figure– occurs for $\varepsilon_y = 0.1105\%$, for which a value of $\sigma_y = 0.452$ GPa is obtained. The figure also shows the 0.2% strain offset criterion, which –by contrast– gives $\varepsilon_y = 0.3167\%$ and $\sigma_y = 0.479$ GPa, *i.e.* a threefold difference in strain and approximately a 6% difference in stress with respect to the stress second derivative criterion.

However, determining the first and second derivatives of the stress-strain relation can become numerically intensive, especially when evaluating thousands of curves as is the case in this work. An approximation to this method that works particularly well for linear-elastic materials that display a clear elastic-to-plastic transition is to take the yield point as the first point in the $\sigma(\varepsilon)$ function that satisfies:

$$\frac{d\sigma}{d\varepsilon} < E(1-\delta)$$

i.e. σ_y is measured as the stress for which a departure from linearity (as set by the elastic regime) larger than some small value δ is observed in the stress-strain relation. We have found that a value of $\delta \approx 0.01$ is sufficient to predict the value of σ_y within a small error relative to the value furnished by the second-derivative method. By way of example, for the curve shown in Fig. 6 and $\delta = 0.01$, we find a values of

[5] Also referred to as elastic limit, proportionality limit, yield stress, etc.

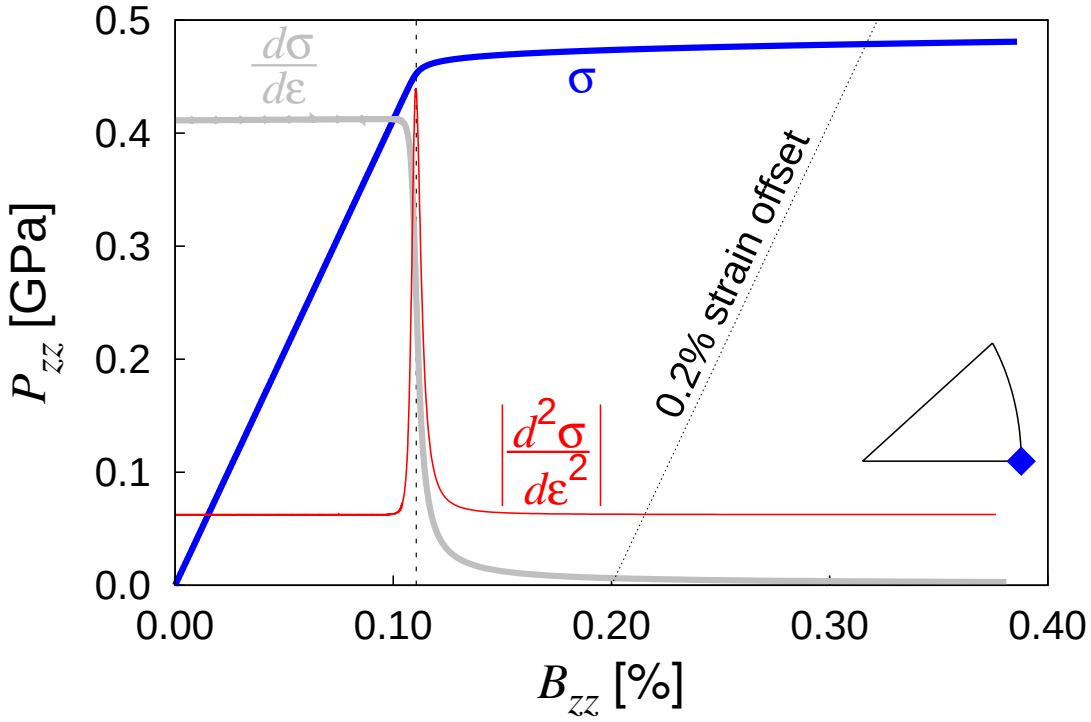

Figure 6: Evolution of the stress P_{zz} with deformation B_{zz} during a CP simulation of a uniaxial tensile test with $[101]$ loading orientation (as depicted in the standard triangle). The first and second derivatives of the stress w.r.t. to the strain are also plotted to illustrate the method of identification of the yield point according to this criterion. Also shown is the intercept of the curve with the 0.2% strain offset criterion line.

$\varepsilon_y = 0.1055\%$ and $\sigma_y = 0.435$ GPa, or less than a 4% difference with the numbers according to the second-derivative criterion. With this reasonable accuracy and the computational advantages alluded to above, we then use the $\delta = 0.01$ criterion in the remainder of this paper.

cite

3.2. Model validation and initial results

Prior to deploying our fully-parameterized CP method for numerically-intensive calculations, it is essential to undergo a thorough exercise of validation. Experimental data from uniaxial tensile tests in single crystal W at low strain rates are scant and sporadic, with the main sources listed below:

1. [116] performed some early experiments at a strain rate of 10^{-4} s^{-1} and temperatures of 77, 199, 293, 373, and 450 K. These authors measured the yield strength for the three vertices of the stereographic triangle $[001]$, $[110]$, and $[111]$ with an initial dislocation density of $\rho_0 \approx 10^{10}$ m^{-2}.
2. [117] analyzed the yielding behavior of arc-melted W between 77 and 680 K at $\dot{\varepsilon} = 8.3 \times 10^{-4}$ s^{-1}. However, the loading orientation is not given and most of the tests were done in compression.
3. [118] has carried out compression tests at 150, 300, and 590 K. This researcher focuses on dislocation density evolution and dislocation substructures, however, with a value of $\rho_0 \approx 1.4 \times 10^{14}$ m^{-2}, notably larger than in other tests. There have been other works that have also focused mainly on compression tests [119; 120].
4. [121; 122] has performed a series of experiments more recently at temperatures between 77 and 800 K. They employed a value of $\dot{\varepsilon} = 8.5 \times 10^{-4}$ s^{-1} and loaded the system uniaxially along the $[\bar{1}4\ 9]$ direction with a starting dislocation density of 5.5×10^9 m^{-2}.

As pointed out in Section 2.3.2, our CP model is parameterized for tensile tests only and so for validation we focus on the works by [116] and [121; 122]. [116] centered on multislip by considering mainly loading orientations coincident with the vertices of the standard triangle. Consequently, we replicate their test conditions in our CP model and compare the results obtained by taking into account all the different elements of the projection tensor (16). The results are shown in Figure 7 for the $[111]$ and the $[110]$ loading orientations, with the insets in both figures showing the relative importance of considering each of the non-Schmid contribution to the projection tensor incrementally. While our calculations are in general good agreement with the $[111]$ test data, they deviate from the experimental results at the two lower temperature points for the $[110]$ orientation. [116] point out that, at low temperatures, deformation by twinning may play a larger role when loading along $[110]$ relative to other orientations. This may be at the origin of the discrepancy, as twinning is not part of the catalog of deformation mechanisms considered in this model.

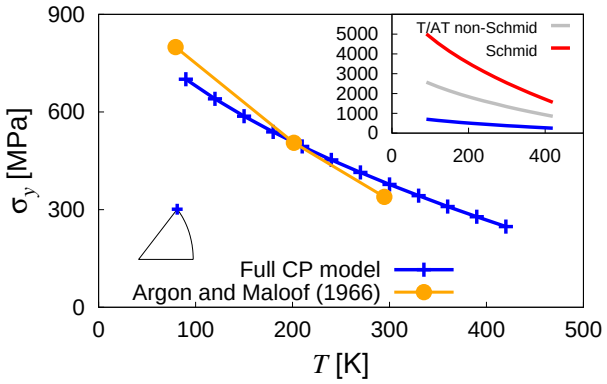

(a) [111] loading

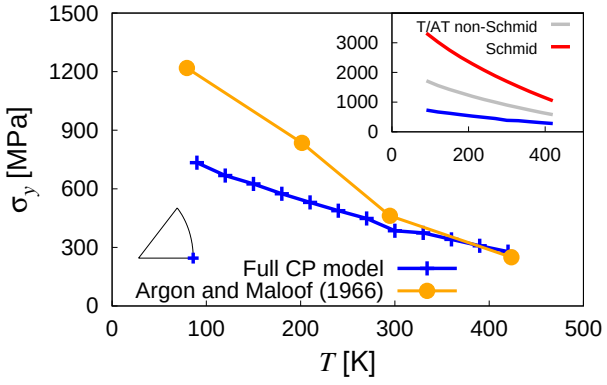

(b) [110] loading

Figure 7: Yield strength of W single crystals at the conditions used by [116] in tensile deformation tests under two different loading orientations. The experimental data is shown for comparison. The inset shows the results of CP calculations with different contributions of the projection tensor activated.

Next we simulate uniaxial tensile tests under single slip conditions, *i.e.* along crystal orientations near the center of the standard triangle. This corresponds to the experiments by [121; 122] referred to above, which were done more recently with more advanced instrumentation. The results are shown in Figure 8, where we also show the curves using the different elements of eq. (16). This time, the agreement is striking,

particularly again at temperatures above 400 K. Specifically, the *athermal* limit (≈ 710 K) is particularly well reproduced, as is the extrapolated critical stress at 0 K (Peierls stress), which is within 10% of the experimental values.

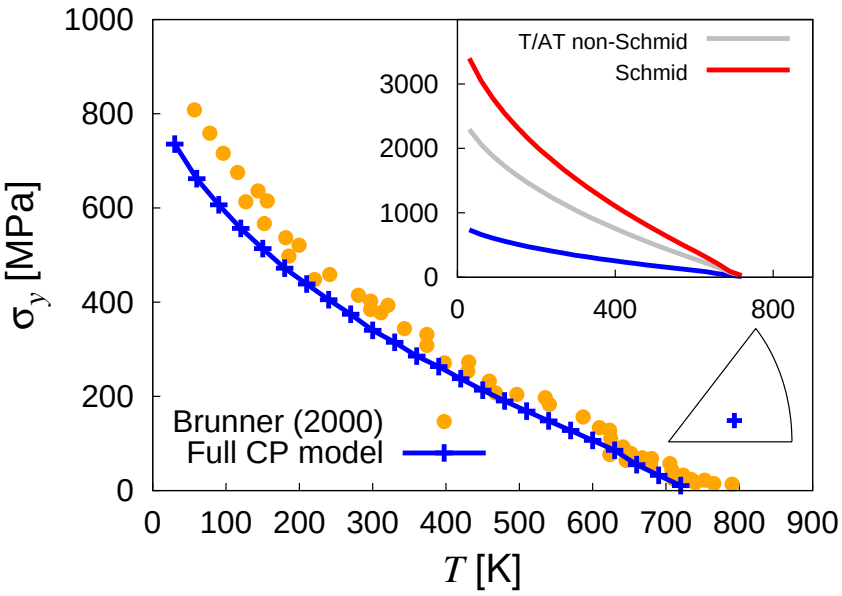

Figure 8: Yield strength of W single crystals under the conditions used by [122] in uniaxial tensile tests. The experimental data is shown for comparison. The inset shows the results of CP calculations with different contributions of the projection tensor activated.

Although, as noted earlier, the main focus of this work is on yielding, we have applied the fully parameterized model to study the flow stress regime for some selected cases in Appendix C. The results shown there demonstrate the performance of the method outside the primary range of application. While the model cannot be assumed to be predictive in the post-yield regime under general loading conditions, these are encouraging results that strengthen the notion that parameter-free CP calculations can perform well under specific deformation scenarios.

With the confidence conferred on our CP model by the validation procedure, next we proceed to calculate the yield strength for a number of numerically-intensive scenarios. This is the object of the following sections.

3.3. Uniaxial tensile tests

In this Section, we report on the uniaxial yielding results as a function of temperature and strain rate. Our results are organized by strain rate, such that we first provide a detailed account of all the calculations at a given strain rate followed by a study on the dependence with $\dot{\varepsilon}$.

3.3.1. Results at $\dot{\varepsilon} = 10^{-3}$ s^{-1}

For these calculations, we have discretized the area of the standard triangle into a uniform grid consisting of 231 nodes, each representing a crystallographic loading orientation. We begin with calculations at a prescribed strain rate of $\dot{\varepsilon} = 10^{-3}$ s^{-1}. Figure 9 shows colored contour plots of the yield stress in the 100-to-600 K temperature range. Areas of high relative yield strength can be seen to concentrate around the vertices of the standard triangle, representing multislip conditions, whereas soft regions develop in two distinct locations of the triangle, one near the $[324]$ zonal axis that then rotates towards $[112]$ above 500 K, and another near $[102]$. Note that, to accentuate the differences between hard and soft regions, each contour plot has its own specific numerical scale.

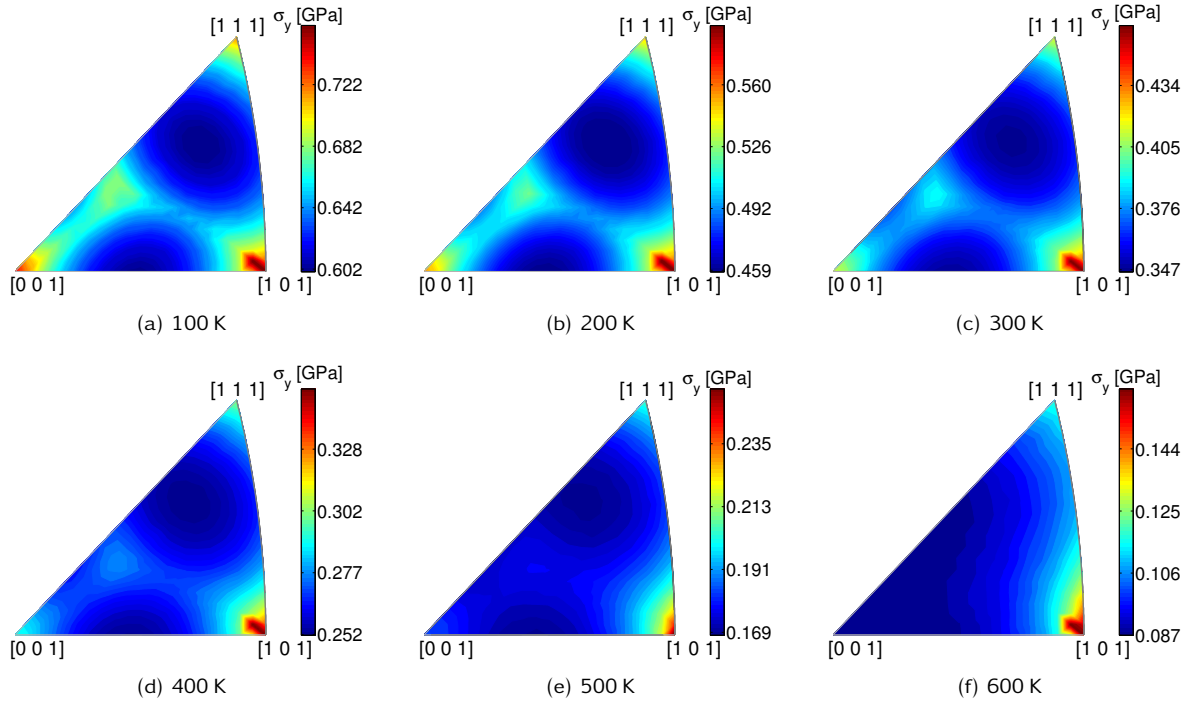

Figure 9: Contour maps of the yield strength from uniaxial tensile test simulations for 231 uniformly distributed crystallographic orientations in the standard triangle at different temperatures. Note that each map has its own distinct numerical scale to aid in the visualization of hard and soft regions.

We have extracted the specific location of the global extrema in the standard triangle and plot it as a function of temperature in Figure 10(a). The hardest direction is consistently the $[101]$, while the softest is seen to revolve around the vicinity of the $[112]$ axis, first along $[30\,18\,41]$ at 100 K, then along $[180\,131\,271]$ between 200 and 500 K, and finally rotating towards $[9\ 9\ 34]$ for $T > 500$ K. Next, we plot the detailed temperature dependence of the yield strength corresponding to the hardest and softest directions –as given by Fig. 10(a)– for this strain rate in Figure 11. As the calculated data show, there is approximately a 30% difference in yield stress between the hardest and softest directions. Interestingly, this gap appears to be fairly independent of temperature. Above 650 K, the curves begin to level off, signaling the onset of the athermal regime.

3.3.2. Dependence on strain rate and strain rate sensitivity

In this Section we expand the analysis presented in the previous Section to strain rates of 10^{-4} and $10^{-5}\ \mathrm{s}^{-1}$. To avoid redundancies, here we show only the temperature trajectory of the softest and hardest loading orientations in Figs. 10(b) and 10(c), which emanate from calculations as those presented in Fig. 9. The results are quantitative similar to the case of $\dot{\varepsilon} = 10^{-3}\ \mathrm{s}^{-1}$, with the only appreciable deviations occurring at temperatures above 450 K. At these high temperatures, the softest orientation rotates clearly towards the vicinity of the $[113]$ zonal axis, without excursions near $[103]$ as was the case for the $\dot{\varepsilon} = 10^{-3}$ calculations.

As above, we add the temperature dependence of the yield stress for the hardest and softest directions at these strain rates to Figure 11. The data show the same qualitative trend for all strain rates, with the same approximate 30% difference between the hard and soft orientations. However, useful information can be extracted if the strain-rate dependence of the yield stress is plotted for selected orientations. Then, one can calculate the so-called *strain rate sensitivity*, characterized by the strain rate sensitivity exponent m, of the material as a function of temperature. Strain rate sensitivity is exceedingly important to delay

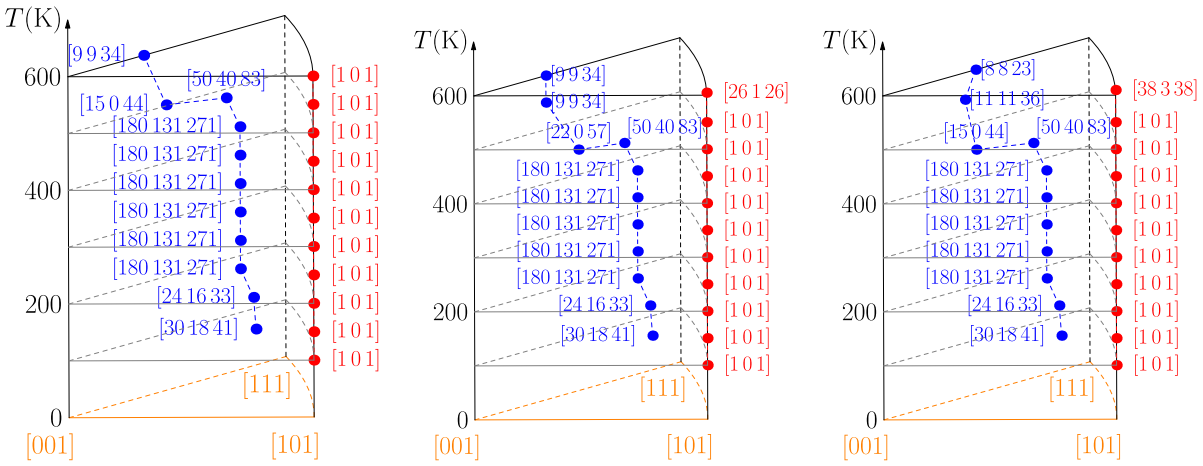

(a) $\dot{\varepsilon} = 10^{-3}$ s^{-1} (b) $\dot{\varepsilon} = 10^{-4}$ s^{-1} (c) $\dot{\varepsilon} = 10^{-5}$ s^{-1}

Figure 10: Temperature path of the softest and hardest yield directions on the standard triangle as a function of strain rate.

the onset of inhomogeneous deformation [123], *e.g.* necking, and is used as a criterion to assess the possibility of superplastic behavior in certain kinds of materials [124; 125]. This belongs more in the realm of failure and is thus outside the scope of this paper. However, it is of interest to calculate the strain rate sensitivity of the yield stress and relate our findings to the larger failure picture if possible.

This precisely what is done in Figure 12 for $[101]$ loading tests. The figure shows the variation of the yield strength at the three strain rates considered here, again in the range $100 < T < 600$ K. The data can then be fitted to the following expression:

$$\sigma_y = C\dot{\varepsilon}^m \tag{30}$$

where C is a fitting constant. The strain rate sensitivity exponent is formally defined as:

$$m = \frac{\partial \log \sigma_y}{\partial \log \dot{\varepsilon}} \tag{31}$$

m is plotted in the inset to Fig. 12, where it can be seen that it increases monotonically with temperature from a value of $m = 0.01$ at 100 K to ≈ 0.2 at 600 K. The implications of these results will be discussed in Section 4.

3.4. Biaxial loading tests and yield surfaces

For non-associated CP formulations such as the present one, yielding is not a separate and independent criterion, but a consequence of the constitutive law of the material behavior [126]. Indeed, with yielding defined on the basis of the identification criterion introduced in Section 3.1, yield surfaces are furnished as a product of the CP calculations. In this Section we calculate the yield curves under biaxial stress conditions for selected pairs of orthogonal loading directions $\boldsymbol{l}_y$ and $\boldsymbol{l}_z$. As noted in Section 2.3.2, the present implementation of the non-Schmid stress projection law is only valid for tensile conditions[6]. Thus, our yield curves are only meaningful in the positive stress quadrant (or octant, for yield surfaces). The procedure to calculate each point of the yield surface consists of deforming the system simultaneously along the prescribed orientations until the material yields on either one according to criterion (29). The stresses P_{zz} and P_{yy} are then measured along both directions and the resulting duplet is added to the curve. Plane stress conditions are adopted along the remaining direction, *i.e.* $P_{xx} = 0$. The calculations

[6] Although this is not a limitation in a strict sense as it is done simply for consistency with non-Schmid treatments published in the literature.

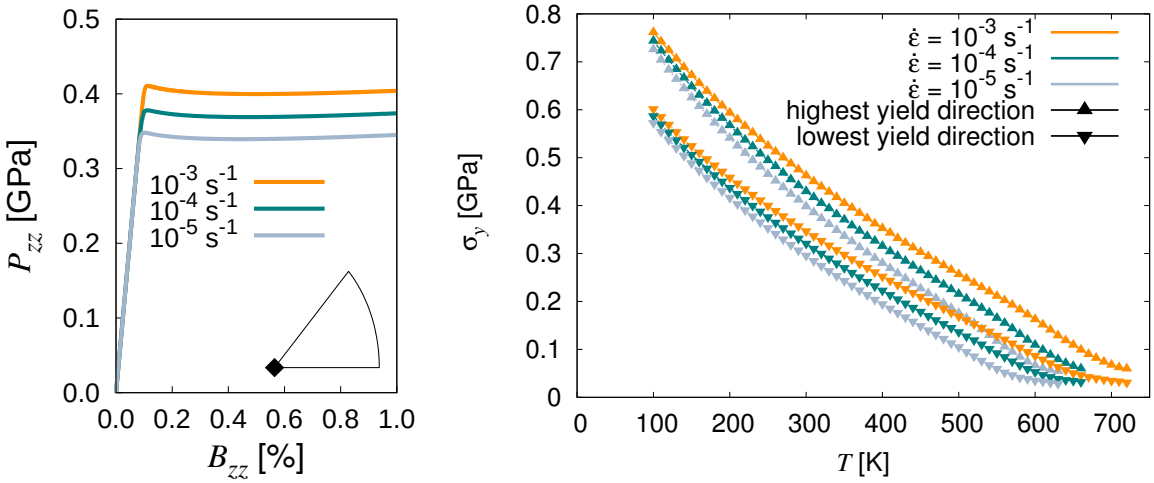

Figure 11: (a) Stress-strain relations at three different strain rates and $T = 300$ K for a $[0\,0\,1]$ loading orientation. (b) Temperature dependence of the yield strength for the softest and hardest directions as a function of strain rate.

are done at a nominal strain rate of $\dot{\varepsilon} = 10^{-4}$ s^{-1}, with slight variations above and below this value in one of the loading directions to accumulate different levels of stress and map the entire stress quadrant.

First we calculate the yield curve for $\boldsymbol{l}_y = [111]$ and $\boldsymbol{l}_z = [1\,1\,\bar{2}]$ as a function of temperature. Results are shown in Figure 13. The curves enclose domains that are everywhere convex, thus satisfying the *Drucker-Prager* criterion for stable plastic flow materials [127; 128]. The absolute values and the temperature sensitivity of the yield stresses for the end cases of $P_{zz} = 0$ and $P_{yy} = 0$ are consistent with the results shown in Section 3.3 for the $\boldsymbol{l}_y$ and $\boldsymbol{l}_z$ chosen here.

The next series of calculations involves determining the entire yield surface of the $[111]$ zone, *i.e.* for a set of directions orthogonal to $[111]$ in 10° intervals, at a fixed temperature of 300 K. Results are shown in Figure 14. Symmetry considerations limit the angular range to be explored to a 60° arc, which is shown in the figure. Yield surfaces such as this one are the culmination of crystal plasticity calculations, and can be used as constitutive input into continuum models to simulate effective mechanical behavior at the engineering scale, for component design and/or to simulate, *e.g.*, thermo-mechanical treatments [129; 130].

4. Discussion and conclusions

In this Section we consider the most important implications of our results. First, we discuss one of the most salient characteristic of the current work. The present CP model uses a standard rate-dependent, finite-deformation, non-associated theory of crystal plasticity. However, while the underlying kinematic formulation serves as the mathematical framework upon which to build a physical methodology, it is via the connection to the material physics that the model is rendered truly predictive. Our technique does so by incorporating the following three features of bcc slip:

- A complete (T/AT plus nonglide) treatment of non-Schmid effects.
- A kinematic flow rule based on a thermally-activated screw dislocation mobility.
- Using accurate interatomic potentials for computing all the free parameters in the model.

We have shown that the full model is capable of predicting the experimentally-measured temperature dependence of yield strength in the entire temperature range for W single crystals without parameter-fitting

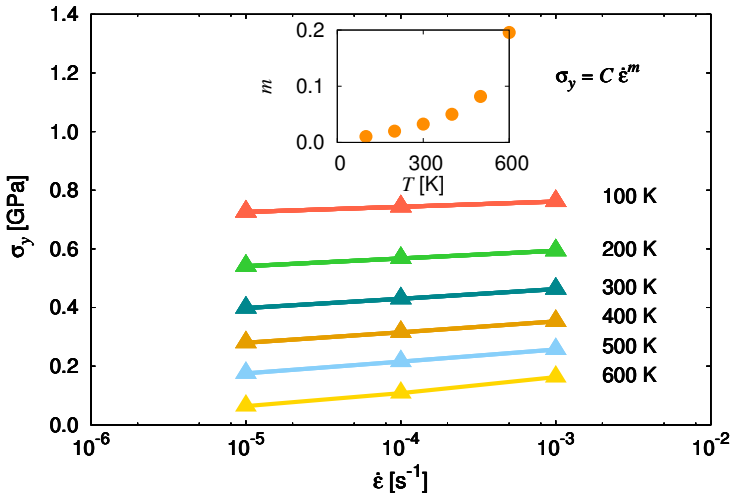

Figure 12: Dependence of yield strength with strain rate for loading along direction $[1\,0\,1]$ as a function of temperature. The inset represents the dependence of the strain rate sensitivity exponent m with temperature.

of any kind[7]. The sole source of material (constitutive) information is a carefully selected semi-empirical interatomic potential fitted exclusively to a DFT-generated dataset that includes the Peierls stress in its full atomistic meaning. This closes the gap seemingly separating electronic structure calculations of fundamental dislocation core properties and real measurements of the yield stress in uniaxial tensile tests of bcc materials.

Indeed, much effort has been devoted to the study of this long-standing experiment/simulation discrepancy, particularly at temperatures < 20 K. Explanations based on collective dislocation dynamics, such as network kinetics [131] and/or mutually interacting dislocations [132] can be more or less discounted in light of recent detailed electron microscopy experiments of isolated screw dislocation motion [97; 98; 133]. A more recent description, based on quantum effects at very low temperatures, has been put forward with reasonable success [78]. On this basis, our first partial conclusion is that, while the present calculations do not provide sufficient grounds to invalidate these theories, they do clearly demonstrate that *models based solely on classical mechanics –and without recourse to fitting to experimental results– can be formulated to predict the temperature dependence of the yield strength of bcc single crystals*. Evidently, we issue this conclusion with caution, as W does not constitute by itself a representative sample to convincingly claim generality, but we believe that it constitutes a step in that direction.

Another important physical aspect of tensile deformation in single bcc crystals is the seemingly distinct slip mechanisms operating in different temperature ranges. According to Seeger and collaborators, there are three clearly distinguishable temperature regions in the flow stress-temperature curves for bcc metals [16; 121; 134], namely, the so-called upper and lower *bend* temperatures, $\check{T}$ and $\hat{T}$, and the *knee* temperature T_k[8]. $\check{T}$, $\hat{T}$, and T_k delimit three different regimes where slip may occur on $\{110\}$, as well as $\{112\}$, glide planes, and give rise to different deformation mechanisms. Although these theories are substantiated by ample experimental data, there are recent studies that indicate that $\{110\}$ slip may be sufficient to explain the most salient features of bcc plasticity [99; 135]. This is consistent with the analysis presented here, backed by atomistic input, which suggests that only $\{110\}$ slip is admissible in bcc

[7] Of course, interatomic potentials –which form the basis of the constitutive information employed here– are subjected to a fair amount of fitting themselves, both to experimental data and first-principles calculations. However, potential fitting is extraneous to our work, in the sense that it was neither performed by us nor done with this application in mind, while the parameter fitting that we refer to here is dedicated specifically to reproduce experimental data of interest to the application of the model.

[8] T_k is understood as the temperature above which the contribution of the kink-pair formation mechanism to the flow stress becomes negligibly small, *i.e.* it signals the athermal limit.

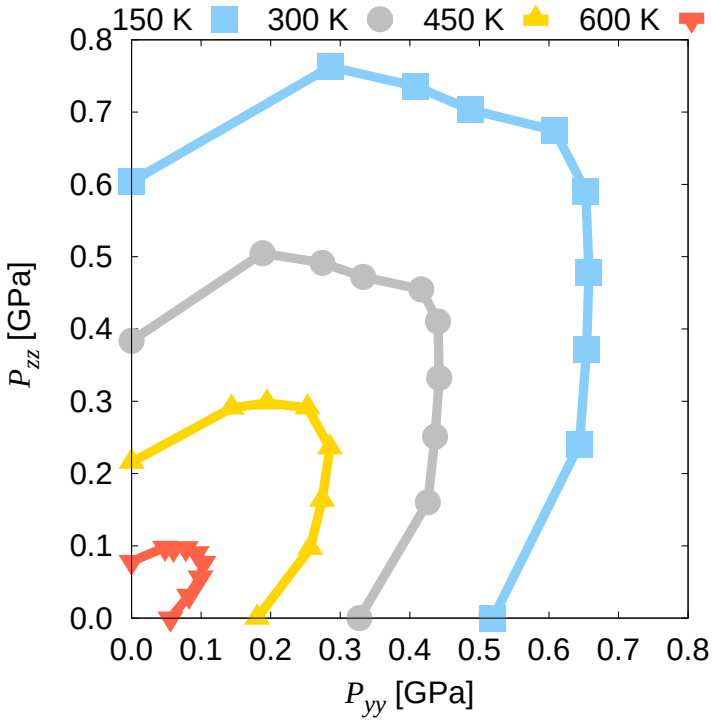

Figure 13: Yield curve for loading along directions $\boldsymbol{l}_y = [111]$ and $\boldsymbol{l}_z = [1\,1\,\bar{2}]$ as a function of temperature.

W. Interestingly, the screw dislocation mobility law employed in this work, where $\{112\}$ slip is disallowed by construction (cf. Section 2.3.1), is sufficient to quantitatively characterize the evolution of the yield stress across the entire temperature spectrum, without any *ad hoc* partition of mechanisms into different temperature regimes. We emphasize once more that the screw mobility law has been fitted exclusively to first-principles data.

In Section 3.3.2 we have provided calculations of the strain rate sensitivity defined as $m = \partial \log \sigma_y / \partial \log \dot{\varepsilon}$. It must be noted that our value of $m = 0.023$ at 300 K obtained in the $10^{-3} > \dot{\varepsilon} > 10^{-5}$ s^{-1} range is consistent with measurements performed by [136] in W compressed uniaxially at strain rates from 10^{-3} to 10^{3} s^{-1}. Notwithstanding the differences in experimental methodology and strain rate regime, this is also encouraging agreement for a result other than yield. m is an important parameter for calculating the kink-pair activation enthalpy and activation volume from stress-relaxation tests. Note that some authors use an alternative definition for the strain rate sensitivity [117; 121], namely, $\lambda = \partial \sigma / \partial \log \dot{\varepsilon}$, which is related to m via $\lambda = m\sigma$. We can then conclude that *the agreement achieved for a derivative quantity of the yield stress such as m is symptomatic of the quality of the method outside the primary validation space.*

The advantages of this and other CP methodologies w.r.t. more accurate techniques such as molecular dynamics, dislocation dynamics, or phase field methods is of course their computational expediency. Backed by the encouraging outcome of the validation exercise, this has enabled us to map the entire loading orientation space in the standard triangle (231 directions) as a function of temperature in a experimentally-meaningful strain rate range. These results can then be used to extract useful information, such as the strongest and softest orientations as a function of temperature and strain rate, or the strain rate sensitivity of our W model system. This information can ultimately be used to define yield criteria under a variety of conditions for more homogenized methods, with the aim put on component design.

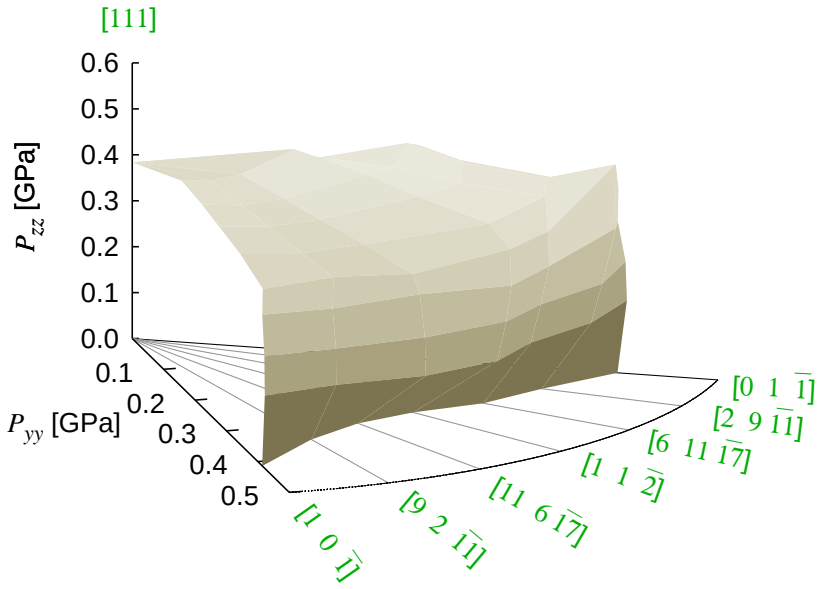

Figure 14: Yield surface at 300 K for biaxial loading along directions belonging to the $[111]$ zone. By symmetry, only the 60°-arc need be explored.

In this sense, the culmination of the CP simulations is the calculation of yield curves and yield surfaces in stress space. The stress space that we have chosen for our yield surface calculations is a purely biaxial one (in plane stress) with one fixed direction, chosen arbitrarily to be $[111]$, and the family of orthogonal directions taken in 10° intervals. This biaxial loading configuration is the elementary basis for pressurized cylinders, *e.g.* pipes, and is thus useful to design components based on this geometry. As well, it can serve as the design premise for loaded plates under plane stress conditions. It is of interest to note that yield surfaces can also serve as the plastic potential in the fundamental theory of plasticity [80]. This equivalence is valid when the critical resolved shear stress is not dependent on the current stress state[9] [80; 137]. However, this may not be applicable in the present model, where the CRSS is seen to display a strong dependence on hydrostatic (nonglide) stress components as discussed in Section 2.3.2. This is also the case in rock and soil plasticity (*e.g.* [138]). In such cases, the normality rule is referred to the pressure-dependent yield surface instead.

A standing limitation of our model is that we have only made use of the tensile region of the dependence of the critical stress τ_c^χ with the nonglide stress σ (cf. eq. (21)). Of course, this dependence is essential to characterize the tension/compression asymmetry customarily observed in bcc crystals, cf. Section 1. However, this is only a weak limitation, as the present CP formulation is sufficiently flexible to admit a full (nonlinear) fit to the data shown in Fig. 4. Finally, we emphasize that the present study focuses on plastic yielding, and consequently, we have not explored the evolution of the flow stress much beyond the extent needed to define a robust yield criterion (cf. Section 3.1). However, this does not detract from the validity of the dislocation density evolution model presented in Section 2.4, which has been used prolifically in many CP studies (cf. Section 1), and which is being investigated in ongoing studies.

This work was performed under the auspices of the U.S. Department of Energy by Lawrence Livermore National Laboratory under Contract No. DE-AC52-07NA27344. J. M. acknowledges support from DOE's

[9] Particularly on non-deviatoric components.

Early Career Research Program. D. C. acknowledges support from the Consejo Social and the PhD program of the Universidad Politécnica de Madrid. The authors are indebted to Dr. M. Victoria for inspiration, encouragement, and guidance throughout this work.

Appendix A. $\{110\}\langle 111\rangle$ slip systems and latent hardening matrix considered for bcc W.

Table A.3: Slip systems considered in our calculations, listing the non-normalized crystallographic vectors $\boldsymbol{m}^\alpha$,$\boldsymbol{n}^\alpha$ and $\boldsymbol{n}_1^\alpha$. Note that in DAMASK each slip system is taken both in its positive and negative sense, which is equivalent to formulations where 24 positive slip systems are employed [35].

α	Reference system	$\boldsymbol{m}^\alpha$	$\boldsymbol{n}^\alpha$	$\boldsymbol{n}_1^\alpha$
1	$[1\bar{1}1]\,(011)$	$[1\bar{1}1]$	$[011]$	$[\bar{1}01]$
2	$[\bar{1}\bar{1}1]\,(011)$	$[\bar{1}\bar{1}1]$	$[011]$	$[\bar{1}\bar{1}0]$
3	$[111]\,(0\bar{1}1)$	$[111]$	$[0\bar{1}1]$	$[1\bar{1}0]$
4	$[\bar{1}11]\,(0\bar{1}1)$	$[\bar{1}11]$	$[0\bar{1}1]$	$[101]$
5	$[\bar{1}11]\,(101)$	$[\bar{1}11]$	$[101]$	$[110]$
6	$[\bar{1}\bar{1}1]\,(101)$	$[\bar{1}\bar{1}1]$	$[101]$	$[011]$
7	$[111]\,(\bar{1}01)$	$[111]$	$[\bar{1}01]$	$[0\bar{1}1]$
8	$[1\bar{1}1]\,(\bar{1}01)$	$[1\bar{1}1]$	$[\bar{1}01]$	$[\bar{1}\bar{1}0]$
9	$[\bar{1}11]\,(110)$	$[\bar{1}11]$	$[110]$	$[01\bar{1}]$
10	$[\bar{1}11]\,(110)$	$[\bar{1}11]$	$[110]$	$[10\bar{1}]$
11	$[111]\,(\bar{1}10)$	$[111]$	$[\bar{1}10]$	$[\bar{1}01]$
12	$[11\bar{1}]\,(\bar{1}10)$	$[11\bar{1}]$	$[\bar{1}10]$	$[011]$

Table A.4: Interaction coefficients $\xi_{\alpha\alpha'}$ for the 12 slip systems defined in Table A.3. The letter coding employed is 'A': self; 'CP': coplanar; 'CL': collinear; 'O': orthogonal; 'G': glissile; 'S': sessile. The reader is referred to Table 1 for the numerical value of each coefficient.

α	1	2	3	4	5	6	7	8	9	10	11	12
1	A											
2	CP	A										
3	S	S	A									
4	S	S	CP	A								
5	G	O	O	CL	A							
6	O	CL	G	O	CP	A						
7	O	G	CL	O	S	S	A					
8	CL	O	O	G	S	S	CP	A				
9	O	G	O	CL	CL	O	G	O	A			
10	CL	O	G	O	O	G	O	CL	CP	A		
11	G	O	CL	O	G	O	CL	O	S	S	S	
12	O	CL	O	G	O	CL	O	G	S	S	CP	A

Appendix B. Details on the atomistic calculations of non-Schmid parameters

Critical stresses are computed by applying shear stresses incrementally to a simulation box containing a screw dislocation lying on a glide plane forming an angle χ with the MRSS plane. The system is schematically shown in Fig. 3. The box dimensions vary slightly with orientation, such that, for $\chi = 0$, the box contains 3024 atoms and the dimensions are $21a \times 24b \times 1c$, where a, b, and c are the moduli of the bcc lattice vectors $x \equiv [\bar{1}21]$, $y \equiv [\bar{1}01]$, and $z \equiv [111]$, respectively. The calculations are performed using the *nudged elastic band* (NEB) method [139] implemented in the parallel molecular dynamics code LAMMPS [140]. Periodic boundary conditions are applied along the dislocation line direction z while non-periodic and shrink-wrapped boundary conditions are applied along the y and x directions. The transition path selected for the NEB calculations is a linear trajectory along the reaction coordinate joining two consecutive Peierls valleys, where the dislocation is relaxed to equilibrium.

Three different forces are applied to different groups of atoms in the simulation box in order to calculate σ_χ^c. These forces recreate the stress tensor (20) in the simulation box:

1. First, an external force f_z is added to the atoms on the boundary surfaces of the simulation box perpendicular to the y-axis to study the T-AT asymmetry. The external force per atom is $f_z = \frac{\tau L_x L_z}{N_z}$, where τ is the desired shear stress, N_z is the number of atoms in each nonperiodic surface along z and $L_x L_z$ is the cross-sectional area of the each of the bounding surfaces along to y.
2. To study the contribution from nonglide stresses, an external force f_x is added to the atoms on the boundaries of the simulation box perpendicular to the x-axis. The external force per atom is obtained as $f_x = \frac{\sigma L_y L_z}{N_x}$, where σ is the applied nonglide stress, N_x is the number of atoms in each surface and $L_y L_z$ is the cross-sectional area of the each of the surfaces along x.
3. Further, an external force f_y is added to the atoms on the surfaces along the y direction, additionally to the shear stress τ. f_y is defined as $f_y = \frac{\sigma L_x L_z}{N_y}$, with $N_y = N_z$ and $L_x L_z$ is the area of the each of the surfaces perpendicular to z.

31 intermediate replicas are used in the NEB calculations to capture the trajectory and measure the critical stress.

cite

Appendix C. Crystal plasticity calculations of flow stress dependence with orientation and temperature

To demonstrate the performance of the model in the flow stress regime, we carry out calculations for a few selected orientations and temperatures up to 10% strain. Figure C.15 shows the stress-strain response at a strain rate of 10^{-3} s^{-1} as a function of temperature for the [001] loading orientation. This is an orientation conducive to multi-slip and thus the system is expected to harden in accordance with eqs. (9), (10), and (28) as the deformation progresses. The figure shows results for the full non-Schmid model. For general viscoplastic materials it is common to represent the σ-ε relation as a power law of the type:

$$\sigma = K\varepsilon^n \tag{C.1}$$

where K is a constant and n is the so-called *hardening exponent*. Accordingly, the hardening rate can be expressed as:

$$\frac{d\sigma}{d\varepsilon} = Kn\varepsilon^{n-1} \tag{C.2}$$

Fits of eq. (C.1) to the data in Fig. C.15 yield values of $n = 0.82$, 0.86, and 0.87 for $T = 200$, 400, and 600 K, respectively. From eq. (C.2), these numbers result in hardening rates of $\frac{d\sigma}{d\varepsilon} \approx 20$ MPa/% in all cases.

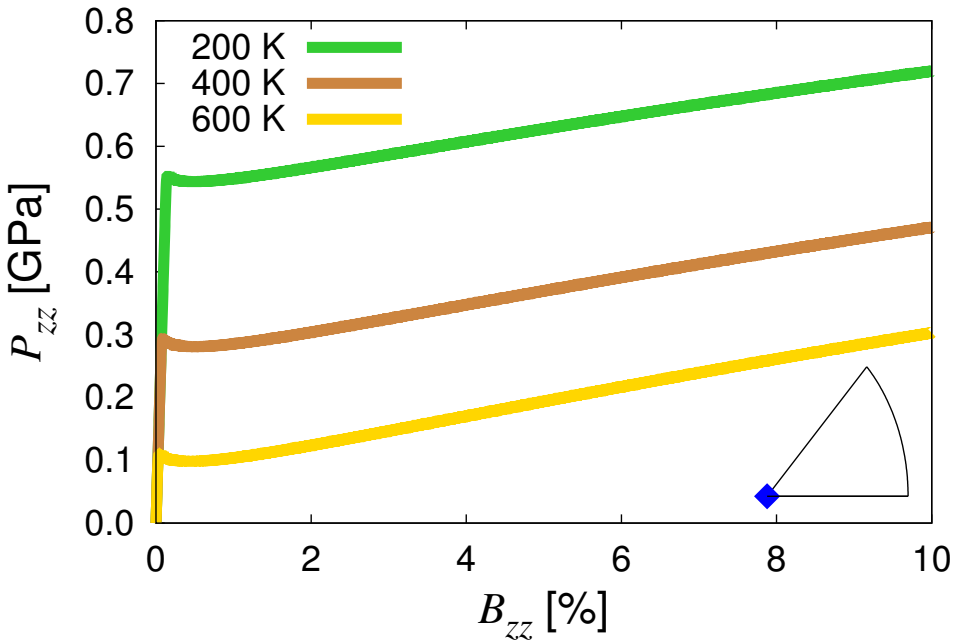

Figure C.15: Stress-strain curves for uniaxial loading along the [001] orientation at a strain rate of 10^{-3} s^{-1} for three different temperatures. These curves are representative of multi-slip conditions where Taylor-type hardening is enabled.

Next, we compare the model against the experimental results of [116] for [111] and [110] loading at $\dot{\varepsilon} = 10^{-4}$ s^{-1}. To avoid comparing in conditions where twinning may be operative (< 200 K), which is not captured by our model, we carry out simulations at 293 K. The results are shown in Figure C.16, which reveals a good agreement between the full non-Schmid model and the experimental data in the [111] loading case. According to [116], yielding under [110] loading occurs at approximately 460 MPa, which is

immediately followed by an abrupt hardening stage that plateaus at $\varepsilon \approx 0.8$ % to a value of ≈ 760 MPa. Whether or not this is the case, this initial hardening period is not captured by our model. Under both loading conditions, however, the model is seen to reproduce the hardening rates in close agreement with the experimental data.

We emphasize that the results shown in Fig. C.16 have been obtained without fitting to experimental (or otherwise) stress-strain curves of any kind, and so the model appears to capture the essential features of plastic flow for the selected conditions showcased here. As noted earlier, these preliminary results do not imply that the model is suitable for calculating the flow stress under general loading conditions.

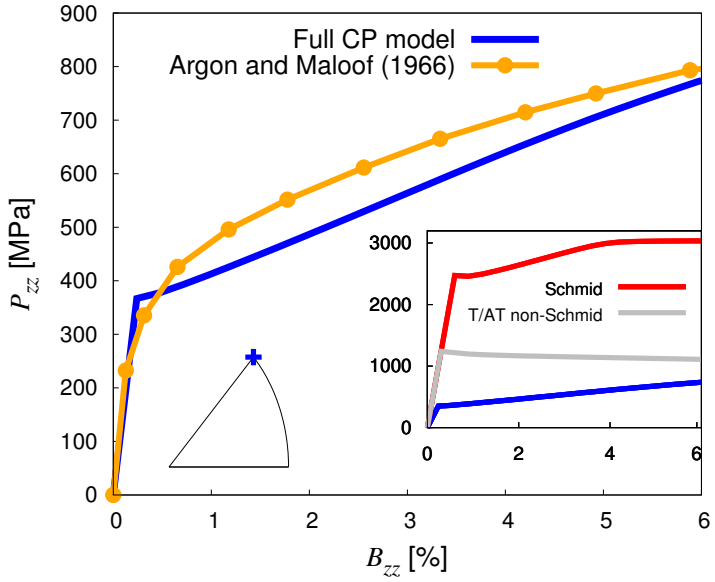

(a) [111] loading

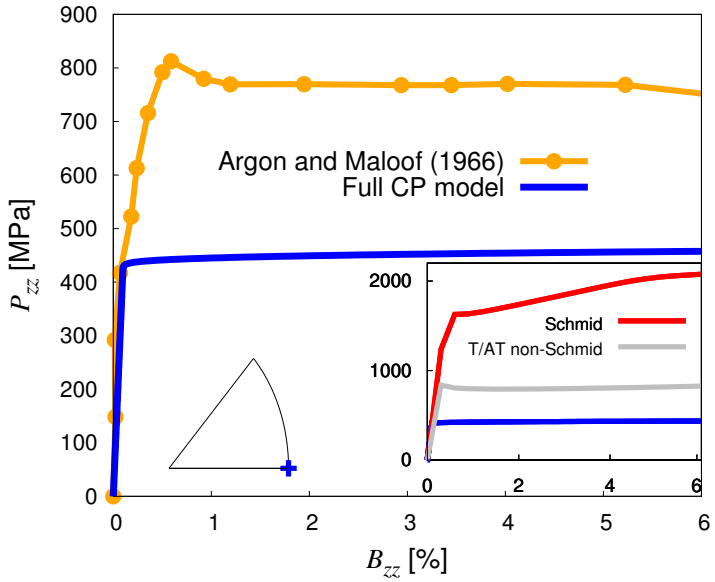

(b) [110] loading

Figure C.16: Flow stress of W single crystals at the conditions used by [116] (cf. Section 3.2) in tensile deformation tests under two different loading orientations. The experimental data is shown for comparison. The inset shows the results of CP calculations with different contributions of the projection tensor activated.

References

[1] V. Vitek, Core structure of screw dislocations in body-centred cubic metals: relation to symmetry and interatomic bonding, Philosophical Magazine 84 (3-5) (2004) 415–428.

[2] S. Wurster, B. Gludovatz, R. Pippan, High temperature fracture experiments on tungsten–rhenium alloys, International Journal of Refractory Metals and Hard Materials 28 (6) (2010) 692–697.

[3] H. Li, S. Wurster, C. Motz, L. Romaner, C. Ambrosch-Draxl, R. Pippan, Dislocation-core symmetry and slip planes in tungsten alloys: Ab initio calculations and microcantilever bending experiments, Acta Materialia 60 (2) (2012) 748–758.

[4] G. D. Samolyuk, Y. Osetsky, R. Stoller, The influence of transition metal solutes on the dislocation core structure and values of the peierls stress and barrier in tungsten, Journal of Physics: Condensed Matter 25 (2) (2013) 025403.

[5] L. Romaner, C. Ambrosch-Draxl, R. Pippan, Effect of rhenium on the dislocation core structure in tungsten, Physical review letters 104 (19) (2010) 195503.

[6] E. Schmid, W. Boas, Kristallplastizität: mit besonderer Berücksichtigung der Metalle, Vol. 17, J. Springer, 1935.

[7] V. Bulatov, O. Richmond, M. Glazov, An atomistic dislocation mechanism of pressure-dependent plastic flow in aluminum, Acta materialia 47 (12) (1999) 3507–3514.

[8] S. Brinckmann, J.-Y. Kim, J. R. Greer, Fundamental differences in mechanical behavior between two types of crystals at the nanoscale, Physical review letters 100 (15) (2008) 155502.

[9] C. Woodward, S. Rao, Ab-initio simulation of isolated screw dislocations in bcc mo and ta, Philosophical Magazine A 81 (5) (2001) 1305–1316.

[10] J. Chaussidon, M. Fivel, D. Rodney, The glide of screw dislocations in bcc fe: Atomistic static and dynamic simulations, Acta materialia 54 (13) (2006) 3407–3416.

[11] R. Gröger, V. Vitek, Breakdown of the schmid law in bcc molybdenum related to the effect of shear stress perpendicular to the slip direction, in: Materials Science Forum, Vol. 482, Trans Tech Publ, 2005, pp. 123–126.

[12] S. Takeuchi, E. Furubayashi, T. Taoka, Orientation dependence of yield stress in 4.4% silicon iron single crystals, Acta metallurgica 15 (7) (1967) 1179–1191.

[13] D. Hull, J. Byron, F. Noble, Orientation dependence of yield in body-centered cubic metals, Canadian Journal of Physics 45 (2) (1967) 1091–1099.

[14] M. Duesbery, The influence of core structure on dislocation mobility, Philosophical Magazine 19 (159) (1969) 501–526.

[15] M. Duesbery, R. Foxall, A detailed study of the deformation of high purity niobium single crystals, Philosophical Magazine 20 (166) (1969) 719–751.

[16] A. Seeger, The temperature and strain-rate dependence of the flow stress of body-centred cubic metals: A theory based on kink–kink interactions, Zeitschrift fur Metallkunde 72 (6) (1981) 369–380.

[17] F. Ackermann, H. Mughrabi, A. Seeger, Temperature-and strain-rate dependence of the flow stress of ultrapure niobium single crystals in cyclic deformation, Acta metallurgica 31 (9) (1983) 1353–1366.

[18] G. Taylor, Thermally-activated deformation of bcc metals and alloys, Progress in materials science 36 (1992) 29–61.

[19] P. Gordon, T. Neeraj, Y. Li, J. Li, Screw dislocation mobility in bcc metals: the role of the compact core on double-kink nucleation, Modelling and Simulation in Materials Science and Engineering 18 (8) (2010) 085008.

[20] L. Yang, P. Söderlind, J. A. Moriarty, Accurate atomistic simulation of (a/2)< 111> screw dislocations and other defects in bcc tantalum, Philosophical Magazine A 81 (5) (2001) 1355–1385.

[21] V. Vitek, M. Yamaguchi, Core structure of nonscrew 1/2 (111) dislocations on (110) planes in bcc crystals. ii. peierls stress and the effect of an external shear stress on the cores, Journal of Physics F: Metal Physics 3 (3) (1973) 537.

[22] G. Taylor, The deformation of crystals of β-brass, Proceedings of the Royal Society of London. Series A 118 (779) (1928) 1–24.

[23] G. Taylor, The mechanism of plastic deformation of crystals. part ii. comparison with observations, Proceedings of the Royal Society of London. Series A, Containing Papers of a Mathematical and Physical Character (1934) 388–404.

[24] G. I. Taylor, The mechanism of plastic deformation of crystals. part i. theoretical, Proceedings of the Royal Society of London. Series A, Containing Papers of a Mathematical and Physical Character (1934) 362–387.

[25] B. Šesták, N. Zárubová, Asymmetry of slip in fe-si alloy single crystals, physica status solidi (b) 10 (1) (1965) 239–250.

[26] P. Sherwood, F. Guiu, H.-C. Kim, P. L. Pratt, Plastic anisotropy of tantalum, niobium, and molybdenum, Canadian Journal of Physics 45 (2) (1967) 1075–1089.

[27] S. Zwiesele, J. Diehl, Temperature and strain rate dependence of the macro-yield stress of high-purity iron single crystals, Strength of Metals and Alloys, 1 (1979) 59–64.

[28] J. Christian, Some surprising features of the plastic deformation of body-centered cubic metals and alloys, Metallurgical Transactions A 14 (7) (1983) 1237–1256.

[29] W. Pichl, Slip geometry and plastic anisotropy of body-centered cubic metals, physica status solidi (a) 189 (1) (2002) 5–25.

[30] B. Escaig, Le Journal de Physique Colloques 29 (225).

[31] B. Escaig, Dissociation and mechanical properties. dislocation splitting and the plastic glide process in crystals, Le Journal de Physique Colloques 35 (C7) (1974) C7–151.

[32] M. a.-S. Duesbery, V. Vitek, Plastic anisotropy in bcc transition metals, Acta Materialia 46 (5) (1998) 1481–1492.

[33] K. Ito, V. Vitek, Atomistic study of non-schmid effects in the plastic yielding of bcc metals, Philosophical Magazine A 81 (5) (2001) 1387–1407.

[34] R. Gröger, A. Bailey, V. Vitek, Multiscale modeling of plastic deformation of molybdenum and tungsten: I. atomistic studies of the core structure and glide of $1/2\langle 1\,1\,1\rangle$ screw dislocations at 0k, Acta Materialia 56 (19) (2008) 5401–5411.

[35] R. Gröger, V. Racherla, J. Bassani, V. Vitek, Multiscale modeling of plastic deformation of molybdenum and tungsten: Ii. yield criterion for single crystals based on atomistic studies of glide of $1/2\langle 1\,1\,1\rangle$ screw dislocations, Acta Materialia 56 (19) (2008) 5412–5425.

[36] S. C. Soare, Plasticity and non-schmid effects, Proceedings of the Royal Society A: Mathematical, Physical and Engineering Science 470 (2161) (2014) 20130440.
[37] L. Ventelon, F. Willaime, Core structure and peierls potential of screw dislocations in α-fe from first principles: cluster versus dipole approaches, Journal of Computer-Aided Materials Design 14 (1) (2007) 85–94.
[38] L. Ventelon, F. Willaime, E. Clouet, D. Rodney, Ab initio investigation of the peierls potential of screw dislocations in bcc fe and w, Acta Materialia 61 (11) (2013) 3973–3985.
[39] C. R. Weinberger, G. J. Tucker, S. M. Foiles, Peierls potential of screw dislocations in bcc transition metals: Predictions from density functional theory, Physical Review B 87 (5) (2013) 054114.
[40] L. Dezerald, L. Ventelon, E. Clouet, C. Denoual, D. Rodney, F. Willaime, Ab initio modeling of the two-dimensional energy landscape of screw dislocations in bcc transition metals, Physical Review B 89 (2) (2014) 024104.
[41] L. Dezerald, L. Proville, L. Ventelon, F. Willaime, D. Rodney, First-principles prediction of kink-pair activation enthalpy on screw dislocations in bcc transition metals: V, nb, ta, mo, w, and fe, Physical Review B 91 (9) (2015) 094105.
[42] M. Gilbert, S. Queyreau, J. Marian, Stress and temperature dependence of screw dislocation mobility in α-fe by molecular dynamics, Physical Review B 84 (17) (2011) 174103.
[43] S. Queyreau, J. Marian, M. Gilbert, B. Wirth, Edge dislocation mobilities in bcc fe obtained by molecular dynamics, Physical Review B 84 (6) (2011) 064106.
[44] J. Chang, W. Cai, V. V. Bulatov, S. Yip, Dislocation motion in bcc metals by molecular dynamics, Materials Science and Engineering: A 309 (2001) 160–163.
[45] R. Komanduri, N. Chandrasekaran, L. Raff, Molecular dynamics (md) simulation of uniaxial tension of some single-crystal cubic metals at nanolevel, International Journal of Mechanical Sciences 43 (10) (2001) 2237–2260.
[46] K. Lin, D. Chrzan, Kinetic monte carlo simulation of dislocation dynamics, Physical Review B 60 (6) (1999) 3799.
[47] W. Cai, V. V. Bulatov, J. F. Justo, A. S. Argon, S. Yip, Kinetic monte carlo approach to modeling dislocation mobility, Computational materials science 23 (1) (2002) 124–130.
[48] C. Deo, D. J. Srolovitz, First passage time markov chain analysis of rare events for kinetic monte carlo: double kink nucleation during dislocation glide, Modelling and Simulation in Materials Science and Engineering 10 (5) (2002) 581.
[49] S. Scarle, C. Ewels, M. Heggie, N. Martsinovich, Linewise kinetic monte carlo study of silicon dislocation dynamics, Physical Review B 69 (7) (2004) 075209.
[50] A. Stukowski, D. Cereceda, T. D. Swinburne, J. Marian, Thermally-activated non-schmid glide of screw dislocations in w using atomistically-informed kinetic monte carlo simulations, International Journal of Plasticity 65 (2015) 108–130.
[51] Q. Qin, J. L. Bassani, Non-schmid yield behavior in single crystals, Journal of the Mechanics and Physics of Solids 40 (4) (1992) 813 – 833.
[52] M. Dao, R. Asaro, Non-schmid effects and localized plastic flow in intermetallic alloys, Materials Science and Engineering: A 170 (1) (1993) 143–160.
[53] M. Brünig, Numerical modelling of finite elastic-plastic deformations of crystalline solids including non-schmid effects, in: Computational plasticity, Vol. 5, 1997, pp. 907–912.
[54] J. Raphanel, P. Van Houtte, Simulation of the rolling textures of bcc metals by means of the relaxed taylor theory, Acta Metallurgica 33 (8) (1985) 1481–1488.
[55] M. Hölscher, D. Raabe, K. Lücke, Rolling and recrystallization textures of bcc steels, Steel Research International (62) (1991) 567–575.
[56] M. Hölscher, D. Raabe, K. Lücke, Relationship between rolling textures and shear textures in fcc and bcc metals, Acta metallurgica et materialia 42 (3) (1994) 879–886.
[57] D. Raabe, G. Schlenkert, H. Weisshaupt, K. Lücke, Texture and microstructure of rolled and annealed tantalum, Materials science and technology 10 (4) (1994) 299–305.
[58] D. Raabe, Investigation of contribution of {123} slip planes to development of rolling textures in bee metals by use of taylor models, Materials science and technology 11 (5) (1995) 455–460.
[59] D. Raabe, Simulation of rolling textures of bcc metals considering grain interactions and crystallographic slip on {110},{112} and {123} planes, Materials Science and Engineering: A 197 (1) (1995) 31–37.
[60] B. Peeters, S. Kalidindi, P. Van Houtte, E. Aernoudt, A crystal plasticity based work-hardening/softening model for bcc metals under changing strain paths, Acta materialia 48 (9) (2000) 2123–2133.
[61] L. Stainier, A. M. Cuitiño, M. Ortiz, A micromechanical model of hardening, rate sensitivity and thermal softening in bcc single crystals, Journal of the Mechanics and Physics of Solids 50 (7) (2002) 1511–1545.
[62] P. Erieau, C. Rey, Modeling of deformation and rotation bands and of deformation induced grain boundaries in if steel aggregate during large plane strain compression, International Journal of Plasticity 20 (10) (2004) 1763–1788.
[63] A. Ma, F. Roters, D. Raabe, A dislocation density based constitutive law for {BCC} materials in crystal plasticity {FEM}, Computational Materials Science 39 (1) (2007) 91 – 95, proceedings of the 15th International Workshop on Computational Mechanics of Materials The 15th International Workshop on Computational Mechanics of Materials.
[64] C. Hamelin, B. Diak, A. Pilkey, Multiscale modelling of the induced plastic anisotropy in bcc metals, International Journal of Plasticity 27 (8) (2011) 1185–1202.
[65] K. Kitayama, C. Tomé, E. Rauch, J. Gracio, F. Barlat, A crystallographic dislocation model for describing hardening of polycrystals during strain path changes. application to low carbon steels, International Journal of Plasticity 46 (2013) 54–69.
[66] Y. J. Lee, G. Subhash, G. Ravichandran, Constitutive modeling of textured body-centered-cubic (bcc) polycrystals, International Journal of Plasticity 15 (6) (1999) 625–645.
[67] S. Kuchnicki, R. Radovitzky, A. Cuitiño, An explicit formulation for multiscale modeling of bcc metals, International Journal of Plasticity 24 (12) (2008) 2173–2191.
[68] A. Koester, A. Ma, A. Hartmaier, Atomistically informed crystal plasticity model for body-centered cubic iron, Acta Materialia

60 (9) (2012) 3894–3901.
[69] C. R. Weinberger, C. C. Battaile, T. E. Buchheit, E. A. Holm, Incorporating atomistic data of lattice friction into bcc crystal plasticity models, International Journal of Plasticity 37 (2012) 16–30.
[70] A. Alankar, D. P. Field, D. Raabe, Plastic anisotropy of electro-deposited pure α-iron with sharp crystallographic // texture in normal direction: Analysis by an explicitly dislocation-based crystal plasticity model, International Journal of Plasticity 52 (0) (2014) 18 – 32, in Honor of Hussein Zbib.
[71] H. Lim, C. R. Weinberger, C. C. Battaile, T. E. Buchheit, Application of generalized non-schmid yield law to low-temperature plasticity in bcc transition metals, Modelling and Simulation in Materials Science and Engineering 21 (4) (2013) 045015.
[72] S. Narayanan, D. L. McDowell, T. Zhu, Crystal plasticity model for {BCC} iron atomistically informed by kinetics of correlated kinkpair nucleation on screw dislocation, Journal of the Mechanics and Physics of Solids 65 (0) (2014) 54 – 68.
[73] A. Patra, T. Zhu, D. L. McDowell, Constitutive equations for modeling non-schmid effects in single crystal bcc-fe at low and ambient temperatures, International Journal of Plasticity 59 (0) (2014) 1 – 14.
[74] M. Knezevic, I. J. Beyerlein, M. L. Lovato, C. N. Tomé, A. W. Richards, R. J. McCabe, A strain-rate and temperature dependent constitutive model for bcc metals incorporating non-schmid effects: Application to tantalum–tungsten alloys, International Journal of Plasticity 62 (2014) 93–104.
[75] H. Lim, C. C. Battaile, J. D. Carroll, B. L. Boyce, C. R. Weinberger, A physically based model of temperature and strain rate dependent yield in bcc metals: Implementation into crystal plasticity, Journal of the Mechanics and Physics of Solids 74 (2015) 80–96.
[76] H. Lim, L. Hale, J. Zimmerman, C. Battaile, C. Weinberger, A multi-scale model of dislocation plasticity in α-fe: Incorporating temperature, strain rate and non-schmid effects, International Journal of Plasticity.
[77] T. Yalcinkaya, W. Brekelmans, M. Geers, Bcc single crystal plasticity modeling and its experimental identification, Modelling and Simulation in Materials Science and Engineering 16 (8) (2008) 085007.
[78] L. Proville, D. Rodney, M.-C. Marinica, Quantum effect on thermally activated glide of dislocations, Nature materials 11 (10) (2012) 845–849.
[79] F. Roters, P. Eisenlohr, L. Hantcherli, D. Tjahjanto, T. Bieler, D. Raabe, Overview of constitutive laws, kinematics, homogenization and multiscale methods in crystal plasticity finite-element modeling: Theory, experiments, applications, Acta Materialia 58 (4) (2010) 1152–1211.
[80] J. Lubliner, Plasticity theory, Courier Corporation, 2008.
[81] E. H. Lee, Elastic-plastic deformation at finite strains, Journal of Applied Mechanics 36 (1) (1969) 1–6.
[82] J. Fish, K. Shek, Finite deformation plasticity based on the additive split of the rate of deformation and hyperelasticity, Computer methods in applied mechanics and engineering 190 (1) (2000) 75–93.
[83] C. Reina, S. Conti, Kinematic description of crystal plasticity in the finite kinematic framework: A micromechanical understanding of F=FeFp, Journal of the Mechanics and Physics of Solids 67 (0) (2014) 40 – 61.
[84] F. Roters, P. Eisenlohr, C. Kords, D. Tjahjanto, M. Diehl, D. Raabe, DAMASK: the Dusseldorf Advanced MAterial Simulation Kit for studying crystal plasticity using an FE based or a spectral numerical solver, Procedia IUTAM 3 (0) (2012) 3 – 10, IUTAM Symposium on Linking Scales in Computations: From Microstructure to Macro-scale Properties.
[85] S. R. Kalidindi, C. A. Bronkhorst, L. Anand, Crystallographic texture evolution in bulk deformation processing of fcc metals, J. Mech. Phys. Solids 40 (1992) 537–569.
[86] S. Dumoulin, O. Hopperstad, T. Berstad, Investigation of integration algorithms for rate-dependent crystal plasticity using explicit finite element codes, Computational Materials Science 46 (4) (2009) 785–799.
[87] D. L. McDowell, Viscoplasticity of heterogeneous metallic materials, Materials Science and Engineering: R: Reports 62 (3) (2008) 67–123.
[88] D. Cereceda, A. Stukowski, M. Gilbert, S. Queyreau, L. Ventelon, M. Marinica, J. Perlado, J. Marian, Assessment of interatomic potentials for atomistic analysis of static and dynamic properties of screw dislocations in w, Journal of Physics: Condensed Matter 25 (8) (2013) 085702.
[89] G. Monnet, C. Domain, S. Queyreau, S. Naamane, B. Devincre, Atomic and dislocation dynamics simulations of plastic deformation in reactor pressure vessel steel, Journal of Nuclear Materials 394 (2â3) (2009) 174 – 181.
[90] S. Naamane, G. Monnet, B. Devincre, Low temperature deformation in iron studied with dislocation dynamics simulations, International Journal of Plasticity 26 (1) (2010) 84 – 92.
[91] G. Monnet, S. Naamane, B. Devincre, Orowan strengthening at low temperatures in bcc materials studied by dislocation dynamics simulations, Acta Materialia 59 (2) (2011) 451 – 461.
[92] M. Tang, J. Marian, Temperature and high strain rate dependence of tensile deformation behavior in single-crystal iron from dislocation dynamics simulations, Acta Materialia 70 (2014) 123–129.
[93] J. E. Dorn, S. Rajnak, Nucleation of kink pairs and the peierls′ mechanism of plastic deformation, Trans. Aime 230 (8) (1964) 1052–1064.
[94] U. Kocks, A. Argon, M. Ashby, Progress in materials science, Thermodynamics and Kinetics of Slip 19 (1975) 110–170.
[95] T. Swinburne, S. Dudarev, S. Fitzgerald, M. Gilbert, A. Sutton, Theory and simulation of the diffusion of kinks on dislocations in bcc metals, Physical Review B 87 (6) (2013) 064108.
[96] D. Cereceda, Multiscale modeling of the plastic behaviour in single crystal tungsten: from atomistic to crystal plasticity simulations, Ph.D. thesis, Univerisdad Politécnica de Madrid (2015).
[97] D. Caillard, Kinetics of dislocations in pure fe. part i. in situ straining experiments at room temperature, Acta Materialia 58 (9) (2010) 3493–3503.
[98] D. Caillard, Kinetics of dislocations in pure fe. part ii. in situ straining experiments at low temperature, Acta Materialia 58 (9) (2010) 3504–3515.
[99] C. Marichal, H. Van Swygenhoven, S. Van Petegem, C. Borca, {110} slip with {112} slip traces in bcc tungsten, Scientific reports

3 (2013) 2547.
[100] C. Marichal, K. Srivastava, D. Weygand, S. Van Petegem, D. Grolimund, P. Gumbsch, H. Van Swygenhoven, Origin of anomalous slip in tungsten, Phys. Rev. Lett. 113 (2014) 025501.
[101] P. Franciosi, L. Le, G. Monnet, C. Kahloun, M.-H. Chavanne, Investigation of slip system activity in iron at room temperature by {SEM} and {AFM} in-situ tensile and compression tests of iron single crystals, International Journal of Plasticity 65 (2015) 226 – 249.
[102] R. Gröger, V. Vitek, Multiscale modeling of plastic deformation of molybdenum and tungsten. iii. effects of temperature and plastic strain rate, Acta Materialia 56 (19) (2008) 5426–5439.
[103] Z. Chen, M. Mrovec, P. Gumbsch, Atomistic aspects of $1/2\langle 1\,1\,1\rangle$ screw dislocation behavior in α-iron and the derivation of microscopic yield criterion, Modelling and Simulation in Materials Science and Engineering 21 (5) (2013) 055023.
[104] H. Mecking, U. Kocks, Kinetics of flow and strain-hardening, Acta Metallurgica 29 (11) (1981) 1865–1875.
[105] Y. Estrin, Dislocation-density-related constitutive modeling, Unified constitutive laws of plastic deformation?,(Eds. AS Krausz and K. Krausz), Academic Press, 1996.
[106] A. Arsenlis, D. M. Parks, Modeling the evolution of crystallographic dislocation density in crystal plasticity, Journal of the Mechanics and Physics of Solids 50 (9) (2002) 1979 – 2009.
[107] N. Barton, J. Bernier, R. Becker, A. Arsenlis, R. Cavallo, J. Marian, M. Rhee, H.-S. Park, B. Remington, R. Olson, A multiscale strength model for extreme loading conditions, Journal of applied physics 109 (7) (2011) 073501.
[108] F. Roters, Advanced material models for the crystal plasticity finite element method: development of a general CPFEM framework, Universitätsbibliothek, 2011.
[109] S. J. Basinski, Z. S. Basinski, Plastic deformation and work hardening, in: F. R. N. Nabarro (Ed.), Dislocations in Solids, Vol. 4, North Holland, Amsterdam, 1979, pp. 261–362.
[110] P. Franciosi, Glide mechanisms in bcc crystals: an investigation of the case of α-iron through multislip and latent hardening tests, Acta Metallurgica 31 (9) (1983) 1331–1342.
[111] P. Franciosi, The concepts of latent hardening and strain hardening in metallic single crystals, Acta Metallurgica 33 (9) (1985) 1601–1612.
[112] R. Madec, L. Kubin, Dislocation interactions and symmetries in bcc crystals, in: IUTAM Symposium on Mesoscopic Dynamics of Fracture Process and Materials Strength, Springer, 2004, pp. 69–78.
[113] S. Queyreau, G. Monnet, B. Devincre, Slip systems interactions in α-iron determined by dislocation dynamics simulations, International Journal of Plasticity 25 (2) (2009) 361 – 377.
[114] R. M. Christensen, Observations on the definition of yield stress, Acta Mechanica 196 (3-4) (2008) 239–244.
[115] P. Bowden, J. Jukes, The plastic flow of isotropic polymers, Journal of Materials Science 7 (1) (1972) 52–63.
[116] A. Argon, S. Maloof, Plastic deformation of tungsten single crystals at low temperatures, Acta metallurgica 14 (11) (1966) 1449–1462.
[117] P. L. Raffo, Yielding and fracture in tungsten and tungsten-rhenium alloys, Journal of the Less Common Metals 17 (2) (1969) 133–149.
[118] J. R. Stephens, Dislocation structures in single-crystal tungsten and tungsten alloys, Metallurgical and Materials Transactions 1 (5) (1970) 1293–1301.
[119] W. D. Klopp, W. R. Witzke, P. L. Raffo, Effects of grain size on the tensile and creep properties of arc-melted and electrobeam-melted tungsten at 2250° to 4140° f, Tech. Rep. E-2681, National Aeronautics and Aerospace Administration, Lewis Research Center, Cleveland, Ohio (July 1964).
[120] I. Gupta, J. Li, Stress relaxation, internal stress, and work hardening in some bcc metals and alloys, Metallurgical Transactions 1 (8) (1970) 2323–2330.
[121] D. Brunner, Comparison of flow-stress measurements on high-purity tungsten single crystals with the kink-pair theory, Materials Transactions JIM 41 (1) (2000) 152–160.
[122] D. Brunner, Temperature dependence of the plastic flow of high-purity tungsten single crystals, International Journal of Materials Research 101 (8) (2010) 1003–1013.
[123] J. Hutchinson, K. Neale, Influence of strain-rate sensitivity on necking under uniaxial tension, Acta Metallurgica 25 (8) (1977) 839–846.
[124] J. Hedworth, M. Stowell, The measurement of strain-rate sensitivity in superplastic alloys, Journal of Materials Science 6 (8) (1971) 1061–1069.
[125] A. Arieli, A. Rosen, Measurements of the strain rate sensitivity coefficient in superplastic ti? 6al? 4v alloy, Scripta Metallurgica 10 (5) (1976) 471–475.
[126] S. Bodner, Constitutive equations for dynamic material behavior, Springer, 1968.
[127] W. Prager, The general theory of limit design, in: Proceedings of the 8th International Congress on theoretical and Applied Mechanics, Istanbul, Vol. 19, 1952, pp. 65–72.
[128] D. Drucker, W. Prager, H. Greenberg, Extended limit design theorems for continuous media, Quaterly of Applied Mathematics 9 (4) (1952) 381–389.
[129] D. Sheng, S. Sloan, A. Gens, A constitutive model for unsaturated soils: thermomechanical and computational aspects, Computational Mechanics 33 (6) (2004) 453–465.
[130] M. Serenelli, M. Bertinetti, J. Signorelli, Investigation of the dislocation slip assumption on formability of {BCC} sheet metals, International Journal of Mechanical Sciences 52 (12) (2010) 1723 – 1734.
[131] V. V. Bulatov, W. Cai, Nodal effects in dislocation mobility, Physical review letters 89 (11) (2002) 115501.
[132] R. Gröger, V. Vitek, Explanation of the discrepancy between the measured and atomistically calculated yield stresses in body-centred cubic metals, Philosophical magazine letters 87 (2) (2007) 113–120.
[133] D. Caillard, On the stress discrepancy at low-temperatures in pure iron, Acta Materialia 62 (2014) 267–275.

[134] A. Seeger, The flow stress of high-purity refractory body-centred cubic metals and its modification by atomic defects, Le Journal de Physique IV 5 (C7) (1995) C7–45.
[135] D. Ali, N. Mushtaq, M. Butt, Investigation of active slip-systems in some body-centered cubic metals, Journal of materials science 46 (11) (2011) 3812–3821.
[136] A. K. Zurek, G. T. Gray III, Dynamic strength and strain rate effects on fracture behavior of tungsten and tungsten alloys, Journal de Physique 1 (C3) (1991) 631–637.
[137] E. Starovoitov, F. B. O. Naghiyev, Foundations of the Theory of Elasticity, Plasticity, and Viscoelasticity, CRC Press, 2012.
[138] W. G. Pariseau, et al., Plasticity theory for anisotropic rocks and soil, in: The 10th US Symposium on Rock Mechanics (USRMS), American Rock Mechanics Association, 1968.
[139] G. Henkelman, G. Johannesson, H. Jonsson, Methods for Finding Saddle Points and Minimum Energy Paths, Kluwer Academic Publishers, 2000.
[140] S. Plimpton, Fast Parallel Algorithms For Short-Range Molecular-Dynamics. http://lammps.sandia.gov., Journal Of Computational Physics 117 (1) (1995) 1–19.

9.1 PRELIMINARY MULTI-PHYSICS DESIGN OF THE FIRST WALL AND BLANKET SYSTEM IN THE FUSION NUCLEAR SCIENCE FACILITY (FNSF) — Yue Huang, Nasr Ghoniem (UCLA), Jake Blanchard, Laila El-Guebaly (UW-Madison), Charles Kessel (Princeton Plasma Physics Laboratory), Siegfried Malang (Nuclear Technology Consulting), Mark Tillack (UCSD)

OBJECTIVE

The objective of this work is to optimize the design of the first wall and blanket system in FNSF so as to develop a reliable configuration that can achieve long lifetime, maintainability, and high reliability. The blanket structural design needs to meet strict temperature and stress design limits while maintaining credible configuration and maintenance characteristics.

SUMMARY

The dual coolant lead-lithium (DCLL) blanket concept is based on a helium-cooled first wall and blanket structure with RAFS (Reduced Activation Ferritic Steel) and a self-cooled Pb-Li breeding zone. 3D solid modeling was achieved with *SOLIDWORKS*, while 3D finite element multiphysics modeling of the DCLL first wall and blanket (mid-plane part of one sector) has been performed by *COMSOL 5.0* via coupling of the CFD, heat transfer in solids, and heat transfer in fluids modules. Design optimization is realized by seamless connection of two main software platforms with life-links. The results of velocity, pressure, and temperature distributions of helium flow, as well as the primary and secondary thermal stress of the structure were obtained. This is followed by determination of the factors of safety based on the ITER design rules of un-irradiated components. Future efforts will consider the effects of radiation on the lifetime and reliability of the design, improvements in the geometric layout of the FW/B structure, improvements in heat transfer and fluid flow models, and integration of multiscale models of plasticity and fracture.

PROGRESS AND STATUS

Introduction

The major design characteristics of the DCLL blanket include helium flow paths for cooling the first wall and blanket structures, and Pb-Li liquid metal paths for cooling all blanket regions[1]. A simplified diagram for the in-board configuration is shown in Figure 1.

The CAD model in Figure 2 for the In-board (IB) blanket represents one of a total of 16 blanket sectors at midplane, showing the breeding zones, tungsten armor, SiC inserts, stiffening and back plates with poloidal cooling channels and separation plates with toroidal cooling. There are 4 radial stiffening plates connecting the first wall and back wall to accommodate the bending stress due to the pressure of helium flow, which is taken to be 8 MPa. The separation wall divides the blanket into two sets of breeding zones. The cooling pathways for the separation wall will be modified from the current toroidal direction to a poloidal direction, similar to the cooling pattern of the back wall. Each breeding cell is 25 cm in the radial direction. The first wall is 3.8 cm thick with a 3 cm cooling channel. The FW structure is curved with a radius of 4.8 m. The first and the back walls are connected by the radial stiffening plates so as to accommodate bending stresses in these walls caused by: (a) the PbLi pressure during normal operation, and (b) the He-pressure during an internal Loss of Coolant Accident (LOCA). There is a 2 mm tungsten (W) armor layer attached to the first wall, designed for (a) accommodating the peak surface heat flux caused by high-temperature plasma transients, and (b) reduce FW surface erosion caused by sputtering.

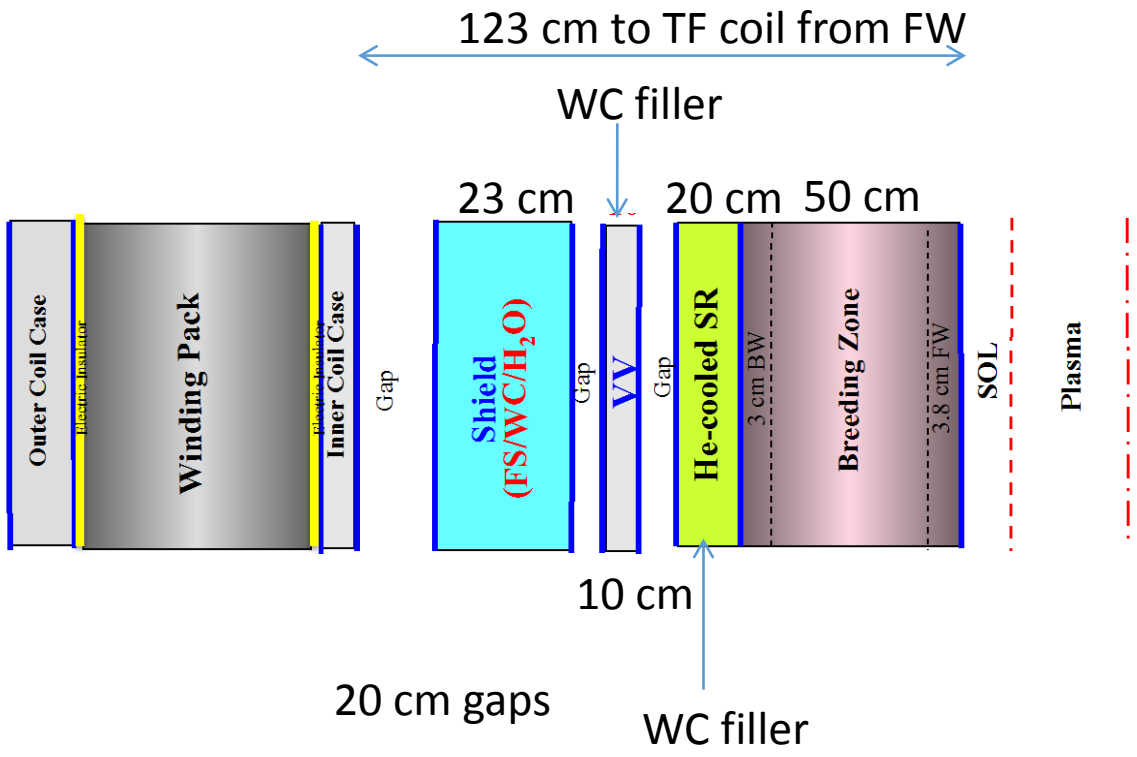

Figure 1. Inboard configuration of FNSF power system.

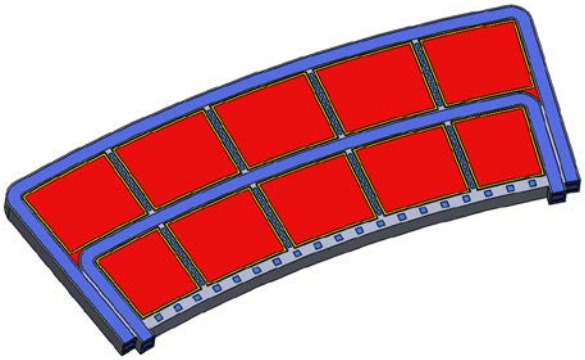

Figure 2: CAD model of Inboard Blanket at midplane

Computer Simulations

Three major multi-physics modules have been coupled in the current design. These are: Non-isothermal Fluid Flow, Heat Transfer in Solids, and Solid Mechanics. They are coupled in the Conjugate Heat Transfer module. Non-isothermal Fluid was used to simulate the helium flow inside the channels. The helium flow was considered as laminar due to the limit of current computation capabilities. Turbulent flow simulations are expected to result in higher heat transfer coefficients, thus reducing the structure temperatures. Turbulent flow will be considered in the future. The temperature and pressure distributions of helium flow can be obtained in this module. Heat Transfer in the Solid was used to compute the temperature distribution of the blanket RAFS structure. Both surface heat flux on the first wall and volumetric heating were considered. The Solid Mechanics module was used to compute the stress

distribution in the structure. The primary stress is due to the helium pressure against the channel wall. To calculate secondary (thermal) stress, the Heat Transfer in Solids and Solid Mechanics were coupled in Multiphysics simulations. Couplings between physics modules are shown schematically in Figure 3.

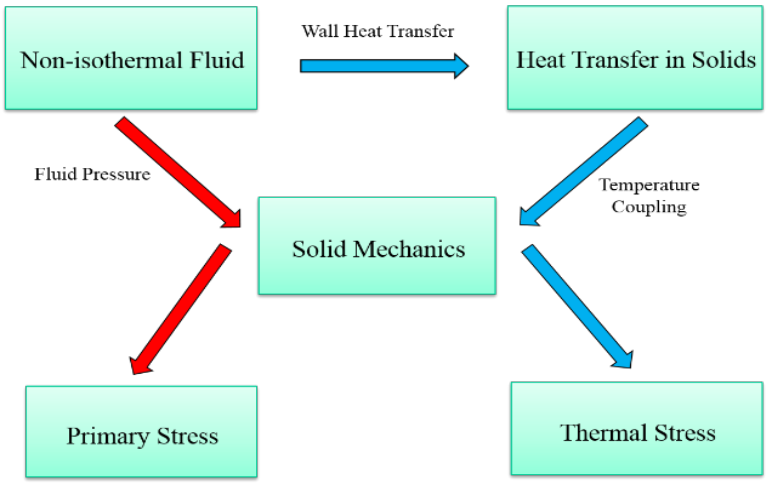

Figure 3. Summary of Models

Results

Helium Flow

The inlet helium operating pressure is assumed to be 8 MPa [1]. As Figure 4 shows, the pressure drops all the way through the helium flow channel. With the laminar flow assumption, the average velocity was set to be over 100 m/s to reach the required heat transfer coefficient.

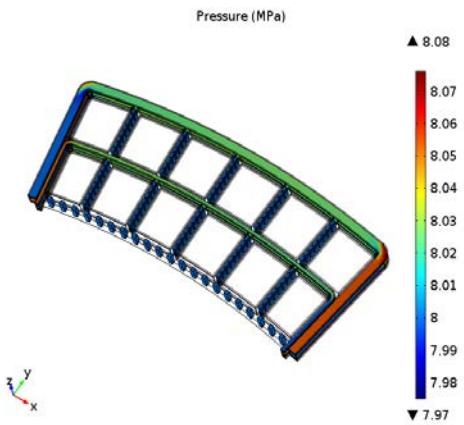

Figure 4. Pressure distribution of helium flow

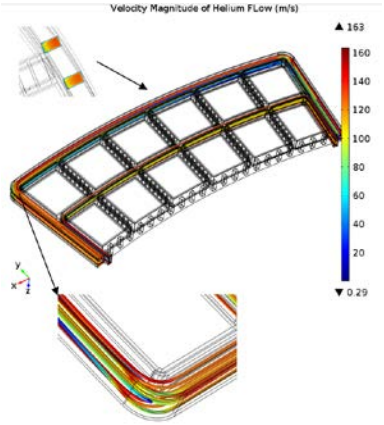

Figure 5. Streamlines of helium flow

The streamlines of helium flow with velocity information are shown in Figure 5. The entire helium flow stream with an inlet temperature of 400 ℃ (Figure 6) enters the blanket sector. So far, only one channel layer at midplane was studied for the present preliminary design. For the entire FW/B design, there are stacks of helium flow channels in the poloidal direction, and an alternating flow configuration will be applied to create a more uniform temperature thus reducing thermal stresses.

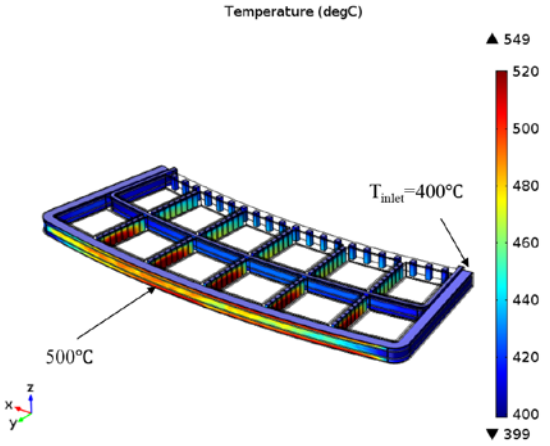

Figure 6. Temperature distribution of helium flow

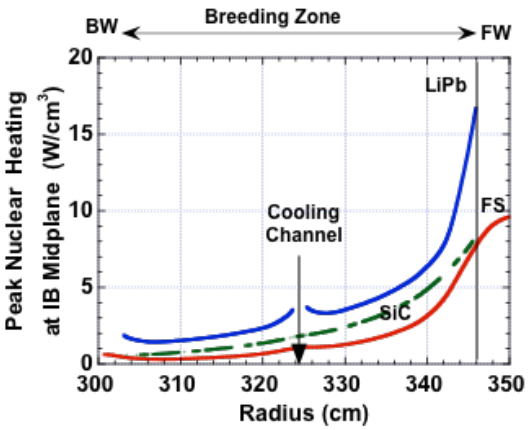

Figure 7. Radial Distribution of Nuclear Heating

Temperature distributions of the solid structure

The heat flux from the plasma results in temperature gradients inside the blanket structure, which cause secondary thermal stresses. The peak heat flux is taken as 1.4 MW/m^2 at the inboard blanket midplane. The dependence of peak volumetric heating on the radial distance at the midplane is shown in Figure 7. The 2 mm thick W armor, which is not shown in the plot, generates the highest heating, which is about 32 W/cm^3.

The surface heat flux and the volumetric heating rates were applied in the Heat Transfer in Solids module in COMSOL. The Pb-Li liquid metal's velocity will go down to 0.075 m/s in the considered temperature range[2,3]. So it is reasonable to consider the breeding zone as a solid, and perform heat transfer simulations in a Pb-Li solid material with appropriate heat flux boundary conditions. The result of the temperature distribution is shown in Figure 8. The maximum temperature of the Pb-Li is slightly above 750 ℃ in the interior parts of breeding cells. However, this is not a concern, since the outlet LiPb temperature is around 700 ℃, while the steel/LiPb interface temperature is kept at 500 ℃.This reveals that helium heat transfer coefficient is not sufficiently high, and this will be modified in the next design iteration. Typically, a heat transfer coefficient around 1000 W/m^{2}K[5] is assumed. In the present simulations, the heat transfer coefficient was not assumed, but rather calculated as a result of the fluid flow and heat transfer simulations. Ribs and grooves may need to be manufactured inside the cooling channels to enhance wall heat transfer. The side effect is that a much higher pressure drop in flow channels will occur.

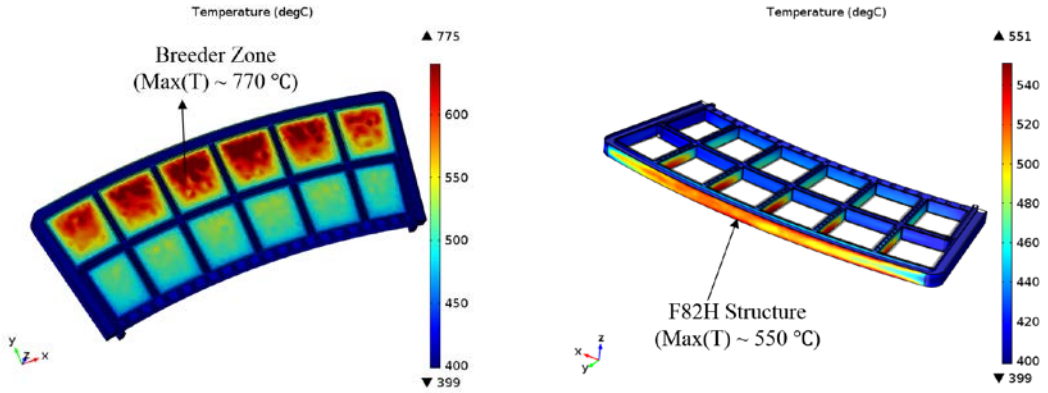

Figure 8. Temperature distribution of global structure

The maximum temperature of the RAFM steel is also about to exceed the limit of 550 ℃. Since the velocity of helium flow is already pretty high, some other methods like roughening the channel wall or changing the structure configuration may need to be applied in future optimizations of the design, if turbulent flow does not result in enhancement of the wall heat transfer coefficient.

Primary stress of solid structure

The helium and Pb-Li flow inside the channel generate the pressure against channel walls, which finally leads to the primary stress in the blanket structure. As discussed before, the pressure load in helium cooling channels and the Pb-Li breeding zone is set to be 8 MPa and 1.6 MPa, respectively. The current analysis of the primary stress is based on normal operating conditions, and future efforts will consider off-normal scenarios as well. Figure 9 shows the global primary stress distribution of the blanket structure. There are stress concentrations at the junctions and corners, which can reach more than 220 MPa. Rounding this junction area will help reduce the stress concentration.

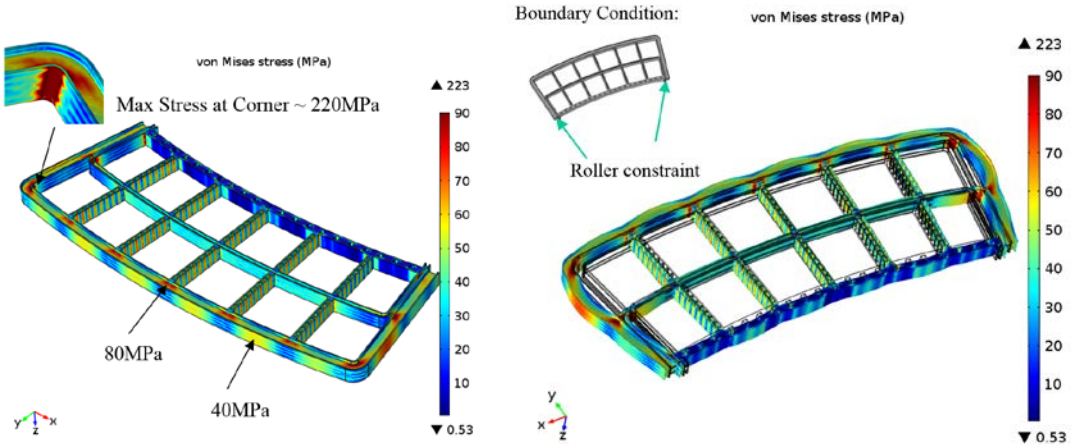

(a) Undeformed configuration (b) Deformed configuration

Figure 9. Primary stress distribution

Deformation resulting from primary stress was also obtained, as shown in Figure 10.

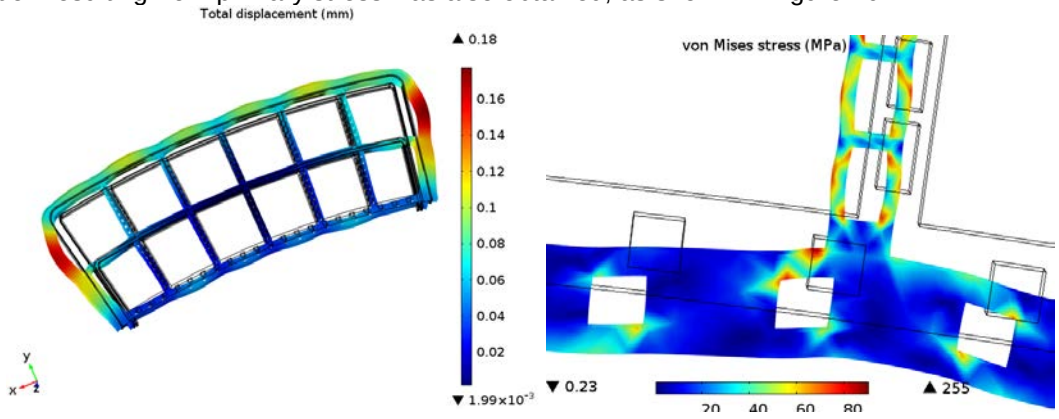

(a) Global deformation (b) Local deformation

Figure 10. Displacement distribution due to the primary stress

Thermal stress of the solid structure

Thermal stress was calculated based on the temperature distributions utilizing the Conjugate Heat Transfer module of COMSOL. As illustrated in Figure 11, the first wall has the largest thermal stress. Also, thermal expansion is shown in Fig 11 (b), illustrating the reason why we need to leave a gap between adjacent sectors during assembly.

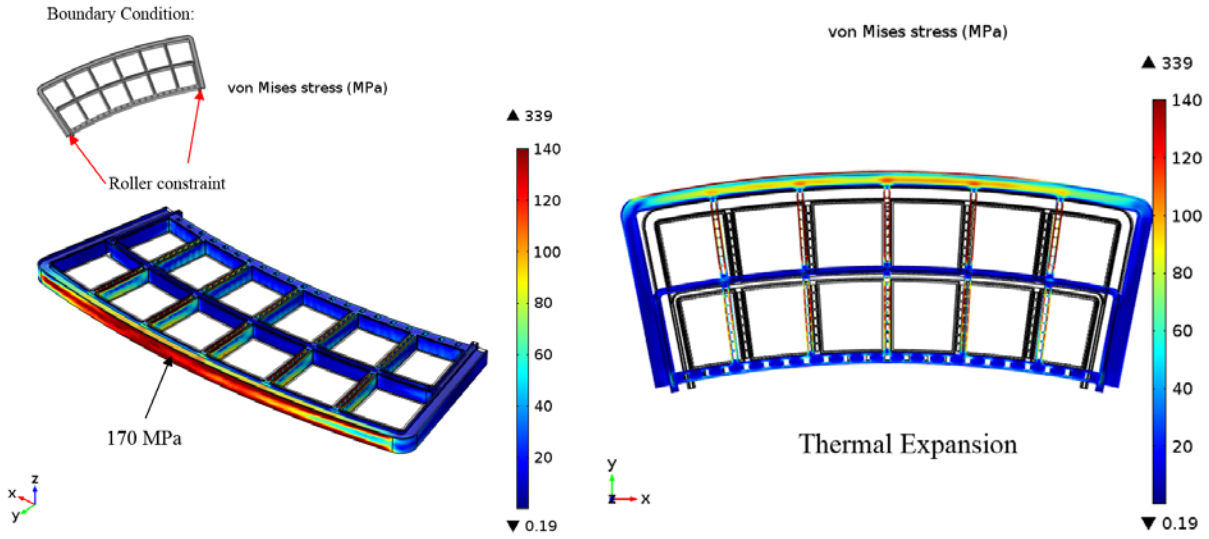

(a) Undeformed configuration (b) Deformed configuration

Figure 11. Thermal stress distribution

Factors of Safety

With the results of the primary and thermal stresses, factors of safety were determined based on three different allowable values. These are: the allowable primary membrane stress intensity (S_m), the allowable total stress intensity (S_d), and the allowable primary plus secondary membrane stress intensity (S_e). The results are shown in the following tables. For reference on the mechanical design procedure, including path definitions and stress intensity parameters, please see reference [6].

Table 1. Factors of safety based on S_m

$\overline{P_m} \leq S_m(T_m, \varphi t_m)$			
Path	$\overline{P_m}[MPa]$	$S_m[MPa]$	Factor of Safety
1	23.6	144.8	6.1
2	32.1	150.1	4.7
3	48.3	154.3	3.2

Table 2. Factors of safety based on S_e

$\overline{P_L + Q_L} \leq S_e(T_m, \varphi t_m)$			
Path	$\overline{P_L + Q_L}[MPa]$	$S_e[MPa]$	Factor of Safety
1	18.4	204.3	11.1
2	65.4	211.8	3.2
3	66.9	217.7	3.3

Table 3. Factors of safety based on S_d

$\overline{P_L + P_B + Q} \leq S_d(T, \varphi t, r_3)$			
Path	$\overline{P_L + P_B + Q}[MPa]$	$S_d[MPa]$	Factor of Safety
1	50.9	408.5	8.0
2	85.1	423.5	5.0
3	57.3	435.5	7.6

Conclusions and Future Research:

We have demonstrated the feasibility of multiphysics design and optimization of the FW/B system, coupling fluid flow, heat transfer in fluids, heat transfer in solids, thermal stress, and mechanical stress simulations. The results are preliminary, as the design will continue to evolve this year. In particular, since the results of heat transfer and fluid flow are based on a laminar flow model for computational expediency, they are not realistic and will be replaced with a turbulent flow model. Future efforts will consider the following: (1) simulations of turbulent heat transfer for helium flow; (2) irradiation effects on material properties, (3) geometric optimization to reduce stress concentrations; (4) simulations of plasma transient effects; (5) multiscale modeling of smaller Representative Volume Elements (RVE) to include dislocation-based plasticity models; (6) Design and analysis of the FW/B system in accidental scenarios.

References

[1] Wang, X. R., et al. "ARIES-ACT2 DCLL Power Core Design and Engineering."*Fusion Science and Technology* 67.1 (2015): 11.

[2] M. S. Tillack and S. Malang, “High Performance PbLi blanket,” proceedings of the 17th IEEE/NPSS Symposium on Fusion Engineering, San Diego CA, October 1997.

[3] M. S. Tillack, X. R. Wang, J. Pulsifer, S. Malang, D. K. Sze, M. Billone, I. Sviatoslavsky and the ARIES Team, “Fusion power core engineering for the ARIES-ST power plant,” Fusion Eng. and Design 65 (2003) 215-261..

[4] Raffray, A. R., et al. "Advanced power core system for the ARIES-AT power plant." *Fusion Engineering and Design* 82.2 (2007): 217-236.

[5] Wang, X. R., et al. "Modular Dual Coolant Pb-17Li Blanket Design for ARIES-CS Compact Stellarator Power Plant." *Fusion Engineering 2005, Twenty-First IEEE/NPS Symposium on*. IEEE, 2005.

[6] S Sharafat, AT Aoyama, N Ghoniem, “Assessment of the DCLL TBM Thermostructural Response Based on ITER Design Criteria,” *Fusion Science and Technology*, 60 (1), 264-271, 2011

10.1 FUSION MATERIAL IRRADIATION TEST STATION (FMITS) AT SNS — Mark Wendel, Phil Ferguson (Oak Ridge National Laboratory)

OBJECTIVE

The Fusion Materials Irradiation Test Station (FMITS) is a plan for an irradiation facility at the Spallation Neutron Source (SNS). The objective of the FY15 effort is to address comments by the reviewers of the 2014 feasibility study and to reduce the technical risks to a potential project by analysis and by building and testing hardware mockups. The 2014 effort produced a Feasibility Study Report, 30% Design Review, and a Preliminary Safety Assessment. The 2014 estimate for implementation of the FMITS at SNS was $13.4 M including a 25% contingency.

SUMMARY

The Fusion Materials Irradiation Test Station (FMITS) is a design concept for installation at the Spallation Neutron Source (SNS) Facility. The project has received funding from OFES during FY15 for (1) performing a mockup test on an FMITS-type target seal, (2) augmenting the safety assessment based on the 2014 technical review, (3) analyzing thermal-hydraulic off-normal transients with a full 3D model to assess the performance of the FMITS sensor array, and (4) remote-handling electrical connector operational mock-up. The main goals of the effort are to remove the project technical risks and prepare for a potential future project.

PROGRESS

1. Seal mockup

FMITS-type (double-pillow) seal hardware (Figure 1) has been received along with a test report from the vendor. This seal is a prototype of the assembly that could be used between the target
module and the core vessel flange for an FMITS harness. It would replace the single-sided version currently in use at SNS. Hardware has also been designed and ordered that would modify the inflatable seal test tank (Figure 2) at SNS to confirm that the new seal operates to required specifications, and to show robust and repeatable performance. The vendor (KSM Corporation) completed a leak test on the double pillow seal with the apparatus shown in Figure 3. The test report indicates that the seal design is highly successful, holding 2.9×10^{-6} torr-liter/s against helium gas. If the ORNL mockup test results confirm, then the technical risk to a proposed FMITS project would be greatly reduced, according to the Feasibility Study Report of 2014.

2. Safety assessment

As mentioned in the previous semi-annual report, deterministic analysis does not seem feasible that can rule out possible FMITS test-section tube rupture severe consequences. It is likely that the FMITS plan will have to keep the engineering control safeguard of a calibrated containment tube with directional failure bias. To that end, a contract has been placed with Fike Company (the same company that designed, tested, and supply HFIR rupture disk) to design and test FMITS tubes that would hold up to 300 psig water pressure, and then fail consistently and without fragmentation in a direction away from the SNS target and moderators. Fike has material on order for their first tests which should begin around August 1, 2015.

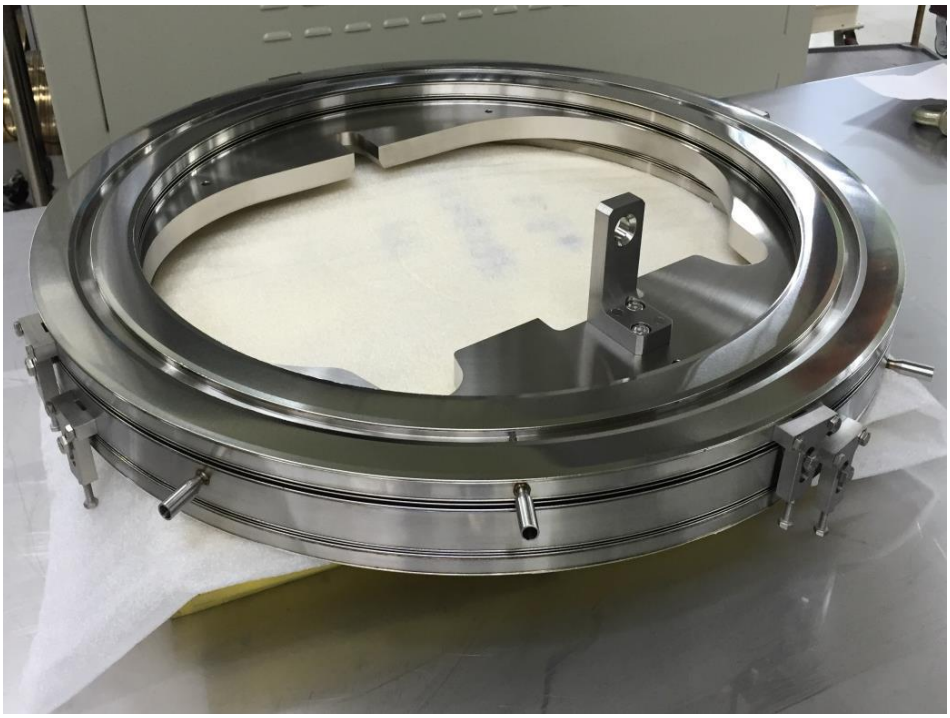

Figure 1. Double-inflatable seal ring received at ORNL from KSM Corporation. Outside diameter is 0.65 meters.

Figure 2. Test tank that will be used to assure robust functional performance of prototype double-inflatable pillow seal. Outside diameter of the tank is 0.91 m.

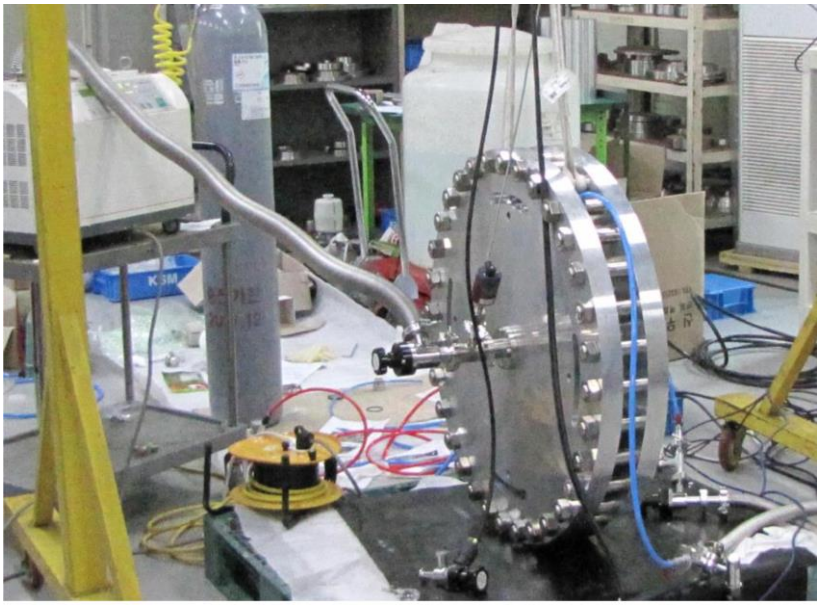

Figure 3. Set-up for double-inflatable seal leak test performed at KSM Corporation.

3. Finite element analysis (FEA) model of FMITS test section

A full 3D model of a representative FMITS capsule has been developed and meshed for finite element analysis. The model includes the outer containment, which is cooled by 37°C water at 5 GPM from the SNS light water system 2, and five sub-capsules containing steel bend bar specimens. As a representative experiment, all five sub-capsules are set to operate between 500°C to 550°C. However, because the axial heat generation profile is strongly peaked at the center, a series of calculations were performed to find individual design diameters that would produce the design temperature in each sub-capsule.

A loss-of-flow transient was completed for which the FMITS capsule experiences a sudden blockage leading to a 50% flow reduction. As shown in Figure 4, within 5 s of the flow blockage event, the hottest thermocouples indicate a 10°C temperature rise. This type of results will be useful in formulating the strategy and timing for machine protection at SNS.

In addition to the thermocouples, the instrumentation described in the FMITS feasibility study includes an RTD-based flow sensor to ensure cooling of the FMITS test section. The flow sensor is not currently available for water, but requires some development. A sub-contract is now in place with Delta M Corporation to test and deliver a prototype water flow sensor that would stand up to the harsh radioactive environment of the FMITS seal ring. The water sensor is scheduled for delivery to ORNL at the beginning of calendar year 2016.

4. Remote-handling connector mockup

Remote handling mockup tests showed that the FMITS electrical connections could be reliably made up using the SNS master-slave manipulators within the available confined space on the back end of the target carriage. Prototypical connectors were used in the mock-up testing, and these results can now be used to confidently move ahead with a preliminary design for the FMITS-specific vent line shield block.

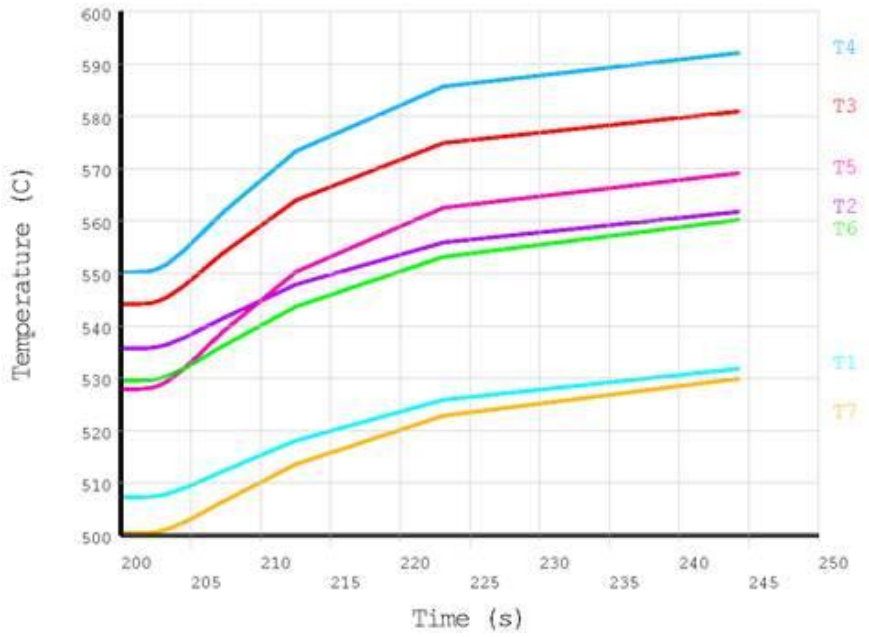

Figure 4. Simulated temperature responses of thermocouples in FMITS test section following an abrupt 50% flow reduction event.

10.2 HFIR IRRADIATION EXPERIMENTS – J.P. Robertson (Oak Ridge National Laboratory)

Status of the Reactor

HFIR completed 2.5 cycles during the first half of 2015. Cycles 458 (January 13 – February 2, 2015) and 459 (February 24 – March 21, 2015) were completed without incident. Cycle 460 started on June 9, 2015, but there was a manual shutdown on June 13, 2015, in response to a reactor setback. The cycle was restarted on June 15 and will continue into July.

Summary of Recent, Current and Planned Fusion Materials Program Experiments

Experiment Designation	Primary Materials	Specimen Types*	Irradiation Temperature (°C)	Max Exposure (dpa)	Number of Reactor Cycles	Irradiation Period (month/year)
Beryllium reflector (RB) irradiation capsules						
RB-15J	F82H	T, F, FT	300, 400	6	10	6/08 – 12/09
RB-19J	F82H, W	T, DCT Disc, Bar	250, 500 800, 1200	2-4	6	3/16 - 4/17
Target zone full-length capsules						
JP-25	F82H	T, FT	300, 500	20	10	2/99 – 1/01
JP-26	F82H	T, FT	300,400,500	9	5	12/03 – 11/04
JP-27	F82H	T, FT	300, 400	21	13	12/03 – 1/08
JP-28	F82H	T, FT	300,400,500	80	46	4/05 – 7/13
JP-29	F82H	T, FT	300,400,500	80	46	1/05 – 7/13
12-DCT	F82H	DCT	50	1.6	1	8/11 – 8/11
JP-30	F82H	T, FT	300,400,650	20	~10	11/11 – 8/13
JP-31	F82H	T, FT	300,400,650	20	~10	11/11 – 8/13
Target zone rabbit capsules (DOE-JAEA)						
F8A1	F82H	T, FT	300	50	29	2/09 – 7/13
F8A2	"	"	"	"	"	" – "
F8B1	"	"	"	"	"	" – "
F8B2	"	"	"	"	"	" – "
JCR-1	SiC/SiC	Bend bars	800	30	15	10/04 – 1/09
JCR-2	"	"	"	"	"	" – "
JCR-3	"	"	"	"	"	" – "
JCR-4	"	"	"	"	"	" – "
JCR-5	"	"	"	>50	>25	10/04 – 2/11
JCR-6	"	"	"	"	"	" – "
JCR-7	"	"	"	"	"	" – "
JCR-8	"	"	"	"	"	" – "
JCR-9	"	"	500	30	15	10/04 – 1/09
JCR-10	"	"	"	"	"	" – "
JCR-11	"	"	"	"	"	" – "
JCR-12	"	"	"	"	"	" – "
F11A3	F82H	T, FT	300	20	12	5/11 – 2/13

Experiment Designation	Primary Materials	Specimen Types*	Irradiation Temperature (°C)	Max Exposure (dpa)	Number of Reactor Cycles	Irradiation Period (month/year)
F11A4	"	"	"	"	"	" – "
F11B3	"	"	"	"	"	" – "
M4-TEN	F82H	DCT	50	1.6	1	8/11 – 8/11
JCR11-01	SiC/SiC	Bend bars	950	50	25	11/12 –
JCR11-02	SiC/SiC	Bend bars	950	10	5	10/12 – 8/13
JCR11-03	SiC/SiC	Bend bars	950	30	15	5/13 –
JCR11-04	SiC/SiC	Bend bars	950	30	15	5/13 –
JCR11-05	SiC/SiC	Bend bars	950	50	25	10/12 –
JCR11-06	SiC/SiC	Bend bars	950	10	5	10/12 – 7/13
JCR11-07	SiC/SiC	Bend bars	950	100	50	10/12 –
JCR11-08	SiC/SiC	Bend bars	950	100	50	10/12 –
JCR11-09	SiC/SiC	UDMC	950	4	2	6/13 – 11/13
JCR11-10	SiC/SiC	UDMC	950	10	8	6/13 – 8/14
JCR11-11	SiC/SiC	UDMC	950	30	15	6/13 –
JCR11-12	SiC/SiC	UDMC	950	100	50	6/13 –
F13A5	F82H	T, FT	300	10	9	1/14 – 3/15
F13A6	F82H	T, FT	300	20	18	1/14 –
F13B4	F82H	T, FT	300	10	9	1/14 – 3/15
F13B5	F82H	T, FT	300	20	18	1/14 –
SCF6	SiC/SiC	Bend bars	600	10	6	11/14 –
SCF7	SiC/SiC	Bend bars	600	30	14	11/14 –
SCF8	SiC/SiC	Bend bars	600	100	45	11/14 –
SCF9	SiC/SiC	Bend bars	600	200	90	11/14 –
SCF10	SiC/SiC	Bend bars	950	10	5	1/15 –
SCF11	SiC/SiC	Bend bars	950	30	14	1/15 –
SCF12	SiC/SiC	Bend bars	950	100	45	1/15 –
Target zone rabbit capsules (DOE-NIFS)						
T8A1	SiC	BSR	300	0.01	HT**	10/09 – 10/09
T8A2	SiC	BSR	300	0.1	HT	10/09 – 10/09
T8B1	SiC	BSR	500	0.01	HT	10/09 – 10/09
T8B2	SiC	BSR	500	0.1	HT	10/09 – 10/09
T8C1	SiC	BSR	500	~1	1	5/09 – 6/09

Experiment Designation	Primary Materials	Specimen Types*	Irradiation Temperature (°C)	Max Exposure (dpa)	Number of Reactor Cycles	Irradiation Period (month/year)
T8D1	SiC	BSR	800	0.1	HT	3/11 – 10/09
T8E1	SiC	BSR	800	~1	1	8/09 – 8/09
T8F1	SiC	BSR	1200	~1	1	8/09 – 8/09
T9A1	W, Ni	Discs	90	0.1	HT	1/09 – 10/09
T9A2	W, Ni	Discs	90	1.2	1	1/09 – 1/09
T9C1	Steels	T, MC	500	5.5	3	11/09 – 2/10
T9C2	Steels	T, MC	500	9.6	5	11/09 – 6/10
T9G1	Steels	T, MC	300	1.2	1	6/09 – 8/09
T9G2	Steels	T, MC	300	9.6	8	6/09 – 8/11
MTTN01	Steels	T, MC	300	4.8	4	1/12 – 8/11
300-LD-1	Steels	SSJ, MC	300	2	1	5/12 – 6/12
300-HD-1	Steels	SSJ, MC	300	12	6	5/12 – 2/13
500-LD-1	Steels	SSJ, MC	500	2	1	5/12 – 6/12
500-HD-1	Steels	SSJ, MC	500	12	6	5/12 – 2/13
500-HD-2	Steels	SSJ, MC	500	12	6	5/12 – 2/13
500-HD-3	Steels	SSJ, MC	500	12	6	5/12 – 2/13
650-LD-1	Steels	SSJ, MC	650	2	1	5/12 – 6/12
650-LD-2	Steels	SSJ, MC	650	2	1	5/12 – 6/12
650-HD-1	Steels	SSJ, MC	650	12	6	5/12 – 2/13
650-HD-2	Steels	SSJ, MC	650	12	6	5/12 – 2/13
300-LD-2	Steels, W	SSJ, MC	300	2	2	7/12 – 8/12
300-MD-1	Steels, W	SSJ, MC	300	7	4	7/12 – 2/13
500-LD-2	Steels, W	SSJ, MC	500	2	2	1/13 – 7/13
300-LD-3	Steels, W	SSJ, MC	300	2	2	7/12 – 11/12
300-HD-2	Steels, W	SSJ, MC	300	12	8	7/12 – 2/14
500-LD-3	Steels, W	SSJ, MC	500	2	1	7/12 – 8/12
500-HD-4	Steels, W	SSJ, MC	500	12	6	7/12 – 7/13
650-LD-3	Steels, W	SSJ, MC	650	2	2	10/12 – 7/13
650-HD-3	Steels, W	SSJ, MC	650	12	8	7/12 – 11/13
PC1	Various	SSJ, MC	80/100	0.02	HT	6/12 – 6/12
PC1A	Various	SSJ, MC	80/100	0.02	HT	6/12 – 6/12
PC2	Various	SSJ, MC	80/100	0.1	HT	6/12 – 6/12
PC2A	Various	SSJ, MC	80/100	0.1	HT	6/12 – 6/12
PC3	Various	SSJ, MC	80/100	0.5	HT	6/12 – 7/12
PC3A	Various	SSJ, MC	80/100	0.5	HT	6/12 – 7/12
PC4	Various	SSJ, MC	80/100	2	1	6/12 – 7/12
PC4A	Various	SSJ, MC	80/100	2	1	6/12 – 7/12
PC5	Various	SSJ, MC	80/100	20	9	6/12 – 11/13
TB-300-1	Steels, W	SSJ, MC	300	0.02	HT	8/12 – 8/12
TB-300-2	Steels, W	SSJ, MC	300	0.1	HT	8/12 – 8/12
TB-300-3	Steels, W	SSJ, MC	300	0.5	HT	8/12 – 8/12
TB-300-4	Steels, W	SSJ, MC	300	7	5	7/12 – 6/13
TB-500-1	Steels, W	SSJ, MC	500	0.1	HT	8/12 – 8/12
TB-500-2	Steels, W	SSJ, MC	500	0.5	HT	8/12 – 8/12
TB-500-3	Steels, W	SSJ, MC	500	7	4	7/12 – 2/13
TB-650-1	Steels, W	SSJ, MC	650	0.1	HT	8/12 – 8/12
TB-650-2	Steels, W	SSJ, MC	650	0.5	HT	8/12 – 8/12
TB-650-3	Steels, W	SSJ, MC	650	7	5	7/12 – 6/13

Experiment Designation	Primary Materials	Specimen Types*	Irradiation Temperature (°C)	Max Exposure (dpa)	Number of Reactor Cycles	Irradiation Period (month/year)
TB-650-4	Steels, W	SSJ, MC	650	20	11	7/12 – 7/14
TTN09	SiC	Joint	500	3.4	2	8/11 – 11/11
TTN10	SiC	Joint	500	4.1	2	8/11 – 11/11
TTN11	SiC	Joint	800	4	2	3/12 – 5/12
TTN01	SiC	BSR	300	1	1	2/11 – 3/11
TTN02	SiC	BSR	300	10	6	2/11 – 12/11
TTN03	SiC	BSR	300	20	11	2/11 – 8/13
TTN04	SiC	BSR	500	10	6	5/11 – 4/12
TTN05	SiC	BSR	500	20	11	5/11 – 8/13
TTN06	SiC	BSR	800	10	6	5/11 – 4/12
TTN07	SiC	BSR	800	20	11	5/11 – 8/13
TTN08	SiC	BSR	1200	10	6	5/11 – 8/12
TTN16	SiC	Fiber BSR	500	1	1	11/11 – 12/11
TTN17	SiC	Fiber BSR	500	10	6	8/11 – 6/12
TTN18	SiC	Fiber BSR	500	20	11	8/11 – 8/13
TTN19	SiC	Fiber BSR	1200	1	1	3/12 – 4/12
TTN20	SiC	Fiber BSR	1200	10	6	3/12 – 11/12
PXW1	W	Discs	800	2	1	–
PXW2	W	Discs	800	2	1	1/15 – 2/15
PXW3	W	Discs	800	6	3	–
PXW4	W	Discs	1100	2	1	–
PXW5	W	Discs	1100	2	1	1/15 – 2/15
PXW8	W	Discs	1100	6	3	–
Target zone rabbit capsules (US-NIFS-JAEA)						
T11-01J	V-4Cr-4Ti	BTC	425	2	1	11/12 – 12/12
T11-02J	V-4Cr-4Ti	BTC	425	6	3	1/13 – 7/13
T11-03J	V-4Cr-4Ti	BTC	425	2	1	11/12 – 12/12
T11-04J	V-4Cr-4Ti	BTC	425	6	3	1/13 – 7/13
T11-05J	SiC	BTC	600	2	1	11/12 – 12/12
T11-06J	SiC	BTC	600	6	3	1/13 – 7/13
T11-08J	SiC	BTC	600	6	3	1/13 – 7/13
T11-09J	SiC	BTC	600	2	1	11/12 – 12/12
T11-11J	SiC	BTC	600	2	1	11/12 – 12/12
T11-13J	Graphite	BTC	600	2	1	11/12 – 12/12
T11-14J	Graphite	BTC	600	6	3	1/13 – 7/13
J12-01	F82H	BTC	300	1.5	1	1/13 – 2/13
J12-02	F82H	BTC	300	6	3	5/13 – 7/13
J12-03	F82H	BTC	300	1.5	1	5/13 – 2/13
J12-04	F82H	BTC	300	6	3	1/13 – 6/13
J12-05	F82H	BTC	300	1.5	1	1/13 – 2/13
J12-06	F82H	BTC	300	6	3	5/13 – 6/13

Experiment Designation	Primary Materials	Specimen Types*	Irradiation Temperature (°C)	Max Exposure (dpa)	Number of Reactor Cycles	Irradiation Period (month/year)
Target zone rabbit capsules (US-IMR)						
MX-1	Ceramics	Various	400	2	1	7/13 – 8/13
MX-2	Ceramics	Various	400	6	3	7/13 – 3/14
MX-3	Ceramics	Various	400	10	6	7/13 – 7/14
MX-4	Ceramics	Various	700	2	1	7/13 – 8/13
MX-5	Ceramics	Various	700	6	3	7/13 – 2/14
MX-6	Ceramics	Various	700	10	5	7/13 – 5/14
MX-7	Ceramics	Various	1000	2	1	7/13 – 8/13
MX-8	Ceramics	Various	1000	6	3	7/13 – 3/14
MX-9	Ceramics	Various	1000	10	5	7/13 – 5/14
IMR1	Various	Various	200	2	1	6/15 –
IMR2	Various	Various	200	2	1	6/15 –
IMR3	Various	Various	200	2	1	6/15 –
IMR4	Various	Various	200	2	1	–
IMR5	Various	Various	200	4	2	6/15 –
IMR6	Various	Various	600	2	1	–
IMR7	Various	Various	600	6	3	–
IMR8	Various	Various	600	10	5	–
IMR9	Various	Various	1000	2	1	–
IMR10	Various	Various	1000	6	3	–
IMR11	Various	Various	1000	10	5	–
Target zone rabbit capsules (US)						
SCJ2-10	Ceramics	Joint	500	3	2	5/14 – 7/14
SCJ2-11	Ceramics	Joint	500	>10	10	5/14 –
SCJ2-12	Ceramics	Joint	500	3	2	5/14 – 7/14
SCJ2-16	Ceramics	Joint	1000	3	2	6/14 – 8/14
SCJ2-17	Ceramics	Joint	1000	3	2	6/14 – 8/14

*T = Tensile, F = Fatigue, FT = Fracture Toughness, MC = Multipurpose Coupon, BSR = Bend Stress Relaxation Creep, DCT = Disc Compact Tension, BTC: Bellows-loaded Tensile Creep, UDMC: Uni-directional Mini-composite. Most experiments also contain TEM disks, other special purpose specimens, and monitors occupying small spaces.
**Hydraulic tube – fractional cycle exposures.